Structural Optimization of Self-Supported Dome Roof Frames under Gust Wind Loads

THESIS

A Thesis submitted in partial fulfilment of the requirements for the degree of Doctor of Philosophy in the School of Engineering at the Newcastle University

Prepared by

Nawfal Nazar Mohammed Hsaine

Supervised by

Dr. Francis J. Franklin, Lecturer in DMM, School of Engineering

Dr. Hemantha Yeddu, Lecturer in DMM, School of Engineering

Newcastle University

United Kingdom

Abstract

Dome roofs are large structures often subject to variable wind, snow and other loading conditions, in addition to their own weight. A wide variety of structural designs are used in practice, and finding the optimal arrangement of trusses or girders, along with suitable section properties, is a common subject for structural optimization studies. This thesis focuses on self-supported dome roofs for fuel storage tanks, and a variety of optimization techniques are adapted, developed and compared.

Various load conditions have been compared using detailed fluid and stress analysis in ANSYS. From results for full and empty storage tanks, with wind and/or snow external loads, the worst cases are for wind loading alone, i.e., snow loading counters the lift force from the wind. Consequently, the case of an empty fuel storage tank subject to wind loading is used as the basis for the structural optimization. To speed up the optimization, a simplified frame analysis was developed in Matlab and integrated with the optimization code. In addition, the wind loads were modelled in ANSYS for a range of dome radii and imported into the Matlab, and a number of different dome designs were used as case studies: these were ribbed, Schwedler, Lamella and geodesic.

The principal method used to optimize the frame is Morphing Evolutionary Structural Optimization (MESO), in which an initial overdesigned frame is iteratively analysed and reduced in overall weight by reducing the sections of key frame members. The frame is progressively weakened, but without compromising the structural integrity, until it is no longer possible to reduce the weight. However, there are additional parameters that MESO is not suited to, such as dome radius and those affecting the overall structure of the dome frame (numbers and placements of rings, etc.), and a variety of metaheuristic optimization techniques have been studied: Artificial Bee Colony (ABC), Bees Algorithm (BA), Differential Evolution (DE), Particle Swarm Optimization (PSO) and Simulated Annealing (SA). These can be used instead of MESO, or in a hybrid form where MESO optimizes the frame member sections. Although the focus in this thesis is on minimizing the total structural weight, the importance of other characteristics of the design, especially structural stiffness, is considered and also integrated with the MESO process. The hybrid methods MESO-ABC and MESO-DE performed best overall.

Acknowledgement

Foremost, I would like to express my sincere gratitude to my graduate advisors Dr Francis Franklin and Dr Hemantha Yeddu for their continuous support to my PhD thesis research over the past four years. Their willingness to provide assistance at all times and understand my struggles throughout the journey are greatly appreciated, and I could not have asked for a better advisor and mentor. I would also like to thank the examination committee Dr Alistair Cree / Plymouth University and Dr Dehong Huo / Newcastle University for volunteering their own valuable time towards helping me to complete my defence.

A special thanks to my family, my wife and my daughters. Words cannot express how grateful I am to my father, my mother, and my siblings for all of the sacrifices that they've made on my behalf. At the end I would like to express my appreciation to all beloved staff of School of Engineering / Newcastle University who spent their valuable time to support me. Finally, I would like to thank my sponsor the Higher Committee for Education Development (HCED), IRAQ for their financial support of my PhD journey.

List of Publications

%%%%%%%%%%%%%%%%%%%%%%%%%%%%%%%%%%%%%

Hsaine, Nawfal N. M., Franklin, Francis J. "Analyzing Fixed Roof Storage Tanks Using FE Principles to Investigate the Stress Relief Degree Caused by Live Loads against Wind Loads" Paper presented at the 1st International Conference for Students on Applied Engineering ICSAE16, 20 – 21, October, 2016, Newcastle upon Tyne, Tyne and Wear, United Kingdom. p.p. 104–113.

%%%%%%%%%%%%%%%%%%%%%%%%%%%%%%%%%%%%%

Hsaine, Nawfal N. M., Franklin, Francis J. "Hybrid Optimization Methodology for Integrating MESO with ABC in Fuel Storage Tank Design" Paper presented at the 20th International Conference on Structural Optimization Methods ICSOM2018, 30 – 31, October, 2018, Rome, Italy.

%%%%%%%%%%%%%%%%%%%%%%%%%%%%%%%%%%%%%

Glossary

ABC	**Artificial Bee Colony**
ACO	**Ant Colony Optimization**
aeDE	**adaptive elitist Differential Evolution**
API	**American Petroleum Institute**
ASCE	**American Society for Civil Engineering**
ASTM	**American Standard for Testing and Materials**
BA	**Bees Algorithm**
BB–BC	**Big Bang–Big Crunch**
BESO	**Bi-directional Evolutionary Structural Optimization**
BFOA	**Bacterial Foraging Optimization Algorithm**
BMESO	**Bi-directional Morphing Evolutionary Structural Optimization**
BS	**British Standard**
C	**Mean Compliance**
CEC	**Caplug Equipment Connector Function**
CF	**Cost Function**
CFD	**Computational Fluid Dynamics**
CG	**Component Group**
CMA-ES	**Covariance Matrix Adaptation Evolution Strategy**
CMLPSA	**Corrected Multi-Level and Multi-Point Simulated Annealing**
CSS	**Charged System Search**
CVP	**Constraint Violation Percentage**
DE	**Differential Evolution**
D-ICDE	**Improved Constrained Differential Evolution with discrete variables**
DM	**Dataset Module**
DPSO	**Democratic Particle Swarm Optimization**
DSO	**Discrete Sizing Optimization**
ER	**Evolutionary Rate**
ERABC	**Efficient and Robust Artificial Bee Colony**
ERO	**Enhanced Ray Optimization**
ESO	**Evolutionary Structural Optimization**
ESs	**Evolution Strategies**
FADE	**Fuzzy Adaptive Differential Evolution**
FFA	**Firefly Algorithm**
FFA-DSO	**Firefly Algorithm with discrete sizing optimization**
FSD	**Fully Stressed Design**
GA	**Genetic Algorithm**
GB	**Global Best**
HBB-BC	**Hybrid Big Bang–Big Crunch**
HGA	**Hybridized Genetic Algorithm**
HHS-BB-BC	**Hybrid Harmony Search and Big Bang–Big Crunch**
HMJCDE	**Hybrid Modified Jointed Constrained Differential Evolution**
HPSACO	**Hybrid Particle Swarm Optimization and Ant Colony Optimization**
HS	**Harmony Search**
ICDE	**Improved Constrained Differential Evolution**

IFA	**Improved Firefly Algorithm**
iPSO	**integrated Particle Swarm Optimization**
IPVS	**Improved Passing Vehicle Search**
JA	**Jaya Algorithm**
JADE	**Jointed Adaptive Differential Evolution**
JA-DSO	**Jaya Algorithm with discrete sizing optimization**
LF	**Lift Force**
MCBA	**Multiple Colony Bees Algorithm**
MCDE	**Multipopulation Crowding Differential Evolution**
MCoDE	**Multipopulation Crossover Differential Evolution**
MESO	**Morphing Evolutionary Structural Optimization**
MHS	**Modified Harmony Search**
MOEA/D	**Multi-objective Evolution Strategy Decomposed**
MP	**Mathematical Programming**
NSA	**Number of Structural Analyses**
OC	**Optimality Criterion**
OF	**Overturning Force**
PF	**Perturbation Force**
PSACO	**Particle Swarm Optimization with Ant Colony Optimization**
PSO	**Particle Swarm Optimization**
PSOPC	**PSO with Passive Congregation**
PSRO	**PSO with Ray Optimization**
RC	**Rejection Criterion**
RR	**Rejection Ratio**
SA	**Simulated Annealing**
SC	**Stopping Criterion**
SE	**Strain Energy**
SED	**Strain Energy Density**
SF	**Safety Factor**
SFSA	**Stochastic Fractal Search Algorithm**
SKO	**Soft Kill Optimization**
SORA-ICDE	**Sequential Optimization with Reliability Assessment ICDE**
SSO	**Simplified Swarm Optimization**
SSODE	**Simplified Swarm Optimization with the Differential Evolution**
TK	**Tank**
TLBO	**Teaching-Learning-Based Optimization**
TLBO-DSO	**Teaching-Learning-Based Optimization with discrete sizing optimization**
TM	**Tipping Moment**
TS	**Tabu Search**

Nomenclatures

Alphabetic Symbols:

a	Crown radius
$\{a^j\}$	Eigenvector corresponding to j^{th} mode
α	Angle formed by the crown based on dome radius
$\bar{\alpha}$	Temperature reduction rate (cooling out coefficient) in SA technique
α_i	Stiffness sensitivity number for i^{th} element
A_{cap}	Surface area of the spherical cap of the tank
$A_{cylinder}$	Surface area of the cylindrical shell of the tank
A_{sc}	Surface area of spherical cap
A_{tank}	Surface area of the whole tank
B	Boltzmann constant for probabilistic distribution in SA technique
$BUCK$	Buckling objective
$\{C\}$	Cumulative summation vector of the probabilistic distribution coefficient of ABC technique
$c1$	Acceleration coefficient for personal component in PSO technique
$c2$	Acceleration coefficient for social component in PSO technique
C_c	Characteristic slenderness coefficient separating between the elastic and inelastic buckling regions
CF	Overall cost function
$COST_i$	Fitness function in ABC
CR_{in}	Radius of inner stiffener of the crown in trimmed ribbed dome model
CR_{out}	Radius of the outer shell of crown in trimmed ribbed dome model
C_{BUCK}	Coefficient used to determine the weighted contribution of buckling in overall cost function
C_{FREQ}	Coefficient used to determine the weighted contribution of frequency in overall cost function
C_{SED}	Coefficient used to determine the weighted contribution of strain energy density SED in overall cost function
C_{SEQV}	Coefficient used to determine the weighted contribution of equivalent stress SEQV in overall cost function
C_W	Coefficient used to determine the weighted contribution of structural mass in overall cost function
d_{basic_offset}	Basic offset of the dome (vertical distance measured from the dome curvature centre to the upper rim of the cylindrical shell)
dx_i	Horizontal linear distance corresponding to the ring "i" measured from the central axis of the tank
$\overrightarrow{DV}$	The vector of overall design variables
$\overrightarrow{DV}_{con}$	The vector of continuous design variables
$\overrightarrow{DV}_{dep}$	The vector of dependent design variables
$\overrightarrow{DV}_{dis}$	The vector of discrete design variables
$\overrightarrow{DV}_{int}$	The vector of integer design variables
$\overrightarrow{DV}_{load}$	The vector of load design variables
E	Elasticity modulus
E_{config}	Activation energy in SA technique
F	Mutation scaling factor
F_i^{comp}	Compressive axial force for i^{th} member

$F_i^{crit\_buck}$	**Critical buckling load for i^{th} member**
F_{lift}	**Lift aerodynamic forces applied to the storage tank**
$F_{overturning}$	**Overturning aerodynamic forces applied to the storage tank**
$F_{resultant}$	**Resultant of aerodynamic forces applied to the storage tank**
$Frac_i$	**Topological fraction corresponding to the local meridional segment "i"**
FREQ	**Frequency objective**
$\vec{g}(t)$	**Global best vector in PSO technique**
H	**Height of the cylindrical shell of the tank**
H1	**Primary height of the tank**
H2	**Secondary height of the tank**
H_{fuel}	**Maximum operating level of the fuel**
h	**Height formed by the spherical cap of the tank**
$\mathcal{H}$	**Bunch of solutions within one patch**
h_i	**Amount of collected food (solution) for the bee (i) within neighbourhood boundaries**
I_{zz}	**Second moment of area for the cross section about local z-axis**
k	**Effective length factor for compressive buckling**
ℶ	**Proximity scaling fraction for integer bounds**
$ℶ(x_j^{max} - x_j^{min})$	**Discretization range of integer subspace used for approximation**
[K]	**Global stiffness matrix**
k_{BUCK}	**Index used to determine the weighted contribution of buckling in overall cost function**
k_{FREQ}	**Index used to determine the weighted contribution of frequency in overall cost function**
k_{SED}	**Index used to determine the weighted contribution of strain energy density SED in overall cost function**
k_{SEQV}	**Index used to determine the weighted contribution of equivalent stress SEQV in overall cost function**
k_W	**Index used to determine the weighted contribution of structural mass in overall cost function**
L	**Member length**
LC	**Abandonment threshold limit for ABC and BA**
L_{circum}	**Virtual length of the element in meridional direction**
L_{merid}	**Virtual length of the element in meridional direction**
L_{PG}	**Arc length of the primary meridional girder**
L_{SG}	**Arc length of the secondary meridional girder**
[M]	**Global mass matrix**
MaxIt	**Maximum number of iterations**
MaxIt1	**Maximum number of iterations for stage 1**
MaxIt2	**Maximum number of iterations for stage 2**
MaxIt3	**Maximum number of iterations for stage 3**
$M_{tipping}$	**Tipping moment applied to the storage tank**
mu	**Mutation rate used to create new neighbours in SA technique**
N	**Number of design variables**
$\mathcal{N}(x, \psi)$	**Neighbourhood search space for BA technique**
ncomp	**Number of components in structural system**
nep	**Population size for Elite patches for BA technique**

ne	**Number of elite patches for BA technique**
nep	**Number of elite bees for BA technique**
Nnodes	**Number of nodes for the dome roof structure**
ns	**Number of selected patches for BA technique**
nscout	**Number of scout patches for BA technique**
nscoutp	**Number of scout bees for BA technique**
nsp	**Number of selected bees for BA technique**
nMove	**Number of neighbours per parent individual in SA technique**
nobj	**Number of sub-objectives in the cost function**
nPop	**Population size**
N_{dr}	**Number of rings for the dense ribs' region of the trimmed ribbed dome**
$N_{Girders}$	**Number of primary meridional girders for integrated model**
$N_{Gussets}$	**Number of crown gussets for integrated model**
N_m	**Topological morphing factor**
N_n	**Number of nodes per circumferential ring**
N_{Rings}	**Number of circumferential rings for integrated model**
N_r	**Number of circumferential rings for simplified model**
N_s	**Topological spacing factor in simplified model**
N_t	**Topological trimming factor in simplified model**
{P}	**Internal load vector**
pbest	**Best individual in the population**
P_{config}	**Probability of distribution in SA technique**
PCR	**Probability crossover constant for DE technique**
$P_{dynamic}$	**Dynamic pressure**
P_i	**Probability distribution value i^{th} recruited bee**
$\vec{p}_j^{it}$	**Trial vector (in DE technique) of j^{th} individual recorded for the iteration "it"**
$\overrightarrow{P_J}(t)$	**Personal best vector in PSO technique**
P_{static}	**Static pressure**
$\hat{q}$	**Buckling coefficient for Euler formula**
R	**Dome roof radius**
$\mathbb{R}^N$	**Predefined subset of integer numbers used to correct the integer parameters in stage 1 of optimization**
$randset_k$	**Vector of random fractures selected from the range $[0, 1]$ in SA method**
R1	**Primary dome radius (dome radius for the upper layer)**
R2	**Secondary dome radius (dome radius for the lower layer)**
r	**Radius of the cylindrical shell of the storage tank**
r_j	**Radius of j^{th} circumferential ring**
SED	**Strain energy density objective**
Seg_i	**Arc length for the local segment "i" in the meridional girder**
SEQV	**Equivalent stress objective**
sigma	**Basic range of mutation in SA technique**
$sigma_0$	**Specified initial range of mutation in SA technique**
T	**Annealing temperature in SA technique**
T_0	**Initial value of annealing temperature in SA technique**
U_{abs}^{max}	**Maximum absolute displacement**

$\{\mathbf{u_i}\}$	**Displacement vector of the i^{th} member**
$\mathbf{U_{ub}}$	**Upper bounds of absolute displacement**
$\boldsymbol{v}$	**Wind speed**
$\mathbf{V}$	**Overall volume of the storage tank**
$\overrightarrow{\mathbf{v_j}}(\mathbf{t})$	**Inertia vector in PSO technique**
$\mathbf{V_{mutation}}$	**Mutation vector in DE algorithm**
$\mathbf{W}$	**Structural weight objective**
$\mathbf{w}$	**Acceleration coefficient for the inertia component in PSO technique**
$\mathcal{X}$	**Solution space**
$\mathbf{x_{i,j}}$	**x-coordinate of a point identified by i^{th} node located on j^{th} ring**
$\vec{\mathbf{x}}_{\mathbf{j}}^{\mathbf{it}}$	**Position vector of j^{th} individual recorded for the iteration "it"**
$\vec{\mathbf{x}}_{\mathbf{j}}^{(\mathbf{0})}$	**Position vector of j^{th} individual recorded for the initial iteration**
$\vec{\mathbf{x}}_{\mathbf{j}}^{\mathbf{it}}$	**Mutant (donor) vector of j^{th} individual recorded for the iteration "it" used in DE technique**
$\mathbf{y_{i,j}}$	**y-coordinate of a point identified by i^{th} node located on j^{th} ring**
$\mathbb{Z}$	**Subset of real parameters used with BA in stage-1**
$\mathbf{z_{dome\_offset}}$	**z-coordinate of the curvature centre of the dome**
$\mathbf{z_{i,j}}$	**z-coordinate of a point identified by i^{th} node located on j^{th} ring**

<u>Greek Symbols:</u>

$\boldsymbol{\psi_r^i}$	**Fraction for neighbourhood radius r of certain patch under iteration i**
$\boldsymbol{\beta}$	**Frequency sensitivity number**
$\boldsymbol{\eta}$	**Height fraction**
$\{\boldsymbol{\epsilon}\}$	**Engineering strain vector**
$\boldsymbol{\Delta C}$	**Change in mean compliance**
$\boldsymbol{\Delta S}$	**Thickness of the double lattice layer at the hub region**
$\{\boldsymbol{\Delta u}\}$	**Change in displacement vector**
$\boldsymbol{\emptyset}$	**Acceleration coefficient for neighbourhood search of ABC, BA and SA**
$\boldsymbol{\kappa}$	**Radius of the base circle of the spherical cap**
$\overline{\boldsymbol{\kappa}}_{\boldsymbol{i}}$	**Radius of gyration for section profile**
$\lambda_{\boldsymbol{i}}$	**Slenderness ratio for i^{th} member**
$\boldsymbol{\lambda_m}$	**Topological morphing fraction**
$\boldsymbol{\lambda_s}$	**Topological spacing fraction**
$\boldsymbol{\lambda_t}$	**Topological trimming fraction**
$\boldsymbol{\omega_j}$	**Natural frequency corresponding to j^{th} mode**
$\boldsymbol{\eth}$	**Dome radius ratio**
$\boldsymbol{\rho}$	**Mass density**
$\{\boldsymbol{\sigma}\}$	**Stress vector**
$\boldsymbol{\sigma_a}$	**Allowable stress**
$\overline{\boldsymbol{\sigma_a}}$	**Allowable compressive stress**
$\lvert\boldsymbol{\sigma_{vm}^{max}}\rvert$	**Absolute value of maximum von Mises stress for the whole structure**
$\boldsymbol{\sigma_{yp}}$	**Yield stress**
$\boldsymbol{\theta}$	**Angle formed by the primary meridional girder based on dome radius**
$\boldsymbol{\theta_{basic}}$	**Rotation angle for one side of the basic polygon of geodesy**
$\boldsymbol{\xi_i^{buck\_ind}}$	**Buckling indicator for i^{th} member**

Table of Contents

List of Figures

List of Tables

Chapter 1. Introduction

1.1 General Overview

Large-scale storage tanks are substantially used to preserve stored products prior to their utilization in industry whether they are liquids, oils, grains, coals, or petrochemical materials. Storage tanks may be classified according to the fixation nature of the roof into fixed, external floating, and internal floating roofs; or according to the geometrical shape of the roof into flat, cone, dome and umbrella (Maraveas *et al.*, 2015). As roof supporting structures, they could be categorized into either column-supported or self-supported depending on the design of the roof and the product nature (Burgos *et al.*, 2015). Furthermore, dome roof structures can be subdivided into single lattice and double lattice depending on the number of structural layers involved (Shirkhanghah *et al.*, 2012). In the oil industry, especially in oil refineries and depots, a high degree of safety should be maintained at the sites of fuel storage tanks, as any fault might cause serious economic and environmental considerations (Moslemi and Kianoush, 2012).

Wind loads are one of most significant environmental influences that impinges on space structures (buildings, bridges and storage tanks) and many researchers have concentrated on computational methods required to estimate the effect of these potential problems on cylindrical tanks (Portela and Godoy, 2005), (Sosa and Godoy, 2010), (Jahangiri *et al.*, 2013), (Zhao and Lin, 2014), (Uematsu *et al.*, 2015). The most severe conditions in the last decades reported by Flores and Godoy (1998) were those due to the devastating hurricane Marilyn that hit the Caribbean islands in 1995 and damaged the set of short tanks operating in this region. Another extraordinary typhoon called "Maemi" was also reported by Cao *et al.* (2015), which hit Japan, Miyako Island in the Okinawa governorate, on September 11, 2003. This hurricane disfigured all topographical features of the region with the maximum sustained wind speed (estimated over 10 minutes) reaching more than 60 m/s. The average gust factor, recorded over this period by the sonic and vane anemometers, was 1.25, which produces an effective wind speed of 75m/s.

Dome roof structures are the most common space frames deployed in the construction of industrial buildings and leisure centers due to their efficiency to cover as large an unobstructed area as possible with minimum utilization of material. Exhibition museums, worship places, swimming pools, sport stadia, and storage tanks are typical applications for the self-supported dome roofs due to the need to enclose a maximum space with a minimum surface. This feature will produce the sufficient economy in the usage of the constructional material (Sarac, 2005).

1.2 Focused Case Study

This work is intending to perform the design optimization for the self-supported dome roof frame needed for fixed roof storage tank. As a practical case study, a typical mid-sized 10000 m^3 capacity fuel storage tank, labeled (50-TK-16) constructed in Al-Samawa new depot project / Iraq, see Figure 1.1, was used in this investigation. The tank has a fixed cylindrical shell diameter of (D=42 m) and fixed height for the tank of (H=8 m). Different dome roof configurations were considered in this optimization to choose the optimum one among them.

The following assumptions have been made:

1. The storage tank is subjected to harsh wind loading conditions identical to that mentioned by Cao *et al.* (2015) about the typhoon Maemi (2003) with maximum 10-min mean wind speed exceeding 60 m/s, so the maximum effective wind speed measured over these events was 75 m/s.
2. As stated in chapter 4, section 4.3.1, Table 4-1, page 18 of the international standard ASCE7-10 (2010), the minimum uniformly distributed live loads for curved roofs was not to be less than 0.96 kN/m^2 including any permissible reduction. Therefore, 1.00 kN/m^2 was applied vertically to the projected area of the dome roof.
3. All structural members within the roof structure are connected as rigid joints to each other, hence the roof structure is expected to behave as a 3D space frame, i.e. it can withstand all types of frame stresses, i.e. axial, shear, bending and torsional stresses (Gidófalvy, 2010).
4. According to the ASTM-Standard, all shell elements of storage tank are manufactured as low carbon steel (A283 Gr C) and the structural sections are manufactured as hot rolled carbon steel (A36) (ASTM-A283/A283M − 13, 2013), (ASTM-A 36/A 36M − 01, 2001), and (API Standard 650, 2013).
5. The linearly varying shell wall thickness is assumed to conform to the linear distribution of fuel hydrostatic pressure exerted on the tank cylindrical shell, so the thicknesses will be varied discretely as 17 mm, 14 mm, 11 mm and 8 mm for the 1^{st}, 2^{nd}, 3^{rd} and 4^{th} cylindrical shell courses respectively.
6. The cylindrical shell of the tank is stiffened by 3 essential circumferential rings, these are a top curb angle at the upper rim of the cylindrical shell, an internal stiffener located 50 cm below the top curb angle internally attached to the cylindrical shell wall, and an external wind girder (stiffener) located 370 cm below the top curb angle (API 620, 2002).
7. The minimum thickness for dome roof shell is 7 mm, which includes the corrosion allowance as per American Petroleum Institute (API) Standard (API Standard 650, 2013).
8. The dome roof shell is joined to the roof structural members underneath.

9. The tank is filled with fuel to the maximum operating level (H_{fuel}=7.55 m) and all of gauge hatches, vents, maintenance manholes, breather valves, and flame arrestors are shut. Hence, there is no air flow inside the tank, so this will generate negligible additional internal pressure.
10. Fixed support boundary conditions are assumed over the entire bottom plate, where the bottom plate is modelled as a circular disk with a constant thickness value of 11 mm.
11. Due to their negligible effects, the tank accessories and other apertures (e.g. spiral stairway, manholes, gauge hatch, vents, inlet, draw off, and outlet nozzles) were omitted from the overall response modelling of the tank structure.
12. The present study is limited to investigate the structural response of the dome roof frame during critical wind gust events. Hence, static structural analysis was utilized to simulate this critical event in order to perform the optimization study for the selected models (Kang *et al.*, 2001) (PARK and KANG, 2003) (Lee and Park, 2013) (Lee and Park, 2015).

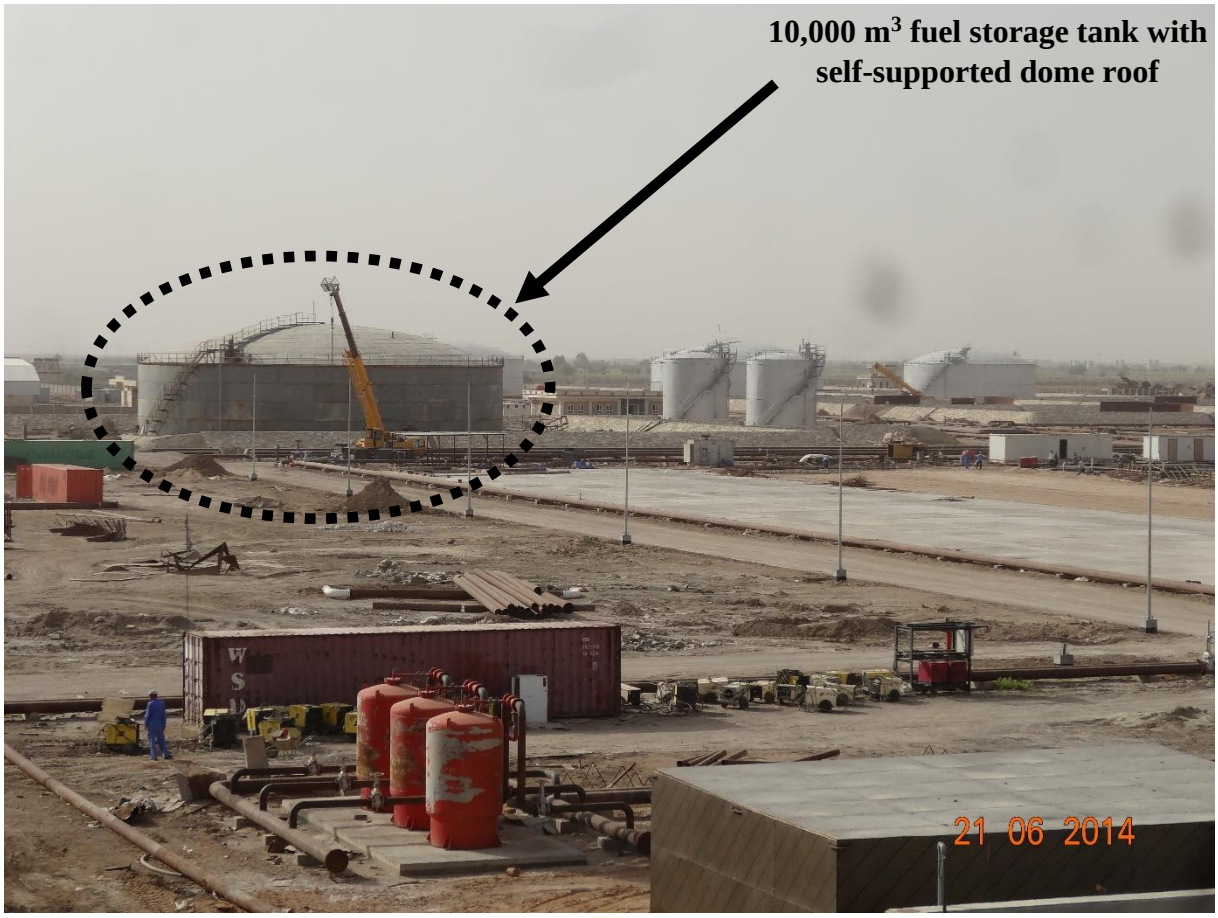

Figure 1.1 Site picture taken at Al-Samawa new depot project showing the general arrangement of the typical 10,000 m^3 storage tank investigated in this work.

1.3 Research Aims

The research focuses on the following aims:

1. A parametric study of the effect of a lift force, an overturning force, and a tipping moment as function of wind speed, dome roof radius, and tank height as a response to wind loading.
2. An investigation of the effect of environmental loads on the output response of the real scale storage tanks with low aspect ratio.
3. The determination, as a cost function, of the combined effect of the different aspects of the structural design, taking into consideration the optimal structural weight, strength, stiffness, buckling, bending strength, torsional strength etc.
4. The identification of the dome roof configuration that has the optimal structural mass through comparing between the diverse configurations adopted in this work.
5. To develop an appropriate optimisation strategy that can reliably provide a good dome design with limited resources (time, computation).
6. The determination of the most critical load case among the set of load cases applied to the external shell of the tank in comparison to the design load case (pure wind).
7. To identify the optimal structural design for each dome type considered.

1.4 Thesis Outline

This dissertation is organized in nine chapters. A general synopsis for the contents of the chapters following this chapter is explained below:

- Chapter 2 is a literature review that includes the simulation of wind loads over the domed roofs, structural analysis of braced domes, viewing the recent advances in the optimization techniques, and the research work carried out against the structural optimization of self-supported domed roofs.
- Chapter 3 studies the wind flow over the external surface of the storage tank, the relevant parametric study is clarified at the end of the chapter.
- Chapter 4 illustrates the modelling procedure for the adopted models. It is split into two tasks: simplified modelling (Matlab frame model) and integrated modelling (ANSYS full structural model) with justification of the main difference between them.
- Chapter 5 sets out the structural optimization problem including objective function, design constraints, configuration of design variables and the generalized form of cost function.
- Chapter 6 focuses on reviewing and discussing the results of the structural optimization for the simplified models.
- Chapter 7 presents the results of structural optimization for the integrated models.
- Chapter 8 presents case study analyses to prove the efficiency and robustness of the proposed optimization strategies in comparison to the classical metaheuristic techniques adopted in this work and those from the literature.
- Chapter 9 summarizes the conclusions and the recommendations for future works.

Chapter 2. Literature Review

This chapter will review the history of structural optimization for the braced domes, taking regard of the loading conditions and the optimization strategies involved. Wind loads affecting the storage tanks will be explored in section 2.1. Section 2.2 reviews the previous trials performed on the structural analysis of the braced domes. In section 2.4, previous work on Evolutionary Structural Optimization (ESO) will be reviewed. Section 2.4 considers diverse metaheuristic techniques and the comparison between them. Section 2.5 will focus on previous attempts to perform the structural optimization for self-supported domed roofs.

2.1 Simulation of Wind Loads Impinging on Storage Tanks

Many researchers were interested in introducing a reliable paradigm that aimed to present a comprehensive understanding of wind action on storage tanks. The primary survey in this field was reported by Purdy *et al.* (1967) when they are modelled wind loads over flat roof tank. They analysed the data numerically for two extreme cases and used them to develop set of equations corresponding to the shell stress and deformation analyses of those cases. Followed by Esslinger *et al.* (1971) works, who are analysed air currents passing through silos tanks groups. They noticed that the open-topped cylindrical shaped silos are more vulnerable to develop axial tensile forces (due to wind loading) than their counterparts with roof-topped. Next, Holroyd (1983) showed the dynamic wind pressures on an open-end storage tank with unstable air surges and low height to diameter ratio (H/D= 0.2). He clarified the significant changes in the structural behaviour of the oil storage tank due to the incident air flow caused by the surrounding environment. In 1985, (Holroyd) verified the structural dynamic response experimentally and suggested innovative wind girder design methods to determine suitable profile measures.

In the same sense, Godoy–PI and Portela–GS (2005) reviewed the effective results of early 20th century tunnel tests. They emphasized that the positive values of wind pressure can be observed at windward region, whereas the maximum negative pressure is presented at the centre of the dome roof and the magnitude of suction pressure applied to the roof is substantially greater than that existing at the suction region of the wall. They considered three cases of shielding two of them are closely spaced silos adopted by Esslinger *et al.* (1971). They observed that the worst scenario occurs in case of the wind being perpendicular to the stacking direction of the silos. Portela and Godoy (2005) also dealt with buckling behaviour of domed roof steel tanks as the response to wind pressure by implementing numerical and experimental trials using a small-scale tank inside the test rig of a wind tunnel. Two models with dome roof and cylindrical walls were considered, the first with a shallow dome, and the second with a deep dome. Later,

Falcinelli *et al.* (2011) succeeded in clarifying topographical influences on the overall estimation of wind forces over the tank surface using computational fluid dynamics as the analysis tool. They concluded that the actual pressure applied to the tank surface depends on the location of the tank with respect to the surround landscape. For instance, the pressure exerted on a tank located on the top of a hill is approximately three times that acting on an isolated tank on flat terrain.

2.2 Structural Analysis of Braced Domes

Auld (1970) concentrated his research on stress distribution and the steadiness principles of radial ribbed domes. He used mathematically efficient methods to obtain the stress function over ribbed pin-jointed dome structure. Experimentally, Blessmann (1996) has performed a series of tests to show the effects of wind forces on the domes installed at the university of Rio Grande do Sul (UFRGS) in Brazil. Similarly, Zamanzadeh *et al.* (2010) investigated the buckling behaviour of reticulated and geodesic dome roof configurations as shown in Figure 2.1. They observed three kinds of buckling taking place, global, local, and member buckling. The buckling loads were estimated using linear and nonlinear buckling analysis finite element software. Gidófalvy (2010) explained the nonlinearity of rotation and stiffness features for semi-rigid dome connections and considered the combination of beam and spring elements to idealize the joint parts.

The natural period of vibration for double lattice dome roofs was the main focus of the work published by Jamshidi (2012). He stated that the dynamic characteristics of the structure was a function of the mass and stiffness matrices. As a result, the structural geometry of the dome frame plays a significant role in determining the dynamic characteristics of the structure as whole. Furthermore, Chacko *et al.* (2014) conducted a parametric study to show the influence of the rise to span ratio on the overall performance of the dome roof. A progressive degradation of the structural characteristics of a large-span reticulated dome was investigated using nonlinear buckling analysis. They remarked that there were 10 governing elements and 3 governing nodes in the single layer structure, and that eliminating these elements or nodes would cause a disastrous failure. Whereas, removing these elements or nodes from a double layer model will not cause any failure at all.

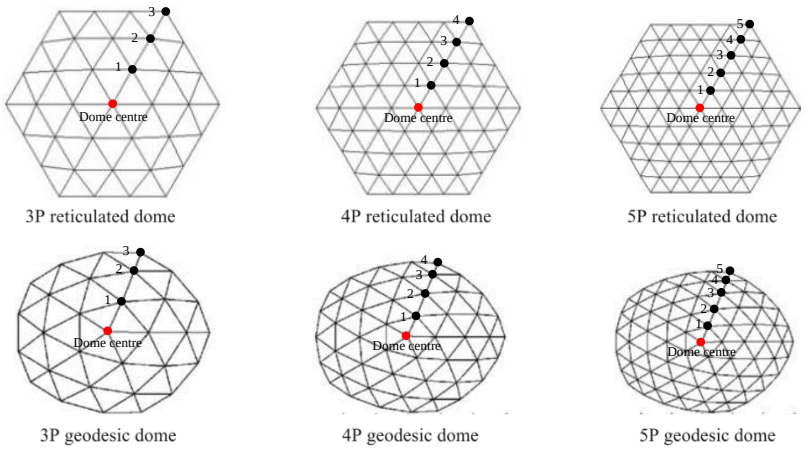

Figure 2.1 Dome roof configurations adopted by Zamanzadeh *et al.* (2010).

2.3 Evolutionary Structural Optimization (ESO)

The basic notion of ESO methods could be explained as the systematic gradual removal of inefficient (superfluous) material from underutilized elements in the structural system. ESO is applicable to both of continuous and discrete structures with slight differences in optimization parameters. The first implementation of layout optimization using ESO was implemented on a 2D continuous structure when Xie and Steven (1993) executed their work on simple beam example to find the ideal distribution of material over the beam.

Later, Chu *et al.* (1996) employed the original concept of the method to find the optimum shape using the hard kill method, i.e. by removing the entire element that satisfies the removal criterion. They performed a simple evolutionary operation supported by finite element technique to minimize the weight while keeping the corresponding changes in the structural stiffness to the lowest level. By eliminating the underutilized elements, or those elements having the minimal influence on the stiffness properties of the structure, the design sensitivity number could be reassessed at each iteration. The progression of the model towards the optimum point continues until reaching the global optimum configuration within prescribed serviceability and displacement constraints.

Further improvement in the generalized methodology of ESO was carried out by Xie and Steven (1996) and Zhao *et al.* (1996) to include the frequency characteristics of plates and continuum structures, whereby the optimality function was guided by frequency constraints obtained by shifting the structure toward the desired configuration.

Nha Chu *et al.* (1997) and Nha *et al.* (1998) developed an extended version of ESO and made some modification to the method to optimize the sizing parameters for the first time. This work was implemented using partial element removal, which is termed Soft Kill Optimization (SKO). In the same field, Querin *et al.* (2000) adopted SKO for plate elements and named it Morphing

Evolutionary Structural Optimization (MESO), also they have conducted a Bidirectional ESO (BESO) for some of workbench examples. In the same aspect, they are defined additive ESO which is working on addition of material for initially undersized design domains. Similarly, Li *et al.* (2000) also demonstrated that the maximum stress can be minimized by regarding the thicknesses of plate elements as design variables.

Improved computer speeds and the recent prevalence of finite element software have caused this type of optimization to become better than its counterparts. The secret behind the outstanding success of this method is attributed to its searching strategy, where there is no arbitrary search, it is moving toward the optimum in a guided and systematic manner utilizing a strict criterion generated by combining both the objective and constraints conditions (Özkal and Uysal, 2009).

This method was further developed by Ghaffarianjam *et al.* (2011) who introduced a new concept performance index to determine the progression rate and the overall performance of morphed form of ESO (MESO). Thereafter, Li *et al.* (1999) inferred the correlation between strength and stiffness criteria by aid of illustrative contours. They noticed an observable closeness in the numerical values of the sensitivity numbers of the two functions.

Working in the same area, Yang (1999) performed extensive studies to prove the capability of ESO to obtain reliable results, based on the reverse theory (addition of material) to boost the efficiency of the active elements in the 2D and 3D continua. The many examples presented attempted to incorporate stiffness optimization with single or multiple displacement constraints as reactions to diverse loads. Yang asserted that BESO is as feasible as ESO, but for some applications it might more practical than ESO. It is noteworthy to mention that ESO has the adequate flexibility of being able to integrate with other optimization functions in order to configure innovative hybrid methodology.

2.4 Metaheuristic Techniques

These are nature-inspired techniques that, when effectively utilized, reduce the computational time and cost for complex engineering problems. They use a stochastic search mechanism to achieve the optimization goal. Metaheuristic techniques, in most cases, incorporate population-based models that are needed to implement the optimization task.

Heuristics are categorized into two groups: specific heuristics and metaheuristics. Specific heuristics (Borenstein and Moraglio, 2014) are designed and prepared for solving particular type of problems like travels salesman and other complicated functions solved by trial and error approach. Metaheuristics, on the other hand, are generic algorithms which have the capability and the sufficient flexibility to adapt for addressing almost any type of optimization problems

(Hasancebi *et al.,* 2010) and (Cao *et al.*, 2017). The terminology "metaheuristic" means the high-level optimization templates act as guiding strategies for the basic heuristic approaches used to solve a particular optimization problem. They are specialized search mechanisms which adopt stochastic modelling principles to solve problems which have a high degree of difficulty. They deal with the mathematical functions that are considered prohibitive in terms of computational effort and time required to attain the solution. Over the last two decades, Metaheuristics have developed rapidly and have gained wide popularity, especially after the discovery of their exceptional capabilities to address the complex optimization problems (Borenstein and Moraglio, 2014). This rapid development is mainly attributed to their strategies in performing the effective search mechanism for global optima within a relatively short time with low computational cost. Thus, a perfect trade-off between the computational accuracy, time, and memory required to obtain optimum results, can be achieved through effective exploitation of this class of optimization strategies.

Metaheuristic methods can be classified into five main strategies including:

- Single-solution based techniques.
- Population-based techniques.
- Multi-objective optimization algorithms.
- Hybrid metaheuristics.
- Parallel and distributed techniques.

In general, Particle Swarm Optimization (PSO), Simulated Annealing (SA), Harmony Search (HS), Genetic Algorithms (GAs), Evolutionary Algorithms (EAs), Ant Colony Optimization (ACO), Tabu Search (TS), Artificial Bee Colony (ABC), Bees Algorithm (BA) can be classified as Metaheuristics regardless whether they are searching for single objective or multi-objective cost functions (Talbi, 2009) (Salam *et al.*, 2015).

2.4.1 Artificial Bee Colony (ABC)

ABC is a metaheuristic optimization technique resembling the foraging habits of honey bees to collect the nectar from the available food sources. The computational efficiency of the strategy is attributed to two main behavioural features for forager bees, self-organization and the allocation of work. In ABC, there are three components essential for planning the required path of search, employed bees, unemployed bees, and food sources. Two distinct modalities of behaviour can be recognized, recruitment, and abandonment of food sources (Karaboga, 2005). There are many factors influence the productivity (dominance) of the food source: its energy value, its richness, its proximity to the hive, and the simplicity to extract the energy latent in it.

The employed (recruited) bees are sharing the required information about their own food sources with other individuals in the hive. While, the main job of unemployed (scout and onlooker) bees is to record the information and decide the profitable food sources with different movement mechanisms. Thus, three types of bees have exploited to perform the task of maximizing the amount of the collected nectar. First, recruited bees which are assigned to seek for the nectar in the food sources visited before and providing the relevant information about those food source sites to the specialized bees (onlooker bees) waiting in the hive. Second, onlooker bees are seeking for the optimum food sources according to the data provided by the first type of bees (employed bees). The decision of selecting the good quality food sources is made by this kind of bees (onlooker bees). Third, scout bees are searching randomly to find new food source depending on pure external evidence (Karaboga and Basturk, 2008).

The information must be exchanged between the honey bees to enhance the collective knowledge of the bees in the hive. Dancing activities are the most dynamic actions utilized by employed bees to deliver their information to other members of the hive. Thus, the specialized bees are communicating and exchanging the required data in the dancing region. Onlooker bees have the ability to read the thoughts of employed bees through watching the advertisement presented by recruited bees in the dancing area. They have the adequate experience to interpret the dancing frequencies to determine the most fertilized food sources relative to others. The dancing frequencies are proportional to the productivities of their respective food sources.

The food sources are standing for all possible solutions of the structural system. In this sense, the nectar quantity indicates the corresponding value of cost function. The more nectar harvested, the fitter the cost function.

Karaboga (2005) is the researcher who proposed the ABC technique when he introduced his idea about the observed behaviour of honey bees. Later, Karaboga and Basturk (2007a) and Karaboga and Akay (2011) adapted the method to work on constrained optimization problems. In addition, Akay and Karaboga (2012) modified the ABC technique to work on discrete sets of design variables. They concluded that standard ABC can effectively find the solution, while a modified ABC can also yields promising results. Karaboga and Akay (2009) and Li *et al.* (2010) claimed that the ABC technique proved its capability to perform an explorative search capability, when compared to the Genetic Algorithm (GA) technique, the Particle Swarm Optimization (PSO) technique and the Differential Evolution (DE) technique.

In comparison with the Bees Algorithm (BA) and DE, Li *et al.* (2010) emphasized that ABC showed its ability to fulfil the best solution for unimodal problems. On the other hand, they also claimed that BA achieved good quality solutions for multimodal functions. ABC can be extended to provide the solution to other forms of optimization problems. For example, Zou *et*

al. (2011b) utilized ABC to solve multi-objective optimization problems by adjusting the Pareto dominance reference used to specify the flight direction of bees to achieve the goal of optimization. (Sonmez, 2011) adopted an adaptive penalty function approach with ABC to minimize the weight of truss structure. He studied five truss examples each counting to 200 members. The results showed considerable improvement in three aspects: independency of initial point and the global search capability, good exploitation to the feedback of the adaptive penalty function to avoid violating the design constraints in the subsequent iterations, and finally the proposed method does not need to evaluate the gradients of objective and constraints as it is relying on the stochastic search to find the optimum.

Xiang and An (2013) concentrated on the work of Karaboga and Basturk (2007b) in order to overcome the weaknesses in the ABC method. They remarked that ABC is lacking in convergence efficiency which will influence the performance of the technique. Consequently, they invented a new ABC strategy called an efficient and robust artificial bee colony (ERABC) based on formulating an innovative search equation to accelerate the searching mechanism by creating a combinatorial solution. To hybridize the method, Kong *et al.* (2013) exploited orthogonal initialization to enhance the performance of ABC. They produced a new hybrid version by merging the explorative capability of ABC with the exploitative ability of PSO to create an effective hybrid strategy capable of achieving an excellent convergence while avoiding being trapped by a local mathematical minimum.

2.4.2 Bees Algorithm (BA)

Swarm Intelligence (SI) algorithms including Bees Algorithm (BA) have attracted the researchers' thoughts to develop innovative ideas to reduce the computational cost of complex mathematical problems. BA is a metaheuristic technique recently proposed by Pham *et al.* (2007) to solve diverse optimization problems. BA is derived from the foraging patterns of honey bees, maintains a number of active search regions, progressively refining each by searching within the neighborhood of the best solution within that region. The entire population is categorized into three groups of bees: elite, selected, and scout, which are collaborating and communicating together to maximize the amount of nectar stored in the hive. When the bees come back to the hive, they are performing dancing activity called waggle dance in the hive to deliver the information of the relevant food sources to other members of the hive. Upon the information provided during the dancing operation, more bees are sent to the locations recommended by the dancing bees, so as to ensure more food will be gathered and stored in the hive (El-Abd, 2012).

The BA was first proposed by Pham *et al.* (2005). It resembles a honeybee colony in terms of their cooperative teamwork and allocation of duties (Rajasekhar *et al.*, 2017). Koc (2010) introduced new coefficients to improve the efficiency of BA by modifying the dynamic recruitment of bees to enhance the method to deal with combinatorial optimization problems. He compared the new method with other conventional algorithms, like GA and Simulated Annealing (SA) and the results were promising. Chai-ead *et al.* (2011) merged two metaheuristic strategies called BA and Firefly algorithm (FA) to generate an optimal solution for noisy nonlinear continuous functions. The firefly algorithm exploits the flashing features to determine the optimal solution. For a high noise level, FA exhibits better performance than BA, because FA is improving individuals' experience needed to avoid the obstacles of the noisy paths. Whereas BA is better in terms of convergence rapidity.

A new method called the multiple colony bees algorithm (MCBA) was developed by Akpinar and Baykasoğlu (2014) to implement a functional optimization technique. The method is suggesting new communication strategy to combine the waggle dance behaviour of bees and the pheromones laid by ants. The results obtained indicated the performance of the proposed method MCBA was improved. Recently, Rajasekhar *et al.* (2017) carried out comprehensive survey for the searching techniques that resembling the honey bees to present the similarities and dissimilarities between the diverse swarm intelligence algorithms. Also, to identify some open research issues incorporated with the bees-inspired computing techniques.

2.4.3 Differential Evolution (DE)

The DE is an innovative computing algorithm. It was first proposed by Storn and Price (1995). It is basically belonging to Evolutionary Algorithms (EA) family, where it is subjected to same rules as EA, represented by mutation, crossover and selection. The new generations (trial vectors) are created by utilizing biological principles in mutation and crossover (Zou *et al.*, 2011a). In the selection process, parents will compete with their offspring for survival and the fittest individuals will be granted the chance to participate in the subsequent iterations (Li *et al.*, 2016).

The simplicity in use and the flexibility in implementation are the most significant merits of DE. Allowing for the mutation to make the required changes to the data set, performing one-way crossover and returning back to select from the generated stochastic data, through employing crossover probability, will make the technique more reliable to perform the stochastic search (Price, 1996). There are many characteristics distinguish this strategy from other metaheuristic methods. First, its capability to solve non-differentiable and multimodal cost functions and this may be attributed to its particular manner in stochastic searching, which

can be applied as verification tool for any experimental minimization. Second, it makes use of parallelizability fundamentals, which significantly affect the computational cost of large-scale structures, as the computational time for such problems might be prohibitive in some of industrial designs. Third, it fulfils a reasonable convergence towards the minimum (Storn and Price, 1997).

Price (1996) utilized the DE technique to optimize real-valued, multi-modal functions. He considered the parameters as floating-point variables subjected to set of statistical operations required to perform the necessary mutation. One-way crossover principles were employed to control the perturbation process of the variables involved. One year later, Storn and Price (1997) pulished work which showed the effectiveness of DE in minimizing nonlinear and non-differentiable continuous functions. They asserted that DE is robust and easy to use and very good for parallel computation. Moreover, Fleetwood (2001) proved that DE is the best global optimization technique in terms of its convergence rate towards the optimum configuration.

Considering the hybridization of DE, Zaharie (2005) proposed a hybrid form of DE called Multipopulation crowding DE (MCDE) and compared it with the typical form of DE to measure its capability to optimize multimodal functions. He defined a multimodal optimization technique as the method having the ability to locate all global (even local) optima of the problem. In the same sense, a new mutation concept was proposed by Ronkkonen and Lampinen (2007) to improve the random selection mechanism of DE and to enable it to deal with general multimodal problems. Consequently, the mutation process has subdivided into two levels, local and global. The main task of global mutation is to control the migration operator, whereas the local one is designated to drive the local search.

On the hybridization aspect of DE, Awad *et al.* (2016) proposed a novel hybridization method to merge DE with another metaheuristic technique called stochastic fractal search algorithm SFSA. The basis of this fusion is to utilize the exploration capability of DE to update processes of SFSA needed to explore the search space efficiently by employing a success-based scheme. This procedure will provide a great explorative extension to the original SFSA.

Additionally, Li *et al.* (2016) combined the merits of two modified DE algorithm called JADE and CoDE. The hybrid mode of the modification for both of JADE and CoDE is termed hybrid modified jointed constrained DE (HMJCDE). The efficiency of the new hybrid technique was tested against 30 standard problems with continuous variables. The results were improved, and the sensitivity analysis was implemented to show the effectiveness of the method. Motivated by the published modifications in the literature, Yi *et al.* (2016) carried out an adaptive form of DE based on pbest (the global best for current population) selection mechanism, i.e. performing the Gaussian mutation for the current individual based on the global best individual

"DE/current-to-pbest/1" as explained in Equation (5.40), to generate a new hybrid offspring suitable for exploitation whilst avoiding the lumping of individuals around pbest in order to diversify the population. The results obtained from this proposed method are highly favourable and indicate the applicability of the method to real-world applications in comparison to the traditional DE.

Recently, Piotrowski (2017) introduced a new concept to correlate the population size to the dimensionality index "d", where "d" represents the number of dimensions (i.e. the number of design variables involved). He made a comprehensive survey of the previous operations and modifications executed on DE. He stated that for problems with dimensionality lower than 30, the recommended population size is 100 individuals. He emphasized that for high-dimensionality problems, the practical range for population size extends from 3d to 5d. He added, guessing the appropriate population size for real-world problems with high dimensionality (d > 40) starts to be a serious problem. Also, he explained that many DE approaches need more choices to be ready for optimizing engineering applications associated with vast number of design variables and there is no clear relationship would be advised for this kind of problems, as the practical range for population size recommended for such applications is extending from 50 to 10d.

2.4.4 Particle Swarm Optimization (PSO)

The PSO technique was introduced for the first time by (Kennedy and Eberhart) in 1995, when they are tested several computational paradigms in this field. They stated that the PSO is inspired by the personal and social habits of bird and fish swarms. There are common features between PSO and Evolutionary Algorithms (EA), where PSO population is initiating with a random set of positions for its particles. They continue to seek for the optimum solution through updating the generations. The distinct feature of PSO as compared to EA is that PSO has no evolutionary operators (i.e. crossover and mutation). Instead, it simulates the collaborative nature of the swarms and apply the principles of the swarm intelligence (Kuo and Huang, 2009). The particles in the system must be engaged in teamwork to execute the task, this cooperation entails to follow the simple rules of communication and learning. Learning the concept of better is the main challenge of the problem, as this is resembling the swarm intelligence, where the intelligent behavior is sustained by means of some agents like birds or fishes. The system contains a population of candidate solutions called swarm and this set of candidate solutions is termed as a swarm of particles (Talukder, 2010) and (Babazadeh *et al.*, 2011).

Zavala *et al.* (2005) utilized the PSO to solve single objective constrained optimization problems. Liang *et al.* (2006) claimed that the learning strategy exploited by PSO helps to avoid

the premature convergence of the paths of flight, and this was tested with multimodal problems. Jiang *et al.* (2007) investigated the stochastic convergence of the PSO algorithm. This was realized by supposing the position of each particle as a stochastic vector within the evolutionary levels of the test. Regarding the recent advancements in PSO, Kaveh and Talatahari (2009a) also developed a hybrid optimization strategy consisting of two different metaheuristic approaches, (PSO) and Ant Colony Optimization (ACO), where ACO is used to control the position of particles in PSO to obtain feasible solutions.

On the modification trials domain, García-Villoria and Pastor (2009) introduced a new concept related to dynamic change in the inertia term of PSO. This modification aims to change the velocity magnitude of the particle to enhance the diversity of the population, where the degree of diversity is changing in a dynamic manner according to the heterogeneity of the population. Vanneschi *et al.* (2010) presented a new method based on creating co-evolving multiple swarms of GA swimming in the PSO space. They tested the method on the typical 25 CEC'05 test functions, which are benchmark functions showing unimodal and multimodal response surfaces used to test the computational performance for different optimization methods as reported by Suganthan *et al.* (2005). The results obtained indicate the improvement in the efficiency of the suggested method relative to the original PSO.

Chang and Yeh (2013) proposed a global optimization tool combining the Simplified Swarm Optimization with the Differential Evolution (SSODE), i.e., the mutational principles of DE are exploited to guide the Simplified Swarm Optimization (SSO) population, which is the proposed form of PSO. Two experiments were conducted to verify the robustness of the proposed strategy and the results obtained exhibited a significant difference when compared to the original DE and SSO. In a practical context, Babaei and Sheidaii (2014) employed PSO to automate the geometry and sizing optimization for latticed space domes. Several examples were taken to prove the efficiency of the proposed design algorithm.

Lately, Kulkarni *et al.* (2015) reviewed the past works on PSO and the relevant applications. They also detailed the improvements performed on this kind of stochastic techniques like Discrete PSO, Hybrid PSO, and Adaptive PSO. Considering the hybridization field of PSO, Patel *et al.* (2016) have hybridized ABC, which is efficient in exploratory search, with PSO, which has a good global search. This hybridization has merged the explorative performance of ABC with the exploitative capability of PSO, which enhanced the convergence speed and supported the technique to avoid the trapping in the local minima.

2.4.5 Simulated Annealing (SA)

During the last period, researchers have paid more attention to use the ideas of natural phenomena in their studies, as this is involved with introducing new thoughts instead of the classical methods used for solving optimization problems in the past. For example, Simulated Annealing (SA) is one of the most important strategies that mimicking the physical phenomenon called annealing process in Metallurgy and resembling the gradual attenuation of activation energy of the metallic atoms involved with the process. SA is a stochastic search algorithm used effectively to optimize functions with multiple variables.

It was first introduced by (Kirkpatrick *et al.*) in 1983. It is well-known member of metaheuristic optimization techniques. As population-based algorithm, SA utilizes the biological operator (mutate) to create new breeding known as neighbours surrounding each parent individual in the original population. The explorative capability of the method is enhanced by the rules of the annealing process through applying the probability distribution of the metallic atoms defined by Steven Boltzmann. Since this metallurgical process is incorporated with minimizing activation energy for the material under annealing, the cost function is chosen to be analogous to the activation energy so as to minimize it as possible.

Corana *et al.* (1987) showed that SA is a stochastic search algorithm suitable for combinatorial optimization. They tested the method against many multimodal functions, and their results proved that SA is the most reliable technique among the methods considered. Later, Rutenbar (1989) prepared an overview of the method and discussed its merits. He described the cost function versus temperature in reference to investigating the effect of temperature on the overall performance of SA.

As physical phenomenon, the process of cooling the metal down is attained gradually, where the metal is initially possessing relatively high energy level and when the time elapsed, the activation energy will reach its minimum value. The mechanism of the process is involved with many features, initial temperature which is assumed at its highest level at the starting of the annealing and then reduced step by step during the optimization, activation energy level, which acts as cost function to be minimized as possible and the new offspring represented by the neighbours for each individual in the assumed population. The mutation operation is employed to create the set of neighbours around each individual to enhance the chance to obtain better solutions and avoid trapping in local minima (KLEIN and DUBES, 1989), (Hasancebi *et al.*, 2010) and (Du and Swamy, 2016).

In 1992, (Goffe *et al.*) confirmed that SA is the suitable method for global optimization by comparing it with set of benchmark methods: UMPOL, UMCGF, and UMINF, which use the mathematical methods of Newton-Raphson and Davidon-Fletcher-Powell.

Henderson *et al.* (2008) published their book about SA strategy. They showed that SA has its own tools to escape the local minima through utilizing hill-climbing mechanism of motion. Hence, a low probability factor for the acceptance of bad solutions is used to enhance the explorative search of the method, and to extend the method to multi-objective optimization problems. Li and Landa-Silva (2011) decompose the complicated multi-objective function into finite number of SA subproblems in order to adapt the existing conventional multi-objective strategy MOEA/D to construct the new hybrid multi-objective strategy called EMOSA. The weight vector of each subproblem is adjusted to the lowest temperature so as to scatter the search directions to increase the chance to land on undiscovered points in the Pareto-optimal front. The method has proved its efficiency to solve the constrained knapsack function and the unconstrained traveling salesman function, which are the most popular multi-objective functions used in literature.

2.4.6 The Application of Metaheuristic Techniques to the Braced Domes

In this field, El-Abd (2012) conducted a comprehensive survey to assess four metaheuristic approaches: Bacterial Foraging Optimization Algorithms (BFOA), BA, ACO, and ABC. He compared them with the most conventional metaheuristic strategies: PSO, DE, GA, and Harmony Search (HS). The test results revealed that PSO is the best algorithm to obtain the solution in terms of convergence rate in case of uni-modal functions, whereas for multi-modal functions, ABC has fulfilled the optimal results, when compared to the adopted methods. Furthermore, Hasancebi *et al.* (2010) employed seven conventional metaheuristic techniques to investigate the structural optimization of different pin-jointed geodesic domes. The design process was implemented to meet the requirements and specifications stated in the standard ASCE 7-98. They announced that Evolution Strategies (ESs), SA and PSO have achieved the optimum designs, especially, when they yielded the same result with high convergence rate, whereas, they observed that Tabu search (TS), ACO and HS methods are fluctuating randomly more than others. Consequently, they deduced that Evolution Strategies (ESs), TS and ACO method are the most promising strategies due to their satisfactory convergence rates.

Kaveh and Talatahari (2008) have implemented the design optimization for the Lamella truss structure by employing the hybrid version of PSO and ACO. The design variables considered in this operation are limited to the cross-sectional area data for the dome roof members. They have explained the searching mechanism in their hybrid methodology, where the local search using the pheromone-guided movement of ACO is exploited to update the positions specified in earlier stage using PSO strategy. Hasancebi *et al.* (2010) developed a metaheuristic search

mechanism to reach the minimum weight of 130-member pin-jointed steel geodesic dome with the aid of seven reliable techniques (i.e. SA, GA, ESs, PSO, TS, ACO and HS methods).

2.5 Structural Optimization of Self-supported Dome Roofs

Structural design of large-scale domed roofs has been the subject of much research, especially when attempting to discover new optimization approaches. In this field, Kameshki and Saka (2007) exploited their work to produce a reliable program to automate the topological optimization process for dome structure by governing the joint coordinates, number of rings and the height of the crown. Their paper showed the influence of axial loads on the bending stiffness of the 3D grid configuration.

Another configuration study of single layer domes, called Lamella lattices, was attempted by Carbas (2008) using HS strategy. He considered the geometric nonlinearity in the analysis of the dome roof frame to calculate the output response. The results indicate that considering the analysis type and supposing the boundary conditions will affect the final design of the dome.

Using HS (based on jazz improvisation), Çarbaş and Saka (2009) listed the optimal design data for geometrically nonlinear network domes. The design objective is limited to the structural weight, whereas the set of geometrical parameters for lamella and network domes are classified such that the number of rings stands for the topological aspect of the optimization, the height of the crown represents the shape part of the problem, and the designations of structural members are assigned to define the sizing parameters of the model.

Kaveh and Talatahari (2010b) implemented the structural topology optimization for Schwedler and ribbed domes exploiting a stochastic search algorithm termed Hybrid Big Bang–Big Crunch (HBB–BC). Three cases were considered depending on the number of rings. The optimization results for the first case showed that the ribbed dome was lighter than the Schwedler dome. Whereas, for the third case, where the number of rings were more numerous, the Schwedler dome yielded better results than the ribbed one. Kaveh and Talatahari (2010a) proposed a new methodology pertaining to the metaheuristic type of optimization techniques called a charged system search to obtain the optimum design of diverse configurations of geodesic dome roofs. The dome roof structural members were modelled using pipe section profiles. The design variables were divided into three categories, size, shape, and topology in order to perform the optimization strategy.

There are researchers carrying out structural optimization for double lattice dome configurations. For example, Babaei and Sheidaii (2013) focused their time on obtaining the optimal design for the scallop special dome roof using the classic genetic algorithm. The dome roof was governed by a set of parametric mathematical formulae to facilitate the optimization

process. They reduced the number of sizing parameters considerably by treating the element section as a single variable. The mathematical functions they used are applicable to wide range of double lattice domes.

Many researchers have carried out sophisticated optimization techniques to investigate the optimal designs for wide range of dome roofs. Another attempts to examine GA in exploring the cost effective optimal designs of domed roofs was conducted by Kameshki and Saka (2007). They use the geometrical nonlinearity in the structural analysis of the braced domes under study to realize a more realistic response for them. Furthermore, a coupled genetic algorithm was used successfully to perform a simultaneous structural optimization by considering a set of tube structural sections to model the individual members of the single layer geodesic dome roof (Saka, 2007b). He included the number of rings, number joints and the height of the dome as topological and shape parameters.

Ho-Huu *et al.* (2016b) suggested an adaptive elitist DE (aeDE) to find the optimal design truss structures using discrete variables. Three key modifications were suggested to improve DE. First, the mutation phase, the mutation operator is selected in a smart manner based on the deviation existing between the objective function of the best individual and the entire population for the preceding generation. Second, to enhance the convergence speed, assigning the elitist group is suggested by choosing the best individuals for the subsequent generation. Third, complementing the method by linking it to the appropriate rounding technique needed to qualify the method in order to address the discrete design parameters. Six design examples were demonstrated to show the efficiency and reliability of the proposed method; aeDE was shown to outperform the classic DE method in terms of the solution quality and the convergence rapidity. Mortazavi and Toğan (2017) have also conducted a study to test the robustness of the proposed integrated particle swarm optimization (iPSO) algorithm, where the iPSO was blended with an improved fly-back mechanism to produce a hybrid version of the two. Four examples were tested with multiple frequency constraints. The optimization results were seen to be excellent when compared to other metaheuristic algorithms mentioned in the literature.

Chapter 3. Impact of Wind Load on the Storage Tank

Large-scale structures are the most vulnerable structural systems to the hazardous actions of nature including extreme weather events such as earthquakes, gusty winds, and snowy storms. This research considers the influence of the intensive wind loads plus the snow loads on the structural design procedure of the dome roof frame of the storage tank. As frequent natural incidences, the conditions recorded by Cao *et al.* (2015) about the typhoon "Maemi" is considered a typical example of the worst windy events occurred in the last few years. However, this research is focusing on the optimization process of the dome roof frame, hence there is no necessity to dive deeply into how to calculate the effective wind speed applied to the storage tank. Thus, the average effective wind speed to be used here, and inferred from the abovementioned events, is 75 m/s. This value is based on an average gust factor of 1.25 with a maximum basic wind speed of 60 m/s.

An integrated computer program was developed using ANSYS Workbench to perform the structural analysis for the whole storage tank. The integrated program consists of two main component parts, ″Fluent″ is the name of the first component, whereas ″static structural″ is the name of the second one. In this chapter, the result of Fluent system (i.e. the numerical data of the wind pressure distributed over the external surface of the tank) will be discussed and the relevant parametric study will be executed at the end of this chapter.

3.1 Airflow Patterns and Bernoulli Equation

The airflow diagram for the current case study, shown in Figure 3.1, indicates the existence of four critical regions: windward (stagnation area), leeward (wake area), low pressure area appearing on the two sides of the tank, and the maximum flow convergence taking place at the hoop region where the dome intersects the cylindrical shell. The airflow path lines, shown in Figure 3.1, and the pressure data, shown in Figure 3.2 and Figure 3.3, indicate that the stagnation point located in the front of the tank (windward) develops the maximum static pressure, while it preserves the minimum dynamic pressure. On the other hand, the lowest static pressure could be seen at the two sides of the tank and some spots on the curb angle hoop, especially that located on the front part of the tank, while the same regions show the highest dynamic pressure at all. The last two statements support the principles of Bernoulli in reservation of pressure, where the static and dynamic pressures are preserved a constant magnitude as given in Eq. (3.1).

$$P_{static} + P_{dynamic} = \text{Constant} \tag{3.1}$$

Eq. (3.1) can define the state of pressure for any particular point on the tank surface. For instance, the pressure of the points 1 and 2, illustrated in Figure 3.1, can be given in Eq. (3.2).

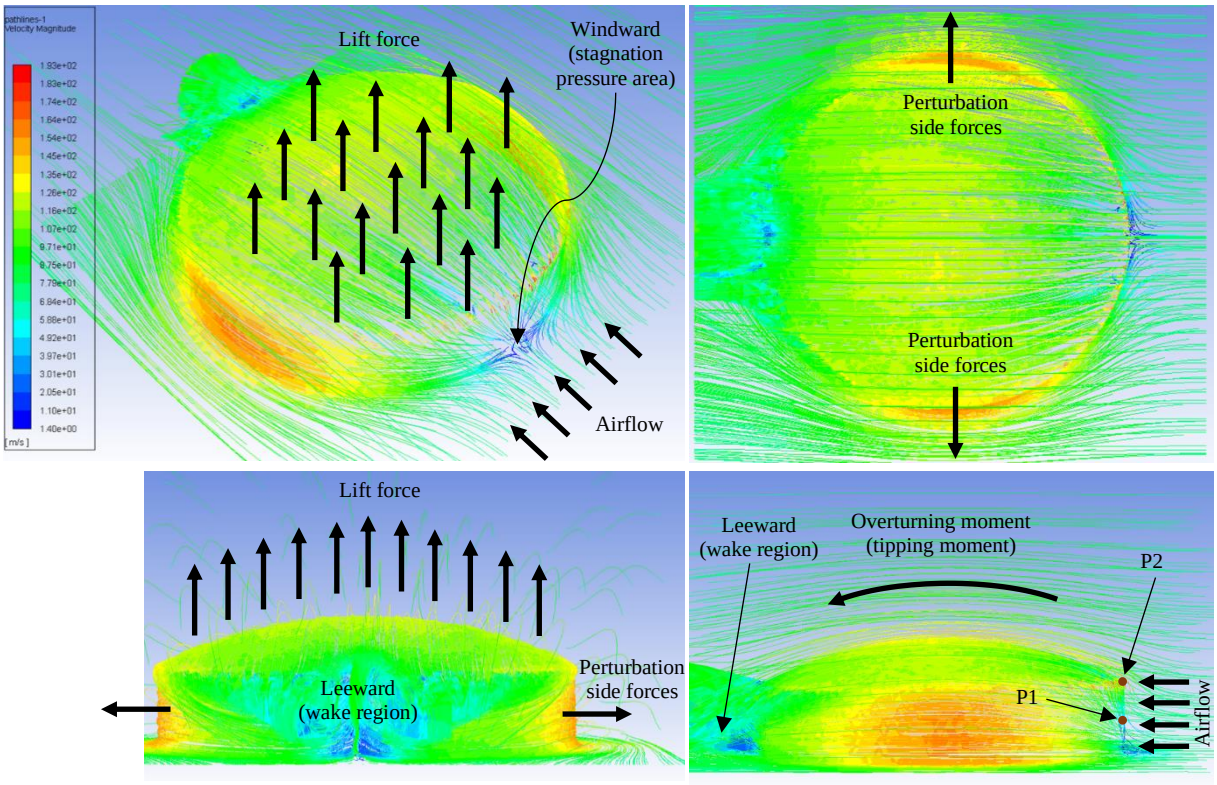

Figure 3.1 3D image for the tank showing the flow path lines (patterns) of wind defined by air velocity distributed around the tank.

$$P_1 + \frac{1}{2}\rho v_1^2 = P_2 + \frac{1}{2}\rho v_2^2 = \text{Constant} \tag{3.2}$$

where, P_1 and P_2 are the values of static pressure for the points 1 and 2 respectively, whereas $\left(\frac{1}{2}\rho v_1^2\right)$ and $\left(\frac{1}{2}\rho v_2^2\right)$ are the values of dynamic pressure for the points 1 and 2 respectively.

Hence, the drop in static pressure between any two points $(P_2 - P_1)$ can be obtained by rearranging Eq. (3.2) as given in Eq. (3.3).

$$P_2 - P_1 = \frac{1}{2}\rho v_1^2 - \frac{1}{2}\rho v_2^2 = \frac{1}{2}\rho(v_1^2 - v_2^2) \tag{3.3}$$

3.2 Evaluation of Wind Load

The output data of the fluid flow system are represented in terms of: static pressure, dynamic pressure, pressure coefficient and the turbulent kinetic energy distributed over the external surface of the tank. The numerical contour plots indicating static pressure, dynamic pressure, and turbulent kinetic energy are shown in Figure 3.2 to Figure 3.4 respectively. For integrated model, the numerical data of wind pressure will be exported directly to the mechanical application to use it as external pressure applied to the finite element model of the tank. In case of simplified model, a pressure file is exported to MATLAB to make use it to generate the relevant nodal forces corresponding to the wind loading analysed by ANSYS/FLUENT. A

detailed explanation of how to calculate the effective lift force, overturning force, and the tipping moment from the individual nodal forces can be found in Appendix A.

According to the CFD results, many findings could be inferred in this section about the aerodynamic characteristics of the air flow passed over storage tank. The contour patterns of Figure 3.2 indicate that there are steep gradients in the static pressure over the roof surface and side walls and these patterns are related to the geometric shape of the storage tank. In overall, the maximum adverse pressure (the lowest pressure) is located at the roof surface, to be precise, at the peripheral rim of the dome, where the dome intersects the cylindrical shell, i.e. the top curb angle region, where the magnitude of static pressure amounts -14.1 kPa as depicted in Figure 3.2. There are also low-pressure regions at the sides of the cylindrical tank wall and the top region of the dome. The criticality of these regions is supported by the airflow patterns depicted in Figure 3.1.

The peak pressure (maximum positive pressure) is occurring at the upwind region of the cylindrical shell, which is located on the anterior section of the cylindrical shell. This region has developed a positive static pressure of 9.31 kPa (pressure coefficient 1.52) due to stagnation pressure. On the other side of the tank (i.e. the leeward area), there is another positive pressure region with minor effect due to the influence of the wake pressure. Also, there is zero-pressure line can be recognized over the cylindrical shell, which is separating between the negative pressure zone and the positive one. Furthermore, there is a relatively weak vacuum pressure at the wake region resulting from the eddy air currents swirling towards the downstream quarter of the wind field causing a turbulent flow as illustrated in Figure 3.1.

In relevance to the distribution nature of the static pressure and regardless of the difference in the absolute magnitudes of the lowest and the highest pressure values, showing clearly in the colour bar of Figure 3.2, the lift force generated by the pressure difference applied to the dome roof is significantly greater than that value of the averaged overturning force exerted on the frontal part of the cylindrical shell due to the projected area withstanding the pressure, as for low aspect ratio ($\frac{H}{D}$) tanks the projected area of the roof is times greater than that of the cylindrical shell. It exactly represents the ratio cylindrical shell radius (r) to the tank height (H), which is for the current study equals ($\frac{r}{H} = \frac{21}{8}$). The difference in negative pressure applied to the roof shell results in equivalent lift force of value (5.69 MN) directed upwards. While, the difference in positive pressure acted upon the windward region of the cylindrical shell is producing an averaged overturning force of value (0.936 MN) due to the direction of wind. The forces acting at the sides of the tank cause a slight perturbation also.

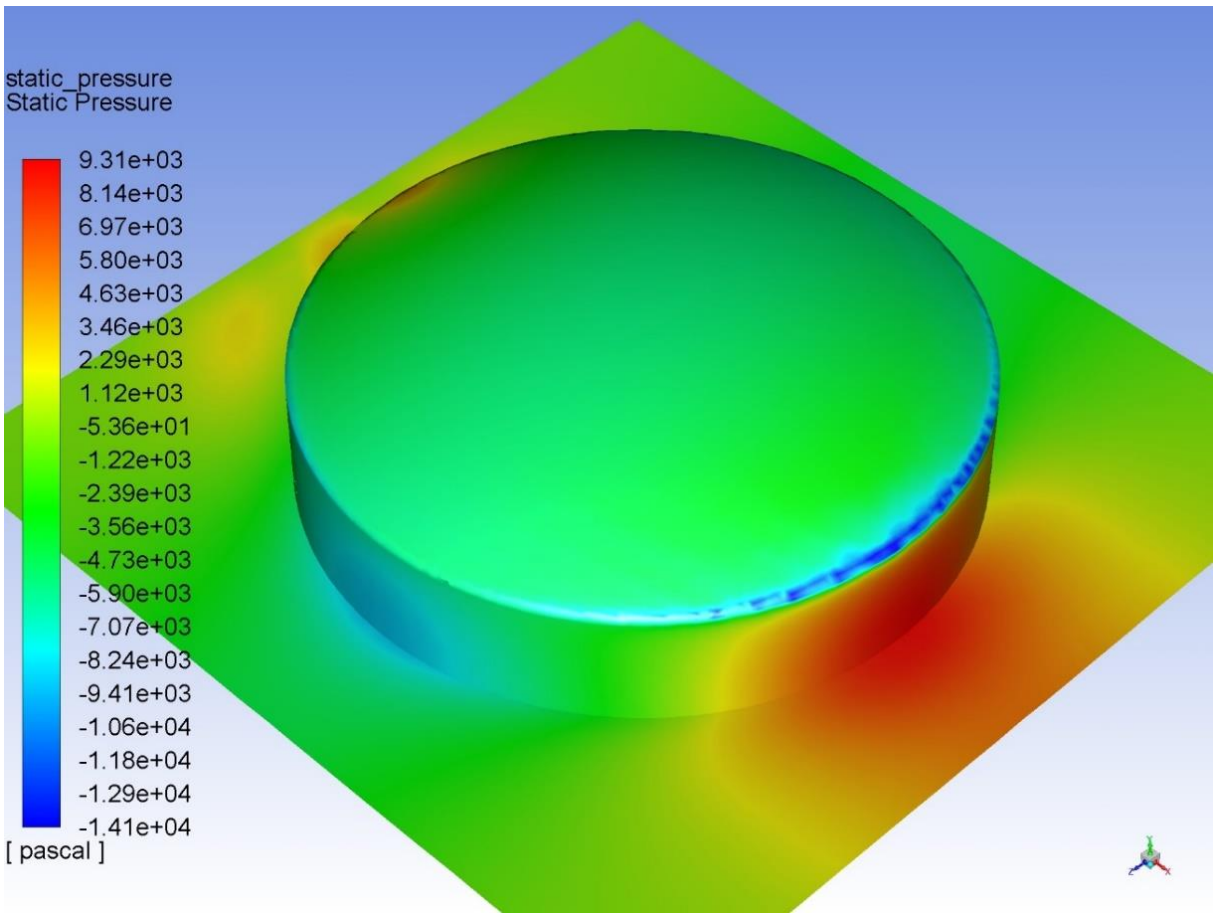

Figure 3.2 Distribution of static pressure over the external surface of the tank.

The dynamic pressure for the air flow over the tank surface is shown in Figure 3.3, which reveals that quasi-stagnation state in air motion is happening at windward and leeward regions with two different styles. In other words, standing whirl is generated at upwind area causing a considerable stagnation in air movement, whereas negative pressure lean eddies are created at wake zone is the reason behind suppressing the air action in this quarter. In the same sense, local twisting waves of air induced at sidewalls are resulting in dramatic increase in dynamic pressure at these regions as explained in the areas shaded with red as shown in Figure 3.3. In this regard, the maximum value of dynamic pressure has developed up to value 16.5 kPa, whereas the minimum value is reached 11.6 Pa.

Through investigating the state of turbulent kinetic energy distributed over the tank surface illustrated in Figure 3.4, two almost symmetrical distinct areas can be specified to account for the considerable turbulence which can give an indication to the presence of local turbulent boundary layers on the tank surface due to its geometrical details. These regions are clearly shown over the frontal part of the dome roof with approximate maximum value of 907 m^2/s^2. While, the lower part of the tank has exhibited negligible magnitudes of turbulent kinetic energy due to the stationary air in this region.

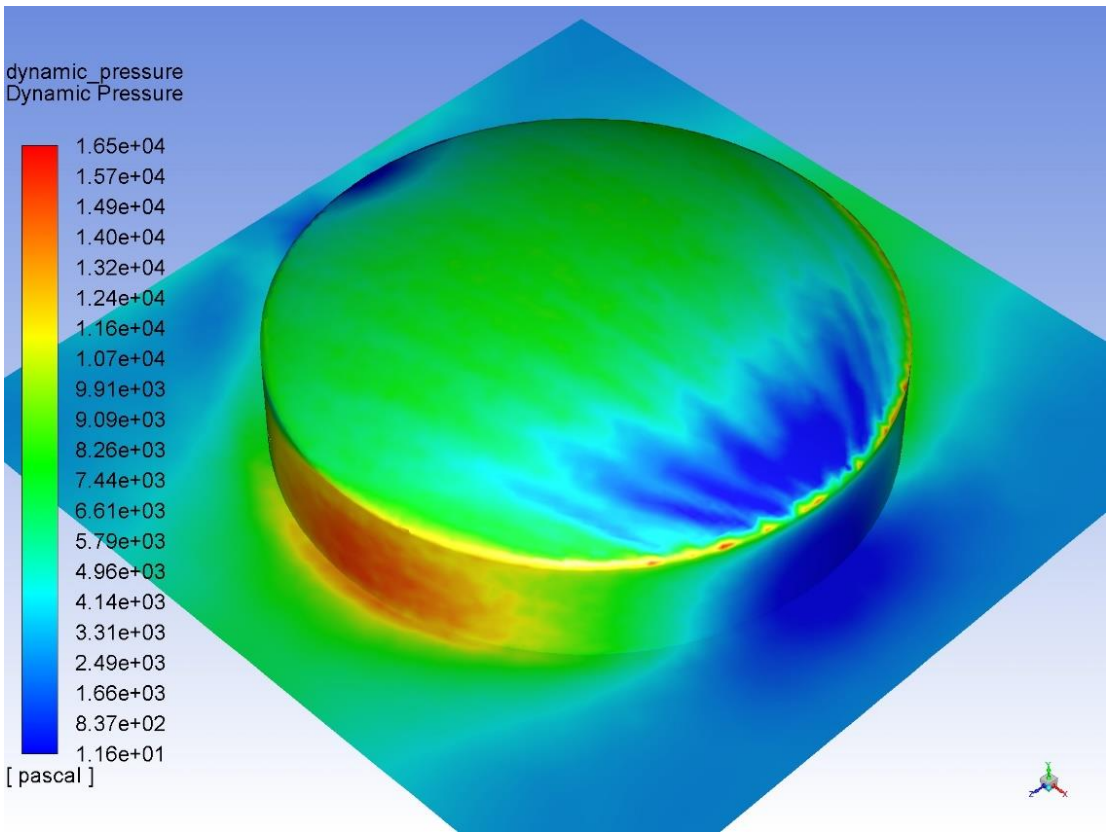

Figure 3.3 Distribution of the dynamic pressure over the external surface of the tank captured for the initial design.

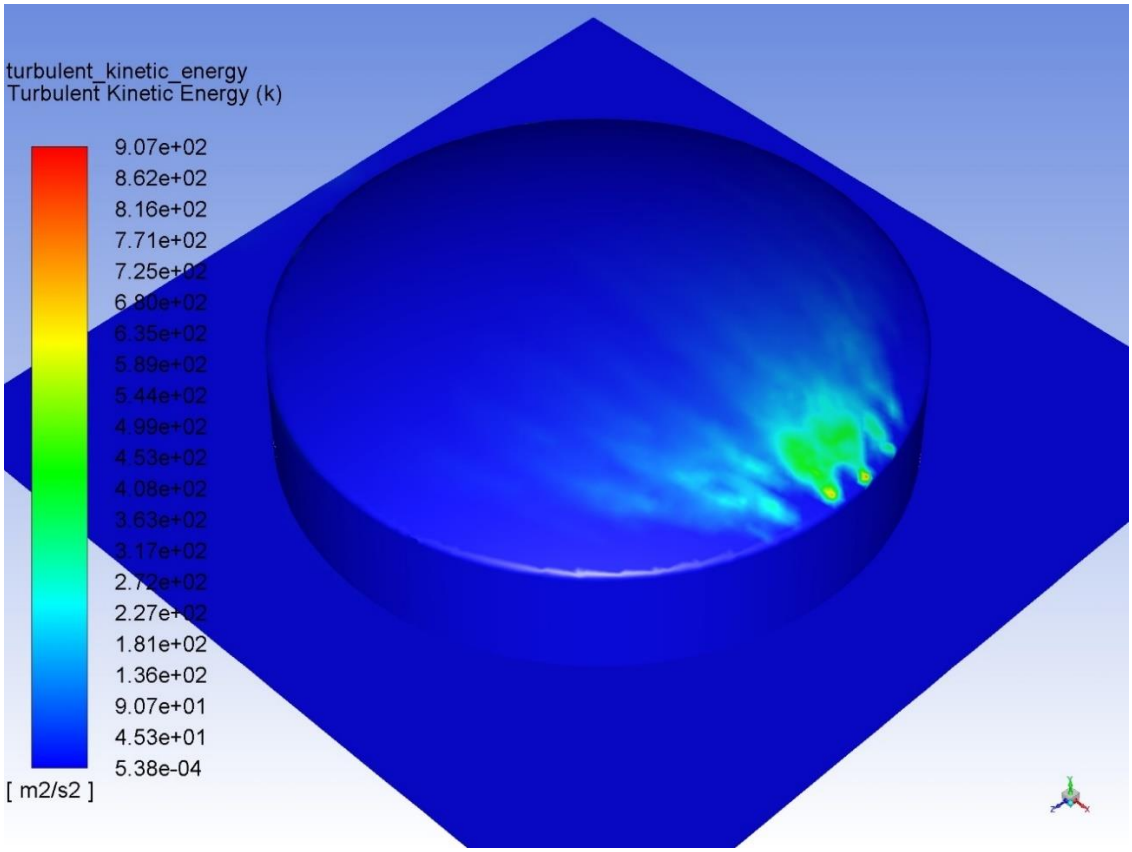

Figure 3.4 Distribution of the turbulent kinetic energy over the external surface of the tank captured for the initial design.

3.3 Relevant Parametric Study

Four output parameters, related to the physical balance of the tank, were considered in this investigation: the lift force, the overturning force, the perturbation side force, and the tipping moment. There are two complementary forces exerted on the external surface of the tank: lift and overturning forces, their resultant is approximately preserving a constant magnitude force ($F_{resultant}$) under the same wind speed, where the resultant force ($F_{resultant}$), detailed in Appendix A, is the effective force responsible of generating the tipping moment applied to the tank structure, which is trying to roll the tank over the ground. While, there is a minor effect caused by the perturbation forces on the two sides of the tank trying to tip the tank on transverse direction to the wind.

3.3.1 Investigation of Aerodynamic Forces under Variable Dome Radius

In this section, a variable wind speed for different dome roof radii was investigated. The range of variation for the dome roof radius was in keeping with the range used in the structural optimization. Consideration of Figure 3.5a will lead to the conclusion that the lift force is inversely proportional to the dome radius of the tank, where the graph shows value of (7.4 MN) for the lift force corresponding to the dome radius (R=30 m), whereas the value (5 MN) is recorded against the radius (R=60 m). Knowing that, these values are computed under constant wind speed (v=75 m/s). Another aspect of the plot indicates that, for a given wind speed, there is direct proportionality between the lift force and the squared wind speed. This is also verified by the correlation between the static pressure difference and the wind speed stated in Eq. (3.3). According to Figure 3.5b, it is noticeable that, in contrary to the conduct followed by the lift force towards the dome radius, the absolute value of overturning force is directly proportional to the dome radius. For instance, the value of (-527 kN) is corresponding to the radius (R=30 m), whereas the value (-627.8 kN) is corresponding to the radius (R=60 m), where the wind speed for this reading is (v=60 m/s).

Figure 3.5c shows a detailed comparison between the different perturbation forces as function of wind speed. It is noticed that the unbalanced side force is proportional to the dome radius except for the radius (R=50 m), which exhibits odd behaviour compared to other radii. The maximum value obtained over the whole plot is reached (43.406 kN), recorded for the radius (R=60 m), whereas the minimum value ever is (0.591 kN), recorded for the radius (R=30 m). It is noteworthy that there is unsteadiness in the perturbation force data measured versus the wind speed for the small values of dome radii.

The set of plots of the tipping moment, depicted in Figure 3.5d, illustrate the fact that this moment is directly proportional to the dome radius due to the high influence of the lift force on

this component. Accordingly, the same correlation built between the lift force and the dome radius can be seen in the tipping moment in relation to the dome radius. The maximum value found for the tipping moment over the whole curves of Figure 3.5d is (461 kN.m), which is measured against radius (R=30 m).

Ultimately, the effect of wind load on the storage tank design is determined through analysing the tipping moment applied to the tank. This reveals that the designs associated with low dome radius are not recommended if the design trends are directed towards reducing the lift force or the tipping moment impinging on the storage tank.

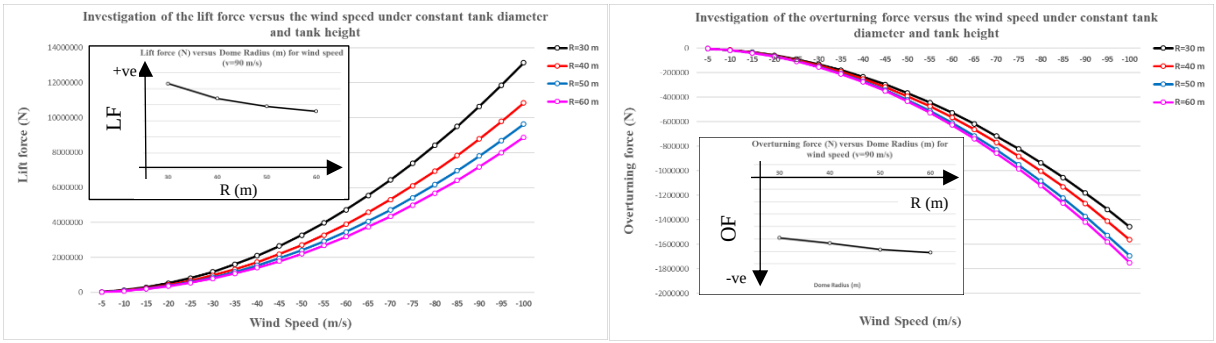

(a) Lift force (b) Overturning force

(c) Side force (d) Tipping moment

Figure 3.5 Parametric investigation for the flow generated force and moment against the wind speed with variable dome radius (R).

3.3.2 Investigation of Aerodynamic Forces under Variable Tank Height

In this section, the height of the tank will be considered in the parametric investigation, so a range of different tank heights will be investigated to demonstrate the significance of the aspect ratio in the design of storage tank under wind load. Thus, the fluid flow parameters are inspected against the practical set of aspect ratios (0.19, 0.238, 0.285, and 0.333) under constant tank diameter and dome radius. Aspect ratio stands for the ratio ($\frac{H}{D}$), where H is the height of the cylindrical shell of the tank and D is the diameter of the cylindrical shell.

Starting with Figure 3.6a, four different heights were used in this survey. The latter figure indicates that, for a given wind speed, the lift force is proportionate with the tank height, i.e. the greater the tank height, the higher lift force. This direct proportionality can be attributed to the considerable geometrical changes caused by altering the aspects ratios for the tank.

It is clear that the lift force has jumped from (10.14 MN) at height (H=8 m) to (15.65 MN) at height (H=14 m), which is a significant change in the state of aerodynamic forces (see Figure 3.6a). By analysing Figure 3.6b, it is concluded that the same behaviour of lift force with the tank height has been conducted by the overturning force, which exhibits dramatic increase proportional to the rise in the tank height. This fact is verified by reading the corresponding output response, where (-1.63 MN) is computed under the height (H=8 m), whereas the value (-3.7 MN) is evaluated for the height (H=14 m). This reading is set at wind speed of (100 m/s).

Figure 3.6c indicates that there is no regular behaviour for the perturbation forces for higher aspect ratios. Consequently, unpredictable side force change will be obtained for different wind speeds for the tanks with considerable height. For instance, the perturbation force is fluctuating from (0.861 kN) for wind speed (v=5 m/s), passing through the value (-15.1 kN) for wind speed (v=50 m/s), ending at the value (56.84 kN) for wind speed (v=100 m/s), hence it is highly oscillating from positive to negative then to positive.

The tipping moment plots shown in Figure 3.6d, illustrate the fact that the tanks with high aspect ratio are more susceptible to the hazards of the wind loads due to developing substantial tipping moments which might cause detrimental effects. This is supported by the small graph fixed in Figure 3.6d showing the relationship between the tipping moment (TM) and the height (H).

In the last investigation, the most hazardous reading of the tipping moment database has a steep jump between the initial value (1.15 kN.m) and the final value (461 kN.m).

Though there is a considerable change in tipping moment, the comparison between the critical values of these parameters for the two investigations reveals that the critical value of the current investigation (618 kN.m) is much greater than the value for the previous investigation. In conclusion, it is recommended to manipulate the dome radius rather than varying the height of the tank as important design feature for storage tanks when the problem is associated with wind loads. Furthermore, the design associated with high aspect ratios are not advisable when aerodynamic forces are the main problem encountered.

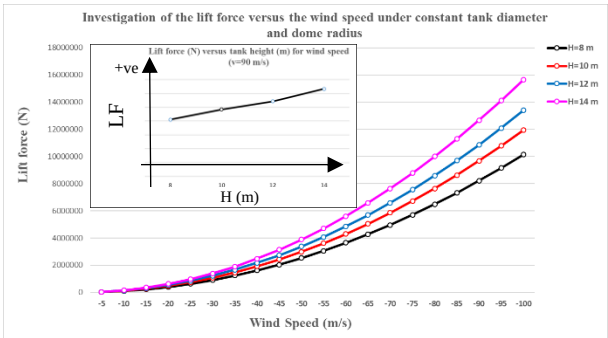

(a) Lift force

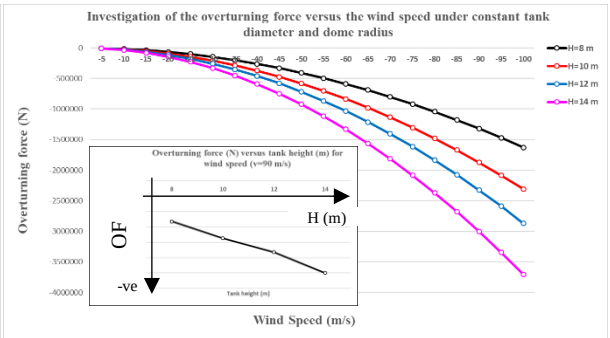

(b) Overturning force

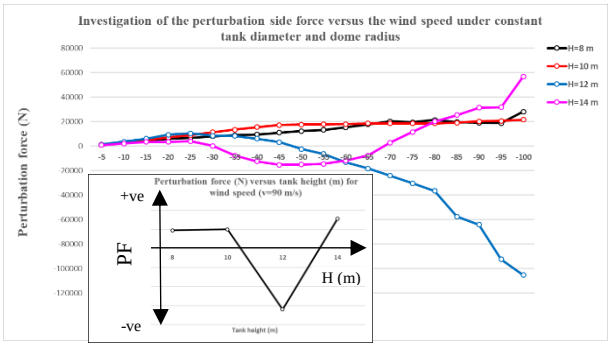

(c) Side force

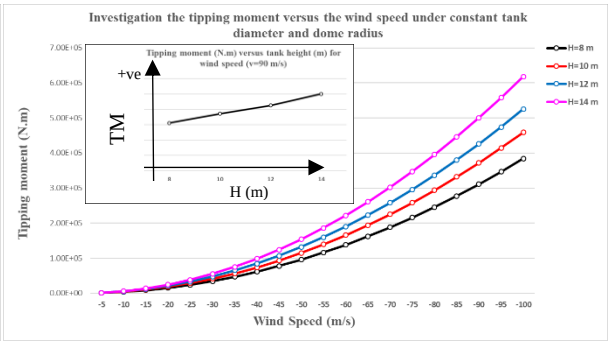

(d) Tipping moment

Figure 3.6 Parametric investigation for the flow generated force and moment against the wind speed with variable tank height (H).

3.4 Empirical Relationship between the Lift Force and the Geometrical Parameters of the Tank

It is possible to construct an empirical formula to relate the lift force to the geometrical parameters of the tank depending on the data viewed in the last section. Such relation discloses some facts about the optimization process performed in chapters 6 to 8. Through analysing the data provided in Figure 3.5a, where the height of the tank (H) is preserved constant at its nominal value (8 m), a simple statistical relationship between F_{lift} and R could be written as in formula (3.4).

$$F_{lift} = \frac{640845}{R} + 11370 \quad (3.4)$$

The same procedure could be repeated, when considering the data viewed in Figure 3.6a, to correlate F_{lift} to the tank height H under constant dome radius (R=45 m) as given in formula (3.5).

$$F_{lift} = 2260.2 \times H + 7079 \quad (3.5)$$

Equations (3.4) and (3.5) are based on constant wind speed (v=75 m/s), which is the design load for the current case study. These two formulae can be combined together to conclude an empirical relationship between the lift force, at that given wind speed, and both of the dome radius and the tank wall height as given in formula (3.6).

$$F_{lift} = 90000\left(\frac{H}{R}\right) + 9000 \quad (3.6)$$

The lift force (F_{lift}), therefore, is reduced by having a low structure with a flat roof, as far as possible within volume constraints. For a fixed volume, H is approximately inversely proportional to the dome roof radius R. Since the tank volume is defined by ($V = \pi r^2 H$), R=30, …, 60, suppose R=2r, then H could be expressed as:

$$H = \left(\frac{V}{\pi r^2}\right) = \left(\frac{4V}{\pi R^2}\right) \quad (3.7)$$

Substitute Eq. (3.7) into Eq. (3.6) would lead to a new relationship between F_{lift} and dome radius (R) and the volume of the tank, which is constant, as given in Eq. (3.8).

$$F_{lift} = 90000\left(\frac{4V}{\pi R^3}\right) + 9000 \quad (3.8)$$

Formula (3.8) indicates that F_{lift} is inversely proportional to R^3.

The data used to derive the formulae (3.4) and (3.5) are illustrated in Table 3.1.

Table 3.1 Empirical data used to correlate the lift force to the geometrical parameters of the storage tank.

Conditions of the experiment	Data used to derive Eq. (3.4), where v=75m/s, H=8m, and r=21m				Data used to derive Eq.(3.5), where v=75m/s, R=45m, and r=21m			
Geometrical variables	R=30 m	R=40m	R=50m	R=60m	H=8m	H=10m	H=12m	H=14m
Lift force (MN)	7.49	6.10	5.42	5.00	5.70	6.72	7.55	8.78

3.5 Summary

- The study indicates that the most peripheral rim of the dome roof (where the dome roof intersects the cylindrical shell of the tank) is the most critical part of the tank in terms of the wind pressure distribution, where this region is subjected to the maximum adverse pressure (the lowest pressure).
- Lift force (LF) applied to the tank structure has inverse proportionality to the dome radius (R) and direct proportionality to the tank height (H).
- Overturning force (OF) applied to the tank structure has inverse proportionality to both of the dome radius (R) and the tank height (H).
- Tipping moment (TM) applied to the tank structure has inverse proportionality to the dome radius (R) and direct proportionality to the tank height (H).

Chapter 4. Geometry and Modelling of the Storage Tank

4.1 Synopsis

Many international standards are devoted to set the appropriate rules used in construction and design of the oil storage tanks such as (API Standard 650, 2013), British Standards BS 2654, The European Standards, and Company standards like shell (DEP) and Petronas (PTS) (Kuan, 2009). The real-world example for the fuel storage tank, shown in Figure 1.1 has adopted in this work. This chapter outlines the geometrical and structural modelling for this application. The current study focuses on performing the design optimization for the dome roof frame, but the whole storage tank consists of two main regions: non-design region and design region. The non-design part represents the external shell of the tank, whereas the design part is characterized by the set of structural components subjected to the design optimization process. Note that the dome roof shell is not a part of the design region, yet it is still subjected to shape change due to the corresponding changes in the supporting frame underneath.

The whole tank structure is modelled using ANSYS software to perform an integrated structural analysis including the fluid flow analysis, as described in Chapter 3, and the structural analysis, which will be demonstrated in this chapter.

Considering the design aspect of the tank, i.e. the design optimization of the self-supported dome roof frame, many objectives may be involved with this task, i.e. structural weight, strength, stiffness, etc. A set of dome roof configurations are constructed for later optimization. Two types of modelling were developed simplified modelling and integrated modelling. Table 4.1 lists the main differences between the two types of modelling.

The simplified frame modelling was implemented in MATLAB to perform the geometric modelling, to create the geometry, and the structural modelling, to discretize the structure into finite number of identified structural components specifying the set of design parameters and executing the required finite element mesh for the structural system to solve the problem. For the integrated modelling, the roof supporting frame has been modelled using the most advanced 3D Timoshenko beam element offered by ANSYS 18.1 (BEAM189)[1].

Considering the non-design region of the tank, i.e. the external shell, represented by the list of structural parts mentioned in Table 4.2, it has been modelled using the most sophisticated 3D shell element available in ANSYS 18.1 library (SHELL281)[2].

Figure 4.1 illustrates the geometrical description of the main structural parts of the storage tank considering a geodesic single lattice dome roof configuration.

[1] Refer to https://www.sharcnet.ca/Software/Ansys/17.0/en-us/help/ans_elem/Hlp_E_BEAM189.html

[2] Refer to https://www.sharcnet.ca/Software/Ansys/16.2.3/en-us/help/ans_elem/Hlp_E_SHELL281.html

Table 4.1 The main differences between the simplified modelling and the integrated modelling.

Simplified Frame Modelling	Integrated Tank Modelling
1. It uses a simple 3D Timoshenko straight beam element in the modelling process (Sarac, 2005) and (Kassim, 2015).	**1.** It uses a sophisticated 3D Timoshenko curved beam element in the modelling process.
2. One analysis takes on average about 30 seconds to execute.	**2.** One analysis takes on average about 30 minutes to execute.
3. The boundary conditions assume that the roof supporting frame is fixed at its edge vertices where it meets the cylindrical shell, because the structural analysis is performed for the dome roof frame only without needing to perform the structural analysis for the whole storage tank.	**3.** The boundary conditions assume that the whole storage tank is fixed at its bottom, because the structural analysis is performed for the whole tank as integrated unit and the results of the dome roof frame is a part of this solution.
4. Due to its swiftness in performing the structural analysis, it is effectively used to check the efficiency and the robustness of the optimization tools to achieve the optimum design under multiple design constraints.	**4.** It cannot be the examination tool for testing the extent of validity for the proposed optimization techniques due to its slowness in performing the required structural analysis compared to the simplified modelling.
5. The model is constructed and solved within MATLAB and numbers of components and joints can be varied with ease.	**5.** Automated construction of the model within ANSYS is very complex, especially when the numbers of components and joints are variables.
6. Less accuracy than the integrated modelling as a result of incorrect boundary conditions and the limitation of straight beams.	**6.** The accuracy is acceptable due to considering more realistic conditions and treating with the storage tank as integrated system.
7. It is created as integrated unit in MATLAB to perform the structural optimization and the Finite element analysis.	**7.** It employs MATLAB as optimization tool, whereas ANSYS is exploited as structural analysis tool, hence interfacing methods are required to integrate the process and perform the optimization task.

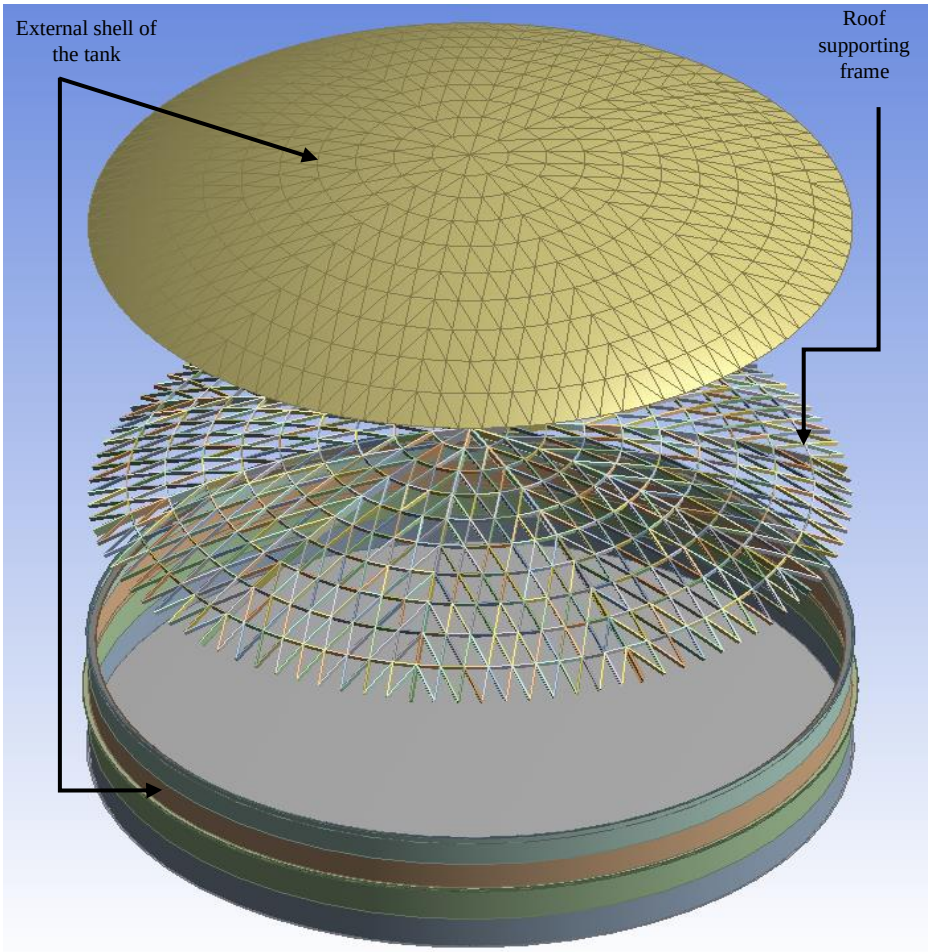

Figure 4.1 Main geometrical parts of the storage tank (with geodesic single lattice modelling).

4.2 Geometric Modelling of the Storage Tank

A simplified illustration for the general shape of the fuel storage tank is shown in Figure 4.2 to explain all geometrical parameters relevant to the general dimensions of the tank, where the diameter of the tank is maintained constant at 42 m. Thus, the curvature angles of the domed roof can be defined as:

$$\alpha + \theta = \sin^{-1}\left(\frac{r}{R}\right) \tag{4.1}$$

$$\alpha = \sin^{-1}\left(\frac{a}{R}\right) \tag{4.2}$$

where, a, r and R stand for the radii of each of the crown, the cylindrical shell of the tank, and the domed roof respectively. C is the centre of curvature of the dome roof, which is simply specified by determining the dome radius (R). α is the angle formed by the crown, θ is the angle of constituted by the primary radial girder (L_{PG}). The length of the major radial girder, L_{PG}, is:

$$L_{PG} = R\theta \tag{4.3}$$

The dome offset (z_{dome_offset}), is given by Eq. (4.4):

$$z_{dome\_offset} = H - d_{basic\_offset} \tag{4.4}$$

where, H is the tank wall height, d_{basic_offset} is the basic offset of the dome, which is represented by the vertical distance measured from the curvature centre of the dome to the top of the tank wall, i.e. the cylindrical shell.

$$d_{basic\_offset} = \sqrt{R^2 - r^2} \tag{4.5}$$

The dimensions and the thicknesses for the different parts of the external shell of the tank for the initial design are shown in Table 4.2. The external surface area of the tank subjected to the environmental loads could be easily calculated by adding the surface area of the cylindrical shell to that of the spherical cap overhead.

$$\begin{aligned} A_{tank} &= A_{cylinder} + A_{cap} = 2\pi rH + 2\pi Rh \\ &= 2\pi\left(rH + R^2\sqrt{1 - \left(\frac{r}{R}\right)^2}\right) \end{aligned} \tag{4.6}$$

The derivation of surface area for spherical cap ($A_{cap} = 2\pi Rh$) is detailed in Appendix A.

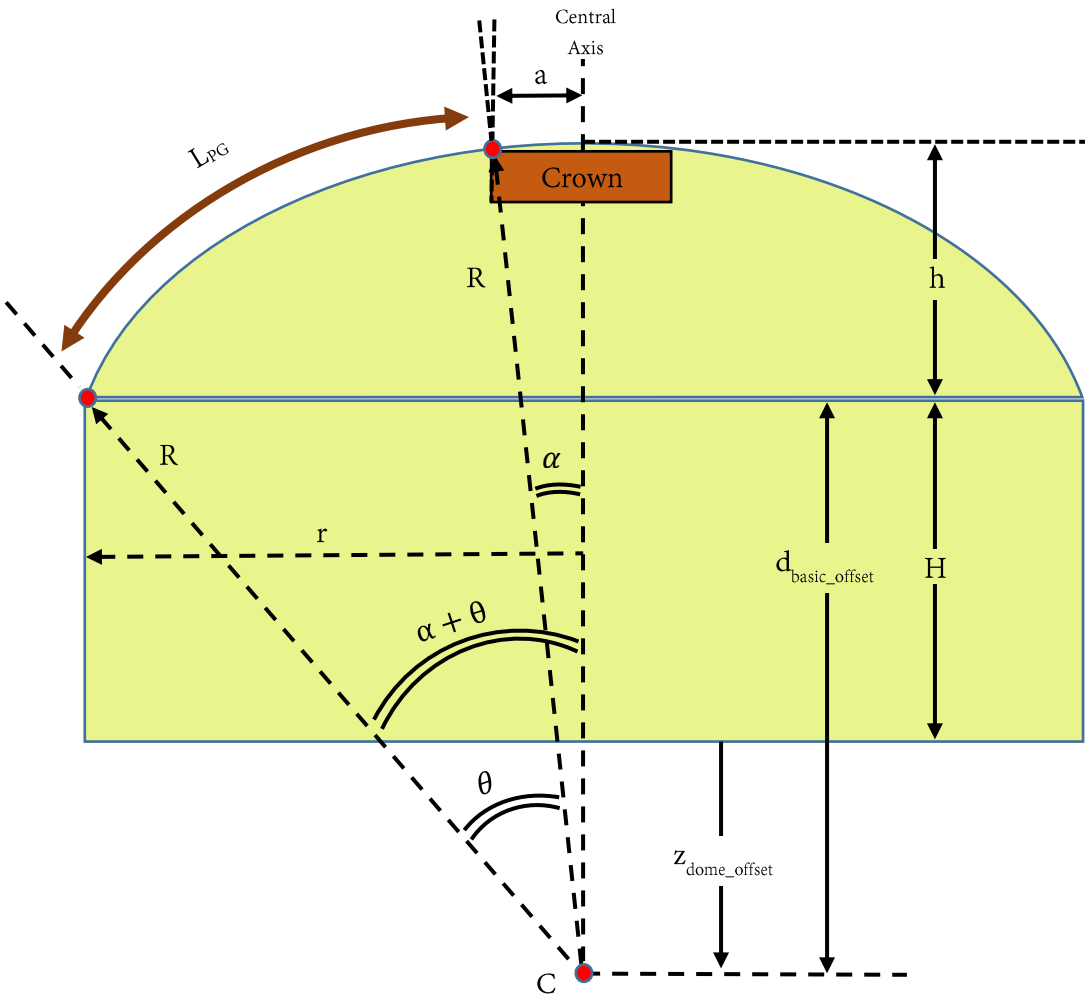

Figure 4.2 Simplified sketch for the tank demonstrating the geometric modelling parameters.

Table 4.2 List of geometrical dimensions and thicknesses (THK) for the structural parts constituting the external shell of the tank (Reference design).

Geometrical dimensions: Tank radius = 21 m, Tank height = 8 m, Dome radius = 45 m.					
Part No.	Part Name	THK. [mm]	Part No.	Part Name	THK. [mm]
1	Bottom Plate	11	8	Web of Top Curb Angle	12
2	Bottom Outer Rim	11	9	Flange of Top Curb Angle	12
3	Cylindrical Shell Course-1	17	10	Web of Internal Stiffener	12
4	Cylindrical Shell Course-2	14	11	Flange of Internal Stiffener	12
5	Cylindrical Shell Course-3	11	12	Web of External Stiffener	10
6	Cylindrical Shell Course-4	8	13	Flange of External Stiffener	10
7	Dome Roof Shell	7			

4.3 Structural Modelling of the Non-design Region (Tank External Shell)

The non-design part of the tank is represented by the external shell, which consists of 13 structural components as detailed in Table 4.2. This preserves the capacity of the tank at constant value during the optimization process, except for the change in the dome roof shape affected by the relevant variation in the roof supporting frame. This significantly reduces the burden of the necessary fluid dynamics calculations for different tank wall heights and corresponding tank radii. An extra shell course would need to be added to the tank height in case of double lattice modelling of the gap generated between the two layers in a double lattice configuration.

Shell components of the tank are modelled as surface bodies using shell element (SHELL281) in ANSYS by choosing the option "Quadratic" for the feature "Element Order" in the mesh setting to account for the geometrical nonlinearity in the structural behaviour of the tank shell. The storage tank is resting directly on a concrete foundation, hence in normal service conditions, negligible values of stresses and strains are induced in the bottom plate, the flat, the interior and the ground-level base of the tank. However, acceptable quality of meshing must be ensured at the critical positions within the tank, i.e. the intersection of the circumferential lines of the cylindrical shell with any of its additional structural attachments, i.e. the intersection with the dome roof shell, bottom plate, and the shell stiffeners. Currently, these critical spots have been meshed appropriately, and consistent meshing has been realized for the external shell of the tank as shown in Figure 4.3. The meshing configuration for the dome roof shell is compatible with the roof frame lattice underneath, hence the number of elements for the external shell will vary slightly according to the dome roof frame involved.

4.3.1 Bottom Plate

This is the basic part of the tank, it is constructed as circular disc through arranging a group of standard, sketch, and annular plates with an overlap no less than 25 mm according to American Petroleum Institute (API Standard 650, 2013). Normally, the standard plate has rectangular outline with a length and breadth of 8 m and 2 m respectively. The annular plates have a constant thickness of 11 mm, which is 2 mm higher than the thicknesses of other bottom plates. The plates are erected and welded together in such manner that they finally constitute the circular shape of the disc, where overlap welding joints are employed to bind the bottom plates together. Also, the bottom plate must be protruded outside the cylindrical shell of the tank to a distance no less than 65 mm as per API Standard 650 (2013). For the sake of simplification, the bottom plate has been modelled as a circular disc with diameter equal to 42 m and constant thickness of 11 mm as shown in Figure 4.3.

4.3.2 Cylindrical Shell Courses

The cylindrical shell (tank wall) consists of 4 courses each with its own constant thickness as given in Table 4.2. The course thickness is designed according to the pressure distribution of the static head of fuel. The shell course is formed by jointing a series of rolled plates with standard dimensions 10 m by 2 m each, where the residual space of the course is filled with nonstandard piece of rolled plate prepared for this purpose. The vertical joints connecting the plates within the single course and the horizontal joints connecting the courses within the cylindrical shell are implemented using a butt joint with v-shaped groove. A T-joint is used to bind the cylindrical shell to the bottom plate. The cylindrical shell has been modelled using a minimum element size of 200 mm, where mapped meshing was used to generate regular meshing patterns.

4.3.3 Dome Roof Shell

The spherical cap at the top of the tank is a thin shell with thickness 7 mm supported by and welded to the roof frame underneath. Many additional component structures are attached to this part of the tank such as breather valves, gauge hatches, roof manholes, etc. Currently, these components are omitted to facilitate the structural analysis of the model. The minimum element size adopted for the dome shell is 200 mm.

4.3.4 Cylindrical Shell Stiffeners

In extreme environmental conditions, the cylindrical shell is exposed to potential buckling incidents due to its weakness as a thin unsupported shell. Therefore, Burgos *et al.* (2015) and Bu and Qian (2015) recommended to stiffen this part of the tank to protect it from potential failure. There are three stiffeners attached to the cylindrical shell: a top curb angle, an internal

stiffener, and an external stiffener. Table 4.3 lists the geometrical dimensions for the set of cylindrical shell stiffeners used in the current tank model. According to API Standard 650 (2013) article 5.9.3.4, shell stiffeners must be seam welded to the cylindrical shell and the splicing welds of the stiffeners must be located at a minimum distance apart from the vertical shell welds.

Table 4.3 Geometrical dimensions for the stiffening rings of the cylindrical shell.

Cylindrical shell appurtenances (stiffening rings)					
Part No.	Part Name	Web height [mm]	Flange width [mm]	Web thickness [mm]	Flange thickness [mm]
1	Top curb angle	120	120	12	12
2	Internal stiffener	400	200	12	12
3	External stiffener	300	200	10	10

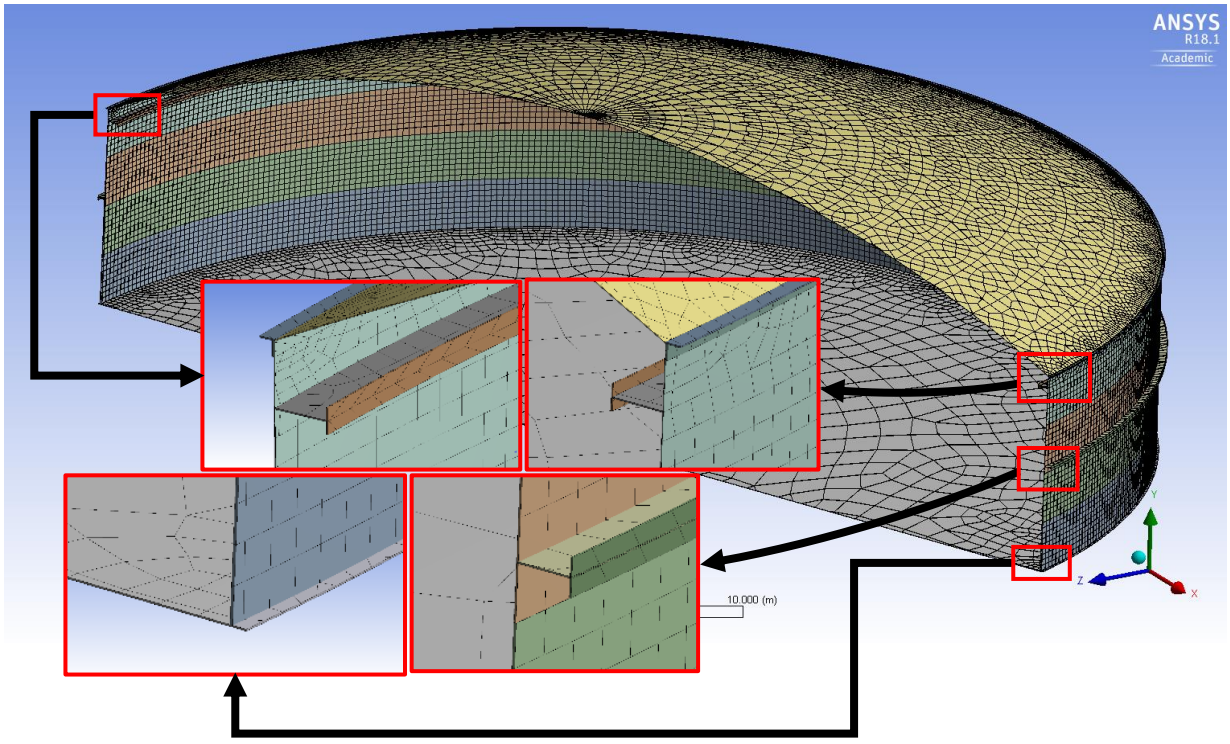

Figure 4.3 Finite element model for the external shell of the storage tank.

4.4 Structural Modelling of the Design Region (Roof Supporting Frame)

In this section, the structural modelling procedure for the most conventional domed roof lattices is described in terms of a finite set of parameters (commercial cross-sections, etc.) that will be used later in the optimization process. In structural modelling process, two distinct features need to be determined to specify the position of any component and reading its cross-sectional specifications within the structural system of the dome roof frame, which is the job of the optimization method to perform the sizing optimization of the structure. These two features are:

- Component group label: This represents the structural components that have the same type of cross section or the same topological nature. For example, model A1 has 3 distinct component groups with 52 structural components as demonstrated in Table 4.5. The first group represented by the set of radial girders, which consists of 20 components, has identified by the CG template (CG-C). According to the dataset stored in the corresponding DM template (DM-C), CG-C selects cross sections from the list of I-beams stored in DM-C, the list of I-beams is found in Appendix Table E.1. The second CG template (CG-D) stands for the group of diagonal braces, which are consisting of 13 components. This representative template (CG-D) is modelled using the set of RHS designations defined in Appendix Table E.4. The third part of the model, i.e. the circumferential rings consisting of 19 components, is represented by the template (CG-E). CG-E is modelled using the set of cross-sections existing in the corresponding DM template (DM-E), where DM-E stores the set of C-channels, described in Appendix Table E.2. Table 4.5 illustrates the data for model A1. The simple example shown in Figure 4.4 illustrates the mechanism of interaction between the model structural components and their corresponding dataset modules, where the colours have been suggested to recognize the different structural components of the model, where the red refers to the meridional girders, the blue refers to the diagonal braces, the green represents the circumferential rings, the brown represents the in-between braces, and the grey refers to the unutilized dataset module.
- Cross section designation: This is the commercial identification of cross sections. Structural sections can also be enumerated in order of decreasing second moment of area, to simplify optimization. These designations are illustrated for each commercial category as shown Appendix Table E.1 to Appendix Table E.8 fixed in Appendix E.

Ultimately, the component group templates {CG-A, CG-B, …, CG-H} and their respective dataset modules {DM-A, DM-B, …, DM-H} are the most substantial tools used to perform the structural modelling needed to perform the sizing optimization for the dome roof frame.

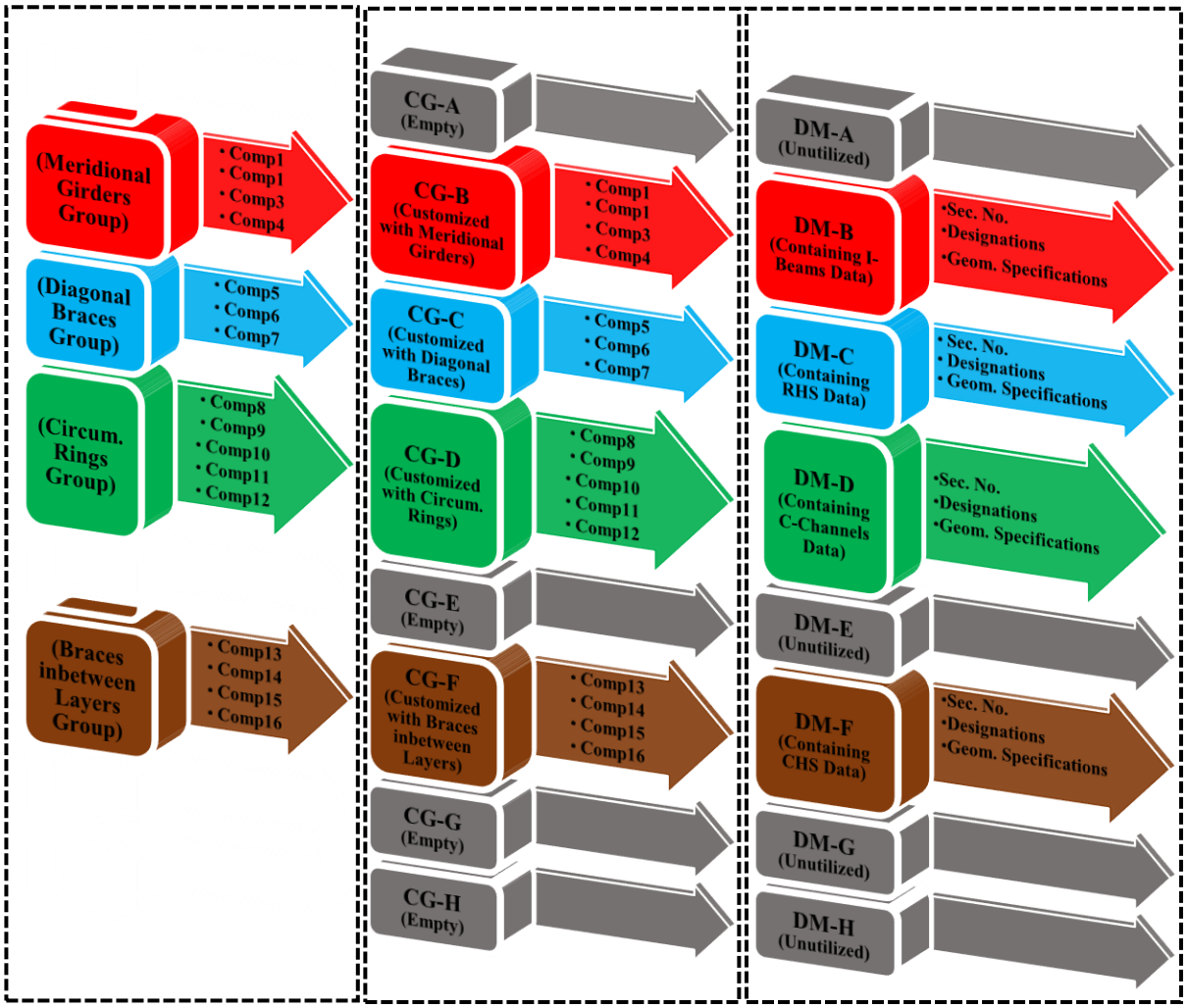

Figure 4.4 Simple example showing how the structural component groupings CGs are linked to their DMs counterparts in structural modelling process.

4.5 Simplified Modelling

Ten simplified frame models corresponding to ten different dome configurations are numerically formulated in this section. Five are single layer lattices (e.g. trimmed ribbed, Schwedler, Lamella, hybrid Schwedler-Lamella and geodesic configurations), and five are double layer lattices with related configurations. For each model, the process of automating the generation of nodes, generation of finite elements, and the discretization of the resulting structure into identifiable structural components is described. The initial values and optimization range of the relevant design variables will be clarified for each model. For the current study, a rigid joint assumption is used to connect the members of the braced domes, i.e. each member in the roof lattice has the frame element capabilities characterised by resisting the axial and transverse forces, whilst accounting for the bending and torsional moments that arise

from this assumption. Each model was characterized by its respective alphabetical designation for referring to it in the subsequent chapters.

4.5.1 Trimmed Ribbed Single Lattice Dome (Model A1)

This configuration can be topologically characterized by two main entities, radial (meridional) girders and circumferential rings. Some extra supporting braces could be added to the original ribbed network to enhance the structural performance of the model. Trimming radial girders to a certain span is behind the difference between the standard and the trimmed ribbed models.

Referring to section 5.1.3, there are five different shape and topological design variables associated with this design. Four of them are integer design variables, as defined by the vector $\overrightarrow{\mathrm{DV}_{\mathrm{int}}}$ which will be defined later in Eq. (5.5), whereas the fifth one is the dome radius (R) characterized as continuous variable defined by the vector $\overrightarrow{\mathrm{DV}_{\mathrm{con}}}$ mentioned in Eq. (5.5). Upon the mathematical classification of design variables, $\overrightarrow{\mathrm{DV}_{\mathrm{int}}}$ for this model essentially includes the following variables:

- Number of nodes (N_n): which stands for the number of nodes per circumferential ring. It is used to determine the angular position for each node in the group of nodes belonging to the same circumferential ring as defined in Eq. (4.1).
- Number of rings (N_r): which represents the number of circumferential rings existing in the model. It is utilized to specify the radius of the circumferential ring as in Eq. (4.4).
- Topological spacing factor (N_s): which controls the diversity of the circumferential rings with respect to each other and with respect to the central hub of the model. It is defined clearly in Eqs. (4.4) & (4.5).
- Topological trimming factor (N_t): which governs the trimming space of the model. In other words, it decides the proportion of the trimmed space to the intact space of the model, which is controlling the length of the secondary meridional girders and the number of rings for the dense ribs' region as demonstrated in Figure 4.6. It is mathematically illustrated in Eqs. (4.2) & (4.3).

Each variable in integer set can select any integer number located within its respective design limits listed in Table 4.4. Appendix F lists the set of designations for optimal designs of this model and others in this chapter.

Table 4.4 Optimization range for the shape and topological parameters of model A1.

Design variable	**N_n (-)**	**N_r (-)**	**N_s (-)**	**N_t (-)**	**R (m)**
Initial value	40	20	24	10	30
Lower bound	30	12	10	4	30
Upper bound	40	20	28	16	60

A. Automatic Generation of Nodes

In each optimization cycle, specifying the values for the design variables mentioned in Table 4.4 along with the tank radius r, which is constant, is more than adequate to configure the governing nodes of the model. Hence, there is no need to use the classic method to create the dome roof nodes. Smart mathematical formulae are prepared for this purpose, where they are formulated in MATLAB to perform this task. The process starts with determining the angular position for each node located within specified circumferential ring, i.e. the angular position θ_i for any node (i) belonging to circumferential ring (j) can be defined as:

$$\theta_i = \left[\frac{2\pi i}{N_n}\right]\begin{cases} i = 1, 3, 5, \dots, N_n & for\ 1 \le j \le N_{dr} \\ i = 1, 2, 3, \dots, N_n & for\ N_{dr} < j \le N_r \end{cases} \quad (4.1)$$

where, i is an integer counter starting from 1 and extending to comprehend the group of nodes belonging to the circumferential ring (j), j is an integer counter beginning with 1 and extending over the group of circumferential rings existing in the model. N_{dr} is the number of rings for the dense ribs' region as illustrated in Figure 4.6. By introducing the variable "trimming fraction" (λ_t), the correlation between the number of rings for the dense ribs' region (N_{dr}) and the total number of rings (N_r) could be posed in formula (4.2):

$$N_{dr} = \|(1 - \lambda_t)N_r\| + 1 \quad (4.2)$$

where, $\|(1 - \lambda_t)N_r\|$ is a rounded integer number that reflects the number of rings for the non-trimmed region. The topological trimming fraction (λ_t) is related to the dummy integer variable called topological trimming factor (N_t) as stated in Eq. (4.3).

$$\lambda_t = 0.05N_t \quad (4.3)$$

Similarly, the radius for the jth circumferential ring (r_j) can be expressed as:

$$r_j = r\left[\frac{j}{N_r}\right]^{\lambda_s}, \quad \text{j=1, 2, 3, …, } N_r \quad (4.4)$$

in which, r is the tank radius, λ_s is the topological spacing fraction, which is inversely proportional to the topological spacing factor as demonstrated in Eq. (4.5).

$$\lambda_s = {}^{1}/_{(0.05N_s)} \quad (4.5)$$

It is remarkable that the coordinates of the nodes, calculated in Eqs. (4.1) & (4.4), are describing the positions of nodes in terms of polar coordinates. Therefore, trigonometric relations are needed to transfer these coordinates to their equivalent Cartesian coordinates as stated in the following equations:

$$x_{i,j} = r_j \cos\theta_i \quad (4.6)$$

$$y_{i,j} = r_j \sin\theta_i \quad (4.7)$$

where, $x_{i,j}$ & $y_{i,j}$ are the Cartesian coordinates for a certain node when it is defined by the radial position (r_j) and the angular position (θ_i). By introducing the parameter dome offset (z_{dome_offset}), the z-coordinate ($z_{i,j}$) for each node could be computed according to Eq. (4.8).

$$z_{i,j} = z_j = z_{dome\_offset} + \sqrt{R^2 - r_j^2} \tag{4.8}$$

where, the relation ($z_{i,j} = z_j$) indicates that the z-coordinate for the set of nodes located within certain circumferential ring (j) is not a function of angular position (θ_i) due to the axisymmetric nature of the dome surface.

The set of key nodes for the initial design of model A1 is shown in Figure 4.5. The total number of generated nodes is 1121, created in systematic manner such that each circumferential ring, located within the dense ribs' region, will have number of nodes equals to $\mathbf{N_n}$, whereas the number of nodes constituting any circumferential ring within the trimmed region equals to the half of $\mathbf{N_n}$. As result, the total number of nodes is ($\mathbf{2Nr \times Nn - (N_r - N_{dr}) \times N_n + 1}$), where $\mathbf{N_r}$ is the number of circumferential rings for the entire model, $\mathbf{N_{dr}}$ is the number of rings for the dense ribs' region. Wind load will be interpreted as nodal loads through manipulating the pressure data file exported by the CFD program, so the distribution of the wind loads is depending on total number of nodes existing in the dome roof frame.

B. Automatic Generation of Connecting Elements

Elements are created by connecting pairs of nodes. The finite element model for the initial design implemented with automatic numbering of elements is clearly described in Figure 4.6. The total number of elements counted for the initial design of model A1 equals 2720.

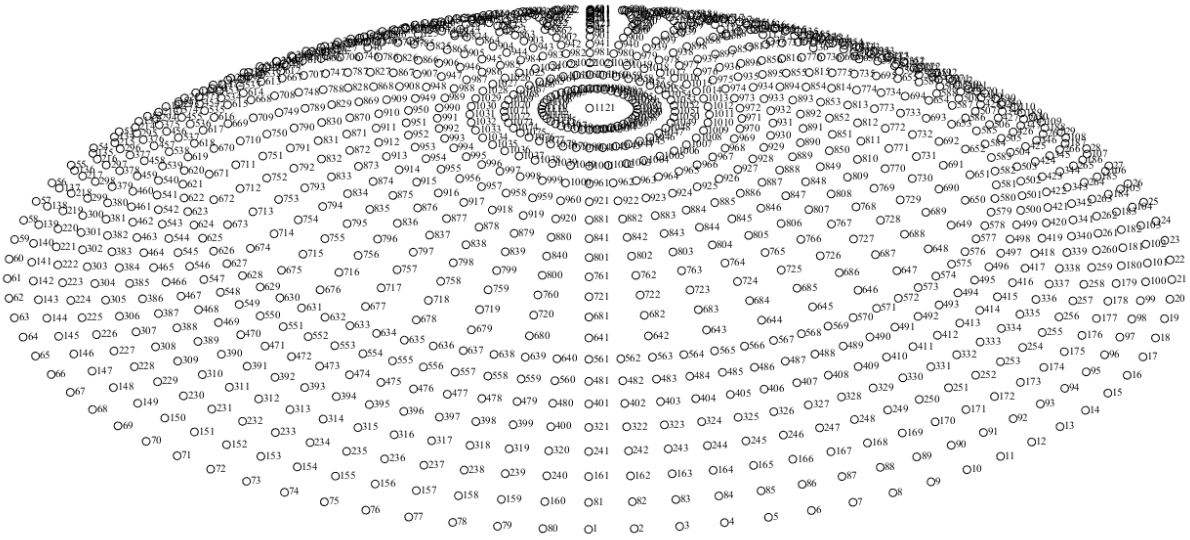

Figure 4.5 Automatic numbering of nodes for the initial design of model A1.

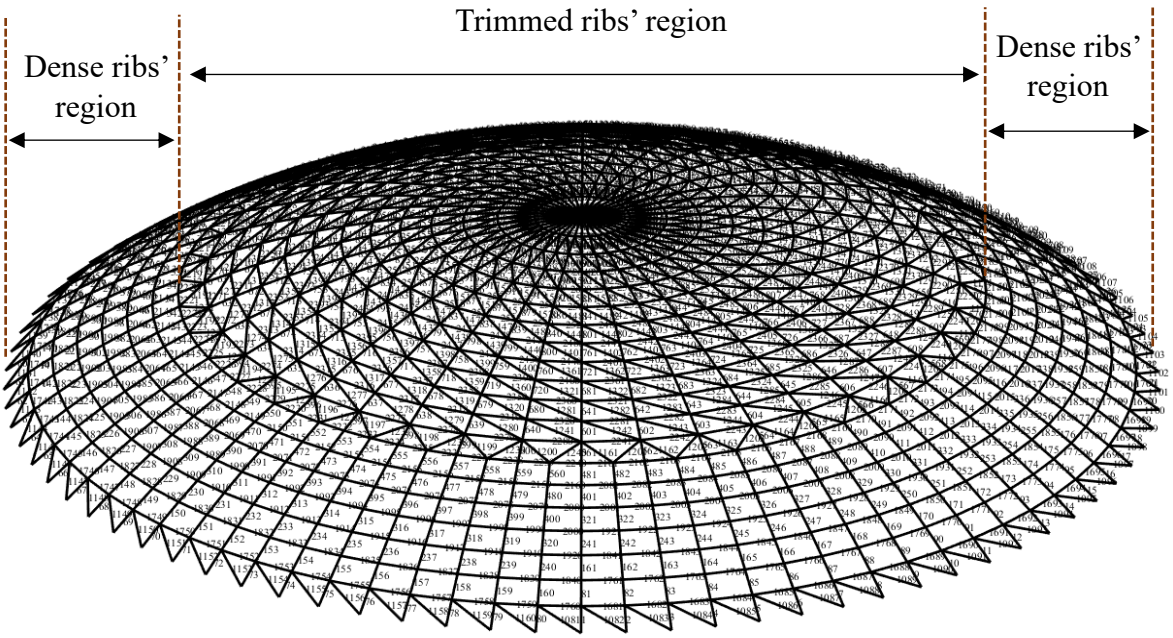

Figure 4.6 Automatic numbering of elements performed for the initial design of model A1.

C. Identification of Structural Components

In this model, there are 52 components allocated as 20 axisymmetric components (CG-C) for the meridional girders, 13 axisymmetric components (CG-D) for the right-inclined braces and 19 axisymmetric components (CG-E) for the circumferential rings (see Table 4.5). Figure 4.7 is designed to show the ID number for each structural group using the available range of colours provided by the MATLAB software, starting at the primary blue, which stands for number 1, ending at the primary red, which represents the ID number for the final component in the system.

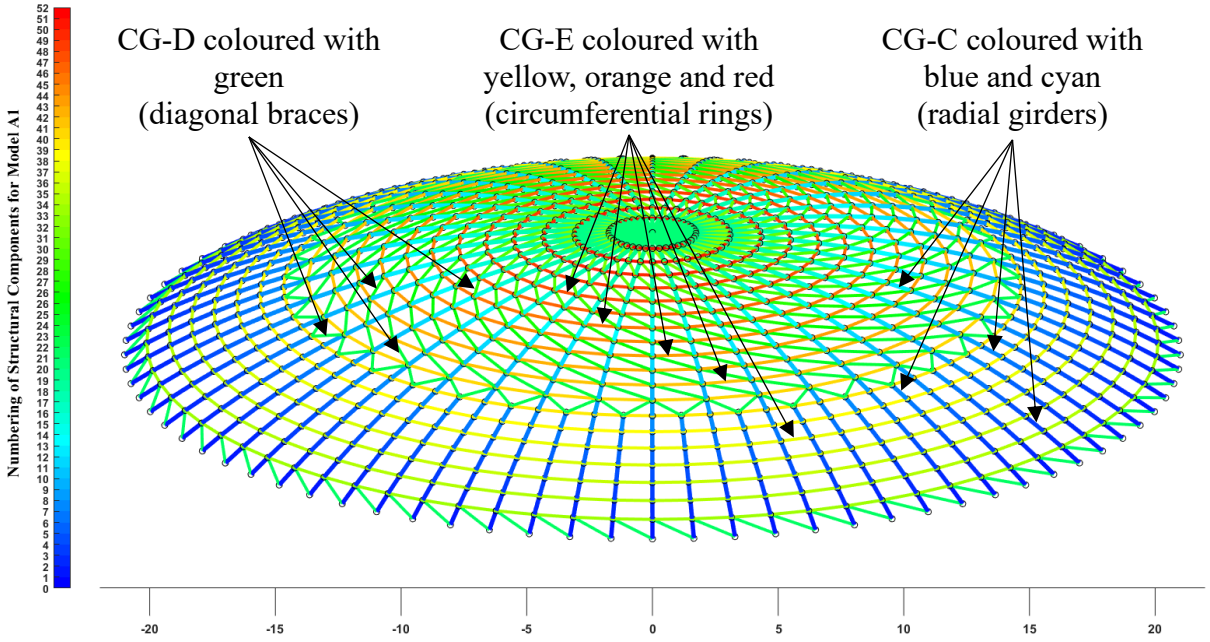

Figure 4.7 Structural component number for the initial design of model A1.

Table 4.5 Data for the initial design of model A1.

Number of Nodes		1121
Number of Elements		2720
Number of Structural Components		20+13+19 = 52
Structural Components	CG-A (Empty)	DM-A (Unutilized)
	CG-B (Empty)	DM-B (Unutilized)
	CG-C (Meridional Girders)	20 comps. modelled by DM-C using 'S20x96'
	CG-D (Right-inclined Braces)	13 comps. modelled by DM-D using '8 x 4 x 5/16'
	CG-E (Circumferential Rings)	19 comps. modelled by DM-E using 'C8x18.75'
	CG-F (Empty)	DM-F (Unutilized)
	CG-G (Empty)	DM-G (Unutilized)
	CG-H (Empty)	DM-H (Unutilized)

4.5.2 Schwedler Single Lattice Dome (Model B1)

This model is characterized as ribbed dome with full diagonal braces, hence there are radial (meridional) girders, circumferential rings and diagonal braces as shown in Figure 4.8. Therefore, Equations (4.1) to (4.8) are applicable to this model with implementing minor changes to them. For instance, Eq. (4.1) could be rewritten as:

$$\theta_i = \left[\frac{2\pi i}{N_n}\right], \; i=1, 2, 3, \ldots, N_n \tag{4.9}$$

where, there is no topological trimming factor (N_t) existing in this model. This model is controlled by three topological parameters (**N_n, N_r & N_s**), 1 shape parameter (R) and 31 sizing parameters, as shown in Table 4.6 and Table 4.7. Other details about generation of nodes are demonstrated in Eqs. (4.3) through (4.8). Hence, the total number of nodes is (**$N_r \times N_n + 1$**), which is equal to 595 for the reference design. The automatic numbering of nodes for this model is shown in Appendix Figure B.1. The finite elements generated for the initial design of model B1 is depicted in Appendix Figure B.2, where the total number of elements recorded for this model is reached 1674 as listed in Table 4.7.

Referring back to the structural discretization mechanism of model A1 and according to Table 4.7, there are 4 main groups containing the 31 structural components of the model. As a result, CG-A represents the radial girders of the model, CG-C stands for the right-inclined braces, CG-D includes the left-inclined braces, and CG-E stands for the circumferential rings. The abovementioned component groups are modelled by their respective dataset modules: DM-A, DM-C, DM-D and DM-E respectively. For instance, the group of meridional girders (CG-A) has modelled by DM-A using S-type I-beams defined in Appendix Table E.1, where CG-A has customized to consist of 5 structural components. Thus, there are 4 templates of component groups (CG-B, CG-F, CG-G & CG-H) left empty without any data, i.e. the number of structural

components for each of these templates is equal to zero. Subsequently, the corresponding dataset modules (DM-B, DM-F, DM-G and DM-H) are left unutilized. Figure 4.8 shows the numbering of structural components for model B1.

Table 4.6 Optimization range for the shape and topological parameters of model B1.

Design variable	**N_n (-)**	**N_r (-)**	**N_s (-)**	**R (m)**
Initial value	54	11	20	30
Lower bound	36	06	10	30
Upper bound	72	16	30	60

Table 4.7 Data for the initial design of model B1.

Number of Nodes		595
Number of Elements		1674
Number of Structural Components		5+11+10+5 = 31
Structural Components	CG-A (Meridional Girders)	05 components modelled by DM-A using 'S20x96'
	CG-B (Empty)	DM-B (Unutilized)
	CG-C (Right-inclined Braces)	11 comps. modelled by DM-C using '9 x 5 x 1/2'
	CG-D (Left-inclined Braces)	10 comps. modelled by DM-D using '9 x 5 x 1/2'
	CG-E (Circumferential Rings)	05 components modelled by DM-E using '9 x 5 x 1/2'
	CG-F (Empty)	DM-F (Unutilized)
	CG-G (Empty)	DM-G (Unutilized)
	CG-H (Empty)	DM-H (Unutilized)

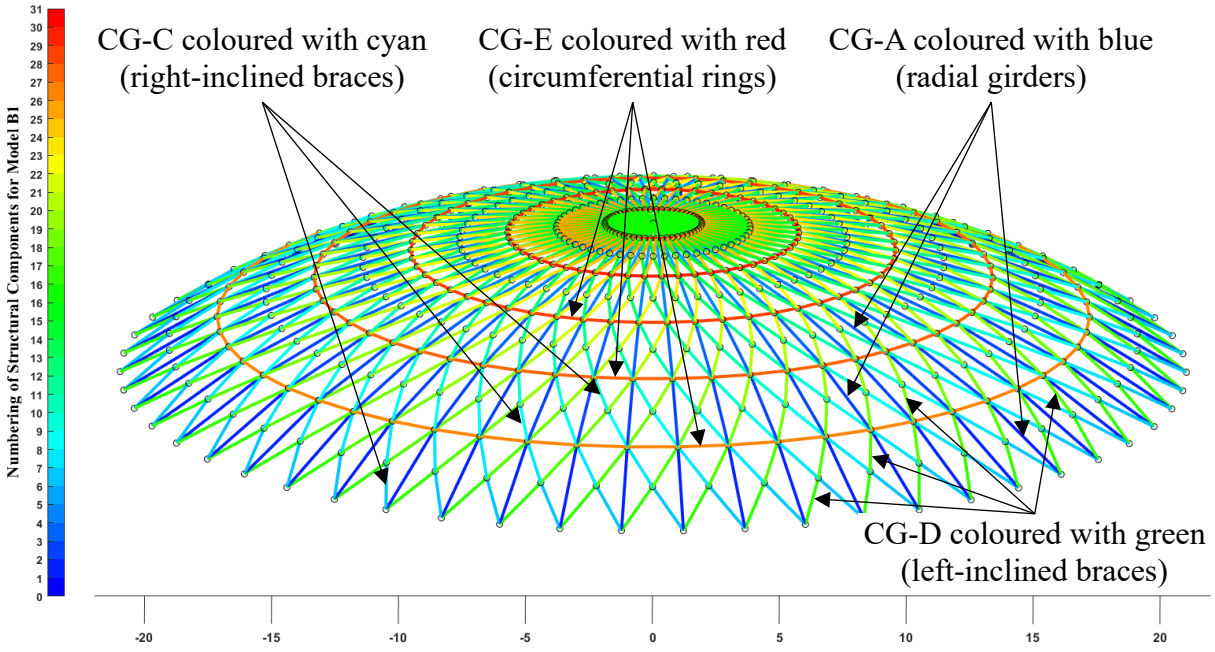

Figure 4.8 Structural component number for the initial design of model B1.

4.5.3 Lamella Single Lattice Dome (Model C1)

The main difference between model C1 and model B1 is attributed to the noticeable topological morphing between the two models, caused by replacing the meridional girders of model B1 by equivalent circumferential elements in model C1. Thus, model C1 has no radial girders, instead it contains a dense mesh of circumferential rings with crossway diagonal braces. An identical configuration of nodes could be seen in the models B1 and C1, hence Eq. (4.9) can be applied for this model. Similarly, Eqs. (4.3) through (4.8) can be exploited to perform the structural modelling for model C1. The set of topological and shape variables for model A1 are listed in Figure 4.9. The total number of nodes counted for the initial design has reached 755, whereas the corresponding number of elements has amounted to 2146.

As noted in Table 4.9, model C1 consists of 37 components allocated over three categories (CG-C, CG-D and CG-E). The structural sections stored in the dataset memory modules are represented by rectangular hollow sections (RHS) as detailed in Appendix Table E.4. Figure 4.9 shows the different structural IDs of model C1 using wide scope of colours as a smart method to avoid the complexity of numbering. Accordingly, the blue refers to the right-inclined braces, the green refers to the left-inclined braces, whereas the yellow refers to the circumferential rings on the outer periphery and the red identifies the circumferential rings closer to the dome hub.

Appendix Figure B.3 illustrate the numbering of nodes for reference design of model C1, whereas Appendix Figure B.4 shows the element numbering for the same model.

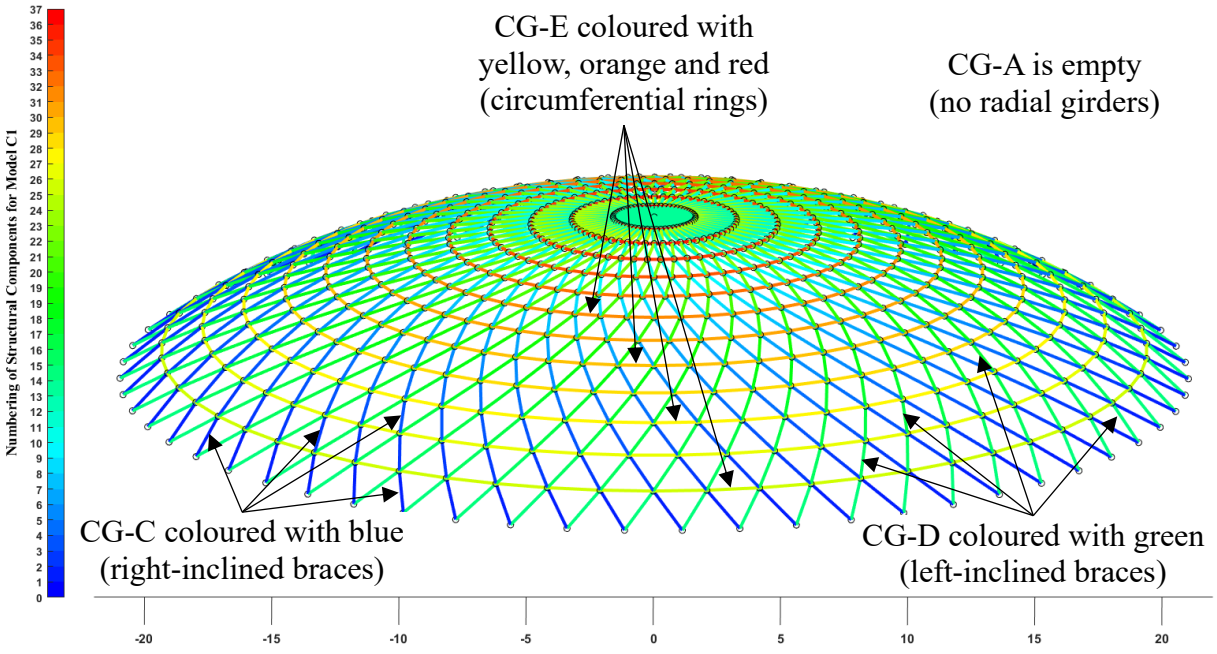

Figure 4.9 Structural component number for the initial design of model C1.

Table 4.8 Optimization range for the shape and topological parameters of model C1.

Design variable	**N_n (-)**	**N_r (-)**	**N_s (-)**	**R (m)**
Initial value	58	13	20	30
Lower bound	36	06	10	30
Upper bound	80	20	30	60

Table 4.9 Data for the initial design of model C1.

Number of Nodes		755
Number of Elements		2146
Number of Structural Components		13+12+12 = 37
Structural Components	CG-A (Empty)	DM-A (Unutilized)
	CG-B (Empty)	DM-B (Unutilized)
	CG-C (Right-inclined Braces)	13 components modelled by DM-C using '9 x 5 x 1/2'
	CG-D (Left- inclined Braces)	12 components modelled by DM-D using '9 x 5 x 1/2'
	CG-E (Circumferential Rings)	12 components modelled by DM-E using '9 x 5 x 1/2'
	CG-F (Empty)	DM-F (Unutilized)
	CG-G (Empty)	DM-G (Unutilized)
	CG-H (Empty)	DM-H (Unutilized)

4.5.4 Hybrid Schwedler-Lamella Single Lattice Dome (Model D1)

This model is hybrid version of models B1 and C1, hence a hybridization parameter termed as topological morphing factor (N_m) will be added as design parameter to the set of integer design parameters defined in Table 4.6. In fact, N_m controls the process of creating meridional or circumferential girders in the basic rhombic grid of the dome roof lattice, i.e. it affects the structural configuration of the dome whether generated as Schwedler, Lamella or blend of them. This process could be further illustrated by introducing the dummy variable called topological morphing fraction (λ_m), which is directly correlated to the integer variable (N_m) as stated in Eq. (4.10).

$$\lambda_m = 0.05 N_m \tag{4.10}$$

The fraction (λ_m) plays a significant role in deciding the appropriate morphological shape of dome roof lattice. The last statement can be interpreted logically in the following formula:

$$\begin{Bmatrix} if\ (\lambda_m L_{circum}) < L_{merid} \rightarrow L_{merid} = 0\ (Lamella) \\ elseif\ (\lambda_m L_{circum}) \geq L_{merid} \rightarrow L_{circum} = 0\ (Schwedler) \end{Bmatrix} \tag{4.11}$$

where, L_{merid} and L_{circum} are the virtual distances measured along the meridional and circumferential lines respectively for each rhombic cell in the basic grid of dome roof as shown in Figure 4.10. Thus, Eq. (4.11) specifies the appropriate morphological shape for the dome roof frame whether Schwedler, Lamella, or hybrid version of them. The concept is based on

creating circumferential elements to establish for Lamella patterns or creating radial elements to establish for Schwedler patterns instead, where the process can be implemented locally and in an axisymmetric manner to enhance the possibility of creating a hybrid version of the two parent configurations.

The shape and topological variables for model D1 are given in Table 4.10. The same approach, as used to create the geometries in models A to C, is adopted for this model. Here the total number of nodes stated in Appendix Figure B.5 and Table 4.11 is 529. The finite elements created for this model is shown in Appendix Figure B.6, which indicates that the number of elements is 1488 as listed in Table 4.11.

There are 31 structural components allocated over 4 main groups CG-A, CG-B, CG-C and CG-D. The components belonging to CG-A are modelled using the cross-sectional specifications found in DM-A, which are the set of universal beams 'UB 356x171x45' introduced by British standard fixed in Appendix Table E.7. The data of component groups for this model are given in Table 4.11. In this aspect, Figure 4.11 shows the ID numbers for the structural components of this model, where the upper numeric value of the colour bar stands for the ID number for the final component in the model represented by the innermost circumferential ring.

Table 4.10 Optimization range for the shape and topological parameters of model D1.

Design variable	**N_n (-)**	**N_r (-)**	**N_s (-)**	**N_m (-)**	**R (m)**
Initial value	48	11	20	35	45
Lower bound	32	06	10	20	30
Upper bound	64	16	30	50	60

Table 4.11 Data for the initial design of model D1.

Number of Nodes		529
Number of Elements		1488
Number of Structural Components		3+10+10+8 = 31
Structural Components	CG-A (Meridional Girders)	03 components modelled by DM-A using 'UB 356x171x45'
	CG-B (Right-inclined Braces)	10 components modelled by DM-B using '9 x 5 x 1/2'
	CG-C (Left- inclined Braces)	10 components modelled by DM-C using '9 x 5 x 1/2'
	CG-D (Circumferential Rings)	08 components modelled by DM-D using '9 x 5 x 1/2'
	CG-E (Empty)	DM-E (Unutilized)
	CG-F (Empty)	DM-F (Unutilized)
	CG-G (Empty)	DM-G (Unutilized)
	CG-H (Empty)	DM-H (Unutilized)

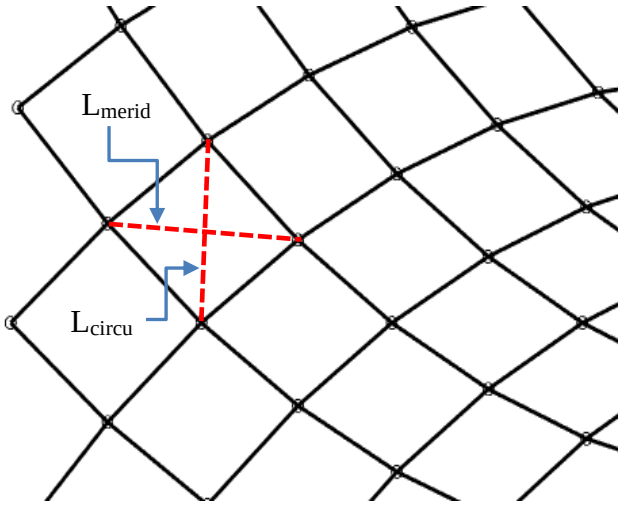

Figure 4.10 Graphical illustration of the morphological elements influencing the formation of the hybrid SL configuration (model D1).

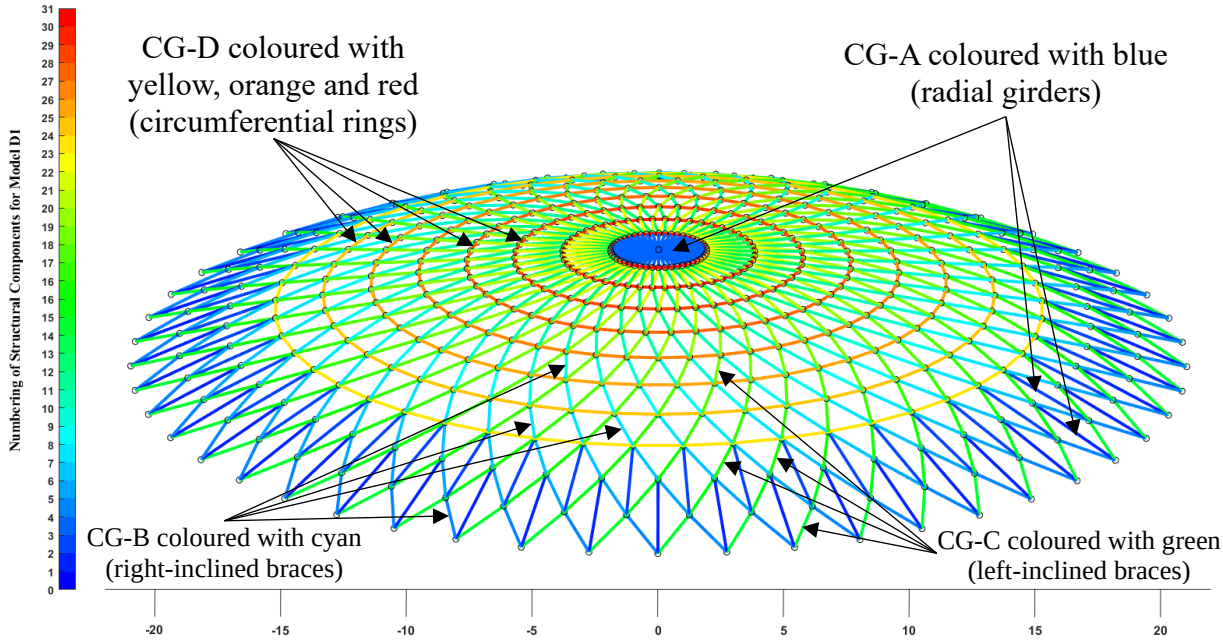

Figure 4.11 Structural component number for the initial design of model D1

4.5.5 Geodesic Single Lattice Dome (Model E1)

This model has a completely different configuration to those for the previous models, where the model is recognized by presence of basic polygon with number of sides (N_n), constructed at the dome hub to represent the crown of the dome roof frame. Accordingly, the number of nodes (N_n) for previous models could be replaced by the number of sides for the basic polygon of this model. The number of sides for each ring is directly proportional to the ring number based on assuming that the counting of rings starts from the dome hub towards the periphery. However, the integer parameter (N_r), standing for the number of rings, is following the same

formulation as the previous models, and the topological spacing factor (N_s) is calculated in the same procedure as the last model. The topological parameters N_m and N_t are not in this model. The design is divided therefore into N_n identical segments and is symmetric under axial rotation of $\theta_{basic} = \left[\frac{2\pi}{N_n}\right]$. The node positions in segment k (k=1, 2, 3, …, N_n) given by Eq. (4.1) can be reformulated as:

$$\theta_{i,j}^{k} = (i-1)\left[\frac{\theta_{basic}}{j}\right] + (k-1) * \theta_{basic} \quad (4.12)$$

(i=1, 2, 3, …, j), (j=1, 2, 3, …, N_r), (k=1, 2, 3, …, N_n)

where, $\theta_{i,j}^{k}$ is the angular position for node located at geodesic ring radius r_j within k^{th} side of the basic polygon, whereas i is a counter extending from 1 to the number of the current circumferential ring (j), i.e. i is an integer counter ranging over the series of nodes belonging to the same circumferential ring (j) and existing in the same side of the basic polygon of geodesy. For instance, substituting i=1, j=1 and k=1 into Eq. (4.12) will result in zero value for angular position, i.e. ($\theta_{1,1}^{1}$=0), which represents the angle of the fundamental radial line of the geodesy. Also, j is an integer counter for the circumferential rings, r_j is the radius of the circumferential ring j as defined in Eq. (4.4). See the previous note.

Hence, Eqs. (4.6) and (4.7) can be reformulated as stated in Eqs. (4.13) and (4.14) respectively.

$$x_{i,j}^{k} = r_j \cos\theta_{i,j}^{k} \quad (4.13)$$

$$y_{i,j}^{k} = r_j \sin\theta_{i,j}^{k} \quad (4.14)$$

where, $x_{i,j}^{k}$ & $y_{i,j}^{k}$ are the Cartesian coordinates for certain node corresponding to the radial position (r_j) and the angular position ($\theta_{i,j}^{k}$). Eqs. (4.4) through (4.8) can be applied directly to this model without any change. The shape and topological variables of model E1 are shown in Table 4.12. The nodes depicted in Appendix Figure B.7 are used to create the geometry of the initial design of model E1 shown clearly in Appendix Figure B.8. The number of nodes developed by the initial design of model E1 is 727, whereas the number of elements used in this structural analysis is 1936. There are 41 structural components existing in this model categorized over 4 structural sets (CG-A, CG-B, CG-C and CG-D). The first group is modelled by DM-A using 'S15x50', whereas the other three groups are modelled by DM-B, DM-C and DM-D as explained in Table 4.13. Figure 4.12 shows the numbering of the structural components included in model E1.

Table 4.12 Optimization range for the shape and topological parameters of model E1.

Design variable	**N_n (-)**	**N_r (-)**	**N_s (-)**	**R (m)**
Initial value	11	11	20	30
Lower bound	06	06	10	30
Upper bound	16	16	30	60

Table 4.13 Data for the initial design of model E1.

Number of Nodes		727
Number of Elements		1936
Number of Structural Components		11+10+10+10 = 41
Structural	CG-A (Meridional Girders)	11 components modelled by DM-A using 'S15x50'
	CG-B (Right-inclined Braces)	10 components modelled by DM-B using '9 x 7 x 1/2'
	CG-C (Left- inclined Braces)	10 components modelled by DM-C using '9 x 7 x 1/2'
	CG-D (Circumferential Rings)	10 components modelled by DM-D using '9 x 7 x 1/2'
	CG-E (Empty)	DM-E (Unutilized)
	CG-F (Empty)	DM-F (Unutilized)
	CG-G (Empty)	DM-G (Unutilized)
	CG-H (Empty)	DM-H (Unutilized)

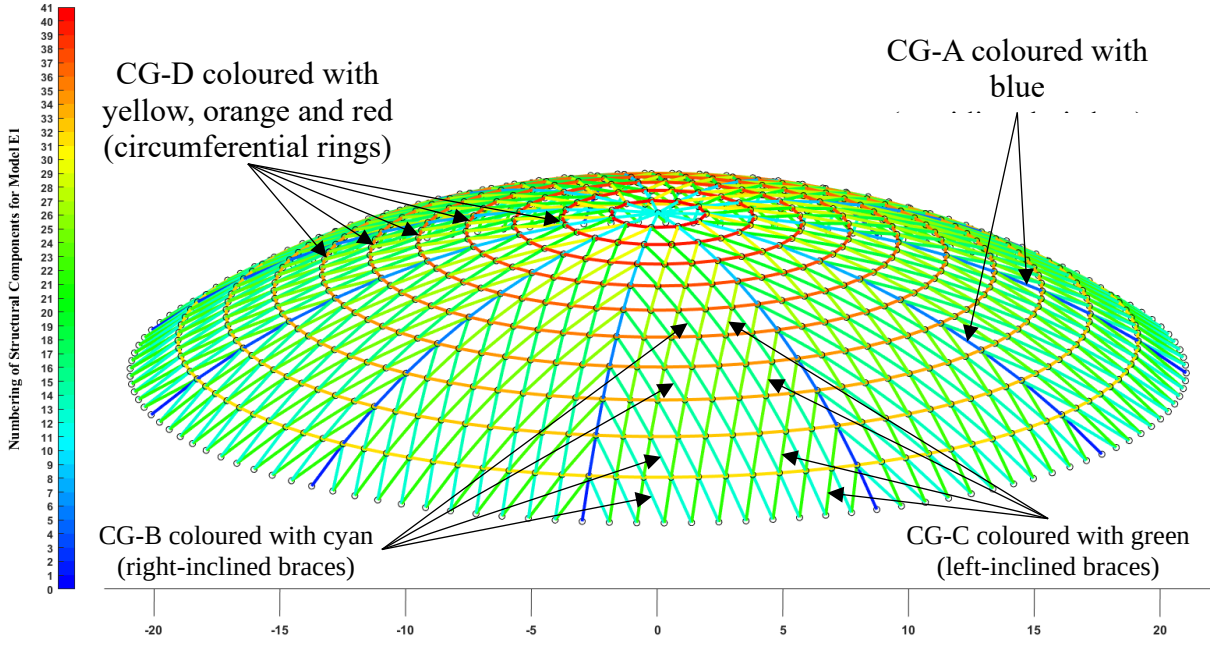

Figure 4.12 Structural component number for the initial design of model E1.

4.5.6 Trimmed Ribbed Double Lattice Dome (Model A2)

Double lattice models are characterized by having two layers of lattices (upper and lower) along with in-between connecting braces as sketched in Figure 4.13. Therefore, in addition to the continuous design parameters ($\overrightarrow{DV_{con}}$), considered in the single lattice models (models A1 to E1), two extra shape variables will be added to the vector of continuous shape variables ($\overrightarrow{DV_{con}}$) of the double lattice models in order to control the shape the in-between space, i.e. the space bounded by the primary and secondary layers of the dome. These two extra variables are:

- Height Fraction (η=H2/H1): this parameter calculates the vertical height (H2) with respect to the primary or nominal height of the tank (H1), where H2 is the vertical height measured from the tank bottom to a point determined by intersecting the lower lattice with the cylindrical shell of the tank.
- Dome Radius Ratio (υ=R2/R1): this parameter determines the radius of curvature for the lower lattice (R2) as function of curvature radius of the upper lattice (R1), where R1 is the primary or nominal radius of curvature for the dome.

Figure 4.13 details the relevant shape parameters existing in the double lattice modelling of the dome roof. C1, C2 are the curvature centres for the upper and lower lattices respectively. ΔS is the gap between the upper and lower lattices along the central axis of the tank (it is a function of η and υ).

$$\Delta S = R1 + z_{dome\_offset1} - \left(R2 + z_{dome\_offset2}\right) \tag{4.15}$$

$$z_{dome\_offset1} = H1 - \left(\sqrt{R1^2 - r^2}\right) \tag{4.16}$$

$$z_{dome\_offset2} = H2 - \left(\sqrt{R2^2 - r^2}\right) \tag{4.17}$$

By substituting Eqs. (4.16) and (4.17) into (4.15), the gap between layers at the hub region of the tank can be rewritten as:

$$\begin{aligned}\Delta S &= R1 + H1 - \left(\sqrt{R1^2 - r^2}\right) - R2 - H2 + \left(\sqrt{R2^2 - r^2}\right) \\ &= R1 - R2 + H1 - H2 - \left(\sqrt{R1^2 - r^2}\right) + \left(\sqrt{R2^2 - r^2}\right)\end{aligned} \tag{4.18}$$

ΔS cannot be negative, otherwise the design will lose its consistency and will be impractical. As consequence, a new design constraint has been introduced for the double lattice models, which ensures ΔS is positive:

$$\Delta S \geq 0.04 \tag{4.19}$$

Eq. (4.19) represents geometrical constraint for the double lattice modelling. If certain design point has dissatisfied the term in Eq. (4.19), it could be healed through adjusting one of the parameters mentioned in Eq. (4.18). Accordingly, it is recommended to select H2 or R2 to implement this task. Currently, H2 has been chosen to perform this task, where H2 must be

recalculated such that to achieve the lower bounds of Eq. (4.19), i.e., the inner lattice is lowered so that the constraint is met.

The number of nodes for model A2 is equal to 1474 as indicated in Table 4.15. Appendix Figure B.9 shows the nodes of the reference design of model A2, whereas the elements of the same model are shown in Appendix Figure B.10. On the other hand, Figure 4.14 shows the ID number for the structural components involved. The data of the model are summarized in Table 4.15, where the overall number of elements is 4353, and the number of components is 102 subdivided into 7 groups, where the template CG-F is left empty. The interfacing mechanism between the model component groups CGs and the relevant DMs illustrated in Figure 4.4 is applicable to this model.

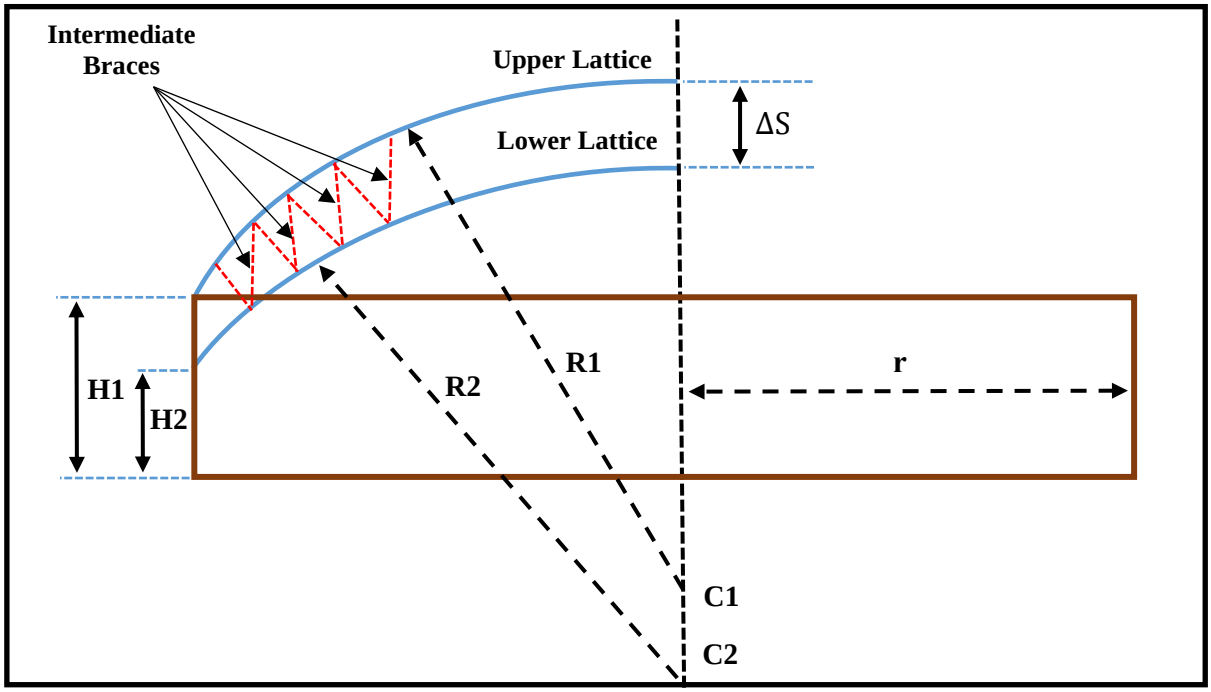

Figure 4.13 Simple sketch for double lattice model demonstrating the extra shape variables added to the continuous set of design parameters.

Table 4.14 Optimization range for the shape and topological parameters of model A2.

Design variable	N_n (-)	N_r (-)	N_s (-)	N_t (-)	R (m)	η (-)	ʊ (-)
Initial value	32	15	20	10	30	0.95	1.10
Lower bound	24	10	10	4	30	0.85	0.90
Upper bound	40	20	30	16	60	0.95	1.10

Table 4.15 Data for the initial design of model A2.

Number of Nodes		1474
Number of Elements		4353
Number of Structural Components		30+14+14+28+14+2 = 102
Structural	CG-A (Meridional Girders)	30 comps. modelled by DM-A using '8 x 6 x 3/8'
	CG-B (Right-inclined Braces)	14 comps. modelled by DM-B using 'L4 x 4 x 3/4'
	CG-C (Left- inclined Braces)	14 comps. modelled by DM-C using 'L4 x 4 x 3/4'
	CG-D (Circumferential Rings)	28 comps. modelled by DM-D using '6 x 6 x 1/4'
	CG-E (in-between Braces)	14 comps. modelled by DM-E using '6.125 x 0.375'
	CG-F (Empty)	DM-F (Unutilized)
	CG-G (Central Hub Beams)	02 comps. modelled by DM-G using '6.125 x 0.375'
	CG-H (Empty)	DM-H (Unutilized)

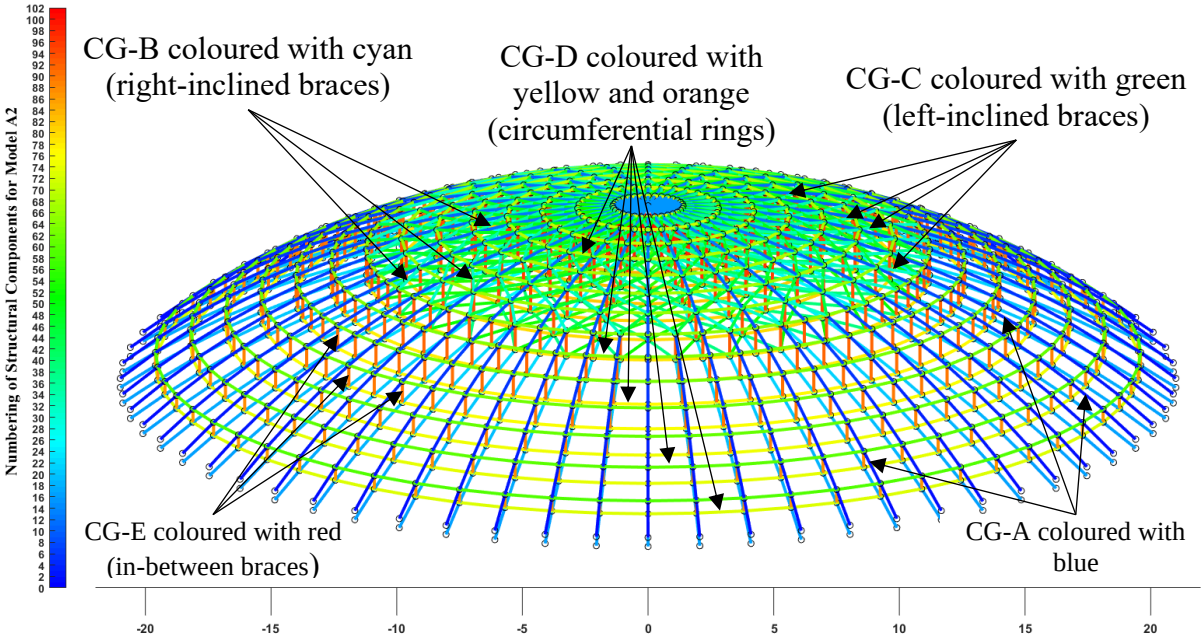

Figure 4.14 Structural component number for the initial design of model A2.

4.5.7 Schwedler Double Lattice Dome (Model B2)

The difference between model B1 and model B2 is attributed to the number of lattices existing in the model. Thus, the characteristic design parameters of the double lattice modelling (ɳ & ʊ) will be added to the set of parameters mentioned in Table 4.6 to produce the new set of design parameters for model B2 as shown in Table 4.16. The number of nodes noticed for this model (see Appendix Figure B.11) counts to 992, whereas the corresponding number of elements counts to 4186 as shown in Appendix Figure B.12. Model B2 consists of 94 structural components categorized over 7 groups as summarized in Table 4.17. These components are numbered in Figure 4.15. It is observed that the meridional girders are modelled using isometric beam section ('ISMB225') designed by Indian standard as indicated in Table E.8.

Table 4.16 Optimization range for the shape and topological parameters of models B2 and C2.

Design variable	**N_n (-)**	**N_r (-)**	**N_s (-)**	**R (m)**	**η (-)**	**υ (-)**
Initial value	45	11	20	30	0.95	1.10
Lower bound	30	06	10	30	0.85	0.90
Upper bound	60	16	30	60	0.95	1.10

Table 4.17 Data for the initial design of model B2.

Number of Nodes		992
Number of Elements		4186
Number of Structural Components		22+20+20+10+10+11+1 = 94
Structural Components	CG-A (Meridional Girders)	22 comps. modelled by DM-A using 'ISMB225'
	CG-B (Right-inclined Braces)	20 comps. modelled by DM-B using '9 x 7 x 1/2'
	CG-C (Left- inclined Braces)	20 comps. modelled by DM-C using '9 x 7 x 1/2'
	CG-D (Circumferential Rings)	10 comps. modelled by DM-D using 'ISLC200'
	CG-E (Shallow Slope in-between Braces)	10 comps. modelled by DM-E using '5 x 5 x 1/2'
	CG-F (Deep Slope in-between Braces)	11 comps. modelled by DM-F using '5 x 5 x 1/2'
	CG-G (Central Hub Beam)	01 comps. modelled by DM-G using '6.125 x 0.375'
	CG-H (Empty)	DM-H (Unutilized)

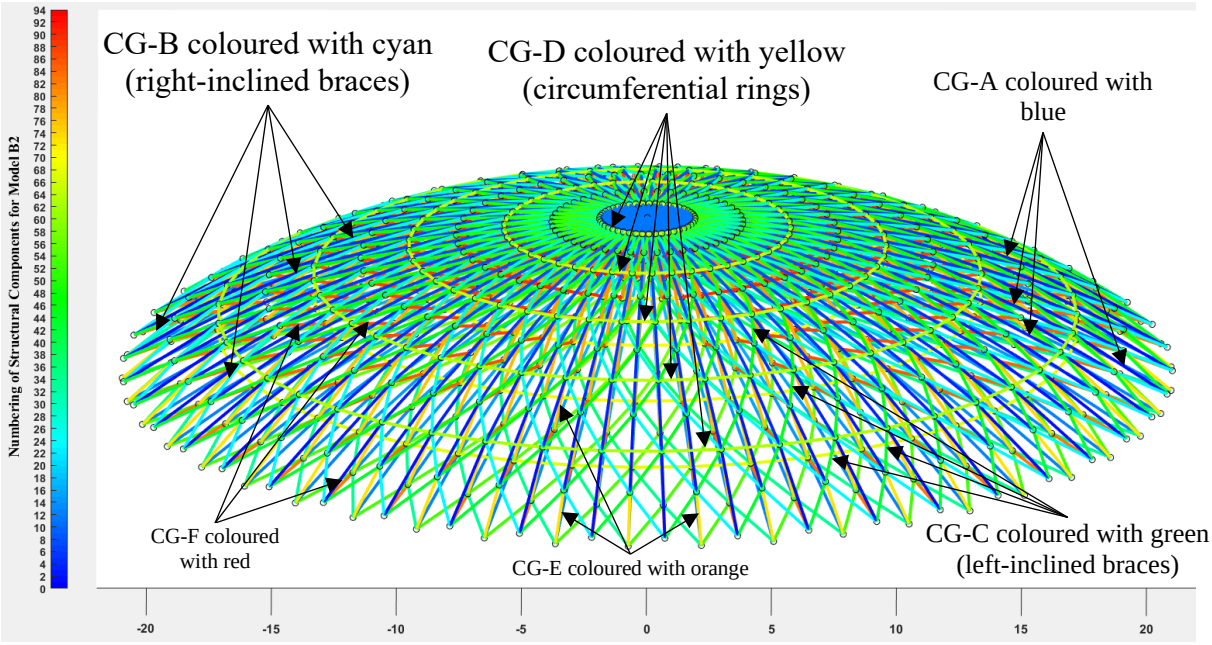

Figure 4.15 Structural component number for the initial design of model B2.

4.5.8 Lamella Double Lattice Dome (Model C2)

There is a significant difference between the number of elements for models B2 and C2, i.e. the number of elements for model C2 is 3736 as fixed in Table 4.18, whereas the number of elements generated for model B2 is 4186 for the same number of nodes. The configuration of nodes for this model is shown in Appendix Figure B.11, i.e., the same as in the Schwedler double lattice, whereas the corresponding finite elements are illustrated in Appendix Figure B.13.

The model is initially designed to consist of 84 components as described in Figure 4.16, they are incorporated with 7 component groups as demonstrated in Table 4.18. Hence, the only unused template is DM-H corresponding to CG-H.

Table 4.18 Data for the initial design of model C2.

Number of Nodes		992
Number of Elements		3736
Number of Structural Components		2+20+20+20+10+11+1 = 84
Structural Components	CG-A (Meridional Girders)	02 comps. modelled by DM-A using 'ISMB225'
	CG-B (Right-inclined Braces)	20 comps. modelled by DM-B using '9 x 7 x 1/2'
	CG-C (Left- inclined Braces)	20 comps. modelled by DM-C using '9 x 7 x 1/2'
	CG-D (Circumferential Rings)	20 comps. modelled by DM-D using 'ISLC200'
	CG-E (Shallow Slope in-between Braces)	10 comps. modelled by DM-E using '5 x 5 x 1/2'
	CG-F (Deep Slope in-between Braces)	11 comps. modelled by DM-F using '5 x 5 x 1/2'
	CG-G (Central Hub Beam)	01 comps. modelled by DM-G using '6.125 x 0.375'
	CG-H (Empty)	DM-H (Unutilized)

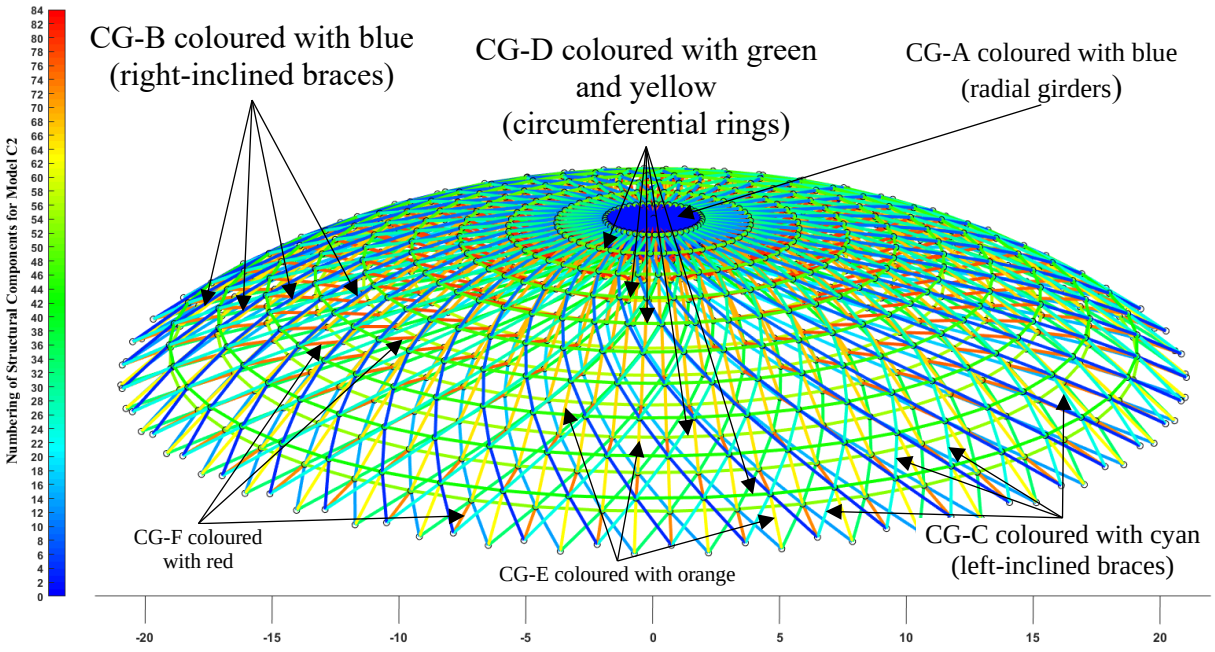

Figure 4.16 Structural component number for the initial design of model C2.

4.5.9 Hybrid Schwedler-Lamella Double Lattice Dome (Model D2)

A hybrid version of models B2 and C2 using the topological morphing parameters in Eqs. (4.10) and (4.11) is used to generate the nodes and create the geometry to perform the structural analysis of the model. Accordingly, the program was created 1058 nodes with two layers arranged in staggered stacking (i.e., rotated a half interval), as shown in Appendix Figure B.14, which are used to generate 3985 elements as depicted in Appendix Figure B.15. The initial design is discretized into 84 parts controlled by 7 separated component groups as summarized in Table 4.20. The radial beams are modelled using American commercial sections 'S15x50'. Figure 4.17 illustrates the numbering of structural components for the initial design of model D2. The colours bar range suggests that there are 84 components managed by 7 CGs. Consequently, the primary blue lines stand for the radial girders, the lighter blue lines represent the right-inclined braces, the cyan-coloured lines represent the left-inclined braces, the green lines denote the circumferential rings, the yellow lines refer to the shallow slope in-between braces, the orange lines refer to the deep slope in-between braces, and the primary red colour identifies the central in-between beam of the dome. Knowing that the structural components in each group, except the in-between braces, are identically distributed over the two layers in axisymmetric form.

Table 4.19 Optimization range for the shape and topological parameters of model D2.

Design variable	**N_n (-)**	**N_r (-)**	**N_s (-)**	**N_m (-)**	**R (m)**	**η (-)**	**$\mho$ (-)**
Initial value	48	11	20	35	30	0.90	1.00
Lower bound	32	06	10	20	30	0.85	0.90
Upper bound	64	16	30	50	60	0.95	1.10

Table 4.20 Data for the initial design of model D2.

Number of Nodes		1058
Number of Elements		3985
Number of Structural Components		6+20+20+16+10+11+1 = 84
Structural Components	CG-A (Meridional Girders)	06 comps. modelled by DM-A using 'S15x50'
	CG-B (Right-inclined Braces)	20 comps. modelled by DM-B using '9 x 7 x 1/2'
	CG-C (Left- inclined Braces)	20 comps. modelled by DM-C using '9 x 7 x 1/2'
	CG-D (Circumferential Rings)	16 comps. modelled by DM-D using '9 x 7 x 1/2'
	CG-E (Shallow Slope in-between Braces)	10 comps. modelled by DM-E using '5 x 5 x 1/2'
	CG-F (Deep Slope in-between Braces)	11 comps. modelled by DM-F using '5 x 5 x 1/2'
	CG-G (Central Hub Beam)	01 comps. modelled by DM-G using '6.125 x 0.375'
	CG-H (Empty)	DM-H (Unutilized)

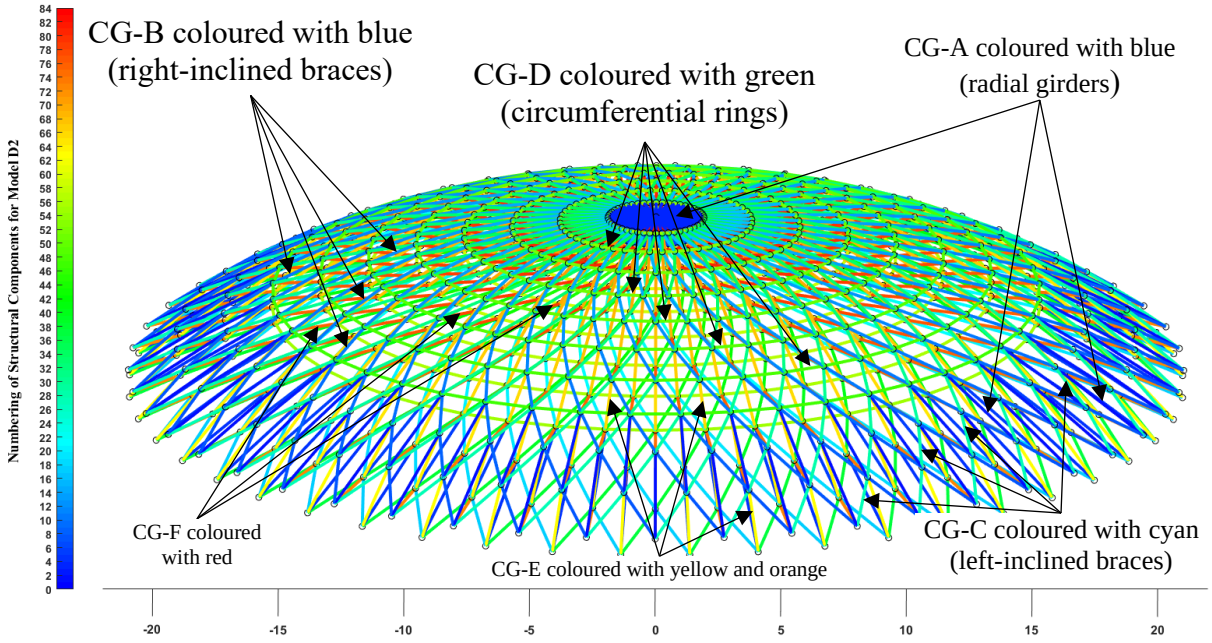

Figure 4.17 Structural component number for the initial design of model D2.

4.5.10 Geodesic Double Lattice Dome (Model E2)

This model is constructed as two geodesic lattices placed in straight stacking. Thus, Eqs. (4.12) through (4.14) are applicable to this model. The design parameters are listed in Table 4.21. The initial design of model E2 is viewed in this section, where the configuration of nodes is shown in Appendix Figure B.16. There are 812 nodes. The elements are shown in Appendix Figure B.17. The number of elements reached 2368 distributed over 75 components as reported in Table 4.22. They are contained in 6 structural groupings. The individual components are numbered in Figure 4.18.

Table 4.21 Optimization range for the shape and topological parameters of model E2.

Design variable	**N_n (-)**	**N_r (-)**	**N_s (-)**	**R (m)**	**η (-)**	**υ (-)**
Initial value	09	09	20	30	0.95	1.10
Lower bound	06	06	10	30	0.85	0.90
Upper bound	12	12	30	60	0.95	1.10

Table 4.22 Data for the initial design of model E2.

Number of Nodes		812
Number of Elements		2368
Number of Structural Components		18+16+16+16+7+2 = 75
Structural Components	CG-A (Meridional Girders)	18 comps. modelled by DM-A using '9 x 7 x 1/2'
	CG-B (Right-inclined Braces)	16 comps. modelled by DM-B using '9 x 7 x 1/2'
	CG-C (Left- inclined Braces)	16 comps. modelled by DM-C using '9 x 7 x 1/2'
	CG-D (Circumferential Rings)	16 comps. modelled by DM-D using '9 x 7 x 1/2'
	CG-E (Braces in-between Layers)	07 comps. modelled by DM-E using '6.125 x 0.375'
	CG-F (Empty)	DM-F (Unutilized)
	CG-G (Empty)	DM-G (Unutilized)
	CG-H (Central Hub Beams)	02 comps. modelled by DM-H using '6.125 x 0.375'

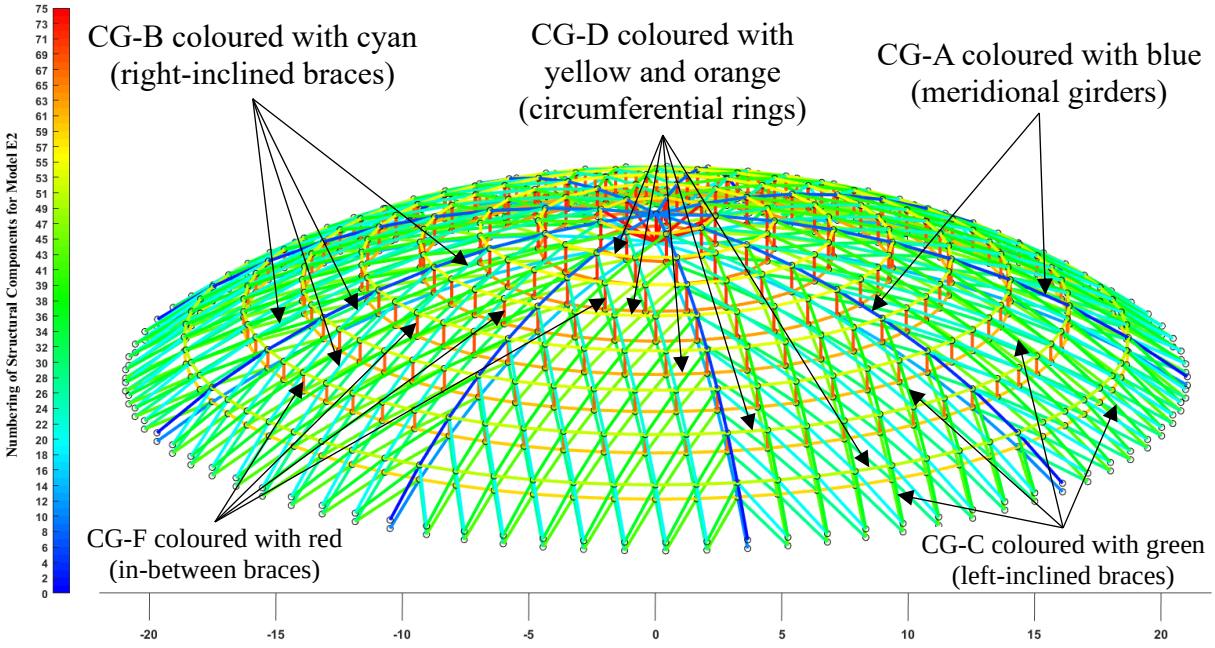

Figure 4.18 Structural component number for the initial design of model E2.

4.6 Integrated Modelling

In this section, 4 kinds of single lattice domed frames will be viewed, as they are modelled using ANSYS 18.1. They are selected to be conformable with the single lattice models mentioned in section 4.5, excluding model D1. Therefore, the integrated models will be labelled with the same sequence of letters adopted in the simplified models, suffixed by number 3 instead of the numbers 1 and 2 adopted for the simplified models. For instance, trimmed ribbed integrated dome model will be labelled as model A3 in reference to its relevance to model A1 as counterpart simplified model. 3D shear capability Timoshenko beam element, existing in ANSYS 18.1 (BEAM189), will be adopted in the structural analysis of the roof frame members.

4.6.1 Trimmed Ribbed Single Lattice Dome (Model A3)

The reference design of this model consists of 40 major meridional girders, 40 minor meridional girders, 10 circumferential rings and the crown structure. Table 4.23 presents the statistical data for the geometric and finite element modelling for the basic design of model A3, where the number of keypoints is 920, the number of line bodies shows 250, the number of nodes is 7145 and the number of elements has reached 8792.

The design variables are classified, according to their mathematical nature, into three groups: integer ($\overrightarrow{\mathrm{DV}_{\mathrm{int}}}$), discrete ($\overrightarrow{\mathrm{DV}_{\mathrm{dis}}}$) and continuous ($\overrightarrow{\mathrm{DV}_{\mathrm{con}}}$) variables. Since this model has single lattice, the shape variables are restricted to the dome radius (R) as stated in section 4.2.

Table 4.23 Data of the reference design of model A3.

Whole Tank Structure	Num. of Nodes	112531
	Num. of Elements	41332
	Num. of Solid Bodies	13+253 = 266
	Structural Mass	520.68 tonnes
Roof Supporting Frame	Num. of Keypoints (Vertices)	920
	Num. of Line Bodies (Edges)	250
	Num. of Nodes	7145
	Num. of Elements	8792
	Num. of Structural Components	4+2+5+1+1 = 13
	Structural Mass	200.4 tonnes
Configuration of Structural Components for the Roof Supporting Frame	CG-A (Major Meridional Girders)	04 comps modelled by DM-A using 'S24x90'
	CG-B (Minor Meridional Girders)	02 comps. modelled by DM-B using 'S15x42.9'
	CG-C (Circumferential Rings)	05 comps modelled by DM-C using 'C8x18.75'
	CG-D (Crown Gussets)	01 comp. modelled by DM-D using plate element with dimensions '2.5 x1.05 x0.021'
	CG-E (Crown Shell)	01 comp. modelled by DM-E using plate element with dimensions '2π*2.5 x1.05 x 0.0375'
	CG-F (Empty)	DM-F (Unutilized)
	CG-G (Empty)	DM-G (Unutilized)
	CG-H (Empty)	DM-H (Unutilized)

The topological variables are divided into two groups: integer ($\mathbf{N_{Gussets}}$, $\mathbf{N_{Girders}}$ and $\mathbf{N_{Rings}}$) and continuous, which are listed in Table 4.24 and defined in the following set of equations:

$$\mathrm{Seg}_A = \mathrm{Frac}_A * \mathrm{L_{PG}} \tag{4.20}$$

$$\mathrm{Seg_B} = \mathrm{Frac_B} * (\mathrm{L_{PG}} - \mathrm{Seg_A}) \tag{4.21}$$

$$\mathrm{Seg}_C = \mathrm{Frac_C} * \left(\mathrm{L_{PG}} - (\mathrm{Seg_A} + \mathrm{Seg}_B)\right) \tag{4.22}$$

$$\mathrm{L_{SG}} = (\mathrm{Seg}_E + \mathrm{Seg}_F) = (\mathrm{Seg}_C + \mathrm{Seg}_D) \tag{4.23}$$

where, the primary meridional girder with arc length $\mathrm{L_{PG}}$, defined in Eq. (4.3), is subdivided into four segments with meridional lengths (Seg_A, Seg_B, Seg_C and Seg_D). Accordingly, the

secondary radial girder with length L_{SG} is subdivided into two segments ($Seg_E + Seg_F$), which are equivalent in length to the last two segments of L_{PG} ($Seg_C + Seg_D$). Therefore, $Frac_A$, $Frac_B$ and $Frac_C$ are dimensionless topological design parameters used to control the arc lengths of the local segments (Seg_A, Seg_B, Seg_C, and Seg_D) and the arc length of the secondary girder L_{SG}. The nondimensional representation for the set of continuous topological design variables existing within these local regions (Seg_A, Seg_B, Seg_C, and Seg_D) is:

$$Frac_{i,j} = d_{i,j}/Seg_i\,,\quad i \in \{A,B,C,D\},\quad j \in \{1,2\} \tag{4.24}$$

They are constrained by the geometrical constraint.

$$0.35 * L_{PG} \le L_{SG} \le 0.70 * L_{PG} \tag{4.25}$$

where, $Frac_{i,j}$ is the fraction of the meridional distance $d_{i,j}$ to the meridional length of the i^{th} segment (Seg_i), as illustrated in Figure 4.19. Table 4.24 lists the optimization range for the shape and topological variables of model A3.

Considering sizing parameters of the model, model A3 has subdivided into 13 structural components as summarized in Table 4.23. This executed as 4 segments (A, B, C and D) for the primary meridional girders, 2 segments (E and F) for the secondary meridional girders, 5 groups (A, B, C, D and E) for the circumferential rings, and the crown itself has subdivided into two components, crown gussets and crown rings.

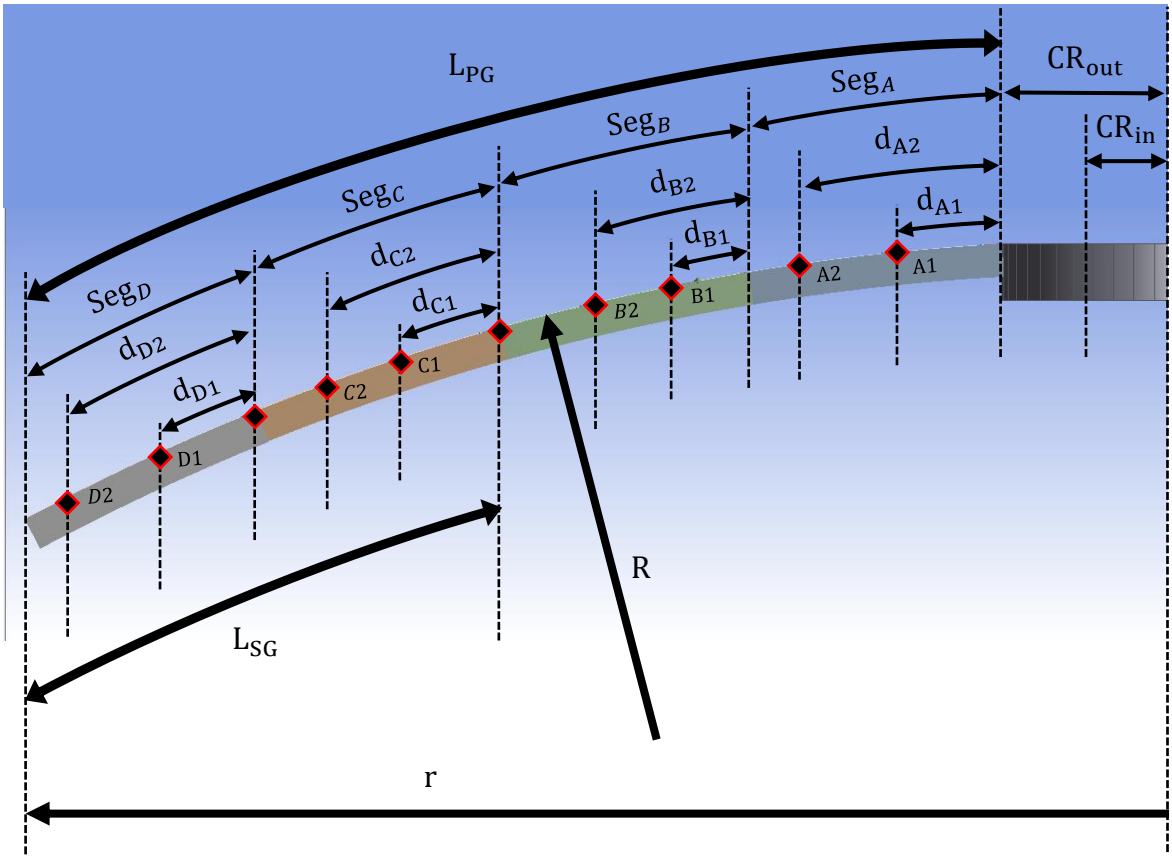

Figure 4.19 Shape and topological parameters for the basic design of model A3.

Table 4.24 Optimization range for the shape and topological parameters of model A3.

Design variable	Initial Value	Lower Bound	Upper Bound
$N_{Gussets}$ [-]	40	30	50
$N_{Girders}$ [-]	40	32	48
N_{Rings} [-]	10	5	10
R [m]	45	30	60
CR_{out} [m]	2.5	1	3.5
CR_{in} [m]	1.25	0.2	3
$Frac_{A}$ [-]	0.25	0.2	0.3
$Frac_{B}$ [-]	0.33	0.3	0.4
$Frac_{C}$ [-]	0.50	0.4	0.6
$Frac_{A1}$ [-]	0.4	0.4	0.6
$Frac_{A2}$ [-]	0.8	0.7	0.8
$Frac_{B1}$ [-]	0.2	0.2	0.3
$Frac_{B2}$ [-]	0.6	0.4	0.6
$Frac_{C1}$ [-]	0.4	0.4	0.6
$Frac_{C2}$ [-]	0.7	0.7	0.8
$Frac_{D1}$ [-]	0.4	0.4	0.6
$Frac_{D2}$ [-]	0.8	0.7	0.8

A. Finite Element Model

The finite element form for the initial design of model A3 is illustrated in Figure 4.20. According to Table 4.23, the crown is modelled using plate elements for this model. Excluding the plate structure of the crown, the number of nodes for the roof beams is equal to 3401, whereas the corresponding elements has reached 4653.

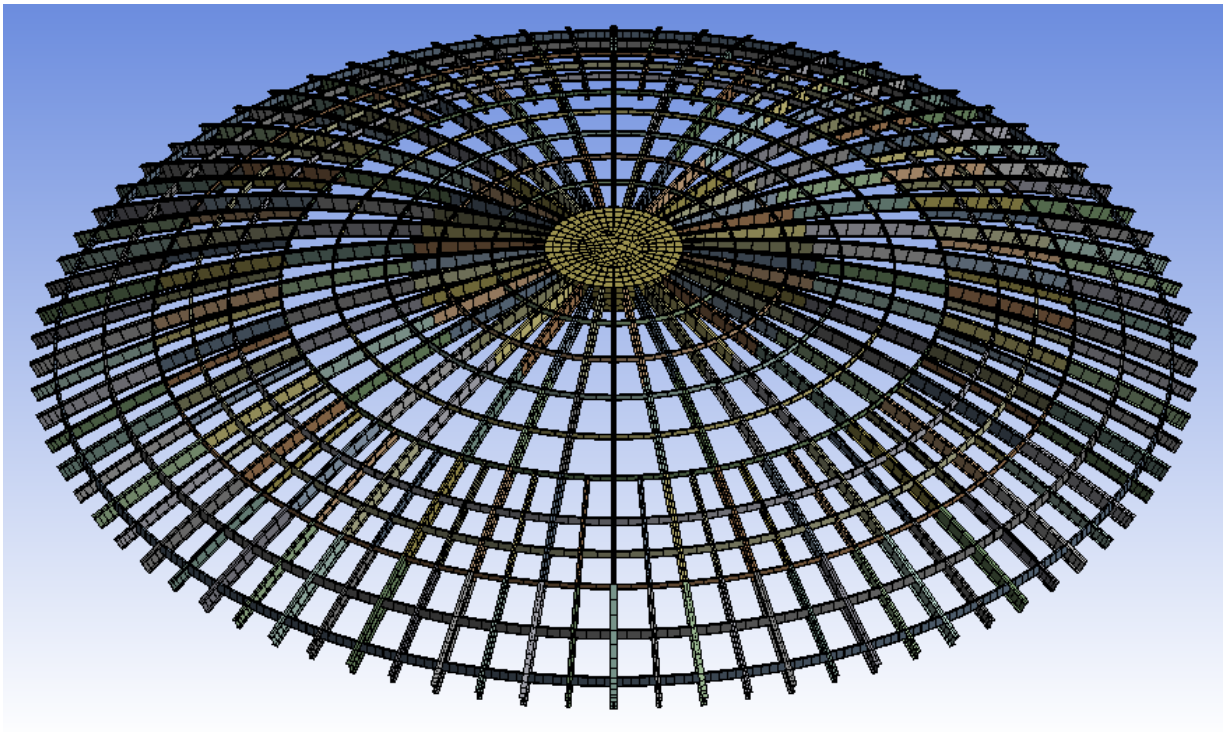

Figure 4.20 Finite element configuration for the basic design of model A3.

B. Identification of Structural Components

The different structural groups for the reference design of model A3 are shown in Figure 4.21. As summarized in Table 4.23, major meridional girders are managed by the component group CG-A and modelled by the dataset module DM-A using 'S24x90', minor meridional Girders are modelled by DM-B using 'S15x42.9', circumferential rings are modelled by DM-C using 'C8x18.75', and the crown components are modelled by DM-D and DM-E for the crown gussets and shell respectively. The only sizing variables for the plate elements considered in the crown modelling are the set of thicknesses and the crown depth, which can be selected from predefined discrete set of values as follow:

1. From 0.7 m to 1.4 m with step 0.027 m assigned for the crown depth.
2. From 0.01 m to 0.032 m with step 0.0008 m assigned for the crown gusset thickness.
3. From 0.015 m to 0.06 m with step 0.0017 m assigned for the crown outer shell thickness.
4. From 0.012 m to 0.045 m with step 0.0012 m assigned for the crown inner shell thickness.

The optimal sets of sizing variables for model A3 are given in Appendix Table F.11.

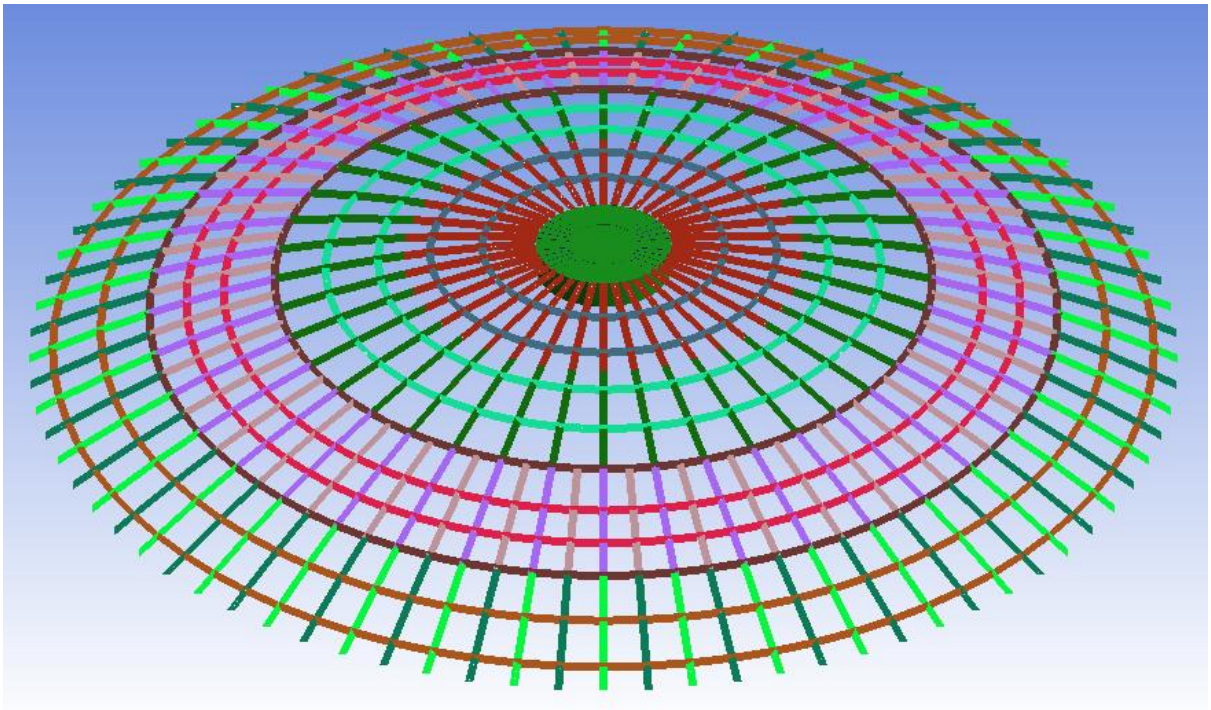

Figure 4.21 Identification of structural components for the basic design of model A3.

4.6.2 Schwedler Single Lattice Dome (Model B3)

Schwedler dome configuration is first introduced in 1863 by the German civil engineer Johann Wilhelm Schwedler. It is one of the common types of braced domes. It is fundamentally created as ribbed dome, i.e. set of meridional beams jointed together by horizontal circumferential rings. Thence, it is supported further by introducing a diagonal member in each trapezoid cell in the basic ribbed dome (Kaveh and Talatahari, 2010b). Thus, model B3 is similar to model A3 with observing that the secondary meridional girders are replaced by their equivalent diagonal braces. Moreover, the crown structure of model B3 has constructed as beam elements instead of the plate elements considered in model A3. Table 4.25 states the statistical facts for the basic design of this model, where 521 keypoints are employed to create the model. There are 1000 line bodies in the roof structure, the number of nodes has counted up to 2441, while the number of elements found in this model is 7730.

Similar to model A3, the shape design parameter is restricted to the dome radius (R). The topological variables are classified into two groups: integer $\overrightarrow{DV_{int}}$ ($N_{Girders}$ and N_{Rings}) and continuous ($\overrightarrow{DV_{con}}$), which are defined in Figure 4.22. The set of topological and shape (integer and continuous) design parameters are listed in Table 4.26. The topological continuous parameters of model B3, defined in Figure 4.22, are expressed in nondimensional form as given in Eq. (4.26).

$$Frac_i = dx_i/r, \quad i = \{1, 2, 3, \dots, N_{Rings}\} \tag{4.26}$$

$Frac_i$ is nondimensional fraction for the i^{th} segment, dx_i is the horizontal distance measured from the central axis of the tank to the end of the i^{th} segment, $i = \{1, 2, 3, \dots, N_{Rings}\}$, where the outermost end of the segment i represents the point where the circumferential ring i intersects the meridional girder as sketched in Figure 4.22. dx_i can be chosen arbitrarily within the following dynamic range.

$$dx_i^0 - \left(\frac{\sqrt{r - dx_i^0}}{10}\right) \le dx_i \le dx_i^0 + \left(\frac{\sqrt{r - dx_i^0}}{10}\right), \quad i = \{1, 2, 3, \dots, N_{Rings}\} \tag{4.27}$$

where the initial values of dx_i (dx_i^0) could be estimated according to:

$$dx_i^0 = i * \left(\frac{r}{N_{Rings} + 1}\right), i = \{1, 2, 3, \dots, N_{Rings}\} \tag{4.28}$$

N_{Rings} is the number of circumferential rings existing in the braced dome. The number of segments depends only on N_{Rings}, i.e. the number of topological continuous variables ($Frac_i$) is changing dynamically during the optimization process according to N_{Rings}. The set of shape and topological parameters are arranged in Table 4.26.

Table 4.25 Statistical data for the fundamental design of model B3.

Whole Tank Structure	Num. of Nodes	133025
	Num. of Elements	45640
	Num. of Solid Bodies	13+1000 = 1013
	Structural Mass	517.01 tonnes
Roof Supporting Frame	Num. of Keypoints (Vertices)	521
	Num. of Line Bodies (Edges)	1000
	Num. of Nodes	2441
	Num. of Elements	7730
	Num. of Structural Components	6+12+5+1+1 = 25
	Structural Mass	196.23 tonnes
Configuration of Structural Components for the Roof Supporting	CG-A (Meridional Girders)	06 comps. modelled by DM-A using 'S20x96'
	CG-B (Right-inclined Braces)	12 comps. modelled by DM-B using '9 x 5 x 1/2'
	CG-C (Circumferential Rings)	05 comps. modelled by DM-C using 'C10x30'
	CG-D (Crown Beams)	01 comps. modelled by DM-D using 'S20x96'
	CG-E (Crown Hoop)	01 comps. modelled by DM-E using 'S20x96'
	CG-F (Empty)	DM-F (Unutilized)
	CG-G (Empty)	DM-G (Unutilized)
	CG-H (Empty)	DM-H (Unutilized)

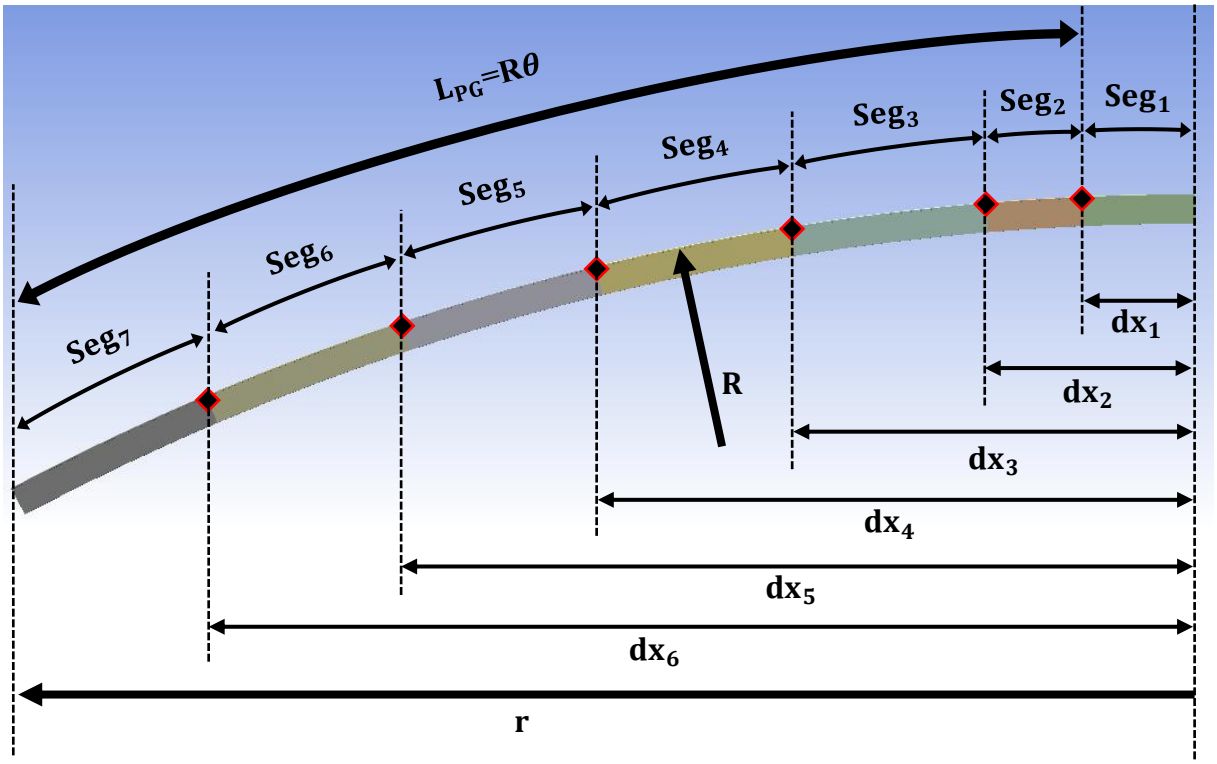

Figure 4.22 Shape and topological parameters for the basic design of model B3.

Table 4.26 Optimization range for the shape and topological parameters of model B3.

Design variable	Initial Value	Lower Bound	Upper Bound
$N_{Girders}$ (-)	40	32	48
N_{Rings} (-)	6	3	8
R (m)	45	30	60
$Frac_i$ (-)	According to Eq. (4.28)	According to Eq. (4.26) and (4.27)	According to Eq. (4.26) and (4.27)

A. Finite Element Model

The finite element form for the basic design of model B3 is illustrated in Figure 4.23, where the number of elements induced from this meshing is 7730 with number of nodes equal to 2441. The structural mass for the initial design was determined to be 196.23 tonnes. The number of elements is lower than those for model A3 due to simplifying the crown structure by modelling it as beam elements rather than plate elements.

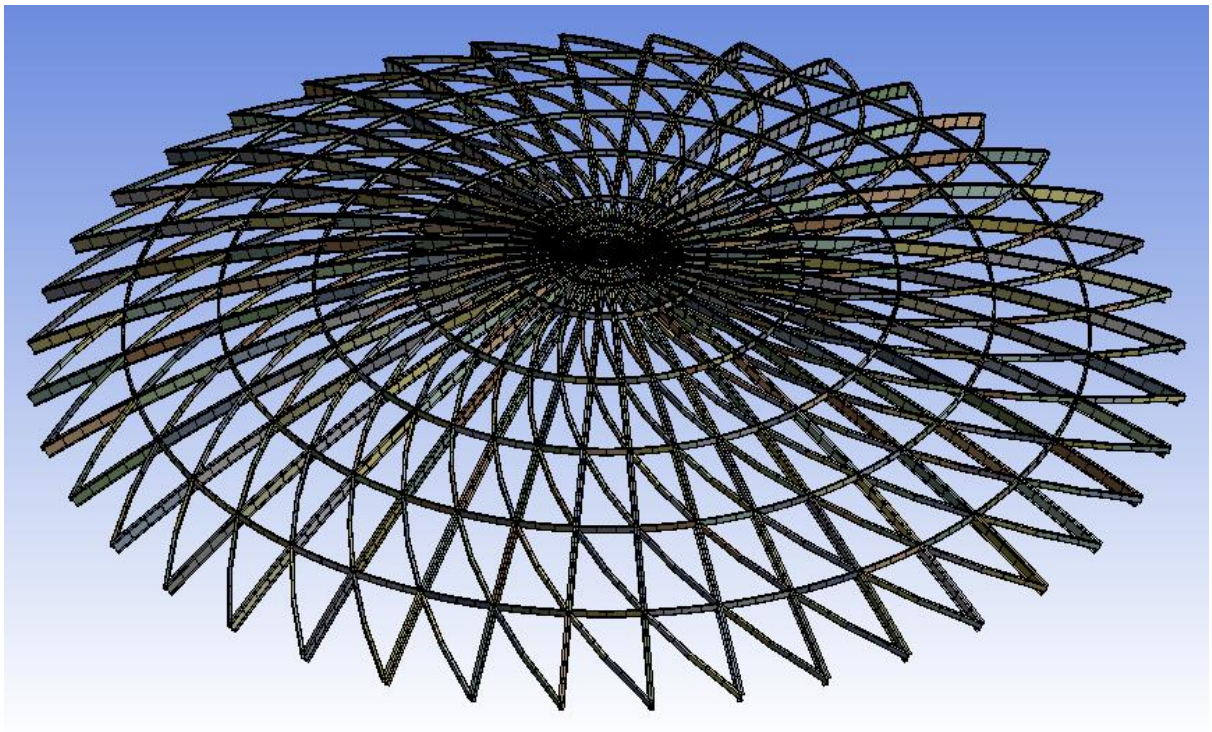

Figure 4.23 Finite element configuration for the basic design of model B3.

B. Identification of Structural Components

There is a significant difference in the geometrical details of the structural components (compare Table 4.23 to Table 4.25). Figure 4.24 and Table 4.25 refer to existence of 25 components in model B3. They are managed by 5 CGs, CG-A includes the meridional girders with 6 components, CG-B represents the right-inclined braces with 12 components, CG-C

denotes the circumferential rings with 5 components, the radial beams of the crown and the crown hoop are included in CG-D and CG-E respectively.

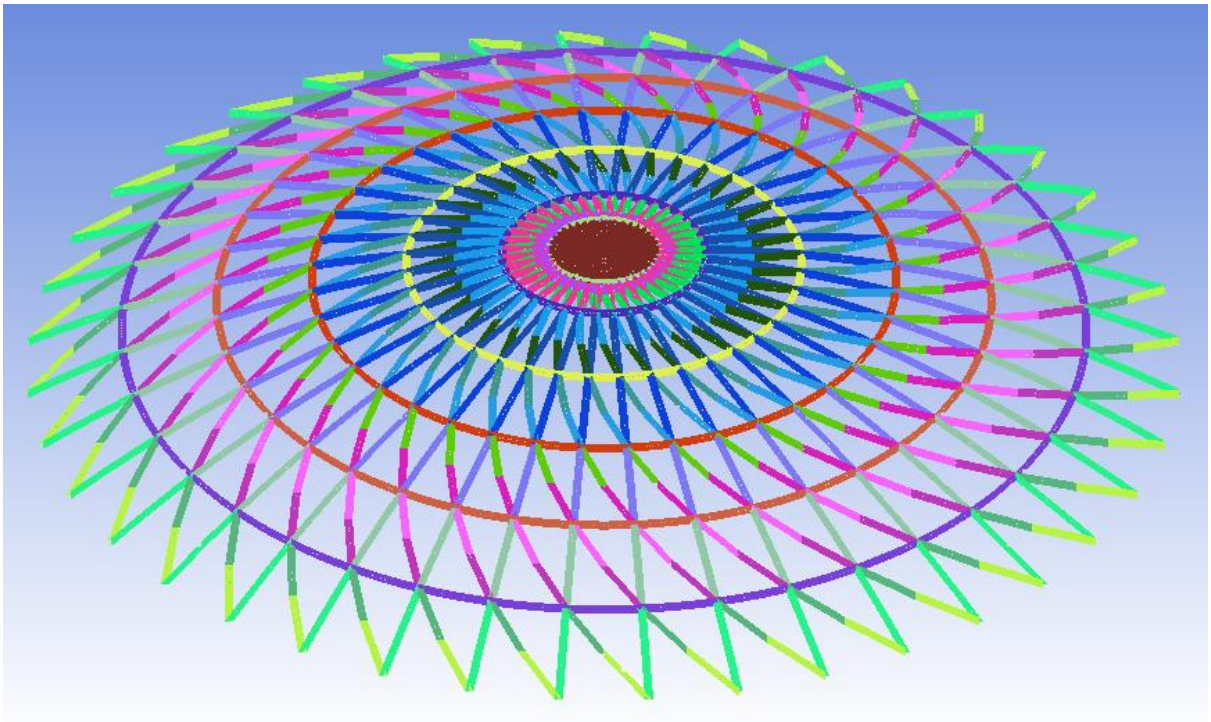

Figure 4.24 Identification of structural components for the basic design of model B3.

4.6.3 Lamella Single Lattice Dome (Model C3)

Model C3 is designed to consist of similar patterns arranged in diamond or rhombic shapes, hence no meridional girders are involved. The shape parameter is represented by the dome radius (**R**), whereas the topological integer variables ($\overrightarrow{\mathrm{DV}_{\mathrm{int}}}$) are restricted to the number of Lamella modules ($\mathbf{N_{Girders}}$) and the number of circumferential rings ($\mathbf{N_{Rings}}$). The continuous set of topological design parameters ($\overrightarrow{\mathrm{DV}_{\mathrm{con}}}$) can be calculated according to Eqs. (4.26) through (4.28) as demonstrated in Figure 4.25. The shape and topology design variables are given in Table 4.28.

Table 4.27 summarizes the finite element formulation for the fundamental design of this model. The roof frame geometry is created using 1360 lines to generate 3601 nodes and 4480 elements, whereas there are 481 vertices utilized to create the model. The total number of nodes over the whole tank was 143989, the corresponding elements show 49338. Accordingly, the mass of the whole tank has recorded the value 530.05 tonnes, whereas for the roof frame it is estimated as 209.27 tonnes.

Table 4.27 Statistical data for the fundamental design of model C3.

Whole Tank Structure	Num. of Nodes	143989
	Num. of Elements	49338
	Num. of Solid Bodies	13+1360 = 1373
	Structural Mass	530.05 tonnes
Roof Supporting Frame	Num. of Keypoints (Vertices)	481
	Num. of Line Bodies (Edges)	1360
	Num. of Nodes	3601
	Num. of Elements	4480
	Num. of Structural Components	11+11+10+1+1 = 34
	Structural Mass	209.27 tonnes
Configuration of Structural Components for the Roof Supporting	CG-A (Right-inclined Braces)	11 comps. modelled by DM-A using '20 x 12 x 1/2'
	CG-B (Left-inclined Braces)	11 comps. modelled by DM-B using 'L8 x 8 x 7/8'
	CG-C (Circumferential Rings)	10 comps. modelled by DM-C using 'C15x33.9'
	CG-D (Crown Beams)	01 comp. modelled by DM-D using 'S24x100'
	CG-E (Crown Hoop)	01 comp. modelled by DM-E using 'S24x100'
	CG-F (Empty)	DM-F (Unutilized)
	CG-G (Empty)	DM-G (Unutilized)
	CG-H (Empty)	DM-H (Unutilized)

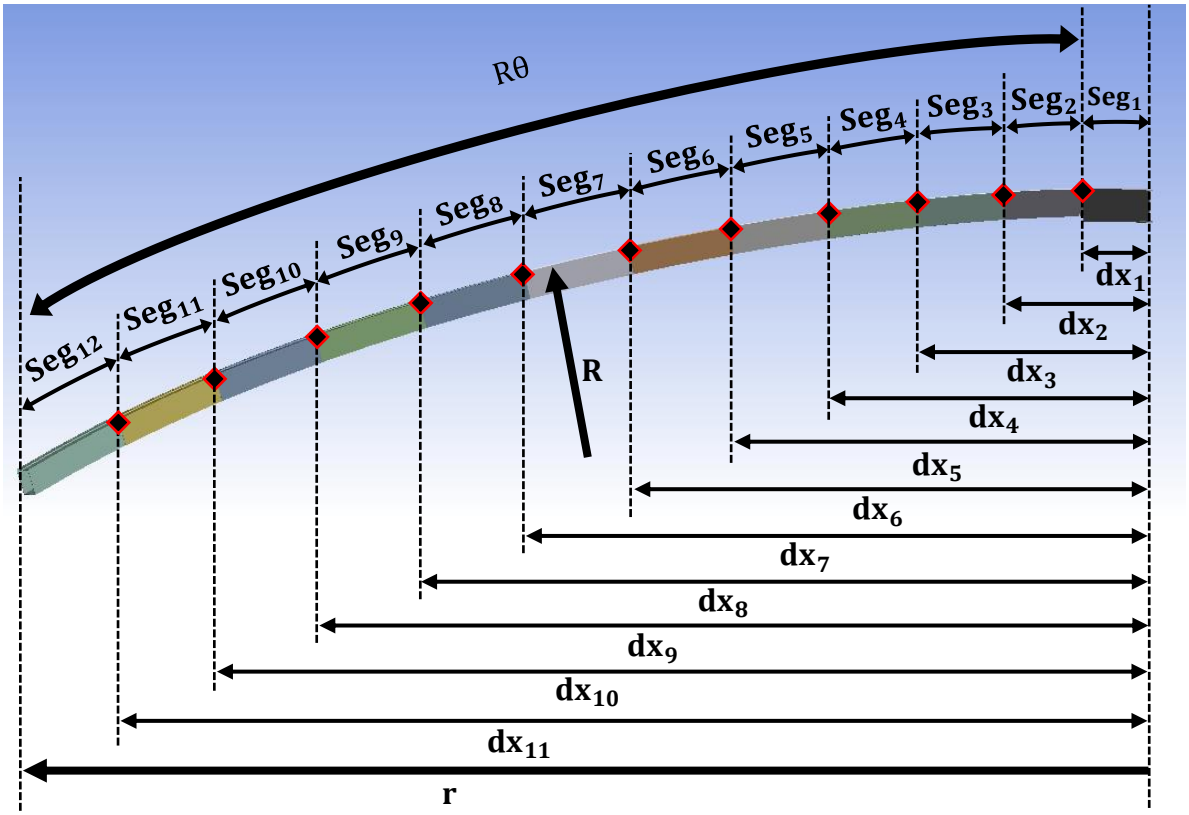

Figure 4.25 Shape and topological parameters for the basic design of model C3.

Table 4.28 Optimization range for the shape and topological parameters of model C3.

Design Variable	Initial Value	Lower Bound	Upper Bound
$N_{Girders}$ (-)	40	30	48
N_{Rings} (-)	11	5	15
R (m)	45	30	60
$Frac_i$ (-)	According to Eq. (4.28)	According to Eq. (4.26) and (4.27)	According to Eq. (4.26) and (4.27)

A. Finite Element Model

The finite element form for the initial design of model C3 is illustrated in Figure 4.26, where a refined mesh sizing (element size = 300 mm) has used to execute the meshing operation of the model.

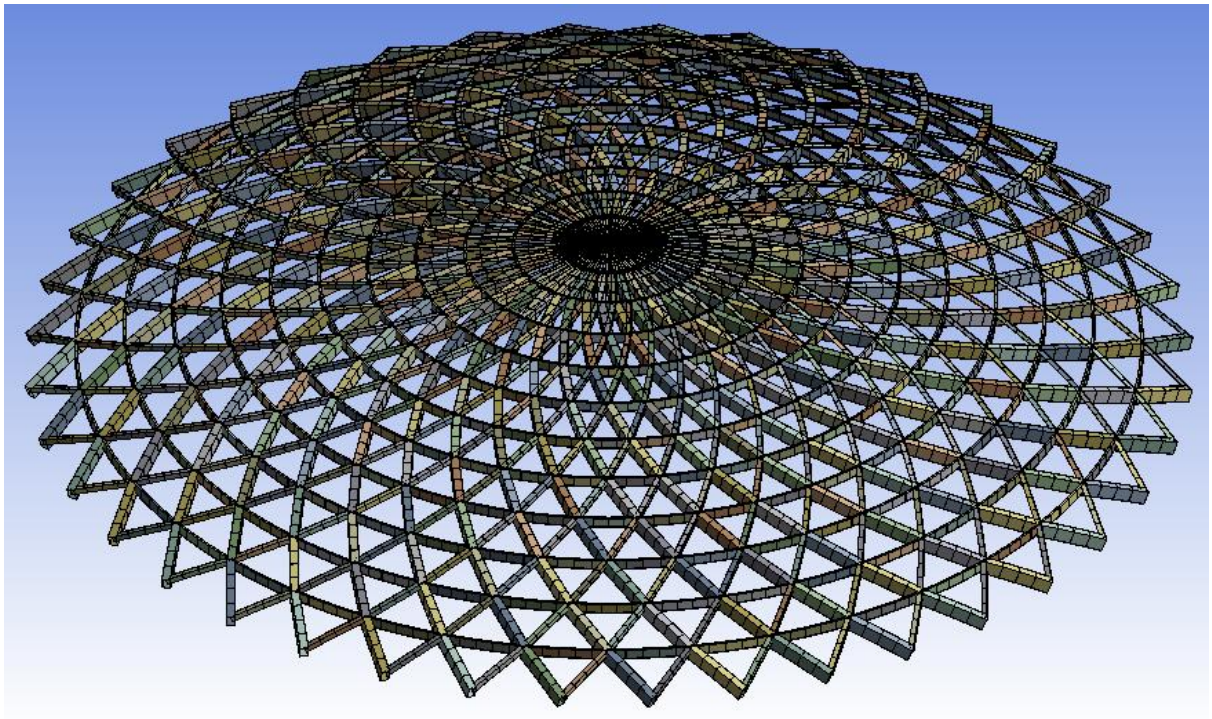

Figure 4.26 Finite element configuration for the basic design of model C3.

B. Identification of Structural Components

The component groups of the reference design of model C3 are shown in Figure 4.27. The statistical data are given in Table 4.27. There are 34 components managed by diverse range of database modules: DM-A with '20 x 12 x 1/2', DM-B with 'L8 x 8 x7/8', DM-C with 'C15x33.9', DM-D with 'S24x100', and DM-E with 'S24x100'. There are 5 CGs needed to control 34 components in model C3. The first group is CG-A represents the right-inclined braces with 11 components, the second is CG-B represents the left-inclined braces with 11 components, the third is CG-C denotes the circumferential rings with 10 components, the fifth and sixth are CG-D and CG-E used to model the radial beams of the crown and the crown hoop respectively.

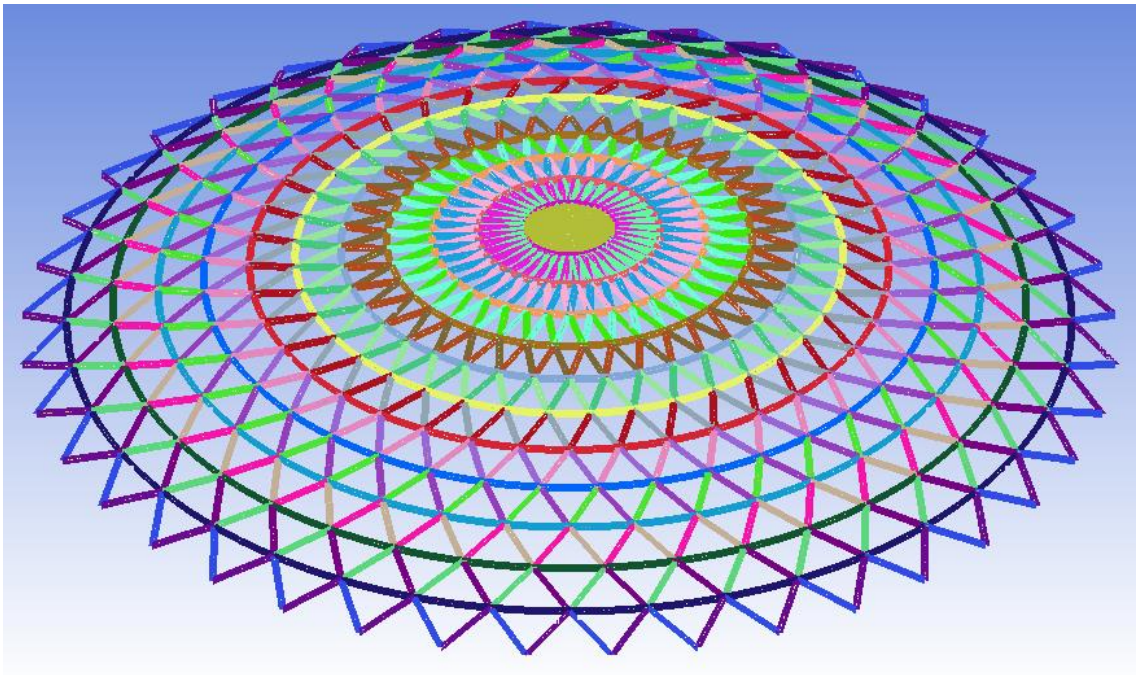

Figure 4.27 Identification of structural components for the basic design of model C3.

4.6.4 Geodesic Single Lattice Dome (Model E3)

For Model E3, the integer design parameters ($\overrightarrow{DV_{int}}$) are defined as the number of sides for basic polygon ($\mathbf{N_{Sides}}$) and the number of circumferential rings ($\mathbf{N_{Rings}}$). Equations (4.26) through (4.28) are applicable to this model to consider the topological continuous variables of the model as illustrated in Figure 4.28. Accordingly, the set of design parameters for model E3 are defined in Table 4.30. The data recorded in Table 4.29 details that there are 50439 elements in the whole tank as basic design for model E3, while the number of nodes has reached 146077, which is the highest in comparison to the previous models due to the configuration nature of the roof frame, which is significantly influencing the meshing patterns of the dome roof shell. Moreover, 1450 lines are used to create this model as illustrated in Figure 4.29 using only 551 keypoints to perform this task. The elements total 5160 to yield initial structural mass of 205.66 tonnes, while the total number of nodes are 4261.

Table 4.29 Statistical data for the fundamental design of model E3.

Whole Tank Structure	Num. of Nodes	146077
	Num. of Elements	50439
	Num. of Solid Bodies	13+1450 = 1463
	Structural Mass	526.44 tonnes
Roof Supporting Frame	Num. of Keypoints (Vertices)	551
	Num. of Line Bodies (Edges)	1450
	Num. of Nodes	4261
	Num. of Elements	5160
	Num. of Structural Components	10+9+9+9 = 37
	Structural Mass	205.66 tonnes
Configuration of Structural Components for the Roof Supporting	CG-A (Meridional Girders)	10 comps. modelled by DM-A using 'S20x96'
	CG-B (Right-inclined Braces)	09 comps. modelled by DM-B using '9 x 5 x 1/2'
	CG-C (Left-inclined Braces)	09 comps. modelled by DM-C using '9 x 5 x 1/2'
	CG-D (Circumferential Rings)	09 comps. modelled by DM-D using 'C10x30'
	CG-E (Empty)	DM-E (Unutilized)
	CG-F (Empty)	DM-F (Unutilized)
	CG-G (Empty)	DM-G (Unutilized)
	CG-H (Empty)	DM-H (Unutilized)

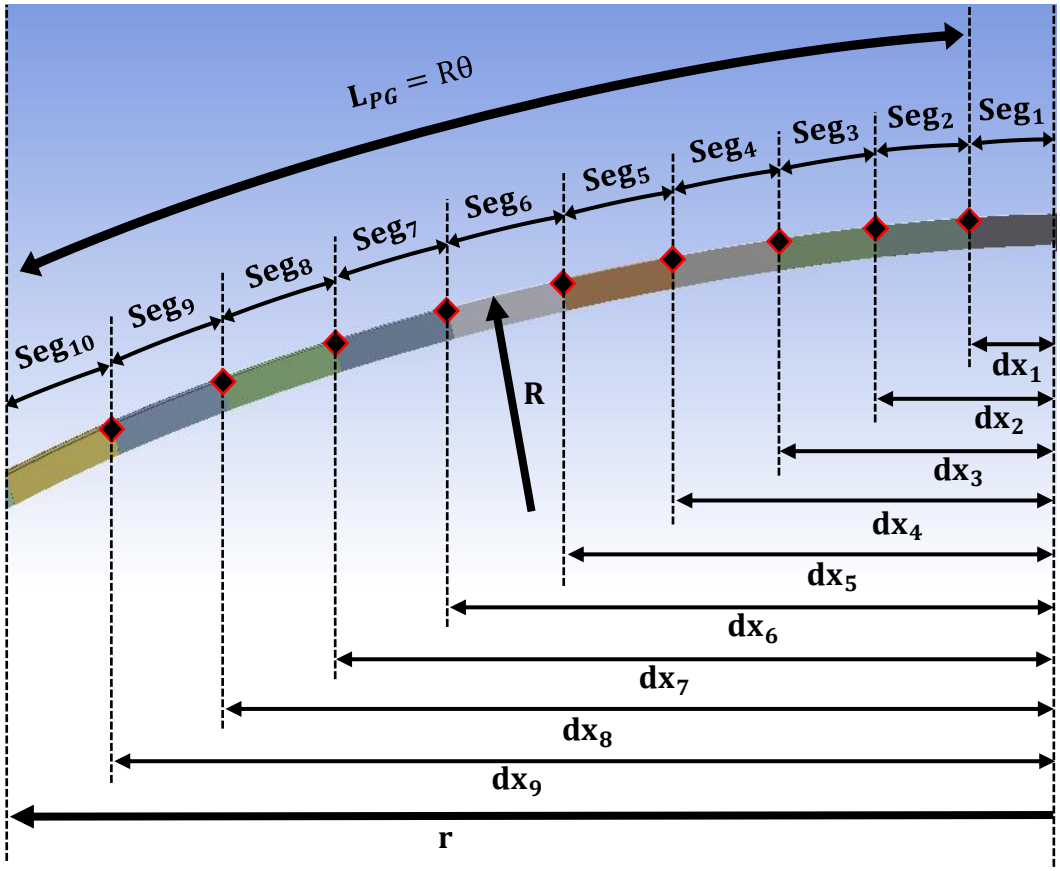

Figure 4.28 Shape and topological parameters for the basic design of model E3.

Table 4.30 Optimization range for the shape and topological parameters of model E3.

Design variable	Initial Value	Lower Bound	Upper Bound
N_{Sides} (-)	10	4	14
N_{Rings} (-)	9	4	14
R (m)	45	30	60
$Frac_i$ (-)	According to Eq. (4.28)	According to Eq. (4.26) and (4.27)	According to Eq. (4.26) and (4.27)

A. Finite Element Model

The discretization of finite elements for the reference design of model E3 is shown in Figure 4.29, where the number of main meridional girders of the model is equal to the number of sides for the basic polygon of the geodesic dome roof configuration.

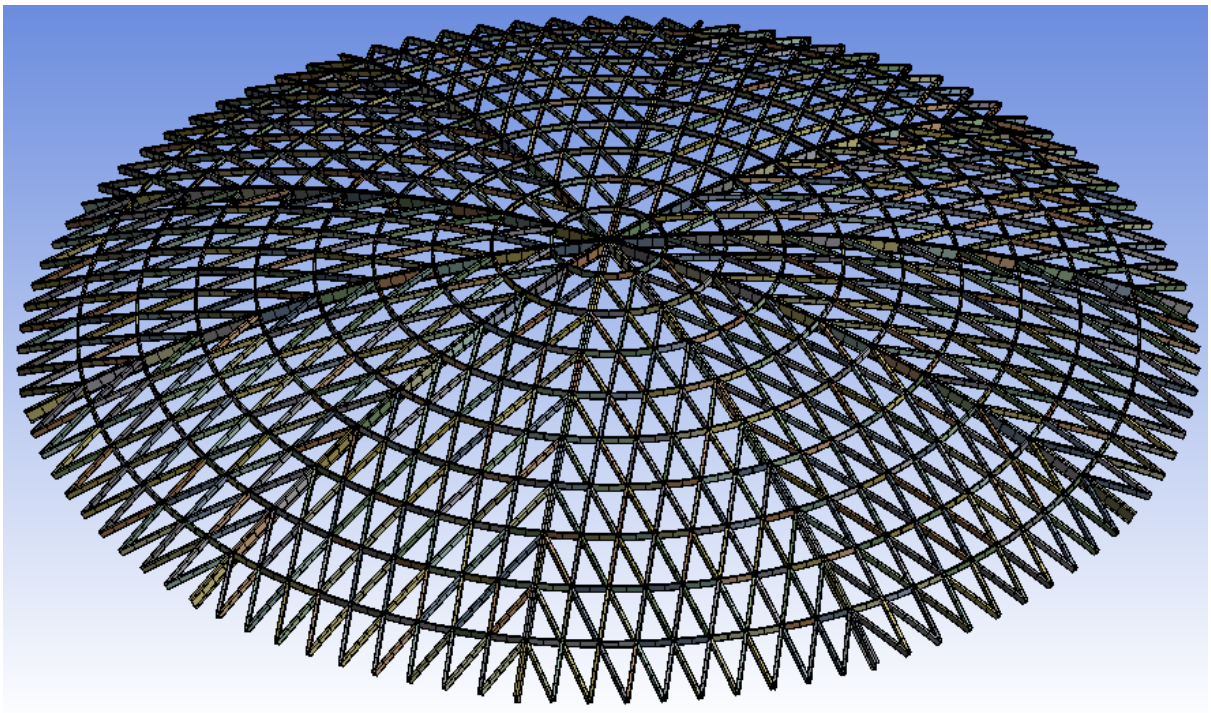

Figure 4.29 Finite element configuration for the basic design of model E3.

B. Identification of Structural Components

Figure 4.30 shows the different component groups of model E3, which consists of 37 components controlled by 4 component groups, where CG-A represents the meridional girders, CG-B and CG-C are used to model inclined braces, whereas CG-D is used to model the circumferential rings– see Table 4.29 for more details. American I-beams, detailed in Appendix Table E.1, are used to model the group of meridional girders, RHS, fixed in Appendix Table E.4, model the inclined braces of the model, whereas S-type C-channels, detailed in Appendix Table E.2, model the circumferential rings of the model.

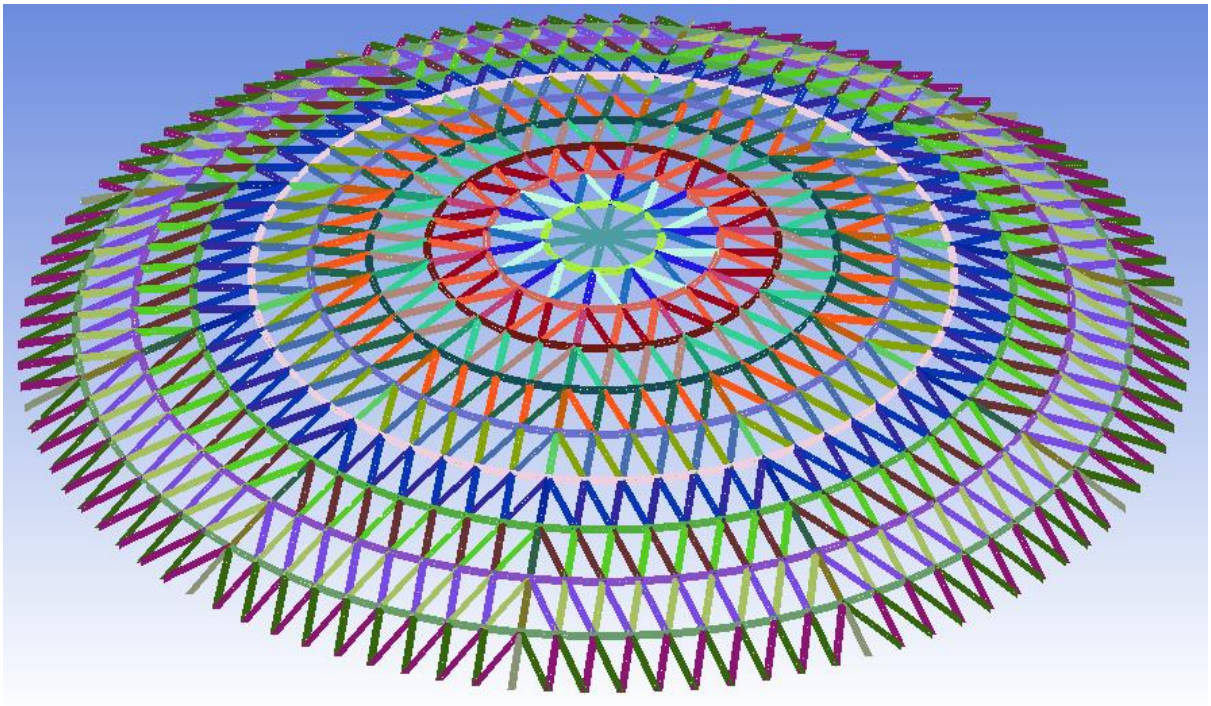

Figure 4.30 Identification of structural components for the basic design of model E3.

4.7 Modelling of Constructional Material

Two types of structural materials are considered in the modelling process. First, low carbon steel hot rolled plates (A283 Gr C) specified to idealize shell elements of the tank which are recommended by (ASTM-A283/A283M − 13, 2013) and the complete schedule for their properties is available in the aforementioned standard. Second, low and intermediate carbon hot rolled structural steel sections (A36) to represent stiffeners, beams, girders, crown elements and other structural sections of the tank which are highly advised by (ASTM-A 36/A 36M − 01, 2001) and (API Standard 650, 2013) for tank construction. The physical and mechanical characteristics for the structural materials adopted in the current model are given in Table 4.31.

Table 4.31 Physical and mechanical properties for the constructional materials of the storage tank as defined by (ASTM-A 36/A 36M − 01, 2001) and (ASTM-A283/A283M − 13, 2013).

Component	Bottom plate, cylindrical shell, dome roof shell, crown components, cylindrical shell stiffeners (hot rolled plates)	Dome roof supporting frame and top curb angle
Designation	A 283 Gr C	A 36
Mass Density [kg/m3]	7850	7850
Elastic Modulus [GPa]	200	200
Poisson Ratio	0.3	0.3
Yield Stress [MPa]	205	250
Ultimate Tensile Strength [MPa]	485	550

Chapter 5. Proposed Optimization Methodology

5.1 Structural Optimization Problem

Optimization problems are often framed in terms of minimizing 'cost', since often the ultimate goal of optimization is to minimize the total financial cost of a product. Thus, the cost to be minimized could include material costs, assembly and maintenance costs, personnel, end-of-life and financial overheads, and so on. In the case of a fuel storage tank, the major cost is related to the bulk mass of steel, and construction (and other) costs generally increase along with the mass of steel. Minimizing the structural mass, therefore, is also minimizing the overall economic cost. However, structural mass is not the only indicator of the quality of a design, and it can be useful to include other aspects of the design in the 'cost' so that the optimization leads to designs with low structural mass without sacrificing other structural requirements.

Each of the fourteen dome roof designs described in the previous chapter can be specified by a finite set of design variables, such as dome roof radius, section numbers (within specified sets of commercial sections), and other numbers affecting the structure and topology. The aim of optimization is to determine values of the design variables that minimize one or more properties of the design, subject to various engineering constraints. This thesis focusses on structural mass of the dome roof frame, but safety, stiffness and overall manufacturing cost, for example, are also properties that could be minimized.

The nature of the dome roof design and analysis is highly non-linear. Not only do the engineering constraints on maximum stress and maximum deflection tend to make heavier designs better from a safety perspective, most of the design variables are integers (e.g., number of rings, section number of each girder) and even a small change in one discrete variable can have a substantial impact on the whole design.

The general form of cost function will be explained in section 5.1.4, where the cost function can includes all kinds of objectives detailed in section 5.1.1 considering the design constraints mentioned in section 5.1.2. However, the current study focuses on minimizing the structural mass of the dome roof frame in order to reduce the material cost of the tank, hence the mass fraction mentioned in the first part of Eq. (5.1) will be the only term used in the formulation of cost function. Therefore, other objectives, mentioned in the second part of Eq. (5.1), will be used as design functions for tracking the structural characteristics corresponding to the mass reduction of the model during the different stages of optimization.

5.1.1 Objective Function

The current study proposes the following individual design functions for the model.

$$\left\{\begin{array}{l}\text{Objective}_{W}=\left(\dfrac{W}{W_0}\right)\\ \text{Objective}_{j}=\dfrac{1}{\text{ncomp}}\displaystyle\sum_{i=1}^{\text{ncomp}}\left(\dfrac{j)_i}{j0)_i}\right), j=\{\text{SEQV, SED, FREQ, BUCK}\}\end{array}\right\} \quad (5.1)$$

where, W_0 and W are the initial and current structural masses respectively. Objective_j is the objective function based on j^{th} structural response, $\left(\frac{j)_i}{j0)_i}\right)$ is the ratio of the current value to the initial value for i^{th} structural component under j^{th} structural response. SEQV, SED, FREQ and BUCK stand for equivalent stress, strain energy density, frequency, and buckling index respectively. They represent the sensitivity numbers of strength, stiffness, frequency, and buckling respectively for certain component in the structural system. These design functions (SEQV, SED, FREQ and BUCK) are detailed in sections 5.4.1, 5.4.2, 5.4.3 and 5.4.4 respectively.

5.1.2 Design Constraints

To ensure a structurally safe and reliable design, the structural behaviour of the dome roof frame must be subjected to a set of design constraints. They are classified upon the requirement of the structural design (Jármai *et al.*, 2006), (Saka, 2007b), (Sui and Yi, 2013), (Savsani *et al.*, 2017). They are:

- Technological or manufacturing constraints: this type of constraints is attributed to practical, manufacturing or fabrication limitations (Seifi *et al.*, 2016).
- Geometrical constraints: these impose relationships among design variables in order to ensure a functional, feasible, safe and stable structure. Such constraints are based on principles of structural reliability and strength to avoid local failure.
- Structural performance constraints: which are subdivided into the following groups:
  - ❖ Stress constraints: in most ductile materials, the von-Mises equivalent stress is considered appropriate for determining the likelihood of plastic failure. Through comparing the value of maximum equivalent von-Mises stress with the limit value (yield stress), as expressed in Eq. (5.2) (Lagaros *et al.*, 2004).
  - ❖ Displacement constraints: The higher the value of maximum displacement, the lower the level of overall structural stiffness. Hence, limiting the value of maximum displacement, as indicated in Eq. (5.3), will ensure a safe and reliable stiffness level (Zhou and Haftka, 1995), (Chu, 1997) and (Liang and Steven, 2002).
  - ❖ Buckling constraints: The buckling formula for slender beams is given in Eq. (5.27),

where the global buckling for compressive members is first introduced by Euler (Bai, 2014). Other types of buckling mentioned in the literature like 'cellular buckling' or 'snaking' (Burke and Knobloch, 2007) are not considered in this work. Hence, the relevant constraints are set on the global buckling calculated according to formula (5.27) with adopting the minimum level for safety factor, i.e. $SF)_{buckling}$=1. Thus, the buckling indicator value for each link in the structure must not exceed the unity according to Eq. (5.26) (Hasancebi *et al.*, 2010).

$$SF * \sigma_{vm}^{max} \leq \sigma_{yp} \tag{5.2}$$

where, SF is the safety factor, σ_{vm}^{max} is the maximum value of the equivalent von Mises stress existing in the roof frame model, σ_{yp} is the yield point (this work considers σ_{yp}=200 MPa for the default structural steel).

$$U_{abs}^{max} \leq U_{ub} \tag{5.3}$$

where, U_{abs}^{max} is the maximum value of absolute displacement observed over the whole structure, U_{ub} is the upper bounds of the displacement constraint (U_{ub}=40 mm, used in this work).

Regarding the buckling limits, the buckling index defined in Eq. (5.26), must not exceed the unity as expressed in Eq.

$$\xi_i^{buck\_ind} \leq 1 \tag{5.4}$$

There are thus two generic types of constraints. There are constraints on the inputs - the design variables that define the structure - and typically these are expressed as a range (or set) of valid values, and can be treated as coordinates in a space of potential solutions. This kind of constraints includes the restriction applied to the dimensions and other geometrical details of the structure. On the other hand, there are constraints on the outputs - on the performance of the structure subject to loading, i.e., the above limits for stress, displacement and buckling. If a structure is being optimized for low mass, it must still meet the constraints, and one way to reflect that is by using the cost function (the quantity being minimized) is the penalty function approach (Ghasemishabankareh *et al.*, 2016), (Yang *et al.*, 2016), (Lieu *et al.*, 2018). The penalty function handles the constraints in a smart manner that the cost function will have a value approaching to infinity when breaching the constraints. Thus, all valid points in design space will have an associated cost. For solutions that meet all constraints, the cost is then (for example) the structural mass, but for solutions that violate the constraints the cost is a value larger than any acceptable structural mass, and these solutions are thus quantified as non-optimal (Gomes, 2011), (Babaei and Sheidaii, 2014) and (Pholdee and Bureerat, 2014).

5.1.3 Configuration of Design Variables

This section presents the characteristics of the design variables considered in this study. The set of variables is classified according to shape, topology, and sizing variables. The design input parameters are subdivided into: integer, discrete and continuous variables. The complete group of variables is subdivided into five subsets, as defined in Eq. (5.5). Each of them is addressed by one of the adopted optimization techniques. For instance, Morphing Evolutionary Structural Optimization (MESO) is used to handle the sizing variables which are classified as discrete subset of variables ($\overrightarrow{\mathrm{DV}_{\mathrm{dis}}}$).

A. Geometric Categorisation

In general, design variables can be geometrically classified into three types: shape, topology and sizing.

- Shape design variables: this set of variables is restricted to the dome radius (R) for all single lattice configurations (models A1 to E1 and models A3 to E3), whereas there are two extra shape parameters (ɳ and ʊ) need to be added to the double lattice configurations (models A2 to E2).
- Topological design variables: they can be classified into types, integer ($\overrightarrow{\mathrm{DV}_{\mathrm{int}}}$) and real (continuous) parameters ($\overrightarrow{\mathrm{DV}_{\mathrm{con}}}$). The first kind is optimized at stage 1, as they have an extreme influence on the structural behaviour which results in high fluctuation at stage 1, these are N_n, N_r, N_s, N_t and N_m. The second kind is optimized at stage 2, as they have a limited influence on the structural behaviour compared to the first kind ($\overrightarrow{\mathrm{DV}_{\mathrm{int}}}$), they are related to minor changes on the structure like the positioning of the circumferential rings and the set of topological fractions controlling the meridional lengths of the local segments of the radial girders and the meridional length of the secondary girder as illustrated in Figure 4.19 and Table 4.24.
- Sizing design variables: they are mathematically classified as discrete variables. This kind of variables can be treated by MESO or any other methods developed to treat with discrete optimization problems. The optimization ranges of the discrete sizing variables are represented by the commercial tables of structural sections are given in Appendix E.

B. Mathematic Categorisation

Mathematically, design variables are categorized into: integer, discrete and continuous. In addition to the design variables, there are a number of dependent variables used to describe the current state of the optimization, needed for instance to represent the corrected integer form of real parameters if applicable.

1) Integer design variables ($\overrightarrow{\mathrm{DV}_{\mathrm{int}}}$): they represent the topological set of parameters, such as number of girders, number of nodes per ring, number of rings, topological trimming factor, topological spacing factor, topological morphing factor etc. They are solved at stage 1, as demonstrated in Figure 5.9, using the adopted list of conventional metaheuristic strategies, introduced in section 5.5.
2) Continuous design variables ($\overrightarrow{\mathrm{DV}_{\mathrm{con}}}$): they represent the dome radius, the other two extra shape optimization parameters, related to the double lattice modelling and the set of topological fractions defined in Table 4.24, Table 4.26, Table 4.28 and Table 4.30, included in section 4.6. They are treated as real (continuous) variables at stage 2 using the adopted standard metaheuristic techniques detailed in section 5.5.
3) Discrete design variables ($\overrightarrow{\mathrm{DV}_{\mathrm{dis}}}$): they stand for the sizing set of variables, which are solved at stage 2. They are handled by the adapted version of MESO if the hybrid optimization technique (MESO-Metaheuristic) is used; otherwise they are handled by the adopted metaheuristic techniques adapted to treat using discrete sizing optimization (DSO) if the conventional metaheuristic method is employed instead.
4) Dependent design variables ($\overrightarrow{\mathrm{DV}_{\mathrm{dep}}}$): these are a set of variables called dependent or intermediate variables like the additional intermediate variables needed to transform some topological variables from dimensional to nondimensional form in order to simplify the optimization problem by reducing (or omitting) the side constraints using these dummy changes in design variables involved.
5) Load design variables ($\overrightarrow{\mathrm{DV}_{\mathrm{load}}}$): the load case(s) to be applied to the model during optimization in Stage 1 and Stage 2, or for verification in Stage 3.

The vector of all input design parameters ($\overrightarrow{\mathrm{DV}}$) is:

$$\overrightarrow{\mathrm{DV}} = \left\{\overrightarrow{\mathrm{DV}_{\mathrm{load}}}, \overrightarrow{\mathrm{DV}_{\mathrm{dep}}}, \overrightarrow{\mathrm{DV}_{\mathrm{int}}}, \overrightarrow{\mathrm{DV}_{\mathrm{dis}}}, \overrightarrow{\mathrm{DV}_{\mathrm{con}}}\right\} \tag{5.5}$$

5.1.4 General Form of the Cost Function

The general form of Cost Function (CF) comprises different sub-objectives of structural optimization, these constituent functions are related to: structural weight, strength, stiffness, buckling etc. Thus, the general form of CF for multi-objective structural optimization problem can be posed as:

$$\mathrm{CF} = \sum_{\mathrm{j}=1}^{\mathrm{nobj}} \mathrm{C_j}\left(\mathrm{Objective_j}\right)^{\mathrm{k_j}}, \quad \mathrm{j} = \{\mathrm{W}, \mathrm{SEQV}, \mathrm{SED}, \mathrm{FREQ}, \mathrm{BUCK}\} \tag{5.6}$$

where, nobj is the number of sub-objectives considered in the problem, $\mathrm{C_j}$ is a constant used to

determine the weighted contribution for the j^{th} sub-objective, k_j is an index used to tune the influence of j^{th} sub-function on the main cost function. Objective_j is defined in Eq. (5.1). However, single objective constrained optimization problem regarding the structural mass minimization is considered in the current work, hence, the last four terms of the formula (5.6) are neglected, i.e. the cost function is only then defined as the fraction of the structural weight divided by the initial weight ($j = \{W\}$) of the structure.

5.2 Morphing Evolutionary Structural Optimization (MESO)

MESO is a modified version of ESO with more flexibility in application, it is extended to cover sizing optimization, as the earlier version of ESO carried out only simultaneous shape-topology optimization of continuous structures. MESO can be applied to optimize large scale skeletal structures for sizing, but it is not ideal for optimizing large scale space frame structures for shape or topology. MESO works by dividing the entire structure into finite number of segments called structural components, each defined by their own cross-sectional dimensions and other sizing parameters.

The level of the inherent stresses and strains is the effective measure for the failure in structural design. However, if the structure shows low level of stress, then this indicates the presence of an inefficient distribution of material over the whole structure (an underutilized material exists). In this sense, a Rejection Criterion (RC) is applied to trim out the unnecessary material (i.e. remove the redundant material from the low stressed parts). Thus, RC is controlling the magnitude of the removed material in each step of optimization through investigating the local stress/strain level for each component in the structure. In the MESO procedure, the initial values of the design variables are assigned to be the maximum values over their own design domain (Abolbashari and Keshavarzmanesh, 2006).

The initial value of Rejection Ratio (RR) must be assumed to initiate the process according to RC principles. RR is increasing progressively as function of the iteration number during the optimization cycles until a specified number is reached. At this stage, an Evolutionary Rate (ER) is introduced and added to the previous value of RR (Steven *et al.*, 2002) and (Ansola *et al.*, 2007):

$$\mathrm{RR}_{\mathrm{it}} = \mathrm{RR}_{\mathrm{it}-1} + \mathrm{ER} \qquad (\mathrm{it} = 2, \dots, \mathrm{MaxIt}) \tag{5.7}$$

where, (it) is a counter which stands for the iteration number incorporated with the current removal of material. $(\mathrm{it} - 1)$ is the iteration number for the preceding cycle. (MaxIt) is the prescribed maximum number of iterations. The new value of RR is utilized to attain more acceptable state of stress in the structure for the subsequent operations Thus, the optimization loop continues searching until it attains the new steady state point at which RR will be changed.

(Li *et al.*, 1999), (Al-Taee *et al.*, 2008) and (Hu *et al.*, 2012). RR value can range from 0 to 1 depending on many factors related to the structural analysis of the problem. RR represents the fraction of the removed material to the whole material. The reference to measure the quantities producing RR depends on the way in which they are eliminated. There is number basis elimination or addition, i.e. the number of components are subjected to a reduction or an increase. Also, there is quantity basis elimination, i.e. the mass to be removed or added. RR_1 is the initial value of RR (at it=1), within the range from 0 to 1. Currently, the number basis is adopted to implement MESO with RR_1= 0.2.

Stopping Criterion (SC) will be satisfied and this terminates the optimization process depending on the conditions of the evolution process. These conditions are: first, when there is no further change in structural dimensions (i.e. the design variables have reached their lower limits), second, when the structure fulfils a uniform distribution of stress/strain energy.

After performing the finite element analysis, the ratio of maximum equivalent stress/strain energy for each structural component to the maximum equivalent stress/strain energy for the entire structure is measured and compared with RR. First, if it meets the necessary conditions (see below), then a different section for that particular component will be chosen (Xie and Steven, 1993).

In this research, MESO has been utilized to optimize the sizing parameters for the adopted models. Different design criteria have been tested under sizing optimization using the MESO strategy to reach the optimum design. The general procedure of MESO strategy used to solve the optimization problem for the sizing variables is explained in Figure 5.1. Different optimization criteria have been applied to the considered dome roof frame models and the optimization results are detailed in Chapter 6, Chapter 7 and Chapter 8. Despite its efficiency to perform the sizing optimization for skeletal structures, MESO cannot perform an integrated simultaneous shape, topology, sizing optimization for the model by itself. Meta-heuristic methods have proved their efficiency to deal with the shape and topology parameters of the model. Therefore, the proposal here is to blend MESO with one of the adopted meta-heuristic techniques to create an integrated hybridized version of optimization capable of performing a simultaneous shape, topology, and sizing optimization with less computational cost than the separated mode of optimization techniques.

According to Figure 5.1, formula (5.6) is used to evaluate the cost function, where it is single objective function with j={W}, C_W=1 and k_W=1. While the optimization parameters used to evaluate the rejection ratio (RR) in Eq. (5.7) are RR1=0.2 and ER=0.001. Next, specify the optimality criterion (e.g. stress, stiffness, buckling etc.) to evaluate the corresponding sensitivity numbers for the structural components. Thereafter, use the general sense of Eqs.

(5.9) and (5.10) to judge the removal or addition of material for the considered structural component. After resizing process (removal and addition of material), a new geometry will be constructed to perform a new structural analysis to obtain the output response and the new design will be tested against the prescribed design constraints using Eq. (5.2), (5.3) and (5.4) for stress, displacement and buckling respectively. If the design is succeeded to pass the test, then it will be recorded in the list of candidates. If not, it will be recorded as penalized solution and another new analysis will be attempted.

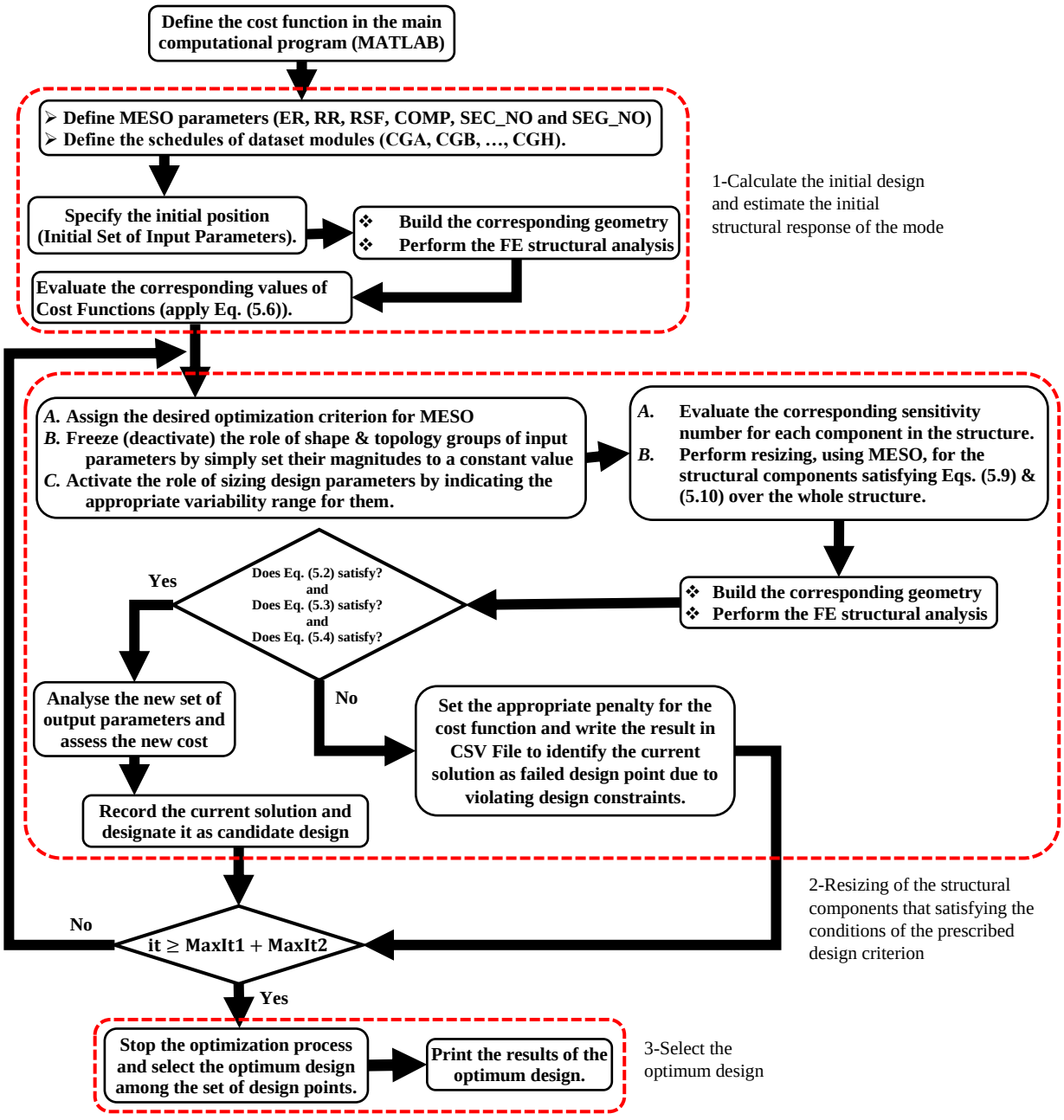

Figure 5.1 Flow chart demonstrating the optimization steps adopted by MESO strategy considered in the present work.

The final statement of the diagram explains how to stop the optimization process and select the optimum design. This is implemented by comparing the current iteration number to the maximum number of iterations specified for stage 2. The maximum number of iterations is supposed according to analysis type, i.e. it is assumed to be (MaxIt1+MaxIt2=12+24=36) for integrated modelling, (MaxIt1+MaxIt2=20+40=60) for simplified single lattice modelling and (MaxIt1+MaxIt2=20+80=100) for simplified double lattice modelling.

5.3 Bi-directional MESO (BMESO)

BMESO is the most flexible approach in ESO family, where there is no necessity to suppose an oversized design domain (background structure) since BMESO can be adapted to include the addition and subtraction in the optimization procedure. Another merit of BMESO, is that it works perfectly on a wide array of engineering applications from large scale space frames to the small size plate samples. The general procedure for BMESO is detailed in the following steps (Yang, 1999) and (Querin *et al.*, 2000):

1. Assign the upper and lower bounds for the design variables, then choose an initial arbitrary set of values for the design variables, provided that the initial set is located within the predefined bounds mentioned above to start the optimization process.
2. Build the corresponding geometry for the model and specify the number of structural components in the system.
3. Assign the Optimality Criterion (OC) for the design, i.e. stress, stiffness etc. and set the design constraints.
4. Perform the structural analysis using appropriate Finite Element (FE) software.
5. Calculate the sensitivity number for each structural part in the system as demonstrated in section 5.4.
6. If a homogenous state for the sensitivity numbers has been reached across the overall structural system or when there is no noticeable change in the overall cost function, then go to step 12.
7. Sort the values of sensitivity numbers calculated in step 5.
8. Reduce the dimensions for the components satisfying Eq. (5.9) by simply selecting the next lower set of discrete values (the cross sectional specifications) available in the prescribed commercial tables listed in Appendix E.

9. Freeze the reduction process for the components in step 8 when they reach their lower bounds, even though they are satisfying Eq. (5.9).
10. Increase the dimensions for elements satisfying Eq. (5.10) by simply selecting the next higher set of discrete values (the cross sectional specifications) available in the prescribed commercial tables listed in Appendix E.
11. Freeze the boosting process for the components in step 10 when they reach their upper bounds, even though they are satisfying Eq. (5.10). Return to step 4.
12. Stop the optimization process and select the optimum trade-off model among the candidate design points.

5.4 Optimality Criteria

The main aim of any structural optimization survey is to reduce the structural weight or minimize the cost function, which is a complicated form of other behavioural, operational, functional, constructional, manufacturing, and practical requirements of the structural design. The most significant design criteria that affect the design procedure is that one correlated to the structural safety issues of the structure, such as (Hasancebi *et al.*, 2010),(Haftka, 2013), (Kaveh and Ghazaan, 2015), (Salam *et al.*, 2015) and (Wu *et al.*, 2017):

1. Overall structural stiffness.
2. Maximum equivalent stress in the structure.
3. Maximum absolute displacement in the structure.
4. Directional displacement at specified point within the structure.
5. Buckling load factor.
6. Natural frequency and compare it to the excitation frequency.

Any of abovementioned functions could be treated as equality or inequality constraint, whereas the constraints that control the design variables are called side constraints (Chu, 1997) (Yang, 1999). However, the current study considers the constraints of the cases 2, 3 and 5 of the abovementioned list, where the stress, displacement and buckling are constrained according to the relations (5.2), (5.3) and (5.4) respectively as illustrated in section 5.1.2. It is noteworthy that the safety factor (SF) is chosen depending on the optimization stage and the severity of the situation, where in stage 1 a relatively high safety extent was assumed, i.e. SF=1.6, 2 and 2 for stress, displacement and buckling respectively, whereas stage 2 was carried out considering strict safety conditions, i.e. SF=1 for each of stress, displacement and buckling constraints.

The earliest design investigations based on rigorous rules of optimality criteria is the Fully Stressed Design (FSD) which is fundamentally scaling the design variables set according the

ratio of element stress to the allowable stress as shown below (Bendsoe, 1989) (Xie and Steven, 1993):

$$x_i^{new} = x_i^{old} * \left[\frac{\sigma_i}{\sigma_a}\right] \tag{5.8}$$

Eq. (5.8) represents the iterative form of FSD optimization, x_i^{new}, x_i^{old} are the values of design variable for the current and the last iterations respectively. σ_i is the element stress, σ_a is the allowable stresses of material.

The strain energy density (SED) is a typical function exploited by optimality criteria rules to obtain minimum level of strain energy over the whole structure. The ideal utilization of optimality criteria can be achieved mathematically through discretising the structure into certain number of structural components as demonstrated in Chapter 4. Each component has its own sensitivity number and share with a weighted value in the overall cost function of the structure as explained in section 5.1.4 (Abolbashari and Keshavarzmanesh, 2006) (Huang and Xie, 2007).

The main merit of this strategy is its practicality to treat with the cost function in an engineered and organized manner to ensure an acceptable progression towards the optimum point. In other words, it is guided by a set of mathematical functions called design sensitivity numbers which are providing the optimization guideline for MESO to attain the optimum point in terms of cost function. It is generally reach the design goal with a relatively small number of analyses compared to MP and metaheuristics (Liang *et al.*, 2001) (Tanskanen, 2002) (Ghaffarianjam and Abolbashari, 2009). In optimality criteria formulation, each objective function in Eq. (5.1) could be a potential participant in the cost function defined in formula (5.6). In this study, a single objective formulation has been implemented considering the structural weight as design objective (i.e. $j = \{W\}$).

5.4.1 Stress Criterion

The earlier studies strength criterion have focused on design variables with continuous-based variability, i.e. the element density is assumed as design variable as adopted by Bendsøe and Kikuchi (1988) and Duysinx and Bendsøe (1998), followed by ESO invented by Xie and Steven (1993) and Xie and Steven (1994), then developed further by Ghaffarianjam *et al.* (2011). When the stress criterion applies, each structural component that satisfies Eq. (5.9) will be subjected to dimensional reduction (Abolbashari and Keshavarzmanesh, 2006) and (Hu *et al.*, 2012):

$$\left|\sigma_{\mathrm{vm)i}}^{\max}\right| \leq \mathrm{RR} * \left|\sigma_{\mathrm{vm}}^{\max}\right| \tag{5.9}$$

On the other hand, if any structural component satisfies (5.10), it will be selected for dimensional boost (Yang, 1999) and (Querin *et al.*, 2000).

$$\left|\sigma_{vm)i}^{max}\right| \geq (1 - RR) * |\sigma_{vm}^{max}| \quad (5.10)$$

where, $\left|\sigma_{vm)i}^{max}\right|$, $|\sigma_{vm}^{max}|$ are the absolute values of the maximum equivalent von Mises stress for the i^{th} structural component, and the whole dome roof structure respectively. RR is the Rejection Ratio as defined in section 5.2.

Ultimately, Eq. (5.9) specifies the structural components eligible for material elimination, whereas, Eq. (5.10) selects the members that must be subjected to material boost. Therefore, $\left|\sigma_{vm)i}^{max}\right|$ is termed as the stress sensitivity number for i^{th} structural component existing in the structure. $\left|\sigma_{vm)i}^{max}\right|$ is used to judge whether the involved member is underutilized or overstressed from stress viewpoint. When applying these principles, it is expected to attain a maximum reduction in structural weight corresponding to a minimum increase in the equivalent stresses of the dome roof structure as a whole (Özkal and Uysal, 2009) and (Hu *et al.*, 2012).

5.4.2 Stiffness Criterion

Strain energy (SE) level for the structure reflects the stiffness specifications of the design model. Thus, the strain energy density (SED) represents the inverse measure of the overall structural stiffness, so by minimizing SE, stiffness properties will improve. For example, reducing cross sectional dimensions of beam element will lead to a remarkable increase in SE, which will cause a degradation in stiffness properties of the entire structure. As analogous state to stress criterion, stiffness criterion is exactly resembling strength criterion and follow the same rules to reach the optimum strength with different sensitivity numbers, where Eqs. (5.9) and (5.10) are applicable for stiffness criterion (Li *et al.*, 2000) (Ansola *et al.*, 2006) (Ansola *et al.*, 2007).

An iterative procedure has been adopted to achieve the stiffness criterion, as this method is derived by the governing design criterion formulated using recursive relationship between SED and the design variables. SED could be simply defined as the amount of energy per unit volume stored in the material as result to its deformation state. Also, the stress-strain curve, presented in Figure 5.2, indicates that SED is graphically equal to the area covered by the curve within elastic limits as expressed in Eq. (5.11).

$$SED = \frac{1}{2}\sigma_1\epsilon_1 \quad (5.11)$$

where, σ_1 and ϵ_1 are the stress and strain for the state of deformation explained in Figure 5.2.

Thus, resizing the structural elements during the optimization is based on the relationships between the optimization parameters defined in Eqs. (5.1) and (5.6), as SE is estimated according to the formula (5.15). While, SED, as defined earlier, is equal to SE divided by the

volume measured on element-basis. This recurrence will be terminated when the convergence of the cost function is accomplished (Nha *et al.*, 1998)and (Saka and Geem, 2013).

To illustrate the sensitivity number concerning stiffness criterion, it is important to appoint the mathematical relationship between structural stiffness and mean compliance of the structure. It is evident that there is an inverse proportionality between the overall structural stiffness and strain energy extent existing in the structural system. The integral form of strain energy can be given in terms of stress and strain vectors as (Kim *et al.*, 2008):

$$\mathrm{SE} = \frac{1}{2}\int \{\sigma\}^T\{\varepsilon\}\, dV \tag{5.12}$$

Referring back to Eq. (5.12), it can be reformulated in an alternative in terms load and displacement to express the mean compliance in the dome roof frame, where the mean compliance is an alternative term for strain energy and can be expressed in the following formula (Ghaffarianjam and Abolbashari, 2010):

$$C = \frac{1}{2}\{P\}^T\{u\} \tag{5.13}$$

where, C is the overall mean compliance for the structure which represents the inverse measure for the overall stiffness of the structural system and this relationship is behind the fact that minimizing the strain energy results in maximizing the structural stiffness (Ansola *et al.*, 2007). Now, The variation in mean compliance (ΔC) can be written as (Chu *et al.*, 1996) (Liang and Steven, 2002) (Ansola *et al.*, 2006) :

$$\Delta C = \frac{1}{2}\{P\}^T\{\Delta u\} = -\frac{1}{2}\{P\}^T[K]^{-1}[\Delta K]\{u\} = \frac{1}{2}\{u_i\}^T[K_i]\{u_i\} \tag{5.14}$$

where, $\{u_i\}$ is the displacement vector of ith constituent part. Finally, the sensitivity number can be formulated in Eq. (5.15) (Nha *et al.*, 1998):

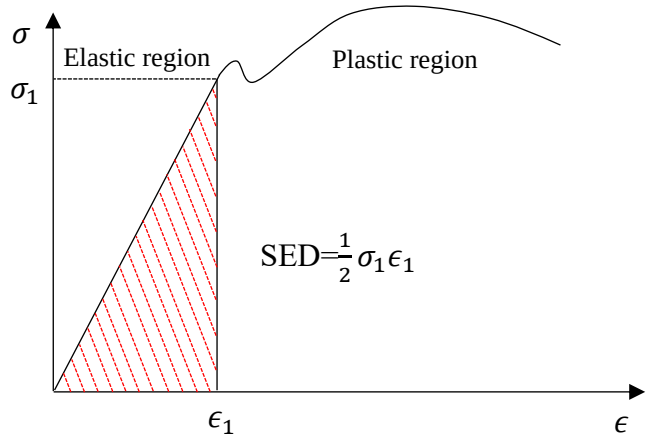

Figure 5.2 Stress-strain curve showing the definition of SED within elastic limits.

$$\alpha_i = \left(\frac{1}{2}\right)\{u_i\}^T[K_i]\{u_i\} \ \ (i = 1, \dots, n) \tag{5.15}$$

where, α_i is the strain energy sensitivity number which reflects the change of strain energy due to the dimensional modifications in the structural parts and it has positive sign. It is noteworthy that for stiffness criterion, it is highly recommended to reduce the dimensions for components with lowest values of α_i in order to attain a minimum increase in compliance.

When the structure is subjected to multiple loading cases, the sensitivity number is adapted to encompass all those conditions effectively. The sensitivity number for i^{th} segment concerning the kth load case is mathematically expressed as (Chu *et al.*, 1996) (Ansola *et al.*, 2006):

$$\alpha_{ik} = \left(\frac{1}{2}\right)\{u_{ik}\}^T[K_i]\{u_{ik}\} \ \ (i = 1, \dots, n) \tag{5.16}$$

where, k refers to the k^{th} load case. $\{u_{ik}\}$ is the displacement vector of i^{th} portion corresponding to k^{th} loading event. It is unusual to obtain a particular element at which its sensitivity number for all loading circumstances is the lowest in the structure. It is necessary to consider each α_{ik} alone depending on the proximity of that function to the limits of corresponding strain energy.

5.4.3 Frequency Criterion

Frequency criterion has been first introduced by (Xie and Steven, 1996) and (Zhao *et al.*, 1996) and developed by (Pedersen, 2000) (Huang *et al.*, 2010). In this criterion, it is easy to distinguish between the inactive components (elements with low frequency sensitivity numbers) and active ones (elements with high frequency sensitivity numbers). Eigenvalue investigation of the structure presents a good estimation for the dynamic nature of the vibrating structure. The dynamic equilibrium equation of motion for the dynamic system can be expressed in terms of stiffness and mass matrices as shown below:

$$\left([\mathrm{K}] - \omega_j^2[\mathrm{M}]\right)\{\mathrm{a}^j\} = 0 \tag{5.17}$$

where [K] is the global stiffness matrix, [M] is the global mass matrix, ω_j^2 is the j^{th} eigenvalue and $\{\mathrm{a}^j\}$ is the j^{th} eigenvector corresponding to ω_j^2. Rayleigh quotient is an essential factor for correlating each of eigenvalue ω_j^2 and eigenvector $\{\mathrm{a}^j\}$ through the following relationship (Zhao *et al.*, 1996):

$$\omega_j^2 = \frac{k_j}{m_j} \tag{5.18}$$

For which, the modal stiffness and mass matrices k_j & m_j can be introduced in formulae (5.30) and (5.31) respectively:

$$k_j = \{\mathrm{a}^j\}^T[\mathrm{K}]\{\mathrm{a}^j\} \tag{5.19}$$

$$m_j = \{a^j\}^T [M] \{a^j\} \tag{5.20}$$

By substituting Eqs. (5.19) and (5.20) into Eq. (5.18), then it can be rewritten in the following form:

$$\Delta(\omega_j^2) \approx \frac{\Delta k_j}{m_j} - \frac{k_j \Delta m_j}{m_j^2} \approx \frac{1}{m_j}(\Delta k_j - \omega_j^2 \Delta m_j) \tag{5.21}$$

To simplify the process of solving Eq. (5.21) to find the roots of the term $\Delta(\omega_j^2)$ mentioned above, a reasonable assumption for $\{a^j\}$ must be carried out to suppose that $\{a^j\}$ is preserved constant over any two consecutive optimization cycles, so the magnitude of change can be neglected between any two sequential iterations. By adopting this assumption, the difference in modal stiffness and mass magnitudes resulting from the reduction or increase of i^{th} element in the structure can be given by:

$$\Delta k_j \approx \{a^{ij}\}^T [K^i] \{a^{ij}\} \tag{5.22}$$

$$\Delta m_j \approx \{a^{ij}\}^T [M^i] \{a^{ij}\} \tag{5.23}$$

For which $[K^i]$ and $[M^i]$ are the stiffness and mass matrices of i^{th} component, [K] and [M] are the global stiffness and mass matrices respectively. Suppose modifying element i due to satisfaction of the criterion condition in the j^{th} mode, $\{a^{ij}\}$ is introduced to cover all of the above features. Thus, from equations (5.21) to (5.23), the differential term for eigenvalue problem might be reformulated as:

$$\Delta(\omega_j^2) \approx \frac{1}{m_j} \{a^{ij}\}^T ([K^i] - \omega_j^2 [M^i]) \{a^{ij}\} \quad (i = 1, \dots, n) \tag{5.24}$$

Hence, the sensitivity number for component change that maximize the vibration frequency for the overall system is detailed in formula (5.25).

$$\beta_{ij} \approx \frac{1}{m_j} \{a^{ij}\}^T ([K^i] - \omega_j^2 [M^i]) \{a^{ij}\} \quad (i = 1, \dots, n) \tag{5.25}$$

The change in the value of β_{ij} indicates the variability in the value of ω_j^2 of the j^{th} mode shape for the vibrating structure. When only one mode is considered, the modal mass m_j in formula (5.34) is correlated the mass properties of the component under consideration.

It is noticeable that the values of β_{ij} are ranging from the positive (maximum) to the negative (minimum). Hence, the removal of material from components associated with low frequency sensitivity number will preserve the reduction occurring in the natural frequency of the structural system as low as possible, and reversely, the removal of material from the component with higher values of sensitivity numbers will cause a noticeable degradation in frequency characteristics of the structural system.

5.4.4 Buckling Criterion

The buckling sensitivity number (buckling index) can be simply defined as:

$$\xi_i^{buck\_ind} = \frac{F_i^{comp}}{F_i^{crit\_buck}} \tag{5.26}$$

where, F_i^{comp} is the compressive axial force in member (i). For members having tensile axial force, the value of $\xi_i^{buck\_ind}$ is zero. The Euler critical buckling load ($F_i^{crit\_buck}$) must be calculated for each member (i) in the braced dome structure:

$$F_i^{crit\_buck} = \hat{q}\pi^2 \left(\frac{E * I_{zz}}{L^2}\right)_i \tag{5.27}$$

where, $\hat{q}$ is a coefficient represent the measure of end loading conditions, i.e. $\hat{q}$=4 for rigidly-jointed members and $\hat{q}$=2 for pin-jointed members. E is Young's elastic modulus, Izz is the second moment of area for the cross section, L is the effective length of the member (i) (Varma, 2015).

5.5 Single Objective Metaheuristic Techniques

Five metaheuristic methods have been chosen to optimize the dome roof frame models considered in this study. These methods are:

- Artificial Bee Colony (ABC).
- Bees Algorithm (BA).
- Differential Evolution (DE).
- Particle Swarm Optimization (PSO).
- Simulated Annealing (SA).

Generally, most metaheuristic techniques use a stochastic search mechanism as a selection strategy for generating new solutions.

5.5.1 Artificial Bee Colony (ABC)

Referring to section 2.4.1, four outstanding roles can be distinguished when describing the general procedure of ABC technique.

A. Initial Population

The initial estimation of metaheuristic variables considered in ABC strategy is performed in a stochastic technicality. Many factors are governing the initial position of the relevant variables. These are: lower bounds, upper bounds, and the population size for the associated design variables. Accordingly, random amounts nectar will be gathered initially by the recruited bees assigned for this task. Thus, the initial position vector for the metaheuristic set of variables can

be formulated in Eq. (Karaboga and Akay, 2011), (Özkis and Babalik, 2013), (Xiang and An, 2013) and (Patel *et al.*, 2016):

$$x_{i,j}^{(0)} = x_i^{min} + rand[0,1] * \left(x_i^{max} - x_i^{min}\right) \quad (5.28)$$

$i \in \{1, 2, 3, \dots, nPop\}$, $j \in \{1, 2, 3, \dots, N\}$. nPop is population size or the number of food sources. N is the number of optimization parameters (design variables). $x_{i,j}^{(0)}$ is the initial value of the i^{th} design variable joining to the j^{th} individual. x_i^{min}, x_i^{max} are the lower and upper bounds for the i^{th} design parameter associated with the j^{th} individual. $rand[0,1]$ stands for a random variable distributed uniformly over the range [0,1]. Trying different seeds for this random set of points would affect the final result of the technique.

B. Recruited Bees

It is remarkable that the number of employed bees is matching exactly the number of food sources. As mentioned earlier in this section, the reason behind the robustness of ABC as optimization tool is attributed to the organizational style of work and the collaborative nature of the hive individuals. That means the work is allocated among the honeybee colony members according to the expertise of each one of them. In this sense, employed bees are designated to perform the primary metaheuristic search within predefined population size. In this mission, recruited bees are expected to obtain the maximum nectar material from the neighboring food sources compared to the amount of nectar collected initially. The relevant position for recruited bees can be posed in Eq.(5.29) (Baykasolu *et al.*, 2007), (Karaboga and Basturk, 2007a), (Karaboga and Basturk, 2008), (El-Abd, 2011), (Karaboga and Akay, 2011), (Akay and Karaboga, 2012), (Gao and Liu, 2012), (Ozkis and Babalik, 2013) and (Yu *et al.*, 2013).

$$v_{i,j}^{it} = x_{i,j}^{it-1} + \emptyset_{i,j} * \left(x_{i,j}^{it-1} - x_{k,j}^{it-1}\right) \quad (5.29)$$

where, $v_{i,j}^{it}$ is the current position of recruited bee i, for the design variable j, calculated for the iteration No. (it). $x_{i,j}^{it-1}$ is the previous position of recruited bee i, for the design variable j, calculated in the iteration No. (it-1). $x_{k,j}^{it-1}$ is the position of a randomly selected bee (k), concerning the design variable j, calculated at iteration No. (it-1). $j = \{1, 2, 3, \dots, N\}$, N is the number of design variables. $\emptyset_{i,j}$ is the acceleration coefficient for the associated mutation process which is a real random number ranging within the period $[-1, +1]$. $k \in \{1, 2, 3, \dots, nPop\}$ is an integer index selected randomly from the mutant vector $\{1, 2, 3, \dots, nPop\}$.

The latter vector is configured as random set of integer numbers corresponding the positions of the previous recruited bees' group with excluding the integer (i) that corresponds the position

of the i^{th} recruited bee under consideration (i.e. $v_{i,j}^{it}$). The perturbation resulting from the difference between the preceding positions $x_{i,j}^{it-1}$ and $x_{k,j}^{it-1}$ is diminishing gradually each optimization cycle. There is some control loop to clip the values of metaheuristic variables that exceed their prescribed limits. Namely, if the parameter exceeds its boundary value, it will be reset equal to its boundary.

C. Onlooker Bees (Roulette Wheel Selection)

To start this stage, the fitness function ($COST_i$) must be estimated for the recruited bees corresponding to the considered onlooker bees (Karaboga and Basturk, 2008), (Zou *et al.*, 2011b) and (Kong *et al.*, 2013):

$$\begin{aligned} COST_i &= {}^{1}/_{(1+f_i)} \quad \text{if} \quad f_i \geq 0 \\ COST_i &= 1 + abs(f_i) \quad \text{if} \quad f_i < 0 \end{aligned} \tag{5.30}$$

where, f_i is the value of cost function corresponding to the position of i^{th} recruited bee (i.e. $v_{i,j}^{it}$). Greedy selection mechanism can be applied to filter out the bad solution and select the minimum between $v_{i,j}^{it}$ & $x_{i,j}^{it-1}$. The profitability of the food source is the only driving parameter towards the optimum point. To control this process, the counter C is set to measure the feasibility of the current position for the i^{th} bee (whether recruited or onlooker). This counter is increasing by one each time the recruited or onlooker bee is failing to improve the nectar amount. As penalty, when this counter exceeds a particular limit defined as constant L (see the parameters C and LC in Figure 5.3), the corresponding bee will be deprived to revisit its respective patch (food source), which causes this failure according to the abandonment rules. When the abandonment condition is satisfied, the counter will be reset to 0.

However, onlooker bees have the choice to land at any of food sources reported by their recruited counterparts. This choice is relying on the probability value produced by applying Roulette Wheel Selection (RWS) approach to the mean value of nectar quantities gathered by the corresponding previous set of recruited bees as given in the Eq. (5.31) (Karaboga and Akay, 2009), (Patel *et al.*, 2016), (Karaboga and Ozturk, 2011), and (Karaboga and Akay, 2011).

$$P_i = \frac{COST_i}{\sum_{i=1}^{nPop} COST_i} \tag{5.31}$$

where, P_i is the probability distribution value. $COST_i$ is the value of cost function for the i^{th} recruited bee. nPop is the number of food sources which is equivalent to the number of employed (recruited) bees.

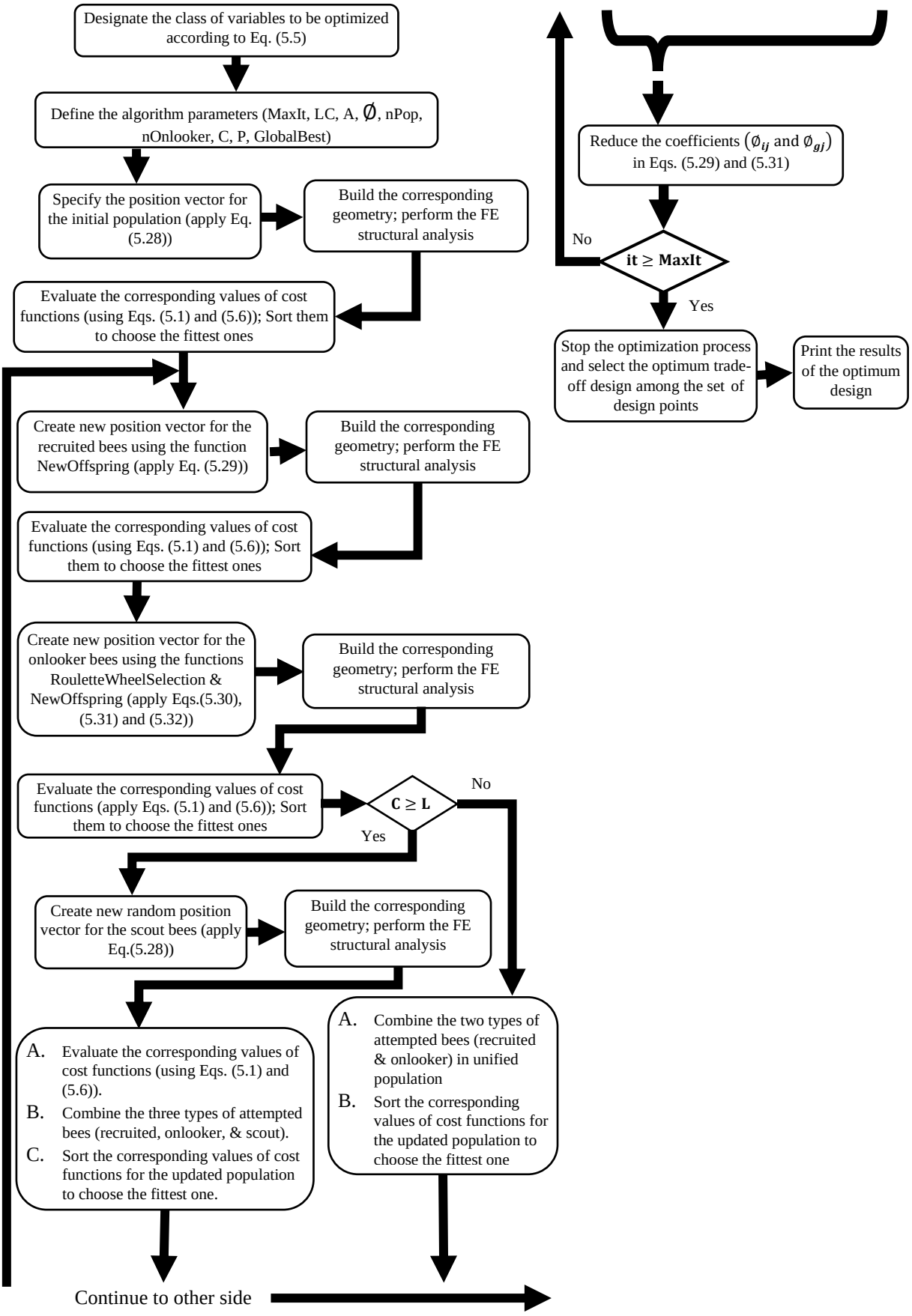

Figure 5.3 Logical steps of standard ABC strategy.

Depending on P_i and RWS, the new mutant position vector for onlooker bees can be estimated according to the formula (5.32) (Akay and Karaboga, 2012) and (Xu *et al.*, 2013) and (Sevim *et al.*, 2016):

$$v_{g,j}^{it} = x_{g,j}^{it} + \emptyset_{g,j} * \left(x_{g,j}^{it} - x_{k,j}^{it}\right) \quad (5.32)$$

where, $j = \{1, 2, 3, \dots, N\}$, N is the number of design variables. $\emptyset_{g,j}$ is the acceleration coefficient defined in the previous section. $k \in \{1, 2, 3, \dots, nPop\}$ is an integer index selected randomly from the mutant vector $\{1, 2, 3, \dots, nPop\}$. The latter vector is configured as random set of integer numbers corresponding the positions selected by exploiting the RWS approach for the previous set of recruited bees with excluding the integer (g) that corresponds the position of g^{th} recruited bee under calculation (i.e. $v_{g,j}^{it}$). where, g is a random integer number calculated as a position for the relevant recruited bee as demonstrated in Eq. (5.33) (Sonmez, 2010), (Kong *et al.*, 2013), (Aydoğdu *et al.*, 2016):

$$g = \text{find}(r \leq \{C\}), \quad r = \text{rand}[0,1], \quad \{C\} = \left\{\sum_{i=1}^{nPop} P_i\right\}, i = \{1, 2, 3, \dots, nPop\} \quad (5.33)$$

where, r is a random real number ranging from 0 to 1. The probabilistic selection is performed to extract the corresponding value of g which is proportional to fitness values when feasible solution exists. While, it is inversely proportional to the set of fitness values when the solution is infeasible. $\{C\}$ is the cumulative summation vector of the probabilistic distribution coefficient P_i (Özkis and Babalik, 2013).

D. Scout Bees (Abandonment Criterion)

The nectar collection of any artificial bee is assessed and updated through the direct comparison with the global ideal one called the (global best cost). Furthermore, there is a record for each bee which lists all activities for that particular bee. This record is managed by the monitoring bees that write down the scores as a feedback for the visited food sites and the corresponding visitor bees. If the position of that specific bee is failed to achieve the required improvement in the nectar magnitude for specific number of cycles, then that position is crossed and assigned as abandoned site. Thus, obtaining such result necessitates the corresponding bee to renounce its food source and start to search for new position as scout bee. The new position ($x_{i,j}^{(0)}$) can be defined in Eq. (5.28) (Karaboga, 2005), (Alatas, 2010) and (Gao *et al.*, 2012).

$x_{i,j}^{(0)}$ is the alternative random position for the i^{th} scout bee concerning the j^{th} decision variable.

The block diagram presented in Figure 5.3 demonstrates the abbreviated steps to execute the optimization process in ABC. The first step is to define the five subsets of design variables as given in Eq. (5.5). The next step is to choose the most appropriate values for the algorithm

parameters needed to perform a reliable and efficient optimization for the considered application. For example, specific values for the optimization parameters of ABC technique, listed in Table 5.1, are used to carry out the optimization process for the current application (storage tanks). The maximum number of iterations are presented in terms of the optimization stages. Thereafter, the position vector for the initial population, represented by N_n, N_r, N_m, N_s, and N_t, for stage 1 or R, ƞ and ʊ for stage 2, needs to be specified according to Eq. (5.28). This position represents the initial patches for the recruited bees. Upon this, build the geometry and perform the analysis to obtain an initial evaluation of cost. Then, update the positions (patches) of recruited bees using Eq. (5.29) and estimate the corresponding cost values. Thereafter, search for new positions (or patches) using the information provided by the parent recruited bees as formulated in Eq. (5.32) by aid of fitness function $COST_i$, defined in Eq. (5.30), probabilistic distribution coefficient P_i, defined in Eq. (5.31), and the integer (g) chosen by RWS mechanism, defined in Eq. (5.33). The exhausted patches will be excluded according to the abandonment limits (L=10) to create new scout bees searching randomly in new spots within the design space. Finally, all types of bees are sorted according to their cost values to choose the fittest one.

Table 5.1 Optimization parameters used to implement ABC technique.

Name	**Description**	**Value**
MaxIt1	Maximum number of iterations for stage 1	12 (integrated single lattice)
		20 (simplified single lattice)
		20 (simplified double lattice)
MaxIt2	Maximum number of iterations for stage 2	24 (integrated single lattice)
		40 (simplified single lattice)
		80 (simplified double lattice)
MaxIt3	Maximum number of iterations for stage 3	7 (integrated single lattice)
		3 (simplified single lattice)
		3 (simplified double lattice)
nPop	Population size	10
nOnlooker	Number of onlooker bees	1
∅	Acceleration coefficient	0.95
L	Abandonment limit parameter	10
Pi	Probabilistic distribution coefficient	According to Eq. (5.31)
g	Rank of individual selected by RWS approach	According to Eq. (5.33)

5.5.2 Bees Algorithm (BA)

BA, like other metaheuristic techniques is starting its stochastic search through determining the initial set of design variables $x_{i,j}^{(0)}$, where foraging bees are starting to search the food sites randomly as given in Eq. (5.28) (Ko$, 2010), (Fahmy, 2012), (Tsai, 2014) and (Rajasekhar *et al.*, 2017).

In which, i $\in \{1, 2, 3, \ldots, \text{nPop}\}$, j $\in \{1, 2, 3, \ldots, \text{N}\}$, i is a counter for population size (nPop), j is a counter for design parameters (N), whereas, nPop is the number of honeybees initializing the population. N is the number of design variables. rand[0,1] is a random number mediating between 0 and 1. This set of initial points is decisive for the subsequent steps as outlined in Figure 5.4.

The size of neighborhood is initially large ($\psi_r^0 \equiv \psi^0$) and reduces gradually:

$$\psi_r^{i+1} = \emptyset \psi_r^i \tag{5.34}$$

where, $\emptyset$ is an acceleration coefficient (cooling off factor is supposed to be between zero and one), and the superscript indicates the number of unsuccessful searches in that region. If after several attempts the search region does not lead to a better solution, it is assumed to be a local minimum, abandoned, and a new search begun elsewhere.

Key to the BA is managing resources in each iteration, such as the number of new potential solutions selected within each active search region, $\mathcal{N}(h_r, \psi_r)$, and the number of new potential solutions selected from across the whole solution space, $\mathcal{X}$.

This ambiguity has an impact on the definition of local neighborhoods, i.e., identifying regions in solution space that are close to existing solutions. Let $\mathcal{X}$ be the set of all potential solutions to the given optimization problem, then the neighborhood of a given solution $x \in \mathcal{X}$ considering spherical search space can be defined as:

$$\mathcal{N}(x, \psi) = \{y \in \mathcal{X}\ s.t. |y - x| < \psi\} \tag{5.35}$$

where ψ is the radius of locality, and $|y - x|$ is the metric, i.e., a measure of the distance between the two solutions. However, in the above case of sections where multiple orderings are possible, neighborhoods can look very different depending on how the metric is defined.

In general, let $f(x)$ be the cost function defined over all of $\mathcal{X}$, and let $\mathcal{H}$ be the subset of all solutions for which the cost is known, then a further subset of solutions, $h_1, h_2, \ldots, h_n \in \mathcal{H}$, ideally with distinct neighborhoods, can be selected for further exploration, with new potential solutions selected randomly from the neighborhoods $\mathcal{N}(h, \psi)$. Reducing the neighborhood radius, ψ, restricts the search space for new solutions, which can improve convergence to an optimum, but can also be overly restrictive if the solution space, $\mathcal{X}$, is not continuous.

Unlike ABC, BA population is subdivided into 3 distinct groups of bees (elite, selected, and non-selected (random)) with Consider n food sources are available to the bees to collect the nectar. Each food spot represents a feasible solution with position and cost, but at the utmost there are set of best sites that provide the colony with a nectar more than other sites (i.e. the global best).

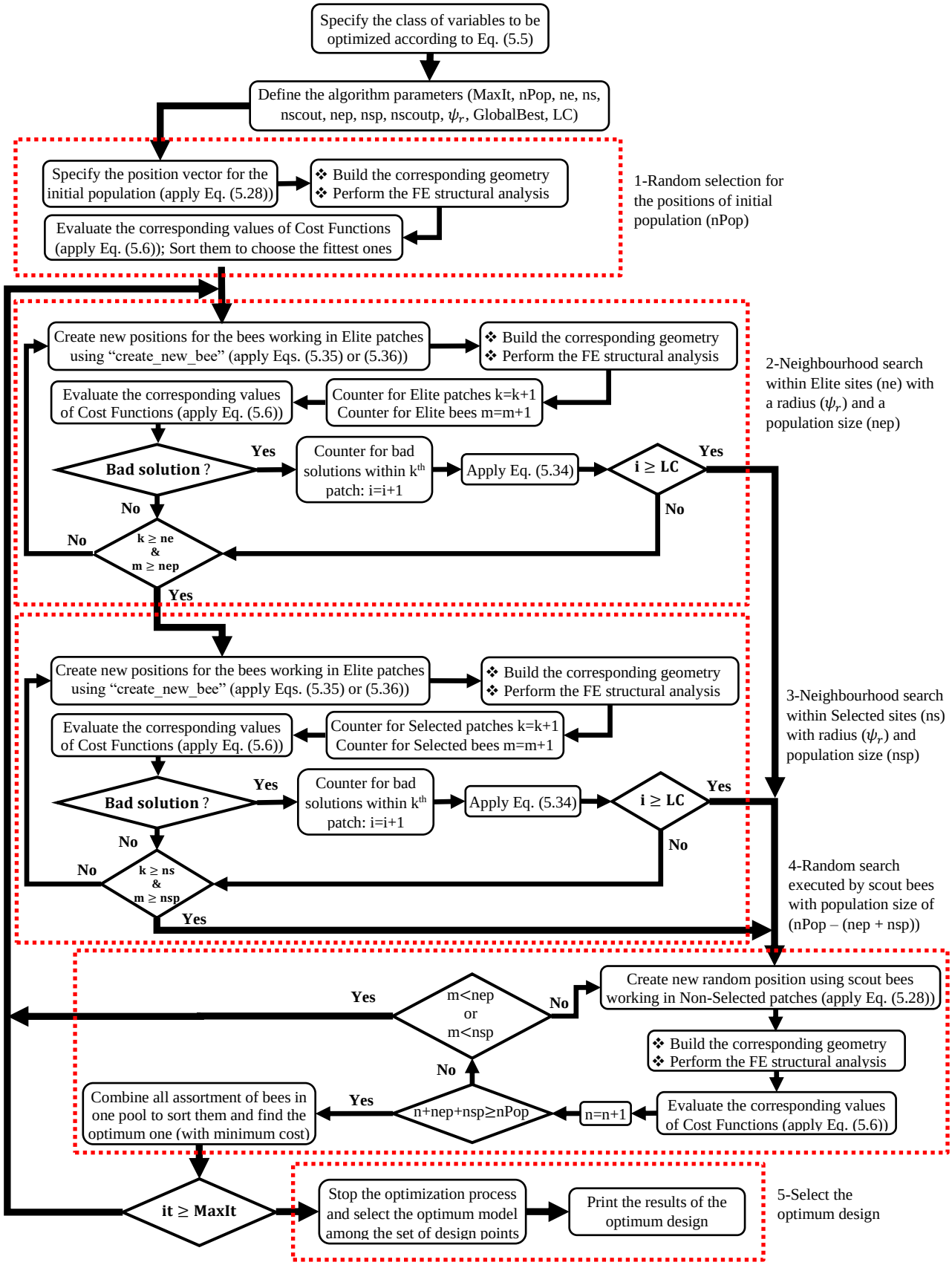

Figure 5.4 General procedure for the standard BA strategy.

In BA, three kinds of recruited bees are committed to perform the search within three types of patches in the lawn. The first is defined as elite sites with number (ne), as those are managed by elite bees with number (nep). The second, category is denoted as selected sites with number (ns), which are controlled by (nsp) selected bees, such that (nep > nsp). Considering cubic neighborhood search space, both of elite and selected bees are executing the local search mechanism with the square bounds $[-\psi_r, +\psi_r]$ as defined in Eq. (5.36). The duties are allocated for them such that each patch will be visited by at least one recruited bee, i.e. in most cases specialized group of bees each are equipped to seek for the nectar within each patch in this field of search. Thus, the position of bees inspecting for the food in the vicinity have the size nep in case of ne patches and nsp in case of ns patches, is defined in formula (5.36) (Aghazadeh and Meybodi, 2011), (Tsai, 2014) and (Rajasekhar *et al.*, 2017):

$$u_{i,j} = x_{i,j} + \text{rand}[-\psi_r, +\psi_r] * \left(\bar{x}_j^{\max} - \bar{x}_j^{\min}\right) \tag{5.36}$$

where, $i \in \{1, 2, 3, \dots, k\}$ & $j \in \{1, 2, 3, \dots, N\}$, k is the population size for the current category of patches (i.e. nep or nsp), N is defined earlier in this section. ψ_r is the radius of neighborhood search for the selected patch, where the term $\text{rand}[-\psi_r, +\psi_r]$ is a random number ranging from the lower bounds $(-\psi_r)$ to the upper bounds $(+\psi_r)$. The cooling out factor $(\emptyset)$ is working on constricting the radius of local search space progressively as formulated in Eq. (5.34) (Koc, 2010) and (Akpinar and Baykasoğlu, 2014).

Hence, the remaining sites is called non-selected spots, which have the number (nscout=nPop-nep-nsp), their positions can be determined randomly through employing the last group of bees (scout bees) with number (nscoutp=nscout), as they are exactly equal to the number of non-selected patches. Thus, the remaining population outside nep and nsp bees is specified to perform the role of scout bees by trying a new uniform random search to discover whether the new patch is a better option or not. Hence, Eq. (5.28) is applicable for the last group of bees, i.e. the scout bees that searching for new sites randomly to improve the quantity of the collected food. The same greedy strategy is applied for this method to decide which bee will continue to work in the colony for the next iterations.

Table 5.2 lists the optimization parameters, with their respective values, used in BA method. There is no necessity to list the data concerning the number of iterations, since they are identical with those carried out in ABC as indicated in Table 5.1. The flow chart shown in Figure 5.4 explains the main steps used to execute BA algorithm for the current dome roof models. These steps can be abbreviated in the following points:

- Create an initial population according to Eq. (5.28).

- ❖ Perform a neighbourhood search within elite sites (ne) with a radius (ψ_r) and population size (nep).
- ❖ Perform a neighbourhood search within selected sites (ns) with a radius (ψ_r) and population size (nsp).
- ❖ Judge whether the current patch needs to be abandoned by checking its productivity for n times and compare it with the number of fails (LC=5) to create new scout bees to perform this task. The population size of scout bees is (nPop – (nep + nsp)).
- ❖ Sort all types of bees to select the minimum cost among them.

Table 5.2 Optimization parameters used to implement BA technique.

Name	**Description**	**Value**
nPop	Population size	10
ne	Number of elite patches	1
ns	Number of selected patches	2
nscout	Number of scout patches	1
nep	Number of elite bees	5
nsp	Number of selected bees	2
nscoutp	Number of scout bees	1
ψ_r	Radius of neighborhood search	0.2
$\emptyset$	Cooling out factor (restriction coefficient)	0.9
LC	Number of fails needed to change the patch	5

5.5.3 Differential Evolution (DE)

As detailed in section 2.4.3, the DE algorithm has its own rules to reproduce new generations (solutions) by utilizing three evolutionary operators (mutation, crossover and selection). The DE collects the required information to create the new offspring from the diverse individuals in the original population. Three governing coefficients are employed to perform this job: scaling factor (F), crossover probability coefficient (PCR), and the population size (nPop). Those constants are depending to some extent on the problem to be solved (Pan *et al.*, 2011), (Mohamed and Sabry, 2012) and (Yang *et al.*, 2013).

A. Initial Population

The standard form of probability distribution is efficiently exploited to decide the effective starting point for the stochastic search carried out by DE. Thus, DE begins with a random distribution in N-dimensional space. The initial set of solutions corresponding to this randomized set of variables can be evaluated. There are upper and lower limits for the design variables and the selection of the random set must be restricted to this range. The uniform random distribution function, used in section 5.5.1 given by Eq. (5.28), is exploited to create

the initial random set for DE (Mallipeddi *et al.*, 2011), (Yu and Zhang, 2012), (Cai and Wang, 2015) and (Das *et al.*, 2016).

B. Mutation Operation

The group of individuals for certain generation, named "target vector", are used to produce new donor (mutant) vector by technique called vector generator. Thereafter, the mutant vector is merged with target vector to produce a trial vector. Consider the arbitrary position vector x_i , i=1, 2, 3, …, N, where N is the number of design variables. The target vector is mutated to produce the trial vector. Active comparison is accomplished for the trial vector against the target vector when it reaches nPop, and the principle of the survival of the fittest is applied in this process. This process results in updating the target vector to select the fittest values. The most common modes of mutation, used in the literature, can be expressed in the formulae (5.37) to (5.41) (Zou *et al.*, 2011a), (Yu and Zhang, 2012), and (Cheng *et al.*, 2016).

$$\acute{x}_j^{it} = x_{r1}^{it-1} + F * \left(x_{r2}^{it-1} - x_{r3}^{it-1}\right) \tag{5.37}$$

$$\acute{x}_j^{it} = x_{best}^{it-1} + F * \left(x_{r1}^{it-1} - x_{r2}^{it-1}\right) \tag{5.38}$$

$$\acute{x}_j^{it} = x_j^{it-1} + F * \left(x_{best}^{it-1} - x_j^{it-1}\right) + F * \left(x_{r1}^{it-1} - x_{r2}^{it-1}\right) \tag{5.39}$$

$$\acute{x}_j^{it} = x_{best}^{it-1} + F * \left(x_{r1}^{it-1} - x_{r2}^{it-1}\right) + F * \left(x_{r3}^{it-1} - x_{r4}^{it-1}\right) \tag{5.40}$$

$$\acute{x}_j^{it} = x_{r1}^{it-1} + F * \left(x_{r2}^{it-1} - x_{r3}^{it-1}\right) + F * \left(x_{r4}^{it-1} - x_{r5}^{it-1}\right) \tag{5.41}$$

where F is the mutation scaling factor, it is real fraction ranging from 0 to 1, it is used to control the difference vectors mentioned in Eqs. (5.37) to (5.41), $\acute{x}_j^{it}$ is the mutant vector belonging to the j^{th} individual estimated at the current iteration (it), x_{best}^{it-1} is the best position for the preceding iteration (it-1), x_{r1}^{it-1} is the position vector for the individual ranked r1 calculated at the preceding iteration (it-1), and so on for other ranks ($r2, r3, r4 \,\&\, r5$). The ranks $r1, r2, r3, r4 \,\&\, r5$ are random integer indices selected from the set of positions defining the individuals vector {1, 2, 3,…, nPop}, provided that those ranks ($r1, r2, r3, r4 \,\&\, r5$) are chosen from the mutation vector ($V_{mutation}$), for which the current index j is excluded. It is also noticed that the condition ($nPop \geq 6$) must be satisfied in order to allow for $r1, r2, r3, r4 \,\&\, r5$ to select their positions freely. (Storn and Price, 1997) (Mallipeddi *et al.*, 2011).

C. Crossover Operation

One of DE merits is the high degree of variance for each design variable within its range, this spattering of data can be realized by implementing high level of perturbation using approximately binomial distribution over N-dimensional space. Thus, the trial vector for any individual (j) could be expressed as series of mutated design parameters as formulated in Eq. (5.42) (Ghosh *et al.*, 2011) and (Trivedi *et al.*, 2016).

$$\vec{\mathrm{p}}_j^{it-1} = \left(\mathrm{p}_{1j}^{it-1}, \mathrm{p}_{2j}^{it-1}, \dots, \mathrm{p}_{Nj}^{it-1}\right) \tag{5.42}$$

To express Eq. (5.42) in terms of decision variables {i=1, 2, …, N}, this entails to introduce the crossover probability constant PCR, hence the following logical sentence could be applied (Storn and Price, 1997), (Mezura-Montes *et al.*, 2010), (Pan *et al.*, 2011) and (Cai and Wang, 2015):

$$\mathrm{p}_{i,j}^{it} = \begin{cases} \acute{\mathrm{x}}_{i,j}^{it} & \text{if } \mathrm{rand}[0,1] \le \mathrm{PCR} \;\; || \;\; \mathrm{i} = \mathrm{rnbr(i)} \\ \mathrm{x}_{i,j}^{it-1} & \text{otherwise} \end{cases} \tag{5.43}$$

According to Eq. (5.43), i={1, 2,…, N} is an integer counter over N-dimensions. $\mathrm{rand}[0,1]$ is a random fraction uniformly distributed over the range [0,1]. PCR is the crossover probability coefficient ranging between 0 and 1. $\mathrm{rnbr(i)}$ is the index of the candidate design variable to be chosen randomly which is an integer number located within the period {1, 2,…, N} to guarantee that the trial vector $\mathrm{p}_{\mathrm{i,j}}^{\mathrm{it}}$ selects at least 1 variable from the mutant vector $\acute{\mathrm{x}}_{\mathrm{i,j}}^{\mathrm{it}}$ (Zaharie, 2005), (Mezura-Montes *et al.*, 2010), (Silva *et al.*, 2011), (Elsayed *et al.*, 2011) and (Li *et al.*, 2016). A comprehensive explanation for the standard DE strategy is shown in Figure 5.5.

D. Selection of Global Optimum

Most of metaheuristic techniques are performing a global search mechanism by the aid of greedy strategy which is nominating a global component called a "global best" to compare it with other individuals in the population at each iteration. For DE strategy, the trial vector $\mathrm{p}_{i,j}^{it}$ is compared to the target vector $\mathrm{x}_{i,j}^{it-1}$ (the original population). Now, if the cost function of the trial vector $\mathrm{p}_{i,j}^{it}$ is less than or equal to the cost function for the original vector $\mathrm{x}_{i,j}^{it-1}$ or mathematically $\left[\mathrm{COST}_{\mathrm{p}_{i,j}^{it}} \le \mathrm{COST}_{\mathrm{x}_{i,j}^{it-1}}\right]$ then $\mathrm{x}_{i,j}^{it} = \mathrm{p}_{i,j}^{it}$ and if $\left[\mathrm{COST}_{\mathrm{p}_{i,j}^{it}} > \mathrm{COST}_{\mathrm{x}_{i,j}^{it-1}}\right]$ then $\mathrm{x}_{i,j}^{it}$ will hold its old value, namely, $\mathrm{x}_{i,j}^{it} = \mathrm{x}_{i,j}^{it-1}$.

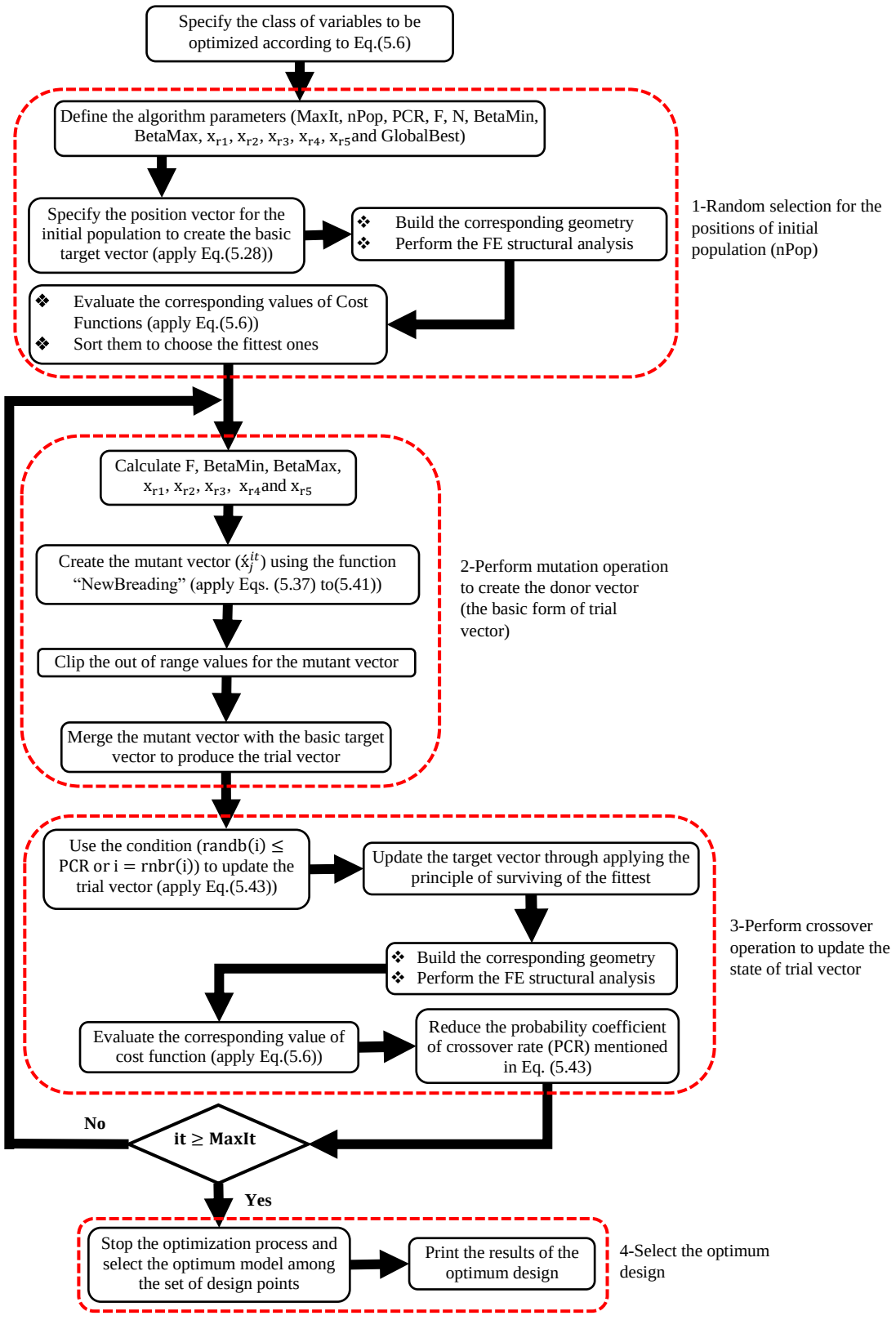

Figure 5.5 Logical steps of the conventional DE strategy.

The flow of the processes in DE strategy is presented in Figure 5.5, where the DE algorithm is used the data listed in Table 5.3 to implement the optimization for the current design models. There is no necessity to list the data concerning the number of iterations, since they are identical with those carried out in ABC as indicated in Table 5.1. Similar to the BA, the DE starts with initial population, hence Eq. (5.28) is used for this purpose. 12 iterations with nPop=10 are specified for stage 1 in case of integrated models, 20 iterations for simplified single and double lattice models. To find the total number of analyses, simply multiply the number of iterations by the population size. For example, the total number of analyses need to be implemented at stage 2 for the simplified double lattice model is MaxIt2×nPop = 80×10 = 800. The scaling factor of mutation (F) for this work is supposed to be ranging between 0.2 and 0.8. While, PCR adopted for the DE technique is 0.3, which is the ideal value for the coefficient to perform the crossover efficiently. According to Figure 5.5, updating the position for any individual in DE strategy needs to significant operations as follow:

- Perform mutation operation based on specifically selected individuals using one of the approaches given in Eqs. (5.37) to (5.41) to produce trial vector.
- Perform 1-way crossover using formula (5.43) and apply the principle of surviving of the fittest to update the target vector.

Table 5.3 Optimization parameters used to implement DE technique.

Name	**Description**	**Value**
nPop	Population size	10
BetaMin	Lower bound of scaling factor	0.2
BetaMax	Upper bound of scaling factor	0.8
F	Scaling factor of mutation	[0.2, 0.8]
PCR	Probability coefficient of crossover rate	0.3

5.5.4 Particle Swarm Optimization (PSO)

Section 2.4.4 states that the PSO employs a swarm of particles benefiting from their personal and social relations to update their positions during the movement to find the optimal path of flight. Thus, the population assumed to represent these particles can be expressed as:

$$\vec{x}_j = \{x_{1,j}, x_{2,j}, x_{3,j,} \dots, x_{N,j}\} \quad (5.44)$$

where, $\vec{x}_j$ stands for the set of design variables existing in the j^{th} voluntary particle swimming in the solution space, (N) is the number design variables, j={1, 2, …, nPop}. Thus, at each iterative step (it), there are nPop number of feasible solutions act as explorative points called "particles". They are communicating, exchanging information, teaching each other to decide the best in terms of their solution values. The transition of position for any particle that remarked

in two sequential iterations is based on the social behavior of the swarm. Each particle tries to change its location to a better one in the next iteration by collecting the useful data related to the set of values of cost functions for other particles in the group (Wetter and Wright, 2004).

It is noticeable that PSO has a fewer number of optimization parameters relative to EA. The general procedure for implementing PSO optimizer can be abbreviated in the following articles (Kuo and Huang, 2009), (Talukder, 2010), and (Rini *et al.*, 2011):

a. Initialize the problem by assigning the number of particles (nPop), specify the initial velocity (Vinitial), maximum and minimum velocity (Vmax, Vmin), assume the coefficient of inertia (w), and the two learning coefficients (c1 & c2) with the two random fractures (rand[0,1]), where$[0 \leq \text{rand}\,[0,1] \leq 1]$.
b. Initialize the position for each particle randomly within the search space, specify the range of velocity for the set of particles.
c. Calculate the value of cost function for each particle in the system.
d. Update the personal best $\vec{P_j}(t)$, and the global best $\vec{g}(t)$.
e. Generate new position $\vec{x_j}(t)$ by adding the three components of motion to the original position of the particle, velocity or inertia component ($\vec{V}_{\text{inertia}}$), cognitive or personal component ($\vec{V}_{\text{local}}$), global or social component ($\vec{V}_{\text{global}}$) as illustrated in Eqs. (5.45) to (5.49).

A. Initial Population

Referring to section 5.5.1, the formula (5.28) is applicable to calculate the position vector for the initial population of PSO (Talukder, 2010) and (Chang and Yeh, 2013). It is noteworthy that Eq. (5.28) affect the final result of PSO as demonstrated in Figure 5.7.

B. Inertia Component

The search space in PSO is the set of all possible solutions for the optimization problem, and the task is to find the best possible solutions in the search space. The position vector of particle (j) is denoted by $\vec{x_j}(t)$, it is a member of search space, where j is the index of the particle and t is a discrete time step. There is another important parameter for the particle which is the velocity denoted by the vector $\vec{v_j}(t)$. The latter vector describes the movement of the particle in the sense of direction, distance, and time step. This component can be given as (Li *et al.*, 2009):

$$\vec{V}_{\text{inertia}} = w * \vec{v_j}(t) \tag{5.45}$$

where, w is the inertia coefficient which reflects the contribution of particle velocity $\vec{v_j}(t)$ in the new position. This component is used to reduce the diversification caused by other components of the particle (Rini, *et al.* 2011) and (Mazhoud, *et al.* 2013).

C. Personal Component

In addition to the particle retardation component represented by $\vec{V}_{\text{inertia}}$, every particle is retaining its local best position (the personal best). Commonly, this component is called the local best of PSO due to the considerable influence of local individuals (neighboring elements) on the magnitude and direction of this component. Hence, the local (best experience) component of the velocity can be posed as (Kuo and Huang, 2009):

$$\vec{V}_{\text{local}} = \text{rand}[0,1] * c1 * \left(\vec{P}_j(t) - \vec{x}_j(t)\right) \tag{5.46}$$

for which, $c1$ is the personal acceleration coefficient used to control the participation of cognitive (personal) component $\vec{P}_j(t) - \vec{x}_j(t)$ in the new position of the particle. rand [0,1] is a random number in the range 0–1 introduced to preserve the swarm diversity. The graphical representation of particle components of movement is shown in Figure 5.6.

D. Social Component

PSO is originally formulated as mathematical form imitating a simplified social environment. The communication between the flock individuals is the secret behind the sufficient knowledge gained about the merits of each particle in the swarm. The aim of this is to recognize the unique choreography that mathematically interprets the unpredictable path of bird flock. The global component for each particle is oriented towards the location of the best ever particle in the swarm at this instant as shown in Figure 5.6. Hence, it can be expressed in (5.47) (Liang *et al.*, 2006) and (Talukder, 2010):

$$\vec{V}_{\text{global}} = \text{rand}[0,1] * c2 * \left(\vec{g}(t) - \vec{x}_j(t)\right) \tag{5.47}$$

where, $c2$ is the global acceleration coefficient utilized to control the tendency towards the global best position $\vec{g}(t) - \vec{x}_j(t)$.

Equations (5.45) through (5.47) can be combined to formulate the general mathematical form for updating the velocity vector of the particle as in (5.48):

$$\vec{v}_j(t+1) = \vec{V}_{\text{inertia}} + \vec{V}_{\text{local}} + \vec{V}_{\text{global}} \tag{5.48}$$

where, $\vec{v}_j(t+1)$ is the updated form of particle velocity, whereas the new position of the particle is determined through adding up the update of velocity to the original position of the particle as formulated in (5.49).

$$\vec{x}_j(t+1) = \vec{x}_j(t) + \vec{v}_j(t+1) \tag{5.49}$$

where, $\vec{x}_j(t+1)$ is the updated form of particle position as plotted clearly in Figure 5.6.

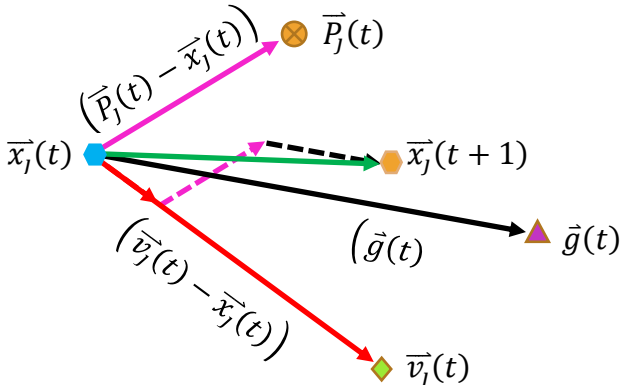

Figure 5.6 Graphical representation for the components contributed in creating the new position of the j[th] particle in PSO.

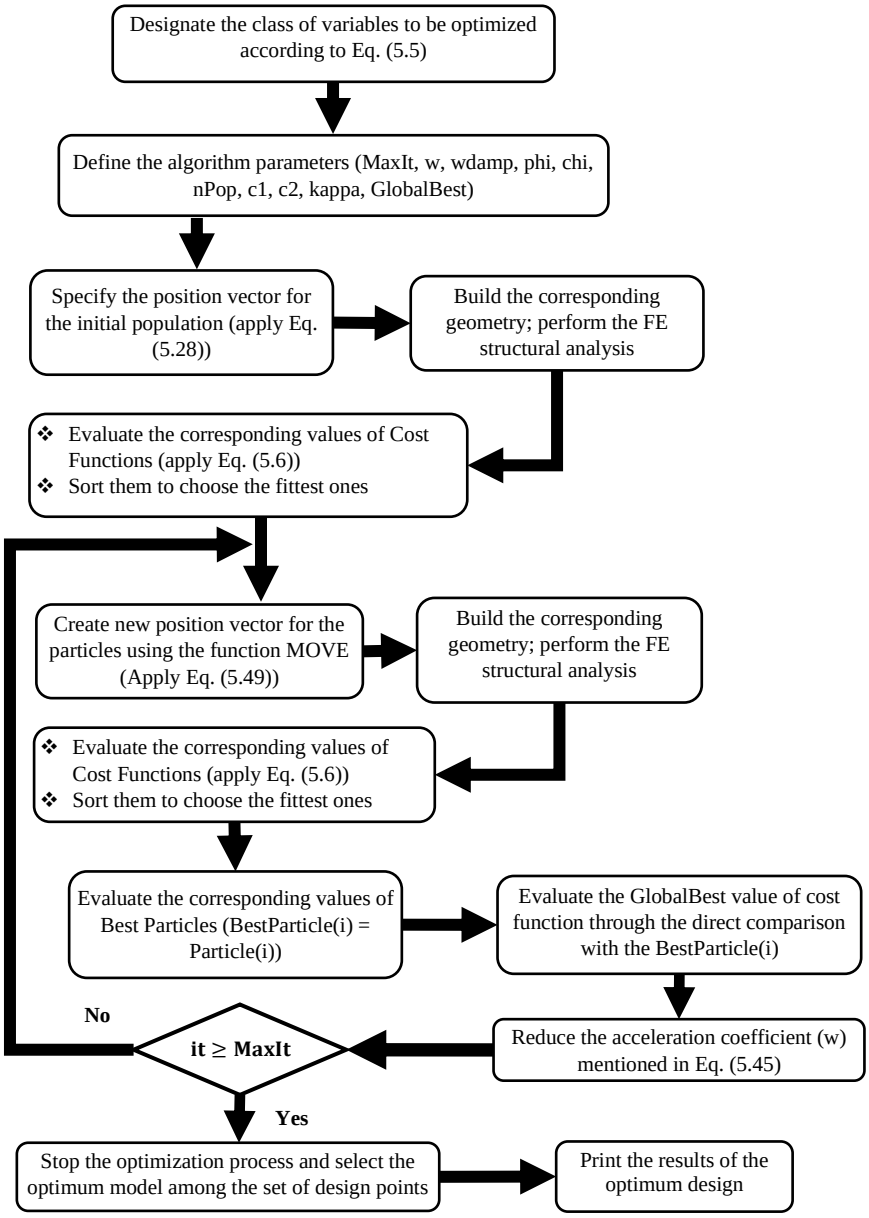

Figure 5.7 Logical steps of the conventional PSO strategy.

The proceeding of operations executed by PSO for the current models is demonstrated in Figure 5.7, where the data used to implement the processes are indicated in Table 5.4. There is no necessity to list the data concerning the number of iterations, since they are identical with those carried out in ABC as indicated in Table 5.1. Similar to DE, PSO starts the journey with initial population by adopting Gaussian random distribution approach, as stated in Eq. (5.28). There are three distinct components affect the new position of the particle: inertia, cognitive and global component. The inertia coefficient (w) for the current application is supposed to be 0.73, whereas the coefficients used for both personal and social components are equal (c1=c2=1.5).

Table 5.4 Optimization parameters used to implement PSO technique.

Name	**Description**	**Value**
nPop	Population size	10
w	Acceleration coefficient for the inertia component	0.73
c1	Acceleration coefficient for personal component	1.5
c2	Acceleration coefficient for social component	1.5

5.5.5 Simulated Annealing (SA)

A. Probability Distribution

When piece of metal is subjected to hot rolling or hot forming, it should be heated to certain temperature. Thence, when the hot working is accomplished, the metal starts to recover its initial temperature by slow cooling. Quenching process is incorporated with certain discrete intervals, thereby the temperature is preserved constant, during the cooling operation. During that particular step, the period of temperature constancy is sufficient for attaining the thermal equilibrium and this implies maintaining orbital motion for its particles under appointed level of activation energy. At this instance of temperature steadiness, the probability of distribution for the microscopic configuration could be expressed in the mathematical exponential form of Boltzmann allocation (Corana *et al.*, 1987) and (Mahfoud and Goldberg, 1995):

$$P_{config} = B * \exp\left(-E_{config}/T\right) \tag{5.50}$$

where, E_{config} is the activation energy of the current configuration of atoms. T is the annealing temperature. B is Boltzmann constant for probabilistic distribution.

B. Initial Population

In SA strategy, the first step is to investigate the initial solution for randomly selected set of positions for the design variables within their respective prescribed optimization ranges. As

consequence, Eq. (5.28) in section 5.5.1 could be applied to conclude the position vector for the initial population.

C. Mutation Rate

The second step of SA is to generate certain number of new offspring (neighbours) for each individual in the original population by utilizing the evolutionary operator (Mutate), which can be mathematically expressed as (Goffe *et al.*, 1992) and (INGBER, 1993):

$$y_k = x_k + \text{sigma}_k * \text{rand}_k \tag{5.51}$$

where, y_k, x_k are the mutated and the original position for the k^{th} rank of the design parameter, sigma_k is the basic scope of mutation corresponding to the design parameter with rank k. rand_k is a random fracture (within the period [0,1]), used to scale the mutated k^{th} parameter. k is the rank of the design variable subjected to mutation, which is specified according to the probabilistic conditions defined in Eq. (5.52) using prescribed value for mutation coefficient (mu) (KLEIN and DUBES, 1989) and (Brown and Huntley, 1992):

$$k = \begin{cases} 1, 2, 3, \dots, n & \text{for } \text{randset}_k \leq \text{mu} \\ 0 & \text{for } \text{randset}_k > \text{mu} \end{cases} \tag{5.52}$$

where, randset_k is a vector of random fractures selected from the range $(0-1)$ with size equal to the size of position vector, zero value for k implies that there is no mutation will be performed for the k^{th} design variable, while the integer value for k in the upper part of Eq. (5.52) indicates the rank of the design variable undergoing mutation process, mu is coefficient stands for the mutation rate of the optimization process. n is the number of design variables chosen to perform the mutation.

D. Explorative Capability

Referring to formula. (5.50), the acceptance of new solution is relying on many factors. First, the difference in activation energy between the current and the previous states. Second, the cooling temperature of the metal under annealing process.

The gap in activation energy could be computed as the difference between the new solution (E_{config}^{it}) as compared to the last solution (E_{config}^{it-1}), i.e. $\left(E_{config}^{it} - E_{config}^{it-1}\right)$. While, the temperature is measured for the current iteration (T_{it}). Ultimately, the acceptance of new solution is realized when the Boltzmann algorithm, with exponential relationship, shown in Eq. (5.53) is satisfied (INGBER, 1993) and (Henderson *et al.*, 2008).

$$\text{rand}[0,1] \leq B * \exp\left(-\left(E_{config}^{it} - E_{config}^{it-1}\right) \Big/ T_{it}\right) \tag{5.53}$$

Where, rand[0,1] is a random fraction ranging within the interval $(0-1)$. While, the temperature T_{it} itself is subjected to systematic reduction during the sequential steps of optimization that is to reduce the chance of accepting bad solutions because the concerns to trap in local optima are diminishing at the final stages of optimization. This reduction can be expressed in Eq. (5.54).

$$T_{it} = \bar{\alpha} * T_{it-1} \quad (5.54)$$

Where, T_{it} , T_{it-1} are the temperatures for the current and the preceding iterations respectively. $\bar{\alpha}$ is the restriction factor which is in this case equal to 0.96.

Similarly, $sigma_{it}$ is subjected to systematic reduction during the optimization process to reduce the jumping peaks (causing low climbs) of the newly generated neighbours and bring the system to equilibrium state and stabilize the activation energy of the system as shown in the formula (5.55) (Henderson *et al.*, 2008) (Li and Landa-Silva, 2011).

$$sigma_{it} = \emptyset * sigma_{it-1} \quad (5.55)$$

Where, $sigma_{it}$, $sigma_{it-1}$ are the mutation coefficients for the current and the previous iterations respectively. $\emptyset$ is the cooling factor, which is in this case equalling to 0.95. The general procedure for implementing SA strategy used to optimize the current dome roof frame model is completely illustrated in Figure 5.8.

The block diagram shown in Figure 5.8 illustrates the implementation steps of SA used to optimize the dome roof models considered in this work. Table 5.5 shows the optimization parameters used in SA, where the number of iterations is the same that used in ABC indicated in Table 5.1. Two cooling coefficients are used: one for the temperature control ($\bar{\alpha}$=0.95), and the second is used to control the mutation process ($\emptyset$=0.95). a mutation rate of (mu=0.5) is utilized to create new generations within neighbourhood radius ($sigma_0$=0.2). While, the initial temperature is taken as (T_0=0.1).

Table 5.5 Optimization parameters used to implement SA technique.

Name	**Description**	**Value**
nPop	Population size	9
nMove	Number of neighbours per parent individual	3
B	Boltzmann coefficient	1.0
mu	Mutation rate used to create new neighbours	0.5
$sigma_0$	Specified initial range of mutation process	0.2
T_0	Initial value of the temperature	0.1
$\bar{\alpha}$	Temperature reduction rate (cooling out coefficient)	0.95
$\emptyset$	Mutation reduction rate	0.95

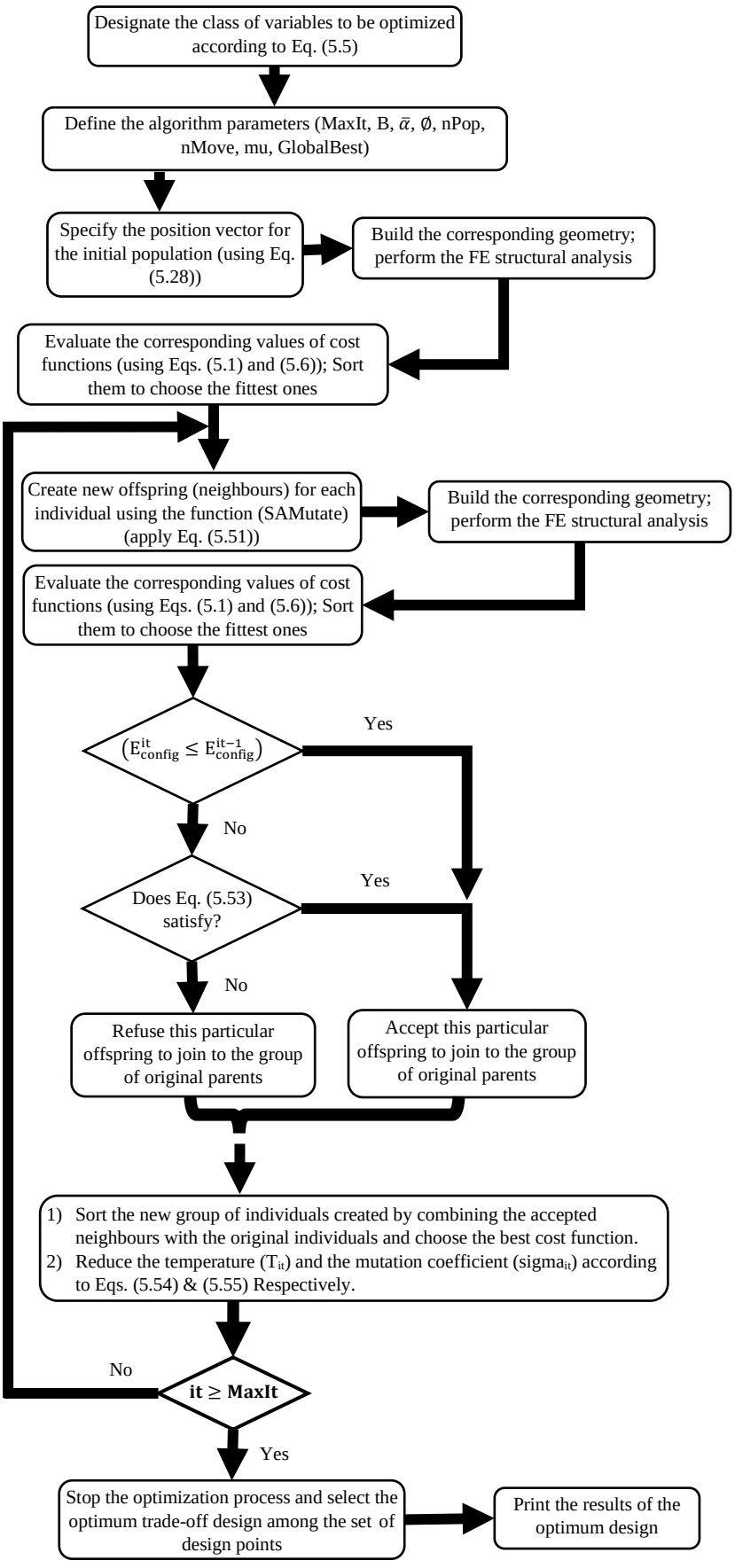

Figure 5.8 Logical steps of the standard SA strategy.

5.5.6 Metaheuristics with Discrete and Integer Variables

Metaheuristic techniques are originally invented to treat with continuous design variables, as they need to be adapted to deal design variables in integer form such as the number of girders and number of rings or other discrete form such as cross-sectional areas of structural members. Treating such variables as continuous sets results in trivial or impractical solutions (Saka *et al.*, 2016) and (Ho-Huu *et al.*, 2016b).

The fuel storage tank, considered in this investigation, has a large number of integer variables, and a large number of discrete variables and the latter variables can be enumerated and also treated as integers. In the case of sections (e.g., the structural sections fixed in Appendix E), the sections are ordered by second moment of area, from the largest to the smallest, although the sections could alternatively be ordered by cross-sectional area. However, MESO is equipped with specialized tool to deal with this mixed nature of variables through identifying the relevant component groups and their respective designations as explained in section 4.5, model A1, the article concerning the identification of structural components illustrated in Figure 4.4 supported by Table 4.5.

On the other hand, in applications associated with discrete or integer variables, metaheuristic techniques need to overcome the problem that design space - the space of potential solutions - is no longer a continuous space and finding new valid coordinates may be non-trivial (Ho-Huu *et al.*, 2015). This study proposes a novel approach to handle such variables through adapting metaheuristic techniques to comprehend these parameters, where the solution space, $\mathcal{X}$, can be described therefore as an N-dimensional space where each of the N dimensions ($\mathcal{X}_j, j = 1 \dots N$) is a bounded predefined subset of integers $\mathbb{Z}$, or a bounded subspace of the real line, $\mathbb{R}$, with minimum and maximum values $\mathcal{X}_j^{\min}$ and $\mathcal{X}_j^{\max}$ respectively. For computational efficiency it is useful to redefine the neighbourhood as:

$$\mathcal{N}(x, Ƕ) = \{y \in \mathcal{X}\ s.t. \left|y_{,j} - x_{,j}\right| < Ƕ\left(\mathcal{X}_j^{\max} - \mathcal{X}_j^{\min}\right), \forall j\} \tag{5.56}$$

where, Ƕ is the fraction determining the proximity scaling to the integer bounds, $x_{,j} \in \mathcal{X}_j$ is the j^{th} component of the N-dimensional solution. This scales each dimension according to its bounds and allows each component of the solution to be changed independently.

The space, $\mathcal{X}$, is a subspace of $\mathbb{R}^N$, and indeed it's convenient to allow the individual to behave as real parameter within continuous scope. Hence, metaheuristic technique is communicating only with the real parameter, which has authority to fly throughout the fully real space rather than be restricted to integer values. The cost function must then be evaluated at the nearest point in $\mathcal{X}$, however, which is potentially not in the current neighbourhood.

5.6 Proposed Optimization Strategies

Metaheuristic techniques, defined in the last section, improve the initial solutions by trial and error until the design constraints are satisfied. They rely on chance even with a degree of intelligence they exploit. For large-scale structures, the number of iterations is strictly limited, since the evaluation of the cost function requires finite element analysis. With this supposition, there are concerns about their success to obtain an acceptable solution, even when alternative approaches are used.

MESO, in contrast, starts with an acceptable but suboptimal design and incrementally improves the solution, and is ideally suited to optimize cross-sectional dimensions. In this work, the reference design is modelled as an overdesigned state and girder sections. During the optimization, the structure is progressively weakened, based on an evaluation of the strain energy density SED. This is fulfilled by maximizing the minimum SED, where the effect is to increase the structural stiffness, thereby reducing deflections and increasing resonant frequencies. The mechanism of structural modelling is illustrated in section 4.4. Depending on SED distribution throughout the whole structure, the structural components can be ordered according to their respective average SEDs, and the components with the lowest selected for weakening. The number of groups selected depends on the reduction ratio (RR), which is typically about 20%.

developing MESO to treat the topological and shape variables is not straightforward since these can cause a significant impact on the state of structural modelling for the whole structure. For instance, changing the number of rings will add or subtract several groups of girders, which leads to serious problems to the application of MESO. This is a reasonable justification for suggesting a two-stage cascade optimization, illustrated in Figure 5.9, with stage 1 using metaheuristic techniques to optimize the integer variables ($\overrightarrow{\mathrm{DV}_{\mathrm{int}}}$), and stage 2 to optimize both of continuous ($\overrightarrow{\mathrm{DV}_{\mathrm{con}}}$) and discrete ($\overrightarrow{\mathrm{DV}_{\mathrm{dis}}}$) variables.

The main notion of the proposed optimization methodology is to nominate the most specialized optimization tool for each category of design variables, illustrated in section 5.1.3, so as to save the cost and time of computation. As large-scale symmetric structure, the symmetry and the consistency of the geometry are requisite features to produce a feasible model during the optimization process. Performing the structural optimization for such large-scale structure entails to treat with numerous numbers of design variables, especially sizing variables. To cope with this, MESO has suggested to control the sizing category of variables by discretizing the whole structure into finite number of structural components as illustrated in Chapter 4. This discretization has contributed effectively in reducing the number of sizing design parameters, where each structural component has its own cross-sectional specifications. Also, it must satisfy

the symmetry conditions as the whole structure does. On the other hand, one of each of the adopted metaheuristic techniques is utilized to optimize the geometry for other design variables. A cascade optimization procedure is used in this methodology as explained by (Kaveh and Ghazaan, 2015), i.e. the result of stage-1 will be utilized in stage-2. And the result of stage-2 will be considered in stage-3 and so on. According to Eq. (5.5), two categories of variables ($\overrightarrow{\mathrm{DV}_{\mathrm{dep}}}$ & $\overrightarrow{\mathrm{DV}_{\mathrm{int}}}$) would be activated at stage-1, namely, integer parameters will be optimized and other design parameters ($\overrightarrow{\mathrm{DV}_{\mathrm{load}}}, \overrightarrow{\mathrm{DV}_{\mathrm{dis}}}, \& \overrightarrow{\mathrm{DV}_{\mathrm{con}}}$) will be preserved frozen at their initial values. Next, at stage-2, the discrete and continuous variables ($\overrightarrow{\mathrm{DV}_{\mathrm{dis}}}$ & $\overrightarrow{\mathrm{DV}_{\mathrm{con}}}$) will be treated. In stage 3, the optimal set of integer, discrete, and continuous variables ($\overrightarrow{\mathrm{DV}_{\mathrm{dep}}}, \overrightarrow{\mathrm{DV}_{\mathrm{int}}}, \overrightarrow{\mathrm{DV}_{\mathrm{dis}}}, \overrightarrow{\mathrm{DV}_{\mathrm{con}}}$) would be kept constant at their optimal values. This stage is suggested to examine the optimal model against constraints for other load cases of the application.

The structural optimization has been directed to minimize the structural weight of the adopted models using stiffness criterion. Five different hybrid optimization strategies, MESO-ABC, MESO-BA, MESO-DE, MESO-PSO and MESO-SA, have been employed to perform this task. These strategies are explained in the next subsections. The first section of the acronym denotes to MESO, which is driven by the optimality criterion detailed in section 5.4, whereas the second section of the abbreviation refers to the conventional metaheuristic technicality used in line with MESO to execute the optimization. The optimization stages for the proposed methodology are illustrated in the details of Figure 5.9. The simplified example, exhibited in Table 5.6, demonstrates how the adapted MESO is treating with the component section No. and the corresponding designation as discrete set of sizing design parameters.

Table 5.6 Simple example showing the incremental progression of MESO with the relevant changes in cross sectional designations.

Structural Component Number	Previous Iteration Data			MESO Manipulation	Current Iteration Data	
	Component Status	Component Section No.	Component Designation		Component Section No.	Component Designation
1	Not Eligible	7	S20x86	7	7	S20x86
2	Candidate Component	8	S20x75	8+1=9	9	S20x66
3	Not Eligible	9	S20x66	9	9	S20x66
4	Not Eligible	10	S18x70	10	10	S18x70
5	Candidate Component	11	S18x54.7	11+1=12	12	S15x50
6	Not Eligible	12	S15x50	12	12	S15x50
7	Candidate Component	13	S15x42.9	13+1=14	14	S12x50

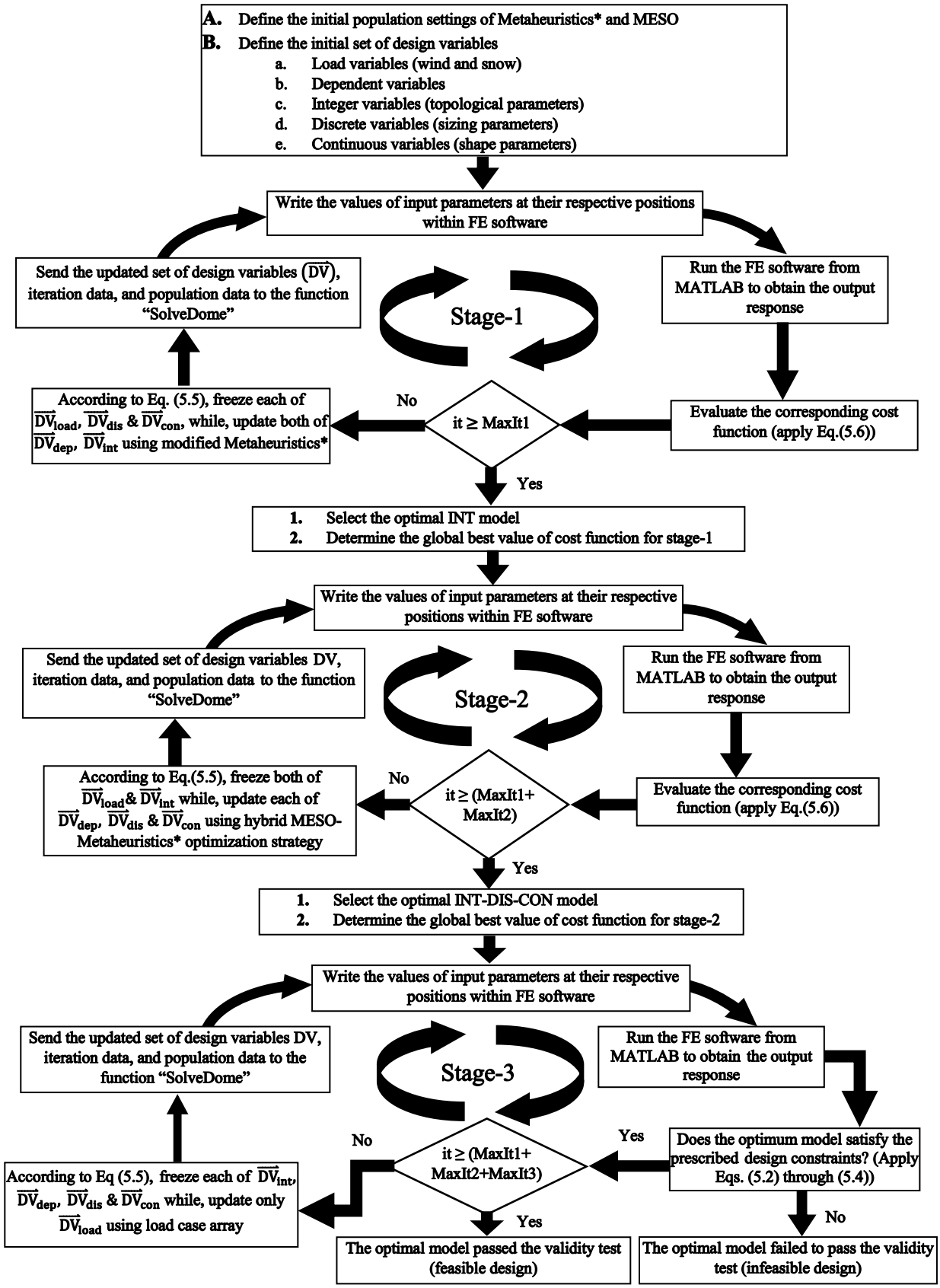

- Metaheuristics denotes to the series of techniques (ABC, BA, DE, PSO and SA), illustrated in section 5.5

Figure 5.9 Simplified flow chart showing the different stages of the proposed optimization methodology.

5.6.1 MESO-ABC

The hybrid optimization strategy MESO-ABC is produced by fusing the optimization features of MESO, mentioned in section 5.2, into the optimization characteristics of ABC, explained in article 5.5.1, to execute the processes in parallel so as to ensure a comprehensive implementation capable of performing a simultaneous shape, topology and sizing optimization. In accordance, MESO embraces the individuals of ABC to carry out the optimization concurrently with ABC at stage-2, where forage bees are communicating and searching for their patches inside MESO plane as illustrated in Figure 5.11. The overall optimization process is proceeding according to the steps illustrated in Figure 5.9. Selecting the optimization methods according to their specializations along with blending their characteristics in one integrated hybrid optimization tool have achieved a significant reduction in computational time and cost. The process is incorporated with dividing the design variables, allocated for stage 2, into two distinct categories. First, is to assign the shape and topology variables to be solved using conventional ABC functions. Second, the sizing design variables of the dome roof frame are appointed to be optimized by exploiting MESO principles. The simple sketch presented in Figure 5.10 demonstrates the sequence of operations implemented in the proposed MESO-ABC strategy. It explains the situation of variables mentioned in the general procedure of the proposed methodology presented in Figure 5.9. For example, in model E3, there are two integer variables ($\overrightarrow{DV_{int}}$={$\mathbf{N_{Sides}}$, $\mathbf{N_{Rings}}$}) need to be optimized at stage 1 to decide the optimal variant for the model using ABC technique adapted to treat this type of variables. Thereafter, the hybrid MESO-ABC algorithm is the responsible of treating the variables at stage 2. This is fulfilled by allocating MESO to deal with the 37 sizing variables (treated as discrete parameters $\overrightarrow{DV_{dis}}$) defined in section 4.6.4 article B (see Table 4.29 and Figure 4.30), while ABC is chosen to deal with the 10 shape and topological variables (treated as continuous parameters $\overrightarrow{DV_{con}}$={R, $Frac_i$} i=1, 2, 3, …, 10) defined in Table 4.30 and Figure 4.28. It is noteworthy that the 37 sizing variables and the 10 shape and topological variables are treated in parallel sequence at stage 2. Subsequently, a simultaneous sizing, shape and topology optimization is realized at this stage using MESO-ABC. Also, there are intermediate design variables incorporated with these subsets represented by ($\overrightarrow{DV_{dep}}$={$\theta_{rot}$, dx_i} i=1, 2, 3, …, 10), where θ_{rot} is the angle between any two consecutive primary girders and dx_i is the linear distance for the i^{th} circumferential ring measured horizontally from the central vertical axis of the storage tank as shown in Figure 4.28. The 4 subsets of design variables are then combined to produce the optimal geometry of the model. Finally, stage 3 is prepared to test the validity of the optimal design against design constraints considering other load cases of the application using the load subset ($\overrightarrow{DV_{load}}$).

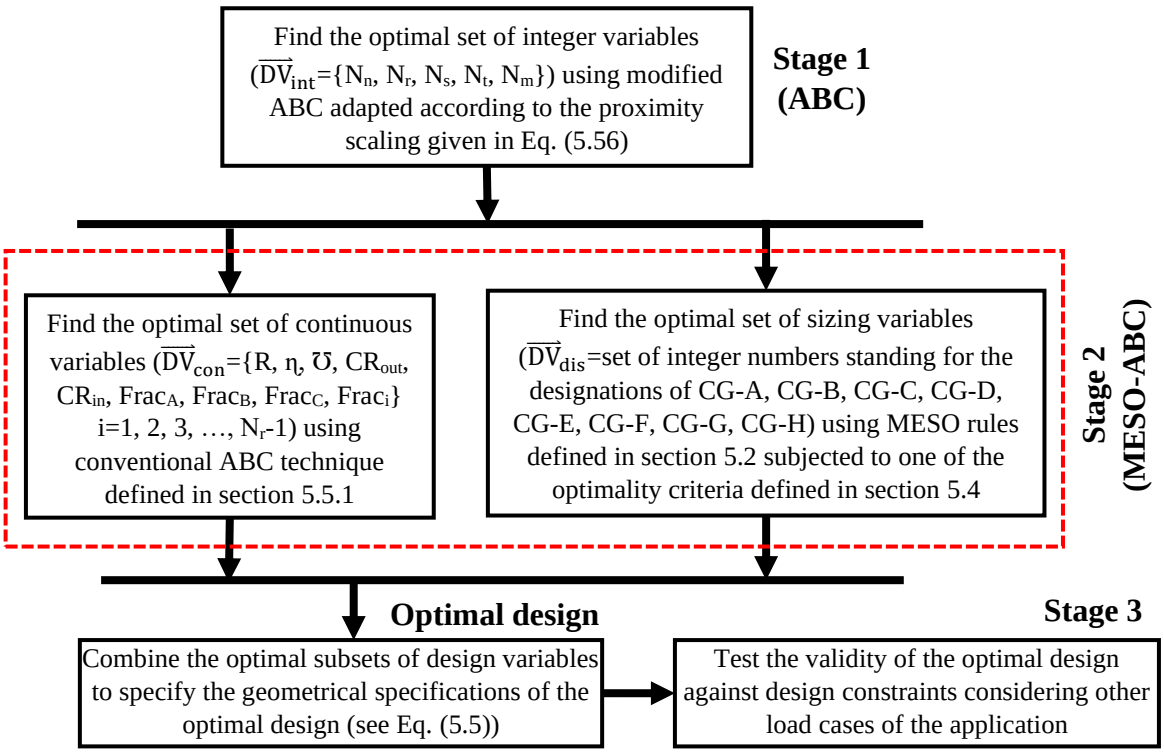

Figure 5.10 Simple sketch showing the sequence of optimization adopted in MESO-ABC.

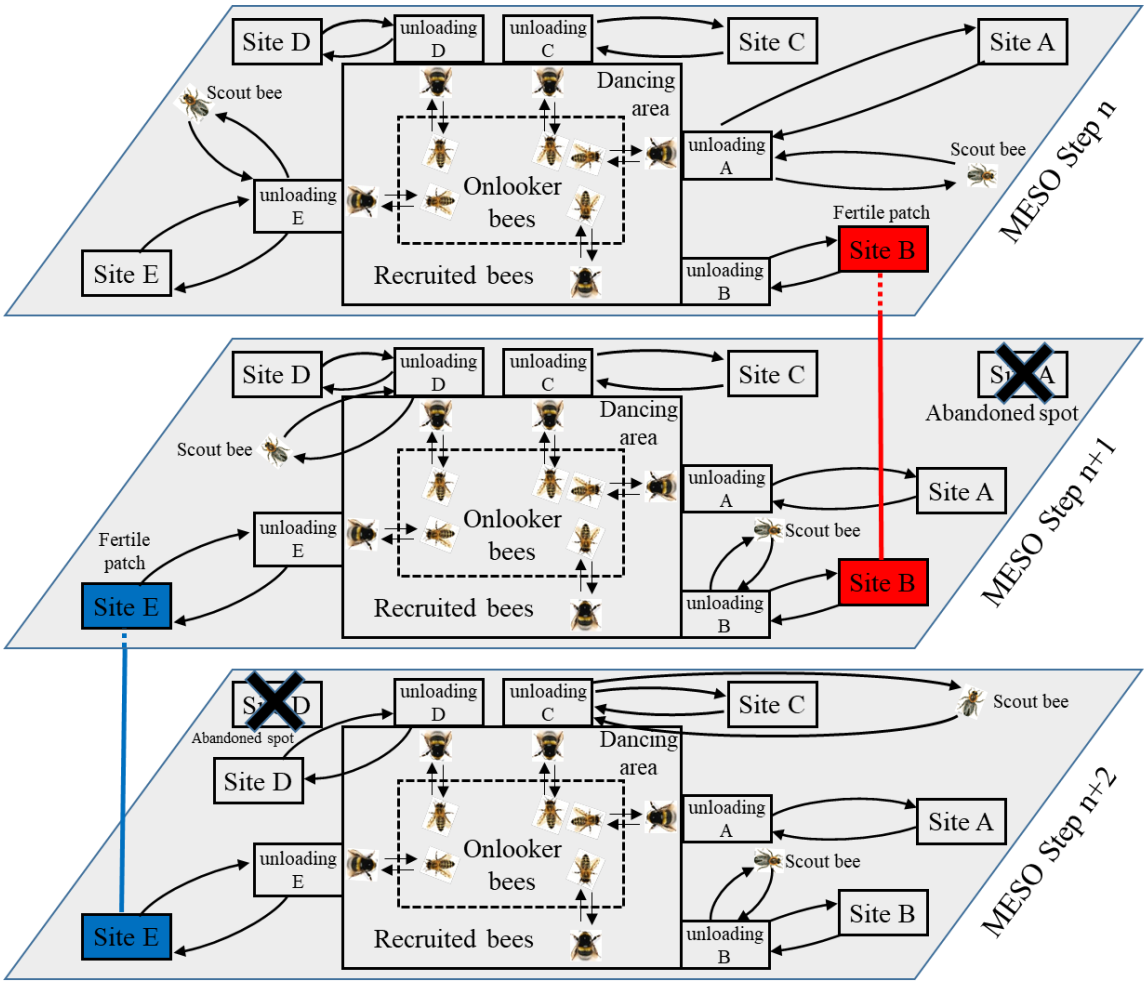

Figure 5.11 Simple sketch showing the nature of connection between MESO and the individuals of ABC.

5.6.2 MESO-BA

The hybridization principles mentioned in section 5.6.1, for MESO-ABC, are applicable in MESO-BA. As consequence, the characteristics of MESO, detailed in section 5.2, will be merged with that for BA, described in section 5.5.2. Similar to MESO-ABC, MESO-BA has different kinds of bees: elite, selected and scout bees. They are hovering around their respective food sources (patches) within specified MESO pool as schematized in Figure 5.12. The same procedure illustrated in Figure 5.10, concerning MESO-ABC, is adopted in this method with replacing ABC by BA in stage 1 and MESO-ABC by MESO-BA in stage 2, where the logical steps delineated in Figure 5.9 indicate that MESO-BA is used in stage 2 to implement an integrated optimization process for the model. Accordingly, BA is used to optimize the continuous variables ($\overrightarrow{DV_{con}}$={R, η, ʊ, CR_{out}, CR_{in}, $Frac_A$, $Frac_B$, $Frac_C$, $Frac_i$} i=1, 2, 3, …, N_r-1), while in parallel MESO is used to optimize the girder sections ($\overrightarrow{DV_{dis}}$). To illustrate this hybridization, suppose that solution space is consisting of a finite number of MESO hyperplanes identified by n MESO steps (see Figure 5.12). Therefore, when MESO proceeds from the current step (n) to the next step (n+1), BA individuals (bees) are transferring accordingly from the current MESO plane (with step n) to the next MESO plane (with step n+1). This implies that the bees are trying a new solution (within the MESO plane n+1) for $\overrightarrow{DV_{con}}$.

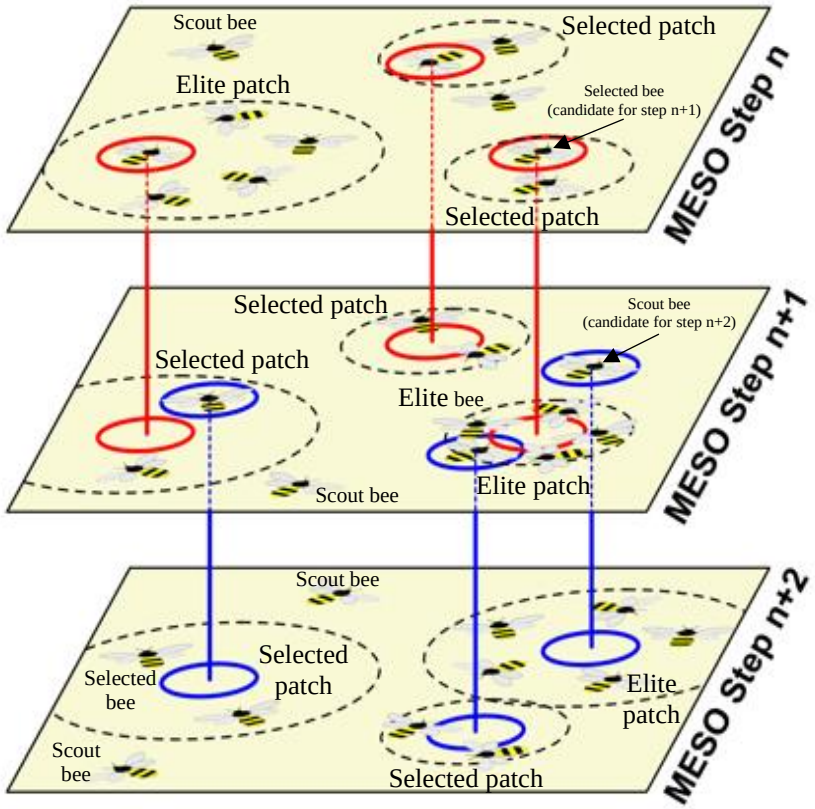

Figure 5.12 Simple sketch showing the relationship between MESO and BA individuals.

5.6.3 MESO-DE

Referring to sections 5.6.1 and 5.6.2, the same hybridization manner will be adopted to produce this version. Obviously, MESO-DE strategy is produced by mixing the optimization steps of MESO, appearing in Figure 5.1 explained in section 5.2, with the logical steps of DE, mentioned in Figure 5.5 of section 5.5.3. As evolutionary and metaheuristic algorithm, there are two outstanding merits for DE strategy. First, it has the capability to escape the local minima and suggest alternative search paths to secure the model against the trivial solutions and determine the global optimum solution. Second, it is robust and reliable enough to handle the multiple design constraints, as it has the capability to recognize the boundary lines of the problem to avoid approaching them in the subsequent iterations. The mechanism of communication between MESO and DE is illustrated in Figure 5.13. While, Figure 5.9 presents the steps of optimization needed to implement the proposed optimization methodology, where MESO-DE is used to solve the variables assigned for stage 2.

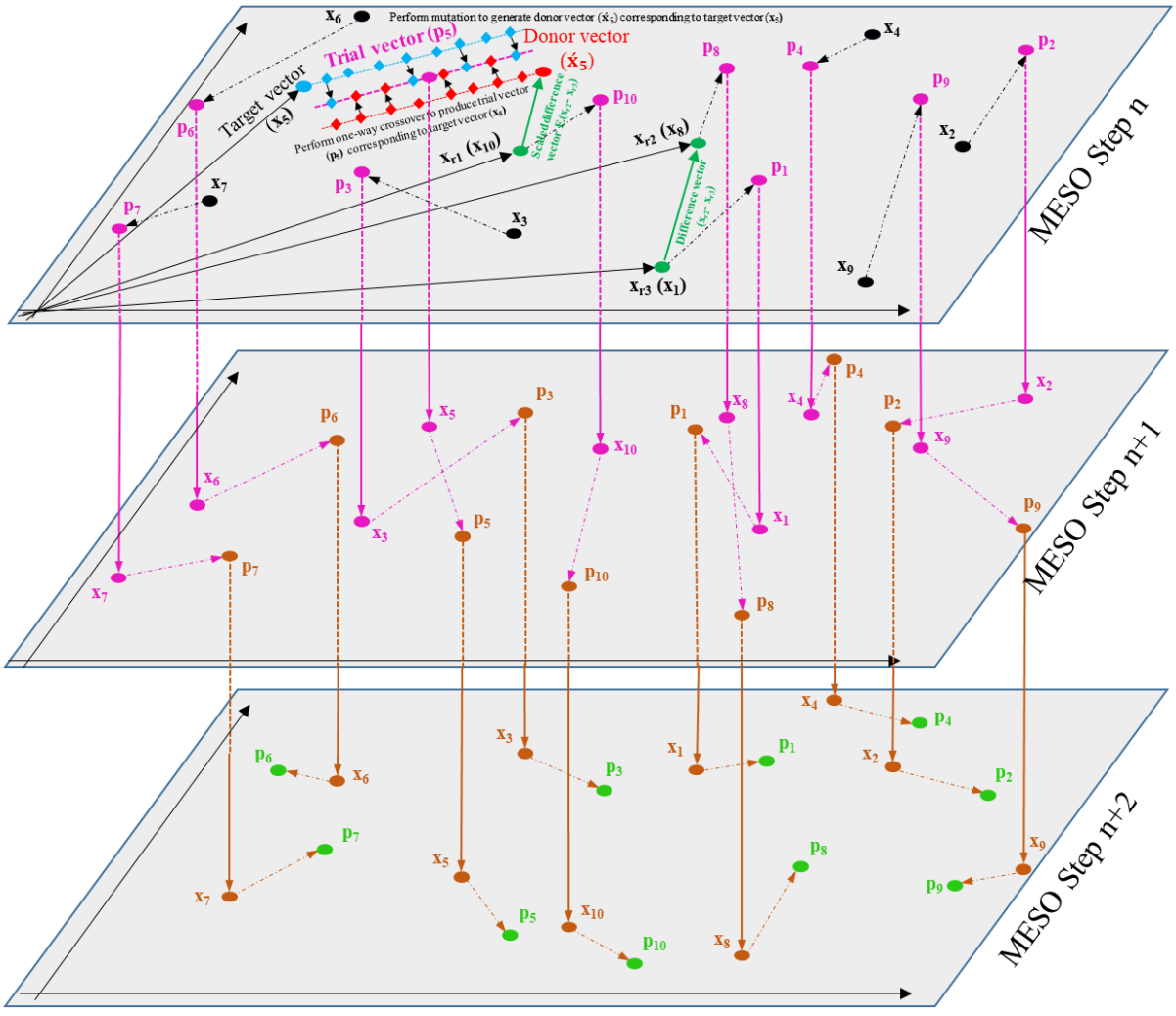

Figure 5.13 Simple sketch showing the relationship between MESO and DE individuals.

The operations demonstrated in Figure 5.10 can be applied to the method MESO-DE with replacing ABC by DE in stage 1 and MESO-ABC by MESO-DE in stage 2. In MESO step n, the trial vector (p5), resulting from the probability one-way crossover of the target vector (x5) with donor vector (ẋ5), transfers to the next level (step n+1) to become x5. In fact, the donor vector (ẋ5) is generated by performing the mutation of the two positions (x1) and (x8) chosen by the roots x_{r2} and x_{r3} respectively. The difference vector (x8-x1) is multiplied by the scaling factor F=[0.2, 0.8] to update the donor vector (ẋ5). Different identities could be recognized for DE individuals in MESO plane n compared to those in MESO plane n+1 and so on. MESO in this case is significantly reduced the dimensionality of search in the design space by nudging the individuals on the most appropriate path to find the optimum point.

5.6.4 MESO-PSO

Referring back to sections 5.2 and 5.5.4, this version is generated by combining the logical based rules of MESO with the exploitative capability of PSO to produce a hybrid version of them. In most cases, it has excellent convergence rate due to the exploitative capability of the method. While, it sometimes fails to jump off the local minimum points, as its explorative capability is limited. In MESO-PSO, PSO particles within one iterative MESO step are allowed to swim within the MESO boundaries, where the movement of particles is limited to the predefined sizing space logically selected by MESO based on engineering intuition. Figure 5.14 is devoted to show how the particles of PSO are behaving with respect each other in MESO plane and how the local and global minima for the current MESO are projected to the next plane. Similar to the previous methods, MESO-PSO follows exactly the same logical steps illustrated in Figure 5.9 to perform the overall optimization process.

The cascade optimization procedure illustrated in Figure 5.9 along with the pertinent illustrative schematic shown in Figure 5.10 are applicable in MESO-PSO. The concept of dividing the solution space into finite number of MESO hyperplanes simplifies the understanding of how hybrid MESO-PSO works. The process could be interpreted as that the complete swarm decides to change the altitude of flight from time to time without any alternation in the habitual features of the group. This decision is made to avoid any obstacles result from any unforeseen environmental circumstances. For instance, the global best (P3′) and the local best (P7′) chosen for the group of particles in the MESO plane (n) will be projected on the plane (n+1) to guide the newly generated swarm of particles in that plane. The same principles will be applied between the MESO attitude at n+1 and that at n+2 (see Figure 5.14).

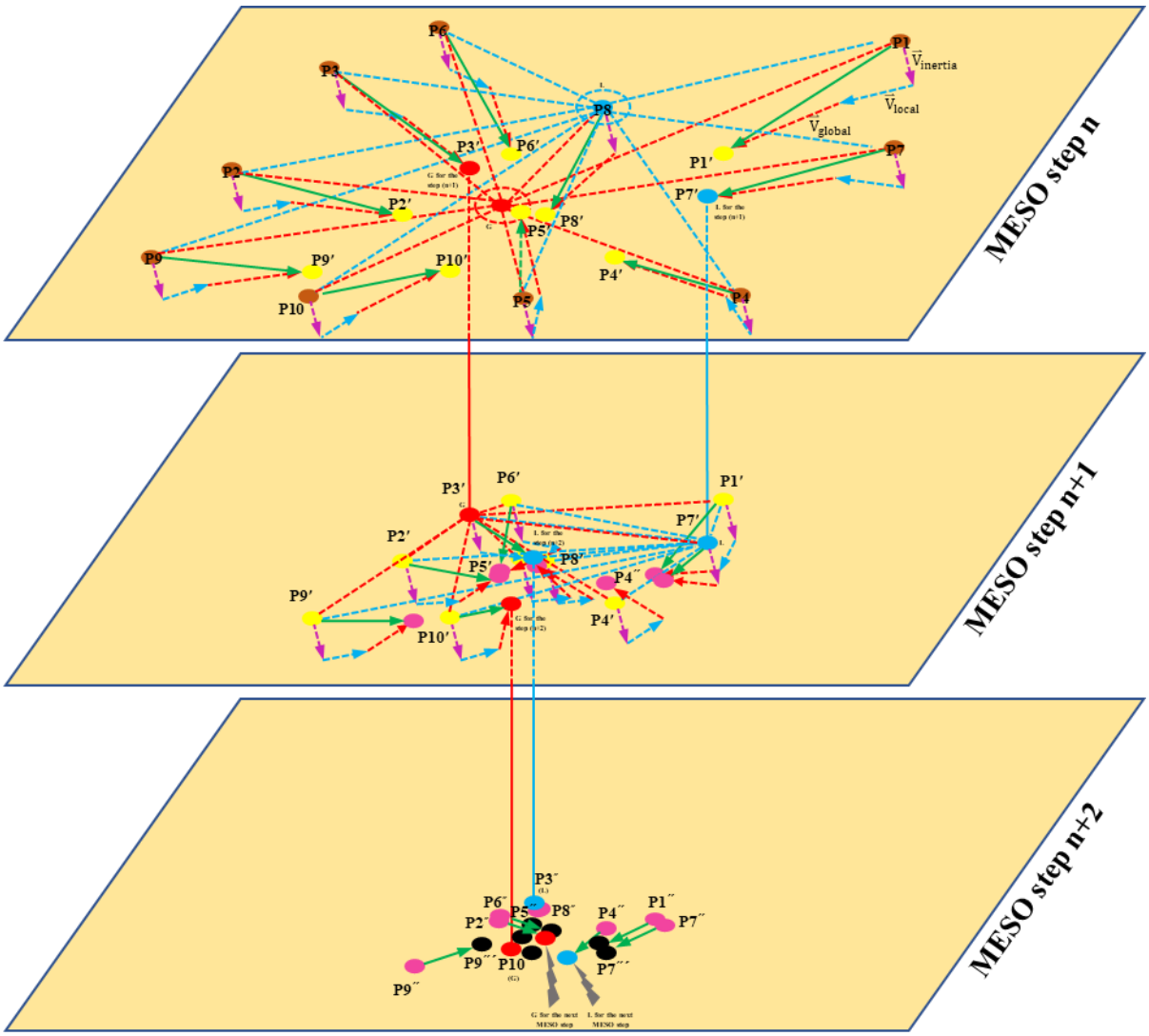

Figure 5.14 Illustrative sketch showing how PSO particles are flying (or swimming) in different MESO attitudes.

5.6.5 MESO-SA

This hybrid version does not differ from its counterparts in the previous sections, where MESO is interacted with the existing individuals of SA to produce the new optimization tool used in stage-2 according to the cascade optimization process demonstrated in Figure 5.9. More details about the classic SA strategy could be found in section 5.5.5. This method is characterized by its capability to treat with multimodal functions due to its ability to climb up the hill (jumping off the local optima) to achieve the global optimum. The cascade optimization steps shown Figure 5.9 aided by the more detailed explanation drawn in Figure 5.10 are applicable to MESO-SA to perform a simultaneous shape, topology and sizing optimization for the dome roof frame. In stage 2, the communication manner between SA individuals and MESO is demonstrated in Figure 5.15, where the search groups are commencing their neighbourhood inspection with radius R_n and temperature T_n at the MESO hyperplane n. The neighbourhood

search radius and the cooling temperature are gradually reduced for the next MESO plane, i.e. $\mathbf{R_{n+2} < R_{n+1} < R_n}$ and $\mathbf{T_{n+2} < T_{n+1} < T_n}$. The SA population consists of 3 subsets called "search groups". They are searching independently with the same neighbourhood radius ($\mathbf{R_n}$) in the same annealing temperature ($\mathbf{T_n}$) in specified MESO plane n. Each group has 3 neighbours (identified by y_j with green and cyan colours, j=1, 2, …, nPop) moving around the parent individual (see Figure 5.15). The chance to accept certain neighbour (identified by y_j with red and brown colours, j=1, 2, …, nPop) to be the candidate as search group parent for the next MESO plane is based on the quality of that neighbour and the probability distribution of the gap in the cost values between the neighbour and the parent individual. More details about accepting the neighbours to be the leaders for the next generation is illustrated in section 5.5.5. It is noteworthy that the proposed optimization methodology illustrated in Figure 5.9 is a general procedure and could be applied to any conventional metaheuristic technique, i.e. MESO could be replaced by any other optimization technique chosen to tackle the discrete sizing variables of the problem at stage 2 (see Chapter 8 for the comparison between the standard metaheuristic techniques and the MESO based algorithms).

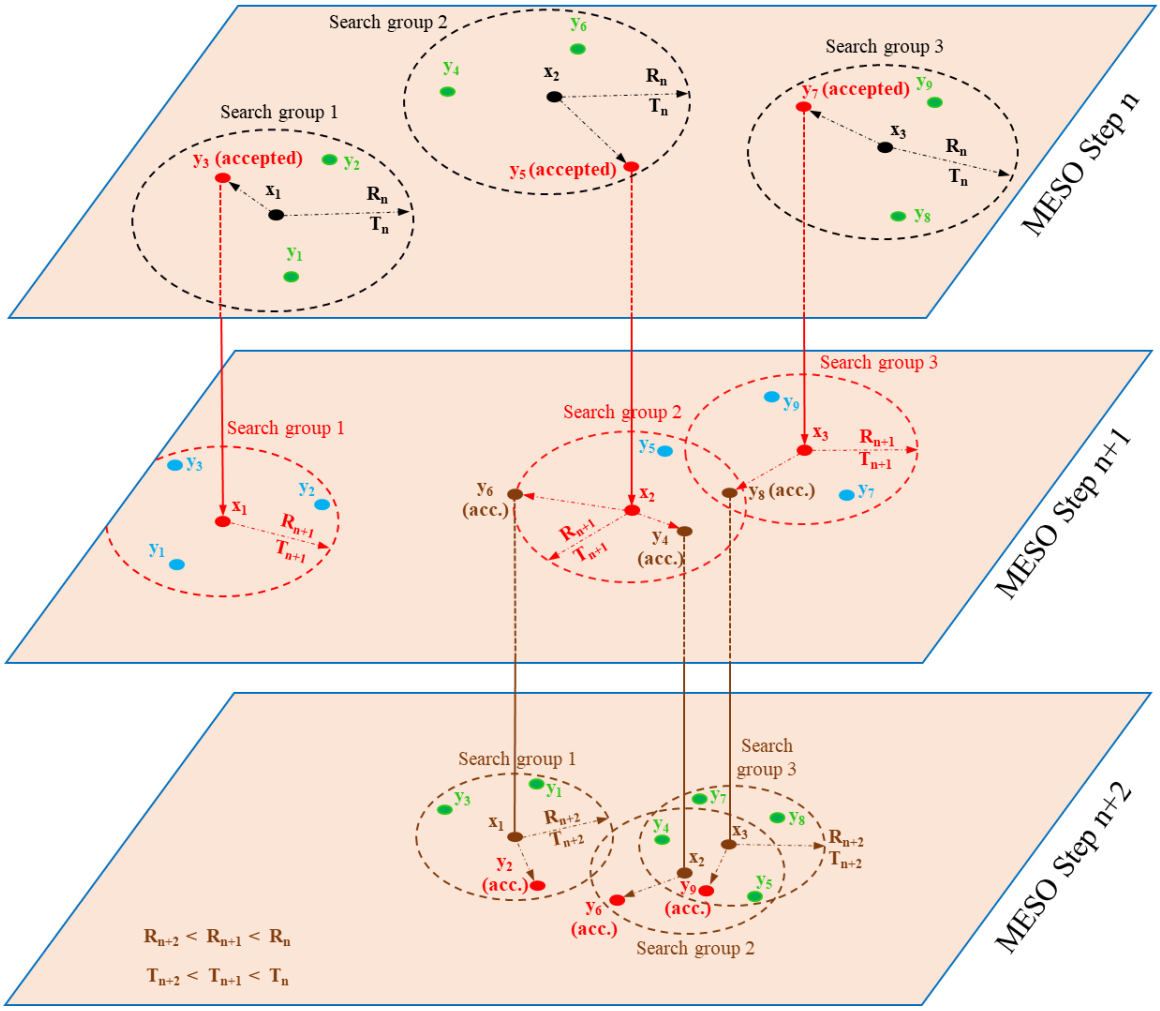

Figure 5.15 Illustrative sketch showing how SA individuals are related to MESO plane.

Chapter 6. Optimization Results of the Simplified Models

The optimization results for the simplified models (models A1 to E1 and A2 to E2), defined in section 4.5, will be viewed in this chapter. Five different hybrid optimization strategies, as clarified in section 5.6, are considered in this investigation by regarding the structural mass of the braced dome as objective function. The design constraints associated with this process are demonstrated in section 5.1.2. The design parameters are stated in section 4.5. At the end of the chapter, the best design will be chosen to specify the most promising model along with the most efficient optimization strategy used to produce that design under the prescribed set of design constraints. Furthermore, the merits and shortcomings of the proposed strategies along with the structural characteristics of their respective designs will be highlighted in this chapter. Finally, the statistical details of the optimization process will also be provided for each model discussed. The model is subjected to pure wind loading which is interpreted as nodal forces applied to the set of keypoints (nodes) of the dome structure. Thus, the forces applied to each node in the dome roof frame are obtained by summing up all forces, resulting from different influences, acted on the same node and in the same direction. for the simplified frame analysis, this is fulfilled by superposing the nodal forces of the wind load with the equivalent nodal forces of the dome shell weight with that result from the dead load of the structural member itself. Therefore, the first two stages of optimization are implemented considering pure wind as design load. While, the third stage of optimization is proposed to check the validity of the optimal design against the design constraints considering other load cases of the problem. Hence, there are two more load cases need to be included in stage 3, these are pure snow and combined snow and wind. Due to this strict test, some of models considered in this chapter are faced serious problem to pass this stage, for instance most of the optimal designs of models B2 and C2 are failed by buckling constraints when pure snow loads are imposed. For more details about the detrimental consequences of this test, review sections 6.5 and 6.6.

6.1 Topological Parametric Investigation

6.1.1 Topological Spacing Factor (N_s)

A comprehensive parametric investigation has been implemented to show the influence of $\mathbf{N_s}$, for the range 10 to 30, on the structural characteristics of the model E1. Figure 6.1 shows the set of critical points depending on the structural response of the model under N_n=6 and N_r=6. The graphs indicate that each of the maximum values of von-Mises stress, SED and buckling index become critical at the same point ($\mathbf{N_s}$=18), whereas the maximum displacement shows slightly different critical point observed at ($\mathbf{N_s}$=21).

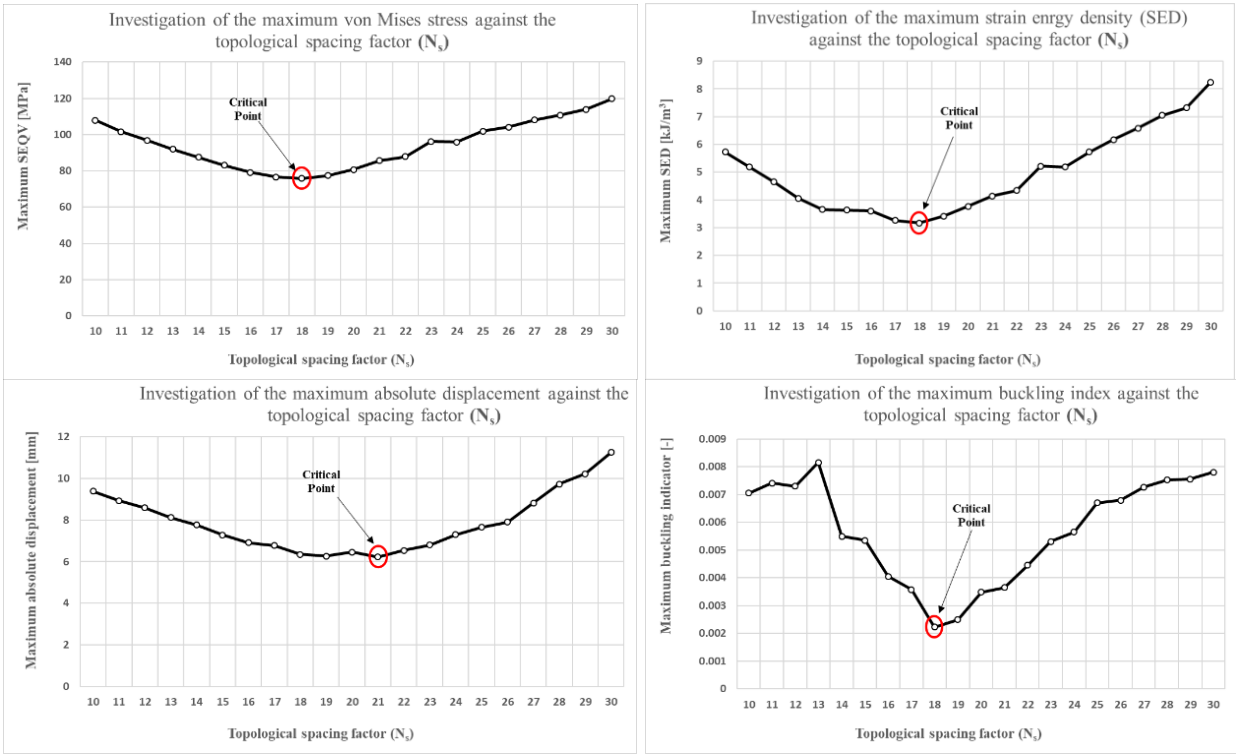

Figure 6.1 Parametric Investigation of $\mathbf{N_s}$ implemented on model E1.

In conclusions, these graphs do not show optima for structural mass, but do suggest that for designs with high safety factors the spacing factor, N_s, should be restricted to a narrow range between 18 and 21 during the optimization for structural mass.

6.1.2 Topological Morphing Factor (N_m)

The effect topological morphing factor ($\mathbf{N_m}$) on the structural response of the hybrid Schwedler-Lamella configuration (model D1) is discussed here. The graphs presented in Figure 6.2 state that there is no morphological change could be seen for low topological spacing ($\mathbf{N_s}$=10), whereas dramatic morphological changes are associated with higher topological spacing ($\mathbf{N_s}$=20, 30). These morphological changes are controlled by the topological morphing factor ($\mathbf{N_m}$), where an observable transition from Lamella to Schwedler configuration could be seen at $\mathbf{N_m}$=31 for $\mathbf{N_s}$=20 and at $\mathbf{N_m}$=21 for $\mathbf{N_s}$=30. Hence, there is an entangled correlation between $\mathbf{N_m}$ and $\mathbf{N_s}$ to determine the new morphology of the structure. In general, there is an obvious increase in the maximum response of the structure during its gradual morphological process within Schwedler zone except for the minor singularities noticed for the stress and buckling of Figure 6.2.

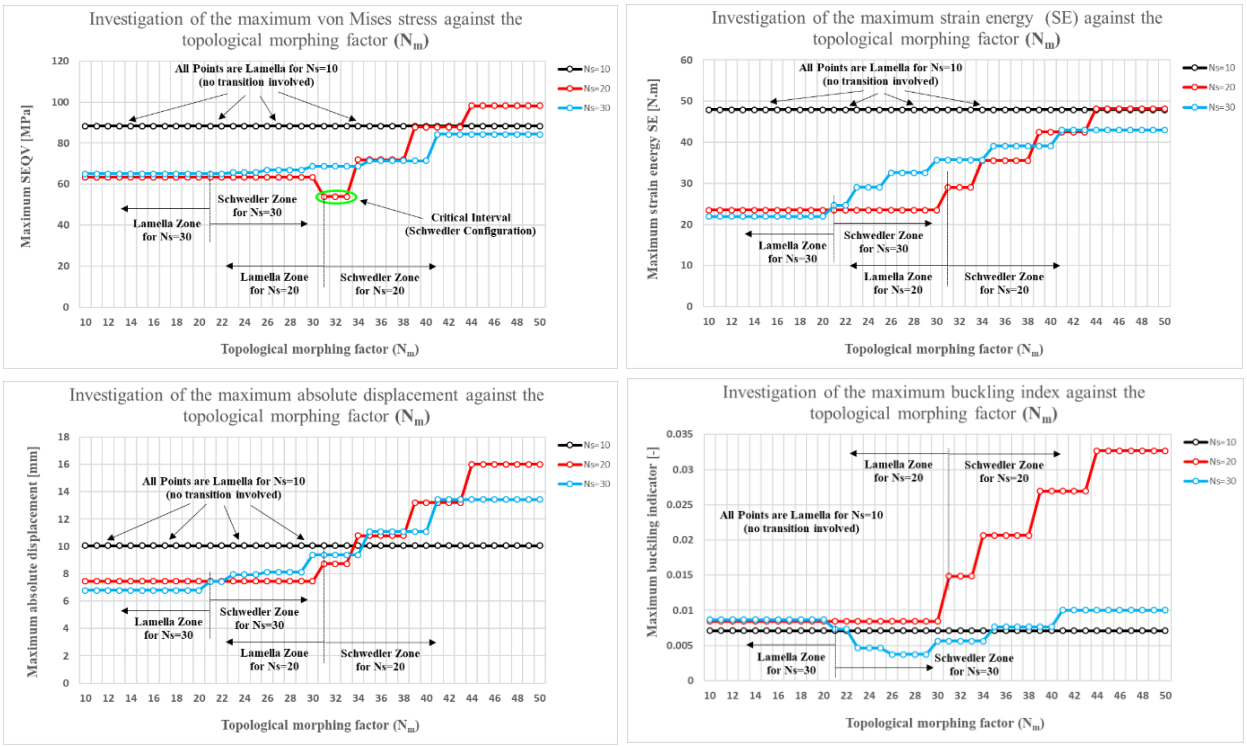

Figure 6.2 Parametric Investigation of **N_m** implemented on model D1.

6.1.3 Topological Trimming Factor (N_t)

The structural characteristics of model A1 are considerably affected by the topological trimming factor (**N_t**). This can be seen in Figure 6.3, where there is direct proportionality between the state of stress, strain and deformation and the trimming factor (**N_t**). The study has been implemented over the range (**N_t**=4 to **N_t**=16) under dome radius R=45 m, number of girders **N_n**=45, number of rings **N_r**=9, and **N_s**=20. As N_t increases, the radius at which the secondary girders also start to increase, and the mass of the structure decreases. The reduced mass correlates with the higher stress and higher strain energy density SED and, perhaps more importantly, the higher deflection. The optimal value of N_t, therefore, is likely to depend on the relative importance of structural mass and maximum deflection during the optimisation. The higher **N_t**, the wider trimmed space, the lower length for secondary girder, which leads to significant reduction in structural weight.

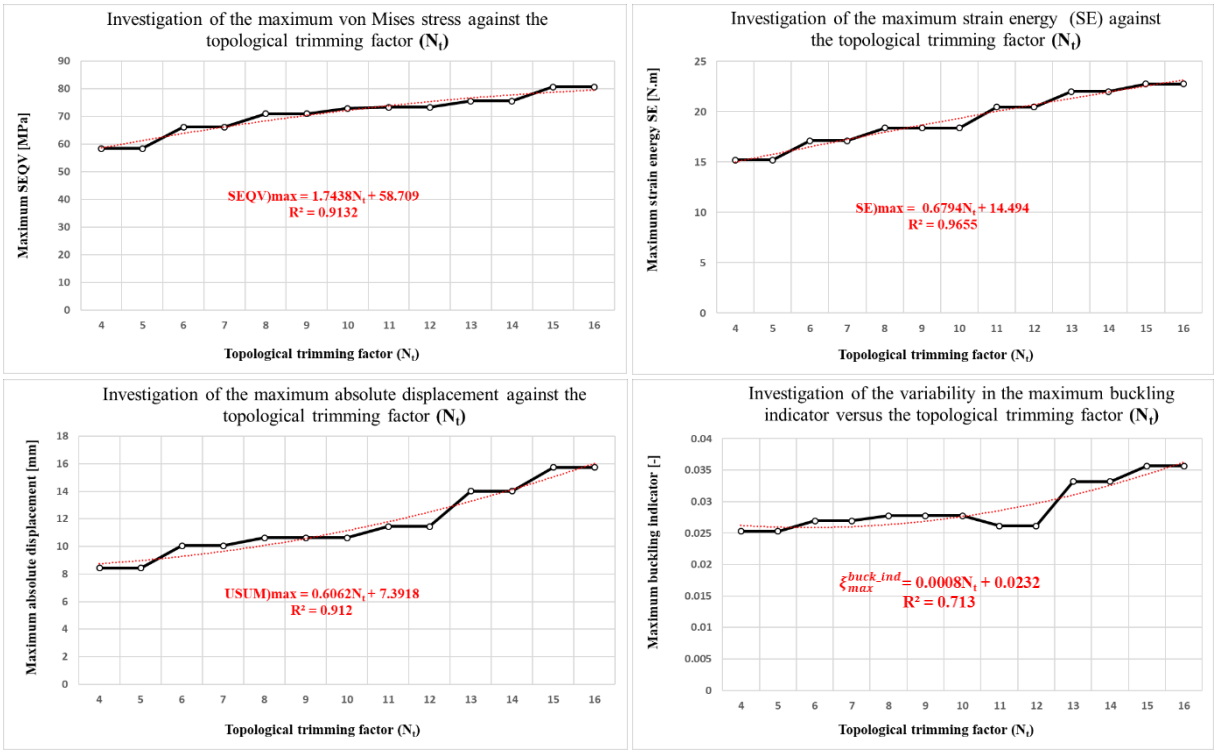

Figure 6.3 Parametric Investigation of $\mathbf{N_t}$ implemented on model A1.

6.2 Trimmed Ribbed Single Lattice Dome (Model A1)

The optimization results for model A1, described in section 4.5.1, using the proposed optimization strategies detailed in section 5.6. are given in Table 6.1 and Table 6.2. The minimum weight was found by MESO-DE (82.664 kg), with MESO-BA a close second, but these designs have been failed to meet the displacement constraints at stage 3 (for the load case with snow but no wind). Hence, the candidate is MESO-PSO, followed by MESO-ABC, which are the only two designs valid for all load cases. Table 6.1 shows that the optimization results from Stage 1 tend towards extreme values, i.e. N_n is set to 30, N_r is set to 12 in most cases. The topological trimming factor (N_t) is set to the highest value of the range (N_t=16), where the number of rings for the dense ribs' region (N_{dr}), defined in Eq. (4.2), has reduced to its minimum range. The optimal set of sizing variables for model A1 is listed in Appendix Table F.1. The design history of cost function for model A1, illustrated in Figure 6.4, states that the number of analyses has reached 210 for stage-1 and 401 for stage-2. This is achieved by assuming the appropriate number of iterations for each stage: MaxIt1=20 and MaxIt2=40, as the design optimization stages are illustrated in Figure 5.9.

The number of design variables, to be optimized at stage-2, has been diminished from (4+52+1=57) to become (4+33+1=38) in total. This reduction is influenced by the significant elimination in N_r (from 20 to 12) implemented at stage-1.

The setting parameters and population size of the of the optimizer play the significant role in determining the number of analyses required to reach the optimum point. For instance, the abandonment rules adopted by ABC strategy will generate an extra explorative design points depending on the abandonment limits supposed for the technique. Furthermore, a considerable number of design points are rejected due to breaching the constraints.

Table 6.1 Optimal set of shape and topological design parameters found for model A1.

Optimization method	N_n (-)	N_r (-)	N_s (-)	N_t (-)	R (m)
Initial design	**40**	**20**	**24**	**13**	**30.000**
MESO-ABC	**31**	**12**	**27**	**16**	**54.033**
MESO-BA	**30**	**12**	**23**	**16**	**59.035**
MESO-DE	**30**	**12**	**23**	**16**	**59.085**
MESO-PSO	**30**	**12**	**23**	**16**	**60.000**
MESO-SA	**30**	**16**	**25**	**13**	**48.422**

Table 6.2 Optimal set of cost functions evaluated for model A1.

Optimization method	Minimum cost $\left(\frac{W}{W_0}\right)$	Corresponding roof frame mass (tonnes)	Corresponding whole tank mass (tonnes)
Initial design	**1.000**	**250.936**	**579.765**
MESO-ABC	**0.366**	**91.705**	**410.949**
MESO-BA*	**0.331**	**82.922**	**401.625**
MESO-DE*	**0.329**	**82.664**	**401.363**
MESO-PSO	**0.341**	**85.524**	**404.140**
MESO-SA*	**0.368**	**92.240**	**412.332**
*** The design has failed by displacement constraints considering pure snow load.**			

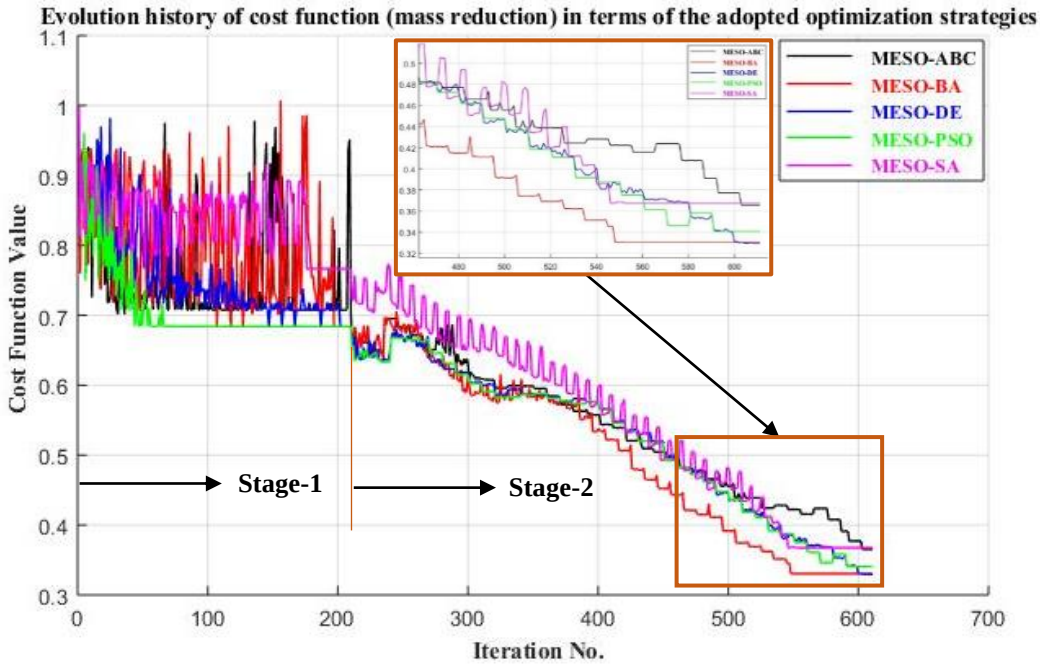

Figure 6.4 Progression history of the cost function towards the optimum for model A1.

6.3 Schwedler Single Lattice Dome (Model B1)

Results for optimization of Model B1 are given in Table 6.3 and Table 6.4. MESO-DE has achieved the minimum of cost function (0.238) among the other designs, with roof structural mass of 60.11 tonnes and whole tank mass of 379 tonnes. All optimal designs obtained for model B1 have passed the test at stage 3.

The sizing parameters of the model B1 are itemized in Appendix Table F.2. In stage-1, for MESO-DE, the number of design variables is considerably reduced from (3+31+1=35) to (3+22+1=26). This reduction is influenced by the reduction in N_r (from 11 to 8) at stage 1.

The numbers of finite element analyses of the optimization process are 207 for stage-1 and 302 for stage-2.

The history of cost function for model B1 is shown in Figure 6.5. Figure 6.6 shows the stress distribution between the initial and optimal designs for model B1.

Table 6.3 Optimal set of shape and topological design parameters found for model B1.

Optimization method	N_n (-)	N_r (-)	N_s (-)	R (m)
Initial design	**54**	**11**	**20**	**30.000**
MESO-ABC	**36**	**6**	**27**	**60.000**
MESO-BA	**36**	**8**	**28**	**59.793**
MESO-DE	**36**	**8**	**30**	**57.212**
MESO-PSO	**36**	**8**	**30**	**60.000**
MESO-SA	**36**	**10**	**16**	**52.667**

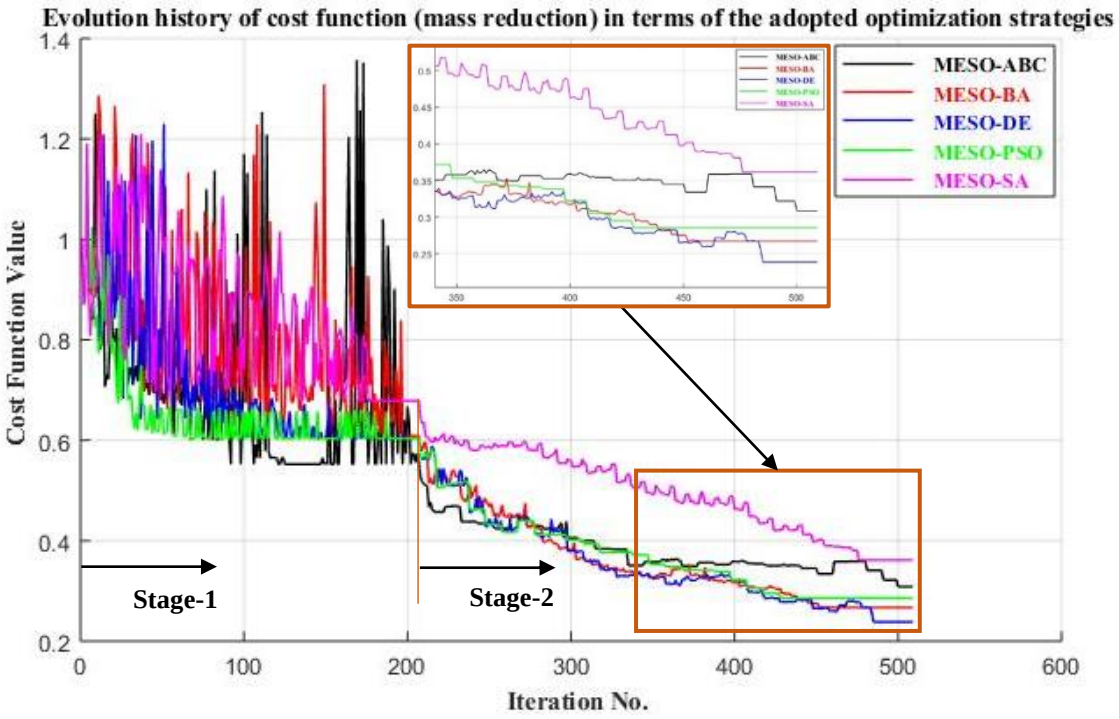

Figure 6.5 Progression history of the cost function towards the optimum for model B1

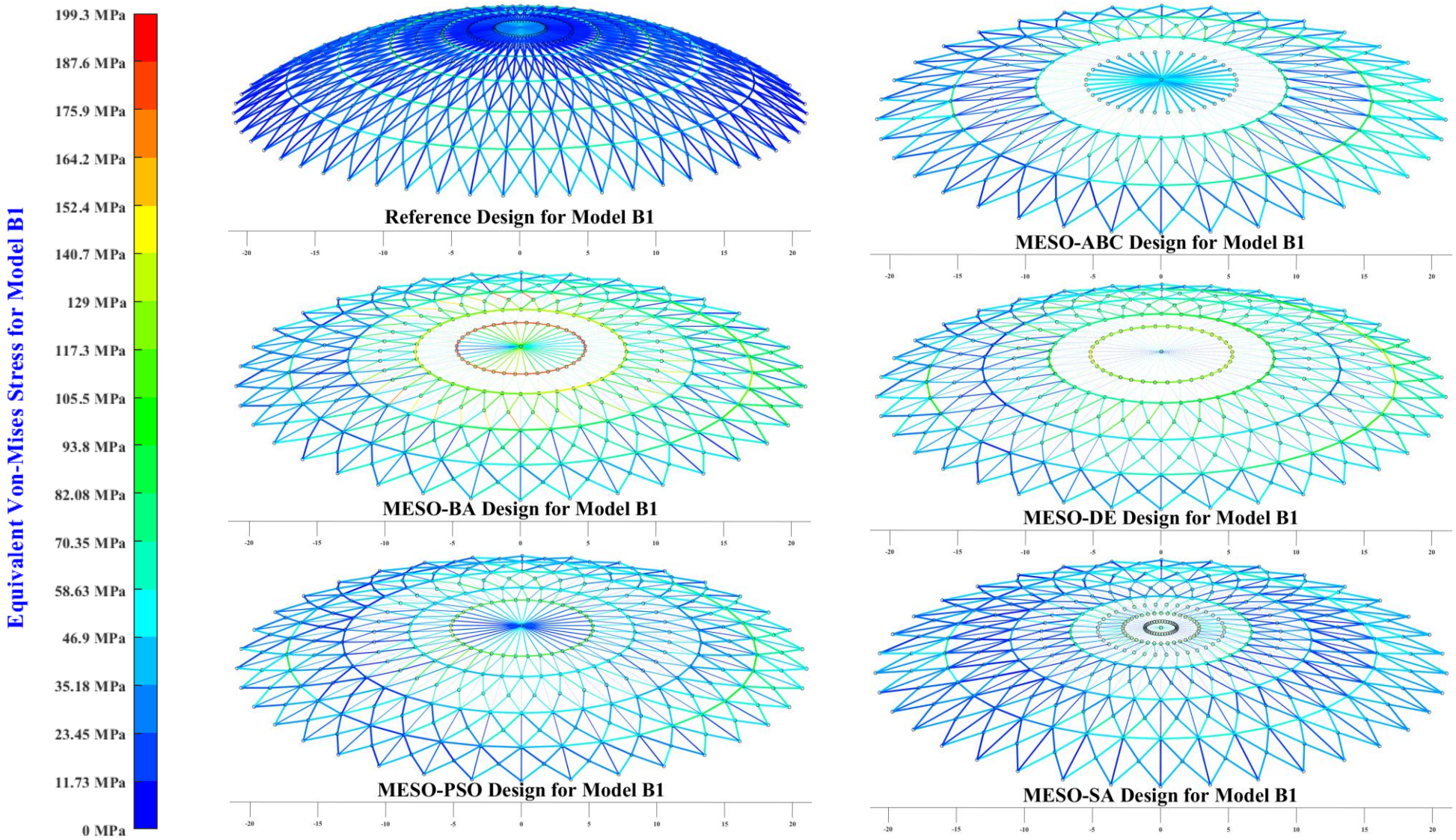

Figure 6.6 Distribution of equivalent (von-Mises) stress showing the difference between the initial and optimal designs for model B1.

Table 6.4 Optimal set of cost functions evaluated for model B1.

Optimization method	Minimum cost $\left(\frac{W}{W_0}\right)$	Corresponding roof frame mass (tonnes)	Corresponding whole tank (tonnes)
Initial design	**1.000**	**252.150**	**580.979**
MESO-ABC	**0.309**	**77.787**	**396.402**
MESO-BA	**0.313**	**78.936**	**397.570**
MESO-DE	**0.238**	**60.110**	**378.992**
MESO-PSO	**0.286**	**71.991**	**390.606**
MESO-SA	**0.361**	**91.115**	**410.537**

6.1 Lamella Single Lattice Dome (Model C1)

Results for Model C1, indicated in Table 6.5 and Table 6.6, show that MESO-ABC is the optimal design with minimum structural mass 54.083 tonnes. Correspondingly, the optimal integer set of design parameters for model C1 is not different from those found by MESO-ABC for model B1, where N_n=36, N_r=6, which are exactly the lower limits of their respective design ranges. The number of design variables for MESO-ABC is appreciably reduced from (3+37+1=41) to (3+16+1=20). This is caused by reducing N_r (from 13 to 6).

The convergence history of cost function, presented in Figure 6.8, shows 207 cycles at high perturbation (stage 1) and 405 cycles at low perturbation (stage 2). The dramatic changes (fluctuations) in the cost (structural weight fraction) at stage 1 are attributed to the correlation nature between the structural weight and the integer design variables involved ($\mathbf{N_n}$, $\mathbf{N_r}$, and $\mathbf{N_s}$). while, other design variables optimized at stage 2 (sizing variables) have lesser influence on the structural mass compared to the topological integer variables. This behaviour could be observed evidently in Figure 6.5, where the fluctuations are depressed to noticeable extent compared to stage 1. However, MESO-SA has stopped to converge after 434 analyses due to breaching the stress limits at this point onwards.

Figure 6.7 shows the stress state for the optimal designs of the model C1. The circumferential rings are the most significant parts influenced by the wind loads applied to the structure. The maximum stress could be observed in the MESO-DE, which reaches 198.5 MPa.

Table 6.5 Optimal set of shape and topological design parameters found for model C1.

Optimization method	N_n (-)	N_r (-)	N_s (-)	R (m)
Initial design	**58**	**13**	**20**	**30.000**
MESO-ABC	**36**	**6**	**16**	**60.000**
MESO-BA	**36**	**6**	**11**	**60.000**
MESO-DE	**36**	**6**	**11**	**59.086**
MESO-PSO	**36**	**7**	**10**	**60.000**
MESO-SA	**52**	**6**	**27**	**51.581**

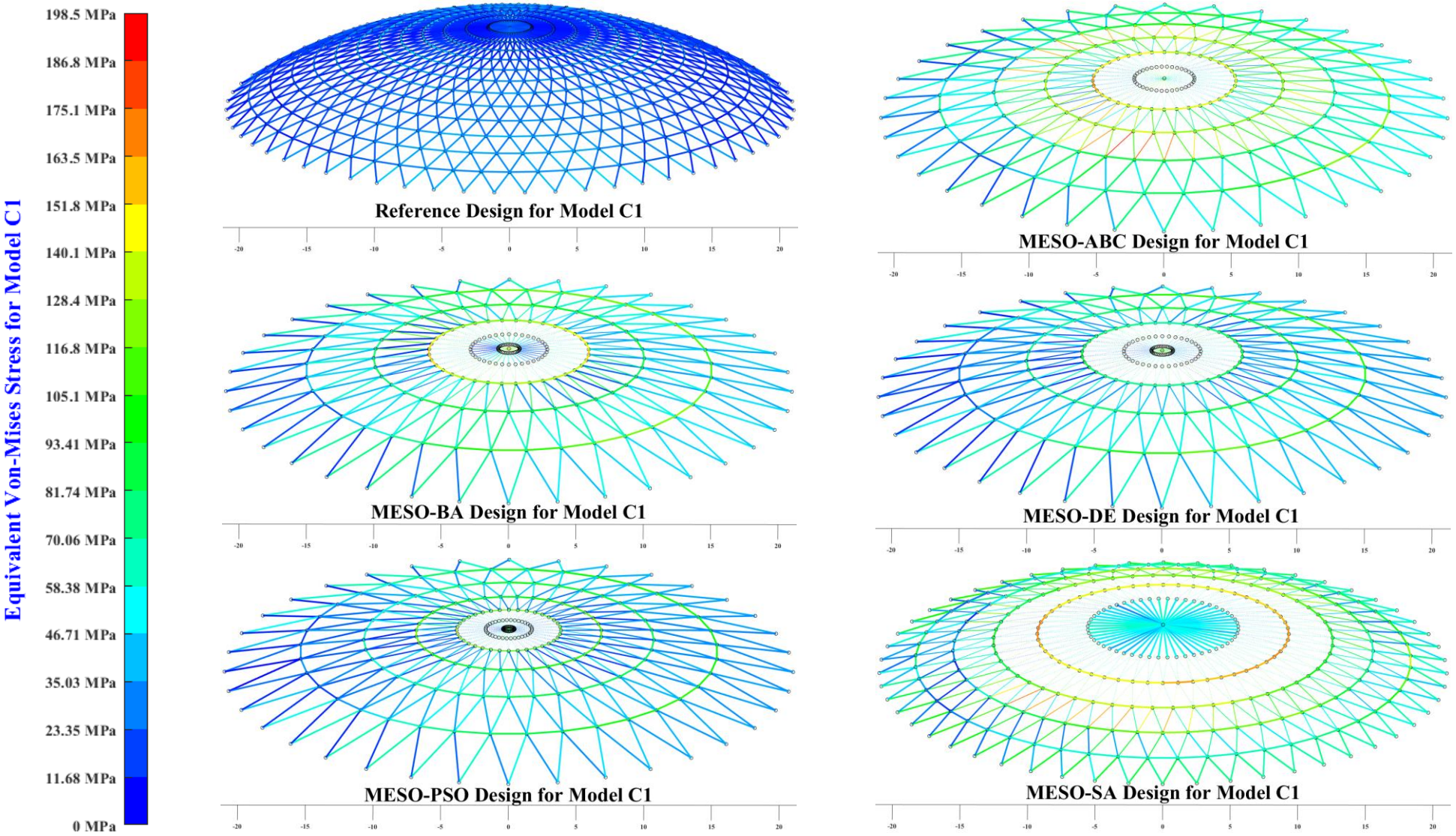

Figure 6.7 Distribution of equivalent (von-Mises) stress showing the difference between the initial and optimal designs of model C1.

Table 6.6 Optimal set of cost functions evaluated for model C1.

Optimization method	Minimum cost $\left(\frac{W}{W_0}\right)$	Corresponding roof frame mass (tonnes)	Corresponding whole tank mass (tonnes)
Initial design	**1**	**208.900**	**537.729**
MESO-ABC	**0.259**	**54.083**	**372.698**
MESO-BA	**0.293**	**61.173**	**379.788**
MESO-DE	**0.330**	**68.835**	**387.533**
MESO-PSO	**0.367**	**76.564**	**395.179**
MESO-SA	**0.299**	**62.539**	**382.115**

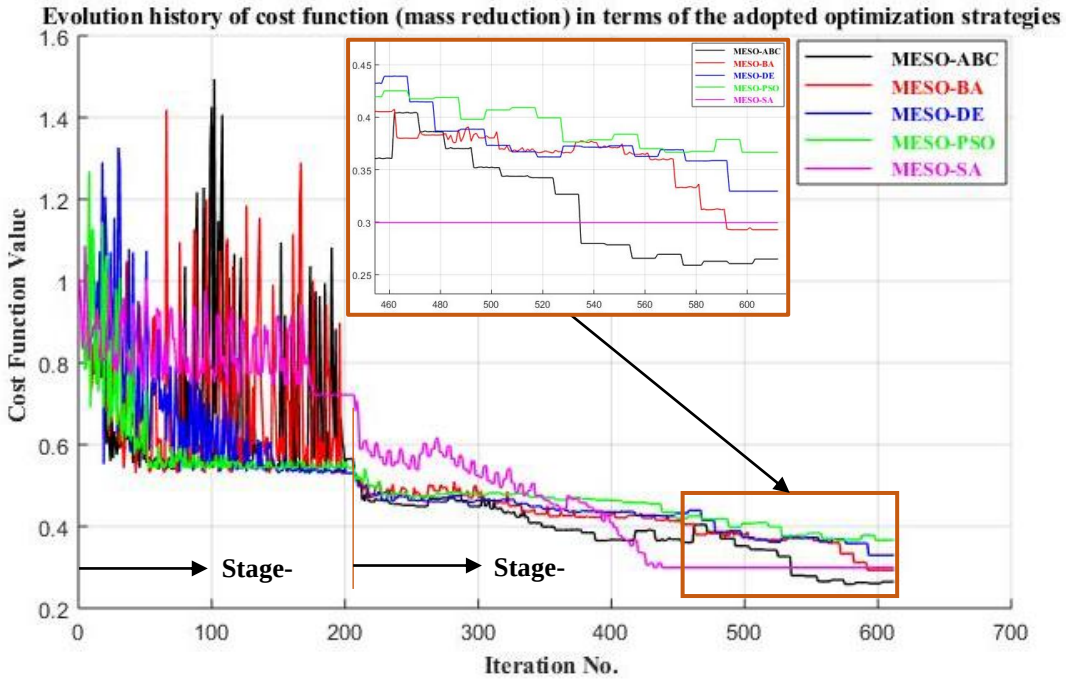

Figure 6.8 Progression history of the cost function towards the optimum for model C1.

6.2 Hybrid Schwedler-Lamella Single Lattice Dome (Model D1)

The results for model D1 reflect the structural characteristics of its parents (models B1 and C1), where the common features existing in both models could be observed in this model. Table 4.11 provides more details about the reference design of model D1. The newly suggested morphological design parameter (**N_m**) is defined in section 4.5.4. Table 6.7 show that the optimal integer set are chosen to be reduced to the lowest value in the range, i.e. N_n=32, N_r=6, N_s=10, and N_m=20 to 23, except MESO-ABC and MESO-BA for N_s. Reducing N_m to the lowest possible level (see the optimization range fixed in Table 4.10) and linking this change to the formulae (4.10) and (4.11) will lead to the conclusion that the topological morphing process has succeeded to minimize the structural weight via transforming the configuration of the considered model from Schwedler to Lamella. The latter statement suggests that the Lamella choice outperforms the Schwedler one to achieve the design goal since both options are

available to execute on this model. Appendix Table F.4 shows the optimal set of the sizing parameters for model D1. In stage 1, the variables have been considerably decreased from (4+31+1=36) to (4+16+1=21) due to reducing the integer design variable N_r (from 11 to 6).

Table 6.7 Optimal set of shape and topological design parameters found for model D1.

Optimization method	**N_n (-)**	**N_r (-)**	**N_s (-)**	**N_m (-)**	**R (m)**
Initial design	**48**	**11**	**20**	**35**	**45.000**
MESO-ABC	**32**	**6**	**19**	**20**	**53.131**
MESO-BA	**32**	**6**	**18**	**22**	**59.475**
MESO-DE	**32**	**6**	**10**	**20**	**60.000**
MESO-PSO	**32**	**6**	**10**	**23**	**60.000**
MESO-SA	**32**	**6**	**10**	**23**	**54.288**

6.2.1 Evolution History of Cost Function

According to Table 6.8, the optimal design obtained for model D1 is MESO-ABC through achieving a minimum cost of 0.204, the corresponding roof frame mass is 34.455 tonnes leading to total mass for the tank 353.815 tonnes. It is the lightest weight indicated for all models considered in this study. The convergence history of cost function is given in Figure 6.9. The first interval is ranging from it=1 to it=207, whereas the second is extending between it=208 and it=618. The model is relatively stable against the design constraints, i.e. it shows a minimum number of violations during the evolution process.

Utilizing lightweight yet strong cross sections (RHS) to model the members of model D1 is one of the reasons behind this success. Looking at stage 1 of Figure 6.9, MESO-PSO has the best convergence rate, which is justified by the high exploitative capability of the method, followed by MESO-DE. At the same time, the randomized motion of MESO-BA and MESO-ABC till the final cycle in stage 1 reflects the explorative capability of these methods. In this sense, the maximum amplitude of MESO-SA as explorative strategy is controlled by the supposed extent of mutation ($sigma_k$) defined in Eqs. (5.50) and (5.54).

Table 6.8 Optimal set of cost functions evaluated for model D1.

Optimization method	**Minimum cost $\left(\frac{W}{W_0}\right)$**	**Corresponding roof frame mass (tonnes)**	**Corresponding whole tank mass (tonnes)**
Initial design	**1**	**168.873**	**489.672**
MESO-ABC	**0.204**	**34.455**	**353.815**
MESO-BA	**0.224**	**37.902**	**356.565**
MESO-DE	**0.243**	**41.009**	**359.624**
MESO-PSO	**0.241**	**40.690**	**359.305**
MESO-SA	**0.244**	**41.210**	**360.423**

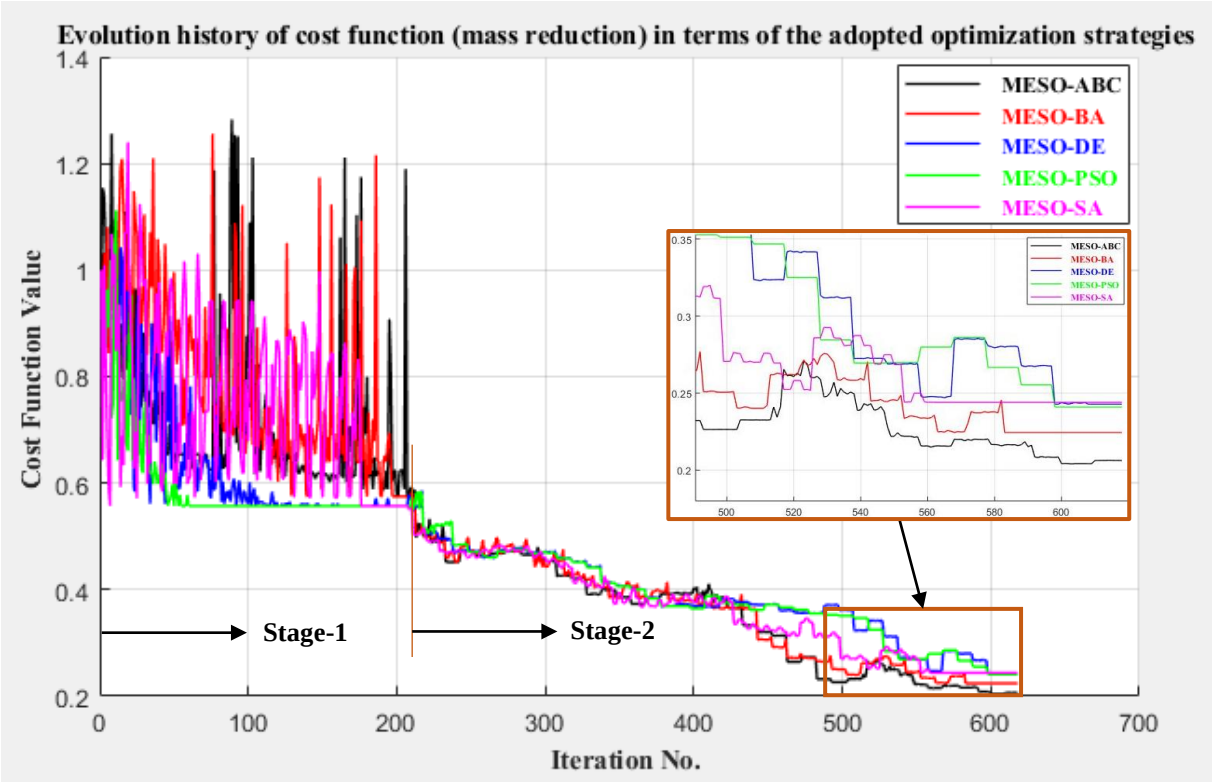

Figure 6.9 Progression history of the cost function towards the optimum for model D1.

6.2.2 Evolution History of Design-related Functions

The stiffness and strength characteristics of this model resemble those for the Lamella model, as the latter model has outperformed the Schwedler model in many aspects. Table 6.9 lists the statistical data about the design characteristics of model D1, where MESO-PSO shows the maximum strength relative to others in terms of the lowest stress ratio (2.8) involved. Similarly, the minimum magnitude of SE function for MESO-PSO reflects the highest stiffness of the design. The further reduction in structural weight implemented on the designs (MESO-ABC and MESO-BA) has caused a worsening of the strength, stiffness and buckling characteristics of the structure, as they show the highest values of normalized stress ratios (4.089 and 3.716), normalized SE ratios (8.986 and 7.905) and normalized buckling ratios (12.278 and 3.697).

Figure 6.10a shows a steep progression in the normalized stress ratio in the curves MESO-ABC and MESO-BA. This increase indicates that the strength features are negatively affected by the reduction in the structural weight. The same justification could be used when looking at the paths delineated by the same designs in each of the graphs in Figure 6.10b-d, where the stiffness characteristics and the buckling resistance are inversely influenced by the mass reduction for these two designs.

6.2.3 History of the Maximum Response (Investigation of the Design Constraints)

The graphs in Figure 6.11 investigate the situation of the model against the design constraints during the optimization process. Statistically, MESO-BA and MESO-DE are the two designs that recorded displacement violations in stage 1, they are penalized 5 and 7 times respectively, whereas there are only 2 solutions discarded by the displacement limits in MESO-SA. On the other hand, the designs MESO-BA and MESO-ABC have missed 128 and 59 solutions due to overstepping the stress constraints during stage 2, whereas the displacement constraints have rejected only one solution as executed on MESO-ABC in stage 2.

Table 6.9 Design data for the initial and optimal statuses executed on model D1.

Optimization method	**Stress function (Stress ratio)**	**SE function (SE ratio)**	**SED function (SED ratio)**	**Buckling function (Buckling ratio)**
Initial design	**1.000**	**1.000**	**1.000**	**1.000**
MESO-ABC	**4.089**	**8.986**	**20.390**	**12.278**
MESO-BA	**3.716**	**7.905**	**15.876**	**3.697**
MESO-DE	**2.812**	**4.709**	**9.247**	**3.149**
MESO-PSO	**2.803**	**4.701**	**8.754**	**3.072**
MESO-SA	**2.866**	**4.831**	**9.795**	**3.959**

Table 6.10 The data of the maximum response induced in model D1.

Optimization Method	**Maximum von-Mises stress [MPa]**	**Maximum absolute displacement [mm]**	**Maximum buckling indicator [---]**
Initial design	**57.471**	**9.055**	**0.0290**
MESO-ABC	**194.343**	**30.183**	**0.1730**
MESO-BA	**185.590**	**29.501**	**0.0460**
MESO-DE	**183.739**	**28.616**	**0.0402**
MESO-PSO	**181.371**	**28.702**	**0.0417**
MESO-SA	**182.044**	**27.397**	**0.0421**

6.2.4 Relevant Design Contours

Figure 6.12 presents the design contours concerning the state of stress for model D1. The different designs in the figure evidence that the circumferential rings are the most critical parts of the structure. The design MESO-ABC has developed the maximum equivalent stress (194.34 MPa) in comparison to others. This is due to the lightest weight produced for this design. Also, it shows the maximum absolute displacement (30.183 mm)

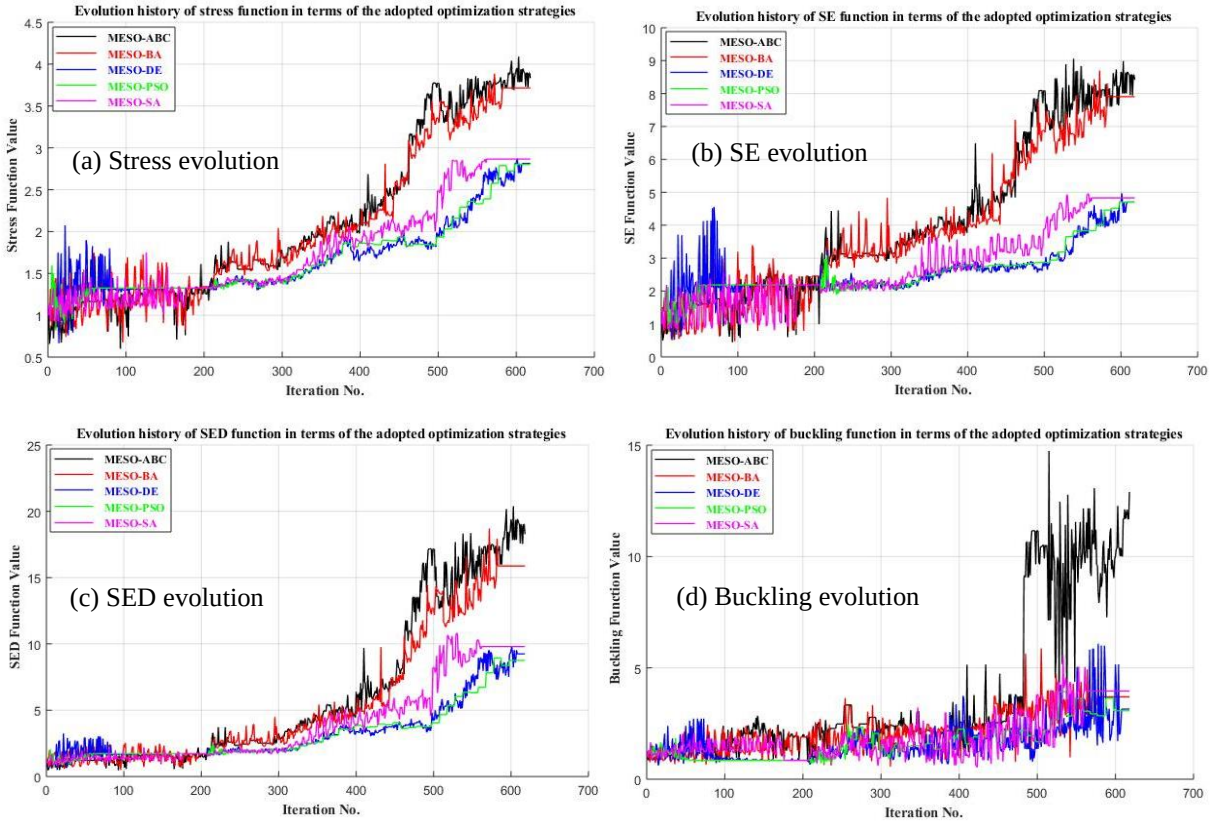

Figure 6.10 Evolution history of the relevant design functions for model D1.

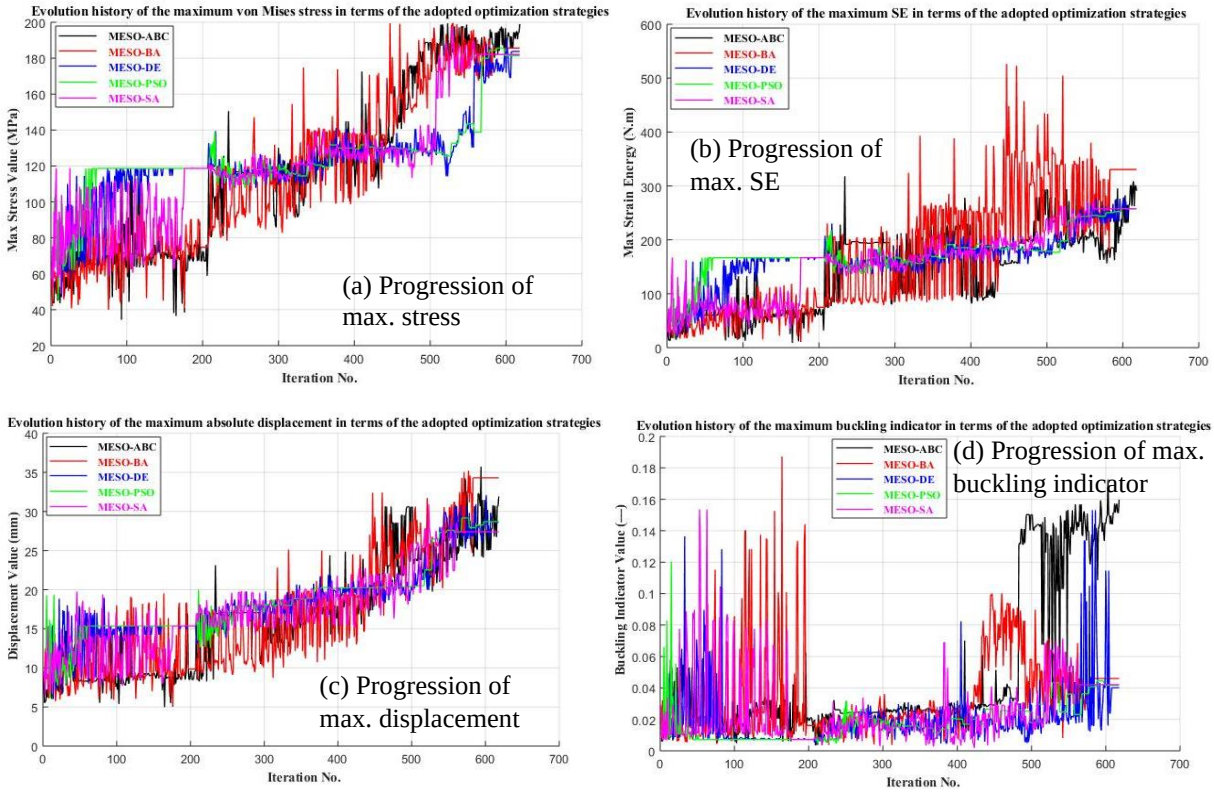

Figure 6.11 Design history of the maximum response induced over the entire structure for model D1.

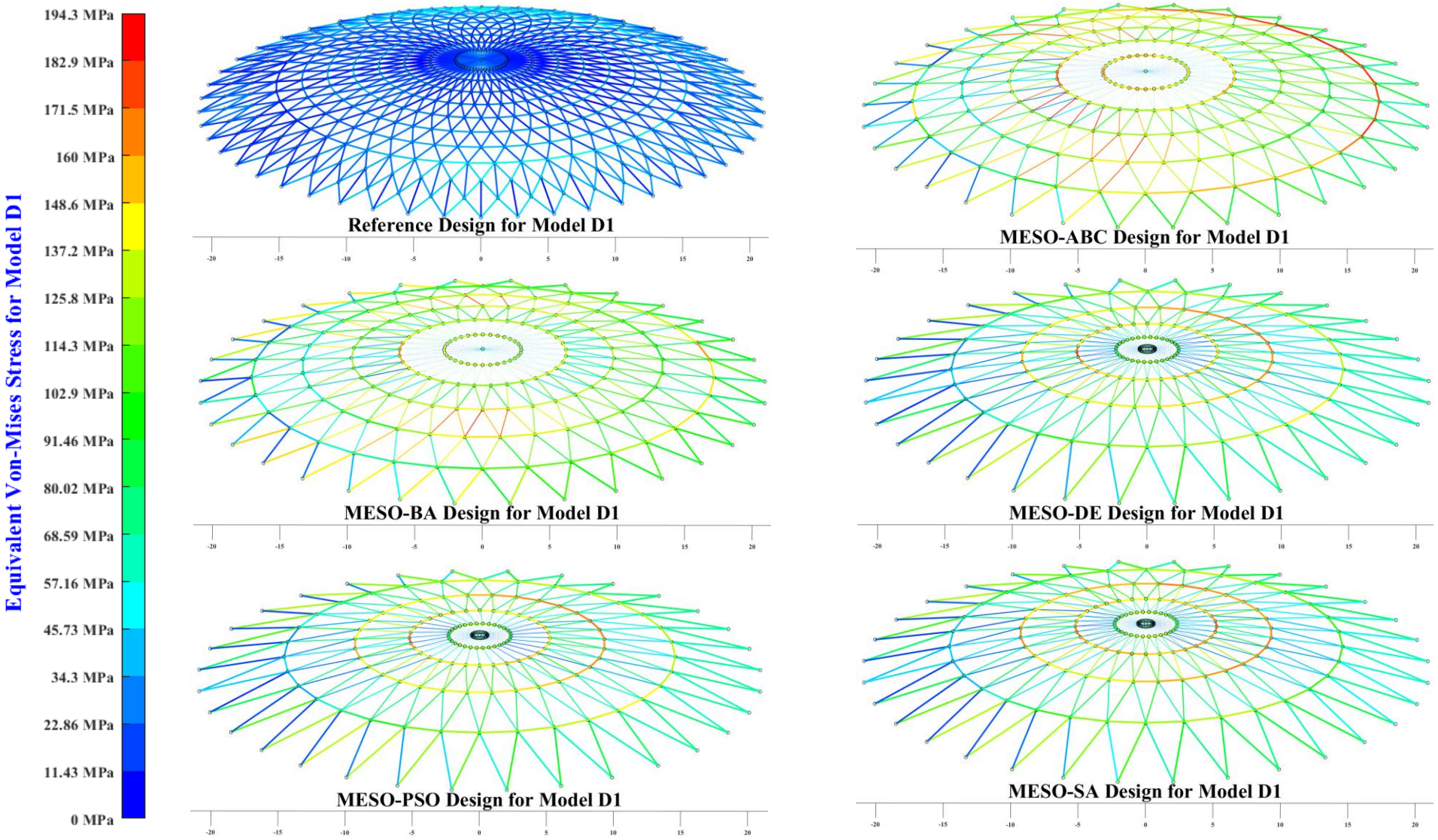

Figure 6.12 Distribution of equivalent (von-Mises) stress showing the difference between the initial and optimal designs for model D1.

6.3 Geodesic Single Lattice Dome (Model E1)

The configuration of model E1 is completely differs from the previous models, where the geometry is created as basic polygon in the dome hub as described in section 4.5.5. Thus, the number of nodes (N_n) is replaced by the number of sides for the basic polygon, as defined in Table 4.12. The results are presented in Table 6.11, N_n and N_r are selected at their lower bounds, i.e. N_n=6 and N_r=6 are recorded as optimal values, whereas the topological spacing parameter (N_s) has increased to the highest level (N_s=30) as optimal value for the designs MESO-ABC, MESO-DE and MESO-PSO. The designs MESO-BA and MESO-SA have lower values. Appendix Table F.5 gives the optimal designations for model E1. The number of design variables is effectively reduced from (3+41+1=45) at stage-1 to (3+21+1=25) at stage 2 due to reducing N_r from 11 to 6.

6.3.1 Evolution History of Cost Function

The optimal design noticed for this model is MESO-DE with weight 37.012 tonnes as fixed in Table 6.12. The plots in Figure 6.13 show the convergence curves of cost function. The evolution is characterized by two intervals: the first is ranging from it=1 to it=208, whereas the second is extending from it=209 to it=448. Hence, the total number of analyses executed during the overall optimization process is (208+240=448).

Table 6.11 Optimal set of shape and topological design parameters found for model E1.

Optimization Method	N_n (-)	N_r (-)	N_s (-)	R (m)
Initial design	**11**	**11**	**20**	**30.000**
MESO-ABC	**6**	**6**	**30**	**60.000**
MESO-BA	**6**	**6**	**25**	**57.514**
MESO-DE	**6**	**6**	**30**	**53.141**
MESO-PSO	**6**	**6**	**30**	**60.000**
MESO-SA	**6**	**6**	**23**	**60.000**

Table 6.12 Optimal set of cost functions evaluated for model E1.

Optimization Method	Minimum cost $\left(\frac{W}{W_0}\right)$	Corresponding roof frame mass (tonnes)	Corresponding whole tank mass (tonnes)
Initial design	**1.000**	**257.006**	**585.834**
MESO-ABC	**0.195**	**50.227**	**368.842**
MESO-BA	**0.262**	**67.196**	**386.047**
MESO-DE	**0.144**	**37.012**	**356.370**
MESO-PSO	**0.191**	**49.096**	**367.711**
MESO-SA	**0.164**	**42.247**	**360.862**

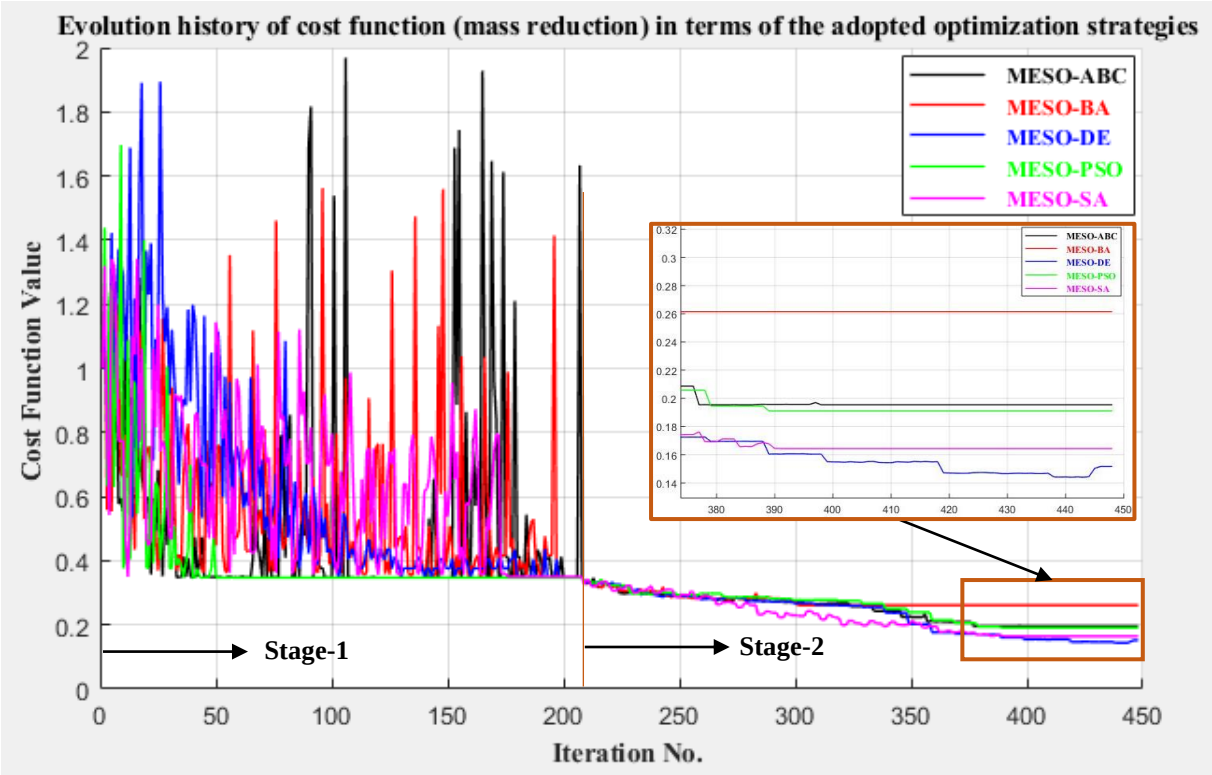

Figure 6.13 Progression history of the cost function towards the optimum for model E1.

6.3.2 Evolution History of Design-related Functions

Normally, stiffness, strength and buckling characteristics for certain design are affected negatively to a higher degree by the reduction in structural weight, especially, when the optimization process is treating with sizing parameters. Simply, this is attributed to the fact that the weight is a linear function of sizing parameters, whereas other design functions (e.g. stress, strain energy and buckling), are reflecting the structural characteristics mentioned above, and are nonlinear functions of sizing parameters.

Table 6.13 Design data for the initial and optimal statuses executed on model E1.

Optimization Method	Stress function (Stress ratio)	SE function (SE ratio)	SED function (SED ratio)	Buckling function (Buckling ratio)
Initial design	**1.000**	**1.000**	**1.000**	**1.000**
MESO-ABC	**5.662**	**38.338**	**49.756**	**26.232**
MESO-BA	**3.464**	**20.867**	**16.542**	**3.003**
MESO-DE	**6.834**	**49.932**	**67.318**	**25.298**
MESO-PSO	**5.847**	**40.460**	**54.670**	**8.654**
MESO-SA	**5.739**	**37.755**	**46.710**	**6.165**

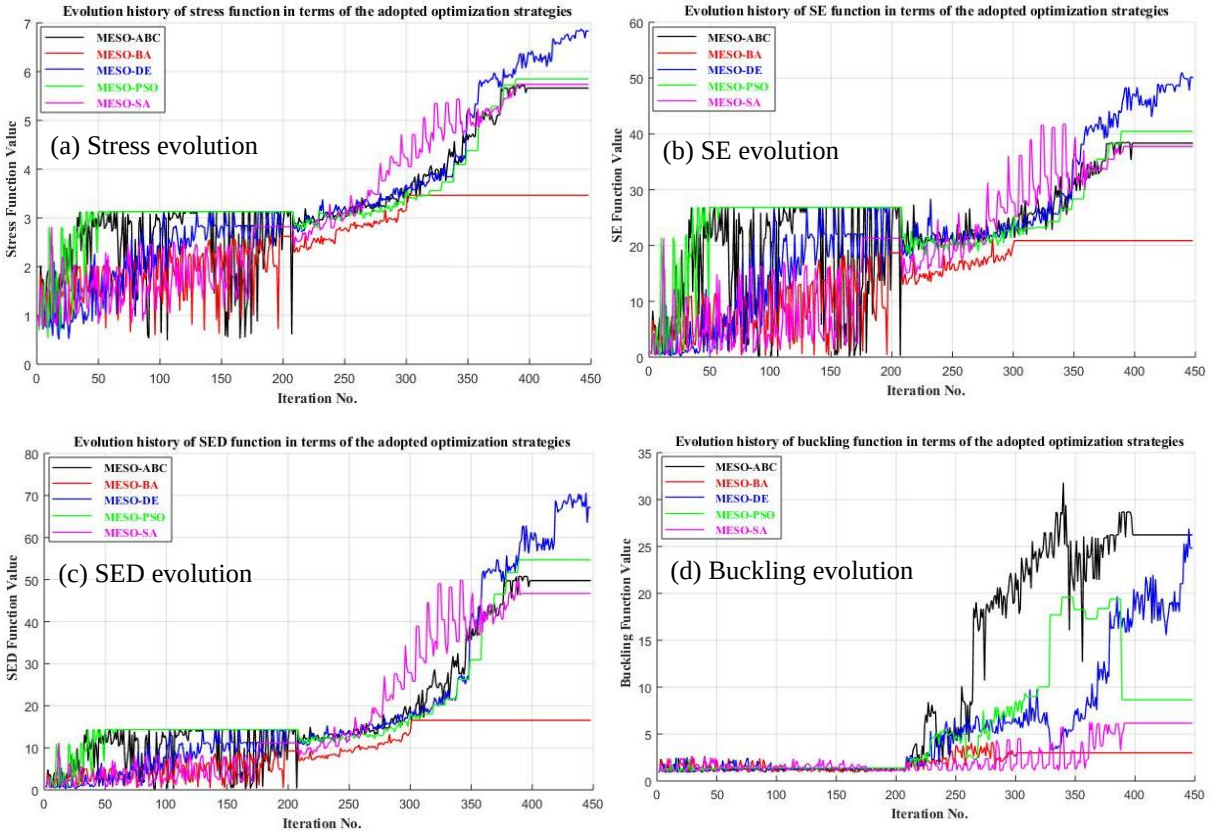

Figure 6.14 Evolution history of the relevant design functions for model E1.

However, the maximum values of normalized stress and SE ratios (6.834 and 49.932) observed in the design MESO-DE indicate the degree of dissipation in their structural characteristics noticed in this design. On the other hand, MESO-BA exhibits the highest buckling resistance as result to the lowest normalized buckling ratio developed by the design (3.003).

Figure 6.14a shows that MESO-DE has increased its progression rate at the final steps of stage 2. Figure 6.14b and Figure 6.14c indicate that MESO-DE is subjected to remarkable lowering in stiffness characteristics and MESO-BA has preserved progressing within the lowest level in the graph. Figure 6.14d demonstrates that MESO-ABC is progressing towards the optimum with extremely high levels causing the buckling characteristics to decline.

6.3.3 History of the Maximum Response (Investigation of the Design Constraints)

Figure 6.16 shows the evolution of the maximum response within the prescribed design constraints. Figure 6.16a shows that model E1 is restricted and constrained by the stress limits, where the permissible stress is defined by two levels of safety: high level (SF=1.6), which is executed at stage 1, and low level (SF=1.0), which is executed at stage 2. The designs MESO-ABC and MESO-DE are the two designs most affected by these limits, i.e. the stress limitations caused those two designs to lose 1008 and 975 solutions respectively. Only 94 evaluations are dismissed by buckling for the design MESO-BA as fixed in Table 6.15.

Figure 6.16c shows that the displacement restrictions is the second rigorous constraint applied to model E1, where the designs MESO-BA and MESO-PSO have been penalized 1462 and 840 times respectively during the optimization process as shown in Table 6.15. It is observed that the maximum stress is realized by MESO-DE with 199.32 MPa, whereas the corresponding maximum displacement is 33.744 mm as shown in Table 6.14. Though the maximum buckling index developed by the model jumps to high values at stage 2, as indicated in Table 6.14 and shown in Figure 6.16d, it is noticeable that this constraint has caused no losses during stage-1 or stage 2 except for the MESO-BA design.

Table 6.14 The data of the maximum response induced in the different designs of model E1.

Optimization method	Maximum von-Mises stress [MPa]	Maximum absolute displacement [mm]	Maximum buckling indicator [unitless]
Initial design	**55.456**	**3.732**	**0.00254**
MESO-ABC	**191.521**	**28.105**	**0.380**
MESO-BA	**198.498**	**21.560**	**0.020**
MESO-DE	**199.320**	**33.744**	**0.234**
MESO-PSO	**197.902**	**31.103**	**0.057**
MESO-SA	**198.72**	**29.663**	**0.105**

Table 6.15 Statistical data about the penalized solutions of model E1 (Stage 1 + Stage 2).

Optimization Method	Solutions lost due to breaching stress	Solutions lost due to breaching displacement	Solutions lost due to breaching buckling
MESO-ABC	**1+1007**	**0+325**	**0+0**
MESO-BA	**1+266**	**0+1462**	**0+94**
MESO-DE	**1+974**	**0+54**	**0+0**
MESO-PSO	**0+420**	**0+840**	**0+0**
MESO-SA	**1+528**	**0+2**	**0+0**

6.3.4 Relevant Design Contours

The design contours of model E1, depicted in Figure 6.15, indicate that the radial girders are the most affected part of the model. Accordingly, MESO-SA and MESO-BA exhibit critical stress at the radial beams of the hub region with values 198.72 MPa and 198.498 MPa respectively. While, MESO-DE has developed the maximum stress of 199.32 MPa and maximum SE of 557.31 J.

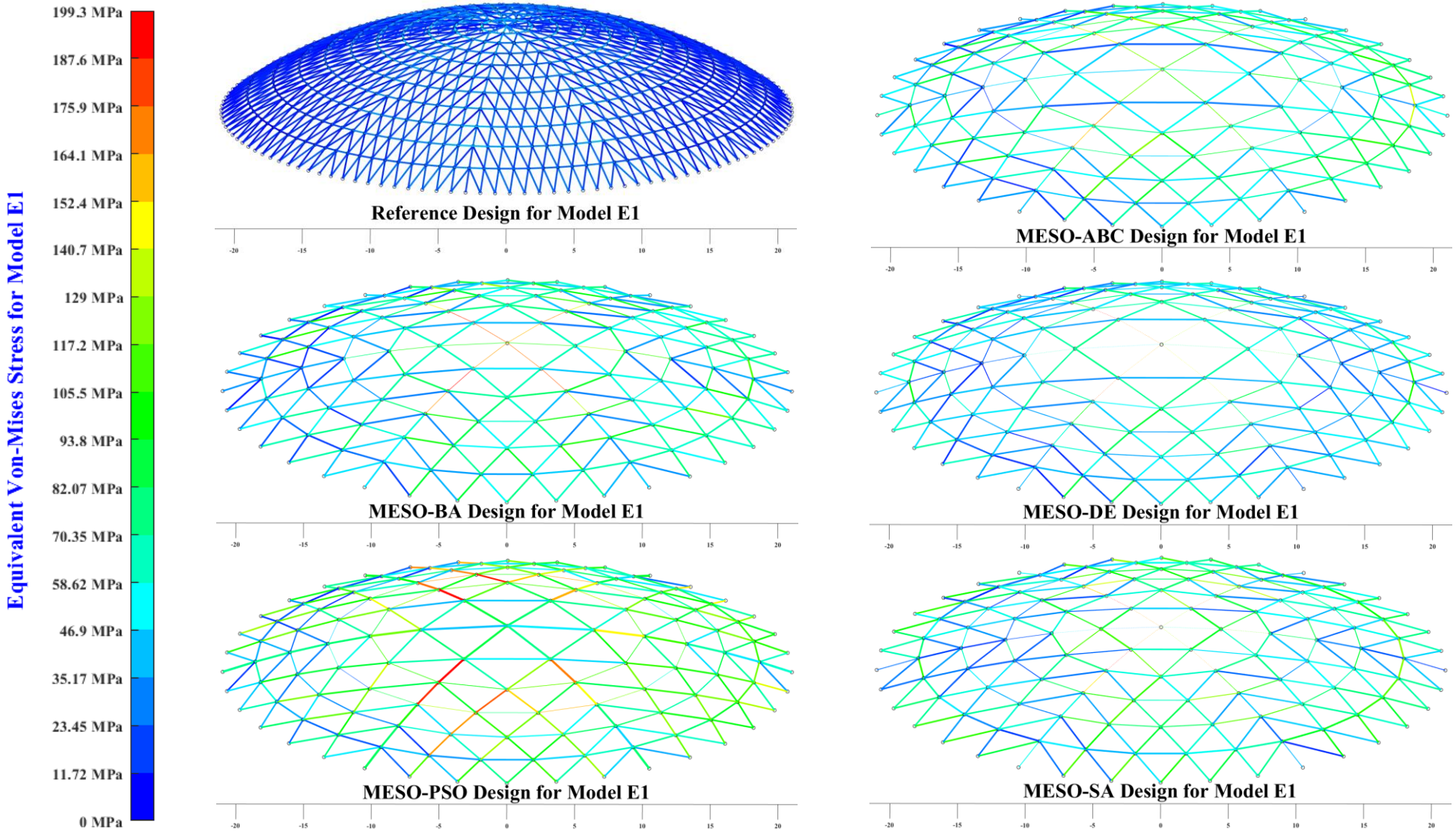

Figure 6.15 Distribution of equivalent (von-Mises) stress showing the difference between the initial and optimal designs for model E1.

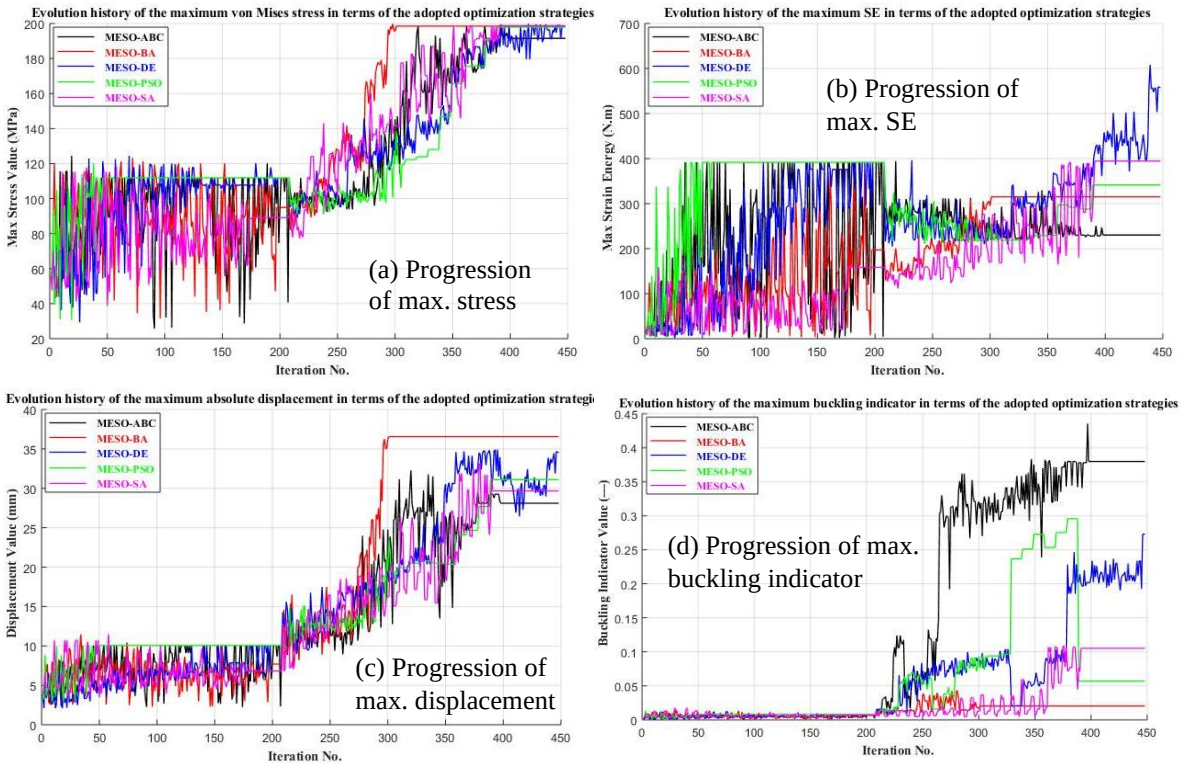

Figure 6.16 Design history of the maximum response induced in model E1.

6.4 Trimmed Ribbed Double Lattice Dome (Model A2)

Model A2, defined in Figure 4.13 (Section 4.5.6), has two extra continuous shape variables: height fraction (η=H2/H1) and dome radius ratio (ϑ=R2/R1). Results of the optimization are presented in Table 6.16 and Table 6.17, N_n and N_r are lowered as much as possible. The designs with low dome radius, i.e. MESO-BA and MESO-DE, are valid also for the other load cases of the problem, whereas the designs with high dome radius fail to meet the displacement constraints (see Table 6.17).

By studying the general trends, η tends to increase, whereas ϑ tends to decrease to achieve the minimum weight. Appendix Table F.6 gives the optimal designations of model A2. The number of design variables are effectively reduced from (4+102+3=109) at stage 1 to (4+69+3=76) at stage 2, as N_r is lowered from 15 to 10.

The optimal design obtained for model A2 is MESO-DE with minimum cost of 0.276, roof frame mass 61.117 tonnes, whole tank mass 391.495 tonnes. Figure 6.17 shows the convergence curves of cost function on two phases: high fluctuations phase (stage 1), incorporated with 206 evaluations, and low fluctuations phase (stage 2), which encompasses 756 cycles. This is produced by assuming an essential number of iterations for each stage: MaxIt1=20, MaxIt2=80 and MaxIt3=3. Hence, the overall optimization process counts to (206+756=962) successful analyses.

Table 6.16 Optimal set of shape and topological design parameters found for model A2.

Optimization Method	N_n (-)	N_r (-)	N_s (-)	N_t (-)	R (m)	η (-)	ϑ (-)
Initial design	**32**	**15**	**20**	**10**	**30.000**	**0.950**	**1.100**
MESO-ABC	**29**	**10**	**29**	**7**	**46.176**	**0.931**	**1.058**
MESO-BA	**24**	**10**	**13**	**16**	**46.892**	**0.927**	**0.902**
MESO-DE	**25**	**10**	**26**	**9**	**40.460**	**0.912**	**0.927**
MESO-PSO	**24**	**10**	**22**	**12**	**56.289**	**0.941**	**0.900**
MESO-SA	**25**	**14**	**28**	**11**	**52.737**	**0.911**	**0.995**

Table 6.17 Optimal set of cost functions evaluated for model A2.

Optimization Method	Minimum cost $\left(\frac{W}{W_0}\right)$	Corresponding roof frame mass (tonnes)	Corresponding whole tank mass (tonnes)
Initial design	**1.000**	**221.368**	**558.483**
MESO-ABC*	**0.338**	**74.868**	**403.689**
MESO-BA	**0.280**	**62.058**	**390.729**
MESO-DE	**0.276**	**61.117**	**391.495**
MESO-PSO*	**0.394**	**87.268**	**414.534**
MESO-SA*	**0.460**	**101.906**	**429.606**
*** The design has failed by displacement constraints considering pure snow load.**			

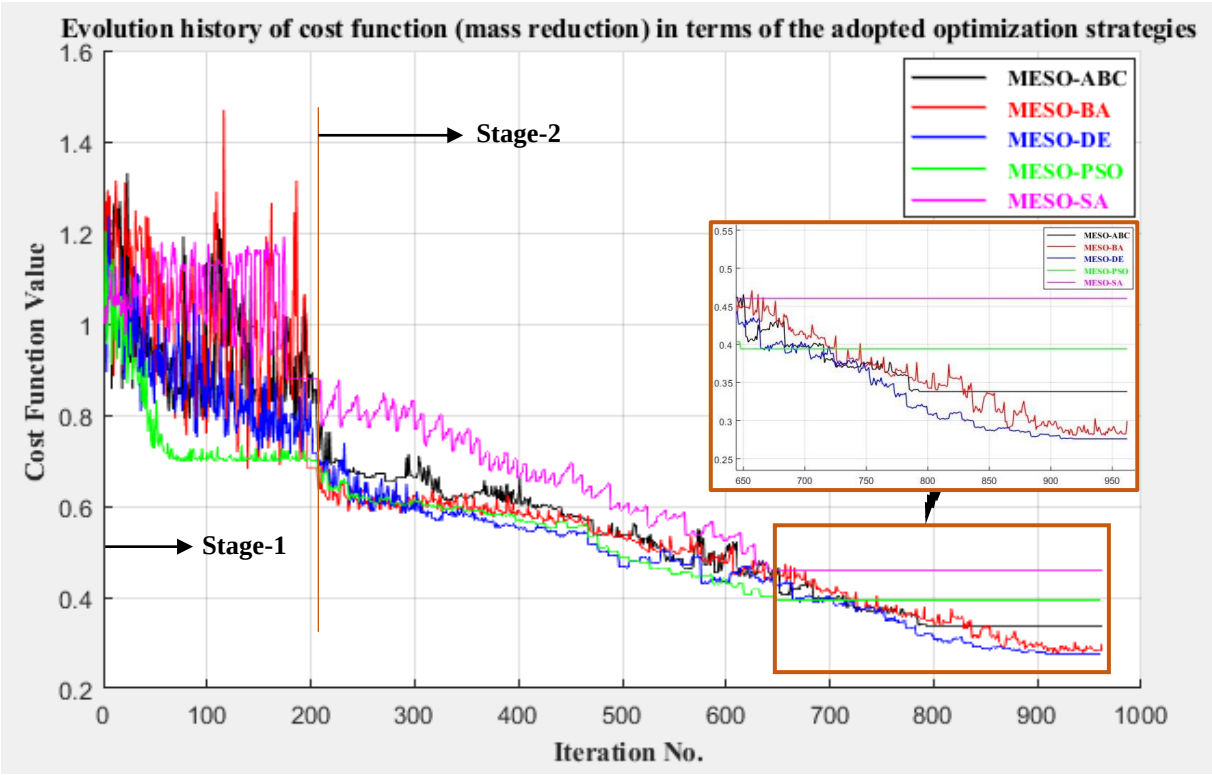

Figure 6.17 Convergence graph of the cost function towards the optimum for model A2.

The dome stresses are shown in Figure 6.18 and it can be seen that there are two critical regions in model A2. First, the periphery of the dome. Second, the circular ring surrounding the trimmed region. Accordingly, the maximum von-Mises stress (190.7 MPa) is indicated in MESO-ABC at the cross girder of the lower lattice as demonstrated in Figure 6.18b.

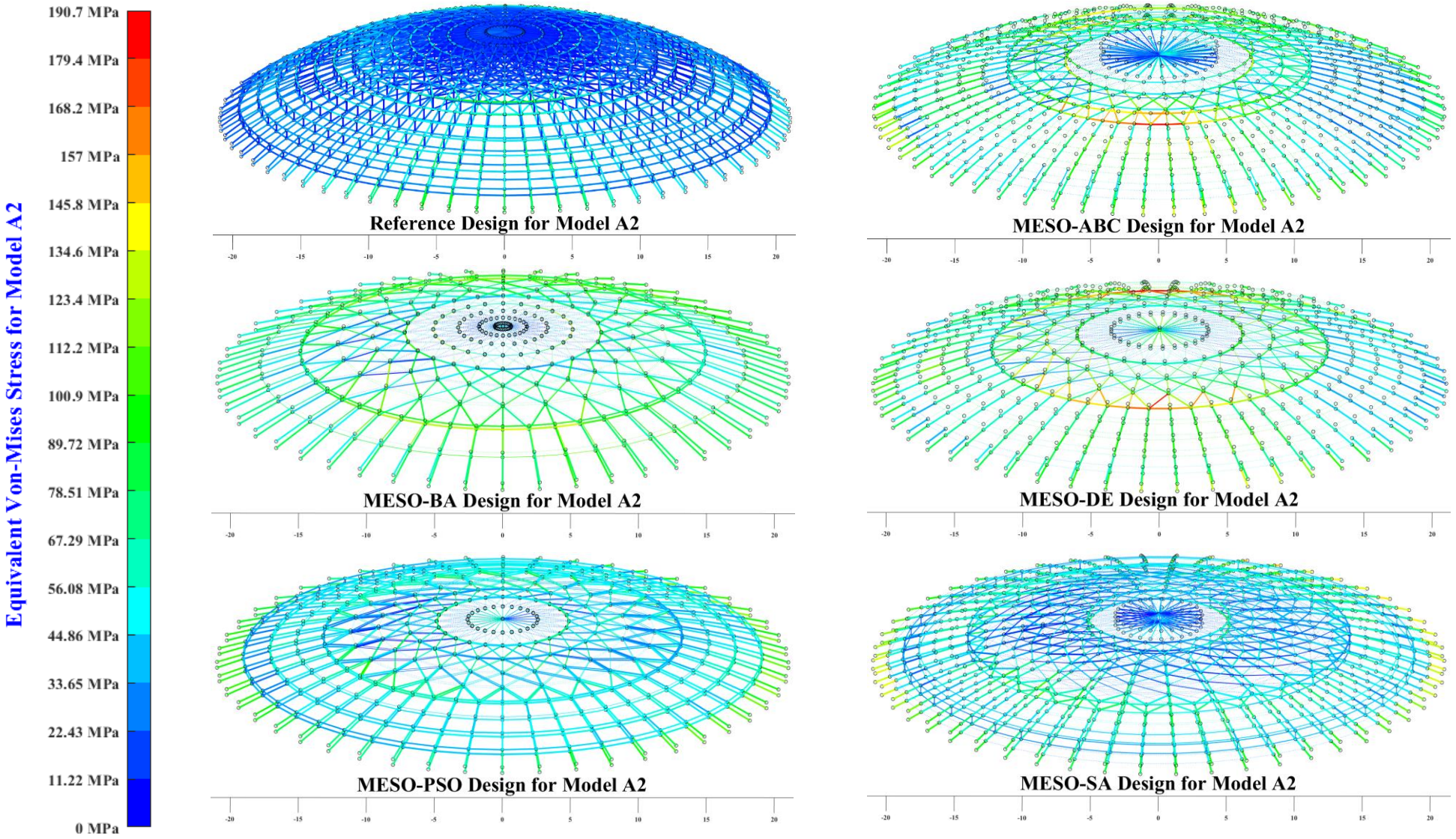

Figure 6.18 Distribution of equivalent (von-Mises) stress showing the difference between the initial and optimal designs for model A2.

The optimal design MESO-DE has developed a maximum stress of 188.8 MPa at the diagonal braces of lower lattice for the region where the transition from the dense rib area to the trimmed area of the dome. The designs produced by MESO-ABC and MESO-DE both have long radial girders, curved across multiple nodes. Although the risk of buckling is very low for individual links, i.e., for the straight girders between pairs of nodes, the cross-bracing is minimal and there is a potential risk of buckling at a global level. Further analysis would be required to ensure full design safety.

6.5 Schwedler Double Lattice Dome (Model B2)

The optimal set of shape and topological variables of model B2 are listed in Table 6.18. According to Table 6.19, the minimum cost function is realized by MESO-BA to be 0.107 corresponding to roof frame mass of 53.348 tonnes and tank mass of 380.495 tonnes. MESO-BA has marginally outperformed other competitive designs MESO-ABC and MESO-SA by a further reduction of 193 kg and 71 kg respectively. However, all five optimal designs failed by buckling under the other load cases considered, highlighting the importance of optimizing for all relevant load cases simultaneously. The evolution of the cost function, shown in Figure 6.19, indicate that MESO-BA and MESO-SA are the most robust methods, as they continue to progress up to the end of the optimization process.

Table 6.18 Optimal set of shape and topological design parameters found for model B2.

Optimization method	N_n (-)	N_r (-)	N_s (-)	R (m)	η (-)	ʊ (-)
Initial design	**45**	**11**	**20**	**30.000**	**0.950**	**1.100**
MESO-ABC	**30**	**6**	**30**	**56.596**	**0.932**	**1.082**
MESO-BA	**30**	**6**	**29**	**57.424**	**0.921**	**1.069**
MESO-DE	**30**	**6**	**30**	**60.000**	**0.852**	**0.946**
MESO-PSO	**30**	**6**	**30**	**60.000**	**0.950**	**1.100**
MESO-SA	**30**	**6**	**25**	**47.109**	**0.904**	**1.065**

Table 6.19 Optimal set of cost functions evaluated for model B2.

Optimization method	Minimum cost $\left(\frac{W}{W_0}\right)$	Corresponding roof frame mass (tonnes)	Corresponding whole tank mass (tonnes)
Initial design	**1.000**	**499.801**	**836.916**
MESO-ABC*	**0.107**	**53.541**	**380.774**
MESO-BA*	**0.107**	**53.348**	**380.495**
MESO-DE*	**0.116**	**57.810**	**384.711**
MESO-PSO*	**0.138**	**68.815**	**395.716**
MESO-SA*	**0.107**	**53.419**	**382.047**
*** The design has failed by buckling constraints considering pure snow load.**			

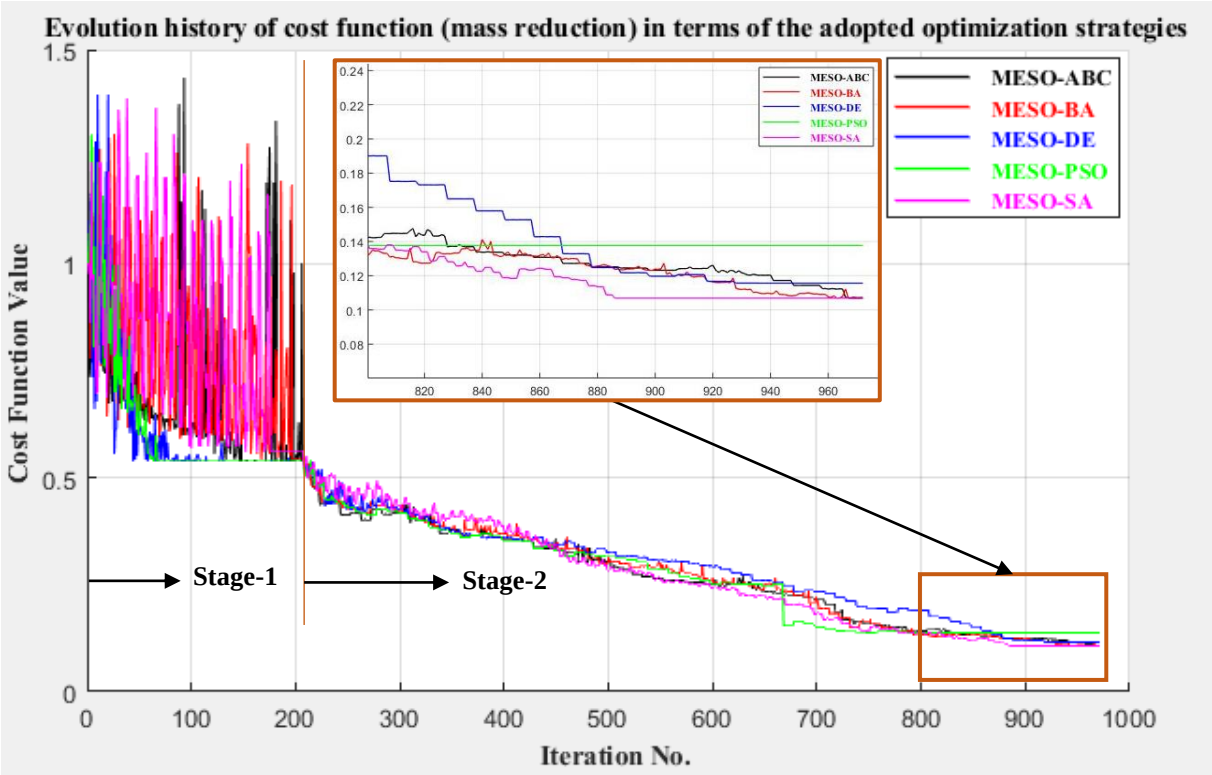

Figure 6.19 Convergence graph of the cost function towards the optimum for model B2.

6.6 Lamella Double Lattice Dome (Model C2)

The optimization results for Model C2 are listed in Table 6.20. During the validation test, implemented at stage 3 (see Figure 5.9), carried out on the optimal designs of model C2, where two extra load cases (pure snow and combined snow+wind) are imposed on the model, four designs failed to pass this test due to violating the buckling limitations under snow load, i.e. the only design which met all conditions is MESO-SA, which in this case was also the lowest mass dome with a cost of 0.106, corresponding to roof frame mass of 42.721 tonnes and tank mass of 369.778 tonnes (see Table 6.21). The convergence history is shown in Figure 6.20.

Despite the minimum structural weight achieved by the design MESO-SA, it exhibits the highest level of overall structural performance. This is attributed to the optimal choice of shape parameters (η and ϑ), as they are selected to increase the gap between the two layers of the dome. Thus, the greater the gap between the lattices, the stronger and stiffer the design.

The other designs of this model (except MESO-SA) have failed to satisfy the buckling constraints set at stage 3 when pure snow load has applied to the structure (although this was not a requirement of the optimization, but ideally should be). The buckling status at the failure point is illustrated in Figure 6.21, where they have exceeded the unity set as upper limits for their buckling indicators as demonstrated in section 5.1.2, Eqs (5.26) and (5.27). Accordingly, the radial beams of the dome hub located within the upper lattice are the most susceptible

members to the local instability problems due to the combined torsional and compressive loads inherent in these parts of the structure. In this sense, MESO-DE, MESO-PSO and MESO-ABC are the most influenced designs by buckling, where they are developed a maximum buckling index of 0.659, 0.501 and 0.464 respectively (see Figure 6.21).

Table 6.20 Optimal set of shape and topological design parameters found for model C2

Optimization method	N_n (-)	N_r (-)	N_s (-)	R (m)	ɳ (-)	ʊ (-)
Initial design	**45**	**11**	**20**	**30.000**	**0.950**	**1.100**
MESO-ABC	**30**	**6**	**30**	**55.460**	**0.905**	**1.061**
MESO-BA	**30**	**6**	**30**	**54.597**	**0.937**	**1.100**
MESO-DE	**30**	**6**	**30**	**47.662**	**0.930**	**1.096**
MESO-PSO	**30**	**6**	**30**	**60.000**	**0.950**	**1.100**
MESO-SA	**30**	**6**	**25**	**58.526**	**0.870**	**1.008**

Table 6.21 Optimal set of cost functions evaluated for model C2

Optimization method	Minimum cost $\left(\frac{W}{W_0}\right)$	Corresponding roof frame mass (tonnes)	Corresponding whole tank mass (tonnes)
Initial design	**1.000**	**403.336**	**740.451**
MESO-ABC*	**0.127**	**51.190**	**378.549**
MESO-BA*	**0.121**	**48.684**	**376.145**
MESO-DE*	**0.126**	**50.989**	**379.508**
MESO-PSO*	**0.132**	**53.328**	**380.230**
MESO-SA	**0.106**	**42.741**	**369.778**
*** The design has failed by buckling constraints considering pure snow load.**			

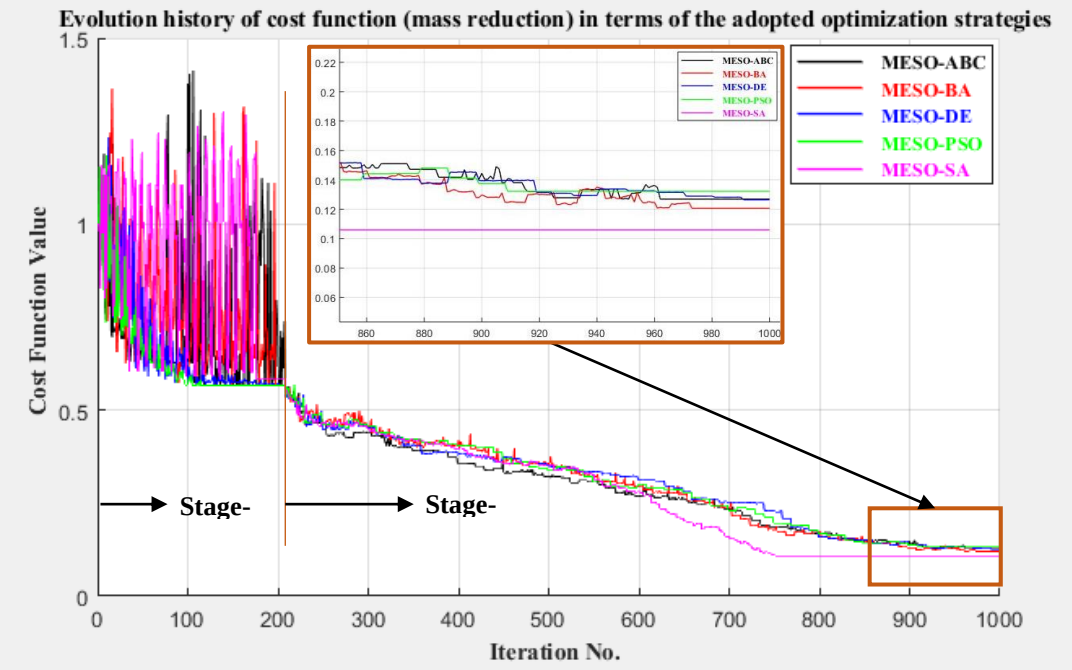

Figure 6.20 Convergence graph of the cost function towards the optimum for model C2.

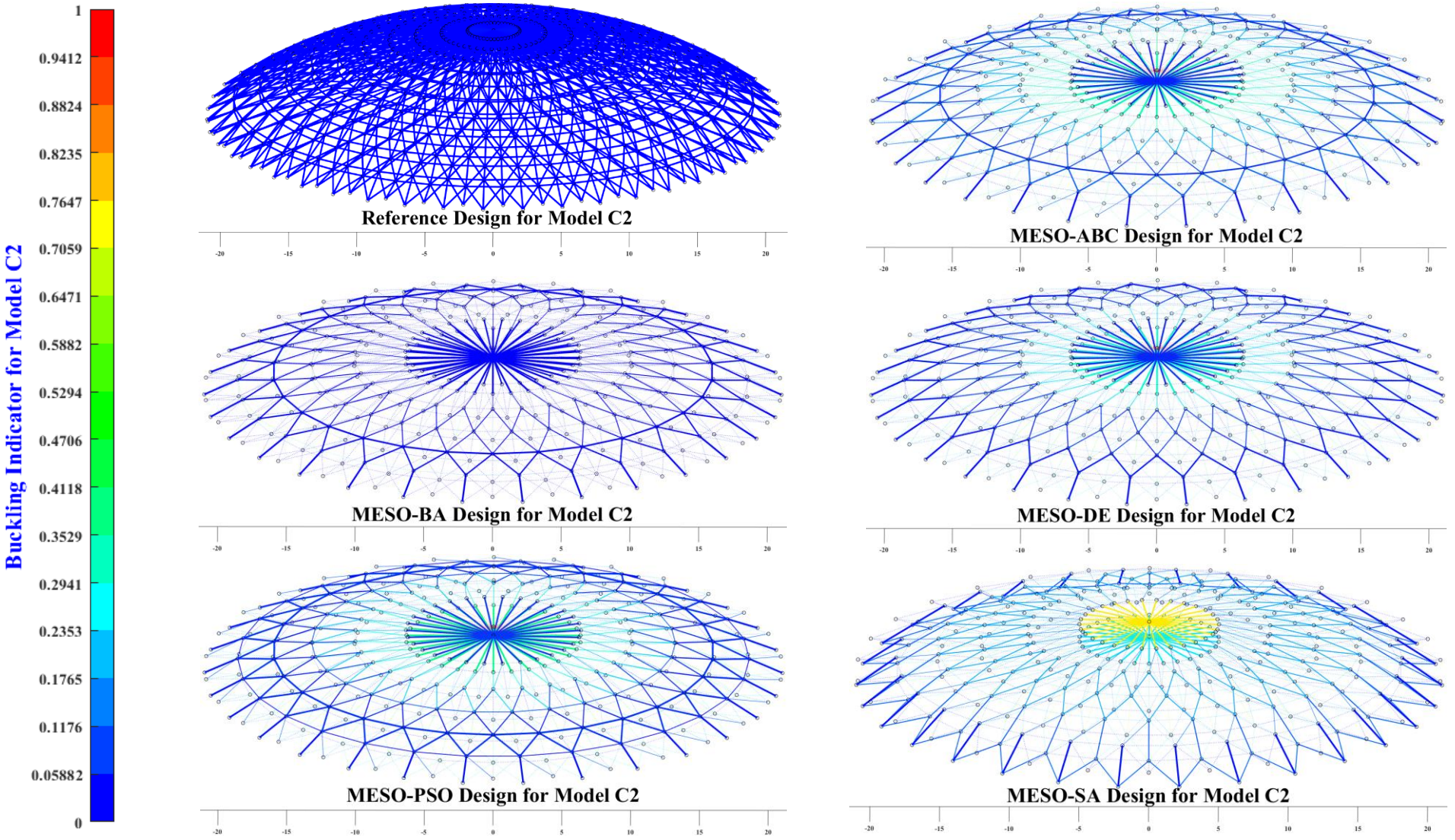

Figure 6.21 Distribution of buckling index showing the difference between the initial and optimal designs for model C2.

6.7 Hybrid Schwedler-Lamella Double Lattice Dome (Model D2)

Four integer topological variables (N_n, N_r, N_s and N_m) and three continuous shape variables (R, ϱ and ϑ) are solved in Model D2. The optimization results are given in Table 6.22. The designs tend towards N_n=32 and N_r=6, whereas there is no consistent value for N_s. The morphological parameter (N_m) was reduced as far as possible to create Lamella configuration for all designs. MESO-PSO fails in buckling for alternative snow loading (see Table 6.23); buckling indicator is plotted in Figure 6.25. This failure is caused by the large dome radius along with thin layer thickness as indicated by the shape variables of MESO-PSO listed in Table 6.22. The optimal topological variables chosen by MESO-DE at phase 1, along with the specific variant selected at phase 2, have enhanced the design to progress rapidly.

The data of optimal designs of model D2 are summarized in Table 6.23, where the minimum cost design is achieved by MESO-DE, which is 0.08, the roof frame weighs 42.598 tonnes, and the whole tank weighs 370.513 tonnes. The convergence plots of cost, shown in Figure 6.22, reveal that the best solution is obtained by MESO-DE, after about 207 evaluations at stage 1 and 835 evaluations at stage 2. MESO-SA in Stage 2 converges more slowly at first but performs well later.

Ultimately, the best design of model D2 (MESO-DE) is 30.3% lighter than best design for model A2, 20.15% lighter than the best design for model B2, 0.34% lighter than the optimal design for model C2, and 17.9% lighter than the best design reported for model E2.

The evolution of design-related functions, shown in Figure 6.23, indicates that the structural characteristics of model D2 are changing dramatically due to reduction in structural weight. This fact is supported by the figures listed in Table 6.24, for their respective design functions. The stress ratio (normalized with the reference design) for MESO-DE is 11.098 obtained after 1042 FE analyses. MESO-ABC and MESO-BA fluctuate with high amplitudes, whereas MESO-PSO develops the lowest values for normalized stress and SE ratios as indicated in Table 6.24, which reflect the high quality of strength and stiffness characteristics. The buckling function is particularly high for the design produced by MESO-PSO.

Table 6.22 Optimal set of shape and topological design parameters found for model D2.

Optimization method	**N_n (-)**	**N_r (-)**	**N_s (-)**	**N_m (-)**	**R (m)**	**ϱ (-)**	**ϑ (-)**
Initial design	**48**	**11**	**20**	**35**	**30.000**	**0.900**	**1.000**
MESO-ABC	**32**	**6**	**10**	**22**	**60.000**	**0.924**	**1.028**
MESO-BA	**32**	**6**	**17**	**21**	**60.000**	**0.901**	**0.921**
MESO-DE	**32**	**6**	**10**	**22**	**51.226**	**0.943**	**1.100**
MESO-PSO	**32**	**6**	**10**	**20**	**60.000**	**0.945**	**0.900**
MESO-SA	**46**	**6**	**29**	**26**	**52.794**	**0.940**	**1.032**

Table 6.23 Optimal set of cost functions evaluated for model D2.

Optimization method	Minimum cost $\left(\frac{W}{W_0}\right)$	Corresponding roof frame mass (tonnes)	Corresponding whole tank mass (tonnes)
Initial design	**1.000**	**532.374**	**869.489**
MESO-ABC	**0.084**	**44.535**	**371.437**
MESO-BA	**0.085**	**45.126**	**372.027**
MESO-DE	**0.080**	**42.598**	**370.513**
MESO-PSO*	**0.106**	**56.653**	**383.554**
MESO-SA	**0.109**	**58.132**	**385.823**
*** The design has failed by buckling constraints considering pure snow load.**			

Table 6.24 Design data for the initial and optimal statuses executed on model D2.

Optimization method	Stress function (Stress ratio)	SE function (SE ratio)	SED function (SED ratio)	Buckling function (ratio)
Initial design	**1.000**	**1.000**	**1.000**	**1.000**
MESO-ABC	**9.368**	**39.164**	**145.761**	**44.324**
MESO-BA	**9.877**	**47.117**	**134.914**	**42.664**
MESO-DE	**11.098**	**63.554**	**240.251**	**46.067**
MESO-PSO	**8.393**	**28.710**	**91.817**	**94.619**
MESO-SA	**9.612**	**29.940**	**117.259**	**28.479**

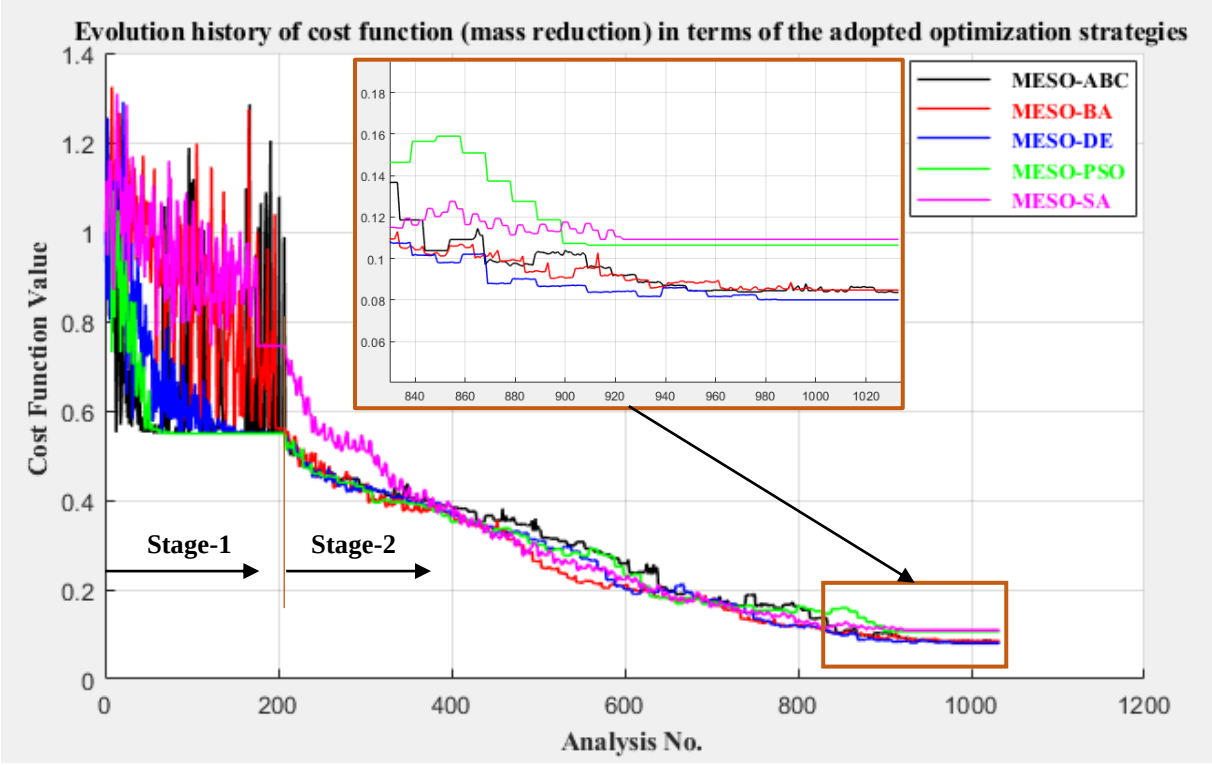

Figure 6.22 Convergence curve of the cost function towards the optimum for model D2.

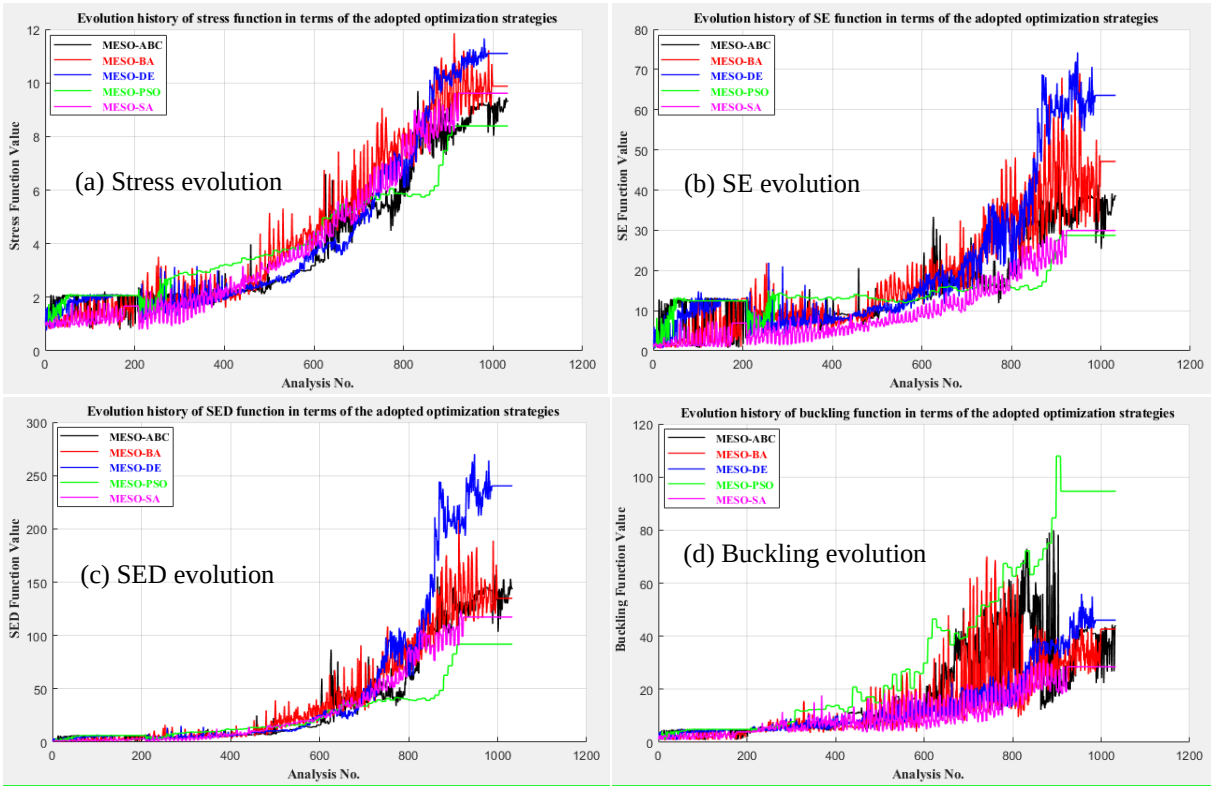

Figure 6.23 Evolution history of the relevant design functions for model D2.

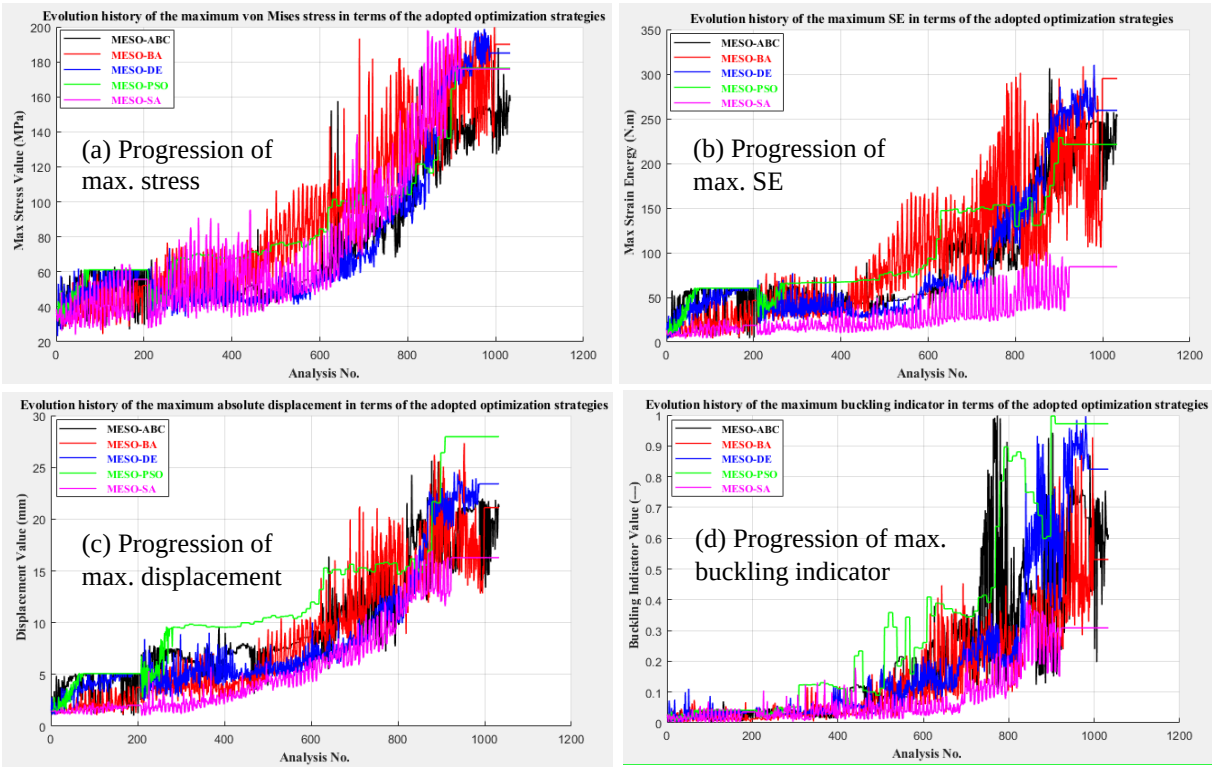

Figure 6.24 Design history of the maximum response induced over the entire structure for model D2.

Table 6.25 The data of the maximum response induced in model D2.

Optimization method	Maximum von-Mises stress [MPa]	Maximum absolute displacement [mm]	Maximum buckling indicator [---]
Initial design	**38.694**	**1.441**	**0.02785**
MESO-ABC	**163.883**	**21.861**	**0.586**
MESO-BA	**190.003**	**21.108**	**0.531**
MESO-DE	**185.073**	**23.402**	**0.824**
MESO-PSO	**176.343**	**27.960**	**0.972**
MESO-SA	**175.891**	**16.277**	**0.309**

Table 6.26 Statistical data about the penalized solutions of model D2 (Stage 1 + Stage 2).

Optimization Method	Solutions lost due to breaching stress	Solutions lost due to breaching displacement	Solutions lost due to breaching buckling
MESO-ABC	**0+5**	**0+0**	**0+9**
MESO-BA	**0+66**	**0+0**	**0+0**
MESO-DE	**0+142**	**0+0**	**0+28**
MESO-PSO	**0+0**	**0+0**	**0+540**
MESO-SA	**0+0**	**0+0**	**0+0**

The stress and buckling limits are the dominant constraints in this model as illustrated in Table 6.26. The statistical data in this table indicate that MESO-DE has failed to achieve the imposed stress conditions about 142 times, and 540 penalties are summarized for MESO-PSO due to exceeding the buckling statement at stage 2. The data for the maximum response presented in Figure 6.24. are listed in Table 6.25.

Ultimately, MESO-SA exhibits a moderate compromise between strength, stiffness and buckling characteristics, whereas MESO-ABC and MESO-BA have achieved a considerable saving in weight, whilst preserving an acceptable extent of structural safety against the design constraints. MESO-PSO is the only design that failed by buckling at stage 3. The patterns of these designs could be visually checked to see the colours appearing in their topologies as illustrated in Figure 6.25. The blue refers to the safe region, whereas the red refers to the unsafe region of the design. Accordingly, the in-between braces in MESO-PSO show red colour with colour scale exceeding unity which signifies that they have exceeded the set buckling limit.

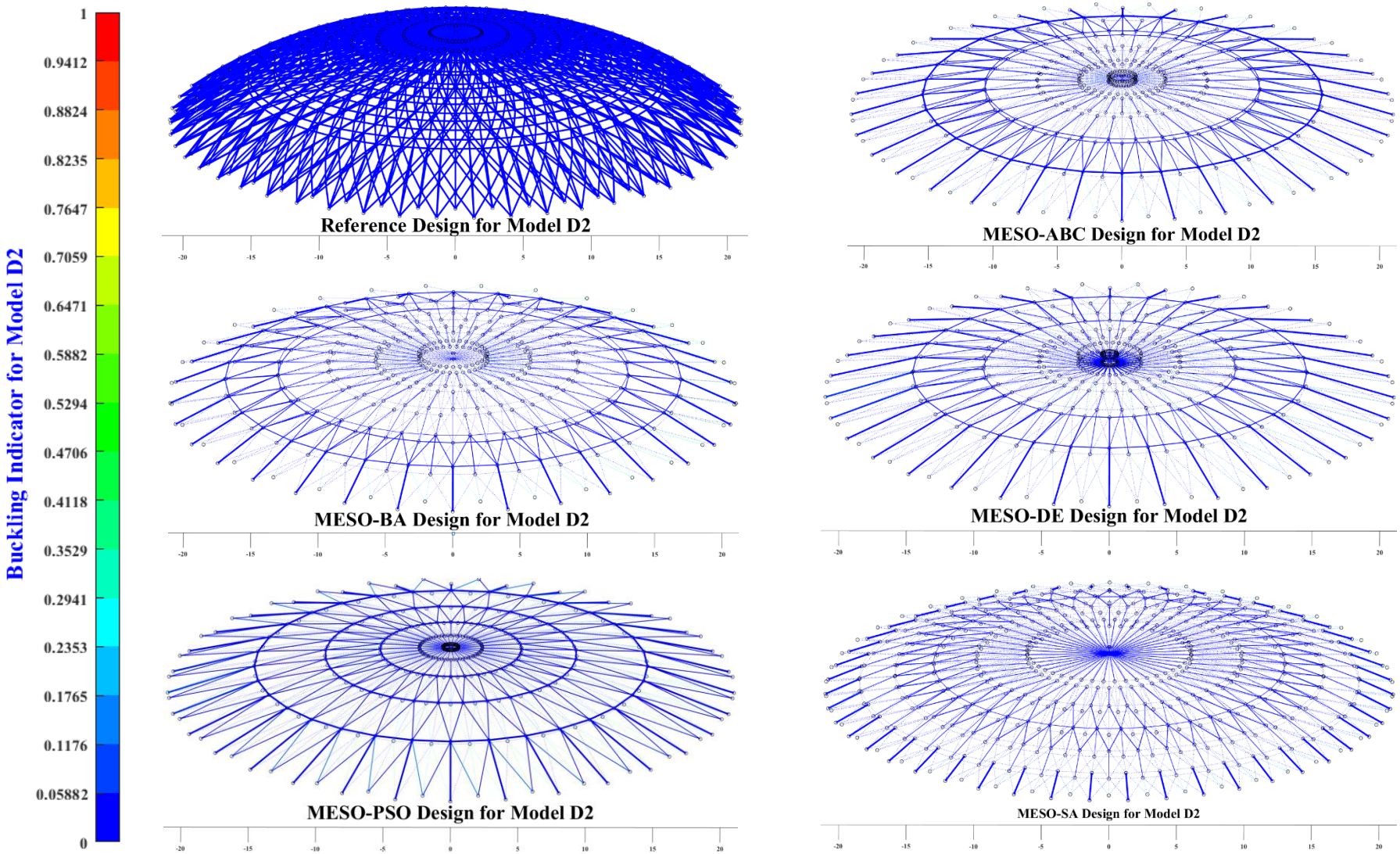

Figure 6.25 Distribution of buckling index showing the difference between the initial and optimal designs for model D2.

6.8 Geodesic Double Lattice Dome (Model E2)

Table 6.27 shows the optimum geometrical parameters of model E2, where N_n=6 and N_r=6 as optimal values needed to reach the optimal weight, whereas N_s=30 except MESO-SA, which shows a slightly different value. The shape variables are optimized at different levels depending on the design. For instance, MESO-PSO is designed as a shallow dome with thick layer thickness tapered towards the periphery of the dome, while MESO-SA is created with moderate deep, and approximately uniform high thickness layer.

MESO-DE achieved a weight fraction of 0.142, the roof frame weighs 51.896 tonnes. The tank mass is then 380.426 tonnes. The number of analyses required to accomplish the task is 209 at stage 1 and 635 analyses at stage 2. The evolution of cost function is plotted in Figure 6.26, where MESO-SA shows to be lagging in the first 658 solutions, but later progresses with an acceptable rate. MESO-BA evolves with a high convergence speed during phase 2 up to it=644, but then progresses no further.

MESO-BA has recorded the greatest number of violations, as it is penalized 764 times by stress (3 times at stage 1 and 761 times at stage 2), 1086 by displacement and 278 by buckling. MESO-ABC had 680 solutions penalized by stress, 476 by displacement and 56 by buckling. MESO-SA had only 636 violations against stress.

Table 6.27 Optimal set of shape and topological design parameters found for model E2.

Optimization method	**N_n (-)**	**N_r (-)**	**N_s (-)**	**R (m)**	**η (-)**	**ʊ (-)**
Initial design	**9**	**9**	**20**	**30.000**	**0.950**	**1.100**
MESO-ABC	**6**	**6**	**30**	**47.662**	**0.883**	**0.900**
MESO-BA	**6**	**6**	**30**	**59.916**	**0.95**	**1.044**
MESO-DE	**6**	**6**	**30**	**47.609**	**0.900**	**0.912**
MESO-PSO	**6**	**6**	**30**	**60.000**	**0.950**	**1.100**
MESO-SA	**8**	**6**	**20**	**47.362**	**0.877**	**0.976**

Table 6.28 Optimal set of cost functions evaluated for model E2.

Optimization Method	**Minimum cost $\left(\frac{W}{W_0}\right)$**	**Corresponding roof frame mass (tonnes)**	**Corresponding whole tank mass (tonnes)**
Initial design	**1.000**	**364.922**	**702.037**
MESO-ABC	**0.150**	**54.540**	**383.060**
MESO-BA	**0.213**	**77.705**	**404.614**
MESO-DE	**0.142**	**51.896**	**380.426**
MESO-PSO	**0.168**	**61.428**	**388.330**
MESO-SA	**0.150**	**54.884**	**383.462**

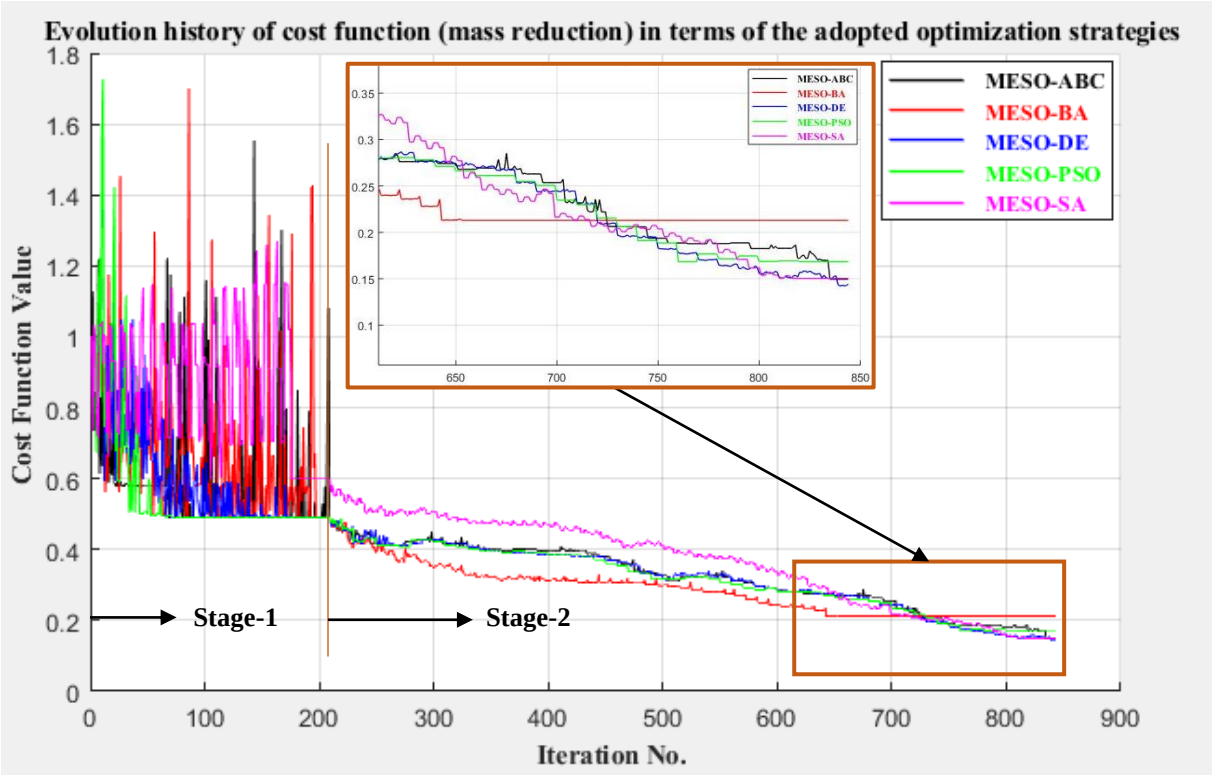

Figure 6.26 Convergence graph of the cost function towards the optimum for model E2

The design data of the model indicate that the critical stress (199.674 MPa) is found in MESO-ABC, also it is developed the critical displacement (33.124 mm), whereas the buckling indicator is critically existing in MESO-DE with value 0.692. The design data also show that MESO-PSO presents the best performance as per the lowest stress and stiffness ratios recorded for the design. While, MESO-SA preserves the best structural behaviour to resist the buckling problems compared to other designs.

Figure 6.27 shows the stress distributions for the model E2. They show that the upper lattice is the key part of the dome frame. Compared to the initial state, the critical spot has transferred from the outermost circumferential ring to diverse spots (e.g. radial girders and diagonal braces) in the optimal designs. The results also suggest the possibility of eliminating the lower layer of the dome, as most designs have reduced the cross sectional dimensions of the lower lattice members to the lowest discrete values available in their respective optimization ranges (as identified by the dotted lines of the relevant topologies) along with minimizing the gap (between the two layers) to the lowest extent.

Unlike other double lattice models, all designs of this model are passed the test at stage-3, where the model is characterized by its exceptional capability to resist the buckling load, especially, MESO-SA and MESO-PSO. Accordingly, the critical buckling region for the latter designs is located in the outermost circumferential ring of the lower layer.

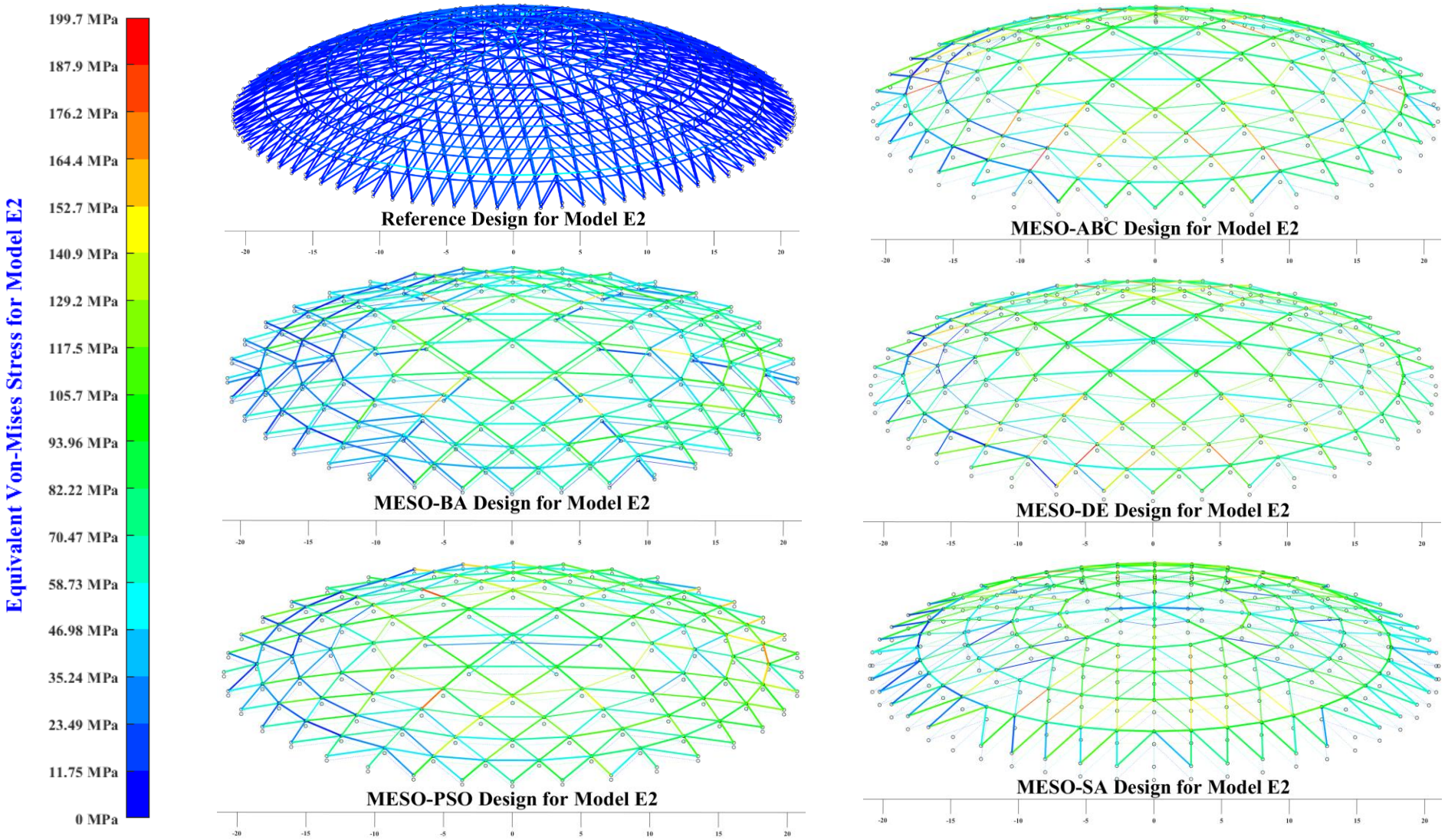

Figure 6.27 Distribution of equivalent (von-Mises) stress showing the difference between the initial and optimal designs for model E2.

6.9 Consistency of Optimization Techniques

Five independent optimization runs have been implemented for each optimization technique to verify consistency in relation to the number of attempts performed. The test results show an acceptable convergence between the adopted methods. The three most successful models are discussed here.

Considering model D1, the maximum number of analyses, i.e. maximum number of iterations multiplied by the population size, was 620 and 602 for MESO-ABC (see Figure 6.28a) and MESO-DE (see Figure 6.29a) respectively. The highest structural masses recorded for this process were 42.177 tonnes and 43.32 tonnes for MESO-ABC and MESO-DE respectively, whereas the lowest structural masses were 34.455 tonnes and 41.009 tonnes for MESO-ABC and MESO-DE respectively. The evolution of standard deviation ($\overline{X}$) of cost (based on five independent runs), presented in Figure 6.30a, indicates that the maximum $\overline{X}$ for MESO-ABC is much higher than that for MESO-DE due to the significant difference between the two algorithms. The average values of $\overline{X}$ found at stage 1 are 0.118 and 0.053 for MESO-ABC and MESO-DE respectively, whereas a considerable decline in average $\overline{X}$ observed at stage 2 to be 0.027 and 0.013 for MESO-ABC and MESO-DE respectively.

Model E1 exhibits a different behaviour, where the number of analyses does not exceed 397 and 442 for MESO-ABC and MESO-DE respectively as plotted in Figure 6.28b and Figure 6.29b. Consequently, the worst designs have masses 66.035 tonnes and 46.06 tonnes for MESO-ABC and MESO-DE respectively, whereas the corresponding optimal designs have masses 50.227 tonnes and 37.012 tonnes. A noticeable gap is found in $\overline{X}$ between MESO-ABC and MESO-DE. For instance, the average values of $\overline{X}$ are 0.178 and 0.123 at stage 1, 0.013 and 0.008 at stage 2 for MESO-ABC and MESO-DE respectively as illustrated in Figure 6.30b.

The number of evaluations needed to reach the optimum for double layer configurations is higher than that for single lattice models.

Figure 6.28c and Figure 6.29c show that the numbers of solutions required to reach the optimum for MESO-ABC and MESO-DE were 1034 and 1002 respectively for Model D2. The highest masses recorded over five optimization runs were 47.867 tonnes and 46.609 tonnes, the lowest mass designs were 44.535 tonnes and 42.6 tonnes for MESO-ABC and MESO-DE in sequence. Figure 6.30c presents the progression history of $\overline{X}$ for different stages of optimization. The maximum $\overline{X}$ reached at stage 1 are 0.459 and 0.312, at stage 2 are 0.031 and 0.052 for the designs MESO-ABC and MESO-DE respectively.

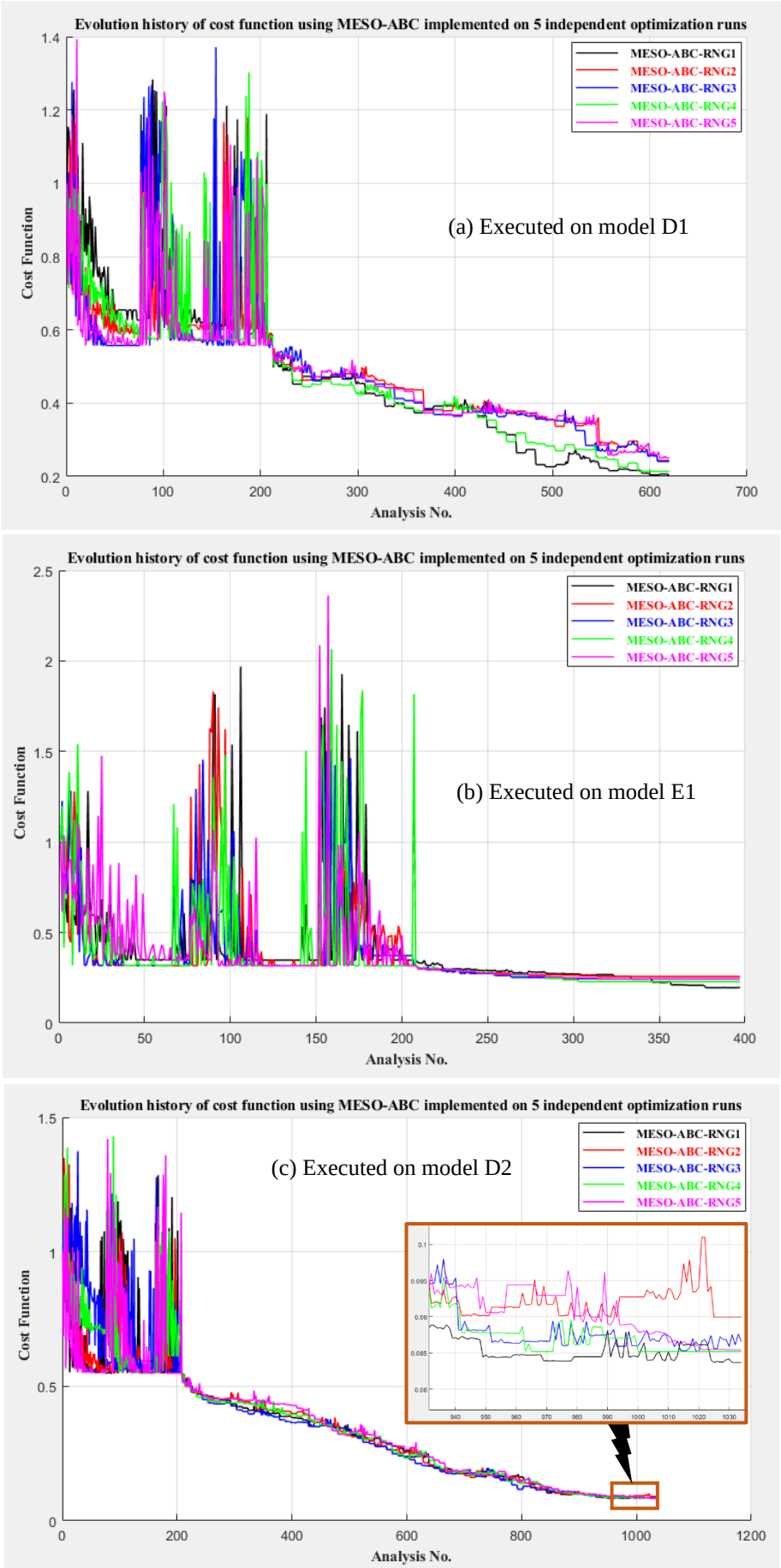

Figure 6.28 Consistency test for MESO-ABC (using 5 independent optimization runs).

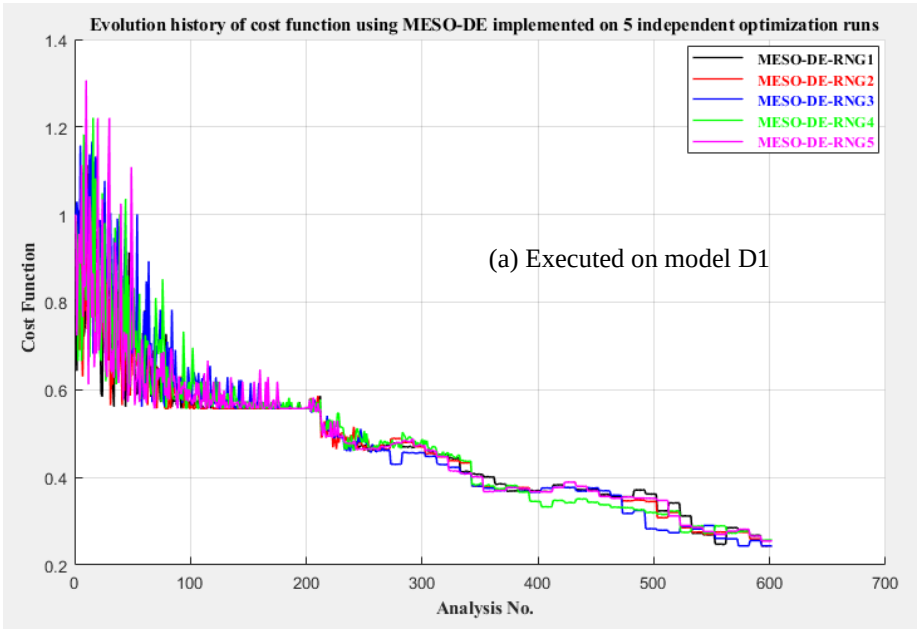

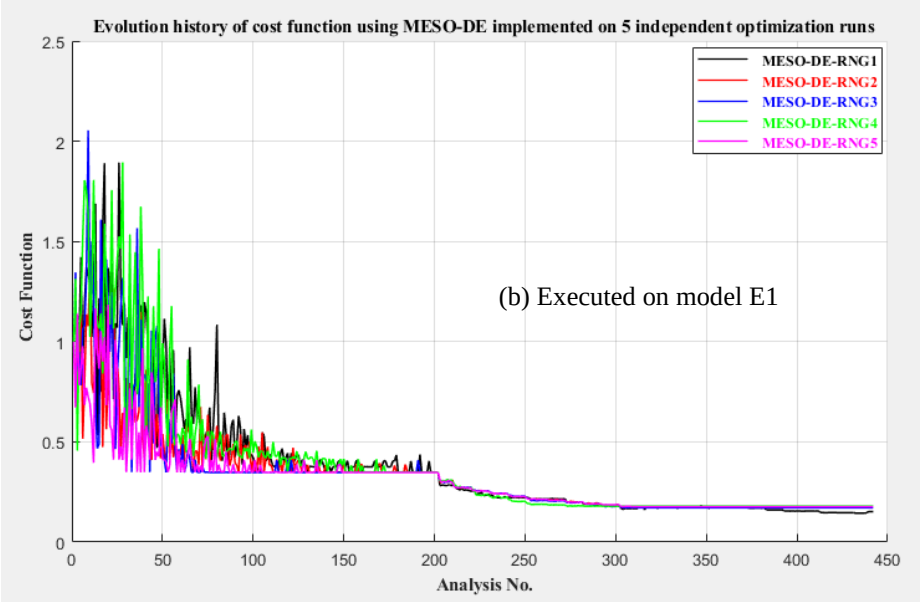

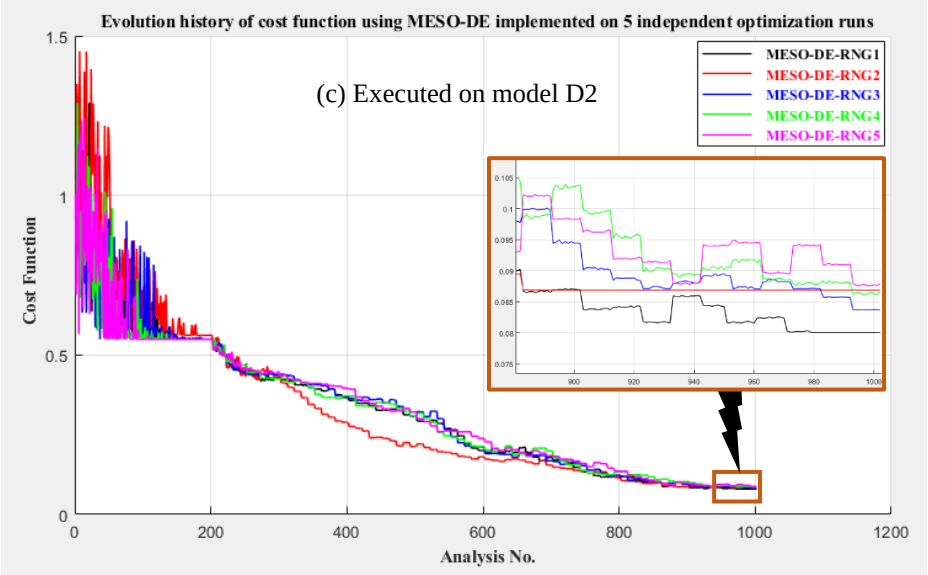

Figure 6.29 Consistency test for MESO-DE (using 5 independent optimization runs).

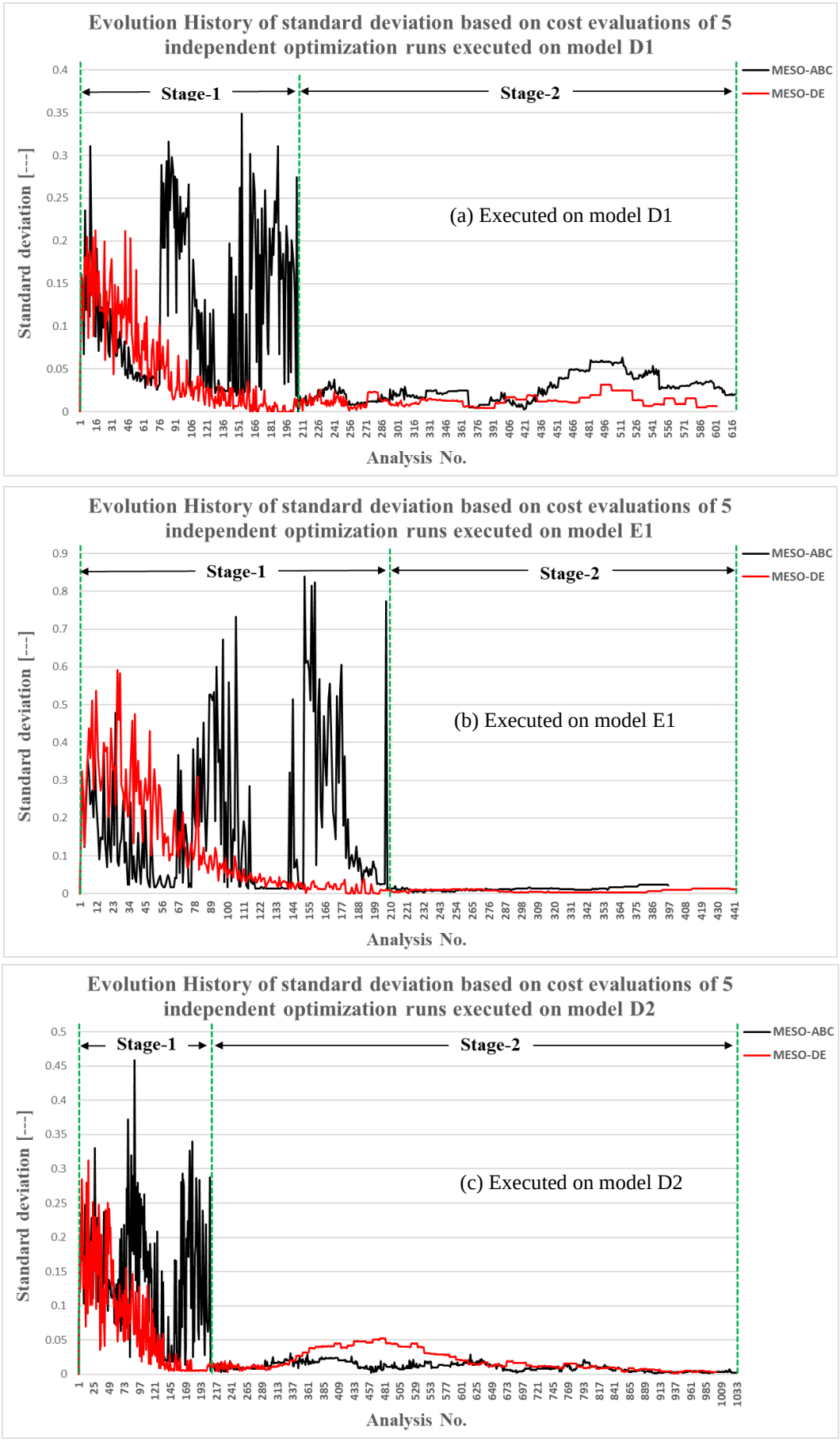

Figure 6.30 History of standard deviation of cost based on 5 independent optimization runs.

6.10 Selection of the Optimum Design

In this section, the best design for the models studied in this chapter will be selected. Two candidates from each family of models will be chosen to discover the latent features in each design and its respective strategy. Thus, according to the first type of models (models A1 to E1) mentioned in Table 6.29, the first candidate is MESO-ABC found in model D1, where the roof frame weighs 34.455 tonnes corresponding to tank weight 353.815 tonnes, whereas the second design is MESO-DE found in model E1 with roof mass of 37.012 tonnes and tank mass of 356.370 tonnes. For the second type of models (models A2 to E2) listed in Table 6.29, it is recommended to perform this selection on a tank mass basis, owing to the discrepancy caused by the dome radius and the extra shell mass. Hence, the first candidate is MESO-SA found in model C2 producing tank mass 369.778 tonnes (with roof mass 42.741 tonnes) and the second design is MESO-DE found in model D2 with tank mass of 370.513 tonnes (with roof mass 42.598 tonnes).

Ultimately, MESO-ABC and MESO-DE are the most efficient and robust optimization techniques for use with single lattice models. MESO-SA and MESO-DE are the most efficient and robust optimization tools for use with double lattice models. Though the standard SA is not that robust metaheuristic optimization tool, unlike DE, a good result is achieved, as its deficiency is compensated for by MESO (by resizing the members), although the optimization process continues for longer through minimizing the penalized solutions in stage 2.

Table 6.29 The set of optimal designs obtained for the simplified models.

Model No.	Associated optimization strategy	Optimal dome frame mass (tonnes)	Optimal whole tank mass (tonnes)
Model A1	**MESO-PSO**	**85.524**	**404.140**
Model B1	**MESO-DE**	**60.110**	**378.992**
Model C1	**MESO-ABC**	**54.083**	**372.698**
Model D1	**MESO-ABC**	**34.455**	**353.815**
Model E1	**MESO-DE**	**37.012**	**356.370**
Model A2	**MESO-DE**	**61.117**	**391.495**
Model B2*	**MESO-BA**	**53.348**	**380.495**
Model C2	**MESO-SA**	**42.741**	**369.778**
Model D2	**MESO-DE**	**42.598**	**370.513**
Model E2	**MESO-DE**	**51.896**	**380.426**
*** The design has failed by buckling constraints considering pure snow load.**			

6.11 Summary

- The topological spacing factor ($\mathbf{N_s}$) has two contradict behaviours, e.g. reducing $\mathbf{N_s}$ in ribbed, Schwedler and Lamella models leads to an observable reduction in the structural mass, whereas reducing $\mathbf{N_s}$ in geodesic model leads to an observable increase in the structural mass.
- For safer designs considering geodesic dome configuration, the spacing factor N_s needs to be adjusted between 18 and 21 during the optimization process in order to obtain the minimum structural mass for the model.
- The morphological shape factor ($\mathbf{N_m}$), proposed for the hybrid Schwedler-Lamella configuration (models D1 and D2), was reduced to the lowest levels to obtain Lamella configuration, which achieves the minimum structural mass of the model.
- The maximum stress and strain energy for the models A1 and A2 have direct proportionality to the topological trimming factor ($\mathbf{N_t}$).
- Compared to single lattice models, double lattice models are more vulnerable to fail by buckling due to pure snow loads when they are designed according to pure wind loads.
- Regardless the optimization algorithm used, models D1 and E1 exhibited the best structural performance compared to other models, which resulted in achieving these models the minimum structural masses of 34.455 tonnes and 37.012 tonnes respectively.
- The proposed optimizers MESO-ABC and MESO-DE are the most efficient methods used to optimize the dome roof frame model.

Chapter 7. Optimization Results of the Integrated Models

This chapter presents the optimization results for the integrated models (models A3 to E3), defined in section 4.6. The proposed optimization methods used in chapter 6 will be adopted in this chapter. The best design for the integrated models will be selected in this chapter to conclude the most robust and reliable optimization strategy. Hence, four models are prepared for this purpose and structurally analysed in ANSYS. The structural details and the degree of refinement for meshing of these models make them spend longer than usual in comparison to the simplified models viewed in the earlier chapter. However, the overall maximum response of the tank not simply the dome frame (as in the simplified model) is included in the results. This investigation is limited to stress and displacement constraints. The integrated model is subjected to pure wind loading when the tank is empty, where this is the design load imposed during stage 1 and stage 2 of the optimization. While, no optimization process noticed at stage 3, instead it only includes 6 extra load cases used to check the optimal designs resulting from stages 1 and 2. These load cases are:

1. Snow + Empty Tank.
2. Wind + Snow + Empty Tank.
3. Wind + Full Tank.
4. Snow + Full Tank.
5. Wind + Snow + Full Tank.
6. Full Tank.

Remarkably, stage 3 is devoted to test the validity of the optimal designs of the considered model against the prescribed design constraints under other load cases of the problem as explained in Figure 7.5 and Figure 7.6. Details of the geometry construction and automated updating are given in Appendix C, and integration with MATLAB is presented in Appendix D.

7.1 Trimmed Ribbed Single Lattice Dome (Model A3)

The optimization results for model A3, described in section 4.6.1, will be investigated in this section using the proposed optimization strategies detailed in section 5.6. According to the proposed optimization methodology, a cascade optimization approach is adopted to obtain the optimum design with three stages, two of them are progressive towards the optimum, whereas the third is designed to check the validity of the optimum design in presence of other load cases of the problem. Phase-1 consists of 12 iterations with each of them involved with population size of 10 individuals (i.e. particles, bees etc.). Thus, stage-1 counts to 120 generations to find the optimal topological integer set of variables. While, 24 iterations with population size of 10

are allocated to phase-2 to investigate the optimal shape, topological, and sizing parameters specified to be variables at this stage as tabulated in Table 4.24 and illustrated in Figure 4.19. It is noteworthy to state that the variables in this phase are segregated into two groups: discrete represented by the set of cross section designations of the model members and continuous characterized by the shape and topology of the model allowed to change in this phase (i.e. the radial positions of the circumferential rings, dome radius, etc.).

Table 7.1 shows the optimum values for shape and topology of model A3. Integer and continuous variables are included in this table, where the integer parameters ($\mathbf{N_{Gussets}}$, $\mathbf{N_{Girders}}$ and $\mathbf{N_{Rings}}$) are solved at stage 1, whereas the continuous and discrete variables are treated at stage 2. The optimal set of discrete variables are tabulated in Appendix Table F.11. Two designs are succeeded to achieve the optimum structural mass as fixed in Table 7.2. Those are MESO-ABC and MESO-PSO with structural weights of 121.772 and 122.393 tonnes respectively, they achieved a further reduction in structural weight by.9%, 6.6% and 2.5% in comparison to MESO-BA, MESO-SA and MESO-DE respectively. The scatter of optimization is markedly diminished by adopting the non-dimensional form of topological variables, as the geometrical constraints are eliminated by exploiting geometrical correlation between the different topological variables. It is important to state that the optimal topology tends to increase the meridional lengths of the segments A and B, shown in Figure 4.19, to minimize the arc length of the secondary girder, which saves a significant amount of constructional material. Furthermore, the radius of the crown has reduced to the lowest values and the circumferential rings are pushed towards the tank hub in most designs.

The optimization tool has been constructed to relate the number of rings ($\mathbf{N_{Rings}}$), optimized at stage 1, to the topological fractions treated at stage 2. For instance, Table 7.1 indicates that when $\mathbf{N_{Rings}}$=5, the design will be directed to discard 4 topological positions, whereas for $\mathbf{N_{Rings}}$=6, only 3 topological fractions will be eliminated at phase 2. Accordingly, the only design that preserved the original topological arrangement is MESO–PSO with $\mathbf{N_{Rings}}$=10.

Figure 7.1 illustrates the progression lines of the cost for model A3. Though MESO-DE outperformed other designs at the end of phase 1, MESO-ABC and MESO-PSO are dominant at the end of phase 2. This could be attributed to two reasons. First, the two variants (MESO-ABC and MESO-PSO) have enabled MESO to progress into a more feasible design space due to their topological arrangements specified at stage 1. This feature has granted the chance to MESO to step further in the design space by realizing an extra reduction in structural weight without exceeding the design constraints. Second, the capability of the relevant metaheuristic techniques in certain circumstances to depart from the local minima, where ABC has succeeded to jump to the dome radius (R=48.7 m) instead of 60 m.

On the other hand, Figure 7.2 shows more clearly the sequence of MESO at phase 2. The graph indicates that the ratio of average SED normalized with respect to the reference design, drawn in Figure 7.2, is inversely proportional to the structural weight of the model. The maximum value of normalized SED is reached by MESO-ABC, which is equal to 2.684, due to reaching the minimum structural weight. While the minimum level of SED ratio (2.055) is indicated by MESO-BA.

On the other hand, Figure 7.3 shows the evolution of the maximum von-Mises stress induced over the whole tank for different designs. The statistical data recorded for the penalties of design constraints indicate that MESO-DE is the worst design with the fact that 33.7% of its cost evaluations have been rejected due to stress. On the other hand, MESO-BA is least affected by the design constraints with the total number of penalized solutions reached being 33.

Table 7.1 Optimal set for shape and topological variables of model A3.

Design variable	Reference design	MESO –ABC	MESO –BA	MESO –DE	MESO –PSO	MESO –SA
$N_{Gussets}$ [-]	40	36	36	30	30	37
$N_{Girders}$ [-]	40	34	35	32	32	33
N_{Rings} [-]	10	6	5	6	10	6
R [m]	45	48.703	56.026	60	56.680	54.821
CR_{out} [m]	2.5	1	1.227	1	1.2333	1.293
CR_{in} [m]	1.25	0.4576	0.538	0.600	0.542	0.509
$Frac_A$ [-]	0.25	0.291	0.265	0.277	0.261	0.290
$Frac_B$ [-]	0.33	0.385	0.391	0.362	0.385	0.382
$Frac_C$ [-]	0.50	0.553	0.528	0.548	0.572	0.508
$Frac_{A1}$ [-]	0.4	0.567	0.487	0.432	0.465	0.512
$Frac_{A2}$ [-]	0.8	---	---	---	0.750	---
$Frac_{B1}$ [-]	0.2	0.237	0.204	0.223	0.257	0.288
$Frac_{B2}$ [-]	0.6	---	---	---	0.546	---
$Frac_{C1}$ [-]	0.4	0.527	0.476	0.400	0.402	0.533
$Frac_{C2}$ [-]	0.7	---	---	---	0.753	---
$Frac_{D1}$ [-]	0.4	0.403	---	0.432	0.455	0.512
$Frac_{D2}$ [-]	0.8	0.730	0.704	0.712	0.724	0.798

Table 7.2 Optimization results for model A3.

Optimization Strategy	Minimum Cost $\left(\frac{W}{W_0}\right)$	Corresponding Roof Frame Structural Mass (tonnes)	Corresponding Whole Tank Structural Mass (tonnes)
Initial design	1.000	200.398	520.680
MESO-ABC	0.608	121.772	441.296
MESO-BA	0.662	132.712	451.202
MESO-DE	0.622	124.558	442.654
MESO-PSO	0.611	122.393	440.813
MESO-SA	0.649	130.065	448.695

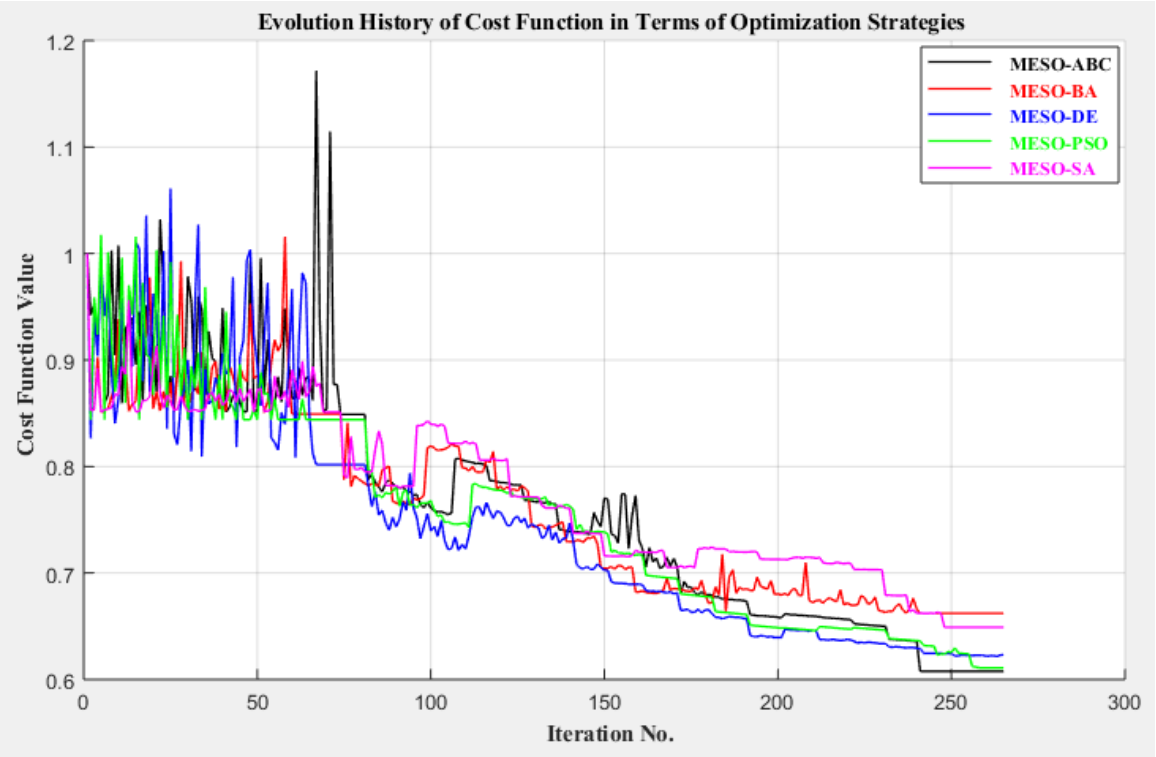

Figure 7.1 Progression history of the cost function towards the optimum for model A3.

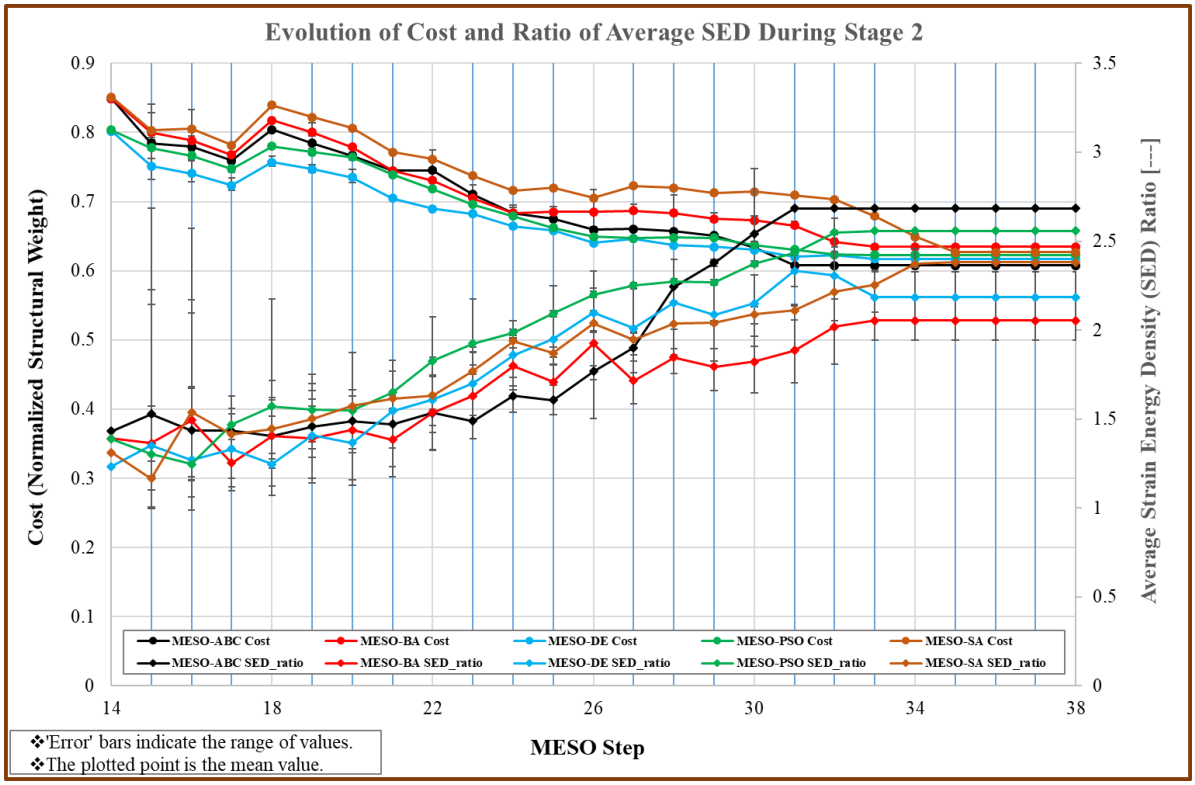

Figure 7.2 Evolution history of the normalized strain energy density SED for model A3.

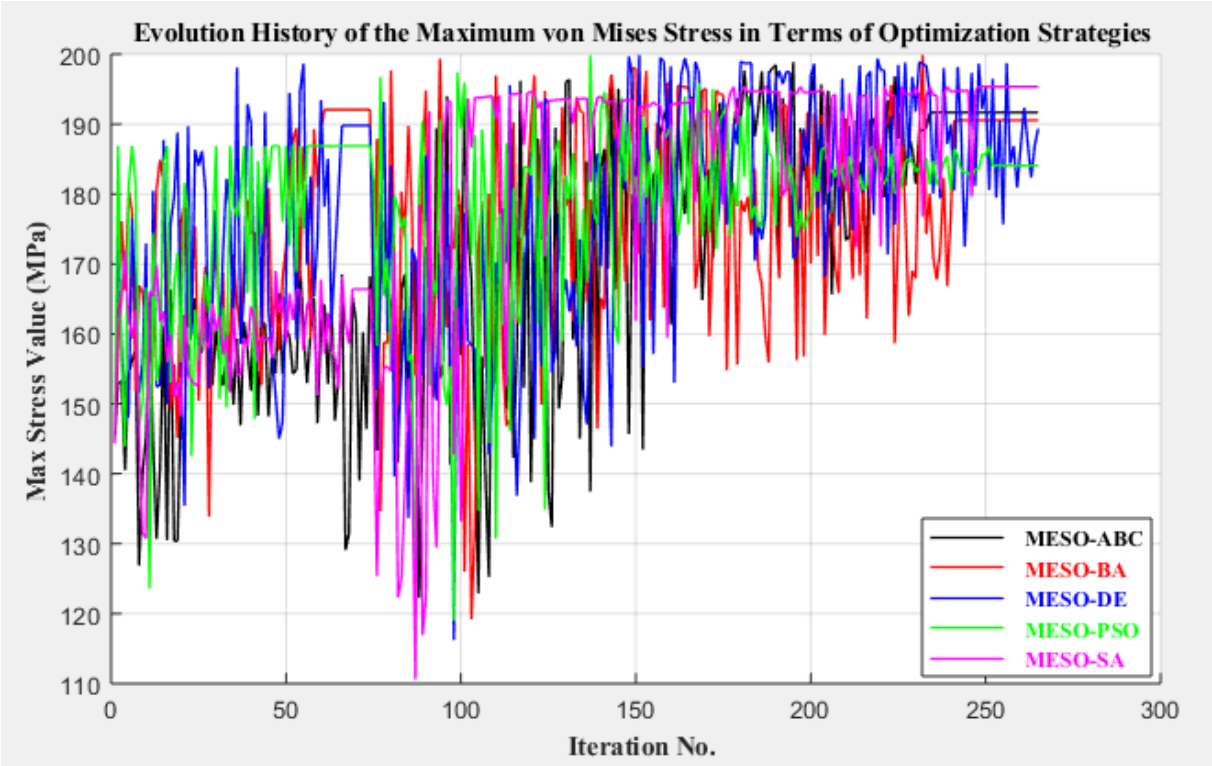

Figure 7.3 Design history of the maximum stress induced over the whole tank for model A3.

The development in the state of SED (illustrated in Figure 7.4) shows the increase in SED for the relevant designs appearing in the graphs of Figure 7.2. It is indicated that the outermost ring is the critical part of the structure. The value 2.88 kJ/m^3 for the SED of MESO-ABC is set as a safe reference level for the maximum SED for the considered designs. Hence, the state of SED for the designs of Figure 7.4 is shown to illustrate the comparative variations between the different designs. Accordingly, MESO-BA shows the minimum level (2.01 kJ/m^3) in comparison to other optimal designs.

There are two critical load cases observed in this investigation (pure wind) and (wind+Hydro) as detailed in Figure 7.5, where the optimal designs are about to fail in the latter case. While, there is a noticeable mitigation in the state of stress for the case (wind+snow) as highlighted by Hsaine and Franklin (2016). Also, the displacement investigation is implemented to show the critical cases as shown in Figure 7.6. The two investigations indicate that the snow could be considered as serious as wind for the displacement investigation, whereas the snow does not make any criticality in the stress state of the model.

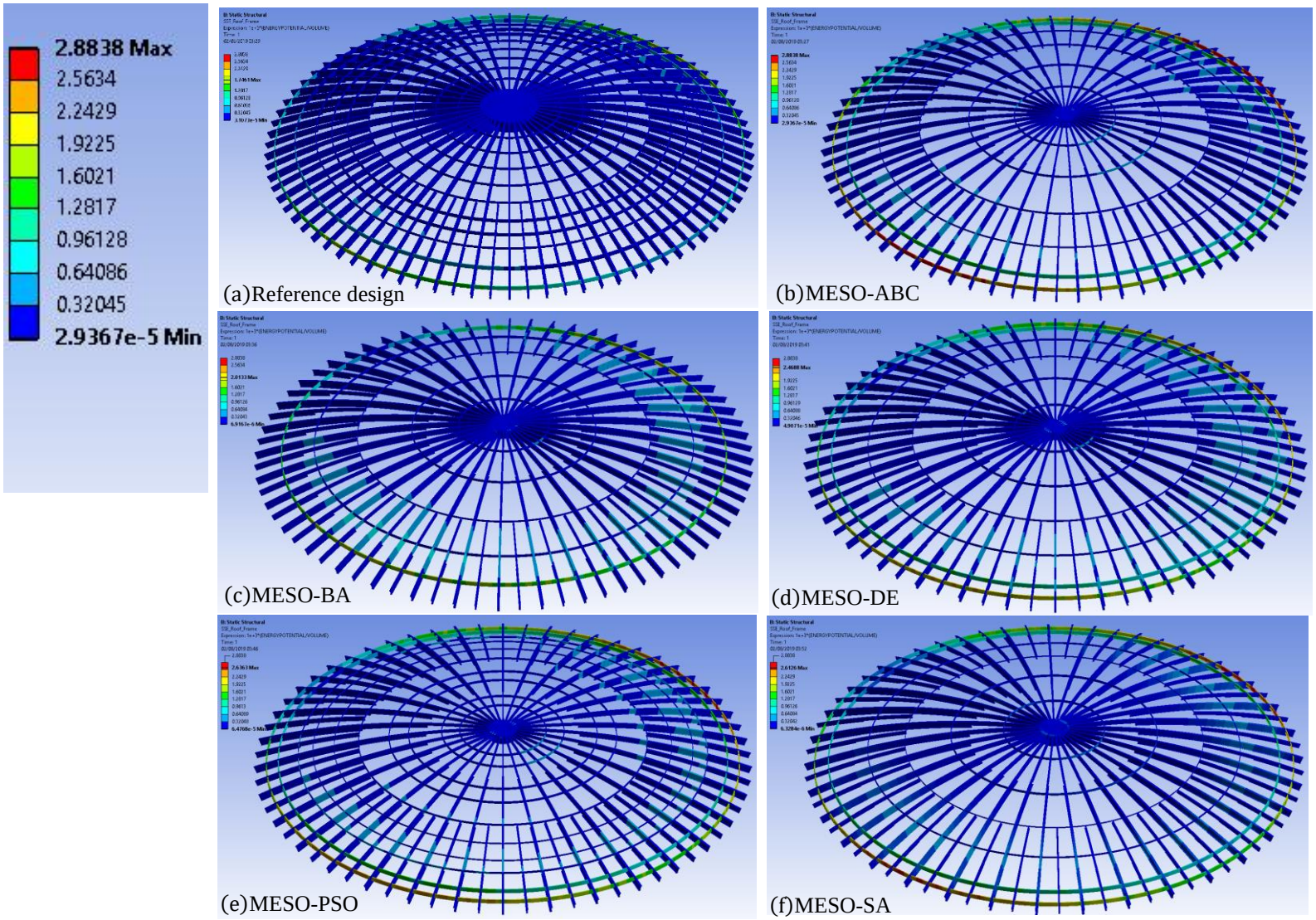

Figure 7.4 Distribution of SED showing the difference between the initial and optimal designs for model A3.

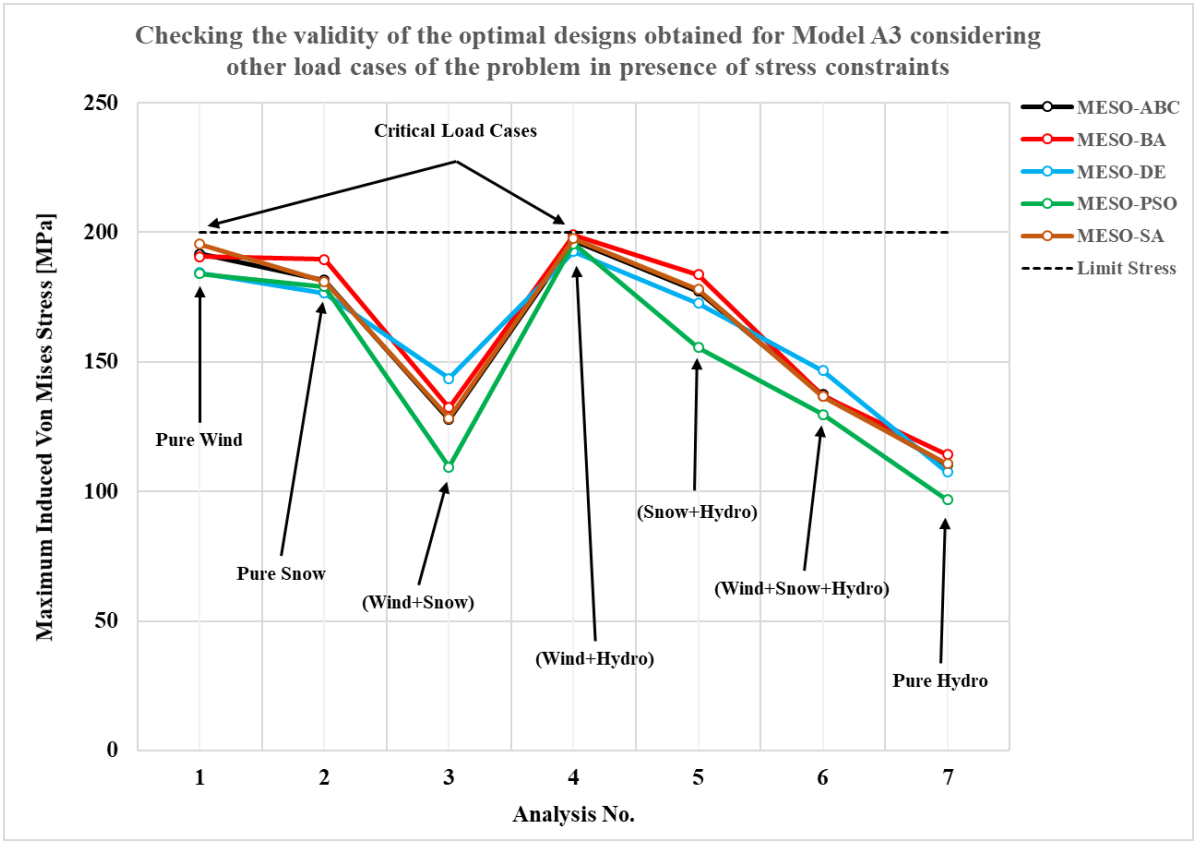

Figure 7.5 Validity test for model A3 executed in stage 3 against stress constraints.

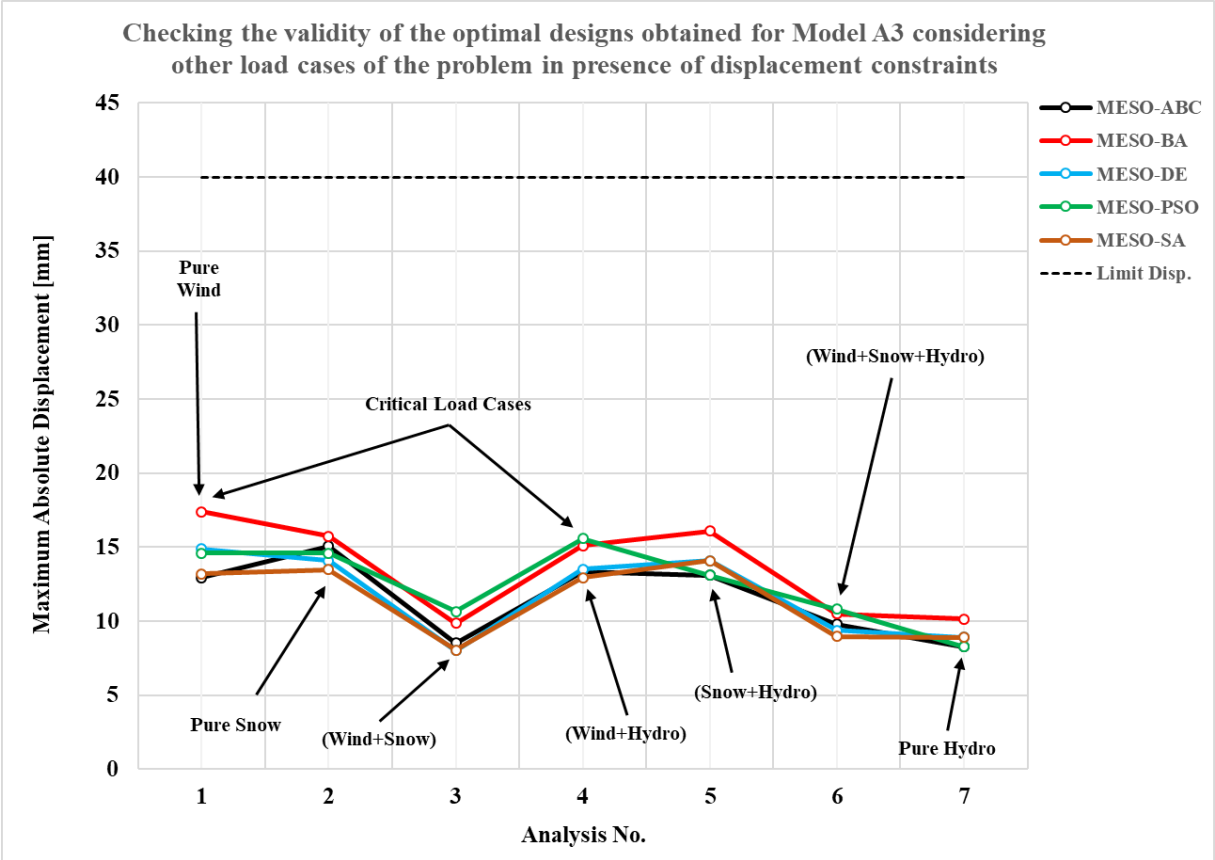

Figure 7.6 Validity test for model A3 executed in stage 3 against displacement constraints.

7.2 Schwedler Single Lattice Dome (Model B3)

Figure 4.22 through Figure 4.24 illustrate the ground structure for model B3; it is constituting of 40 Schwedler modules reinforced by 6 circumferential rings. Hence, the evolution process is commencing at 196.231 tonnes and the convergence rate is depending on the nature of the adopted optimization algorithm. Table 4.26 aided by Figure 4.22 is prepared to show the scopes of variability for the design variables. While, Appendix E lists the commercial ranges of diverse structural sections used in the modelling of roof frame members. The optimization results fixed in Table 7.3 reveal that the minimum possible number of girders for model B3 is 34, whereas the number of rings could be reduced to 4. The dome radius is the only parameter that control the structural behaviour globally at stage 2, so the relevant metaheuristic method is obviously manipulating this parameter to escape from the local minimum. For instance, the first three designs (MESO-ABC, MESO-BA and MESO-DE) outperform other designs to achieve the global optimum when they depart from the local minimum at R=60 m. Furthermore, the topological fractions fixed in Table 7.3 are chosen in most cases to compress the rings towards the dome hub without sacrificing the design constraints.

The design MESO-ABC has achieved the optimum weight at 105.342 tonnes in only 54 structural analyses at phase 1 and 160 structural analyses at phase 2, as plotted in Figure 7.7. The optimal solution achieved by MESO-ABC could be justified by the different topology efficiently chosen by ABC at stage 1 to complement with the simultaneous shape, topology, and size optimization implemented at stage 2. The optimal values of sizing variables for this model are listed in terms of their designations in Appendix Table F.12. The reference design consists of 25 structural components as detailed in Table 4.25. for MESO-ABC, the number of design variables was reduced from (2+25+7=34) to (2+17+5=24), i.e. 2 continuous topological variables and 8 discrete sizing variables were omitted in this process as illustrated in Table 7.3 and Appendix Table F.12 respectively. This is only affected by the considerable elimination in $\mathbf{N_{Rings}}$ (from 6 to 4) executed at stage 1.

The remarkable reduction in the structural weight expressed in terms of MESO steps at stage 2 (see Figure 7.8) has caused the normalized SED to increase. For instance, SED for MESO-ABC has developed dramatically from 4.365 to 24.195, whereas other designs are observed to progress with lower extent. 194.77 MPa is the maximum stress reached in the entire optimization process, it is induced by MESO-PSO as illustrated in Figure 7.9. On the other hand, high fluctuations in the state of maximum stress could be observed in MESO-ABC, MESO-BA and MESO-SA. These fluctuations are dependent on many factors. For instance, in MESO-ABC, they depend on the population size, threshold of abandonment, space (radius) of the searching spot, and the fitness-based selection scheme.

Table 7.3 Optimal set for shape and topological variables of model B3.

Design variable	Reference design	MESO –ABC	MESO –BA	MESO –DE	MESO –PSO	MESO –SA
$N_{Girders}$ [-]	40	34	34	35	35	35
N_{Rings} [-]	6	4	5	4	4	5
R [m]	45	47.302	50.088	44.424	48.508	52.460
$Frac_1$ (-)	0.0952	0.0477	0.0532	0.0512	0.0918	0.1228
$Frac_2$ (-)	0.286	0.407	0.343	0.389	0.383	0.342
$Frac_3$ (-)	0.429	0.589	0.508	0.591	0.588	0.503
$Frac_4$ (-)	0.571	0.799	0.675	0.791	0.802	0.660
$Frac_5$ (-)	0.714	-	0.839	-	-	0.829
$Frac_6$ (-)	0.857	-	-	-	-	-

Table 7.4 Optimization results for model B3.

Optimization Strategy	Minimum Cost $\left(\frac{W}{W_0}\right)$	Corresponding Roof Frame Structural Mass (tonnes)	Corresponding Whole Tank Structural Mass (tonnes)
Initial design	1.000	196.231	517.009
MESO-ABC	0.537	105.342	425.626
MESO-BA	0.540	105.911	425.696
MESO-DE	0.537	105.374	426.292
MESO-PSO	0.546	107.098	427.154
MESO-SA	0.578	113.406	432.836

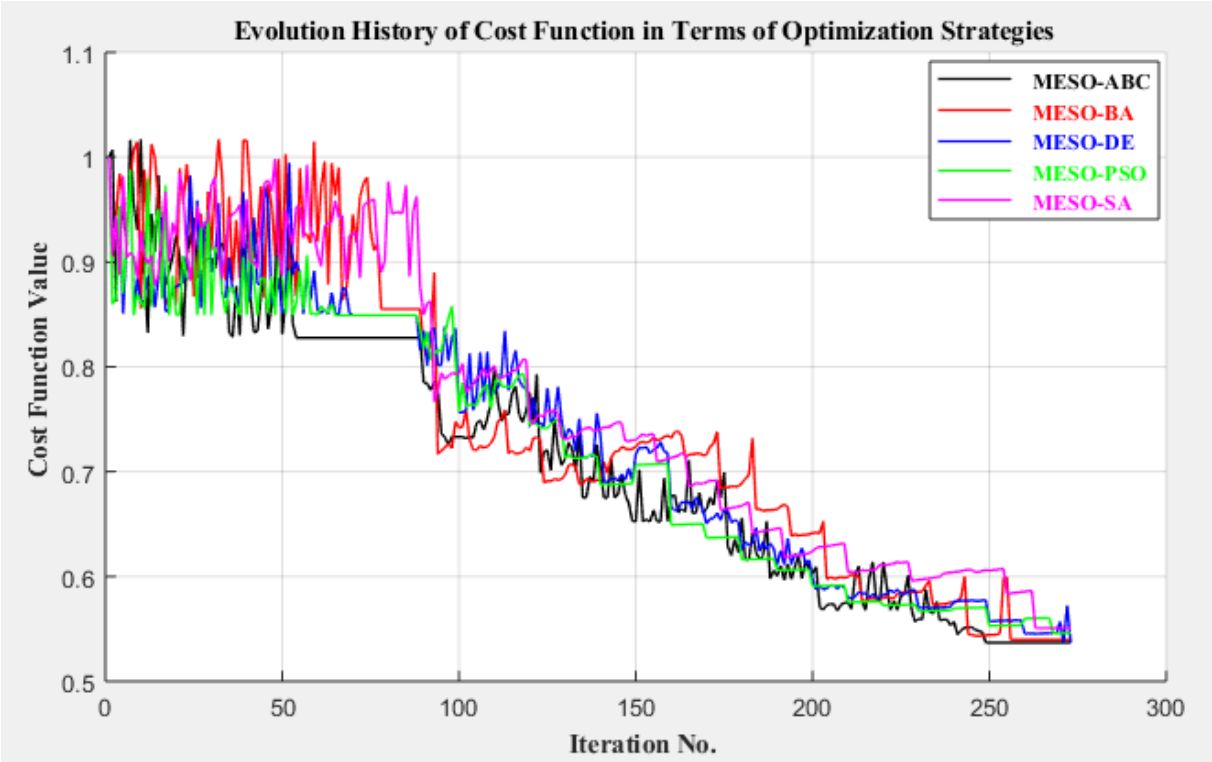

Figure 7.7 Progression history of the cost function towards the optimum for model B3.

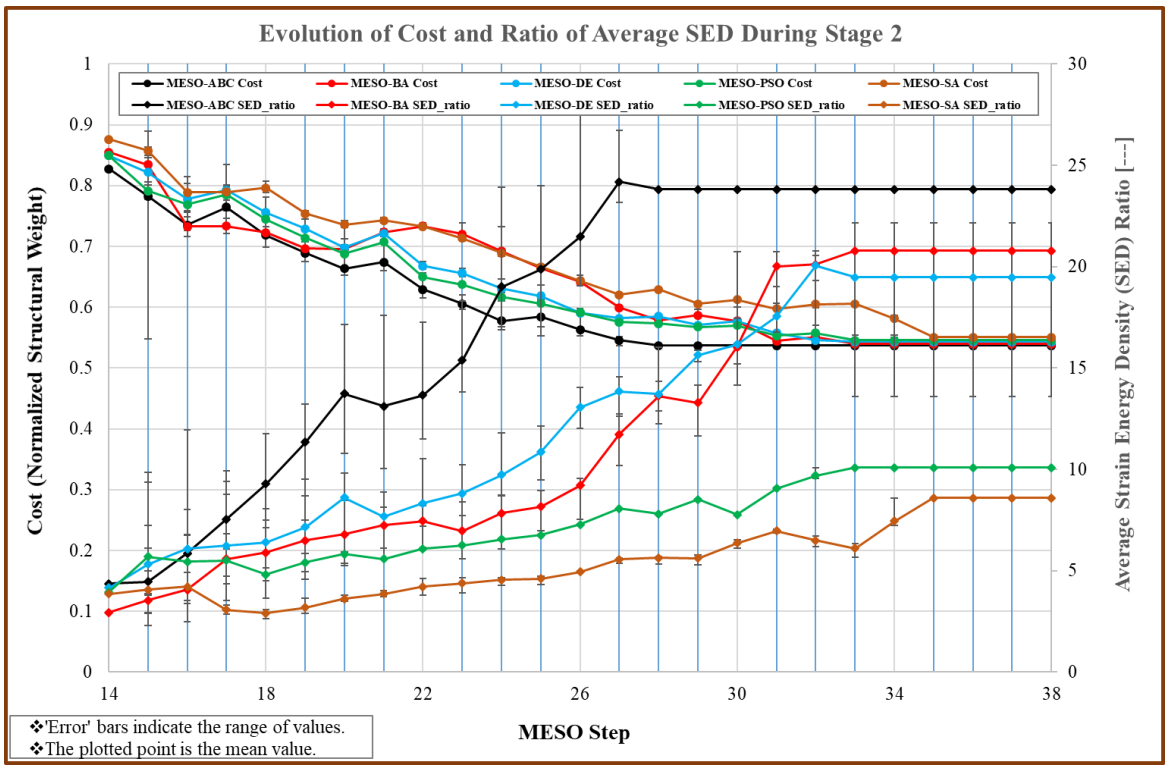

Figure 7.8 Evolution history of the normalized strain energy density SED for model B3.

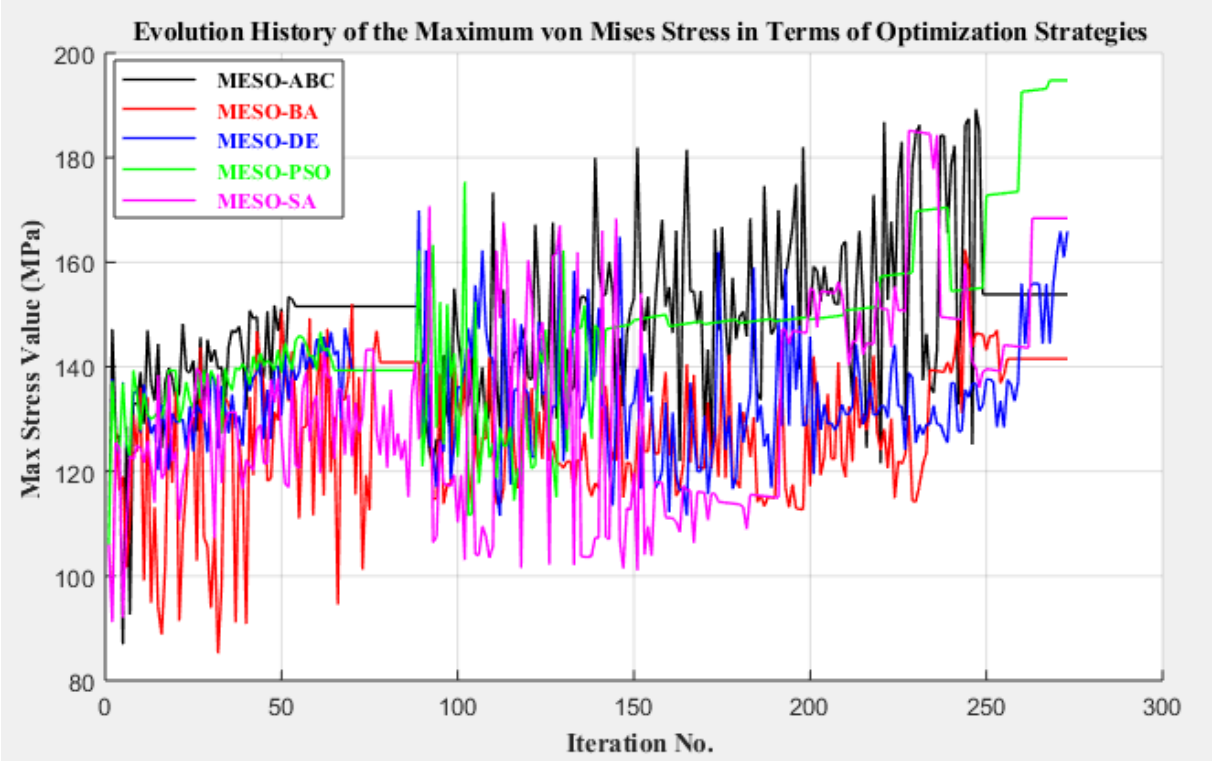

Figure 7.9 Design history of the maximum stress induced over the whole tank for model B3.

Figure 7.10 describes the variations in the state of SED between the initial and optimal designs for model B3, as the design MESO-ABC exhibits the maximum value of SED (1.1629 kJ/m^3).

It is observable that the maximum SED is located in the peripheral part of the dome roof frame, as the same spot shows the maximum stress of the model. The maximum strain energy reached in this case is 22.839 J, the maximum displacement is 19.246 mm as recorded by MESO-ABC. It is noteworthy to state that there are no penalties indicated in this optimization, as the progression of the maximum response is hovering much below the limit lines with an appreciable gap. The only problem with this model is belonging to the violations noticed at stage 3, where other load cases are applied. Accordingly, Figure 7.11 shows that MESO-PSO has exceeded the stress limits in the case (Wind+Hydro) with maximum stress of 204.837 MPa, i.e. the tank structure will fail when it is full and subjected to wind loads only for this particular design.

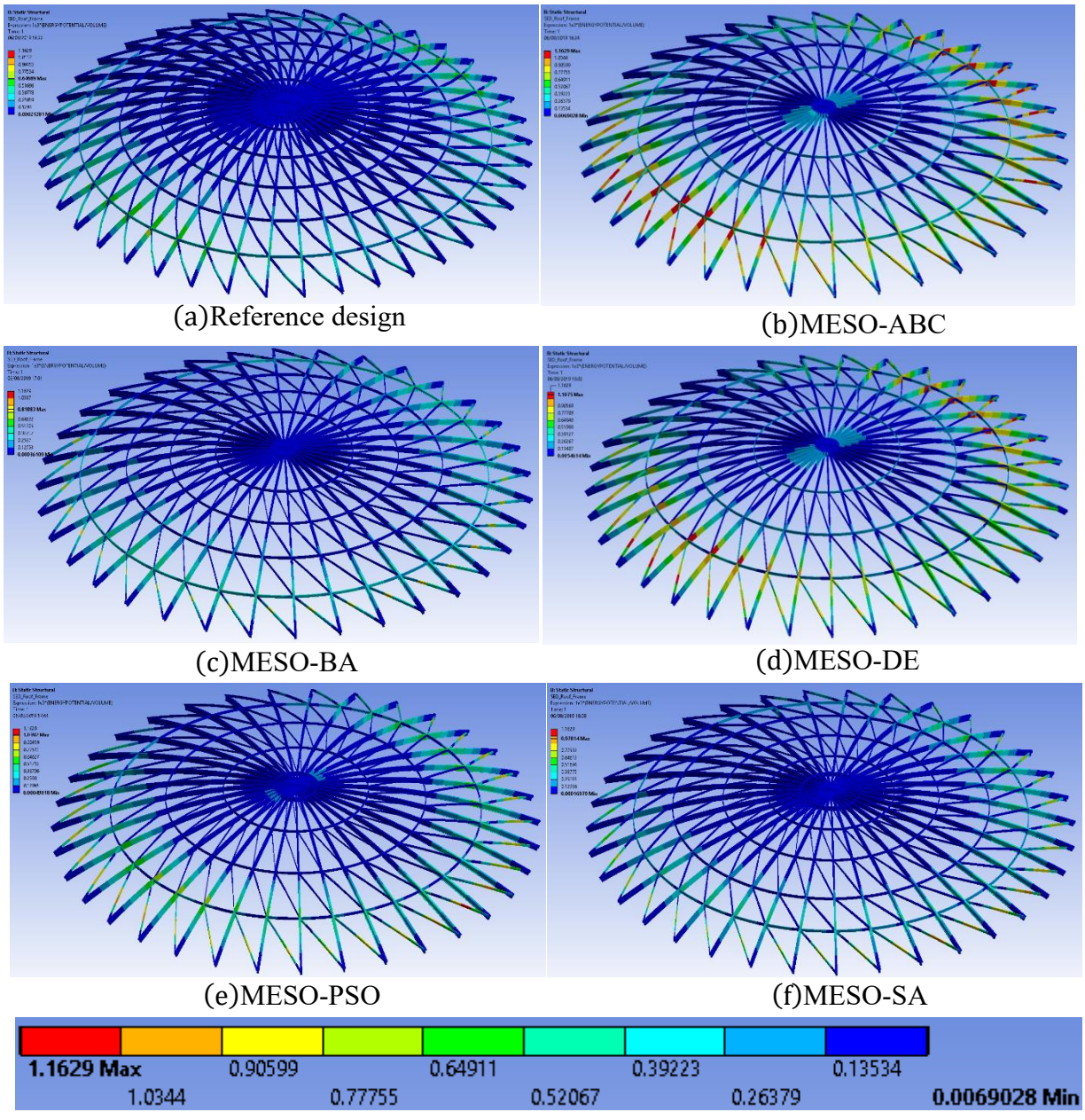

Figure 7.10 Distribution of SED showing the difference between the initial and optimal designs for model B3.

Due to exceeding stress limits at stage 3, MESO-PSO will be excluded from being a candidate design for this model. On the other side, the deformation inspection shows the same critical load cases as stress: (wind + empty tank) and (wind + full tank) as shown in Figure 7.12.

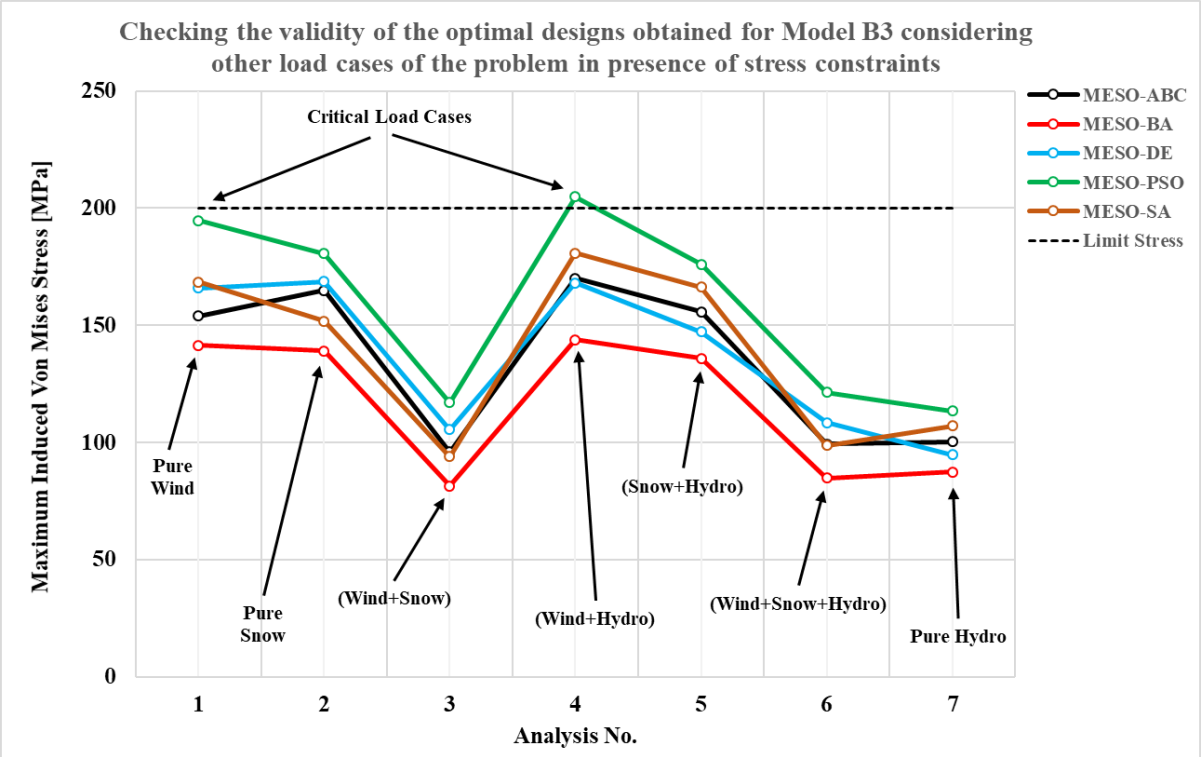

Figure 7.11 Validity test for model B3 executed in stage 3 against stress constraints.

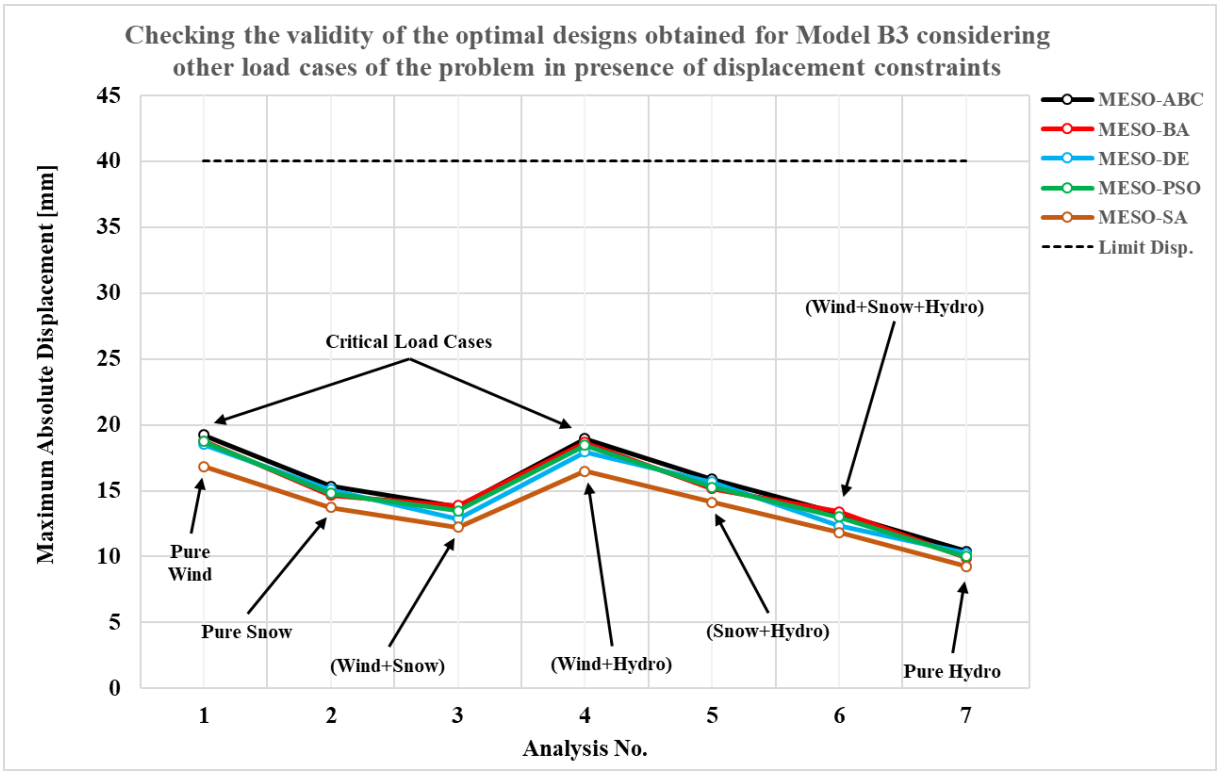

Figure 7.12 Validity test for model B3 executed in stage 3 against displacement constraints.

7.3 Lamella Single Lattice Dome (Model C3)

The reference design of this model is detailed in section 4.6.3. The design MESO-PSO has achieved the optimum weight at 113.121 tonnes after consuming 78 structural analyses at stage 1 and 179 structural analyses at stage 2 (look at Table 7.6 and Figure 7.13). The best two solutions are MESO-PSO and MESO-ABC, which have the same topology at the beginning of stage 2. However, a significant gap could be noticed in their topologies and their girder sections at the end of stage 2. The sizing variables for model C3 are listed in Appendix Table F.13. The reference design consists of 34 structural components as detailed in Table 4.27. For MESO-PSO, the number of design variables is reduced from (2+34+12=48) to (2+22+8=32), i.e. 4 continuous topological variables and 12 discrete sizing variables were omitted to prepare the design for stage 2 as illustrated in Table 7.5 and Appendix Table F.13 respectively. This is only affected by the considerable elimination in $\mathbf{N_{Rings}}$ (from 11 to 7) implemented at stage 1.

Despite MESO-ABC and MESO-PSO showing parallel progression in the first 100 generations at stage 2, the final result indicates the domination of MESO-PSO as illustrated in Figure 7.13. The maximum strain energy SE (18.922 N.m) is induced by MESO-PSO. Similarly, the maximum SED was produced by MESO-PSO to be 2.233 kJ/m^3, whereas the maximum deformation (17.96 mm) is generated at MESO-SA.

The evolution of normalized strain energy at stage 2 described in MESO sequence, as depicted in Figure 7.14, reveals that MESO-ABC is progressing rapidly at the beginning of the stage 2 up to step 25. Thereafter, MESO-PSO will step over MESO-ABC to stabilize at the value 7.56. While, MESO-BA and MESO-DE are preserved their progression at the lowest level to reach the values at 4.53 and 4.67 respectively.

Table 7.5 Optimal set for shape and topological variables of model C3.

Design variable	Reference design	MESO –ABC	MESO –BA	MESO –DE	MESO –PSO	MESO –SA
$N_{Girders}$ [-]	40	34	34	30	34	35
N_{Rings} [-]	11	7	8	8	7	7
R [m]	45	52.044	50.130	47.034	53.607	55.306
$Frac_1$ (-)	0.0952	0.0563	0.0490	0.1265	0.0776	0.0895
$Frac_2$ (-)	0.1667	0.2681	0.2183	0.2331	0.2437	0.2682
$Frac_3$ (-)	0.25	0.3785	0.3357	0.3383	0.3683	0.3621
$Frac_4$ (-)	0.3333	0.4886	0.4395	0.4564	0.5139	0.4889
$Frac_5$ (-)	0.4167	0.6226	0.5455	0.5652	0.6116	0.6299
$Frac_6$ (-)	0.5	0.7431	0.6694	0.6597	0.7519	0.7552
$Frac_7$ (-)	0.5833	0.8714	0.7843	0.7675	0.8723	0.8693
$Frac_8$ (-)	0.6667	-	0.8895	0.8816	-	-
$Frac_9$ (-)	0.75	-	-	-	-	-
$Frac_{10}$ (-)	0.8333	-	-	-	-	-
$Frac_{11}$ (-)	0.9167	-	-	-	-	-

Table 7.6 Optimization results for model C3.

Optimization Strategy	Minimum Cost $\left(\frac{W}{W_0}\right)$	Corresponding Roof Frame Structural Mass (tonnes)	Corresponding Whole Tank Structural Mass (tonnes)
Initial design	**1.000**	**209.269**	**530.048**
MESO-ABC	**0.5577**	**116.706**	**435.983**
MESO-BA	**0.5854**	**122.505**	**442.400**
MESO-DE	**0.5619**	**117.577**	**437.909**
MESO-PSO	**0.5406**	**113.121**	**432.348**
MESO-SA	**0.5788**	**121.116**	**440.523**

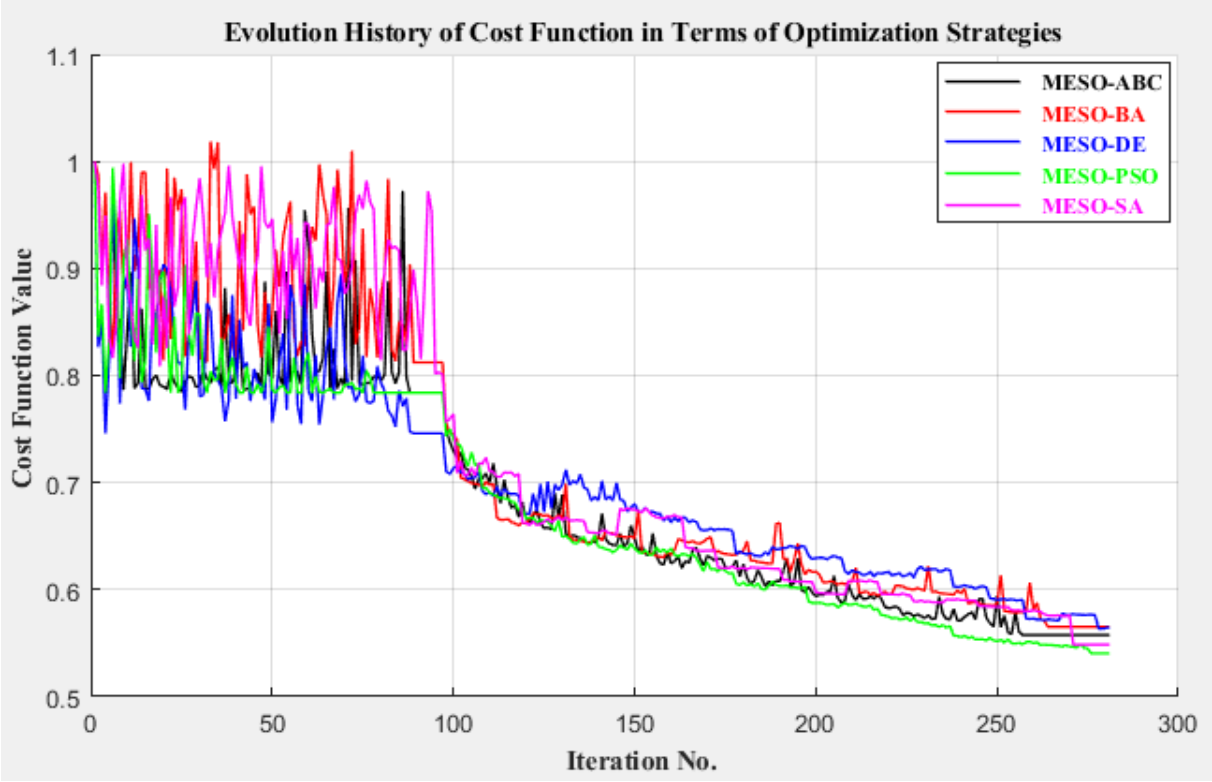

Figure 7.13 Progression history of the cost function towards the optimum for model C3.

Figure 7.15 states that MESO-BA is the most design that breached the stress constraints at phase 1, as it was penalized 14 times due to high fluctuations of cost noticed in this algorithm at phase 1, whereas it is remarked that MESO-PSO has discarded 61 evaluations at phase 2 due to stress. Furthermore, Figure 7.15 indicates that the maximum stress is induced in MESO-PSO with value of 188.958 MPa. On the other hand, the minimum stress is recorded by MESO-BA (158.029 MPa). Also, statistical data state that MESO-BA and MESO-DE show no violations to the stress constraints, as they have different variants compared to other designs.

The distribution of SED for model C3, depicted in Figure 7.16, indicates that the maximum SED (2.233 kJ/m^3) is generated in MESO-PSO. Hence, this is considered as reference value for other designs to show the SED state for them comparatively. It can be inferred that the outermost ring experiences a compressive load as result of lift force applied to the model.

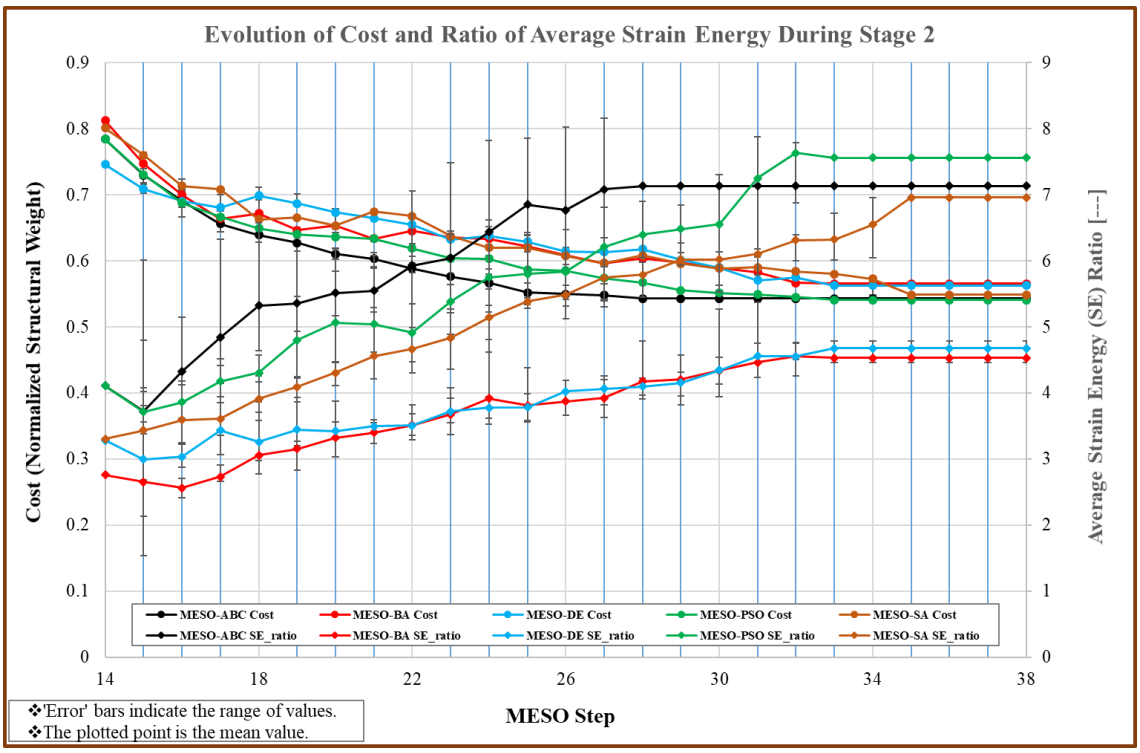

Figure 7.14 Evolution history of the normalized strain energy SE for model C3.

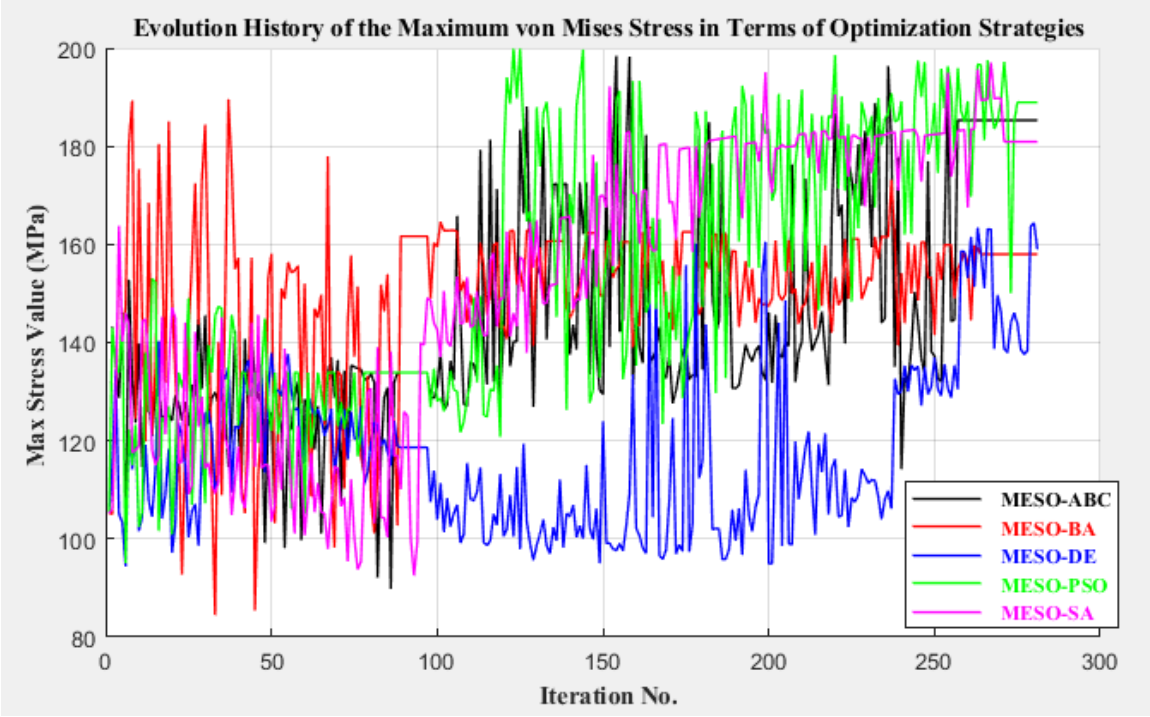

Figure 7.15 Design history of the maximum stress induced over the whole tank for model C3.

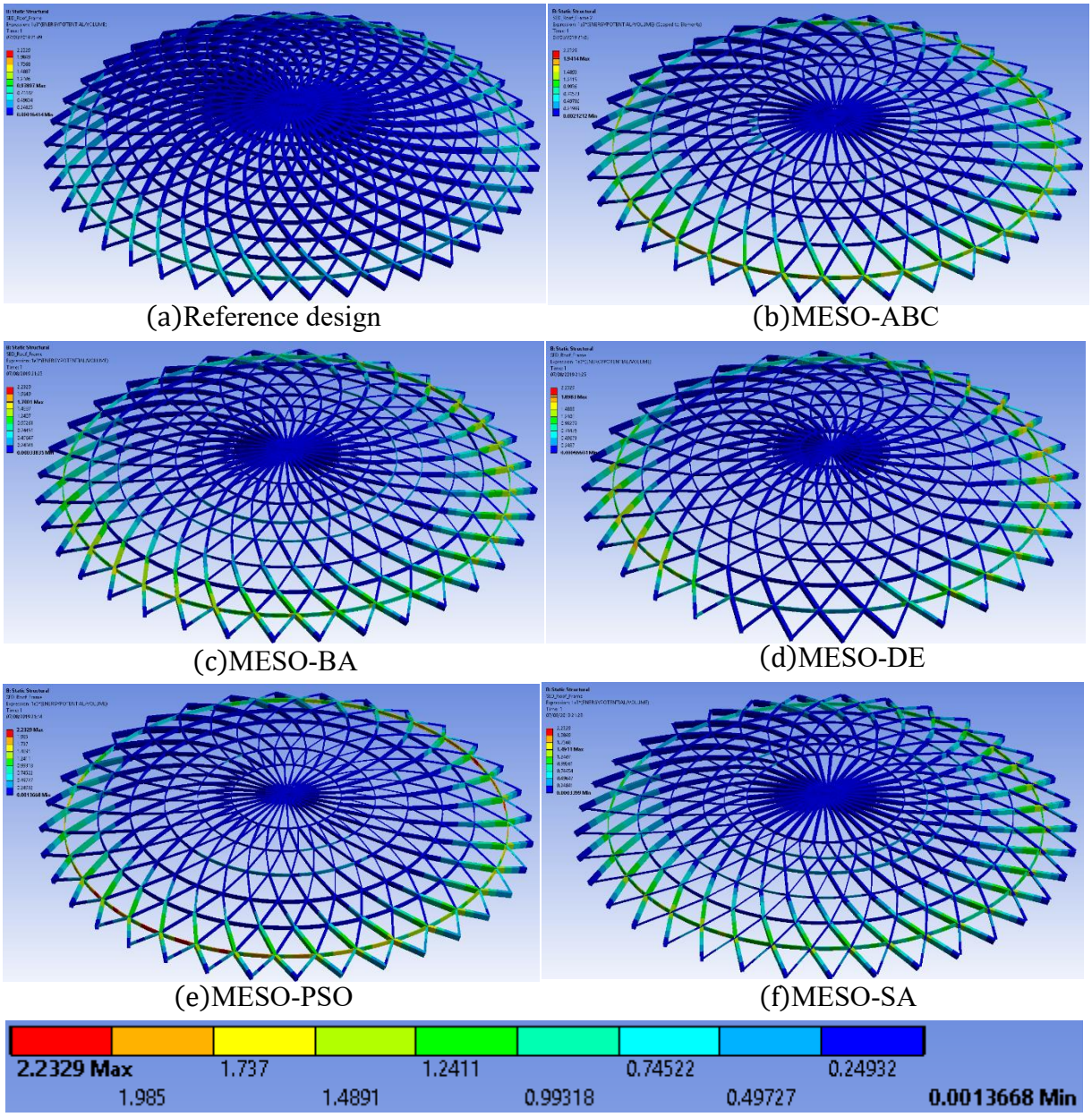

Figure 7.16 Distribution of SED showing the difference between the initial and optimal designs for model C3.

The validity test of the optimal designs performed against stress constraints, plotted in Figure 7.17, shows that two designs (MESO-ABC and MESO-PSO) are breached the stress limits for two load cases (pure snow and snow+hydro), hence those two designs are crossed and excluded from being candidate designs. Thus, the next candidate design to be selected for model C3 is MESO-DE with weight 117.577 tonnes, as illustrated in Table 7.6. However, the displacement test, shown in Figure 7.18, clarifies that there are no violations to the displacement constraints.

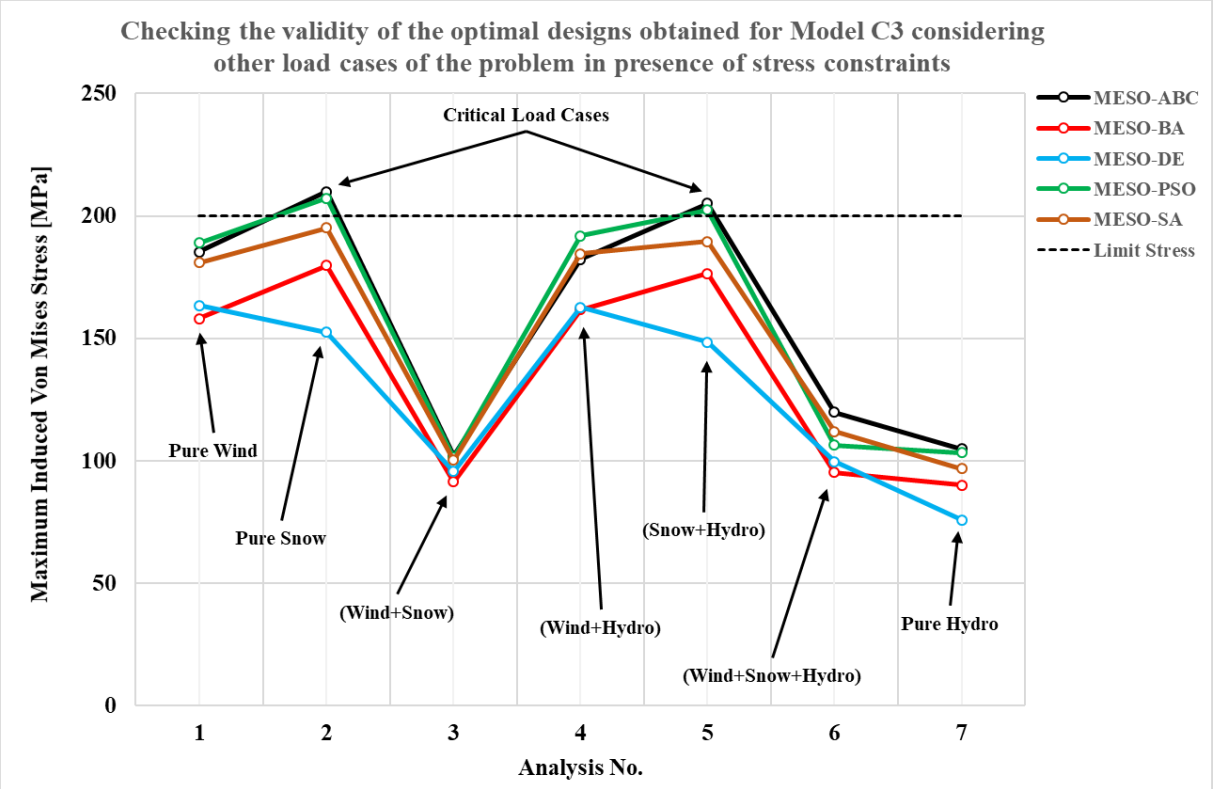

Figure 7.17 Validity test for model C3 executed in stage 3 against stress constraints.

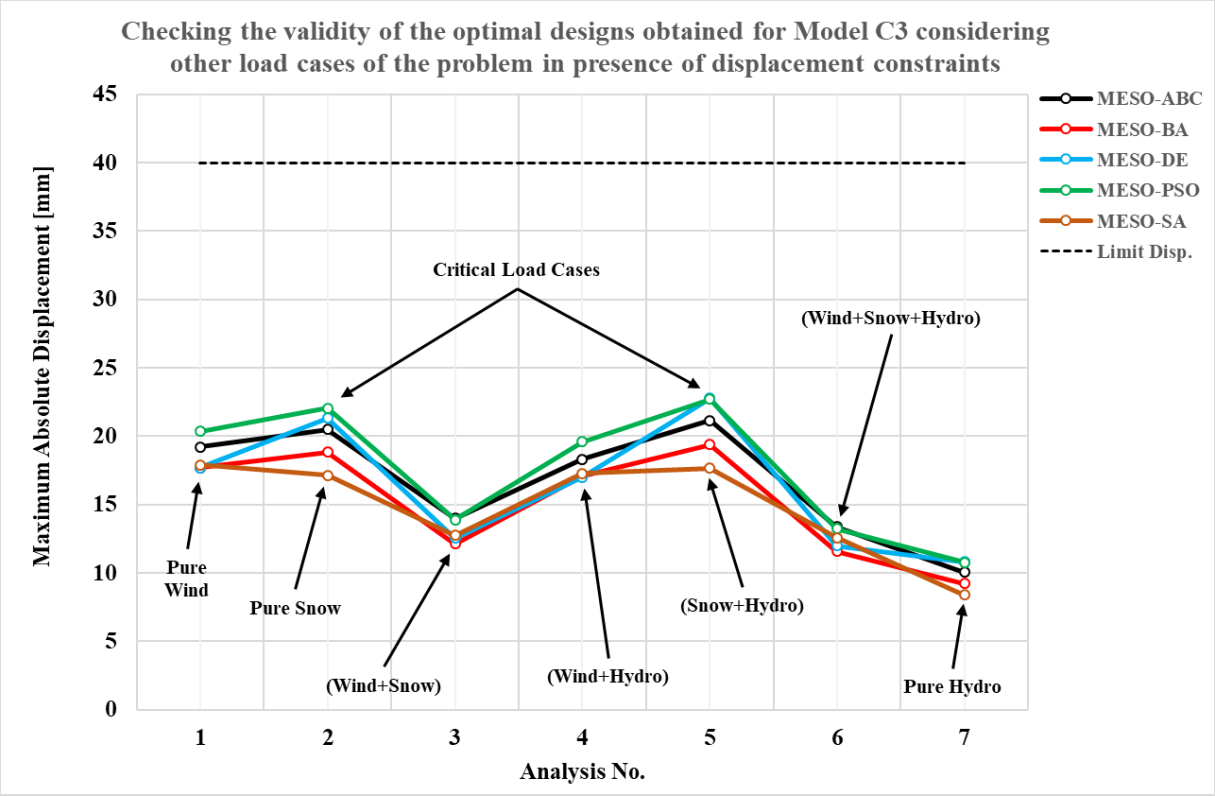

Figure 7.18 Validity test for model C3 executed in stage 3 against displacement constraints.

7.4 Geodesic Single Lattice Dome (Model E3)

The main difference between this model and the previous models could be justified by the configuration of the braces. The number of braces is determined as multiples of ring number. For instance, if the number of radial girders ($\mathbf{N_{Girders}}$=6), then the number of braces for $\mathbf{N_{Rings}}$=4 will be calculated simply as (6×1+6×2+6×3+6×4=60) as illustrated in formulae (4.12) in terms of the circumferential nodes involved. The reference design of this model is detailed in section 4.6.4. However, MESO-DE has achieved an exceptional optimum weight at 74.256 tonnes after 103 structural analyses at stage 1 and 184 structural analyses at stage 2 as illustrated in Table 7.8 and Figure 7.19. Model E3 is characterized by low number of radial girders, which are compensated by the radially increasing braces.

Initially, the model has 10 radial girders and 9 circumferential rings, these are reduced to 6 by 6 in each of MESO-ABC, MESO-DE and MESO-SA, 6 by 7 in MESO-BA and 7 by 7 in MESO-PSO as stated in Table 7.7. The dome radii of all designs are concentrated at the upper half of the optimization range. Unlike models A3 to C3, the optimizer is trying to push the circumferential rings radially towards the dome periphery to achieve the minimum weight (review the topological fractions mentioned in Table 7.7 with the radial distances of circumferential rings shown graphically in Figure 7.23). A parametric study has been conducted in Chapter 6 to highlight this relationship. A significant reduction in design variables from (2+37+10=49) to (2+25+7=34) was remarked in stage 2 for the designs MESO-ABC, MESO-DE and MESO-SA due to reducing the rings from 9 to 6.

The sizing variables for the set of optimal designs of this model are listed in Appendix Table F.14. While, Appendix E is devoted to list the industrial cross sections used in the modeling of structural members.

Table 7.7 Optimal set for shape and topological variables of model E3.

Design variable	Reference design	MESO –ABC	MESO –BA	MESO –DE	MESO –PSO	MESO –SA
$N_{Girders}$ [-]	10	6	6	6	7	6
N_{Rings} [-]	9	6	7	6	7	6
R [m]	45	50.339	52.326	54.943	56.812	51.325
$Frac_1$ (-)	0.1	0.1001	0.0943	0.1359	0.1398	0.1355
$Frac_2$ (-)	0.2	0.7536	0.2689	0.2931	0.2439	0.2897
$Frac_3$ (-)	0.3	0.4451	0.3774	0.4121	0.3888	0.4394
$Frac_4$ (-)	0.4	0.5603	0.4888	0.5727	0.5084	0.5857
$Frac_5$ (-)	0.5	0.7190	0.6371	0.7260	0.6116	0.7129
$Frac_6$ (-)	0.6	0.8574	0.7436	0.8619	0.7598	0.8654
$Frac_7$ (-)	0.7	-	0.8793	-	0.8688	-
$Frac_8$ (-)	0.8	-	-	-	-	-
$Frac_9$ (-)	0.9	-	-	-	-	-

The graph shown in Figure 7.19 indicate that MESO-ABC, MESO-DE and MESO-SA are progressing with high convergence rate to achieve the minimum at the end of stage 2. The evolution of normalized average strain energy density SED, appearing in Figure 7.20, states that the strain energy increases for any structure subjected to material removal. Subsequently, the stiffness characteristics will be negatively affected. The highest value for SED ratio is 23.66 as noticed in MESO-DE, whereas the lowest value is 11.44 observed in MESO-PSO. Consequently, MESO-DE has developed the maximum SED (3.165 kJ/m^3), and the maximum vertical deformation (24.618 mm).

Table 7.8 Optimization results for model E3.

Optimization Strategy	Minimum Cost $\left(\frac{W}{W_0}\right)$	Corresponding Roof Frame Structural Mass (tonnes)	Corresponding Whole Tank Structural Mass (tonnes)
Initial design	**1.000**	**209.269**	**530.048**
MESO-ABC	**0.382**	**78.494**	**398.239**
MESO-BA	**0.388**	**79.818**	**399.266**
MESO-DE	**0.361**	**74.256**	**393.368**
MESO-PSO	**0.426**	**87.661**	**406.563**
MESO-SA	**0.376**	**77.261**	**396.854**

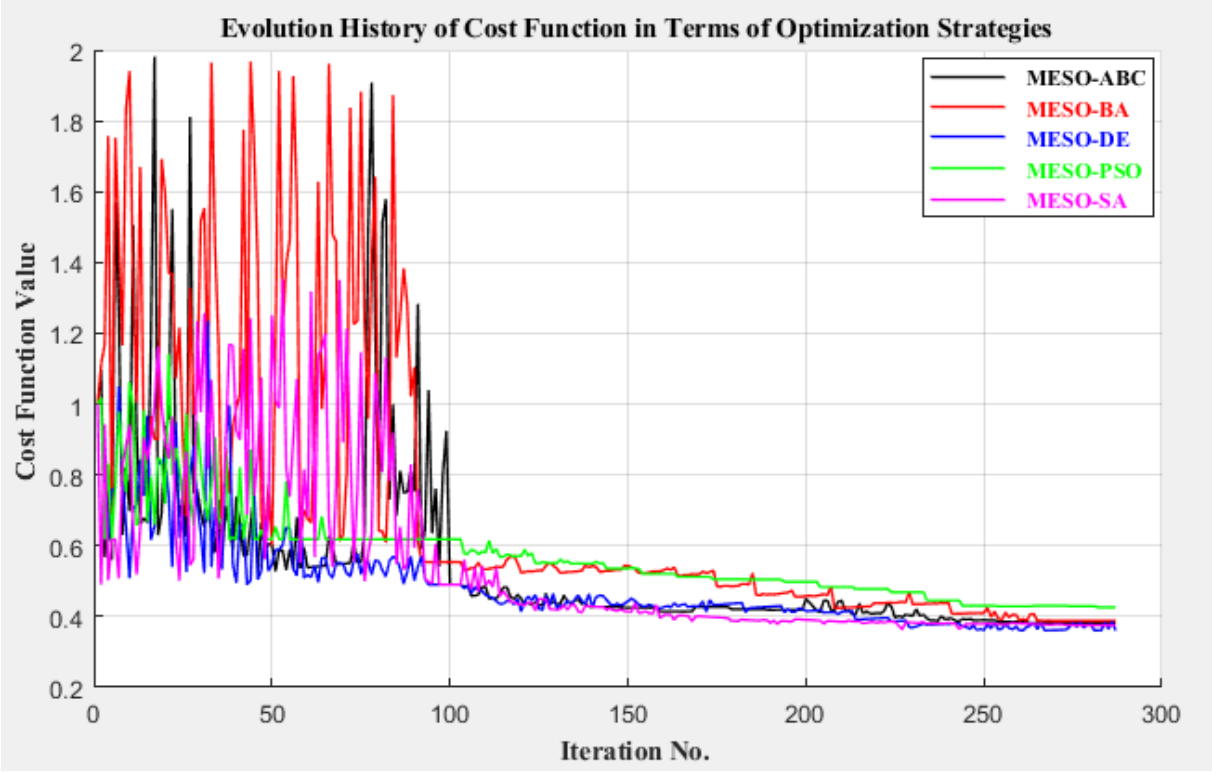

Figure 7.19 Progression history of the cost function towards the optimum for model E3.

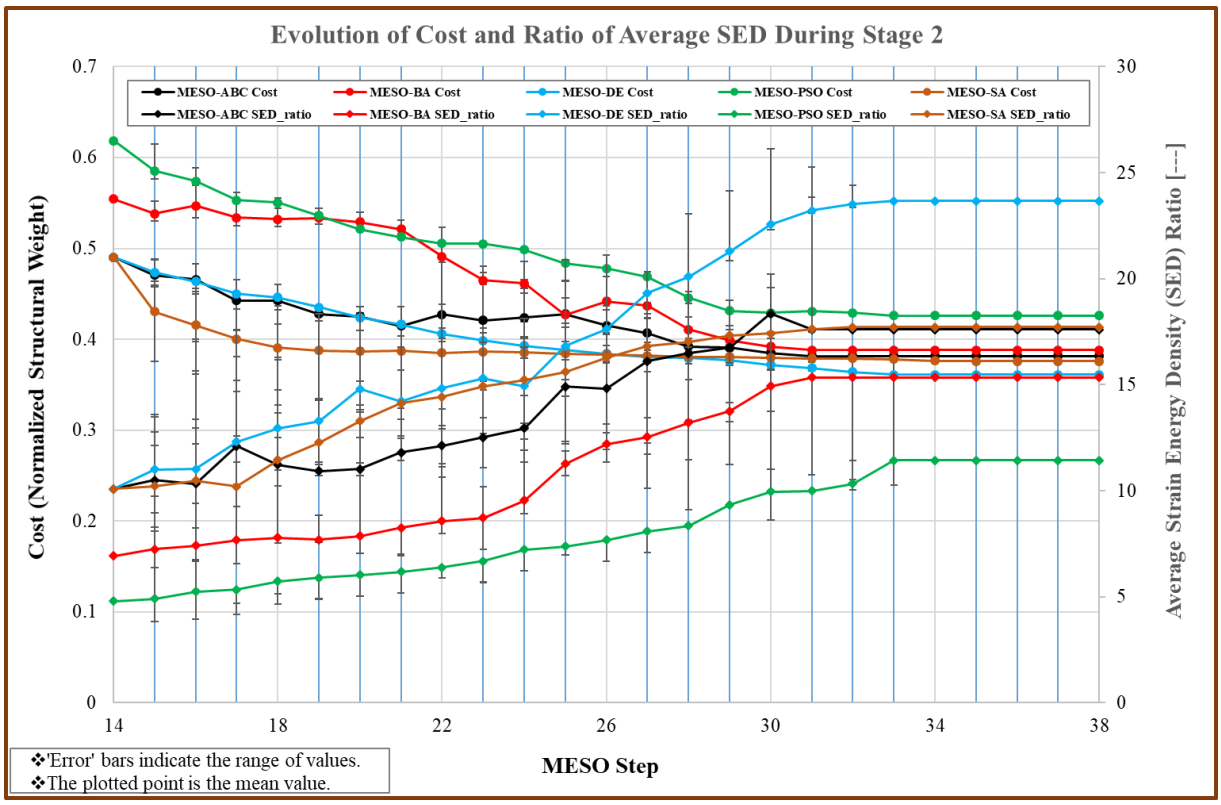

Figure 7.20 Evolution history of the normalized strain energy density SED for model E3.

MESO-DE is the most susceptible design to the penalties of stress limits, where it has lost 86 solutions during this optimization task. Followed by MESO-SA with violations equal to 72, whereas MESO-PSO has recorded zero violations to stress. The evolution history of maximum von Mises stress described for different designs, as shown in Figure 7.21, reflects the state of satisfaction to the stress constraints. The lumping of design points for certain design around the limit line of certain constraint will enhance the chance to be penalized by that constraint more than other designs.

The design contours for model E3, illustrated in Figure 7.23, indicate that the maximum SED is located on the peripheral part of the radial girders for all designs. This is the same situation seen in model B3, as the radial girders are the most vulnerable parts of the dome frame (look at Figure 7.10). On the contrary, models A3 and C3 exhibit a different situation towards the pure wind loads as depicted in Figure 7.4 and Figure 7.16, where the outermost circumferential ring is the critical part of the dome structure.

Though the presence of other critical load case (full tank subjected to pure wind) during the test implemented at stage 3 against stress limits as clarified in Figure 7.22, all designs were passed the test without any breaching to the prescribed stress limits. Since there are no violations to the displacement limits, as indicated in Figure 7.24, MESO-DE is now eligible to be chosen as candidate for model E3 with weight 74.256 tonnes, as illustrated in Table 7.8.

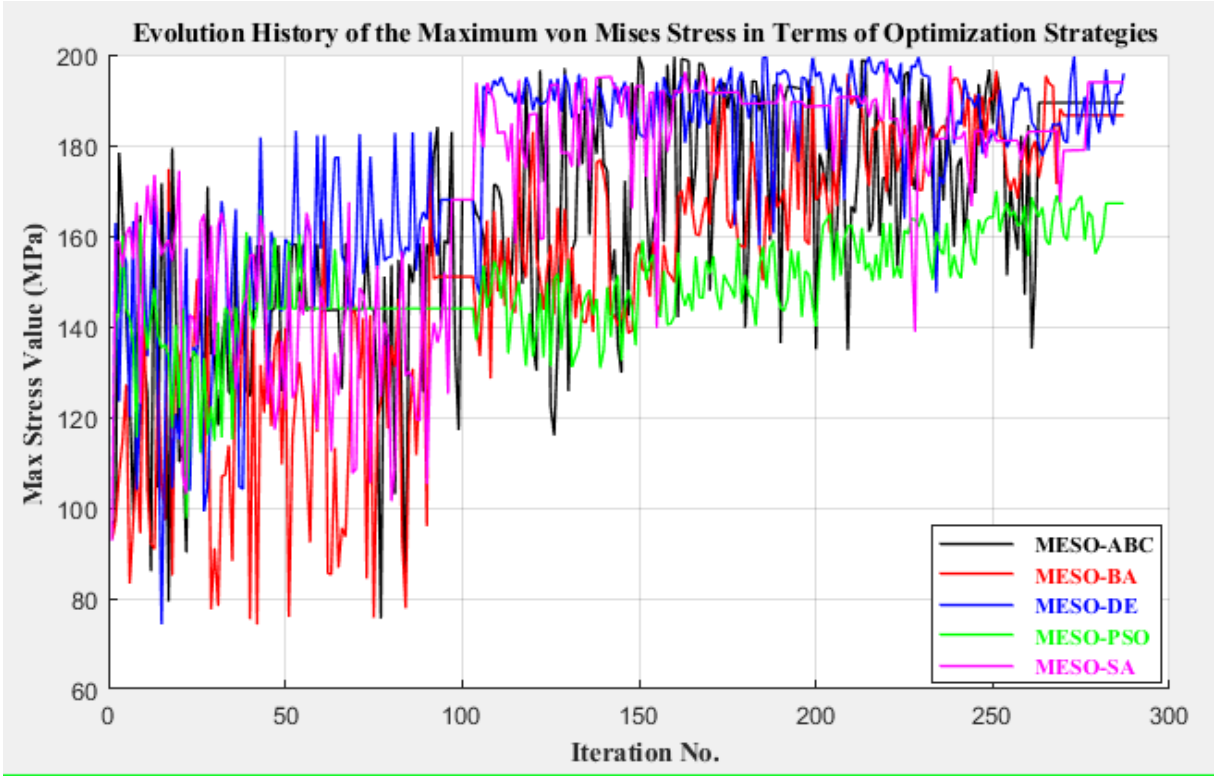

Figure 7.21 Design history of the maximum stress induced over the whole tank for model E3.

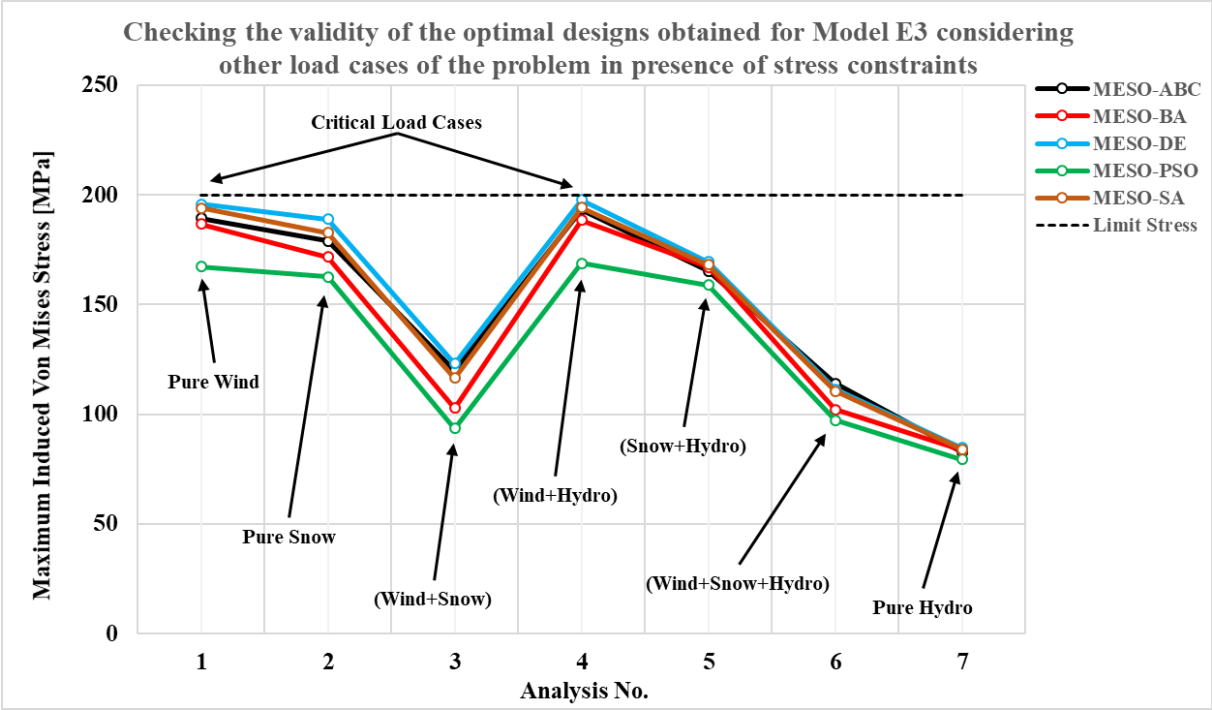

Figure 7.22 Validity test for model E3 executed in stage 3 against stress constraints.

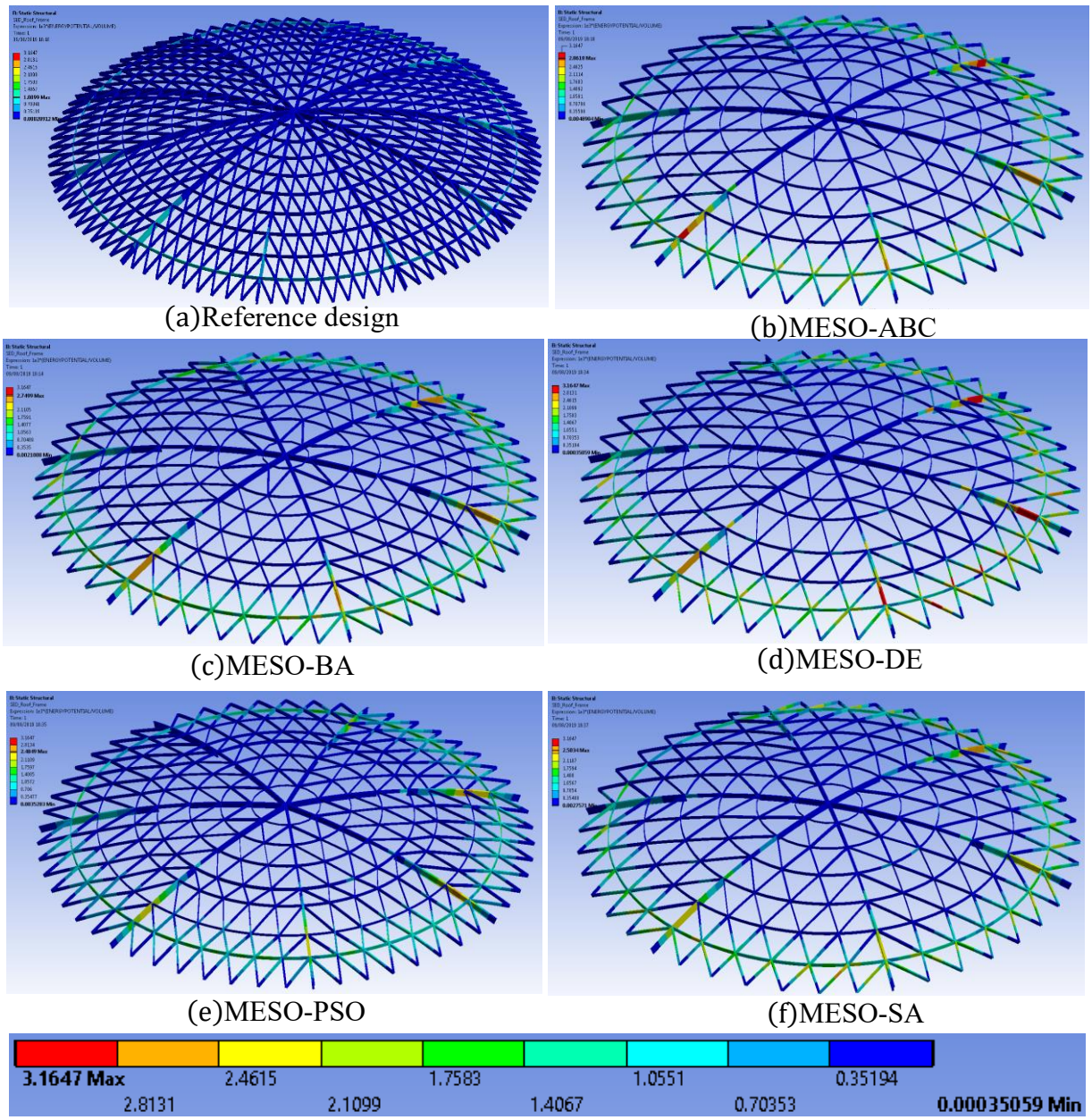

Figure 7.23 Distribution of SED showing the difference between the initial and optimal designs for model E3.

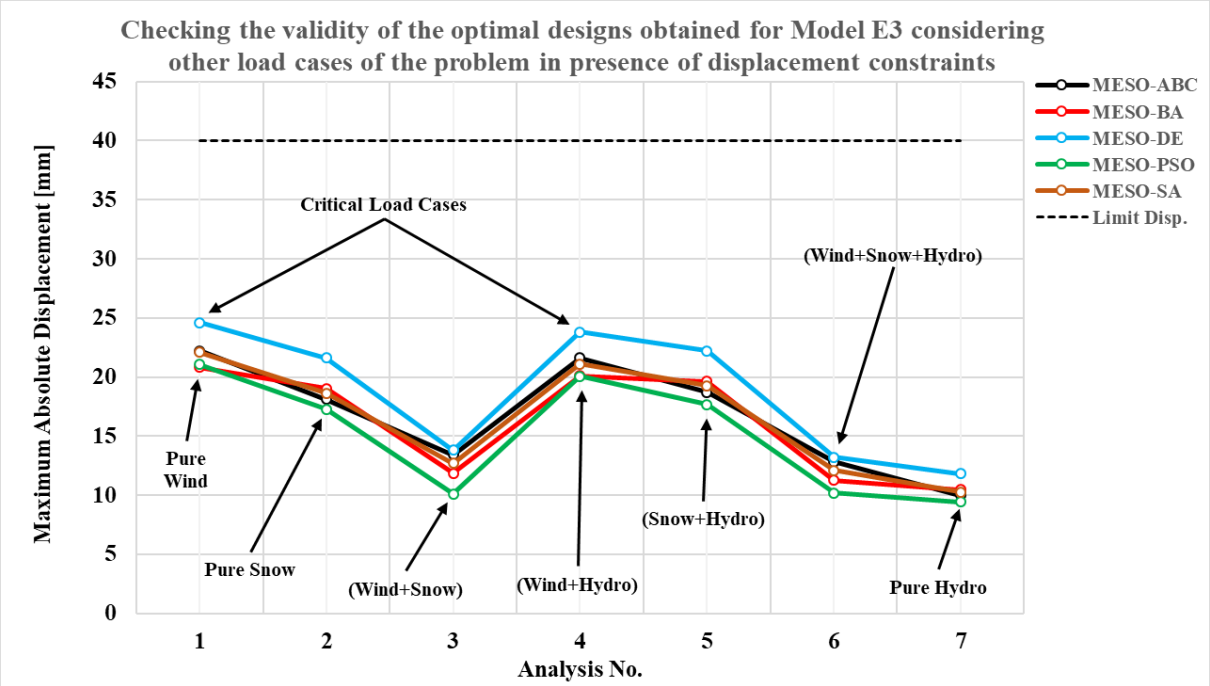

Figure 7.24 Validity test for model E3 executed in stage 3 against displacement constraints.

7.5 Selection of the Optimum Design

It is observed that MESO-ABC, MESO-DE and MESO-SA are the most efficient algorithms for global search associated with multiple and strict design constraints. They can treat with multimodal problems, where multiple paths are possible to achieve the optimum. However, the significant part of their success is attributed to using MESO, as it conducts a single path of search intelligently depending on prescribed design criterion, as detailed in section 5.4. One of the merits of MESO is that it produces a feasible solution acceptable to both practical and manufacturing perspectives, as it resizes the member dimensions systematically, whereas this feature does not exist in the conventional metaheuristic techniques.

According to Table 7.2, the best candidate, for model A3, is MESO-ABC with weight 121.772 tonnes corresponding to tank weight 441.296 tonnes. Similarly, the contribution of model B3 is MESO-ABC, which developed a minimum weight of 105.342 tonnes, the corresponding tank mass was 425.626 tonnes as given in Table 7.4. The third candidate is MESO-DE to represent model C3, with roof mass 117.577 tonnes, and tank mass 437.909 tonnes as indicated in Table 7.6. The last candidate is MESO-DE found in model E3, which recorded a minimum roof frame mass of 74.256 tonnes and a tank mass of 393.368 tonnes (see Table 7.8). The latter design is selected to be the best design for the set of models and algorithms evaluated in this chapter. The smart configuration of the model (model E3) along with the exceptional characteristics of the adopted optimization technique (MESO-DE) are the main two reasons behind this success. Table 7.9 lists the set of best optimal designs for the integrated dome roof models investigated in this chapter.

Table 7.9 The set of optimal designs obtained for the integrated models.

Model ID	Associated optimization technique	Optimal mass for the dome roof frame (tonnes)	Optimal mass for the whole tank (tonnes)
Model A3	**MESO-ABC**	**121.772**	**441.296**
Model B3	**MESO-ABC**	**105.342**	**425.626**
Model C3	**MESO-DE**	**117.577**	**437.909**
Model E3	**MESO-DE**	**74.256**	**393.368**

7.6 Summary

- It is more complicated to treat the design variables in the integrated models to be easier to optimize compared to the simplified models.
- Three more critical load cases need to be considered in the design process: a full tank subjected to pure wind loading (from stress perspective), and an empty and full tank subjected to pure snow loading (from displacement perspective).
- In appreciable closeness to the results obtained for the simplified modelling, the integrated model E3 exhibited the best structural performance compared to other models, where the minimum structural mass obtained for the roof supporting frame is **74.256** tonnes, which is corresponding to a whole tank mass of **393.368 tonnes**.
- Compared to other methods adopted in this work, MESO-DE showed its robustness to find the optimal solution for the applications involved with strict and multiple design constraints.

Chapter 8. Efficiency and Robustness of the Proposed Strategies

8.1 Synopsis

This chapter discusses the computational performance (convergence rate) of the hybrid optimizers proposed in this work compared to the classic metaheuristic ones used in the literature for the same field of optimization, i.e. large-scale structural optimization. The reliability and robustness of the adopted optimizers is compared to the conventional metaheuristic techniques based on five different models along with five different optimization strategies posed in two modes: the hybrid mode (MESO based algorithms) and the standard or conventional mode (STD based algorithms). Five different case studies are considered in this investigation to verify the computational efficiency and the feasibility of the proposed optimizers (MESO based algorithms) compared to other conventional metaheuristic techniques used in the literature. Two of them are taken from this research and the others are selected from the literature. The same conditions (objective constraints and loading cases) as the study performed in Chapter 6 are applicable to the first two case studies. While, the remaining case studies have their own specified constraints and loading condition as stated in their respective subsections.

8.2 Trimmed Ribbed Staggered Double Lattice Dome (Model A4)

Model A4 is a variation of Model A2 in which the lower frame is staggered, i.e., rotated axially by half an interval (180/$\mathbf{N_n}$) with respect to the upper (primary) layer. Hence, a zigzag style of in-between bracing is introduced for this type of modelling, where the number of structural components will increase by ($\mathbf{N_r}$**-1)**, i.e. the reference design is consisting of (30+14+14+28+14+14+2=116) components, 1474 nodes, and 5025 elements. The numbering of structural components for initial design is shown in Figure 8.1.

The optimization data are listed in Table 8.1. $\mathbf{N_n}$ and $\mathbf{N_r}$ both reduce to the lowest values of their respective ranges, i.e. 24 and 10 respectively, while $\mathbf{N_s}$ ranges from 17 to 22, as seen in the parametric study of $\mathbf{N_s}$ discussed in section 6.1.1. The optimal values of $\mathbf{N_t}$ range from 4 to 10, which matches with the investigation results for $\mathbf{N_t}$ in section 6.1.3. More details about the optimum dome radii and other two extra shape parameters concerning the double lattice modelling are shown in Table 8.1.

As explained earlier, this investigation is directed to show the significant difference between the proposed MESO based algorithms and the classic or conventional metaheuristic algorithms. To recognize these methods, the adopted metaheuristic techniques (ABC, BA, DE, PSO, and SA) hybridized with MESO are prefixed by “MESO”, whereas the conventional ones are

prefixed by “STD”. For instance, the hybrid BA is labelled as MESO-BA, whereas the standard BA is referred to as STD-BA as defined in Table 8.1 and Figure 8.2.

The evolution curves of cost function for model A4, appearing in Figure 8.2, are represented by 10 different optimization algorithms. Five of them are hybrid metaheuristic algorithms (MESO–ABC, MESO–BA, MESO–DE, MESO–PSO, and MESO–SA) with their procedure explained in section 5.6 and Figure 5.9. Another five algorithms are the conventional metaheuristic algorithms (STD–ABC, STD–BA, STD–DE, STD–PSO, and STD–SA), which are working on the same procedure explained in Figure 5.9, but without using MESO, i.e. they are using pure metaheuristic rules to treat with all variables at Stage 1 and Stage 2.

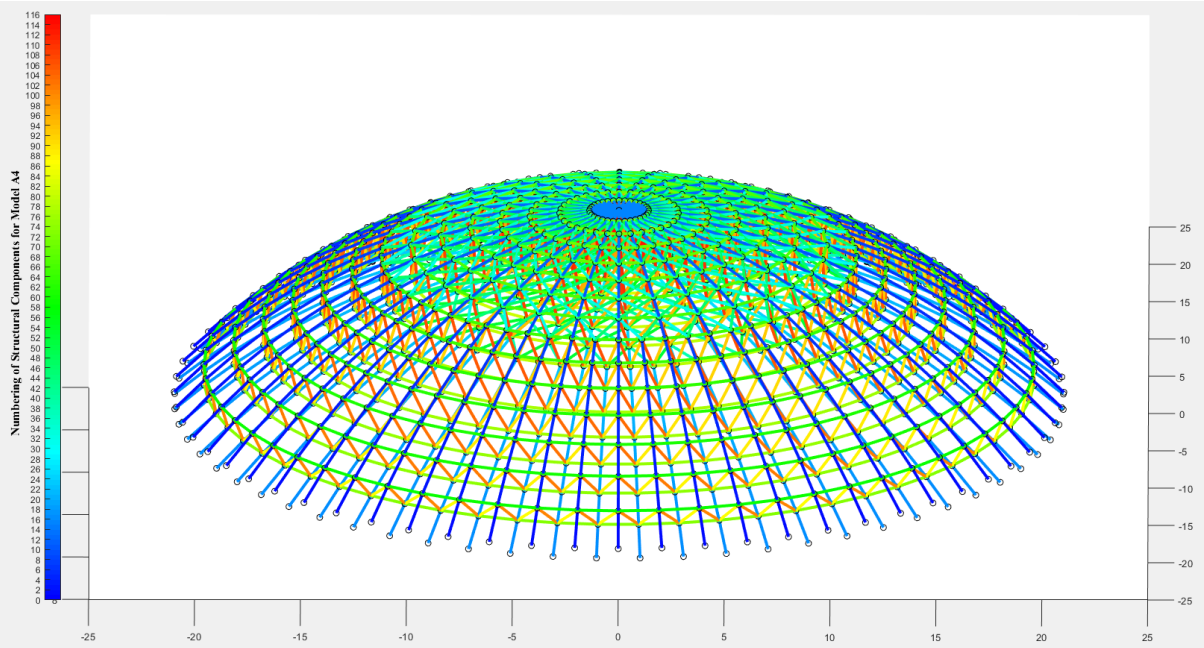

Figure 8.1 Reference design of model A4, showing identification of the structural components.

Table 8.1 Optimal set for shape and topological variables of model A4.

Optimization Method	N_n [-]	N_r [-]	N_s [-]	N_t [-]	R1 [m]	η [-]	ʊ [-]
Initial design	**32**	**15**	**20**	**10**	**30.000**	**0.9500**	**1.1000**
MESO-ABC	**24**	**10**	**18**	**9**	**38.056**	**0.8666**	**1.0618**
MESO-BA	**24**	**10**	**22**	**4**	**34.677**	**0.9311**	**1.0011**
MESO-DE	**24**	**10**	**22**	**6**	**37.178**	**0.9216**	**1.1000**
MESO-PSO	**24**	**10**	**18**	**10**	**39.503**	**0.9499**	**1.0578**
MESO-SA	**25**	**10**	**17**	**10**	**40.471**	**0.9479**	**1.0011**
STD-ABC	**24**	**10**	**18**	**9**	**36.956**	**0.8729**	**0.9123**
STD-BA	**24**	**10**	**22**	**4**	**58.956**	**0.9216**	**1.0414**
STD-DE	**24**	**10**	**22**	**6**	**57.225**	**0.9497**	**0.9980**
STD-PSO	**24**	**10**	**18**	**10**	**37.173**	**0.8883**	**0.9054**
STD-SA	**25**	**10**	**17**	**10**	**56.274**	**0.9457**	**1.0221**

The optimal structural mass for each of the ten methods is summarized in Table 8.2. MESO–ABC has outperformed other algorithms with MESO-DE a close second (59.2 tonnes and 60.2 tonnes respectively). Phase 1 is identical for both MESO and STD methods (see Figure 8.2 to Figure 8.4) due to the fact that they are optimizing the same integer topological variables allocated for this phase and the MESO method itself is only introduced at Stage 2.

As can be seen in Figure 8.2, MESO-BA and MESO-SA were trapped in local minima early on, as they stopped progress after 294 and 328 analyses at stage 2 respectively. STD-BA has lost a lot of solutions, hence after 587 successful evaluations it was given up to reach the steady state after 381 successful evaluations at phase 2. Only 206 successful evaluations are consumed to pass stage 1 for both MESO and STD techniques, while the statistical data reveal that MESO algorithms reached the optimum after only 512 successful solutions at stage 2. On the other hand, STD methods are consumed 842 successful solutions to reach the optimum. Though the high number of analyses remarked in STD curves, they have achieved poor results in comparison to the proposed MESO algorithms.

In general, the diversity ranges of cost function (i.e. the difference between the max and min values of cost evaluations for the bunch of individuals found in only one iteration), plotted in Figure 8.3, indicate that MESO algorithms have significantly lower ranges of diversity at stage 2 in comparison to STD algorithms. This is attributed to the engineering intuition exploited by MESO to follow the optimal path of evolution instead of swimming randomly in full solution space, as seen in STD algorithms. The corresponding evolution maximum stresses is shown in Figure 8.4. The data provided in Table 8.3, indicate that MESO-ABC breached the stress limits more than other designs, it was recorded 11 violations at stage 1 and 562 violations at stage 2.

Table 8.2 Optimization results for model A4.

Optimization Strategy	**Minimum Cost $\left(\frac{W}{W_0}\right)$**	**Corresponding Roof Frame Structural Mass [tonnes]**	**Corresponding Whole Tank Structural Mass [tonnes]**
Initial Design	**1.0000**	**227.575**	**564.690**
MESO-ABC	**0.2603**	**59.228**	**390.538**
MESO-BA	**0.3037**	**69.106**	**402.181**
MESO-DE	**0.2646**	**60.207**	**391.916**
MESO-PSO	**0.2800**	**63.717**	**394.440**
MESO-SA	**0.3709**	**84.416**	**414.791**
STD-ABC	**0.4621**	**105.152**	**436.967**
STD-BA	**0.5529**	**125.831**	**452.827**
STD-DE	**0.3230**	**73.497**	**400.664**
STD-PSO	**0.3897**	**88.694**	**420.405**
STD-SA	**0.4424**	**100.669**	**427.937**

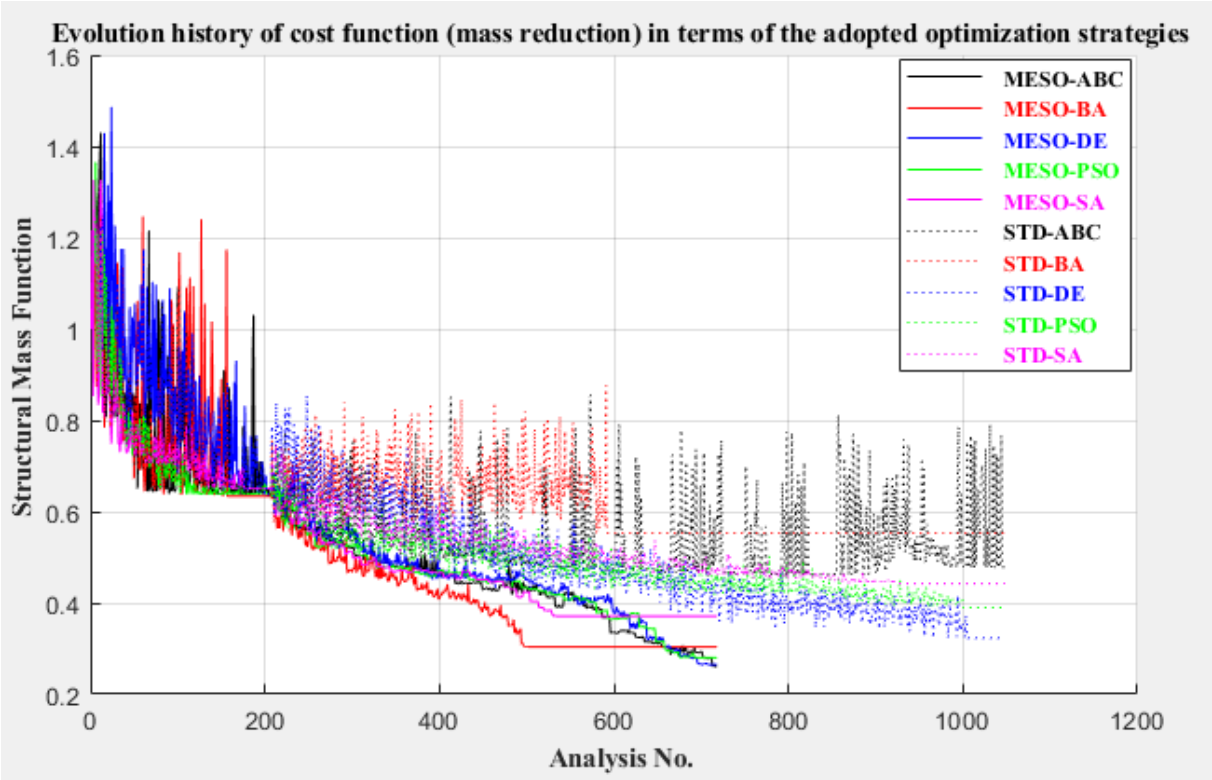

Figure 8.2 Progression history of the cost function towards the optimum for model A4.

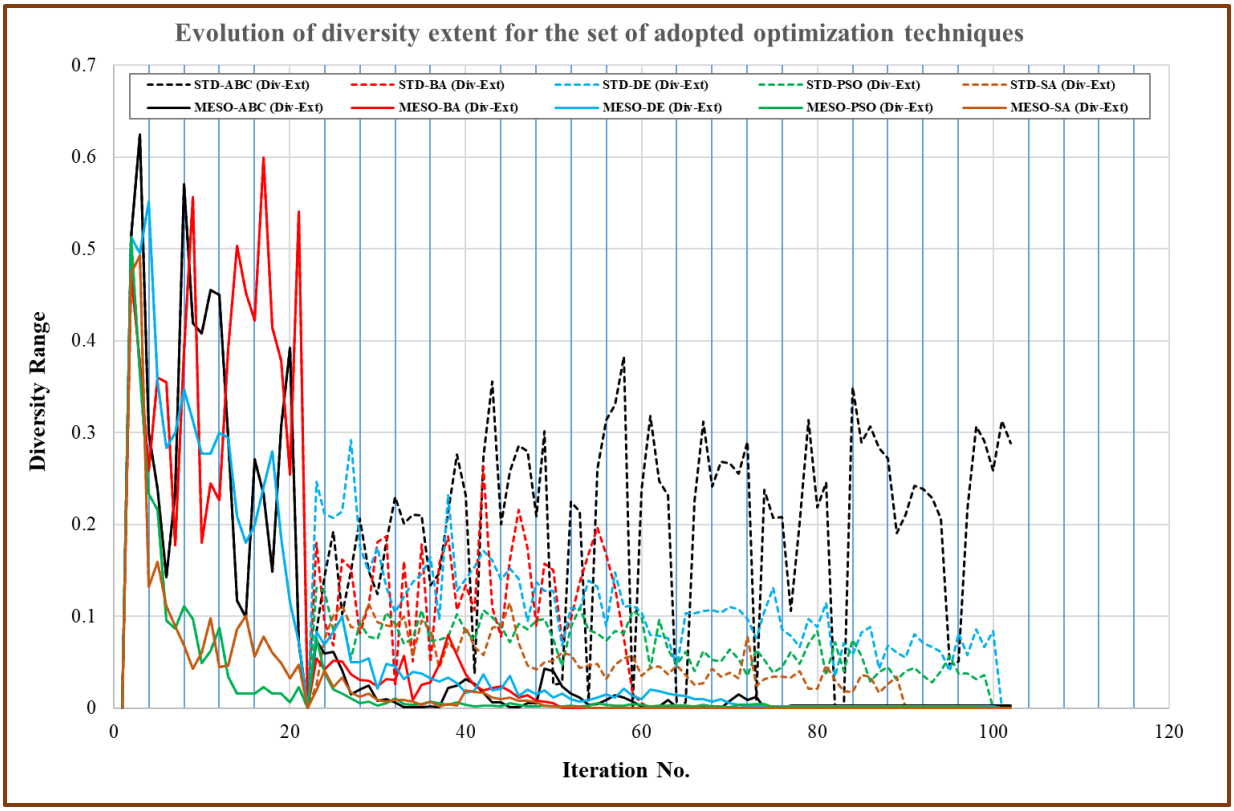

Figure 8.3 Diversity ranges of cost function for the adopted algorithms executed on model A4.

Table 8.3 also reveals that the displacement constraints are much more restrictive than the stress limitations for this model, as the violations recorded for displacement are many times the violations recorded by stress, especially for MESO designs, where MESO-SA has discarded 9 solutions at phase 1 and 2615 solutions at phase 2 due to breaching displacement limits.

MESO-ABC has developed the maximum value of stress 199.69 MPa, whereas the critical absolute displacement (39.96 mm) is found in MESO-SA. The second design affected by the limitations of displacement is MESO-PSO, where 39 penalties are implemented at phase 1 and 2269 penalties are reported at stage 2.

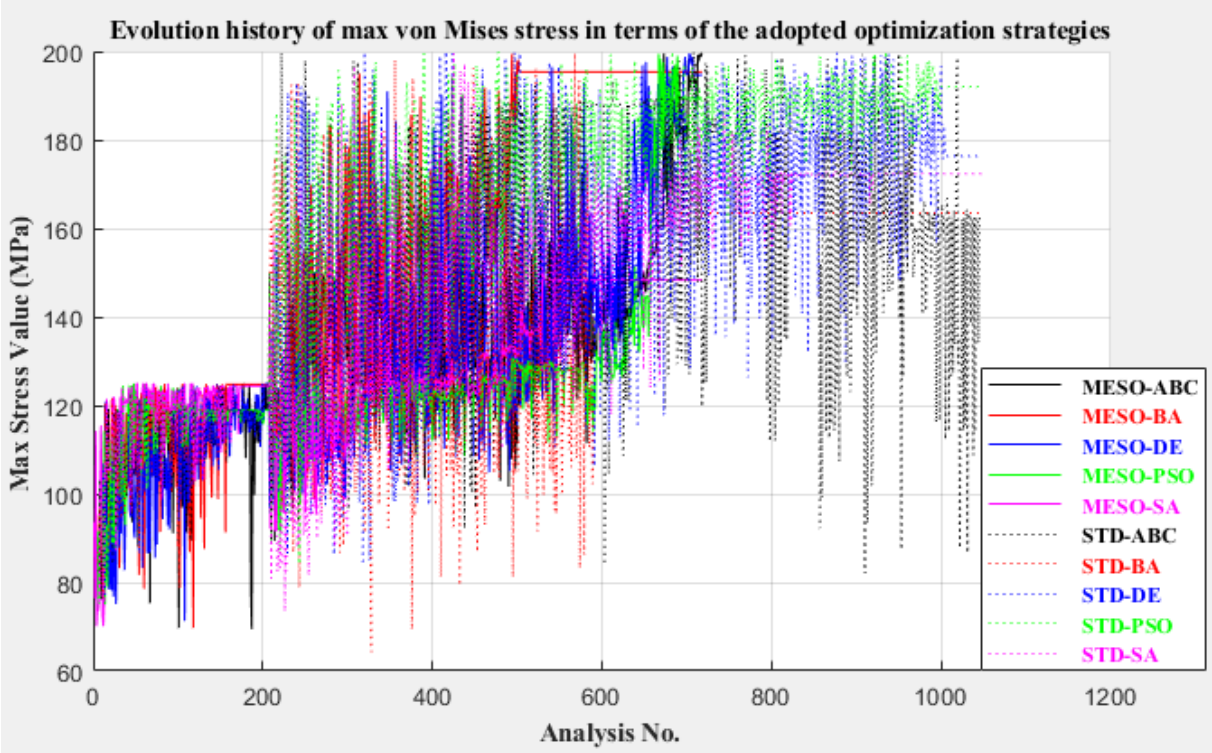

Figure 8.4 Design history of the maximum equivalent stress induced in model A4.

Table 8.3 Data of model A4 showing the number of violations (Stage 1 + Stage 2).

Optimization Method	Solutions lost due to breaching stress	Solutions lost due to breaching displacement	Solutions lost due to breaching buckling
MESO-ABC	**11+562**	**12+1537**	**0+0**
MESO-BA	**28+28**	**12+722**	**0+0**
MESO-DE	**29+81**	**20+1902**	**0+0**
MESO-PSO	**54+8**	**39+2269**	**0+0**
MESO-SA	**38+0**	**9+2615**	**0+0**
STD-ABC	**11+32**	**12+103**	**0+0**
STD-BA	**28+22**	**12+446**	**0+0**
STD-DE	**29+74**	**20+307**	**0+0**
STD-PSO	**54+133**	**39+433**	**0+0**
STD-SA	**38+7**	**9+249**	**0+0**

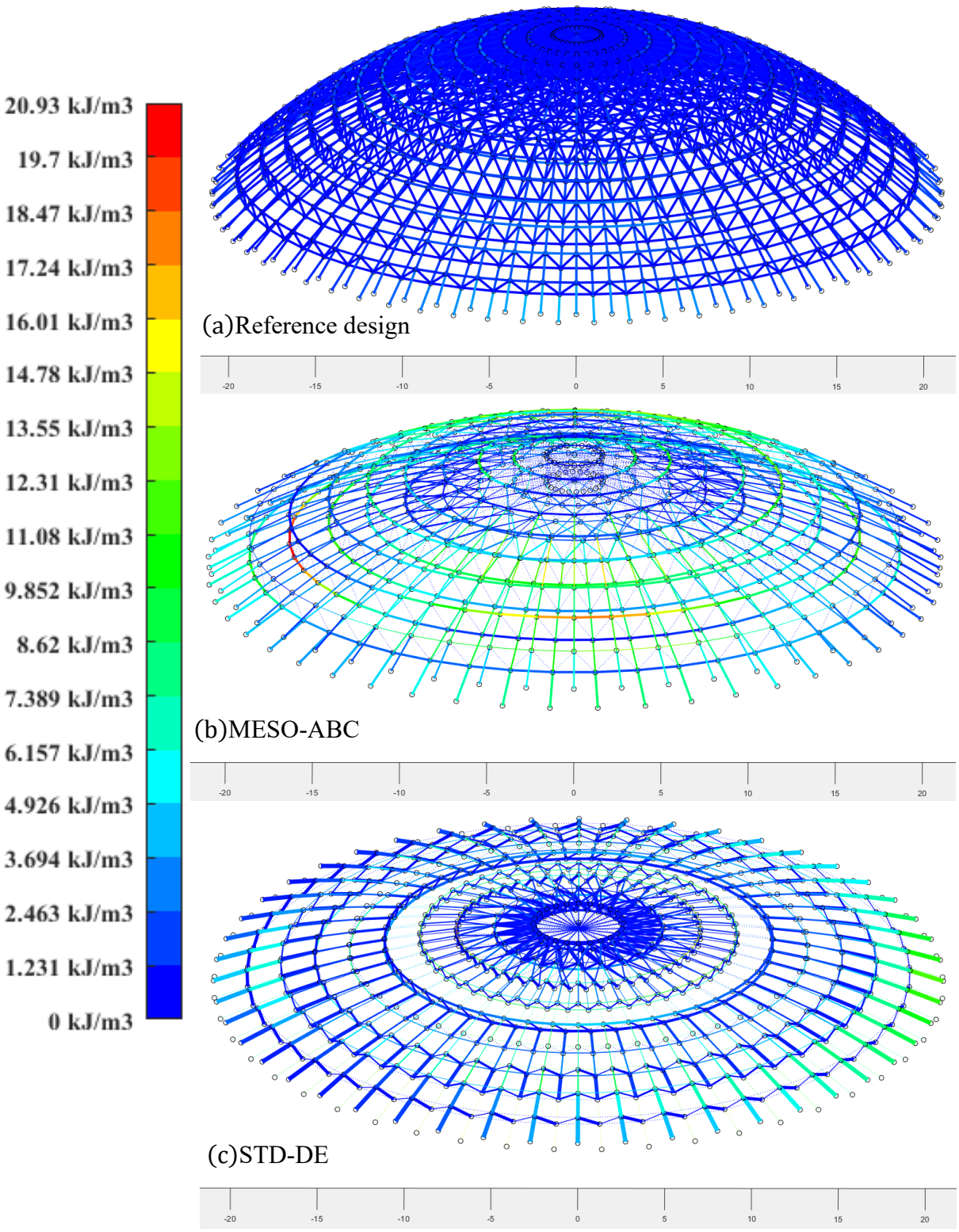

Figure 8.5 Distribution of SED for model A4 (a) Reference design (b) Optimal MESO-based design (MESO-ABC) (c) Optimal STD-based design (STD-DE).

Figure 8.5 shows the difference in the strain energy density SED between the reference design and optimal designs for both of MESO and STD algorithms. The design contours disclose the main merits of MESO compared to STD. First, the resizing operation in MESO based algorithms is implemented in a more systematic manner rather than the multi-dimensional random search adopted by STD based algorithms to produce more consistent geometry with a more homogeneous distribution of constructional material. Second, in addition to the extra saving in structural material, MESO based algorithms produce feasible designs with more conformity with the strict limitations of manufacturing and assembly through selecting more limited ranges for the girders sections in comparison to STD based algorithms.

8.3 Hybrid Schwedler-Lamella Double Lattice Dome (Model D2)

The only difference between this model and the model discussed in section 6.7 is attributed to the adopted optimization ranges between the two models. Accordingly, for the current model the upper bounds of $\mathbf{N_n}$ and $\mathbf{N_r}$ are 80 and 20, whereas the lower bounds are 60 and 12 respectively, the bounds of other variables are identical for the two models. The lower layer for model D2 is axially rotated by $180/\mathbf{N_n}$ with respect to the upper (primary) layer. The reference design comprises of (14+40+38+24+1+19+20=156) components (see Figure 8.6), the number of nodes is 3202, and the number of elements is 12401. Many challenges are associated with this model. First, the size and the nature of the geometry require an efficient optimizer to deal with the situation. Second, the newly proposed topological and shape parameters ($\mathbf{N_s}$, $\mathbf{N_m}$, $\boldsymbol{\eta}$ and $\boldsymbol{\mho}$) along with the strict rules of multiple design constraints represent a significant challenge for the optimizer to solve the problem.

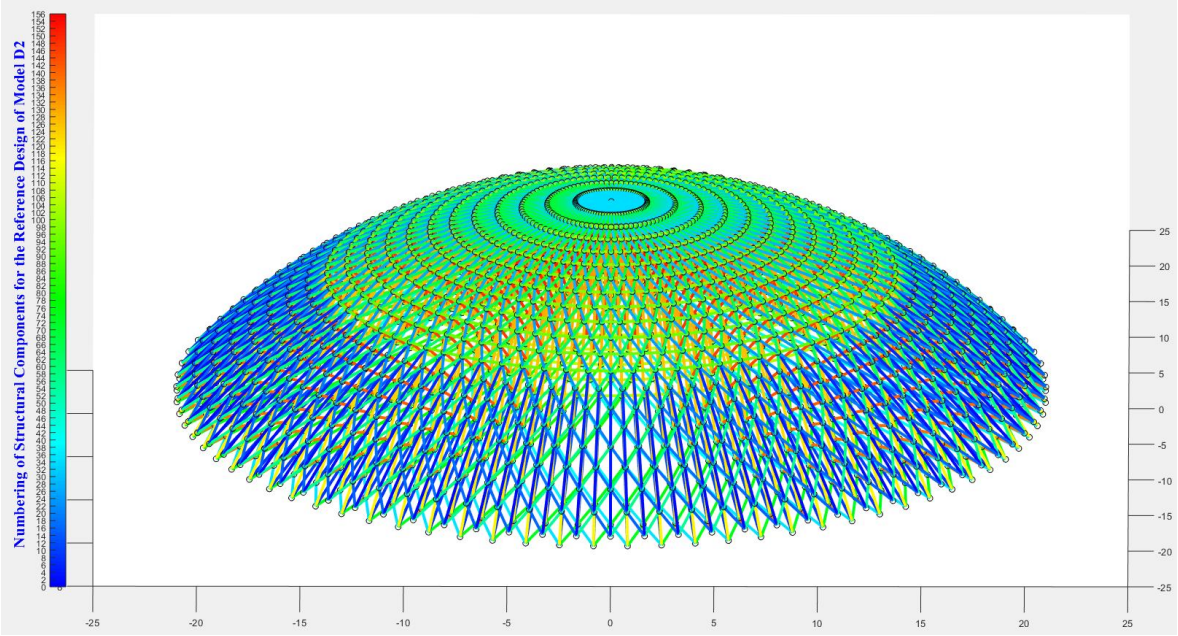

Figure 8.6 Reference design of model D2, showing identification of the structural components.

The convergence curves for cost, plotted in Figure 8.7, highlight the exceptional convergence rates of MESO based methods, where a significant gap in the convergence rates could be recognized evidently between MESO based techniques and STD techniques after 300 analyses onwards at stage 2. The optimum masses for each method are summarized in Table 8.5. Once again, $\mathbf{N_n}$ and $\mathbf{N_r}$ reduce to the lowest possible values of their prescribed design ranges, i.e. 60 and 12 respectively. The optimum values of $\mathbf{N_s}$ are set to the upper limits for the methods ABC and BA, but to lower limits for other designs (DE, PSO, and SA).

The morphological factor $\mathbf{N_m}$ in all optimum solutions has reduced to trim out all radial girders in the structure to generate pure Lamella configuration. The results obtained for $\mathbf{N_m}$ by the designs DE, PSO, and SA for both modes of optimization (MESO and STD) are compatible with the parametric investigation performed for $\mathbf{N_m}$ in section 6.1.2.

The diversity range of cost is plotted against iteration number (MESO step) as illustrated in Figure 8.8 to show how MESO is achieved its goal to reduce the scope of variation gradually during the evolution. MESO and STD are identical at stage 1 (up to it=22), whereas stage 2 show an evident gap between the two groups of strategies (MESO and STD). Accordingly, the average values of diversity ranges recorded by MESO based algorithms in phase 2 are 0.0115, 0.0136, 0.0083, 0.0016, and 0.0019, whereas the average diversity ranges remarked in their counterparts in STD based techniques are 0.1515, 0.1227, 0.072, 0.0531, and 0.0394, which exhibit a considerable gap with respect to MESO based techniques.

Table 8.4 Optimal set for shape and topological variables of model D2.

Optimization Method	**N_n [-]**	**N_r [-]**	**N_s [-]**	**N_m [-]**	**R1 [m]**	**η [-]**	**ʊ [-]**
Initial design	**80**	**20**	**24**	**33**	**30.000**	**0.950**	**1.100**
MESO-ABC	**60**	**12**	**26**	**11**	**56.217**	**0.95**	**0.920**
MESO-BA	**60**	**12**	**28**	**12**	**60**	**0.95**	**0.957**
MESO-DE	**60**	**12**	**10**	**11**	**59.655**	**0.947**	**0.904**
MESO-PSO	**60**	**12**	**10**	**10**	**60**	**0.945**	**0.900**
MESO-SA	**60**	**12**	**10**	**11**	**60**	**0.95**	**0.909**
STD-ABC	**60**	**12**	**26**	**11**	**47.755**	**0.907**	**0.918**
STD-BA	**60**	**12**	**28**	**11**	**49.940**	**0.913**	**0.999**
STD-DE	**60**	**12**	**10**	**10**	**49.611**	**0.939**	**0.962**
STD-PSO	**60**	**12**	**10**	**12**	**49.295**	**0.909**	**0.914**
STD-SA	**60**	**12**	**10**	**10**	**54.373**	**0.880**	**0.910**

Table 8.5 Optimization results for model D2.

Optimization Strategy	Minimum Cost $\left(\frac{W}{W_0}\right)$	Corresponding Roof Frame Structural Mass (tonnes)	Corresponding Whole Tank Structural Mass (tonnes)
Initial Design	**1**	**491.890**	**829.005**
MESO-ABC	**0.1759**	**86.543**	**413.818**
MESO-BA	**0.1580**	**77.716**	**404.617**
MESO-DE	**0.1728**	**84.988**	**411.920**
MESO-PSO	**0.1742**	**85.700**	**412.602**
MESO-SA	**0.1766**	**86.849**	**413.751**
STD-ABC	**0.3908**	**192.247**	**520.749**
STD-BA	**0.4368**	**214.877**	**542.993**
STD-DE	**0.2217**	**109.027**	**437.197**
STD-PSO	**0.2990**	**147.068**	**475.292**
STD-SA	**0.3413**	**167.881**	**495.370**

The design history of maximum equivalent von-Mises stress, demonstrated in Figure 8.9, indicate that the algorithms STD-DE is the most susceptible to the penalties of stress limitations, as it has experienced 99 penalties during the optimization task. In the same topic, only 6 violations are confirmed on the design MESO-BA. There are no outstanding violations to the displacement and buckling constraints noticed for this model.

The design contours, presented in Figure 8.10, compare the state of stress between the reference and optimal results obtained for MESO and STD based algorithms. The optimal design selected for MESO group is MESO-BA with weight 77.716 tonnes, while the optimal design chosen for STD group is STD-DE with weight 109.027 tonnes.

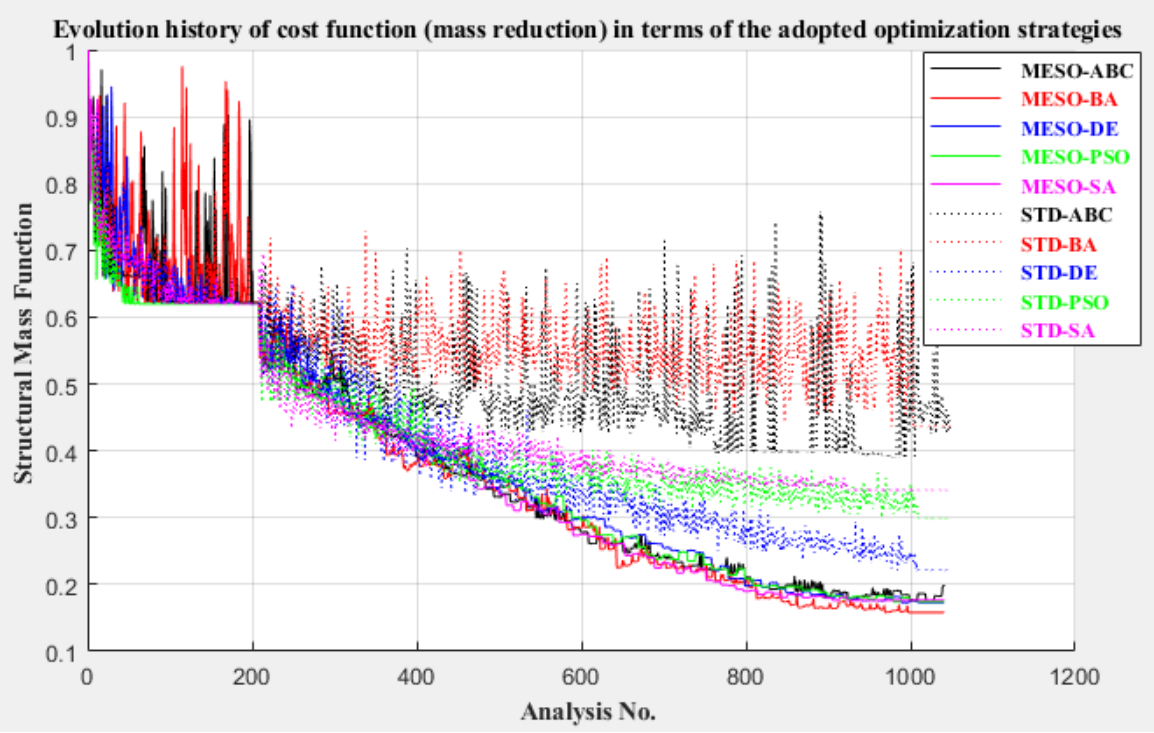

Figure 8.7 Progression history of the cost function towards the optimum for model D2.

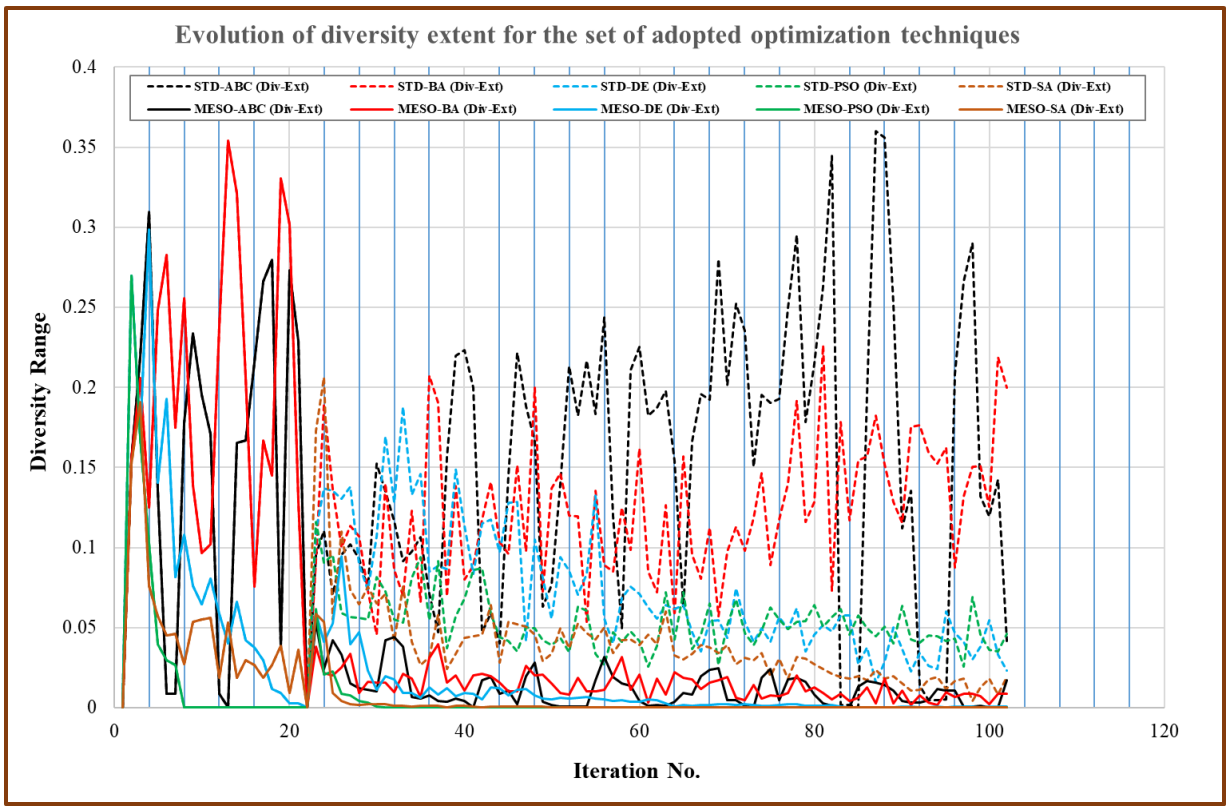

Figure 8.8 Diversity ranges of cost function for the adopted algorithms executed on model D2.

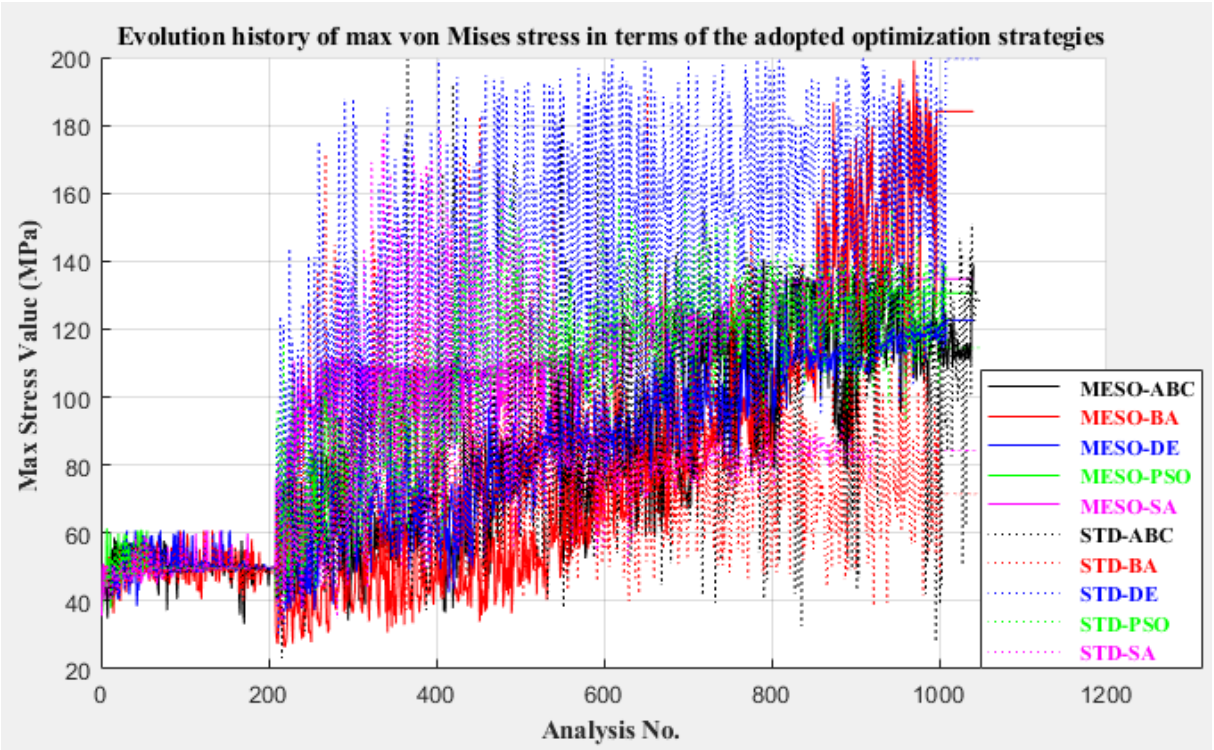

Figure 8.9 Design history of the maximum equivalent stress induced in model D2.

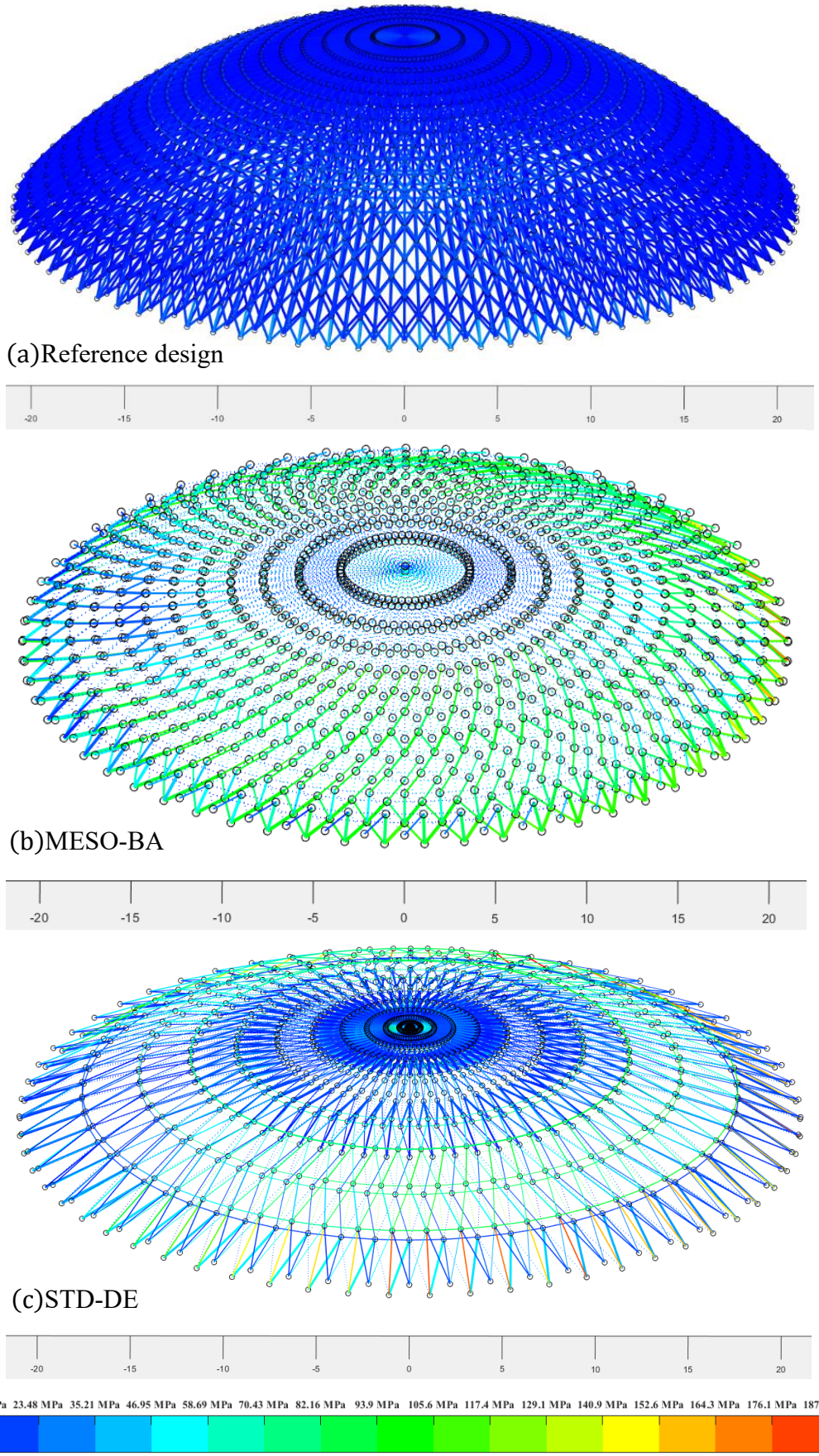

Figure 8.10 Distribution of von-Mises stress for model D2 (a) Reference design (b) Optimal MESO-based design (MESO-BA) (c) Optimal STD-based design (STD-DE).

8.4 The 25-bar Spatial Transmission Tower (Fox and Schmit Model)

The 25-bar 3D transmission tower, see Figure 8.11, is the most popular design example used for comparison in the literature. The optimization results for this example are viewed and discussed considering two different cases for the problem. First, the model is subjected to static design constraints (stress and deflection). Second, the model is subjected to dynamic (frequency) constraints.

The mass density of the structural material is taken as 2767.990 kg/m^3, the modulus of elasticity is 68.950 GPa. The whole structure is subdivided into eight groups modelled using circular cross-sections. The cross-sectional areas of the truss members are the only sizing variables of the problem. Thus, there are 13 design variables in total, 8 of them are sizing variables and 5 are layout variables represented by the coordinates of the nodes 4 and 8, i.e. X4, Y4, Z4, X8 and Y8. The cross-sectional areas are distributed over the range 0.1 in^2 to 3.4 in^2. The model is symmetric about the planes XZ and YZ and nodes 1 and 2 are fixed as shown in Figure 8.11 (at height 200 in and separation 75 in). Manipulating the coordinates for only two nodes (4 and 8) is sufficient to control the geometrical shape of the model. The side constraints imposed on the geometrical variables are given as:

$20 \leq X4 = X5 = -X3 = -X6 \leq 60$ in, $40 \leq Y3 = Y4 = -Y5 = -Y6 \leq 80$ in,

$90 \leq Z3 = Z4 = Z5 = Z6 \leq 130$ in, $40 \leq X8 = X9 = -X7 = -X10 \leq 80$ in,

$100 \leq Y7 = Y8 = -Y9 = -Y10 \leq 140$ in.

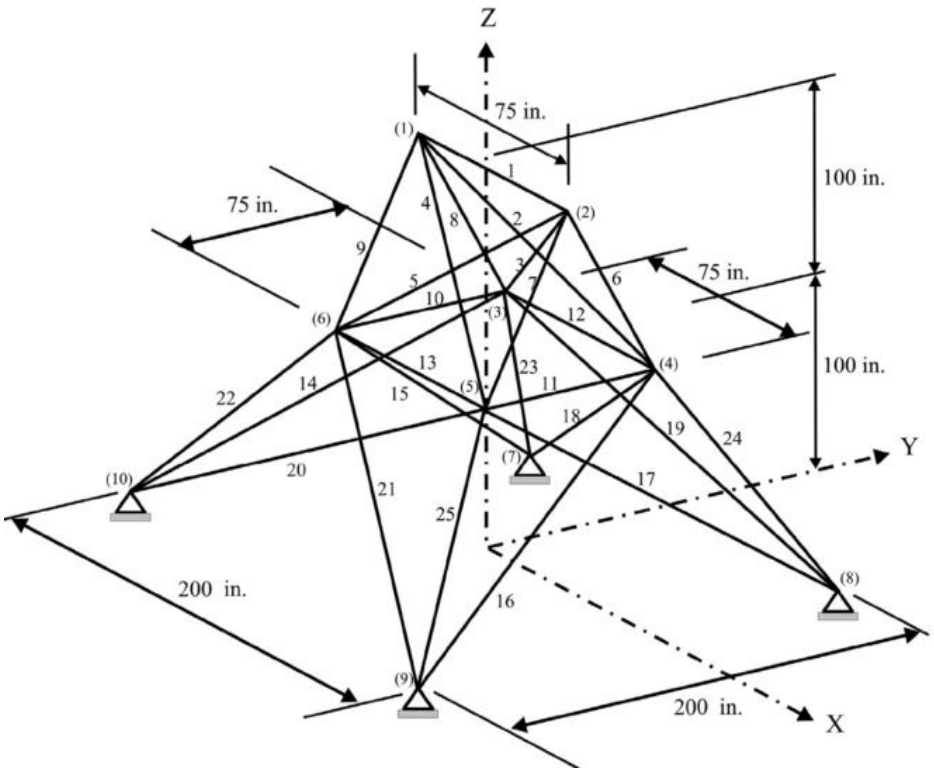

Figure 8.11 Schematic of the 25-bar spatial transmission tower illustrating the boundary conditions and numbering of nodes and elements (Asl *et al.*, 2016).

8.4.1 Optimization Results for Stress and Displacement Constraints (Case 1)

This section will discuss the optimization results for the 25-bar spatial truss subject to displacement and stress constraints. The model is constrained by stress limitations of 40 ksi (275.79 MPa) for tension and compression, and the displacement of all nodes in all directions are restricted to the scope ±0.35 in (±8.89 mm) - see Table 8.8. The model is subjected to the static loading specified in Table 8.7. The results are given in Table 8.9. Group numbers 1, 2, 4, 5, 6 and 7 are inactive components in the structural system, hence their cross-sectional areas have been reduced to the lowest values in their optimization ranges.

This example is used to test many metaheuristic algorithms against robustness and efficiency as summarized in Table 8.6.

Table 8.6 The set of metaheuristic techniques executed on the 25-bar truss (case 1).

Optimization method	Executed by:
JA[1] JA-DSO[2]	Degertekin *et al.* (2018)
HS[3]	Lee and Geem (2004)
Modified HS	Gholizadeh *et al.* (2011)
BB-BC[4]	Kaveh and Talatahari (2009c)
Hybrid HS-BB-BC	Lamberti and Pappalettere (2013)
CMLPSA[5]	Lamberti (2008)
FFA[6]	Degertekin and Lamberti (2013) Degertekin and Hayalioglu (2013)
FFA-DSO[7]	Miguel *et al.* (2013) Talatahari *et al.* (2014)
TLBO-DSO[8]	Cheng *et al.* (2013) Degertekin and Hayalioglu (2013)
D-ICDE[9]	Ho-Huu *et al.* (2015)
iPSO[10]	Mortazavi and Toğan (2016)

[1] Jaya Algorithm.
[2] Jaya Algorithm with discrete sizing optimization.
[3] Harmony Search.
[4] Big Bang–Big Crunch.
[5] Corrected Multi-Level and Multi-Point Simulated Annealing.
[6] Firefly Algorithm.
[7] Firefly Algorithm with discrete sizing optimization.
[8] Teaching-Learning-Based Optimization with discrete sizing optimization.
[9] Improved Constrained Differential Evolution with discrete variables.
[10] integrated Particle Swarm Optimization.

Table 8.9 summarizes the statistical information for the most recent studies implemented on the 25-bar spatial truss including the values of the optimized variables with the corresponding optimum weight, the number of structural analyses (NSA) and the percentage of constraint violations CVP (%) of the considered optimizers. The current optimization strategies (MESO-ABC, MESO-BA, MESO-DE, MESO-PSO, MESO-SA) have achieved a remarkable saving in

computational time, i.e. they fulfilled a considerable reduction in the number of cost evaluations needed to reach optimal weight close to that obtained by other methods mentioned in the table. For instance, MESO-DE has reached the weight 52.080 kg after only 1398 analyses, whereas each of CMLPSA, HHS-LS, HS-BB-BC-LS, FFA-LS, JA, JA-DSO, Modified HS-DSO, iPSO, D-ICDE and TLBO-DSO are executed 3981, 3338, 3734, 4076, 3097, 3795, 5000, 4870, 6000, 50007 structural analyses to reach the steady state evolution at 54.535, 54.847, 54.820, 54.305, 53.049, 53.219, 53.243, 53.186, 53.869, 53.187 kg respectively. The only drawback noticed in the proposed optimization strategies is that they show a slight rise in the number of violations to the design constraints, for instance MESO-PSO has penalized 60 times during this optimization run.

Table 8.7 Loading conditions of the 25-bar truss structure (Ho-Huu *et al.*, 2016b).

Node	F_x (kips)	F_y (kips)	F_z (kips)
1	1	-10	-10
2	0	-10	-10
3	0.5	0	0
6	0.6	0	0

Table 8.8 Element group, stress, and displacement limits of the 25-bar truss (Lamberti, 2008).

Group No.	Element No.	Tension/Compression stress limit [MPa]	Node No.	Displacement limit [mm]
1	1	275.79	1	8.89
2	2, 3, 4, 5	275.79	2	8.89
3	6, 7, 8, 9	275.79	3	8.89
4	10, 11	275.79	4	8.89
5	12, 13	275.79	5	8.89
6	14, 15, 16, 17	275.79	6	8.89
7	18, 19, 20, 21	275.79	-	-
8	22, 23, 24, 25	275.79	-	-

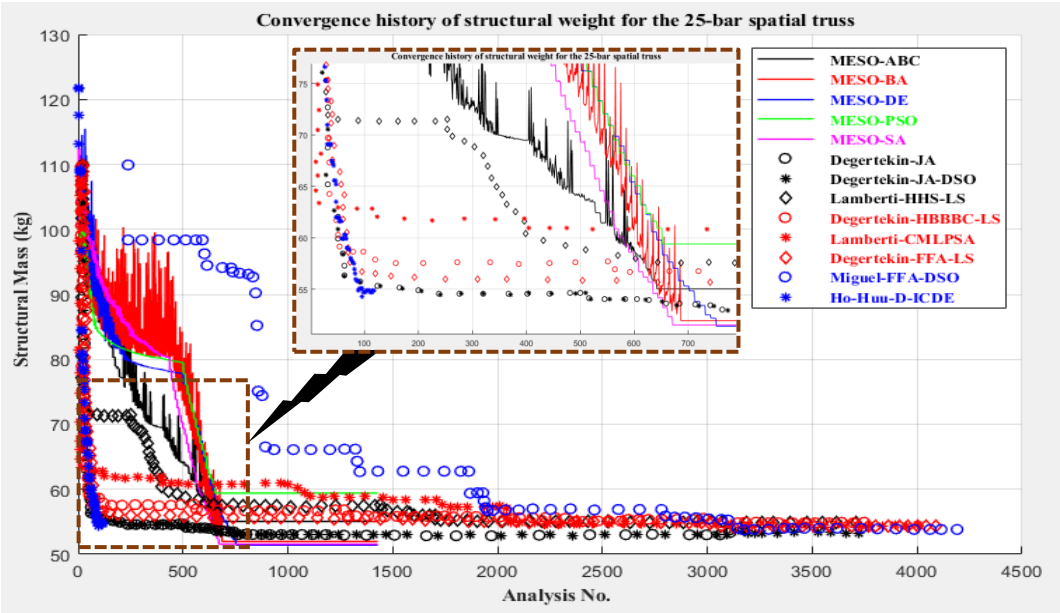

Figure 8.12 Convergence curves for the recent studies executed on the 25-bar truss (case 1).

Table 8.9 Comparison of the optimized designs for the sizing and layout optimization of the 25-bar transmission tower (case 1).

Design variables	CMLPSA[1]	HHS-LS[2]	HS-BB-BC-LS[3]	FFA-LS[4]	JA[5]	JA-DSO (2 stages)[6]	Modified HS-DSO[7]	iPSO-DSO[8]	D-ICDE[9]	TLBO-DSO[10]	MESO-ABC	MESO-BA	MESO-DE	MESO-PSO	MESO-SA
A1 (in^2)	0.1246	0.1041	0.1049	0.1223	0.1	0.1	0.1	0.1	0.1	0.1	0.1	0.1	0.1	0.1	0.1
A2 (in^2)	0.1251	0.1189	0.1274	0.1197	0.1	0.1	0.1	0.1	0.1	0.1	0.1	0.1	0.1	0.1	0.1
A3 (in^2)	0.9462	0.9156	0.9090	0.8684	0.9374	1.0	1.0	1.0	0.9	1.0	0.7926	0.9490	1.0384	1.2432	1.0384
A4 (in^2)	0.1001	0.1028	0.1038	0.1007	0.1	0.1	0.1	0.1	0.1	0.1	0.1	0.1	0.1	0.1	0.1
A5 (in^2)	0.1093	0.1424	0.1006	0.1009	0.1	0.1	0.1	0.1	0.1	0.1	0.1	0.1	0.1	0.1	0.1
A6 (in^2)	0.1137	0.1192	0.1128	0.1160	0.1	0.1	0.1	0.1	0.1	0.1	0.1	0.1	0.1	0.1	0.1
A7 (in^2)	0.1407	0.1405	0.1484	0.2392	0.1057	0.1	0.1	0.1	0.1	0.1	0.1433	0.1433	0.1	0.1	0.1
A8 (in^2)	0.9094	0.9254	0.9392	0.8280	0.9219	0.9	0.9	0.9	1.0	0.9	1.1362	1.0384	1.0384	1.2432	1.0384
X4 (in)	33.245	34.161	33.556	31.565	37.801	37.107	37.820	37.6	36.83	37.657	20	20.109	20.526	20	20.213
Y4 (in)	57.016	62.049	61.749	56.007	55.063	54.255	55.485	54.46	58.53	54.496	48.549	50.339	42.270	40	41.595
Z4 (in)	125.645	119.690	119.176	129.824	129.998	129.998	128.730	130.00	122.67	130.000	108.307	99.420	90	90	90.094
X8 (in)	44.745	44.006	42.825	41.620	51.023	52.008	52.068	51.89	49.21	51.887	48.034	44.395	40.029	40	40.994
Y8 (in)	136.458	136.921	136.160	139.939	140.000	140.000	139.590	139.55	136.74	139.521	132.137	106.380	100.045	100	100.002
Weight (kg)	54.535	54.847	54.820	54.305	53.049	53.219	53.243	53.186	53.869	53.187	55.486	52.295	52.080	60.586	52.129
CVP (%)	None	None	0.2	None	None	None	0.0826	None	0.266	0.114	0.0763	0.0791	0.7439	3.3538	2.5437
NSA	3981	3338	3734	4076	3097	3795	5000	4870	6000	50007	1311	1264	1398	1789	1486

[1] Lamberti, L. (2008).
[2] Degertekin, S. O. and Lamberti, L. (2013).
[3] Lamberti and Pappalettere (2013).
[4] Degertekin, S. O. and Lamberti L. (2013).
[5] Degertekin, Lamberti et al. (2018).
[6] Degertekin, Lamberti et al. (2018).
[7] Gholizadeh, Barzegar et al. (2011).
[8] Mortazavi and Toğan (2016).
[9] Ho-Huu, Nguyen-Thoi et al. (2015).
[10] Cheng, Liu et al. (2013).

Figure 8.12 compares diverse convergence rates for the methods used in the previous works. The graph indicates that MESO-DE is the most promising method used to perform a simultaneous shape, topology and sizing optimization for the adopted truss model. MESO-DE, MOSO-SA and MESO-BA resulted in the lowest structural masses: 52.080, 52.129 and 52.295 kg respectively. The optimal topology of the best design (MESO-DE) was compared to those found in the literature in Figure 8.13.

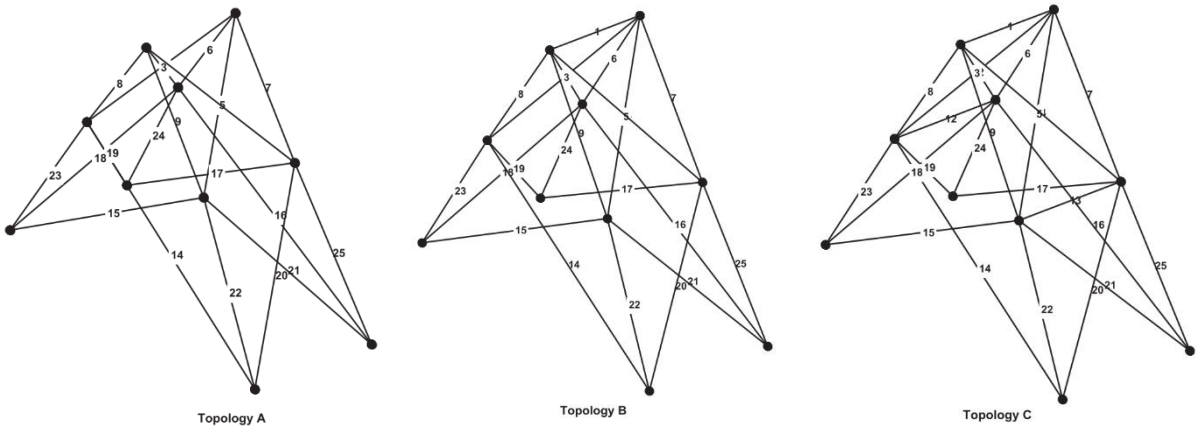

(a) Multimodal optimization using FFA adopted by Miguel *et al.* (2013).

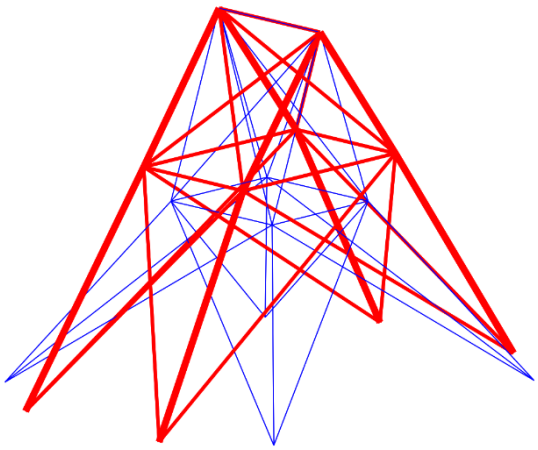

(b) D-ICDE with DSO adopted by Ho-Huu *et al.* (2015).

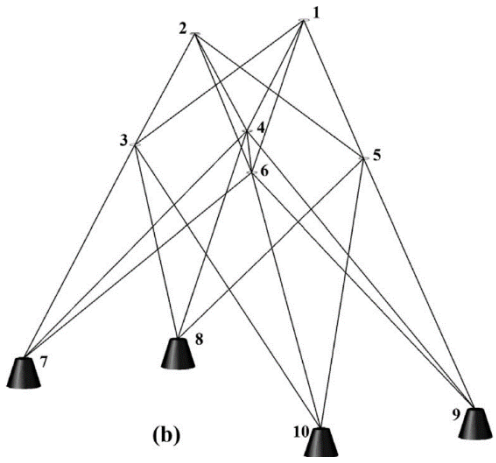

(c) Improved Passing Vehicle Search (IPVS) adopted by Tejani *et al.* (2018).

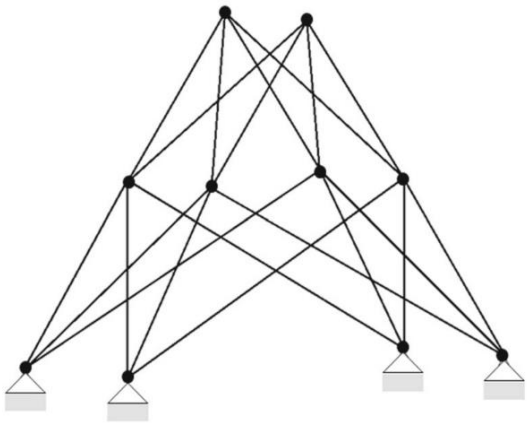

(d) iPSO with DSO adopted by Mortazavi and Toğan (2016).

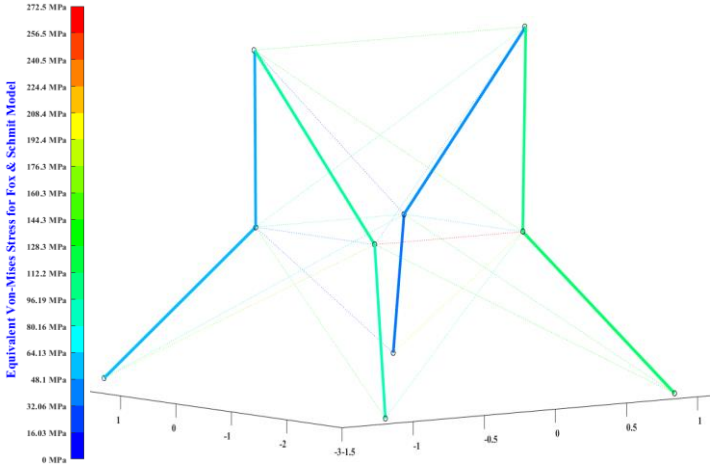

(e) MESO-DE with DSO (current study).

Figure 8.13 Samples of the optimal topologies determined for the size, shape, and topology optimization of the 25-bar 3D transmission tower (case 1).

8.4.2 Optimization Results for Stress, Displacement and Buckling Constraints (Case 2)

In addition to stress and displacement constraints defined in section 8.4.1, the model will be subject to buckling constraints through introducing compressive stress limits as illustrated in Table 8.11. The eight cross-sectional areas of the truss members are the only design variables of the problem, i.e. there is no shape or topology optimization in this case. Thus, MESO can be used to obtain the optimum solution through introducing the buckling indicator ($\xi_i^{buck\_ind}$) as given in Eq. (8.1).

$$\xi_i^{buck\_ind} = \frac{F_i^{comp}}{\overline{\sigma_a}} \tag{8.1}$$

which is evaluated for each member (i). F_i^{comp} is the axial stress for member (i), $\overline{\sigma_a}$ is the allowable compressive stress for each member (i) as explained in Table 8.11. The main purpose of this investigation is to show the robustness and efficiency of MESO to treat with sizing variables compared to the results produced by the conventional metaheuristic techniques. This case was considered by many researchers as detailed in Table 8.10.

Table 8.10 The set of metaheuristic techniques executed on the 25-bar truss (case 2).

Optimization method	Executed by:
TLBO[1]	Camp and Farshchin (2014)
HGA[2]	Asl *et al.* (2016)
aeDE[3]	Ho-Huu *et al.* (2016b)
IFA[4]	Kaveh and Talatahari (2009c)
[1] Teaching-Learning-Based Optimization. [2] Hybridized Genetic Algorithm. [3] adaptive elitist Differential Evolution. [4] Improved Firefly Algorithm.	

Table 8.11 Stress (tension/compression) limits for the 25-bar spatial truss (Lamberti, 2008).

Group No.	**Elements**	**Compression stress limit $\overline{\sigma_a}$ [MPa]**	**Tension stress limit σ_{yp} [MPa]**
1	**1**	**-242.04**	**275.79**
2	**2, 3, 4, 5**	**-79.939**	**275.79**
3	**6, 7, 8, 9**	**-119.36**	**275.79**
4	**10, 11**	**-242.04**	**275.79**
5	**12, 13**	**-242.04**	**275.79**
6	**14, 15, 16, 17**	**-46.619**	**275.79**
7	**18, 19, 20, 21**	**-47.998**	**275.79**
8	**22, 23, 24, 25**	**-76.435**	**275.79**

Table 8.12 Comparison of optimization results with the recent works executed on the 25-bar truss problem (case 2).

Design variables	TLBO[1]	HGA[2]	aeDE[3]	IFA[4]	MESO	STD-ABC	STD-BA	STD-DE	STD-PSO	STD-SA
A1 (in^2)	0.100	0.010	0.100	0	0.1	0.206	0.157	0.100	0.100	0.246
A2 (in^2)	0.300	1.986	0.300	1.687	0.1	0.522	0.100	0.100	0.100	0.100
A3 (in^2)	3.400	2.998	3.400	3.344	3.346	3.043	3.205	2.955	3.077	3.346
A4 (in^2)	0.100	0.010	0.100	0	0.1	0.462	0.100	0.100	0.225	0.143
A5 (in^2)	2.100	0.010	2.100	0	0.1	1.636	0.125	0.108	0.100	0.189
A6 (in^2)	1.000	0.681	1.000	1.004	0.246	0.725	0.108	0.100	0.100	0.100
A7 (in^2)	0.500	1.673	0.500	1.972	1.782	1.175	0.433	0.100	0.246	0.580
A8 (in^2)	3.400	2.664	3.400	2.269	3.346	3.315	2.802	2.234	2.037	3.346
Best Weight (kg)	219.838	247.057	219.84	256.910	215.578	227.922	215.195	215.001	215.851	218.481
NSA	2000	5000	1440	9960	110	490	1316	1035	1063	1032

[1] Camp and Farshchin (2014).
[2] Asl, Aslani et al. (2016).
[3] Ho-Huu, Nguyen-Thoi et al. (2016).
[4] Wu, Li et al. (2017).

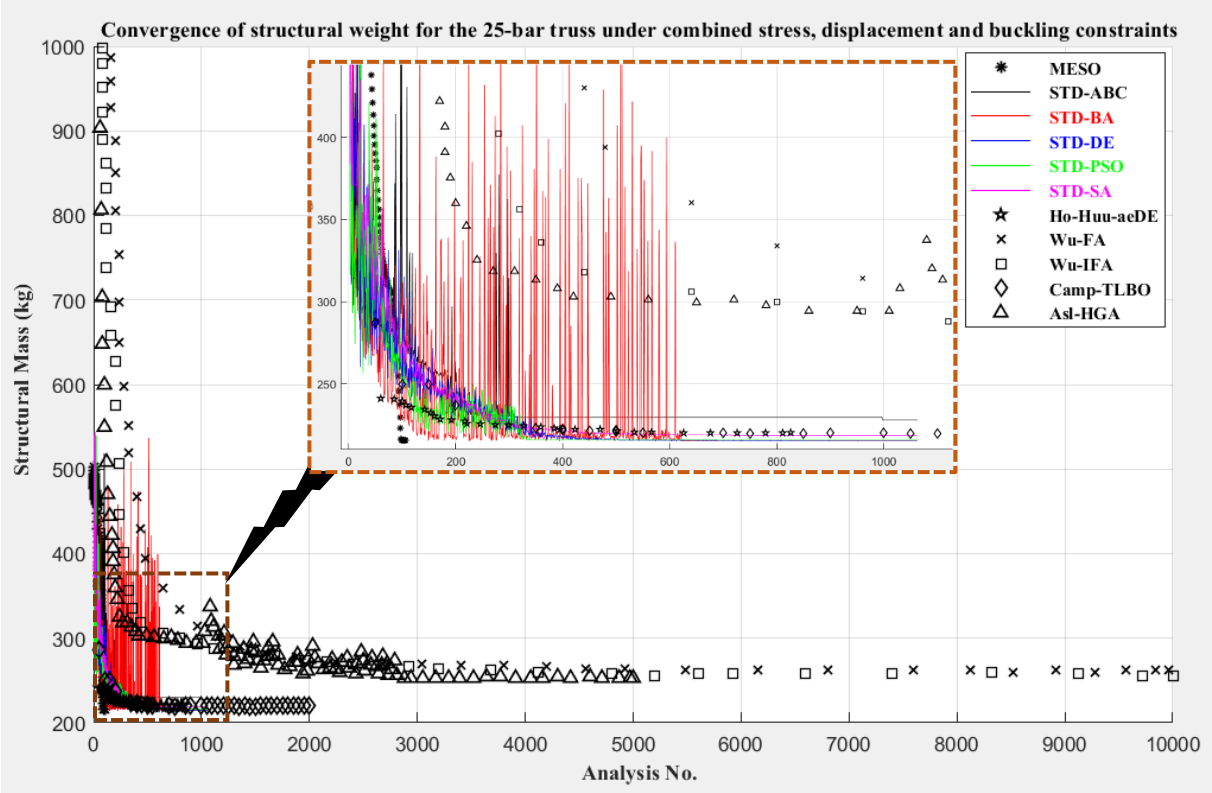

Figure 8.14 Comparison of the convergence history for the 25-bar truss subjected to combined stress, deflection and buckling constraints (case 2).

The results are listed in Table 8.12. MESO has achieved promising reduction in structural weight (from 501.938 kg to 215.578 kg) in only 110 analyses using buckling criterion, where MESO removes superfluous material depending on the buckling sensitivity numbers defined in Eq. (5.26). The results show that the conventional metaheuristic techniques, adopted in this work, have gave an acceptable result after consuming much more analyses. The lightest weight is obtained by MESO. It also achieved a significant saving in computational time.

8.5 The 120-bar Spatial Dome Truss (Soh and Yang Model)

The popular example 120-bar dome truss is considered for the comparison with other literature. The general outline of this truss structure is clearly sketched in Figure 8.15 to show the group number and node number. The modulus of elasticity is 210 GPa and the material density is 7971.810 kg/m^3. The structural material is steel with yield stress 400 MPa.

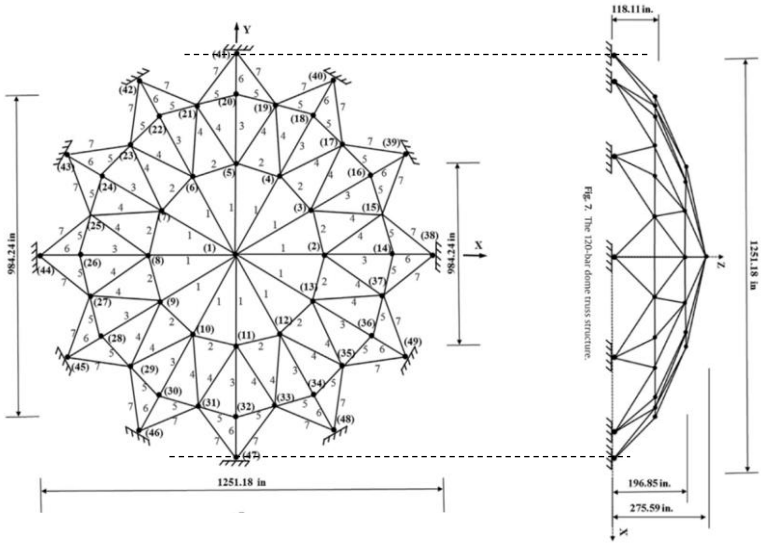

Figure 8.15 Schematic of the 120-bar space dome truss.

Vertical nodal loads have been applied at all unsupported joints such that 60 kN is applied at node 1, 30 kN at nodes 2 through 13 and 10 kN at nodes 14 through 37. There is no topological or shape optimization associated with this model, hence the sizing variables represented by the cross-sectional areas of the structural members are the only design variables of the problem. With discretising the model into 7 axisymmetric components, only 7 sizing variables need to be optimized to obtain the optimum design. The minimum cross-sectional area found in the discrete set circular sections is 5 cm^2, whereas the maximum area is 129.032 cm^2.

Static (stress, displacement and buckling) and dynamic (frequency) constraints are considered.

8.5.1 Optimization Results for Static Analysis (Case 1)

Three constraints are considered in this case (Kaveh and Talatahari, 2009c):

- Stress constraints: defined by the allowable stress ($\sigma_a = 0.6 * \sigma_{yp}$), where σ_{yp} is the yield stress of the structural material (400 MPa).
- Displacement constraints: 5 mm is imposed on all nodes in all directions.
- Compressive instability: a specific allowable stress ($\overline{\sigma_a}$) for each compressively stressed member is introduced.

$$\overline{\sigma_a} = \begin{cases} \dfrac{\left[\left(1 - \dfrac{\lambda_i^2}{2C_c^2}\right)\sigma_{yp}\right]}{\left(\dfrac{5}{3} + \dfrac{3\lambda_i}{8C_c} + \dfrac{\lambda_i^3}{8C_c^3}\right)} & \text{for } \lambda_i < C_c \\ \dfrac{12\pi^2 E}{23\lambda_i^2} & \text{for } \lambda_i \geq C_c \end{cases} \quad (8.2)$$

where, E is the elastic modulus, C_c is the characteristic slenderness coefficient separating between the elastic and inelastic buckling regions ($C_c = \sqrt{2\pi^2 E/\sigma_{yp}}$), λ_i is the slenderness ratio for member (i), which is given as ($kL_i/\bar{\kappa}_i$), k is the effective length factor, L_i is the length of the member (i) and $\bar{\kappa}_i$ is the radius of gyration, which is correlated to the cross section area (A_i) of the member (i), i.e. $\bar{\kappa}_i = aA_i^b$, where a = 0.4993 and b= 0.6777 are adopted for bars with circular sections.

Many optimization methods have been tested for computational efficiency using this example such as the methods listed in Table 8.13.

Table 8.13 The set of metaheuristic techniques executed on the 120-bar dome truss (case 1).

Optimization method	Executed by:
PSACO[1]	Kaveh and Talatahari (2008)
HPSACO[2]	Kaveh and Talatahari (2009b)
HBB-BC[3]	Kaveh and Talatahari (2009c)
CMA-ES[4]	Kaveh *et al.* (2011)
PSRO[5] PSOPC[6]	Kaveh and Javadi (2013)
ICDE[7] SORA-ICDE[8]	Ho-Huu *et al.* (2016a)
[1] PSO and ACO. [2] Hybrid PSO and ACO. [3] Hybrid Big Bang–Big Crunch. [4] Covariance Matrix Adaptation Evolution Strategy. [5] PSO with Ray Optimization. [6] PSO with Passive Congregation. [7] Improved Constrained Differential Evolution. [8] Sequential Optimization with Reliability Assessment ICDE.	

Table 8.14 Comparison of the optimized designs for the sizing optimization of the 120-bar space dome truss (case 1).

Design variables	PSACO[1]	HPSACO[2]	HBB-BC[3]	CMA-ES[4]	ICDE[5]	SORA-ICDE[6]	MESO (current)	STD-ABC (current)	STD-BA (current)	STD-DE (current)	STD-PSO (current)	STD-SA (current)
A1 (in^2)	3.026	3.095	3.037	3.025	2.4896	2.4700	4.495	4.495	3.875	2.635	9.455	2.945
A2 (in^2)	15.222	14.405	14.431	14.73	15.2608	18.6943	6.045	10.385	6.665	9.765	6.975	15.655
A3 (in^2)	4.904	5.020	5.130	5.153	5.0172	6.7604	8.525	4.805	4.495	7.905	4.495	8.525
A4 (in^2)	3.123	3.352	3.134	3.136	2.5952	2.9971	4.805	2.325	5.115	2.945	4.185	2.325
A5 (in^2)	8.341	8.631	8.591	8.437	9.0277	11.8378	4.185	4.805	3.255	2.015	2.325	2.015
A6 (in^2)	3.418	3.432	3.377	3.306	3.4898	4.2042	0.775	2.015	5.735	1.085	0.775	0.775
A7 (in^2)	2.498	2.499	2.500	2.495	2.3657	2.3672	0.775	8.215	4.495	2.325	5.735	0.775
Weight (kg)	15082.347	15075.546	15093.229	15078.856	14678.450	17714.978	14693.480	15628.236	15285.724	12673.108	13801.876	14384.611
CVP (%)	2.5	None	1.2	2	None	None	None	11.333	10.889	5.667	4.1333	3
NSA	32600	10000	10000	10000	9030	93990	180	900	900	900	750	900

[1] Kaveh and Talatahari (2008).
[2] Kaveh and Talatahari (2009).
[3] Kaveh and Talatahari (2009).
[4] Kaveh, Kalateh-Ahani et al. (2011).
[5] Kaveh and Javadi (2013).
[6] Kaveh and Javadi (2013).

Table 8.14 presents the optimal designs for this model obtained by this work (MESO and STDs) and other algorithms from the literature. The optimum design found by STD-DE is the best overall. However, in terms of the lowest number of cost evaluations, MESO has occupied the first rank, since it announced a feasible design with weight 14693.48 kg in only 180 structural analyses. It was followed by STD-PSO with appreciably heavier weight (13801.876 kg) obtained after 750 successful evaluations. Thus, MESO is the ideal method used to alleviate the burden of computation, especially for large-scale integrated structures, where executing only one optimization cycle for such structures might consume tens of minutes or several hours. Ultimately, MESO has effectively reduced the computational time, to obtain approximately the same result as other techniques or (in some cases) better. Also, the conventional metaheuristics adopted in this work have experienced many penalties, for instance, STD-ABC, STD-BA and STD-DE have penalized 102, 98 and 51 times due to breaching displacement and buckling limits. Figure 8.16 compares the convergence curves recorded for the optimization runs of this model. A high perturbation can be seen in STD-ABC and STD-BA due to the high degree of randomization adopted by these methods.

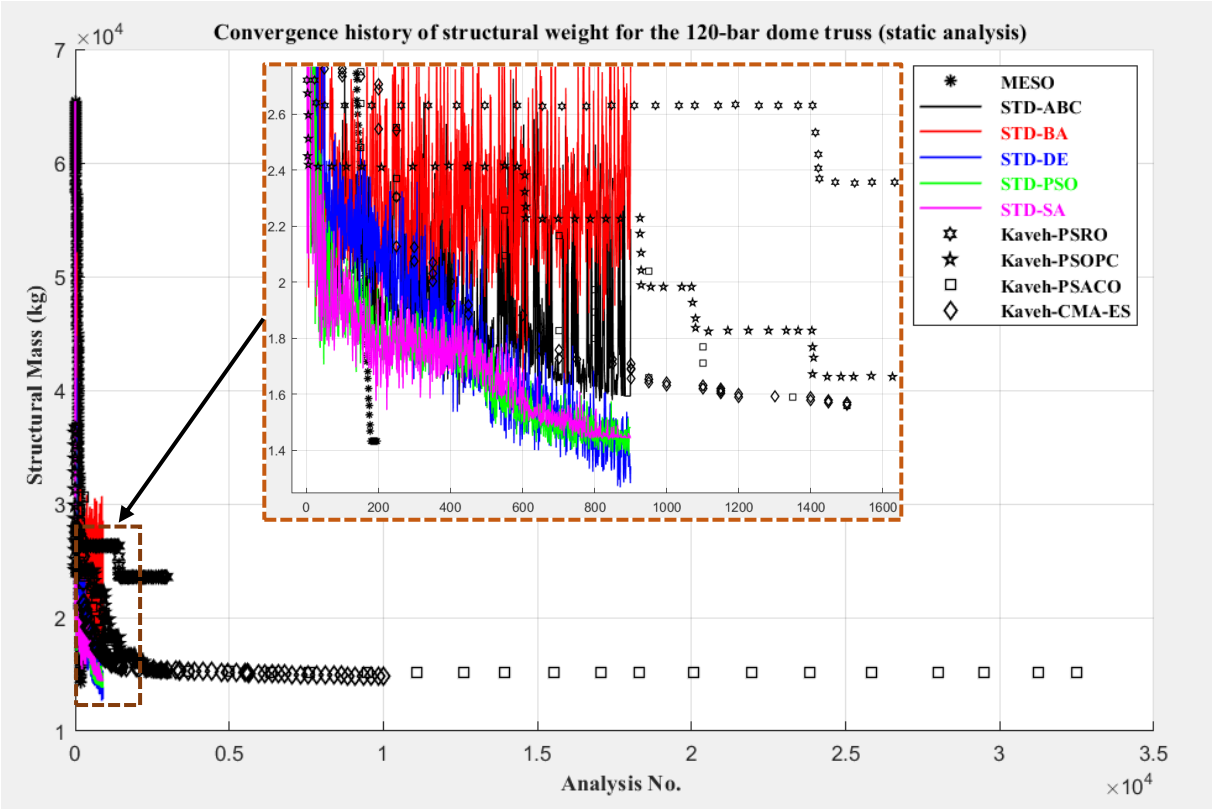

Figure 8.16 Convergence curves for the most recent studies implemented on the 120-bar truss (case 1).

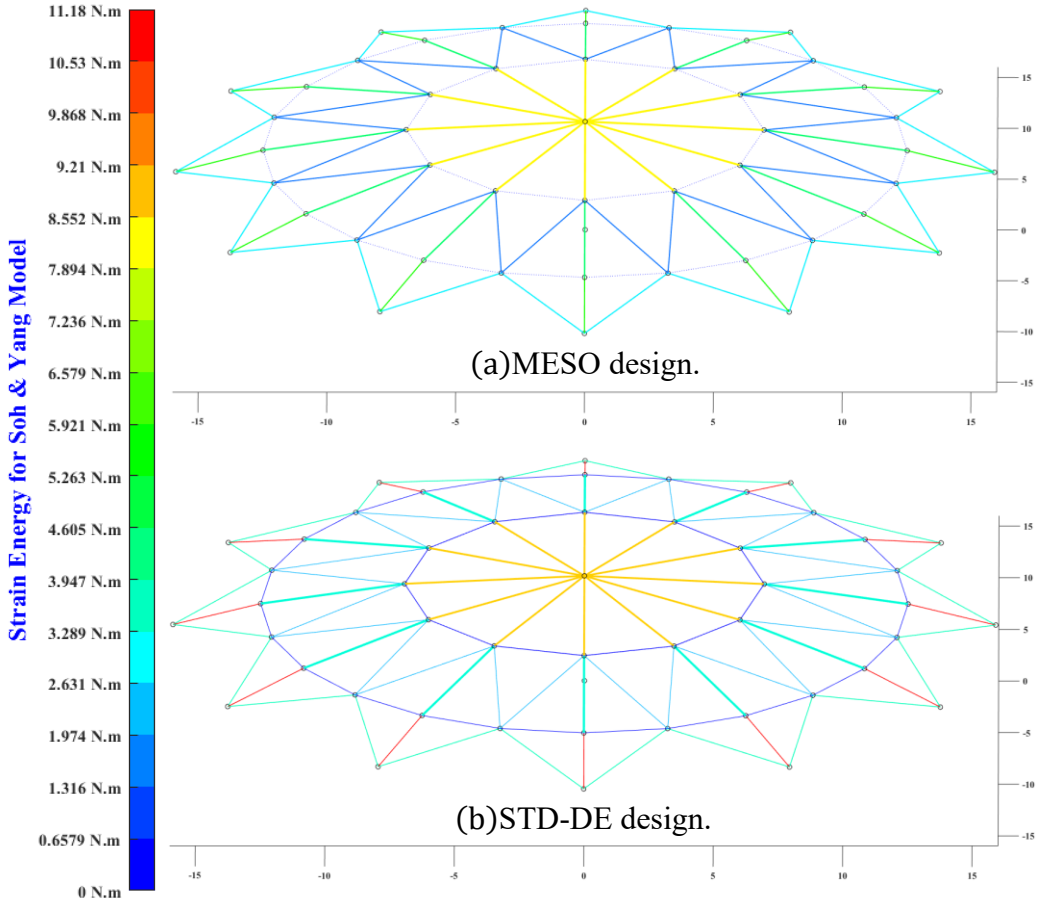

Figure 8.17 The state of strain energy for the optimum designs of the 120-bar truss (case 1).

A steep progression can be seen in MESO curve to achieve the optimum within 180 cost evaluations. However, lighter masses are achieved by STD-DE, STD-PSO and STD-SA with 12673.108, 13801.876 and 14384.611 kg after 900, 750 and 900 evaluations respectively. Ultimately, MESO has achieved appreciable reduction in weight with a significant gain in the number of analyses compared to conventional metaheuristic methods. STD-DE has achieved the lowest mass in the group (12673.108 kg) after 900 analyses. The distribution of strain energy for the optimal designs, shown in Figure 8.17, indicates that the radial girders are the most influenced part of the dome frame, as they bear axial compressive loads causing buckling problems.

8.5.2 Optimization Results for Dynamic (Frequency) Analysis (Case 2)

This case considers the frequency characteristics of the model. The same geometry data mentioned in section 8.5.1 is used, but the design constraints are restricted to the limitations set on the natural frequency of the system, where the first mode natural frequency (ω_1) must be greater than 9 Hz and the second mode natural frequency (ω_2) must be greater than 11 Hz. Lumped masses were added to the nodes with the magnitudes: 3000 kg added to node 1, 500 kg added to nodes 2 through 13 and 100 kg added to the nodes 14 through 37. The frequency optimality criterion, defined in section 5.4.3, will be utilized to guide MESO technique to the optimum point.

Five metaheuristic techniques (HS[1], BB-BC[2], FA[3], CSS[4], ERO[5]), selected from the literature as reported by Kaveh and Zolghadr (2014), will be compared with the current results represented by MESO and the five conventional metaheuristic techniques adopted in this work (STD-ABC, STD-BA, STD-DE, STD-PSO and STD-SA). A diversity index was first introduced by Kaveh and Zolghadr (2012) to measure the capability of the metaheuristic technique to explore/exploit the data within design space. Thence, it was modified by Kaveh and Zolghadr (2014) to estimate the average (normalized) distance of particles from the global optimum.

$$Diversity\ Index = \frac{1}{nPop}\sum_{j=1}^{nPop}\sqrt{\sum_{i=1}^{N}\left(\frac{GB(i)-X_j(i)}{X_i^{max}-X_i^{min}}\right)^2} \tag{8.3}$$

nPop is the number of particles (population size), N is the number of design variables. $X_j(i)$ is the value of the ith variable concerning the jth particle. X_i^{max} and X_i^{min} are the upper and lower

[1] Harmony Search
[2] Big Bang-Big Crunch
[3] Firefly Algorithm
[4] Charged System Search
[5] Enhanced Ray Optimization

bounds for the ith variable. $GB(i)$ is the ith variable belonging to the position vector of the (current) global optimum.

The optimal results for this example are provided in Table 8.15. The data included disclose two merits for MESO. First, it converges rapidly compared to the metaheuristic algorithms such that it found the optimum in only 194 optimization cycles, while other methods are executed at least 845 cycles (STD-ABC) to reach approximately the same result as MESO does. Some cases are carried out 4000 analyses to reach the optimum, such as HS adopted by Kaveh and Talatahari (2009b). MESO achieved the lowest mass for this model (8771.12 kg) - see Table 8.15. MESO chooses the appropriate optimality criterion for the case, therefore MESO will be guided to the optimum without the need to adopt the trial and error approach of metaheuristic techniques.

Figure 8.18 shows the state of strain energy for the two most promising designs. It shows that the stiffness optimality criterion adopted for this case has directed MESO to enhance the radial girders and reduce the dimensions for other parts of the dome structure.

Figure 8.19 explains the progression history of diversity index for various metaheuristic algorithms. The smoothest progression is observed in STD-PSO and STD-SA, whereas STD-BA (by its nature) keeps progressing randomly with no convergence. Other methods are located in-between. Since this factor is set to measure the capability of the method to explore or exploit, it could be inferred that STD-BA has an extraordinary explorative capability, whereas STD-PSO and STD-SA could be classified as highly exploitative tools.

Table 8.15 Comparison of optimization results with the recent works executed on the 120-bar truss problem (case 2).

Design variables	**HS** (Kaveh)	**BB-BC** (Kaveh)	**FFA** (Kaveh)	**CSS** (Kaveh)	**ERO** (Kaveh)	**MESO** (current)	**STD-ABC** (current)	**STD-BA** (current)	**STD-DE** (current)	**STD-PSO** (current)	**STD-SA** (current)
A1 (in^2)	**3.0713**	**3.0214**	**3.0532**	**3.0154**	**3.2823**	**3.5650**	**2.6350**	**9.4550**	**0.7750**	**0.7750**	**10.3850**
A2 (in^2)	**6.2355**	**6.7197**	**6.4610**	**6.8470**	**5.5027**	**3.8750**	**1.7050**	**15.6550**	**1.0850**	**2.3250**	**0.7750**
A3 (in^2)	**1.7569**	**1.7422**	**1.7369**	**1.6833**	**1.8352**	**10.0750**	**2.0150**	**6.6650**	**1.3950**	**1.3950**	**0.7750**
A4 (in^2)	**3.4655**	**3.2997**	**3.3015**	**3.2555**	**3.4672**	**1.0850**	**6.0450**	**19.0650**	**3.5650**	**3.8750**	**3.8750**
A5 (in^2)	**1.5644**	**1.4730**	**1.4861**	**1.4043**	**1.7227**	**0.7750**	**7.9050**	**8.8350**	**2.9450**	**2.6350**	**1.3950**
A6 (in^2)	**2.0226**	**1.9882**	**1.9746**	**2.0373**	**1.9980**	**0.7750**	**6.0450**	**0.7750**	**4.1850**	**2.9450**	**2.9450**
A7 (in^2)	**2.1887**	**2.3393**	**2.3528**	**2.3943**	**2.3267**	**0.7750**	**3.8750**	**12.8650**	**3.8750**	**4.8050**	**1.0850**
Best Weight (kg)	**8905.37**	**8923.51**	**8890.64**	**8922.85**	**9021.27**	**8771.12**	**9007.71**	**9376.94**	**8788.5**	**8940**	**8906.15**
NSA	**4000**	**3900**	**3940**	**2040**	**1320**	**194**	**845**	**1084**	**872**	**892**	**855**

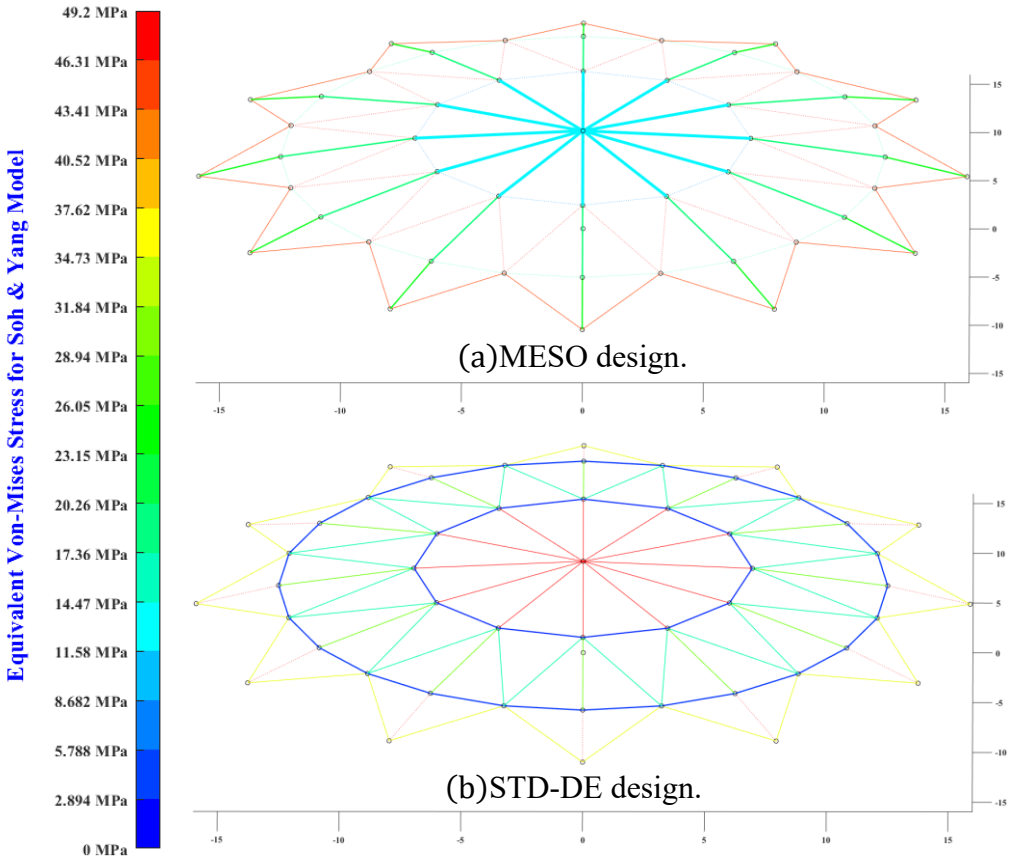

Figure 8.18 The state of stress for the best two designs of the 120-bar dome truss (case 2).

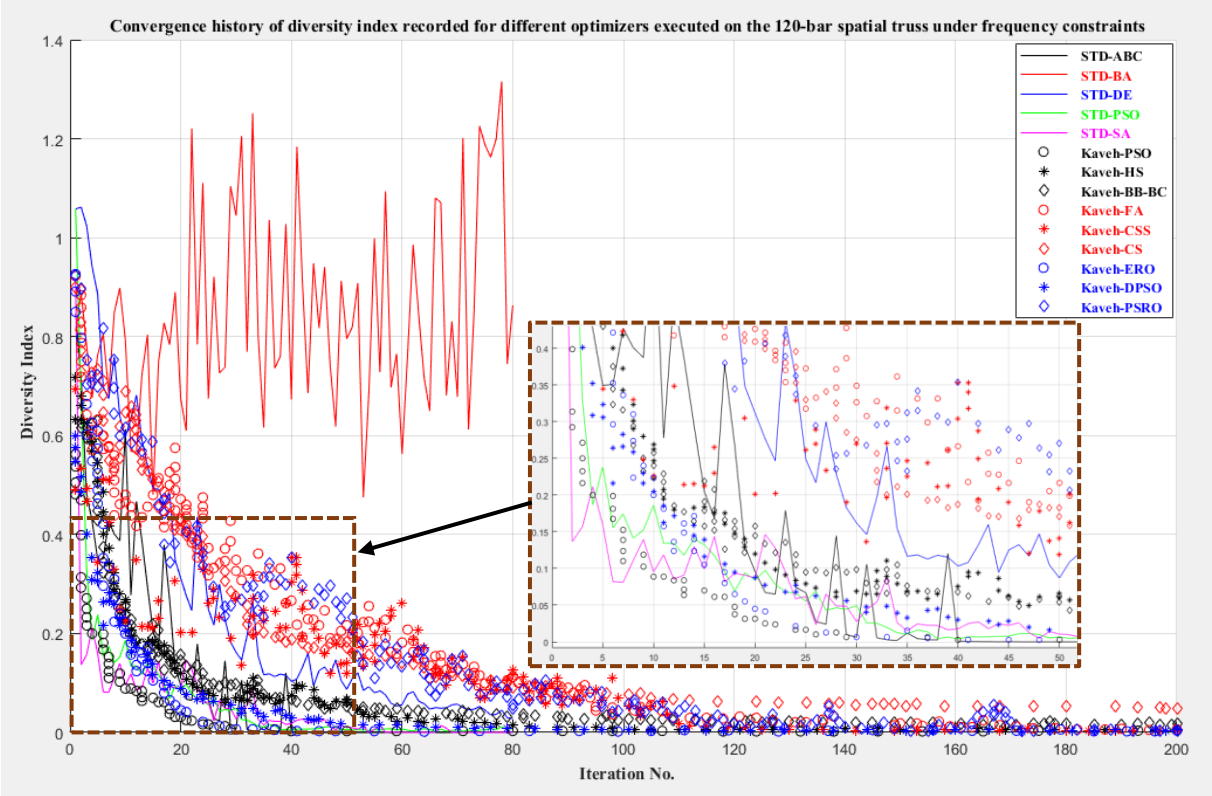

Figure 8.19 Diversity index recorded for different algorithms executed on the 120-bar dome truss under frequency constraints (case 2).

8.6 Geodesic Single Lattice Dome (Saka Model)

The optimization results for the geodesic dome truss designed by Saka (2007a) will be viewed and discussed in this section. Many dome roof configurations are solved by Saka (3, 4, 5 and 6 rings). However, the current study focuses on the last model (5 radial girders with 6 rings), which consists of 51 nodes and 255 elements, the outer periphery is clamped by 20 fixed supports, a vertical concentrated load P=1000 kN is applied at the central point of the dome as illustrated in Figure 8.20. The outermost ring could be discarded since it is zero stress member. Overall, there are 13 design variables in this problem, 12 of them are sizing represented by the set of section areas of the 12 element groupings of the model, whereas the last one is shape variable defined by the height of the crown. The structural material is steel Grade 43 with elasticity modulus E=205 GPa. A commercial set of 64 circular hollow sections designed and manufactured according to "Steelwork design guide to BS5950 (1990)" was considered as discrete optimization range for the sizing variables. This range starts with the designation PIP212.6 and ends with PIP2735.0. The crown height is extending over the range from 1 m to 8.75 m with step 0.25 m. Displacement constraints restrict the (absolute) movement of node 1 within the period 0 to 28 mm in Z direction, whereas the nodes 2 and 3 are restricted to the range 0 to 33 mm in X and Y directions and 0 to 28 mm in Z direction.

In this example, the proposed methods MESO-ABC, MESO-BA, MESO-DE, MESO-PSO and MESO-SA are tested against the mixed discrete-continuous optimization problem considered by Saka (2007a), where the sizing variables must be selected from the predefined discrete set of commercial sections and the crown height is the only continuous variable of the problem.

Table 8.16 shows results of the two investigations. MESO-BA has achieved an optimal weight of 1429.165 kg after 658 cost evaluations, which is lighter than the weight presented by Saka (1445.3 kg) for the same configuration in addition to the appreciable saving in the number of cost evaluations from 4500 to 658. The next best design is MESO-ABC, where it yielded 1438.694 kg, which is 0.46% lesser than that reported by Saka, in only 609 cycles. In conclusion, MESO-based algorithms are able to produce further reduction in the structural weight along with realizing a considerable saving in computational time.

The convergence history of this example is given in Figure 8.21, where the maximum number of iterations for the proposed methods is set to 1000, population size is set to equivalent to 10 individuals, reduction ratio of MESO is set to 0.25. Some of algorithms have terminated the optimization process earlier than others after becoming trapped in a local minimum. For instance, MESO-PSO stopped after 561 solutions with an unpromising result. In MESO algorithms, the involved metaheuristic technique plays a significant role in escaping from the local minimum through manipulating the set of continuous variables involved.

The design contours shown in Figure 8.22 describe the state of strain energy for the optimal designs. The results show that the radial girders are the most susceptible part of the dome structure, as they are experiencing a compressive load.

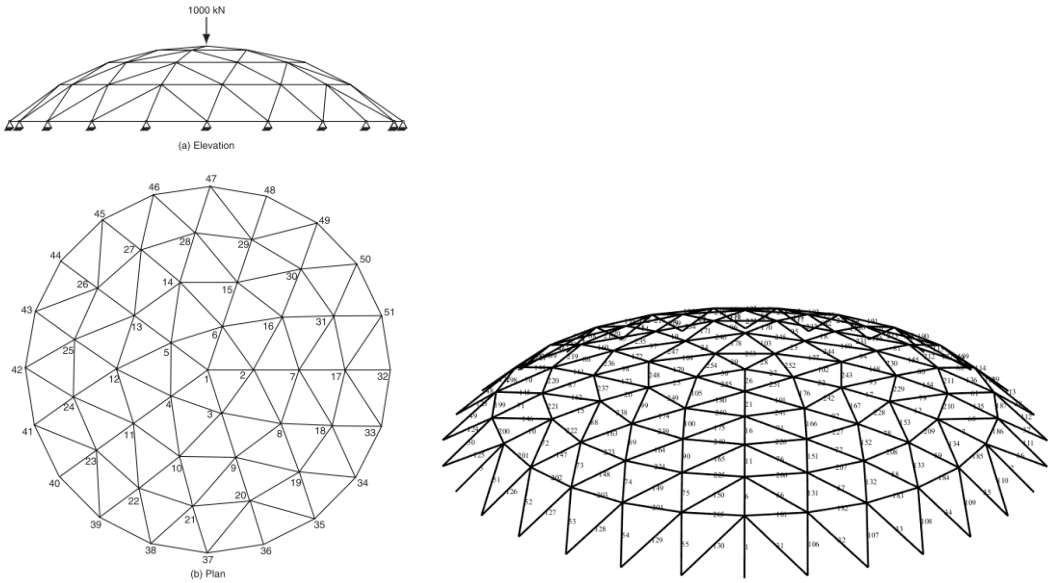

Figure 8.20 Boundary and load conditions with illustration of nodes and elements for the 6-rings geodesic model adopted by Saka (2007a).

Table 8.16 Comparison of optimization results obtained for Saka model (Saka, 2007a).

Group No.	Work implemented by Saka using HS				Current study implemented on Saka geodesic model with 6-rings				
	3-rings	4-rings	5-rings	6-rings	MESO-ABC	MESO-BA	MESO-DE	MESO-PSO	MESO-SA
1	**PIP1393.6**	**PIP1393.6**	**PIP886.3**	**PIP886.3**	**PIP883.2**	**PIP767.1**	**PIP885.0**	**PIP886.3**	**PIP888.0**
2	**PIP1143.0**	**PIP1143.0**	**PIP765.0**	**PIP884.0**	**PIP767.1**	**PIP762.9**	**PIP762.9**	**PIP886.3**	**PIP764.5**
3	**PIP603.6**	**PIP485.0**	**PIP763.6**	**PIP763.6**	**PIP602.9**	**PIP605.6**	**PIP602.9**	**PIP762.9**	**PIP602.9**
4	**PIP483.2**	**PIP483.6**	**PIP483.6**	**PIP483.6**	**PIP423.6**	**PIP422.6**	**PIP482.6**	**PIP486.3**	**PIP423.6**
5	**PIP423.2**	**PIP482.5**	**PIP423.2**	**PIP483.6**	**PIP422.9**	**PIP422.9**	**PIP334.5**	**PIP602.9**	**PIP483.2**
6	**PIP213.2**	**PIP333.0**	**PIP333.2**	**PIP333.6**	**PIP332.9**	**PIP332.6**	**PIP333.6**	**PIP422.9**	**PIP334.0**
7	**NA**	**PIP333.2**	**PIP333.0**	**PIP333.0**	**PIP332.6**	**PIP332.9**	**PIP334.0**	**PIP334.0**	**PIP333.2**
8	**NA**	**PIP213.2**	**PIP422.6**	**PIP263.2**	**PIP262.6**	**PIP262.6**	**PIP332.9**	**PIP332.9**	**PIP334.5**
9	**NA**	**NA**	**PIP263.2**	**PIP263.2**	**PIP263.6**	**PIP263.2**	**PIP332.6**	**PIP422.6**	**PIP333.6**
10	**NA**	**NA**	**PIP213.2**	**PIP263.2**	**PIP262.6**	**PIP262.6**	**PIP263.2**	**PIP332.6**	**PIP262.9**
11	**NA**	**NA**	**NA**	**PIP263.2**	**PIP213.2**	**PIP213.2**	**PIP212.9**	**PIP262.9**	**PIP212.9**
12	**NA**	**NA**	**NA**	**PIP213.2**	**PIP212.6**	**PIP212.6**	**PIP212.6**	**PIP212.6**	**PIP212.6**
Crown height (m)	**2**	**2**	**1.5**	**1.5**	**1.184**	**2.455**	**2.838**	**1**	**1.276**
Best Weight (kg)	**1244.42**	**2721.45**	**1477.08**	**1445.3**	**1438.694**	**1429.165**	**1521.821**	**1930.986**	**1518.117**
Max Disp. (mm)	**31.7**	**30.9**	**32**	**29.3**	**32.29**	**32.51**	**32.07**	**31.85**	**32.16**
NSA	**4500**	**4500**	**4500**	**4500**	**609**	**658**	**652**	**561**	**552**

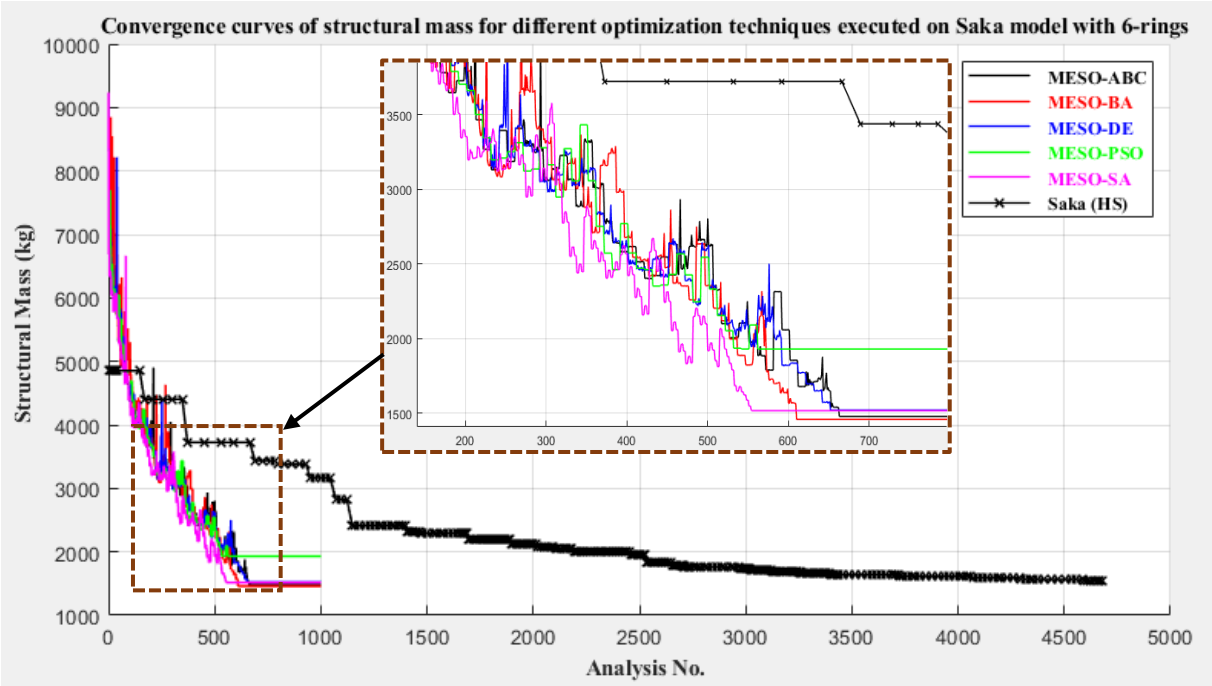

Figure 8.21 Convergence curves of structural mass for different optimization techniques executed on Saka model with 6-rings.

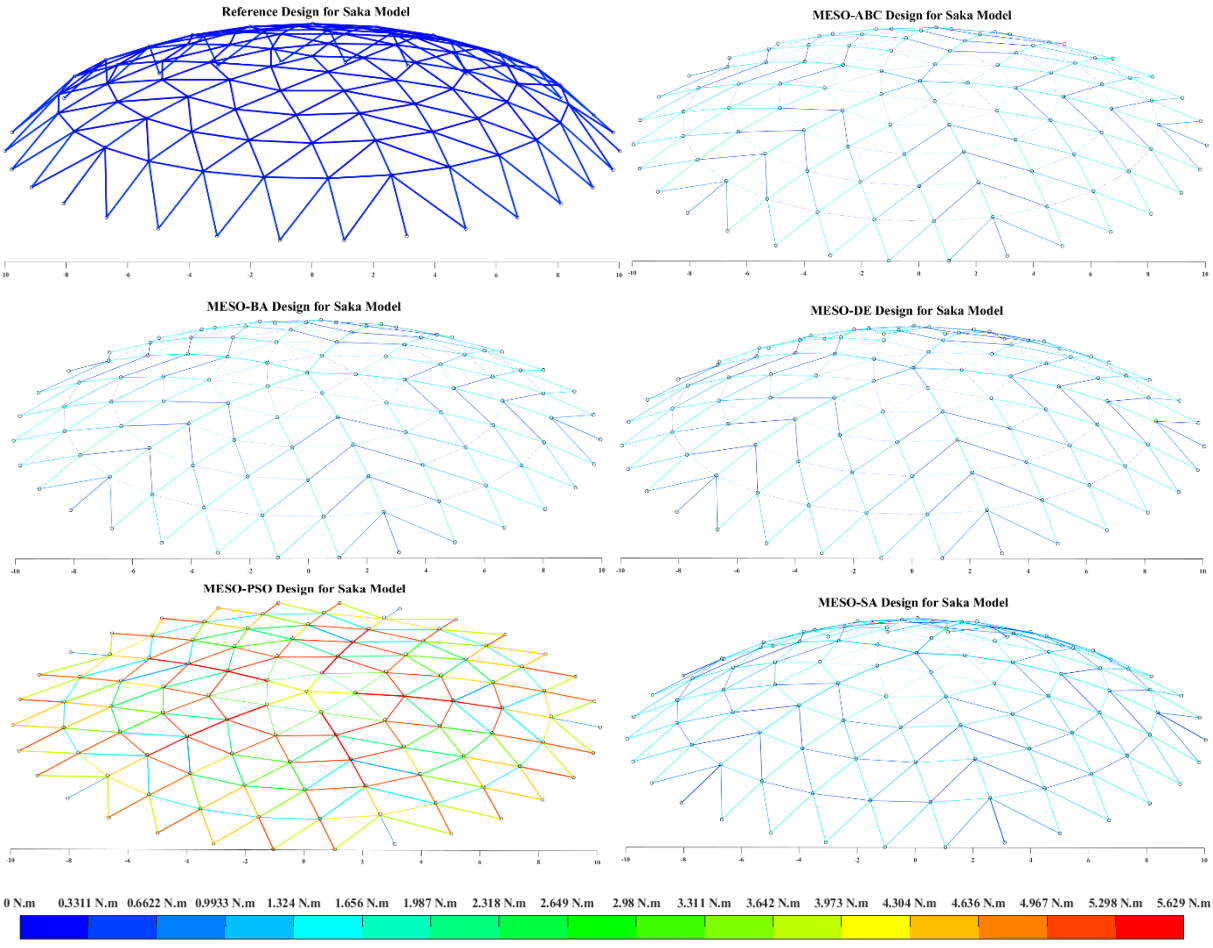

Figure 8.22 3D contours showing the state of strain energy for the initial and optimal designs (produced by different optimization algorithms) of Saka model.

8.7 Summary

- The cascade optimization procedure allowed MESO to guide the process with great efficiency to build an intelligent optimization tool by utilizing the engineering intuition.
- The proposed optimizers (MESO based algorithms) have appreciably saved the computational cost, by enhancing the convergence rate of the relevant metaheuristic technique.
- One of the merits of MESO based algorithms is that MESO employs a specific optimality criterion to solve the optimization problem without the need to exploit any population to perform the task. Thus, MESO has the sufficient reliability and efficiency to deal with any size of the optimization problem in contrary to other conventional metaheuristic techniques, which are significantly influenced by the problem size (number of design variables).
- MESO based metaheuristic algorithms essentially produce consistent geometries, also reliable and attractive from manufacturing perspective, as a systematic distribution of girder sections can be ensured in contrast with the classic metaheuristic techniques.
- A diversity index is a reliable measure to the capability of the metaheuristic technique to explore/exploit the data within design space

Chapter 9. Conclusions and Future Work

This chapter will summarize the contributions of the proposed optimization methodology and will list the main conclusions drawn about the adopted MESO based metaheuristic algorithms implemented in the preceding chapters. Recommendations are then set forward for future research.

9.1 Conclusions

Using a 10,000 m^3 fuel storage tank as the target application, this thesis has set out to study and develop a methodology for optimizing dome roof frame structures subject to wind loading. The optimization problem is one with 30+ design variables, most of which relate to choosing engineering sections for the girders and are therefore discrete variables, while some variables relate to the overall structure of the frame. Given the engineering constraints on the structure (stress, deflection, buckling), the optimization aim of reducing the structural mass leads to a highly non-linear problem that requires a stochastic approach to its solution.

Five metaheuristic optimization methods have been used as a basis for developing a hybrid approach. The MESO principles of gradual material removal are used to optimize girder sections, coupled with one of the metaheuristic methods for optimizing other design variables. A cascading approach was used to simplify the analysis, so that major variables (e.g., numbers of rings, number of nodes per ring) are optimized initially, and then MESO was introduced to further optimize girder sections. The result was a novel method that combines the stochastic exploration of metaheuristic methods with the high convergence rate of evolutionary optimization.

Five basic designs of roof frame structure were modelled. Single and double lattice versions were constructed and solved using a simplified model in MATLAB, primarily for the purpose of studying the behaviours of the optimization methods. Full finite element (integrated) models were constructed also in ANSYS and optimized. For both the simplified and integrated models, wind loads were determined with ANSYS Fluent.

The following conclusions can be inferred from the optimization results obtained:

1. Implementing a cascade optimization procedure via separating the design variables into a 'high energy' set that have a large impact on the whole structure at Stage 1 and a 'low energy' set for incremental optimization at Stage 2 allows MESO to be employed at Stage 2 to guide the optimization with great efficiency and an excellent convergence rate. Engineering principles can be built into MESO to make it an intelligent optimization tool, targeting the specific application, whereas metaheuristic methods are far more random. For the hybrid

model, there is still an element of randomness, but MESO can be used to guide the optimization towards better solutions.

2. The proposed optimization strategies appreciably saved the computational cost, by enhancing the convergence rate of the relevant metaheuristic technique.
3. MESO based metaheuristic algorithms essentially produce feasible designs with consistent geometries. They are also reliable and attractive from manufacturing perspective, since a systematic distribution of girder sections can be ensured in contrast with the other classic metaheuristic techniques.
4. The single lattice Lamella and geodesic domes are the two most promising design models, with structural mass of the frame 34.455 tonnes and 37.012 tonnes respectively, as compared to other configurations adopted in this work.
5. The peripheral section of a radial girder is the critical part of dome structure in a geodesic configuration, whereas the outermost circumferential ring is the key part for Lamella dome structure.
6. Double lattice designs tend to be stiffer and stronger when the inner and outer layers are further apart at the periphery, tapering towards the hub.
7. The higher the dome radius, the lower the lift force generated by wind loads, whereas the snow becomes a critical load case at higher dome radii. Dome roofs that are optimized for pure wind loads can fail when subjected to snow loads alone. Snow loading tends to be an issue especially for double layer truss dome roofs.
8. Following on from the previous point, other load cases need to be considered during the optimization to achieve a safe and optimal design. In addition to the basic load case of an empty tank under pure wind loading, the following cases should also be considered:
    a. A full tank subjected to pure wind, is another critical load case from a stress perspective.
    b. An empty and full tank subjected to pure snow loading, are critical load cases from a displacement perspective.
9. The approach used in the hybrid models is to have an initial reference solution that is acceptable, although non-optimal, and to search for better solutions while aggressively rejecting designs that fail to meet the imposed constraints. The consequence of this is that there will always be a solution, and an 'optimal' design will be achieved within an acceptable time frame. In addition, the MESO process focusses on improving an already acceptable design.
10. Design functions have been proposed for assessing the strength and stiffness of the dome roof frame relative to the reference design. These functions can be used instead of, or in

addition to, the simple ratio of structural mass used as the cost function to be minimized throughout the majority of this thesis.

9.2 Recommendations for Future Works

The following suggestions have been made to complement and extend this research:

1. The hybrid method developed in this research has focussed on reducing the structural mass but with an intelligent approach that tries to limit the increasing strain energy. While it is possible and relatively simple to modify the cost function to make this an explicit target of the optimization, for example by including the proposed design function for strain energy, an alternative approach is to have multiple explicit cost functions that must be optimized simultaneously. This leads to a competitive scenario where there is not one unique global optimum but rather a set of optimal solutions (the Pareto front) that the designer must ultimately choose from. For example, this could lead to a set of potential dome designs of varying masses, each with different resonant frequencies.
2. The current strategy can be used to optimize other operational units in oil industry where the thermal effects and machinery vibrations are the most two substantial design constraints of the optimization (e.g. oil refinement towers, piping networks, etc.). The thermal effects would require more load cases to be modelled and considered during the optimization, while a fatigue analysis would need to be included with the structural analysis.
3. Large scale structures such as fuel storage tanks often have strict requirements in terms of response to seismic loads. Only wind and snow loads have been included so far, but to be used in practice for optimizing structures, the models need to be developed to include seismic response.
4. The assumption throughout this work is that the dome roof is spherical. In the case of the double lattice, both inner and outer layers are assumed to be spherical. Primarily this assumption has been made for simplicity, especially in the wind load modelling to avoid having to solve fluid flow with each new shape of the dome roof. However, a set of convex roof designs could be investigated to study the impact on wind loading, and consequently on the frame design. For the double lattice designs, the inner layer can be changed without changing the spherical outer layer, so an investigation of non-spherical inner-layer designs would be relatively straight forward.
5. The computationally intensive nature of the dome roof optimization has limited the time and resources available to conduct a full statistical analysis of the hybrid method. For a more secure comparison of the dome roofs and the optimization methods, these trials should be repeated multiple times (typically 20-100). This would also be interesting in terms of

studying the hybrid Lamella-Schwedler designs; typically, the optimizer prefers the pure Lamella designs, but hybrid designs can be optimized and can be visually attractive.

6. One of the main conclusions from this research is that multiple load cases need to be considered during the optimization. This creates difficulties for the MESO process, since multiple load cases need to be solved and analysed together, and then structural changes proposed that lead to a solution that is at least acceptable for all load cases, and ideally better.
7. Steel has been used for the fuel storage tank components in this thesis, and research generally into dome roofs and structures uses steel and aluminium alloys. For lightweight structures, there is certainly benefit in using aluminium alloys, but in practice the higher weight of steel can be beneficial in resisting the lifting force of the wind. But there is certainly scope for further study into the use of different materials - and not just aluminium alloys. Composite panels could be used instead of the steel shell, and pultruded GRP is used for industrial girders that could be used for the frame structure. Careful consideration needs to be given, of course, to environmental and loading conditions, and to fabrication and assembly costs, but there is potential for new designs that are both cheaper and safer than conventional heavy engineering designs.
8. If the current optimization methodology is used to find the optimal design for a storage tank subjected to dynamic loads (e.g. seismic loads), then an appropriate tool needs to be developed to validate the structural analysis results according to the practice.

Appendix A. Calculation of Fluid-related Design Parameters.

In this Appendix, the design parameters concerning the fluid flow problem will be reviewed.

In addition to the pressure data produced by CFD analysis, there are four extra output parameters have been calculated by CFD and exported to the grand parametric table built in Ansys. First, the lift force (F_{lift}), which is applied normally to the roof structure directed upwards. Second, the overturning force ($F_{overturning}$), which is applied to the windward region, it tries to push the cylindrical shell of the tank towards the leeward quarter in horizontal direction. Third, the perturbation side force, it is unbalanced force exerted horizontally due to possible asymmetry in wind loading on the two sides of the cylindrical shell, it is fluctuating unbalanced force. Fourth, the tipping moment ($M_{tipping}$), which stands for the moment trying to overthrow the tank. In fact, this moment is generated from multiplying the resultant of lift and overturning forces by the orthogonal distance (d) measured from the line of action of the resultant force ($F_{resultant}$) to the pivot point (O) of the tank as demonstrated in Figure A.1. The suitable formulation for the tipping moment can be posed in the following form:

$$M_{tipping} = F_{resultant} \times d = \sqrt{F_{lift}^2 + F_{overturning}^2} \times d \qquad (A.1)$$

where, $M_{tipping}$, $F_{resultant}$, F_{lift}, $F_{overturning}$ & d are graphically demonstrated in the simple sketch of Figure A.1, which is prepared to illustrate the most substantial aerodynamic forces applied to the external surface of the storage tank. Also, Portela and Godoy (2005) shows the numerical values for these aerodynamic forces exerted on external shell of the storage tank as calculated for the initial design.

The aerodynamic model for the current case study has been built in ANSYS/FLUENT, which is used to calculate the wind pressure data for 10,000 m^3 tank with 8m-high walls, for dome roof radii from 30m to 60m in 20cm intervals, for a wind speed of 75m/s. The nearest was then imported during the optimization. Weights and external forces are summed up locally and applied at nodes. ANSYS/FLUENT also provides the 3D coordinates of the nodes where the local forces applied. Therefore, to calculate the effective distance (d) in Eq. (A.1), it is necessary to know that the overturning moment is simply represents the summation of the individual moments caused by the local forces applied at the nodes of the external surface of the tank. Hence, $M_{tipping}$ can be easily formulated as given in Eq. (A.2).

$$M_{tipping} = F_{resultant} \times d = \sum_{i=1}^{Nnodes} Fx)_i \times dy)_i + Fy)_i \times dx)_i \qquad (A.2)$$

In the same sense, $F_{overturning}$ and F_{lift} can be calculated as summation of the nodal forces acting on their respective directions as expressed in Eq. (A.3) – see Figure A.1.

$$F_{overturning} = \sum_{i=1}^{Nnodes} Fx)_i \quad , F_{lift} = \sum_{i=1}^{Nnodes} Fy)_i \qquad (A.3)$$

The perpendicular distance (d) can now be evaluated by substituting the values of $M_{tipping}$, $F_{overturning}$, and F_{lift} into Eq. (A.1), where the nodal forces $(Fx)_i$ and $Fy)_i$) and their respective nodal coordinates $(dx)_i$ and $dy)_i$) are provided by the software (ANSYS/FLUENT)

Table A.1 Aerodynamic forces and moments acting on storage tank.

Parameter name	Lift force [N]	Overturning force [N]	Perturbation force [N]	Tipping moment [N.m]
Parameter value	5689471	-935754	25761.67	2.15E+05

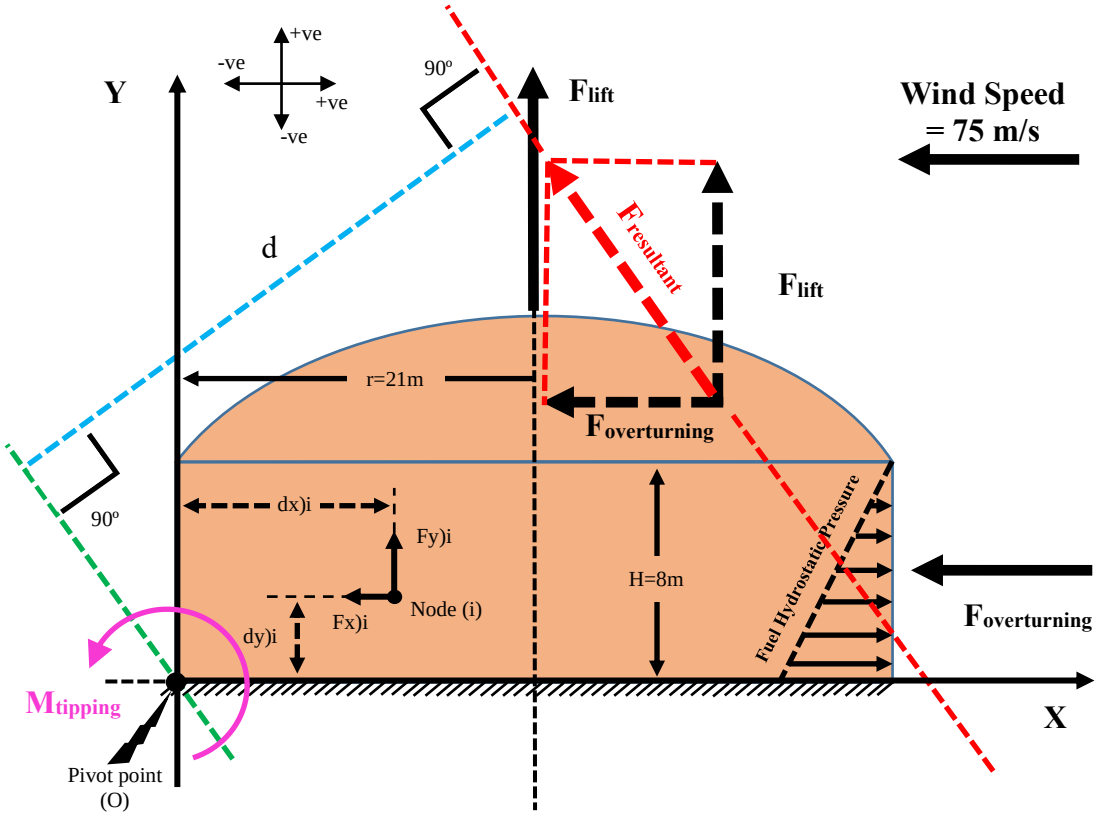

Figure A.1 Simple sketch showing the principal aerodynamic forces applied to the storage tank.

To find the surface area for the spherical cap, shown in Figure A.2, consider the geometric dimensions and the reference axes fixed for the sphere, hence y-coordinate represents the vertical distance from the origin of the sphere to the base circle of the spherical cap. While, x-coordinate equals the radius of the base circle, where the origin of the reference frame is located on the sphere centroid, x-coordinate is given by formula (A.4).

$$x = \sqrt{R^2 - y^2} \tag{A.4}$$

Where, R is the sphere radius (constant), hence the derivative of x with respect to y ($\frac{dx}{dy}$) could be given in formula (A.5).

$$\frac{dx}{dy} = -\frac{y}{\sqrt{R^2 - y^2}} = -\frac{y}{x} \tag{A.5}$$

According to Figure A.2, the surface area of the spherical cap is generated by revolving the red dotted arc about Y-axis, hence to find this surface of revolution, it is necessary to integrate the arc length for the infinitesimal segment ($ds=Rd\theta$) over the distance from $(R-h)$ to R. The infinitesimal arc length (ds) could be expressed in terms of Cartesian coordinates as given in Eq. (A.6).

$$ds = Rd\theta = \sqrt{dx^2 + dy^2} = \sqrt{1 + \left(\frac{dx}{dy}\right)^2}\, dy \tag{A.6}$$

Substituting Eq. (A.5) into Eq. (A.6) will lead to the following formula:

$$ds = \sqrt{1 + \left(-\frac{y}{x}\right)^2}\, dy = \frac{\sqrt{x^2 + y^2}}{x} dy = \left(\frac{R}{x}\right) dy \tag{A.7}$$

Hence, the surface area of the spherical cap (A_{sc}) is obtained by integrating the horizontal slice ($dA_{sc} = 2\pi\kappa ds$) within the interval $[R-h, R]$, where $(2\pi\kappa)$ is the circumference of the horizontal circle mediating the integration slice (identified by the brown dotted curve in Figure A.2) and κ is the radius of this circle, which is essentially replaced by x as a variable to perform the integration with respect to dy, whereas ds is the meridional length of the slice to be integrated from R to (R-h) as given in Eq. (A.8).

$$A_{sc} = \int_{R-h}^{R} dA_{sc} = 2\pi\kappa \int_{R-h}^{R} ds = 2\pi \int_{R-h}^{R} x\, ds \tag{A.8}$$

To perform the above integration, substitute the value of ds, expressed in terms of dy as given in Eq. (A.7), into Eq. (A.8) to obtain Eq. (A.9).

$$A_{sc} = 2\pi \int_{R-h}^{R} x \frac{R}{x} dy = 2\pi R[y]_{R-h}^{R} = 2\pi R\big(R - (R-h)\big) = 2\pi Rh \tag{A.9}$$

Where, R is the sphere radius (dome radius), which is constant, h is the height of the dome.

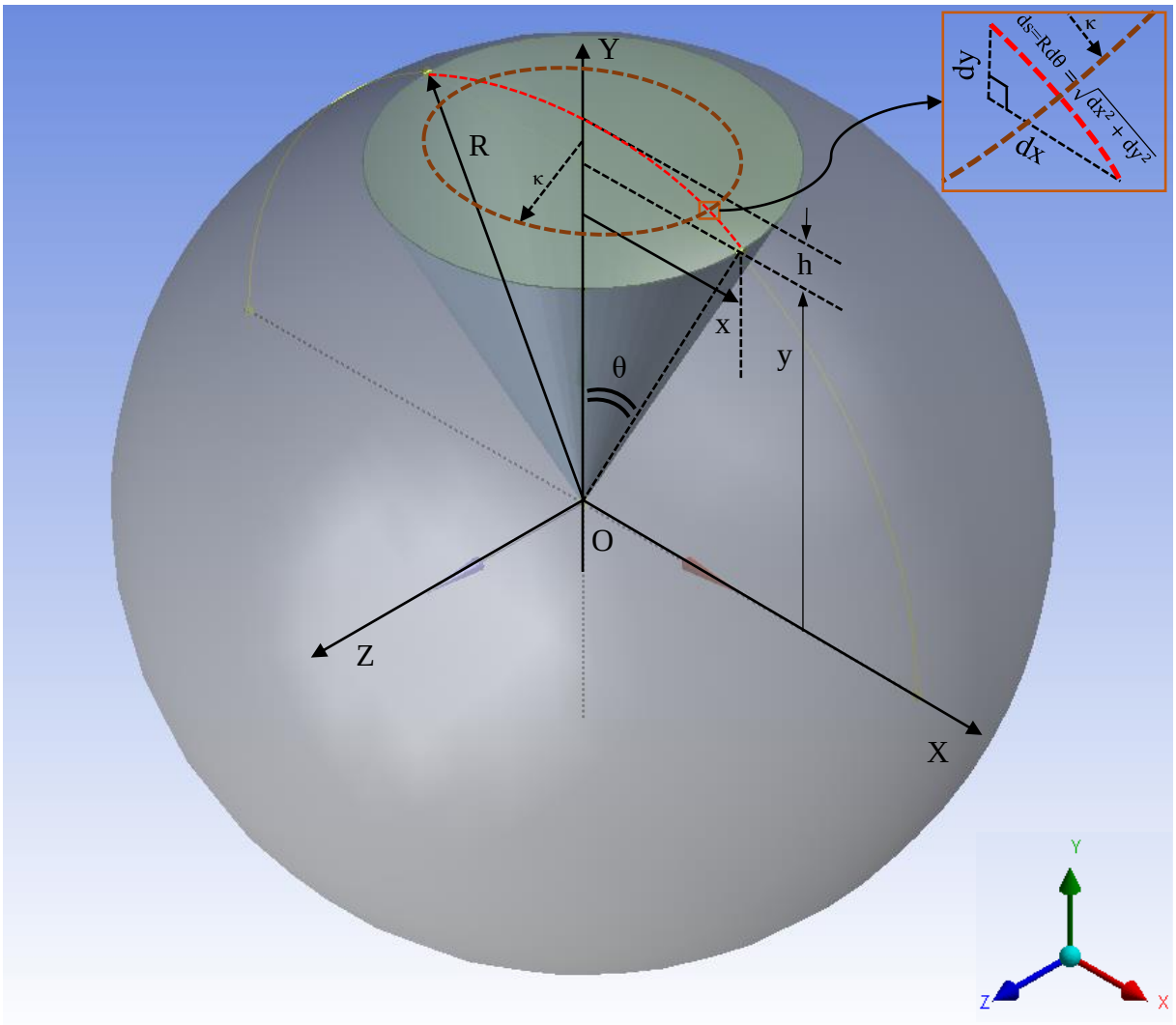

Figure A.2 Geometric parameters of spherical cap.

Appendix B. FINITE ELEMENT MODELLING OF THE SIMPLIFIED FRAME ANALYSIS.

This appendix shows the numbering of nodes and elements for the simplified frame models.

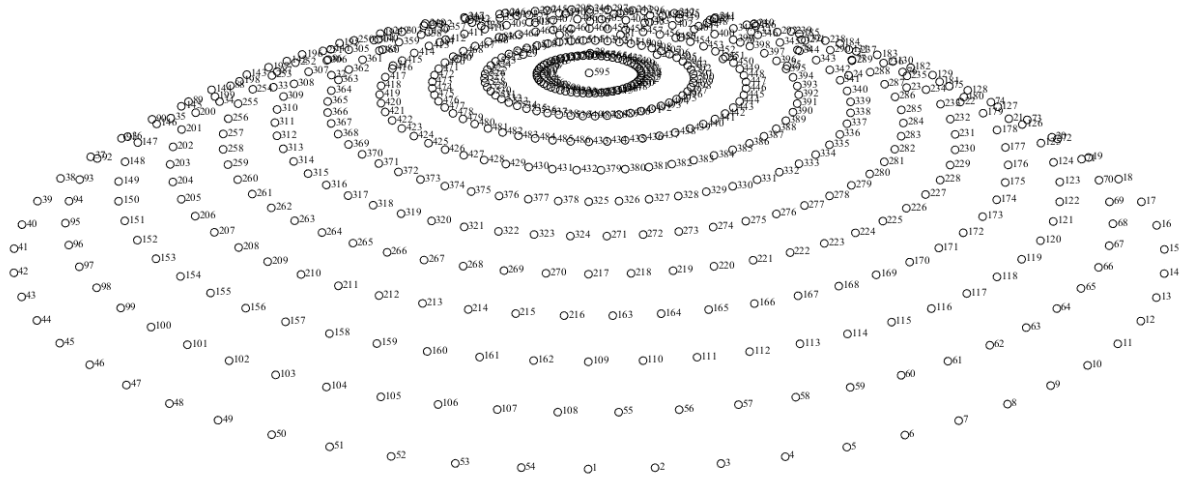

Figure B.1 Automatic numbering of nodes for the initial design of model B1.

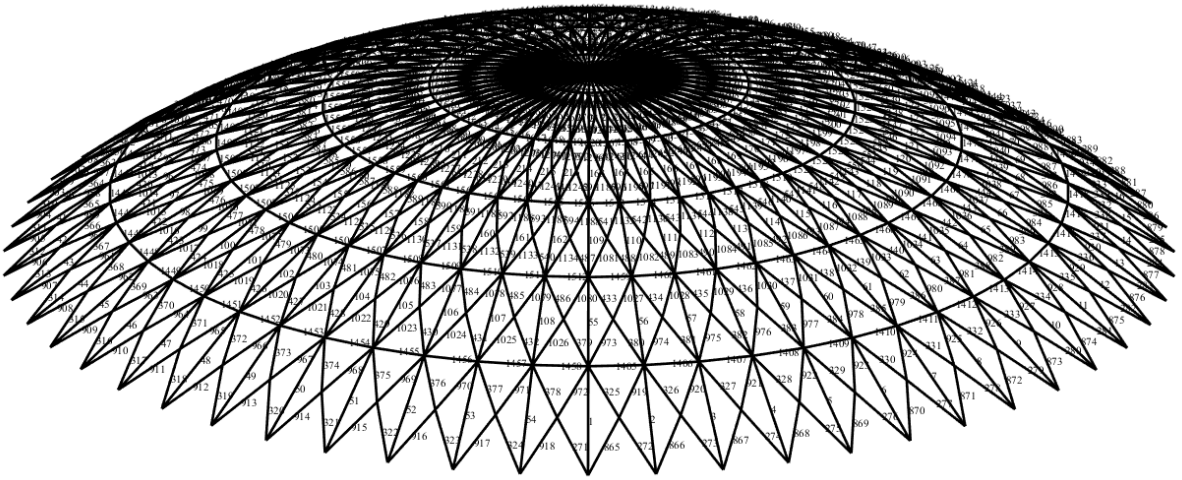

Figure B.2 Automatic numbering of elements performed for the initial design of model B1.

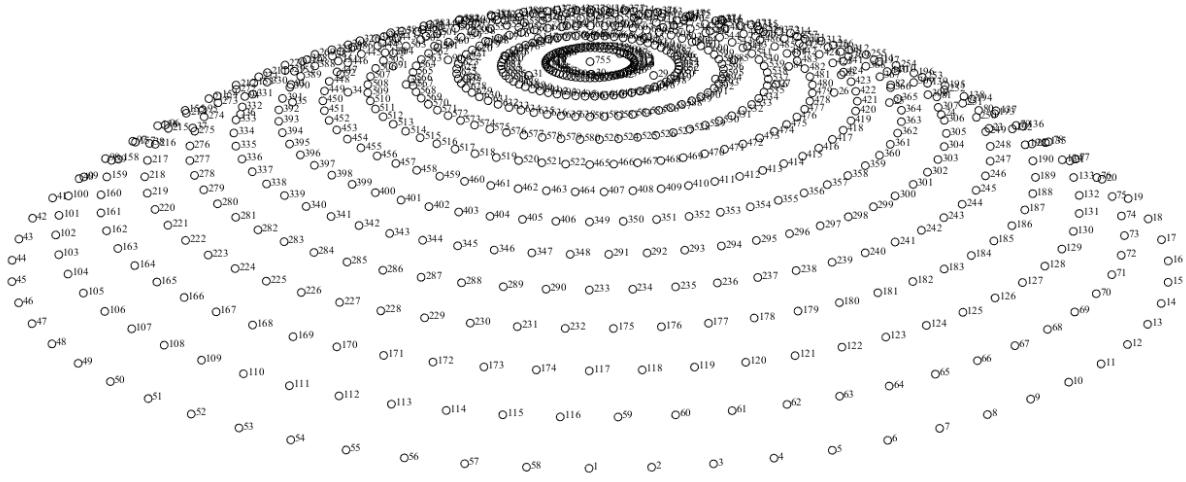

Figure B.3 Automatic numbering of nodes for the initial design of model C1.

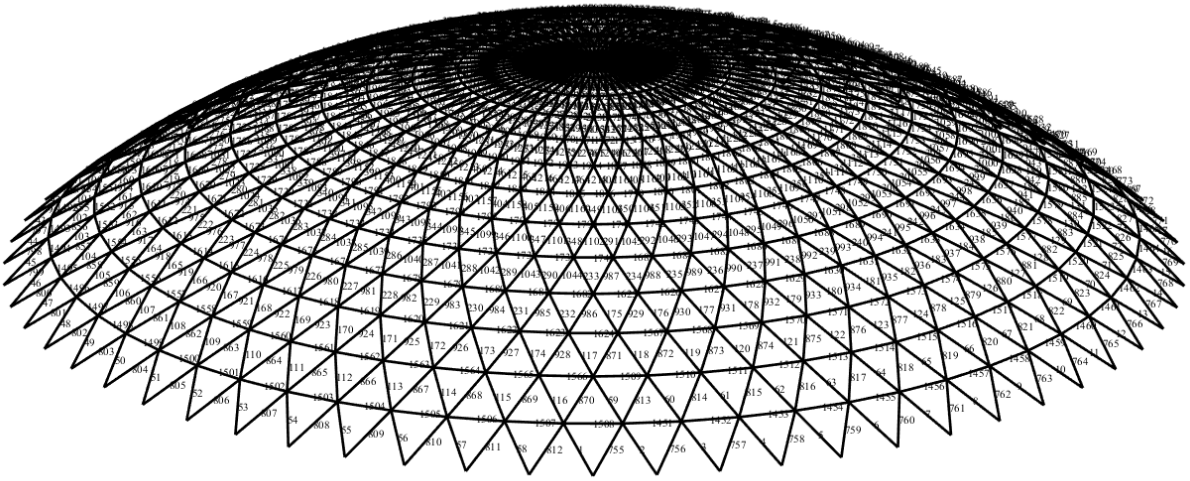

Figure B.4 Automatic numbering of elements performed for the initial design of model C1.

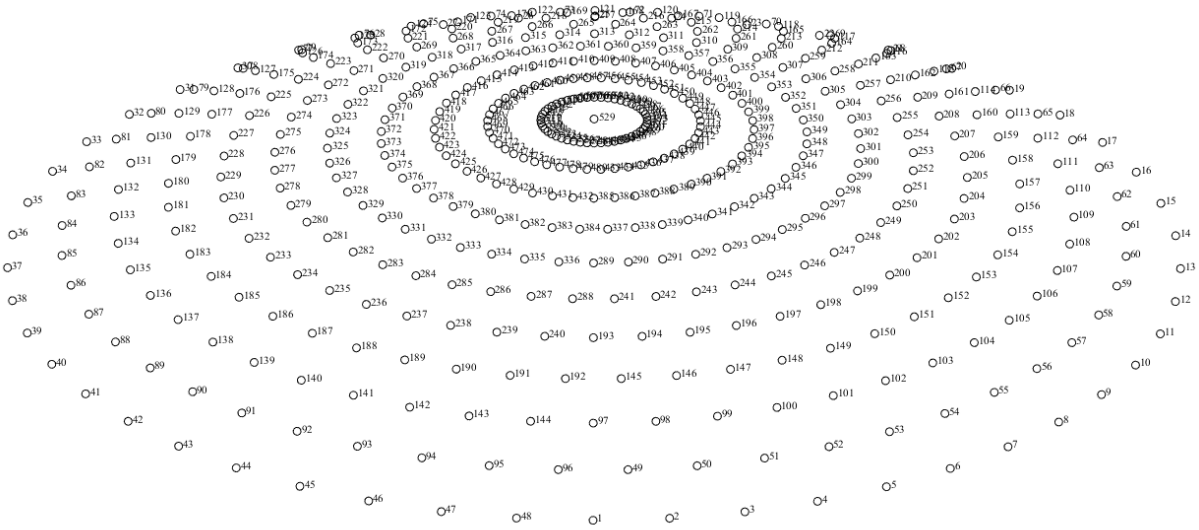

Figure B.5 Automatic numbering of nodes for the initial design of model D1.

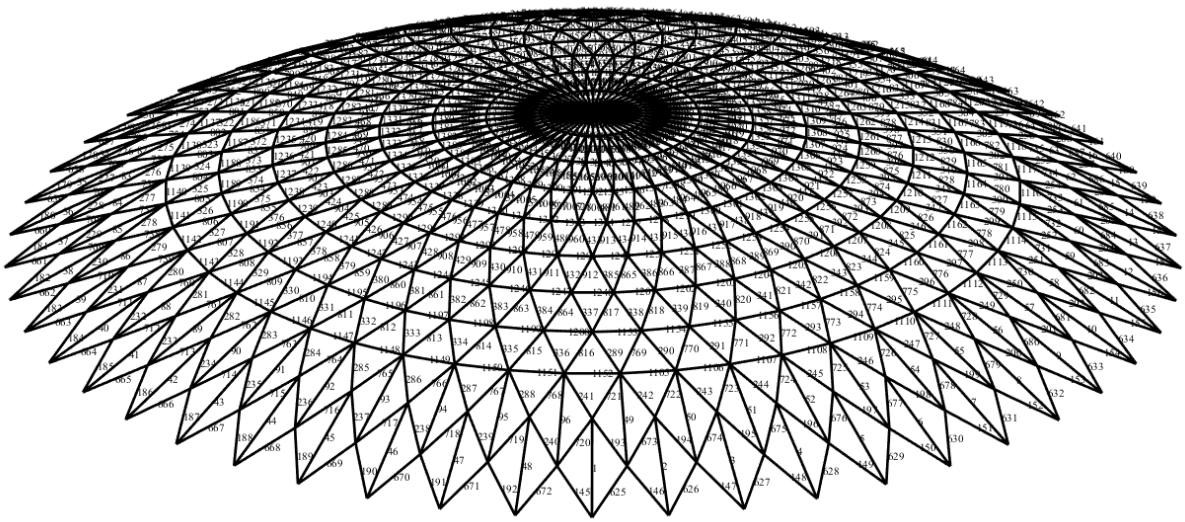

Figure B.6 Automatic numbering of elements performed for the initial design of model D1.

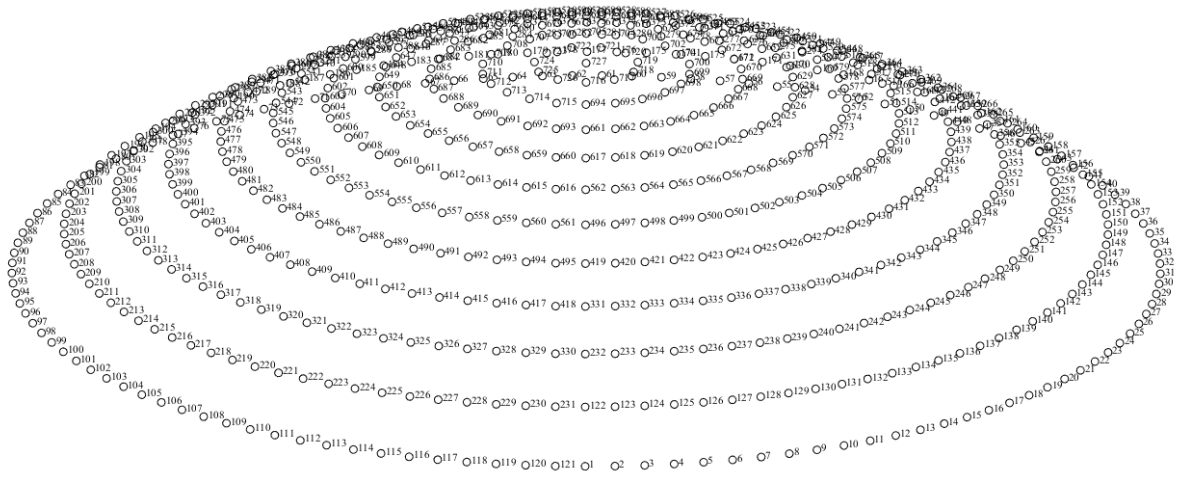

Figure B.7 Automatic numbering of nodes for the initial design of model E1.

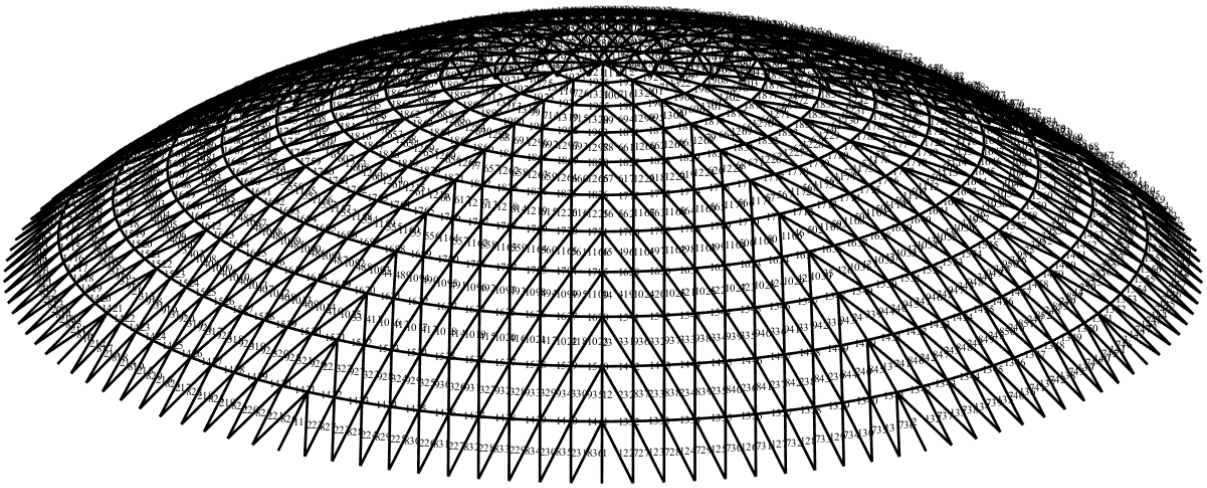

Figure B.8 Automatic numbering of elements performed for the initial design of model E1.

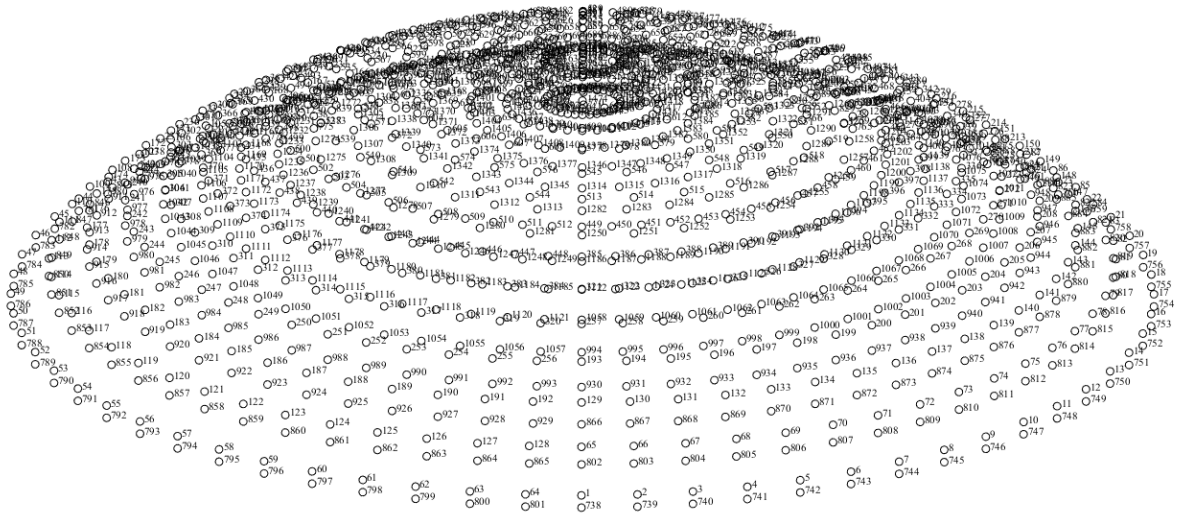

Figure B.9 Automatic numbering of nodes for the initial design of model A2.

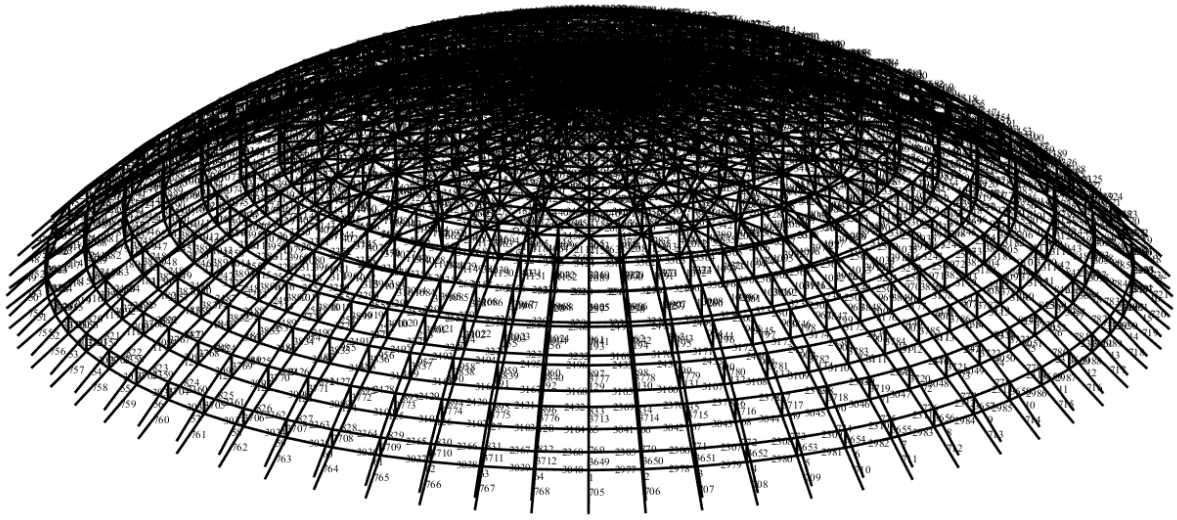

Figure B.10 Automatic numbering of elements executed on the initial design of model A2.

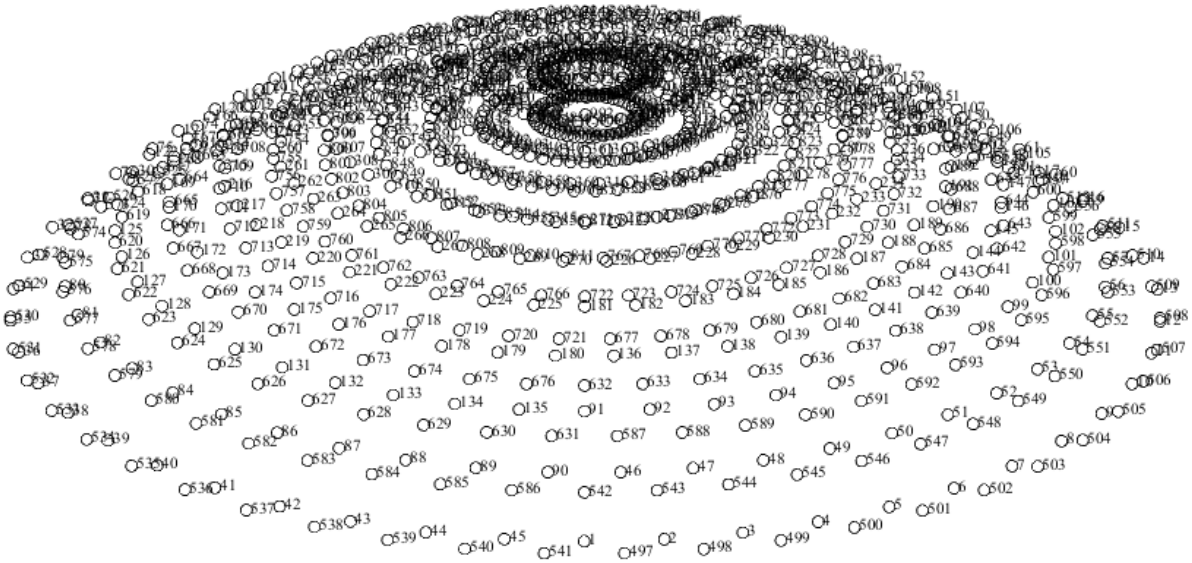

Figure B.11 Automatic numbering of nodes for the initial design of models B2 and C2.

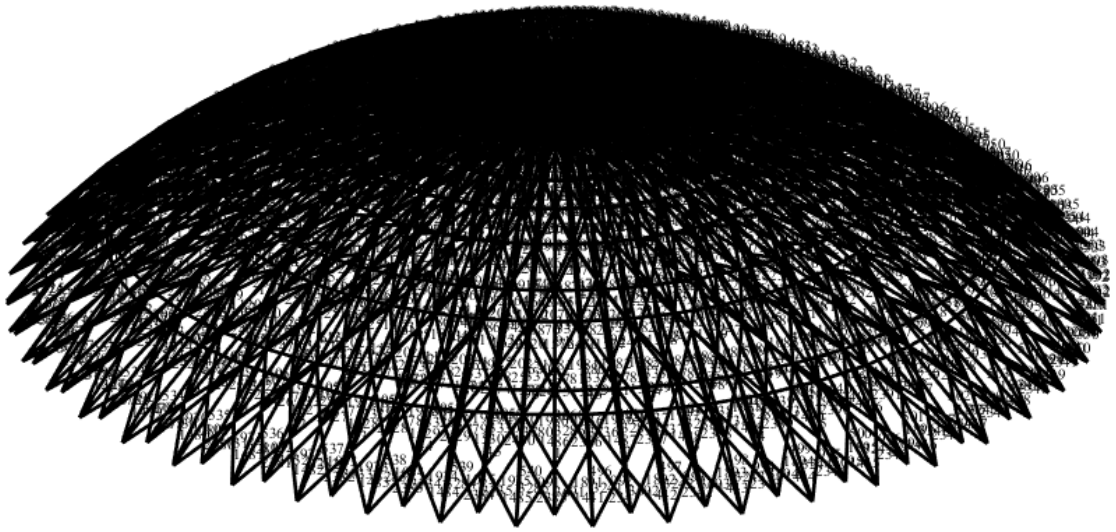

Figure B.12 Automatic numbering of elements performed for the initial design of model B2.

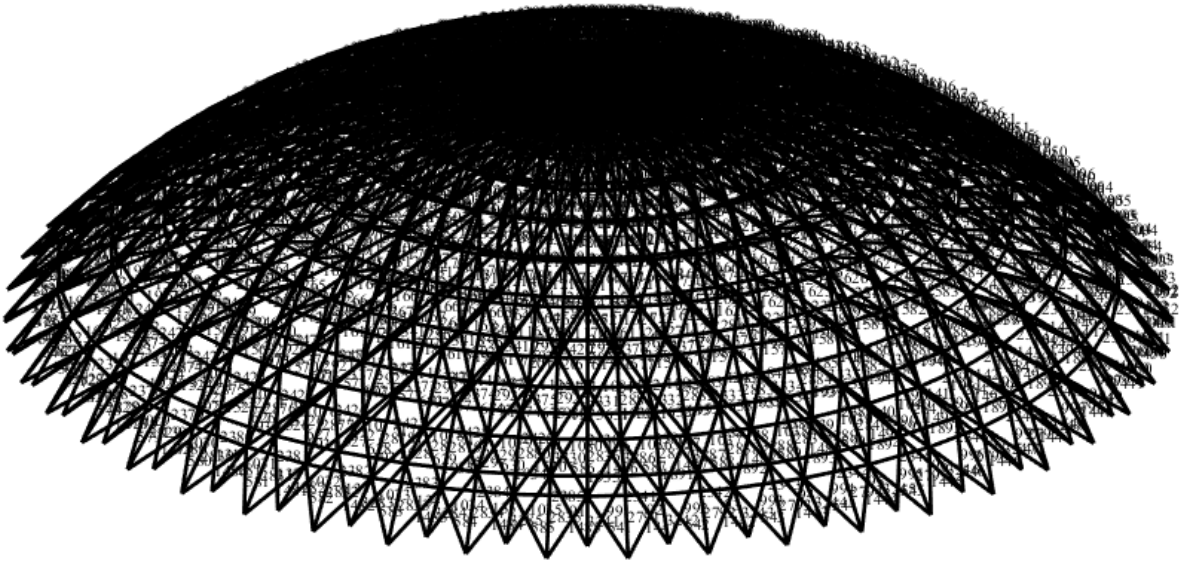

Figure B.13 Automatic numbering of elements performed for the initial design of model C2.

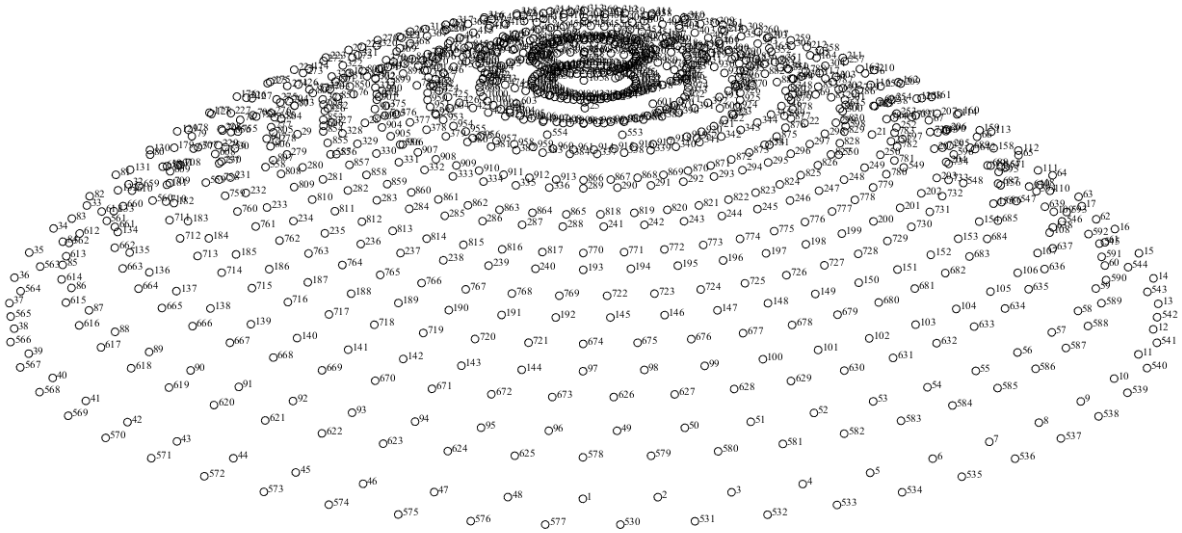

Figure B.14 Automatic numbering of nodes for the initial design of model D2.

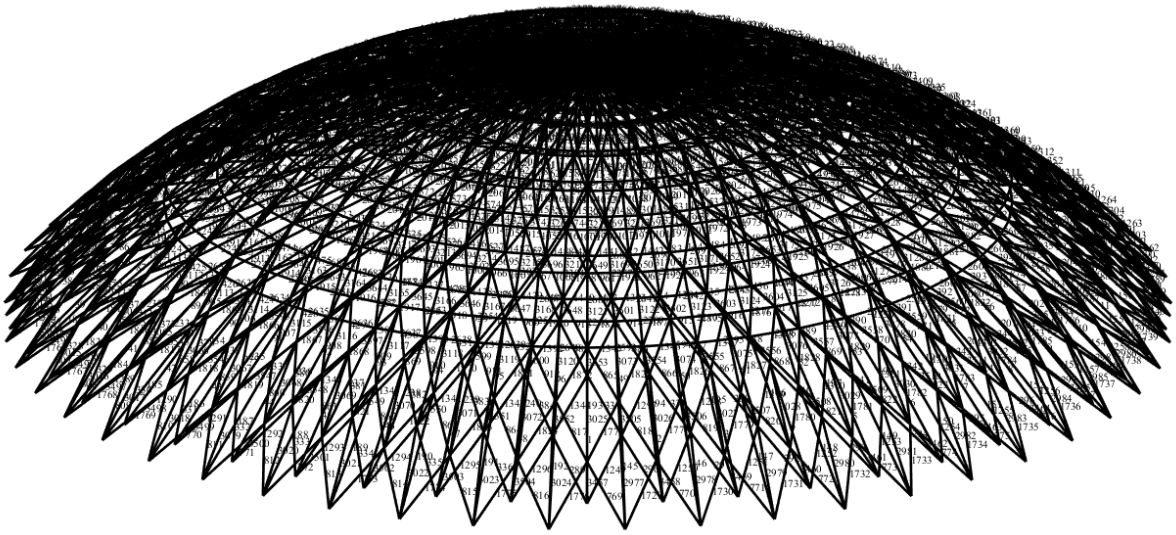

Figure B.15 Automatic numbering of elements performed for the initial design of model D2.

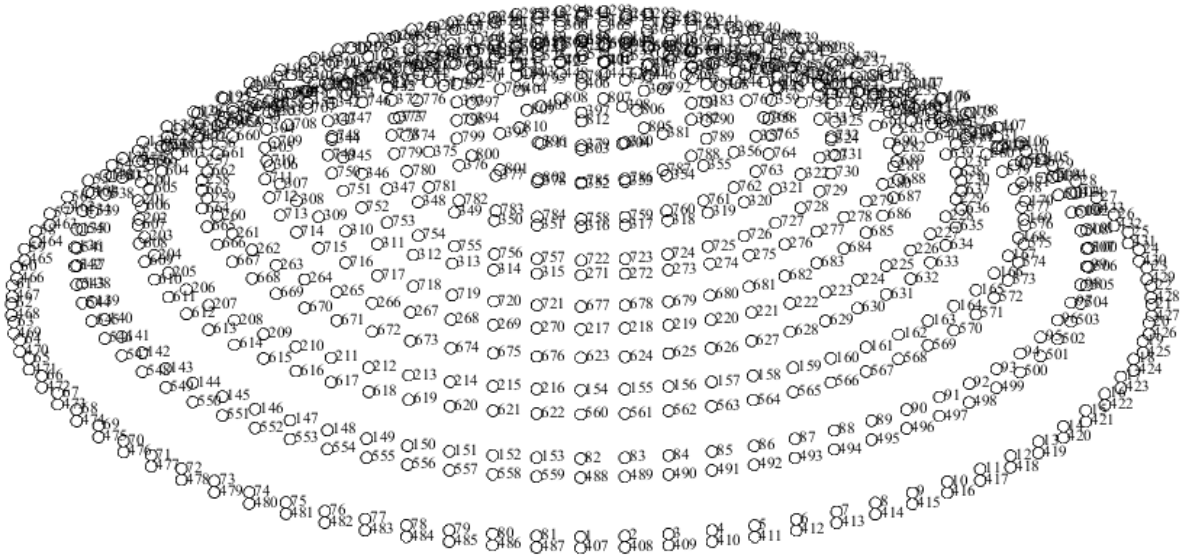

Figure B.16 Automatic numbering of nodes for the initial design of model E2.

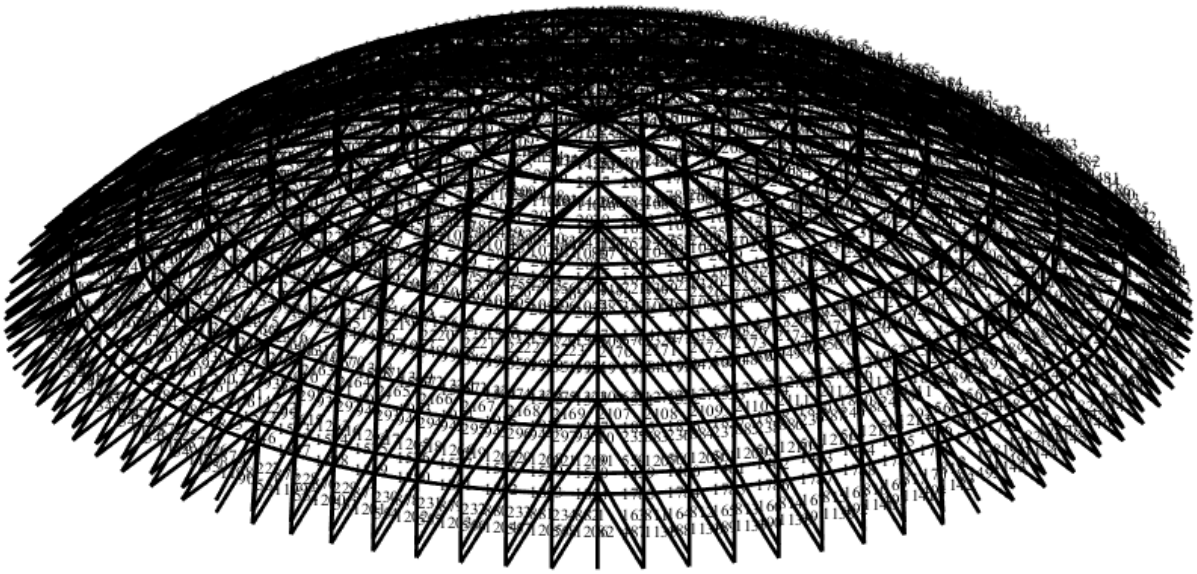

Figure B.17 Automatic numbering of elements performed for the initial design of model E2.

Appendix C. The General Procedure for Building up the Geometry and Performing the Finite Element Analysis for the Integrated Models.

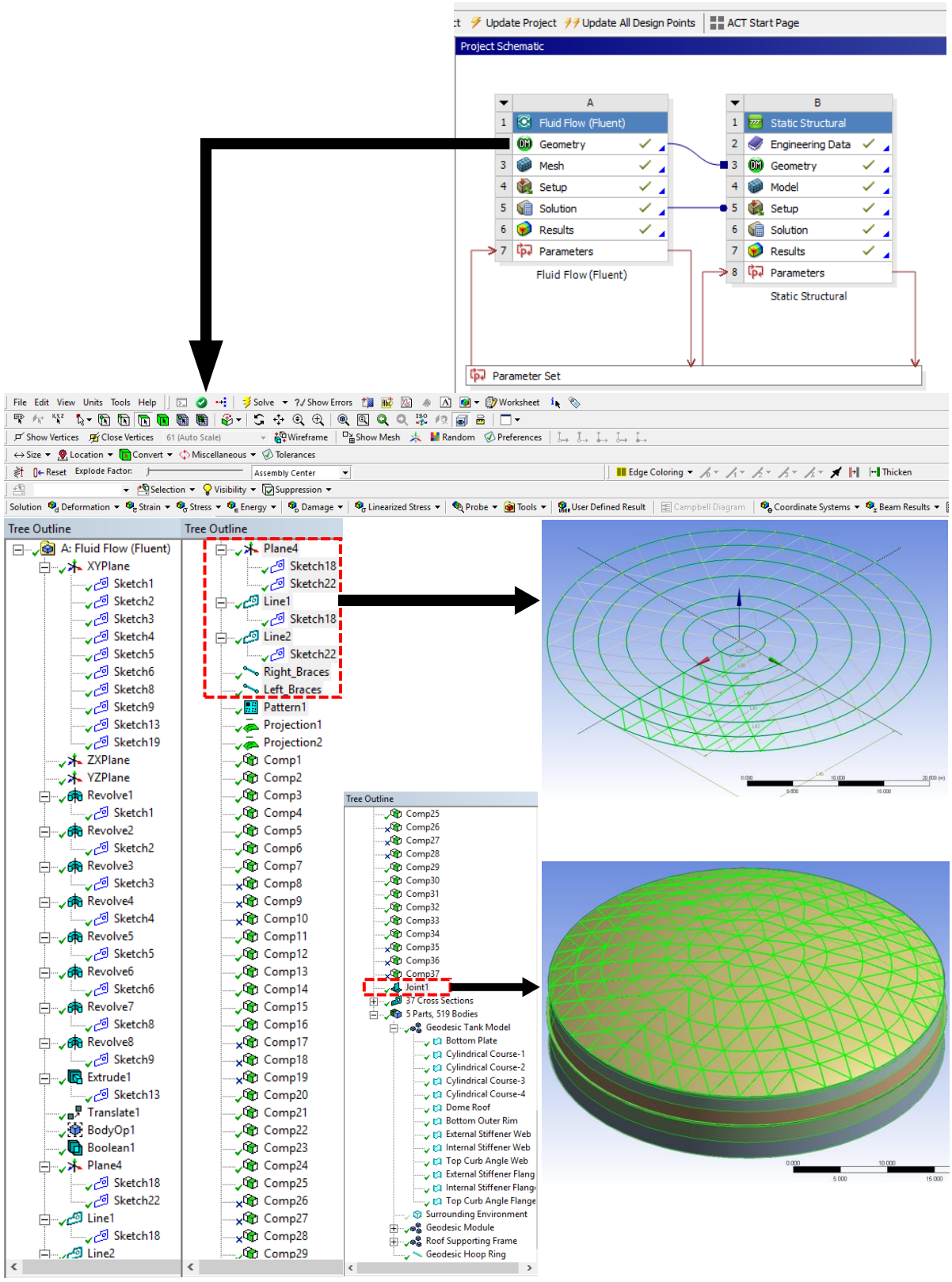

Figure C.1 Illustrative diagram showing the different features and commands needed to create the geometry for the analysis system.

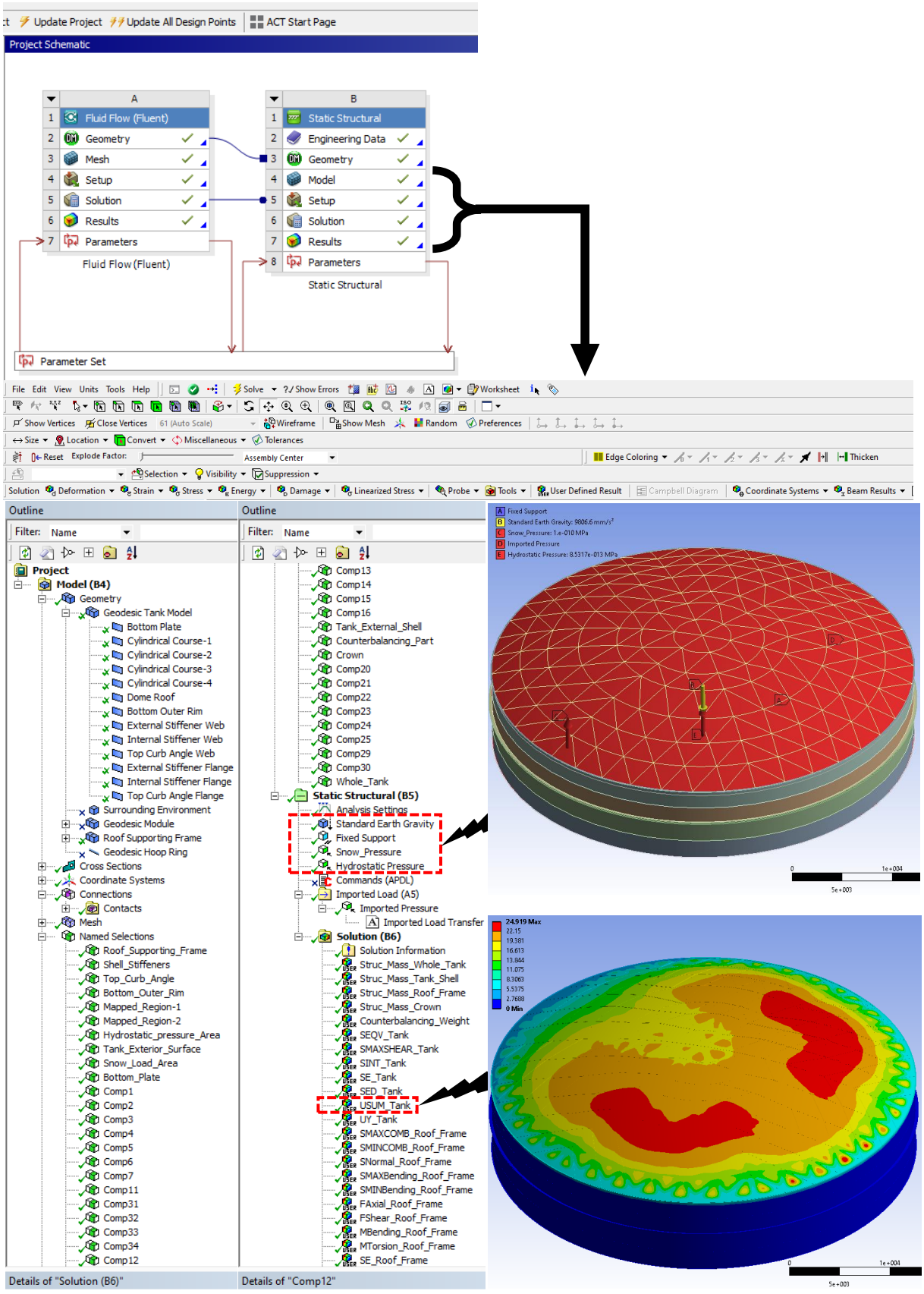

Figure C.2 Illustrative diagram showing the features and commands used to control the structural analysis of the tank in ANSYS Mechanical system.

Appendix D. The Software Codes Used to Create and Modify the Geometry, Perform the Structural Analysis and Execute the Structural Optimization Process for Simplified Frame Analysis.

The executables used to modify the geometry of integrated models posted in the forum CFD-Online, more details can be found on the following link:

https://www.cfd-online.com/Forums/main/194966-jscript-command-used-suppressing-joint-feature-designmodeler.html#post743572

The files concerning the structural analysis of the simplified frame models have been uploaded to Mathworks website, use the following link to browse the relevant executables:

https://uk.mathworks.com/matlabcentral/fileexchange/72635-static-structural-analysis-of-dome-roof-structure

The MATLAB files used to perform the structural optimization of the dome roof frame using Particle Swarm Optimization (PSO) have been uploaded to Mathworks website, use the following link to browse the relevant executables:

https://uk.mathworks.com/matlabcentral/fileexchange/72639-optimization-code-for-pso-strategy

Appendix E. COMMERCIAL TABLES OF STRUCTURAL STEEL SECTIONS (DESIGNED ACCORDING TO AMERICAN STANDARD OF BEAM SECTIONS).

Table E.1 Commercial S-type I-Beams sorted according to their second moment of area.

Designation	Web Height [mm]	Flange Width [mm]	Web Thickness [mm]	Flange Thickness [mm]	Second Moment of Area Iyy [m^4]	Second Moment of Area Izz [m^4]	Torsional Constant J [m^4]
S24x121	0.6223	0.20447	0.02032	0.027686	0.0013153	3.467E-05	4.6332E-06
S24x106	0.6223	0.199898	0.015748	0.027686	0.0012237	3.209E-05	3.6382E-06
S24x100	0.6096	0.184023	0.018923	0.022098	0.0009948	1.985E-05	2.7007E-06
S24x90	0.6096	0.180975	0.015875	0.022098	0.0009365	1.869E-05	2.1149E-06
S24x80	0.6096	0.1778	0.0127	0.022098	0.0008741	1.756E-05	1.6953E-06
S20x96	0.51562	0.18288	0.02032	0.023368	0.0006951	2.089E-05	2.9978E-06
S20x86	0.51562	0.179324	0.016764	0.023368	0.0006576	1.948E-05	2.3352E-06
S20x75	0.508	0.162179	0.016129	0.020193	0.0005328	1.24E-05	1.6007E-06
S20x66	0.508	0.158877	0.012827	0.020193	0.0004953	1.153E-05	1.2295E-06
S18x70	0.4572	0.158775	0.018059	0.017551	0.0003854	1.003E-05	1.4699E-06
S18x54.7	0.4572	0.152425	0.011709	0.017551	0.0003347	8.658E-06	7.9408E-07
S15x50	0.381	0.143256	0.01397	0.015799	0.0002023	6.535E-06	7.2286E-07
S15x42.9	0.381	0.139725	0.010439	0.015799	0.0001861	5.994E-06	5.1181E-07
S12x50	0.3048	0.139116	0.01745	0.016739	0.000127	6.535E-06	9.7478E-07
S12x40.8	0.3048	0.133401	0.011735	0.016739	0.0001132	5.661E-06	5.8126E-07
S12x35	0.3048	0.128981	0.010871	0.013818	9.532E-05	4.108E-06	3.5738E-07
S12x31.8	0.3048	0.127	0.00889	0.013818	9.074E-05	3.896E-06	2.9474E-07
S10x35	0.254	0.125578	0.015088	0.012471	6.119E-05	3.48E-06	4.5317E-07
S10x25.4	0.254	0.118389	0.007899	0.012471	5.161E-05	2.826E-06	1.9483E-07
S8x23	0.2032	0.105943	0.011201	0.01082	2.701E-05	1.794E-06	1.8467E-07
S8x18.4	0.2032	0.101625	0.006883	0.01082	2.397E-05	1.553E-06	1.0792E-07
S6x17.25	0.1524	0.090551	0.011811	0.009119	1.095E-05	9.615E-07	1.2947E-07
S6x12.5	0.1524	0.084633	0.005893	0.009119	9.199E-06	7.575E-07	5.3174E-08
S5x10	0.127	0.076302	0.005436	0.00828	5.12E-06	5.078E-07	3.5678E-08
S4x9.5	0.1016	0.071018	0.00828	0.007442	2.826E-06	3.759E-07	3.8743E-08
S4x7.7	0.1016	0.06764	0.004902	0.007442	2.531E-06	3.18E-07	2.2577E-08
S3x7.5	0.0762	0.063729	0.008865	0.006604	1.22E-06	2.439E-07	2.993E-08
S3x5.7	0.0762	0.059182	0.004318	0.006604	1.049E-06	1.894E-07	1.3409E-08

Table E.2 Commercial S-type C-Beams sorted according to their second moment of area.

Designation	Web Height [mm]	Flange Width [mm]	Web Thickness [mm]	Flange Thickness [mm]	Second Moment of Area Iyy [m^4]	Second Moment of Area Izz [m^4]	Torsional Constant J [m^4]
C15x50	0.381	0.0943864	0.0181864	0.01651	0.000168157	4.57855E-06	1.04708E-06
C15x40	0.381	0.089408	0.013208	0.01651	0.000145265	3.84182E-06	5.60863E-07
C15x33.9	0.381	0.08636	0.01016	0.01651	0.000131113	3.38396E-06	3.92287E-07
C12x30	0.3048	0.080518	0.012954	0.0127254	6.74295E-05	2.13943E-06	3.31466E-07
C12x25	0.3048	0.0773938	0.0098298	0.0127254	5.99373E-05	1.86055E-06	2.02822E-07
C12x20.7	0.3048	0.0747268	0.0071628	0.0127254	5.36939E-05	1.61498E-06	1.39995E-07
C10x30	0.254	0.0770382	0.0170942	0.0110744	4.28718E-05	1.63995E-06	4.92671E-07
C10x25	0.254	0.0733044	0.0133604	0.0110744	3.79603E-05	1.39854E-06	2.68288E-07
C10x20	0.254	0.0695706	0.0096266	0.0110744	3.28407E-05	1.16961E-06	1.38524E-07
C10x15.3	0.254	0.06604	0.006096	0.0110744	2.8054E-05	9.49008E-07	7.89757E-08
C9x20	0.2286	0.0672592	0.0113792	0.0104902	2.53485E-05	1.00728E-06	1.64037E-07
C9x15	0.2286	0.063119	0.007239	0.0104902	2.12278E-05	8.03327E-07	7.74812E-08
C9x13.4	0.2286	0.0617982	0.0059182	0.0104902	1.99375E-05	7.32567E-07	6.33539E-08
C8x18.75	0.2032	0.0641858	0.0123698	0.009906	1.83142E-05	8.24138E-07	1.69794E-07
C8x13.75	0.2032	0.0595122	0.0076962	0.009906	1.5026E-05	6.36834E-07	6.94425E-08
C8x11.5	0.2032	0.057404	0.005588	0.009906	1.35691E-05	5.49425E-07	4.90185E-08
C7x12.25	0.1778	0.0557276	0.0079756	0.0092964	1.00728E-05	4.86991E-07	5.99157E-08
C7x9.8	0.1778	0.053086	0.005334	0.0092964	8.86573E-06	4.02912E-07	3.74277E-08
C6x13	0.1524	0.0547878	0.0110998	0.0087122	7.24243E-06	4.37043E-07	9.36242E-08
C6x10.5	0.1524	0.0516636	0.0079756	0.0087122	6.32672E-06	3.60456E-07	4.85478E-08
C6x8.2	0.1524	0.048768	0.00508	0.0087122	5.45263E-06	2.88448E-07	2.81589E-08
C5x9	0.127	0.047879	0.008255	0.008128	3.70446E-06	2.63058E-07	4.09534E-08
C5x6.7	0.127	0.04445	0.004826	0.008128	3.11757E-06	1.99375E-07	2.06703E-08
C4x7.25	0.1016	0.0437134	0.0081534	0.0075184	1.9105E-06	1.80228E-07	3.07412E-08
C4x5.4	0.1016	0.0402336	0.0046736	0.0075184	1.60249E-06	1.32778E-07	1.48563E-08
C3x6	0.0762	0.0405384	0.0090424	0.0069342	8.61599E-07	1.26951E-07	2.77901E-08
C3x5	0.0762	0.0380492	0.0065532	0.0069342	7.70028E-07	1.02809E-07	1.56055E-08
C3x4.1	0.0762	0.035814	0.004318	0.0069342	6.90944E-07	8.19976E-08	1.00055E-08

Table E.3 Commercial unequal angles sorted according to their second moment of area.

Designation	Web Height [mm]	Flange Width [mm]	Web Thickness [mm]	Flange Thickness [mm]	Second Moment of Area Iyy [m^4]	Second Moment of Area Izz [m^4]	Torsional Constant J [m^4]
L8 x 8 x 11/8	0.2032	0.2032	0.028575	0.028575	4.08E-05	4.07907E-05	3.16073E-06
L8 x 8 x 7/8	0.2032	0.2032	0.022225	0.022225	3.31E-05	3.3132E-05	1.48715E-06
L8 x 8 x 5/8	0.2032	0.2032	0.015875	0.015875	2.47E-05	2.47241E-05	5.41963E-07
L8 x 4 x 3/4	0.2032	0.1016	0.01905	0.01905	2.29E-05	3.89593E-06	7.02384E-07
L8 x 6 x 5/8	0.2032	0.1524	0.015875	0.015875	2.25E-05	1.09469E-05	4.74217E-07
⋮	⋮	⋮	⋮	⋮	⋮	⋮	⋮
L6 x 31/2 x 3/8	0.1524	0.0889	0.009525	0.009525	5.36939E-06	1.39021E-06	6.95067E-08
L5 x 31/2 x 5/8	0.127	0.0889	0.015875	0.015875	4.99478E-06	2.0104E-06	2.87918E-07
L6 x 4 x 5/16	0.1524	0.1016	0.007938	0.007938	4.74504E-06	1.73985E-06	4.23408E-08
L5 x 5 x 7/16	0.127	0.127	0.011113	0.011113	4.16231E-06	4.16231E-06	1.16183E-07
L5 x 3 x 7/16	0.127	0.0762	0.011113	0.011113	3.50883E-06	9.65657E-07	9.29466E-08
⋮	⋮	⋮	⋮	⋮	⋮	⋮	⋮
L4 x 4 x 1/4	0.1016	0.1016	0.00635	0.00635	1.26534E-06	1.26534E-06	1.73428E-08
L4 x 31/2 x 1/4	0.1016	0.0889	0.00635	0.00635	1.21123E-06	8.69924E-07	1.62589E-08
L4 x 3 x 1/4	0.1016	0.0762	0.00635	0.00635	1.15296E-06	5.66075E-07	1.5175E-08
L31/2 x 31/2 x 5/16	0.0889	0.0889	0.0079375	0.0079375	1.01977E-06	1.01977E-06	2.96386E-08
L31/2 x 3 x 5/16	0.0889	0.0762	0.0079375	0.0079375	9.69819E-07	6.57646E-07	2.75215E-08
⋮	⋮	⋮	⋮	⋮	⋮	⋮	⋮
L21/2 x 21/2 x 1/4	0.0635	0.0635	0.00635	0.00635	2.92611E-07	2.92611E-07	1.08393E-08
L21/2 x 2 x 1/4	0.0635	0.0508	0.00635	0.00635	2.72215E-07	1.54838E-07	9.75533E-09
L2 x 2 x 3/8	0.0508	0.0508	0.009525	0.009525	1.99375E-07	1.99375E-07	2.9266E-08
L2 x 2 x 1/4	0.0508	0.0508	0.00635	0.00635	1.44849E-07	1.44849E-07	8.6714E-09
L2 x 2 x 1/8	0.0508	0.0508	0.003175	0.003175	7.9084E-08	7.9084E-08	1.08393E-09

Table E.4 Commercial Rectangular Hollow Sections (RHSs) sorted according to their second moment of area.

Designation	Web Height [mm]	Flange Width [mm]	Web Thickness [mm]	Flange Thickness [mm]	Second Moment of Area Iyy [m^4]	Second Moment of Area Izz [m^4]	Torsional Constant J [m^4]
32 x 24 x 1/2	0.8128	0.6096	0.0127	0.0127	0.003396448	0.0021977	0.004203937
32 x 24 x 3/8	0.8128	0.6096	0.009525	0.009525	0.002601446	0.0016857	0.003192495
28 x 24 x 1/2	0.7112	0.6096	0.0127	0.0127	0.002484902	0.0019688	0.003467208
26 x 24 x 1/2	0.6604	0.6096	0.0127	0.0127	0.002089482	0.0018522	0.003105086
22 x 20 x 5/8	0.5588	0.508	0.015875	0.015875	0.001469297	0.0012737	0.00224765
⋮	⋮	⋮	⋮	⋮	⋮	⋮	⋮
14 x 10 x 5/8	0.3556	0.254	0.014757	0.014757	0.000285951	0.0001694	0.000346305
16 x 12 x 5/16	0.4064	0.3048	0.007391	0.007391	0.000247658	0.0001598	0.0003026
16 x 8 x 3/8	0.4064	0.2032	0.008865	0.008865	0.000221019	7.534E-05	0.000181477
14 x 6 x 1/2	0.3556	0.1524	0.011811	0.011811	0.000167325	4.37E-05	0.000116129
12 x 10 x 5/16	0.3048	0.254	0.007391	0.007391	0.000109885	8.325E-05	0.000148178
⋮	⋮	⋮	⋮	⋮	⋮	⋮	⋮
8 x 6 x 3/8	0.2032	0.1524	0.008865	0.008865	3.29239E-05	2.106E-05	4.16231E-05
10 x 2 x 3/8	0.254	0.0508	0.008865	0.008865	2.98438E-05	1.952E-06	6.61808E-06
7 x 5 x 1/2	0.1778	0.127	0.011811	0.011811	2.52236E-05	1.482E-05	3.15503E-05
9 x 3 x 5/16	0.2286	0.0762	0.007391	0.007391	2.40166E-05	4.112E-06	1.20291E-05
8 x 4 x 5/16	0.2032	0.1016	0.007391	0.007391	2.12278E-05	7.159E-06	1.77315E-05
⋮	⋮	⋮	⋮	⋮	⋮	⋮	⋮
3 x 2 x 1/4	0.0762	0.0508	0.005918	0.005918	8.82411E-07	4.62E-07	1.0489E-06
3 x 1 1/2 x 1/4	0.0762	0.0381	0.005918	0.005918	6.99269E-07	2.252E-07	5.99373E-07
3 x 1 x 1/8	0.0762	0.0254	0.002946	0.002946	3.40061E-07	5.744E-08	1.69822E-07
2 1/2 x 1 1/2 x 1/8	0.0635	0.0381	0.002946	0.002946	2.78043E-07	1.245E-07	2.85951E-07
2 x 1 x 3/16	0.0508	0.0254	0.00442	0.00442	1.45265E-07	4.662E-08	1.25286E-07

Table E.5 Commercial Square Hollow Sections (SHSs) sorted according to their second moment of area.

Designation	Web Height [mm]	Flange Width [mm]	Web Thickness [mm]	Flange Thickness [mm]	Second Moment of Area Iyy [m^4]	Second Moment of Area Izz [m^4]	Torsional Constant J [m^4]
32 x 32 x 5/8	0.8128	0.8128	0.015875	0.015875	0.00512	0.00512	0.0082
30 x 30 x 1/2	0.762	0.762	0.0127	0.0127	0.003463	0.003463	0.005411
28 x 28 x 5/8	0.7112	0.7112	0.015875	0.015875	0.003388	0.003388	0.005453
32 x 32 x 3/8	0.8128	0.8128	0.009525	0.009525	0.003226	0.003226	0.004995
26 x 26 x 1/2	0.6604	0.6604	0.0127	0.0127	0.002227	0.002227	0.003509
⋮	⋮	⋮	⋮	⋮	⋮	⋮	⋮
12 x 12 x 5/8	0.3048	0.3048	0.014757	0.014757	0.000228	0.000228	0.000368
12 x 12 x 3/8	0.3048	0.3048	0.008865	0.008865	0.000149	0.000149	0.000234
10 x 10 x 1/2	0.254	0.254	0.011811	0.011811	0.000107	0.000107	0.000171
12 x 12 x 1/4	0.3048	0.3048	0.005918	0.005918	0.000103	0.000103	0.00016
10 x 10 x 5/16	0.254	0.254	0.007391	0.007391	7.16E-05	7.16E-05	0.000113
⋮	⋮	⋮	⋮	⋮	⋮	⋮	⋮
4 1/2 x 4 1/2 x 1/2	0.1143	0.1143	0.011811	0.011811	7.49E-06	7.49E-06	1.3E-05
5 1/2 x 5 1/2 x 3/16	0.1397	0.1397	0.00442	0.00442	7.08E-06	7.08E-06	1.11E-05
6 x 6 x 1/8	0.1524	0.1524	0.002946	0.002946	6.45E-06	6.45E-06	9.95E-06
4 1/2 x 4 1/2 x 5/16	0.1143	0.1143	0.007391	0.007391	5.62E-06	5.62E-06	9.28E-06
5 x 5 x 3/16	0.127	0.127	0.00442	0.00442	5.24E-06	5.24E-06	8.28E-06
⋮	⋮	⋮	⋮	⋮	⋮	⋮	⋮
2 x 2 x 3/16	0.0508	0.0508	0.00442	0.00442	2.66E-07	2.66E-07	4.54E-07
1 3/4 x 1 3/4 x 3/16	0.04445	0.04445	0.00442	0.00442	1.69E-07	1.69E-07	2.91E-07
1 5/8 x 1 5/8 x 1/8	0.041275	0.041275	0.002946	0.002946	1.02E-07	1.02E-07	1.71E-07
1 1/2 x 1 1/2 x 1/8	0.0381	0.0381	0.002946	0.002946	7.83E-08	7.83E-08	1.32E-07
1 1/4 x 1 1/4 x 1/8	0.03175	0.03175	0.002946	0.002946	4.2E-08	4.2E-08	7.24E-08

Table E.6 Commercial Circular Hollow Sections (CHSs) sorted according to their second moment of area.

Designation	Web Height [mm]	Flange Width [mm]	Web Thickness [mm]	Flange Thickness [mm]	Second Moment of Area Iyy [m^4]	Second Moment of Area Izz [m^4]	Torsional Constant J [m^4]
20.000 x 0.500	0.508	0.508	0.011811	0.011811	0.000566075	0.000566075	0.001132
18.000 x 0.500	0.4572	0.4572	0.011811	0.011811	0.000409988	0.000409988	0.00082
16.000 x 0.500	0.4064	0.4064	0.011811	0.011811	0.000285119	0.000285119	0.00057
16.000 x 0.375	0.4064	0.4064	0.008865	0.008865	0.000218938	0.000218938	0.000437
14.000 x 0.500	0.3556	0.3556	0.011811	0.011811	0.000188553	0.000188553	0.000378
⋮	⋮	⋮	⋮	⋮	⋮	⋮	⋮
10.000 x 0.188	0.254	0.254	0.00442	0.00442	2.69718E-05	2.69718E-05	5.41E-05
8.625 x 0.250	0.219075	0.219075	0.005918	0.005918	2.25181E-05	2.25181E-05	4.5E-05
7.625 x 0.375	0.193675	0.193675	0.008865	0.008865	2.20186E-05	2.20186E-05	4.41E-05
7.000 x 0.500	0.1778	0.1778	0.011811	0.011811	2.1311E-05	2.1311E-05	4.25E-05
7.500 x 0.375	0.1905	0.1905	0.008865	0.008865	2.08948E-05	2.08948E-05	4.16E-05
⋮	⋮	⋮	⋮	⋮	⋮	⋮	⋮
6.625 x 0.125	0.168275	0.168275	0.002946	0.002946	5.24452E-06	5.24452E-06	1.04E-05
5.000 x 0.312	0.127	0.127	0.007391	0.007391	4.99478E-06	4.99478E-06	9.99E-06
5.000 x 0.250	0.127	0.127	0.005918	0.005918	4.13734E-06	4.13734E-06	8.28E-06
6.000 x 0.125	0.1524	0.1524	0.002946	0.002946	3.86263E-06	3.86263E-06	7.74E-06
5.563 x 0.134	0.1413	0.1413	0.003175	0.003175	3.28823E-06	3.28823E-06	6.58E-06
⋮	⋮	⋮	⋮	⋮	⋮	⋮	⋮
2.375 x 0.218	0.060325	0.060325	0.005182	0.005182	3.44223E-07	3.44223E-07	6.87E-07
2.375 x 0.154	0.060325	0.060325	0.003632	0.003632	2.60977E-07	2.60977E-07	5.2E-07
2.500 x 0.125	0.0635	0.0635	0.002946	0.002946	2.57647E-07	2.57647E-07	5.16E-07
1.900 x 0.145	0.04826	0.04826	0.003429	0.003429	1.21956E-07	1.21956E-07	2.44E-07
1.660 x 0.140	0.042164	0.042164	0.003302	0.003302	7.65866E-08	7.65866E-08	1.53E-07

Table E.7 Commercial I-Beams designed according to the British Standard, sorted according to their second moment of area.

Designation	Web Height [mm]	Flange Width [mm]	Web Thickness [mm]	Flange Thickness [mm]	Second Moment of Area Iyy [m^4]	Second Moment of Area Izz [m^4]	Torsional Constant J [m^4]
UB 1016x305x584	1.056	0.314	0.036	0.064	0.012461	0.00033	7.12977E-05
UB 1016x305x494	1.036	0.309	0.031	0.054	0.01028	0.00027	4.2725E-05
UB 1016x305x438	1.026	0.305	0.027	0.049	0.009098	0.00023	3.06532E-05
UB 1016x305x415	1.02	0.304	0.026	0.046	0.008531	0.00022	2.57023E-05
UB 1016x305x393	1.016	0.303	0.0244	0.0439	0.008077	0.00021	2.20096E-05
⋮	⋮	⋮	⋮	⋮	⋮	⋮	⋮
UB 686x254x125	0.6779	0.253	0.0117	0.0162	0.00118	4.4E-05	1.07899E-06
UB 610x229x140	0.6172	0.2302	0.0131	0.0221	0.001118	4.5E-05	2.11898E-06
UB 610x229x125	0.6122	0.229	0.0119	0.0196	0.000986	3.9E-05	1.49338E-06
UB 610x229x113	0.6076	0.2282	0.0111	0.0173	0.000873	3.4E-05	1.06468E-06
UB 533x210x122	0.5445	0.2119	0.0127	0.0213	0.00076	3.4E-05	1.73691E-06
⋮	⋮	⋮	⋮	⋮	⋮	⋮	⋮
UB 356x171x57	0.358	0.1722	0.0081	0.013	0.00016	1.1E-05	3.15631E-07
UB 406x140x46	0.4032	0.1422	0.0068	0.0112	0.000157	5.4E-06	1.75445E-07
UB 356x171x51	0.355	0.1715	0.0074	0.0115	0.000141	9.7E-06	2.21836E-07
UB 406x140x39	0.398	0.1418	0.0064	0.0086	0.000125	4.1E-06	9.49053E-08
UB 356x171x45	0.3514	0.1711	0.007	0.0097	0.000121	8.1E-06	1.44281E-07
⋮	⋮	⋮	⋮	⋮	⋮	⋮	⋮
UB 203x133x25	0.2032	0.1332	0.0057	0.0078	2.34E-05	3.1E-06	5.46834E-08
UB 203x102x23	0.2032	0.1018	0.0054	0.0093	2.11E-05	1.6E-06	6.52539E-08
UB 178x102x19	0.1778	0.1012	0.0048	0.0079	1.36E-05	1.4E-06	3.98177E-08
UB 152x89x16	0.1524	0.0887	0.0045	0.0077	8.34E-06	9E-07	3.16252E-08
UB 127x76x13	0.127	0.076	0.004	0.0076	4.73E-06	5.6E-07	2.49505E-08

Table E.8 Commercial Isometric Beams (ISMB) designed according to the Indian Standard, sorted according to their second moment of area.

Designation	Web Height [mm]	Flange Width [mm]	Web Thickness [mm]	Flange Thickness [mm]	Second Moment of Area Iyy [m^4]	Second Moment of Area Izz [m^4]	Torsional Constant J [m^4]
ISMB600	0.6	0.21	0.012	0.0203	0.000918	0.0000265	1.51674E-06
ISLB600	0.6	0.21	0.0105	0.0155	0.000728	0.0000182	7.5286E-07
ISMB550	0.55	0.19	0.0112	0.0193	0.000649	0.0000183	1.16817E-06
ISLB550	0.55	0.19	0.0099	0.015	0.000532	0.0000134	6.05382E-07
ISMB500	0.5	0.18	0.0102	0.0172	0.000452	0.0000137	7.87474E-07
⋮	⋮	⋮	⋮	⋮	⋮	⋮	⋮
ISMB300	0.3	0.14	0.0077	0.0131	0.0000899	0.00000486	2.55473E-07
ISLB(P)300	0.3	0.14	0.007	0.0116	0.0000813	0.00000414	1.79982E-07
ISLB300	0.3	0.15	0.0067	0.0094	0.0000733	0.00000376	1.13134E-07
ISLB275	0.275	0.14	0.0064	0.0088	0.0000538	0.00000287	8.7633E-08
ISMB250	0.25	0.125	0.0069	0.0125	0.0000513	0.00000335	1.90134E-07
⋮	⋮	⋮	⋮	⋮	⋮	⋮	⋮
ISJB225	0.225	0.08	0.0037	0.005	0.0000131	0.000000405	1.04655E-08
ISMB175	0.175	0.085	0.0058	0.009	0.0000126	0.000000767	5.2691E-08
ISLB175	0.175	0.09	0.0051	0.0069	0.000011	0.000000796	2.74482E-08
ISLB(P)175	0.175	0.08	0.0052	0.0077	0.0000107	0.000000573	3.25502E-08
ISJB200	0.2	0.06	0.0034	0.005	0.00000781	0.000000173	7.62019E-09
⋮	⋮	⋮	⋮	⋮	⋮	⋮	⋮
ISJB150	0.15	0.05	0.003	0.0046	0.00000322	0.000000092	4.59449E-09
ISMB100	0.1	0.05	0.0047	0.007	0.00000183	0.000000129	1.4894E-08
ISLB(P)100	0.1	0.05	0.0043	0.007	0.00000178	0.000000132	1.40834E-08
ISLB100	0.1	0.05	0.004	0.0064	0.00000168	0.000000127	1.08714E-08
ISLB75	0.075	0.05	0.0037	0.005	0.000000727	0.0000001	5.43294E-09

Appendix F. THE OPTIMAL SETS OF SIZING PARAMETERS FOR THE CONSIDERED MODELS.

Table F.1 Optimal sets of sizing parameters for model A1.

Structural Component No.	Cross Section Designation				
	MESO-ABC	MESO-BA	MESO-DE	MESO-PSO	MESO-SA
1	S20x96	S20x96	S20x96	S20x96	S20x96
2	S20x96	S20x75	S20x96	S20x96	S20x96
3	S6x12.5	S6x12.5	S6x12.5	S6x12.5	S20x86
4	S15x42.9	S12x50	S15x42.9	S15x42.9	S15x42.9
5	S12x50	S15x42.9	S15x42.9	S15x42.9	S10x35
6	S12x35	S10x35	S12x31.8	S12x31.8	S8x23
7	S10x25.4	S8x18.4	S10x25.4	S10x25.4	S6x12.5
8	S8x18.4	S6x12.5	S8x18.4	S8x18.4	S15x42.9
9	S8x18.4	S6x12.5	S6x12.5	S6x12.5	S12x35
10	S6x12.5	S6x12.5	S6x12.5	S6x12.5	S12x31.8
11	S12x50	S6x17.25	S12x31.8	S12x35	S8x23
12	S20x96	S8x18.4	S12x50	S12x35	S8x18.4
13	6 x 3 x 1/4	7 x 4 x 1/2	8 x 2 x 3/8	8 x 3 x 3/8	S6x12.5
14	6 x 5 x 5/16	3 x 2 x 1/4	6 x 4 x 5/16	7 x 3 x 1/2	S6x12.5
15	3 x 2 x 1/4	3 x 2 x 1/4	3 x 2 x 1/4	3 x 2 x 1/4	S12x40.8
16	3 x 2 x 1/4	3 x 2 x 1/4	3 x 2 x 1/4	3 x 2 x 1/4	S20x66
17	3 x 2 x 1/4	3 x 2 x 1/4	3 x 2 x 1/4	3 x 2 x 1/4	6 x 4 x 5/16
18	3 x 2 x 1/4	3 x 2 x 1/4	3 x 2 x 1/4	3 x 2 x 1/4	6 x 5 x 5/16
19	3 x 2 x 1/4	3 x 2 x 1/4	3 x 2 x 1/4	3 x 2 x 1/4	3 x 2 x 1/4
20	3 x 2 x 1/4	3 x 2 x 1/4	3 x 2 x 1/4	3 x 2 x 1/4	3 x 2 x 1/4
21	3 x 2 x 1/4	7 x 4 x 1/2	3 x 2 x 1/4	3 x 2 x 1/4	3 x 2 x 1/4
22	3 x 2 x 1/4	6 x 4 x 5/16	3 x 2 x 1/4	3 x 2 x 1/4	3 x 2 x 1/4
23	C8x18.75	C8x11.5	C8x18.75	C8x18.75	3 x 2 x 1/4
24	C5x6.7	C3x5	C6x8.2	C4x7.25	3 x 2 x 1/4
25	C3x4.1	C6x13	C8x11.5	C8x13.75	3 x 2 x 1/4
26	C8x13.75	C6x10.5	C6x13	C6x13	3 x 2 x 1/4
27	C8x18.75	C8x18.75	C8x18.75	C8x18.75	C8x18.75
28	C7x12.25	C5x9	C6x10.5	C6x10.5	C6x13
29	C8x18.75	C8x18.75	C8x18.75	C8x13.75	C3x4.1
30	C8x18.75	C8x11.5	C8x13.75	C8x13.75	C3x4.1
31	C8x18.75	C8x18.75	C8x18.75	C8x18.75	C3x4.1
32	C3x4.1	C3x4.1	C3x4.1	C3x4.1	C7x12.25
33	C3x4.1	C3x4.1	C3x4.1	C3x4.1	C5x9
34	NA	NA	NA	NA	C7x9.8
35	NA	NA	NA	NA	C8x18.75
36	NA	NA	NA	NA	C8x18.75
37	NA	NA	NA	NA	C8x18.75
38	NA	NA	NA	NA	C8x18.75
39	NA	NA	NA	NA	C8x18.75
40	NA	NA	NA	NA	C3x4.1
41	NA	NA	NA	NA	C3x4.1

Table F.2 Optimal sets of sizing parameters for model B1.

Structural Component No.	Cross Section Designation				
	MESO-ABC	MESO-BA	MESO-DE	MESO-PSO	MESO-SA
1	S12x50'	S6x12.5	S12x31.8'	S12x35'	S15x42.9'
2	S10x35'	S6x12.5	S6x17.25'	S8x23'	S10x35'
3	9 x 5 x 1/2'	S6x12.5	S6x12.5'	S6x12.5'	S6x12.5'
4	9 x 5 x 1/2'	9 x 5 x 1/2	9 x 5 x 1/2'	9 x 5 x 1/2'	S6x12.5'
5	6 x 5 x 5/16'	9 x 5 x 1/2	8 x 6 x 3/8'	9 x 5 x 1/2'	9 x 5 x 1/2'
6	6 x 2 x 3/16'	5 x 4 x 3/16	6 x 4 x 5/16'	9 x 3 x 5/16'	9 x 5 x 1/2'
7	3 x 2 x 1/4'	4 x 2 1/2 x 1/4	6 x 3 x 1/4'	9 x 3 x 5/16'	9 x 3 x 5/16'
8	9 x 5 x 1/2'	3 x 2 x 1/4	6 x 3 x 1/4'	5 x 4 x 3/16'	8 x 4 x 5/16'
9	9 x 5 x 1/2'	3 x 2 x 1/4	6 x 3 x 1/4'	6 x 2 x 3/16'	6 x 5 x 5/16'
10	9 x 5 x 1/2'	3 x 2 x 1/4	3 x 2 x 1/4'	5 x 3 x 1/8'	7 x 4 x 1/2'
11	6 x 4 x 5/16'	3 x 2 x 1/4	3 x 2 x 1/4'	6 x 3 x 1/4'	3 x 2 x 1/4'
12	6 x 5 x 5/16'	9 x 5 x 1/2	9 x 5 x 1/2'	9 x 5 x 1/2'	3 x 2 1/2 x 1/4'
13	3 x 2 x 1/4'	9 x 5 x 1/2	9 x 5 x 1/2'	9 x 5 x 1/2'	3 x 2 x 1/4'
14	9 x 5 x 1/2'	7 x 5 x 1/2	6 x 5 x 5/16'	9 x 3 x 5/16'	3 x 2 x 1/4'
15	9 x 5 x 1/2'	7 x 3 x 1/2	6 x 4 x 5/16'	9 x 3 x 5/16'	9 x 5 x 1/2'
16	3 x 2 x 1/4'	3 x 2 x 1/4	6 x 2 x 3/16'	6 x 4 x 5/16'	9 x 5 x 1/2'
17	NA	3 x 2 x 1/4	6 x 2 x 3/16'	6 x 4 x 5/16'	9 x 3 x 5/16'

18	**NA**	**3 x 2 x 1/4**	**3 x 2 x 1/4'**	**4 x 3 x 5/16'**	**9 x 5 x 1/2'**
19	**NA**	**8 x 6 x 3/8**	**9 x 3 x 5/16'**	**9 x 5 x 1/2'**	**6 x 3 x 1/4'**
20	**NA**	**9 x 5 x 1/2**	**9 x 5 x 1/2'**	**9 x 5 x 1/2'**	**6 x 4 x 5/16'**
21	**NA**	**9 x 3 x 5/16**	**9 x 3 x 5/16'**	**9 x 5 x 1/2'**	**5 x 3 x 1/8'**
22	**NA**	**5 x 3 x 1/8**	**8 x 2 x 3/8'**	**6 x 5 x 5/16'**	**3 1/2 x 2 1/2 x 1/4'**
23	**NA**	**NA**	**NA**	**NA**	**3 x 2 x 1/4'**
24	**NA**	**NA**	**NA**	**NA**	**9 x 5 x 1/2'**
25	**NA**	**NA**	**NA**	**NA**	**9 x 5 x 1/2'**
26	**NA**	**NA**	**NA**	**NA**	**9 x 5 x 1/2'**
27	**NA**	**NA**	**NA**	**NA**	**3 1/2 x 2 1/2 x 1/4'**
28	**NA**	**NA**	**NA**	**NA**	**3 x 2 x 1/4'**

Table F.3 Optimal sets of sizing parameters for model C1.

Structural Component No.	**Cross Section Designation**				
	MESO-ABC	**MESO-BA**	**MESO-DE**	**MESO-PSO**	**MESO-SA**
1	**9 x 5 x 1/2**	**9 x 5 x 1/2**	**9 x 5 x 1/2**	**9 x 5 x 1/2**	**9 x 3 x 5/16**
2	**9 x 3 x 5/16**	**9 x 3 x 5/16**	**9 x 3 x 5/16**	**9 x 5 x 1/2**	**7 x 5 x 1/2**
3	**6 x 2 x 3/16**	**8 x 4 x 5/16**	**6 x 4 x 5/16**	**7 x 4 x 1/2**	**4 x 3 x 5/16**
4	**4 x 2 1/2 x 1/4**	**3 x 2 x 1/4**	**3 x 2 x 1/4**	**6 x 3 x 1/4**	**3 x 2 x 1/4**
5	**3 x 2 x 1/4**	**3 1/2 x 2 1/2 x 1/4**	**3 x 2 x 1/4**	**3 x 2 x 1/4**	**3 x 2 x 1/4**
6	**3 x 2 x 1/4**	**3 x 2 x 1/4**	**3 x 2 x 1/4**	**3 x 2 x 1/4**	**9 x 5 x 1/2**
7	**9 x 5 x 1/2**	**9 x 5 x 1/2**	**9 x 5 x 1/2**	**3 x 2 x 1/4**	**8 x 3 x 3/8**
8	**9 x 3 x 5/16**	**9 x 3 x 5/16**	**9 x 5 x 1/2**	**9 x 5 x 1/2**	**6 x 2 x 3/16**
9	**5 x 3 x 1/8**	**6 x 2 x 3/16**	**8 x 2 x 3/8**	**9 x 5 x 1/2**	**5 x 3 x 1/8**
10	**3 x 2 1/2 x 1/4**	**3 x 2 x 1/4**	**3 x 2 x 1/4**	**7 x 3 x 1/2**	**3 x 2 x 1/4**
11	**3 x 2 x 1/4**	**3 x 2 x 1/4**	**3 x 2 x 1/4**	**4 x 3 x 5/16**	**3 x 2 x 1/4**
12	**9 x 5 x 1/2**	**9 x 5 x 1/2**	**9 x 5 x 1/2**	**3 x 2 x 1/4**	**9 x 5 x 1/2**
13	**9 x 5 x 1/2**	**9 x 5 x 1/2**	**9 x 5 x 1/2**	**3 x 2 x 1/4**	**9 x 3 x 5/16**
14	**7 x 5 x 1/2**	**9 x 3 x 5/16**	**9 x 5 x 1/2**	**9 x 5 x 1/2**	**9 x 3 x 5/16**
15	**7 x 5 x 1/2**	**3 x 2 x 1/4**	**3 x 2 x 1/4**	**9 x 5 x 1/2**	**9 x 3 x 5/16**
16	**3 x 2 x 1/4**	**3 x 2 x 1/4**	**3 x 2 x 1/4**	**9 x 3 x 5/16**	**3 x 2 x 1/4**
17	**NA**	**NA**	**NA**	**6 x 2 x 3/16**	**NA**
18	**NA**	**NA**	**NA**	**3 x 2 x 1/4**	**NA**
19	**NA**	**NA**	**NA**	**3 x 2 x 1/4**	**NA**

Table F.4 Optimal sets of sizing parameters for model D1.

Structural Component No.	**Cross Section Designation**				
	MESO-ABC	**MESO-BA**	**MESO-DE**	**MESO-PSO**	**MESO-SA**
1	**UB 127x76x13**	**UB 127x76x13**	**UB 127x76x13**	**UB 127x76x13**	**UB 127x76x13**
2	**8 x 2 x 3/8**	**8 x 4 x 5/16**	**9 x 3 x 5/16**	**9 x 3 x 5/16**	**9 x 3 x 5/16**
3	**6 x 3 x 1/4**	**6 x 2 x 3/16**	**6 x 5 x 5/16**	**6 x 5 x 5/16**	**6 x 5 x 5/16**
4	**6 x 2 x 3/16**	**6 x 2 x 3/16**	**6 x 2 x 3/16**	**6 x 2 x 3/16**	**6 x 2 x 3/16**
5	**5 x 3 x 1/8**	**5 x 3 x 1/8**	**4 x 2 1/2 x 1/4**	**4 x 3 x 5/16**	**4 x 2 1/2 x 1/4**
6	**3 x 2 x 1/4**	**3 x 2 x 1/4**	**3 x 2 x 1/4**	**3 x 2 x 1/4**	**3 x 2 x 1/4**
7	**8 x 2 x 3/8**	**8 x 6 x 3/8**	**9 x 3 x 5/16**	**9 x 3 x 5/16**	**9 x 3 x 5/16**
8	**6 x 3 x 1/4**	**6 x 3 x 1/4**	**6 x 5 x 5/16**	**6 x 4 x 5/16**	**6 x 5 x 5/16**
9	**6 x 2 x 3/16**	**6 x 2 x 3/16**	**6 x 2 x 3/16**	**6 x 2 x 3/16**	**6 x 2 x 3/16**
10	**6 x 2 x 3/16**	**5 x 2 x 5/16**	**3 1/2 x 2 1/2 x 1/4**	**3 x 2 x 1/4**	**3 1/2 x 2 1/2 x 1/4**
11	**3 x 2 x 1/4**	**3 x 2 x 1/4**	**3 x 2 x 1/4**	**3 x 2 x 1/4**	**3 x 2 x 1/4**
12	**9 x 3 x 5/16**	**9 x 5 x 1/2**	**9 x 5 x 1/2**	**9 x 5 x 1/2**	**9 x 5 x 1/2**
13	**8 x 3 x 3/8**	**8 x 4 x 5/16**	**9 x 3 x 5/16**	**9 x 3 x 5/16**	**9 x 3 x 5/16**
14	**7 x 5 x 1/2**	**8 x 2 x 3/8**	**9 x 3 x 5/16**	**9 x 3 x 5/16**	**9 x 3 x 5/16**
15	**9 x 3 x 5/16**	**9 x 3 x 5/16**	**9 x 3 x 5/16**	**9 x 3 x 5/16**	**9 x 3 x 5/16**
16	**9 x 3 x 5/16**	**8 x 2 x 3/8**	**6 x 2 x 3/16**	**6 x 3 x 1/4**	**6 x 2 x 3/16**

Table F.5 Optimal sets of sizing parameters for model E1.

Structural Component No.	Cross Section Designation				
	MESO-ABC	MESO-BA	MESO-DE	MESO-PSO	MESO-SA
1	S12x40.8'	S15x50	S12x40.8'	S15x42.9	S10x25.4'
2	S12x35'	S15x50	S12x35'	S12x35	S15x42.9'
3	S10x25.4'	S15x50	S12x31.8'	S12x31.8	S12x40.8'
4	S8x18.4'	S6x12.5	S10x35'	S10x35	S8x18.4'
5	S8x23'	S6x12.5	S12x35'	S12x40.8	S6x12.5'
6	S8x23'	S6x12.5	S15x42.9'	S12x35	S6x12.5'
7	9 x 7 x 1/2'	3 x 2 x 1/4	9 x 3 x 5/16'	9 x 3 x 5/16'	9 x 3 x 5/16'
8	9 x 3 x 5/16'	6 x 2 x 3/16	9 x 3 x 5/16'	9 x 3 x 5/16'	9 x 3 x 5/16'
9	9 x 3 x 5/16'	7 x 3 x 1/2	9 x 3 x 5/16'	9 x 3 x 5/16'	8 x 3 x 3/8'
10	9 x 3 x 5/16'	9 x 7 x 1/2	9 x 3 x 5/16'	9 x 3 x 5/16'	8 x 6 x 3/8'
11	9 x 5 x 1/2'	9 x 5 x 1/2	8 x 2 x 3/8'	9 x 5 x 1/2'	6 x 3 x 1/4'
12	9 x 7 x 1/2'	3 x 2 x 1/4	9 x 3 x 5/16'	9 x 5 x 1/2'	9 x 3 x 5/16'
13	9 x 3 x 5/16'	4 x 2 1/2 x 1/4	8 x 6 x 3/8'	9 x 3 x 5/16'	9 x 3 x 5/16'
14	9 x 3 x 5/16'	7 x 5 x 1/2	9 x 3 x 5/16'	9 x 3 x 5/16'	9 x 3 x 5/16'
15	9 x 3 x 5/16'	9 x 7 x 1/2	9 x 3 x 5/16'	9 x 3 x 5/16'	9 x 3 x 5/16'
16	9 x 5 x 1/2'	9 x 7 x 1/2	8 x 4 x 5/16'	9 x 3 x 5/16'	6 x 5 x 5/16'
17	8 x 2 x 3/8'	3 x 2 x 1/4	9 x 3 x 5/16'	9 x 5 x 1/2'	9 x 7 x 1/2'
18	8 x 4 x 5/16'	3 x 2 x 1/4	6 x 3 x 1/4'	7 x 4 x 1/2'	6 x 3 x 1/4'
19	4 x 3 x 5/16'	3 x 2 x 1/4	6 x 2 x 3/16'	3 1/2 x 2 1/2 x 1/4'	6 x 2 x 3/16'
20	6 x 2 x 3/16'	7 x 3 x 1/2	6 x 2 x 3/16'	5 x 2 x 5/16'	8 x 4 x 5/16'
21	9 x 7 x 1/2'	9 x 7 x 1/2	9 x 3 x 5/16'	9 x 7 x 1/2'	9 x 3 x 5/16'

Table F.6 Optimal sets of sizing parameters for model A2.

Structural Component No.	Cross Section Designation				
	MESO-ABC	MESO-BA	MESO-DE	MESO-PSO	MESO-SA
1	8 x 6 x 3/8	8 x 6 x 3/8	8 x 6 x 3/8	8 x 6 x 3/8	8 x 6 x 3/8
2	3 x 2 1/2 x 1/4	6 x 2 x 3/16	3 x 2 1/2 x 1/4	5 x 3 x 1/8	8 x 6 x 3/8
3	3 x 2 1/2 x 1/4	3 x 2 1/2 x 1/4	3 x 2 1/2 x 1/4	3 x 2 1/2 x 1/4	8 x 4 x 5/16
4	3 x 2 1/2 x 1/4	3 x 2 1/2 x 1/4	3 x 2 1/2 x 1/4	3 x 2 1/2 x 1/4	5 x 3 x 1/8
5	3 x 2 1/2 x 1/4	3 x 2 1/2 x 1/4	3 x 2 1/2 x 1/4	3 x 2 1/2 x 1/4	3 1/2 x 2 1/2 x 1/4
6	3 x 2 1/2 x 1/4	3 x 2 1/2 x 1/4	3 x 2 1/2 x 1/4	3 x 2 1/2 x 1/4	3 x 2 1/2 x 1/4
7	3 x 2 1/2 x 1/4	3 x 2 1/2 x 1/4	3 x 2 1/2 x 1/4	3 x 2 1/2 x 1/4	3 x 2 1/2 x 1/4
8	3 x 2 1/2 x 1/4	3 x 2 1/2 x 1/4	3 x 2 1/2 x 1/4	3 x 2 1/2 x 1/4	6 x 3 x 1/4
9	3 x 2 1/2 x 1/4	3 x 2 1/2 x 1/4	3 x 2 1/2 x 1/4	3 x 2 1/2 x 1/4	6 x 2 x 3/16
10	3 x 2 1/2 x 1/4	3 x 2 1/2 x 1/4	3 x 2 1/2 x 1/4	3 x 2 1/2 x 1/4	5 x 3 x 1/8
11	8 x 6 x 3/8	8 x 6 x 3/8	8 x 6 x 3/8	8 x 6 x 3/8	3 x 2 1/2 x 1/4
12	8 x 6 x 3/8	8 x 6 x 3/8	8 x 6 x 3/8	8 x 6 x 3/8	3 x 2 1/2 x 1/4
13	8 x 4 x 5/16	8 x 4 x 5/16	8 x 6 x 3/8	8 x 4 x 5/16	3 x 2 1/2 x 1/4
14	8 x 2 x 3/8	6 x 5 x 5/16	8 x 6 x 3/8	6 x 5 x 5/16	3 x 2 1/2 x 1/4
15	6 x 4 x 5/16	3 x 2 1/2 x 1/4	8 x 4 x 5/16	6 x 2 x 3/16	8 x 6 x 3/8
16	7 x 4 x 1/2	3 x 2 1/2 x 1/4	5 x 3 x 1/8	6 x 4 x 5/16	8 x 6 x 3/8
17	5 x 3 x 1/8	3 x 2 1/2 x 1/4	5 x 3 x 1/8	3 x 2 1/2 x 1/4	7 x 4 x 1/2
18	3 x 2 1/2 x 1/4	3 x 2 1/2 x 1/4	3 x 2 1/2 x 1/4	3 x 2 1/2 x 1/4	6 x 3 x 1/4
19	3 x 2 1/2 x 1/4	3 x 2 1/2 x 1/4	3 x 2 1/2 x 1/4	3 x 2 1/2 x 1/4	6 x 3 x 1/4
20	6 x 3 x 1/4	3 x 2 1/2 x 1/4	5 x 3 x 1/8	3 x 2 1/2 x 1/4	6 x 2 x 3/16
21	L3 x 2 x 5/16	L3 x 2 x 5/16	L3 x 2 x 5/16	L3 x 2 x 1/2	6 x 2 x 3/16
22	L3 x 2 x 5/16	L3 x 2 x 5/16	L3 x 2 x 5/16	L3 x 2 x 5/16	8 x 4 x 5/16
23	L3 x 2 x 5/16	L3 x 2 x 5/16	L3 x 2 x 5/16	L3 x 2 x 5/16	6 x 4 x 5/16
24	L31/2 x 21/2 x 1/4	L3 x 2 x 5/16	L3 x 2 x 5/16	L3 x 2 x 5/16	6 x 3 x 1/4
25	L3 x 2 x 5/16	L3 x 2 x 5/16	L31/2 x 3 x 1/2	L3 x 2 x 5/16	3 x 2 1/2 x 1/4
26	L3 x 2 x 5/16	L3 x 2 x 5/16	L4 x 3 x 1/4	L31/2 x 21/2 x 1/4	3 x 2 1/2 x 1/4
27	L3 x 2 x 5/16	L3 x 2 x 5/16	L3 x 2 x 5/16	L3 x 2 x 5/16	3 x 2 1/2 x 1/4
28	L3 x 2 x 5/16	L4 x 4 x 3/8	L3 x 2 x 5/16	L3 x 2 x 5/16	3 x 2 1/2 x 1/4
29	L3 x 2 x 5/16	L4 x 4 x 1/4	L3 x 2 x 5/16	L3 x 2 x 5/16	L31/2 x 21/2 x 1/2
30	L3 x 21/2 x 1/4	L4 x 4 x 3/8	L3 x 2 x 5/16	L3 x 2 x 5/16	L3 x 2 x 5/16
31	L3 x 2 x 5/16	L3 x 2 x 5/16	L3 x 2 x 5/16	L3 x 2 x 5/16	L3 x 2 x 5/16
32	L3 x 2 x 5/16	L3 x 2 x 5/16	L3 x 2 x 5/16	L3 x 2 x 5/16	L3 x 2 x 5/16
33	3 x 3 x 3/16	L3 x 2 x 5/16	L31/2 x 21/2 x 1/2	L3 x 2 x 5/16	L3 x 2 x 5/16
34	3 x 3 x 3/16	L3 x 2 x 5/16	L31/2 x 21/2 x 1/4	L3 x 2 x 5/16	L3 x 2 x 5/16
35	3 x 3 x 3/16	L3 x 2 x 5/16	L3 x 2 x 5/16	L3 x 2 x 5/16	L3 x 2 x 5/16
36	3 x 3 x 3/16	L3 x 2 x 5/16	L3 x 2 x 5/16	L31/2 x 21/2 x 1/4	L4 x 31/2 x 1/4
37	3 x 3 x 3/16	L3 x 2 x 5/16	3 x 3 x 3/16	L3 x 2 x 5/16	L3 x 2 x 5/16
38	3 x 3 x 5/16	L3 x 2 x 5/16	3 x 3 x 3/16	L3 x 2 x 5/16	L3 x 2 x 5/16
39	3 x 3 x 3/16	L3 x 2 x 5/16	3 x 3 x 3/16	L3 x 2 x 5/16	L3 x 2 x 5/16
40	3 x 3 x 3/16	L3 x 2 x 5/16	3 x 3 x 3/16	L3 x 2 x 5/16	L3 x 2 x 5/16
41	3 x 3 x 3/16	L3 x 2 x 5/16	3 x 3 x 3/16	3 x 3 x 3/16	L3 x 2 x 5/16

42	3 x 3 x 3/16	L4 x 4 x 3/8	3 x 3 x 3/16	3 x 3 x 3/16	L3 x 2 x 5/16
43	3 x 3 x 3/16	L31/2 x 3 x 5/16	3 x 3 x 3/16	3 x 3 x 3/16	L31/2 x 21/2 x 1/4
44	3 x 3 x 3/16	L4 x 4 x 3/8	3 x 3 x 3/16	3 x 3 x 3/16	L3 x 2 x 5/16
45	3 x 3 x 3/16	L3 x 2 x 5/16	3 x 3 x 3/16	3 x 3 x 3/16	L3 x 2 x 5/16
46	3 x 3 x 3/16	L3 x 2 x 5/16	3 x 3 x 3/16	3 x 3 x 3/16	L3 x 2 x 5/16
47	4 x 4 x 3/16	L3 x 2 x 5/16	3 x 3 x 3/16	3 x 3 x 3/16	L3 x 2 x 5/16
48	4 1/2 x 4 1/2 x 3/16	L3 x 2 x 5/16	3 x 3 x 3/16	3 x 3 x 3/16	L3 x 2 x 5/16
49	5 x 5 x 3/16	3 x 3 x 3/16	3 x 3 x 3/16	3 x 3 x 3/16	L3 x 2 x 5/16
50	3 x 3 x 3/16	5 x 5 x 5/16	6 x 6 x 1/8	3 x 3 x 3/16	L4 x 4 x 1/4
51	3.000 x 0.134	3 x 3 x 3/16	3 x 3 x 3/16	6 x 6 x 1/4	L3 x 2 x 5/16
52	3.000 x 0.134	3 x 3 x 3/16	4 x 4 x 3/16	3 x 3 x 3/16	L3 x 2 x 5/16
53	3.000 x 0.134	3 x 3 x 3/16	6 x 6 x 1/8	5 x 5 x 3/16	L3 x 2 x 5/16
54	3.000 x 0.134	3 x 3 x 3/16	3 x 3 x 3/16	3 x 3 x 3/16	L3 x 2 x 5/16
55	3.000 x 0.134	3 x 3 x 3/16	3.000 x 0.134	3 x 3 x 3/16	L3 x 2 x 5/16
56	3.000 x 0.134	3 x 3 x 3/16	3.000 x 0.134	3 1/2 x 3 1/2 x 1/4	L3 x 2 x 5/16
57	3.000 x 0.134	3 x 3 x 3/16	3.000 x 0.134	5 x 5 x 3/16	3 x 3 x 3/16
58	3.000 x 0.134	3 x 3 x 3/16	3.000 x 0.134	3 x 3 x 3/16	3 x 3 x 3/16
59	3.000 x 0.134	6 x 6 x 1/8	3.000 x 0.134	3.000 x 0.134	3 x 3 x 3/16
60	3.000 x 0.134	3 x 3 x 3/16	3.000 x 0.134	3.000 x 0.134	3 x 3 x 3/16
61	3.000 x 0.134	3 x 3 x 3/16	3.000 x 0.134	3.000 x 0.134	3 x 3 x 3/16
62	NA	5 1/2 x 5 1/2 x 3/16	3.000 x 0.134	3.000 x 0.134	3 x 3 x 3/16
63	NA	3 x 3 x 3/16	3.000 x 0.134	3.000 x 0.134	3 x 3 x 3/16
64	NA	3 x 3 x 3/16	3.000 x 0.134	3.000 x 0.134	3 x 3 x 3/16
65	NA	3 x 3 x 3/16	3.000 x 0.134	3.000 x 0.134	3 x 3 x 3/16
66	NA	3 x 3 x 3/16	NA	3.000 x 0.134	3 x 3 x 3/16
67	NA	3.000 x 0.134	NA	3.000 x 0.134	3 x 3 x 3/16
68	NA	3.000 x 0.134	NA	3.000 x 0.134	3 x 3 x 3/16
69	NA	3.000 x 0.134	NA	3.000 x 0.134	3 x 3 x 3/16
70	NA	3.000 x 0.134	NA	NA	3 x 3 x 3/16
71	NA	3.000 x 0.134	NA	NA	3 x 3 x 3/16
72	NA	3.000 x 0.134	NA	NA	3 x 3 x 3/16
73	NA	3.000 x 0.134	NA	NA	3 x 3 x 3/16
74	NA	3.000 x 0.134	NA	NA	3 x 3 x 3/16
75	NA	3.000 x 0.134	NA	NA	3 x 3 x 3/16
76	NA	3.000 x 0.134	NA	NA	3 x 3 x 3/16
77	NA	3.000 x 0.134	NA	NA	3 x 3 x 3/16
78	NA	NA	NA	NA	3 x 3 x 3/16
79	NA	NA	NA	NA	3 x 3 x 3/16
80	NA	NA	NA	NA	3 x 3 x 3/16
81	NA	NA	NA	NA	3 x 3 x 3/16
82	NA	NA	NA	NA	3 x 3 x 3/16
83	NA	NA	NA	NA	3.000 x 0.134
84	NA	NA	NA	NA	3.000 x 0.134
85	NA	NA	NA	NA	3.000 x 0.134
86	NA	NA	NA	NA	3.000 x 0.134
87	NA	NA	NA	NA	3.000 x 0.134
88	NA	NA	NA	NA	3.000 x 0.134
89	NA	NA	NA	NA	3.000 x 0.134
90	NA	NA	NA	NA	3.000 x 0.134
91	NA	NA	NA	NA	3.000 x 0.134
92	NA	NA	NA	NA	3.000 x 0.134
93	NA	NA	NA	NA	3.000 x 0.134
94	NA	NA	NA	NA	3.000 x 0.134
95	NA	NA	NA	NA	3.000 x 0.134
96	NA	NA	NA	NA	3.000 x 0.134
97	NA	NA	NA	NA	3.000 x 0.134

Table F.7 Optimal sets of sizing parameters for model B2.

Structural Component No.	Cross Section Designation				
	MESO-ABC	MESO-BA	MESO-DE	MESO-PSO	MESO-SA
1	ISLB75	ISLB75	ISLB75	ISLB75	ISLB75
2	ISLB75	ISLB75	ISLB75	ISLB75	ISLB75
3	ISLB75	ISLB75	ISLB75	ISLB75	ISLB75
4	ISLB75	ISLB75	ISLB75	ISLB75	ISLB75
5	ISLB75	ISLB75	ISJB225	ISLB75	ISLB75
6	ISLB75	ISLB75	ISLB75	ISLB75	ISLB75
7	ISLB75	ISLB75	ISLB75	ISLB75	ISLB75
8	ISLB75	ISLB75	ISLB75	ISLB75	ISLB75
9	ISLB75	ISLB75	ISLB75	ISLB75	ISLB75
10	ISLB225	ISLB225	ISMB225	ISMB225	ISMB225
11	3 x 2 x 1/4	3 x 2 x 1/4	3 x 2 x 1/4	8 x 4 x 5/16	3 x 2 x 1/4

12	8 x 4 x 5/16	9 x 3 x 5/16	3 x 2 x 1/4	9 x 3 x 5/16	5 x 2 x 5/16
13	6 x 2 x 3/16	6 x 2 x 3/16	3 x 2 x 1/4	6 x 2 x 3/16	6 x 3 x 1/4
14	5 x 3 x 1/8	5 x 3 x 1/8	3 1/2 x 2 1/2 x 1/4	6 x 2 x 3/16	6 x 2 x 3/16
15	3 x 2 x 1/4	3 x 2 x 1/4	3 x 2 x 1/4	3 x 2 x 1/4	3 x 2 x 1/4
16	3 x 2 x 1/4	3 x 2 x 1/4	9 x 3 x 5/16	3 x 2 x 1/4	6 x 2 x 3/16
17	3 x 2 x 1/4	3 x 2 x 1/4	3 x 2 x 1/4	3 x 2 x 1/4	3 x 2 x 1/4
18	3 x 2 x 1/4	3 x 2 x 1/4	3 x 2 x 1/4	3 x 2 x 1/4	3 x 2 x 1/4
19	3 x 2 x 1/4	3 x 2 x 1/4	3 x 2 x 1/4	3 x 2 x 1/4	3 x 2 x 1/4
20	3 x 2 x 1/4	3 x 2 x 1/4	3 x 2 x 1/4	3 x 2 x 1/4	3 x 2 x 1/4
21	3 x 2 x 1/4	3 x 2 x 1/4	3 x 2 x 1/4	3 x 2 x 1/4	3 x 2 x 1/4
22	8 x 4 x 5/16	9 x 3 x 5/16	3 x 2 x 1/4	9 x 3 x 5/16	5 x 3 x 1/8
23	6 x 2 x 3/16	6 x 2 x 3/16	3 x 2 x 1/4	6 x 2 x 3/16	6 x 2 x 3/16
24	6 x 2 x 3/16	5 x 3 x 1/8	3 x 2 x 1/4	5 x 4 x 3/16	6 x 2 x 3/16
25	3 x 2 x 1/4	3 x 2 x 1/4	3 x 2 x 1/4	3 x 2 x 1/4	3 x 2 x 1/4
26	3 x 2 x 1/4	3 x 2 x 1/4	9 x 3 x 5/16	3 x 2 x 1/4	5 x 3 x 1/8
27	3 x 2 x 1/4	3 x 2 x 1/4	3 x 2 x 1/4	3 x 2 x 1/4	3 x 2 x 1/4
28	3 x 2 x 1/4	3 x 2 x 1/4	3 x 2 x 1/4	3 x 2 x 1/4	3 x 2 x 1/4
29	3 x 2 x 1/4	3 x 2 x 1/4	3 x 2 x 1/4	3 x 2 x 1/4	3 x 2 x 1/4
30	3 x 2 x 1/4	3 x 2 x 1/4	3 x 2 x 1/4	3 x 2 x 1/4	3 x 2 x 1/4
31	ISLC200	ISLC200	ISLC75	ISLC200	ISLC75
32	ISLC75	ISLC75	ISLC75	ISLC75	ISLC75
33	ISLC75	ISLC75	ISLC75	ISLC75	ISLC75
34	ISLC75	ISLC75	ISLC75	ISLC75	ISLC75
35	ISLC75	ISLC75	ISLC75	ISLC75	ISLC75
36	ISLC75	ISLC75	ISLC75	ISLC75	ISLC75
37	5 x 5 x 1/2	5 x 5 x 1/2	5 x 5 x 1/2	5 x 5 x 1/2	5 x 5 x 1/2
38	1 1/2 x 1 1/2 x 1/8	1 1/2 x 1 1/2 x 1/8	5 x 5 x 3/16	1 1/2 x 1 1/2 x 1/8	3 1/2 x 3 1/2 x 1/4
39	1 1/2 x 1 1/2 x 1/8	1 1/2 x 1 1/2 x 1/8	1 1/2 x 1 1/2 x 1/8	1 1/2 x 1 1/2 x 1/8	1 1/2 x 1 1/2 x 1/8
40	1 1/2 x 1 1/2 x 1/8	1 1/2 x 1 1/2 x 1/8	1 1/2 x 1 1/2 x 1/8	1 1/2 x 1 1/2 x 1/8	1 1/2 x 1 1/2 x 1/8
41	1 1/2 x 1 1/2 x 1/8	1 1/2 x 1 1/2 x 1/8	1 1/2 x 1 1/2 x 1/8	1 1/2 x 1 1/2 x 1/8	1 1/2 x 1 1/2 x 1/8
42	1 1/2 x 1 1/2 x 1/8	1 1/2 x 1 1/2 x 1/8	1 1/2 x 1 1/2 x 1/8	1 1/2 x 1 1/2 x 1/8	1 1/2 x 1 1/2 x 1/8
43	1 1/2 x 1 1/2 x 1/8	1 1/2 x 1 1/2 x 1/8	1 1/2 x 1 1/2 x 1/8	1 1/2 x 1 1/2 x 1/8	1 1/2 x 1 1/2 x 1/8
44	1 1/2 x 1 1/2 x 1/8	1 1/2 x 1 1/2 x 1/8	1 1/2 x 1 1/2 x 1/8	1 1/2 x 1 1/2 x 1/8	1 1/2 x 1 1/2 x 1/8
45	1 1/2 x 1 1/2 x 1/8	1 1/2 x 1 1/2 x 1/8	1 1/2 x 1 1/2 x 1/8	1 1/2 x 1 1/2 x 1/8	1 1/2 x 1 1/2 x 1/8
46	3 1/2 x 3 1/2 x 1/8	2 1/2 x 2 1/2 x 3/16	1 5/8 x 1 5/8 x 1/8	3 1/2 x 3 1/2 x 1/8	3 1/2 x 3 1/2 x 1/8
47	5 x 5 x 3/16	5 x 5 x 3/16	5 x 5 x 3/16	5 x 5 x 5/16	4 1/2 x 4 1/2 x 3/16
48	3.000 x 0.134	3.000 x 0.134	3.000 x 0.134	3.000 x 0.134	3.000 x 0.134

Table F.8 Optimal sets of sizing parameters for model C2.

Structural Component No.	Cross Section Designation				
	MESO-ABC	MESO-BA	MESO-DE	MESO-PSO	MESO-SA
1	ISLB75	ISLB75	ISLB75	ISLB75	ISJB225
2	ISMB225	ISMB225	ISMB225	ISMB225	ISLB200
3	3 x 2 x 1/4	3 x 2 x 1/4	3 x 2 x 1/4	3 x 2 x 1/4	3 x 2 x 1/4
4	7 x 4 x 1/2	8 x 2 x 3/8	8 x 4 x 5/16	7 x 5 x 1/2	3 x 2 x 1/4
5	6 x 3 x 1/4	6 x 3 x 1/4	6 x 4 x 5/16	6 x 2 x 3/16	6 x 2 x 3/16
6	6 x 2 x 3/16	6 x 2 x 3/16	6 x 3 x 1/4	6 x 2 x 3/16	6 x 2 x 3/16
7	3 x 2 x 1/4	3 x 2 x 1/4	3 x 2 x 1/4	3 x 2 x 1/4	3 x 2 x 1/4
8	3 x 2 x 1/4	3 x 2 x 1/4	3 x 2 x 1/4	3 x 2 x 1/4	6 x 3 x 1/4
9	3 x 2 x 1/4	3 x 2 x 1/4	3 x 2 x 1/4	3 x 2 x 1/4	3 x 2 x 1/4
10	3 x 2 x 1/4	3 x 2 x 1/4	3 x 2 x 1/4	3 x 2 x 1/4	3 x 2 x 1/4
11	3 x 2 x 1/4	3 x 2 x 1/4	3 x 2 x 1/4	3 x 2 x 1/4	3 x 2 x 1/4
12	3 x 2 x 1/4	3 x 2 x 1/4	3 x 2 x 1/4	3 x 2 x 1/4	3 x 2 x 1/4
13	3 x 2 x 1/4	3 x 2 x 1/4	3 x 2 x 1/4	3 x 2 x 1/4	3 x 2 x 1/4
14	7 x 4 x 1/2	7 x 5 x 1/2	8 x 4 x 5/16	8 x 2 x 3/8	3 x 2 1/2 x 1/4
15	6 x 2 x 3/16	6 x 2 x 3/16	6 x 3 x 1/4	6 x 2 x 3/16	6 x 2 x 3/16
16	6 x 2 x 3/16	6 x 2 x 3/16	6 x 3 x 1/4	6 x 2 x 3/16	6 x 2 x 3/16
17	3 x 2 x 1/4	3 x 2 x 1/4	3 x 2 x 1/4	3 x 2 x 1/4	3 1/2 x 2 1/2 x 1/4
18	3 x 2 x 1/4	3 x 2 x 1/4	3 x 2 x 1/4	3 x 2 x 1/4	6 x 3 x 1/4
19	3 x 2 x 1/4	3 x 2 x 1/4	3 x 2 x 1/4	3 x 2 x 1/4	3 x 2 x 1/4
20	3 x 2 x 1/4	3 x 2 x 1/4	3 x 2 x 1/4	3 x 2 x 1/4	3 x 2 x 1/4
21	3 x 2 x 1/4	3 x 2 x 1/4	3 x 2 x 1/4	3 x 2 x 1/4	3 x 2 x 1/4
22	3 x 2 x 1/4	3 x 2 x 1/4	3 x 2 x 1/4	3 x 2 x 1/4	3 x 2 x 1/4
23	ISLC75	ISLC75	ISLC75	ISLC75	ISLC75
24	ISMC150	ISJC200	ISLC75	ISLC200	ISLC75
25	ISLC75	ISLC75	ISLC75	ISLC75	ISLC75
26	ISLC75	ISLC75	ISLC75	ISLC75	ISLC75
27	ISLC75	ISLC75	ISLC75	ISLC75	ISLC75
28	ISLC75	ISLC75	ISLC75	ISLC75	ISLC75
29	ISLC75	ISLC75	ISLC75	ISLC75	ISLC75
30	ISLC75	ISLC75	ISLC75	ISLC75	ISLC75

31	ISLC75	ISLC75	ISLC75	ISLC75	ISLC75
32	ISLC75	ISLC75	ISLC75	ISLC75	ISLC75
33	5 x 5 x 1/2	5 x 5 x 1/2	5 x 5 x 1/2	5 x 5 x 1/2	5 x 5 x 1/2
34	1 1/2 x 1 1/2 x 1/8	1 1/2 x 1 1/2 x 1/8	1 1/2 x 1 1/2 x 1/8	1 1/2 x 1 1/2 x 1/8	3 1/2 x 3 1/2 x 1/8
35	1 1/2 x 1 1/2 x 1/8	1 1/2 x 1 1/2 x 1/8	1 1/2 x 1 1/2 x 1/8	1 1/2 x 1 1/2 x 1/8	1 1/2 x 1 1/2 x 1/8
36	1 1/2 x 1 1/2 x 1/8	1 1/2 x 1 1/2 x 1/8	1 1/2 x 1 1/2 x 1/8	1 1/2 x 1 1/2 x 1/8	1 1/2 x 1 1/2 x 1/8
37	1 1/2 x 1 1/2 x 1/8	1 1/2 x 1 1/2 x 1/8	1 1/2 x 1 1/2 x 1/8	1 1/2 x 1 1/2 x 1/8	1 1/2 x 1 1/2 x 1/8
38	1 1/2 x 1 1/2 x 1/8	1 1/2 x 1 1/2 x 1/8	1 1/2 x 1 1/2 x 1/8	1 1/2 x 1 1/2 x 1/8	1 1/2 x 1 1/2 x 1/8
39	1 1/2 x 1 1/2 x 1/8	1 1/2 x 1 1/2 x 1/8	1 1/2 x 1 1/2 x 1/8	1 1/2 x 1 1/2 x 1/8	1 1/2 x 1 1/2 x 1/8
40	1 1/2 x 1 1/2 x 1/8	1 1/2 x 1 1/2 x 1/8	1 1/2 x 1 1/2 x 1/8	1 1/2 x 1 1/2 x 1/8	1 1/2 x 1 1/2 x 1/8
41	1 1/2 x 1 1/2 x 1/8	1 1/2 x 1 1/2 x 1/8	1 1/2 x 1 1/2 x 1/8	1 1/2 x 1 1/2 x 1/8	1 1/2 x 1 1/2 x 1/8
42	1 5/8 x 1 5/8 x 1/8	2 1/4 x 2 1/4 x 1/8	2 1/4 x 2 1/4 x 1/8	2 1/4 x 2 1/4 x 1/8	1 1/2 x 1 1/2 x 1/8
43	4 x 4 x 1/2	4 1/2 x 4 1/2 x 3/16	5 x 5 x 3/16	4 1/2 x 4 1/2 x 3/16	1 1/2 x 1 1/2 x 1/8
44	3.000 x 0.134	3.000 x 0.134	3.000 x 0.134	3.000 x 0.134	3.000 x 0.134

Table F.9 Optimal sets of sizing parameters for model D2.

Structural Component No.	Cross Section Designation				
	MESO-ABC	MESO-BA	MESO-DE	MESO-PSO	MESO-SA
1	S6x12.5	S6x12.5	S6x12.5	S6x12.5	S6x12.5
2	S6x12.5	S6x12.5	S6x12.5	S6x12.5	S6x12.5
3	3 x 2 x 1/4	3 x 2 x 1/4	3 x 2 x 1/4	3 x 2 x 1/4	3 x 2 x 1/4
4	5 x 3 x 1/8	4 x 3 x 5/16	3 x 2 x 1/4	5 x 3 x 1/8	3 x 2 x 1/4
5	3 x 2 x 1/4	3 x 2 x 1/4	3 x 2 x 1/4	4 x 3 x 5/16	5 x 3 x 1/8
6	3 x 2 x 1/4	3 x 2 x 1/4	3 x 2 x 1/4	3 x 2 x 1/4	5 x 3 x 1/8
7	3 x 2 x 1/4	3 x 2 x 1/4	3 x 2 x 1/4	3 x 2 x 1/4	3 x 2 x 1/4
8	3 x 2 x 1/4	3 x 2 x 1/4	3 x 2 x 1/4	3 x 2 x 1/4	3 x 2 x 1/4
9	3 x 2 x 1/4	3 x 2 x 1/4	3 x 2 x 1/4	3 x 2 x 1/4	3 x 2 x 1/4
10	3 x 2 x 1/4	3 x 2 x 1/4	3 x 2 x 1/4	3 x 2 x 1/4	3 x 2 x 1/4
11	3 x 2 x 1/4	3 x 2 x 1/4	3 x 2 x 1/4	3 x 2 x 1/4	3 x 2 x 1/4
12	3 x 2 x 1/4	3 x 2 x 1/4	5 x 2 x 5/16	3 x 2 x 1/4	3 x 2 x 1/4
13	3 x 2 x 1/4	3 x 2 x 1/4	3 x 2 x 1/4	3 x 2 x 1/4	3 x 2 x 1/4
14	5 x 3 x 1/8	5 x 3 x 1/8	3 x 2 x 1/4	6 x 2 x 3/16	3 x 2 x 1/4
15	3 x 2 x 1/4	3 x 2 x 1/4	3 x 2 x 1/4	5 x 3 x 1/8	5 x 3 x 1/8
16	3 x 2 x 1/4	3 x 2 x 1/4	3 x 2 x 1/4	3 x 2 x 1/4	3 1/2 x 2 1/2 x 1/4
17	3 x 2 x 1/4	3 x 2 x 1/4	3 x 2 x 1/4	3 x 2 x 1/4	3 x 2 x 1/4
18	3 x 2 x 1/4	3 x 2 x 1/4	3 x 2 x 1/4	3 x 2 x 1/4	3 x 2 x 1/4
19	3 x 2 x 1/4	3 x 2 x 1/4	3 x 2 x 1/4	3 x 2 x 1/4	3 x 2 x 1/4
20	3 x 2 x 1/4	3 x 2 x 1/4	3 x 2 x 1/4	3 x 2 x 1/4	3 x 2 x 1/4
21	3 x 2 x 1/4	3 x 2 x 1/4	3 x 2 x 1/4	3 x 2 x 1/4	3 x 2 x 1/4
22	3 x 2 x 1/4	3 x 2 x 1/4	5 x 3 x 1/8	3 x 2 x 1/4	3 x 2 x 1/4
23	8 x 4 x 5/16	5 x 3 x 1/8	6 x 2 x 3/16	9 x 3 x 5/16	3 x 2 x 1/4
24	3 x 2 1/2 x 1/4	3 x 2 x 1/4	3 x 2 x 1/4	9 x 3 x 5/16	3 x 2 x 1/4
25	3 x 2 x 1/4	3 x 2 x 1/4	3 x 2 x 1/4	8 x 2 x 3/8	4 x 2 1/2 x 1/4
26	3 x 2 x 1/4	3 x 2 x 1/4	3 x 2 x 1/4	3 x 2 x 1/4	3 x 2 x 1/4
27	3 x 2 x 1/4	3 x 2 x 1/4	3 x 2 x 1/4	3 x 2 x 1/4	3 x 2 x 1/4
28	3 x 2 x 1/4	3 x 2 x 1/4	3 x 2 x 1/4	3 x 2 x 1/4	3 x 2 x 1/4
29	5 x 3 x 1/8	5 x 4 x 3/16	5 x 3 x 1/8	3 x 2 x 1/4	3 x 2 x 1/4
30	3 x 2 x 1/4	3 x 2 x 1/4	3 x 2 x 1/4	3 x 2 x 1/4	3 x 2 x 1/4
31	3 x 2 x 1/4	3 x 2 x 1/4	3 x 2 x 1/4	3 x 2 x 1/4	3 x 2 x 1/4
32	5 x 4 x 3/16	3 x 2 x 1/4	6 x 3 x 1/4	3 x 2 x 1/4	3 x 2 x 1/4
33	5 x 5 x 5/16	5 x 5 x 5/16	5 x 5 x 3/16	5 x 5 x 5/16	5 x 5 x 5/16
34	2 1/4 x 2 1/4 x 1/8	2 1/4 x 2 1/4 x 1/4	2 1/4 x 2 1/4 x 1/8	1 1/2 x 1 1/2 x 1/8	2 1/4 x 2 1/4 x 1/8
35	1 1/2 x 1 1/2 x 1/8	1 5/8 x 1 5/8 x 1/8	1 1/2 x 1 1/2 x 1/8	1 1/2 x 1 1/2 x 1/8	1 5/8 x 1 5/8 x 1/8
36	1 1/2 x 1 1/2 x 1/8	1 1/2 x 1 1/2 x 1/8	1 1/2 x 1 1/2 x 1/8	1 1/2 x 1 1/2 x 1/8	1 1/2 x 1 1/2 x 1/8
37	1 1/2 x 1 1/2 x 1/8	1 1/2 x 1 1/2 x 1/8	1 1/2 x 1 1/2 x 1/8	1 1/2 x 1 1/2 x 1/8	1 1/2 x 1 1/2 x 1/8
38	1 1/2 x 1 1/2 x 1/8	1 1/2 x 1 1/2 x 1/8	1 1/2 x 1 1/2 x 1/8	1 1/2 x 1 1/2 x 1/8	1 1/2 x 1 1/2 x 1/8
39	3 1/2 x 3 1/2 x 1/8	2 1/4 x 2 1/4 x 1/4	3 1/2 x 3 1/2 x 1/8	1 1/2 x 1 1/2 x 1/8	1 1/2 x 1 1/2 x 1/8
40	2 1/4 x 2 1/4 x 1/8	1 5/8 x 1 5/8 x 1/8	2 1/4 x 2 1/4 x 1/8	1 1/2 x 1 1/2 x 1/8	1 1/2 x 1 1/2 x 1/8
41	1 5/8 x 1 5/8 x 1/8	2 1/4 x 2 1/4 x 1/8	1 5/8 x 1 5/8 x 1/8	1 1/2 x 1 1/2 x 1/8	1 1/2 x 1 1/2 x 1/8
42	1 1/2 x 1 1/2 x 1/8	1 5/8 x 1 5/8 x 1/8	1 1/2 x 1 1/2 x 1/8	1 1/2 x 1 1/2 x 1/8	2 1/4 x 2 1/4 x 1/8
43	1 1/2 x 1 1/2 x 1/8	1 1/2 x 1 1/2 x 1/8	1 1/2 x 1 1/2 x 1/8	1 1/2 x 1 1/2 x 1/8	2 1/4 x 2 1/4 x 1/8
44	3.000 x 0.134	3.000 x 0.134	3.000 x 0.134	3.000 x 0.134	3.000 x 0.188

Table F.10 Optimal sets of sizing parameters for model E2.

Structural Component No.	Cross Section Designation				
	MESO-ABC	MESO-BA	MESO-DE	MESO-PSO	MESO-SA
1	3 x 2 x 1/4	9 x 7 x 1/2	3 x 2 x 1/4	3 x 2 x 1/4	3 x 2 x 1/4
2	3 x 2 x 1/4	9 x 7 x 1/2	3 x 2 x 1/4	3 x 2 x 1/4	3 x 2 x 1/4
3	5 x 4 x 3/16	9 x 7 x 1/2	6 x 2 x 3/16	5 x 3 x 1/8	7 x 3 x 1/2
4	6 x 3 x 1/4	3 x 2 x 1/4	6 x 3 x 1/4	6 x 3 x 1/4	9 x 3 x 5/16
5	9 x 3 x 5/16	3 x 2 x 1/4	9 x 3 x 5/16	9 x 3 x 5/16	9 x 3 x 5/16
6	9 x 7 x 1/2	3 x 2 x 1/4	9 x 3 x 5/16	9 x 7 x 1/2	9 x 5 x 1/2
7	3 x 2 x 1/4	3 x 2 x 1/4	3 x 2 x 1/4	3 x 2 x 1/4	3 x 2 x 1/4
8	3 x 2 x 1/4	3 x 2 x 1/4	3 x 2 x 1/4	3 x 2 x 1/4	3 x 2 x 1/4
9	3 x 2 x 1/4	3 x 2 x 1/4	3 x 2 x 1/4	3 x 2 x 1/4	3 x 2 x 1/4
10	3 x 2 x 1/4	3 x 2 x 1/4	3 x 2 x 1/4	3 x 2 x 1/4	3 x 2 x 1/4
11	3 x 2 x 1/4	3 x 2 x 1/4	3 x 2 x 1/4	3 x 2 x 1/4	3 x 2 x 1/4
12	3 x 2 x 1/4	3 x 2 x 1/4	3 x 2 x 1/4	3 x 2 x 1/4	3 x 2 x 1/4
13	6 x 2 x 3/16	9 x 7 x 1/2	5 x 3 x 1/8	5 x 3 x 1/8	7 x 4 x 1/2
14	4 x 2 1/2 x 1/4	3 x 2 x 1/4	5 x 3 x 1/8	3 1/2 x 2 1/2 x 1/4	5 x 3 x 1/8
15	5 x 3 x 1/8	9 x 3 x 5/16	6 x 2 x 3/16	3 1/2 x 2 1/2 x 1/4	5 x 3 x 1/8
16	6 x 2 x 3/16	8 x 6 x 3/8	6 x 2 x 3/16	5 x 3 x 1/8	3 x 2 x 1/4
17	6 x 4 x 5/16	9 x 3 x 5/16	6 x 5 x 5/16	6 x 2 x 3/16	3 x 2 x 1/4
18	3 x 2 x 1/4	3 x 2 x 1/4	3 x 2 x 1/4	3 x 2 x 1/4	3 x 2 x 1/4
19	3 x 2 x 1/4	3 x 2 x 1/4	3 x 2 x 1/4	3 x 2 x 1/4	3 x 2 x 1/4
20	3 x 2 x 1/4	3 x 2 x 1/4	3 x 2 x 1/4	3 x 2 x 1/4	3 x 2 x 1/4
21	3 x 2 x 1/4	3 x 2 x 1/4	3 x 2 x 1/4	3 x 2 x 1/4	3 x 2 x 1/4
22	3 x 2 x 1/4	3 x 2 x 1/4	3 x 2 x 1/4	3 x 2 x 1/4	3 x 2 x 1/4
23	5 x 4 x 3/16	3 x 2 x 1/4	6 x 2 x 3/16	9 x 7 x 1/2	9 x 3 x 5/16
24	4 x 3 x 5/16	3 x 2 x 1/4	3 1/2 x 2 1/2 x 1/4	5 x 3 x 1/8	4 x 3 x 5/16
25	5 x 3 x 1/8	3 x 2 x 1/4	5 x 3 x 1/8	5 x 3 x 1/8	3 x 2 1/2 x 1/4
26	6 x 2 x 3/16	8 x 6 x 3/8	6 x 2 x 3/16	6 x 2 x 3/16	3 x 2 x 1/4
27	6 x 2 x 3/16	9 x 3 x 5/16	6 x 5 x 5/16	6 x 2 x 3/16	3 x 2 x 1/4
28	3 x 2 x 1/4	3 x 2 x 1/4	3 x 2 x 1/4	3 x 2 x 1/4	3 x 2 x 1/4
29	3 x 2 x 1/4	3 x 2 x 1/4	3 x 2 x 1/4	3 x 2 x 1/4	3 x 2 x 1/4
30	3 x 2 x 1/4	3 x 2 x 1/4	3 x 2 x 1/4	3 x 2 x 1/4	3 x 2 x 1/4
31	3 x 2 x 1/4	3 x 2 x 1/4	3 x 2 x 1/4	3 x 2 x 1/4	3 x 2 x 1/4
32	3 x 2 x 1/4	3 x 2 x 1/4	3 x 2 x 1/4	3 x 2 x 1/4	3 x 2 x 1/4
33	9 x 3 x 5/16	9 x 7 x 1/2	9 x 3 x 5/16	9 x 7 x 1/2	9 x 7 x 1/2
34	3 x 2 x 1/4	3 x 2 x 1/4	3 x 2 x 1/4	4 x 2 1/2 x 1/4	6 x 2 x 3/16
35	3 x 2 x 1/4	3 x 2 x 1/4	3 x 2 x 1/4	3 x 2 x 1/4	5 x 2 x 5/16
36	3 x 2 x 1/4	3 x 2 x 1/4	3 x 2 x 1/4	3 x 2 x 1/4	8 x 2 x 3/8
37	5 x 2 x 5/16	3 x 2 x 1/4	7 x 3 x 1/2	3 x 2 x 1/4	3 x 2 x 1/4
38	3 x 2 x 1/4	3 x 2 x 1/4	3 x 2 x 1/4	3 x 2 x 1/4	3 x 2 x 1/4
39	3 x 2 x 1/4	3 x 2 x 1/4	3 x 2 x 1/4	3 x 2 x 1/4	3 x 2 x 1/4
40	3 x 2 x 1/4	3 x 2 x 1/4	3 x 2 x 1/4	3 x 2 x 1/4	3 x 2 x 1/4
41	3 x 2 x 1/4	3 x 2 x 1/4	3 x 2 x 1/4	3 x 2 x 1/4	3 x 2 x 1/4
42	3 x 2 x 1/4	3 x 2 x 1/4	3 x 2 x 1/4	3 x 2 x 1/4	3 x 2 x 1/4
43	3.000 x 0.134	3.000 x 0.134	3.000 x 0.134	3.000 x 0.134	3.000 x 0.134
44	3.000 x 0.134	3.000 x 0.134	3.000 x 0.134	3.000 x 0.134	3.000 x 0.134
45	3.000 x 0.134	3.000 x 0.134	3.000 x 0.134	3.000 x 0.134	3.000 x 0.134
46	3.000 x 0.134	3.000 x 0.134	3.000 x 0.134	3.000 x 0.134	3.000 x 0.134
47	3.000 x 0.134	3.000 x 0.134	3.000 x 0.134	3.000 x 0.134	3.000 x 0.134
48	3.000 x 0.134	3.000 x 0.134	3.000 x 0.134	3.000 x 0.134	3.000 x 0.134

Table F.11 Optimal sets of sizing parameters for model A3.

Structural Component No.	Cross Section Designation				
	MESO-ABC	MESO-BA	MESO-DE	MESO-PSO	MESO-SA
1	S12x35	S18x70	S18x54.7	S18x54.7	S15x50
2	S18x54.7	S24x80	S24x80	S24x90	S24x80
3	S24x90	S24x90	S24x90	S24x90	S24x90
4	S24x121	S24x121	S24x121	S24x121	S24x121
5	S15x42.9	S12x40.8	S15x42.9	S15x42.9	S12x40.8
6	S20x66	S20x66	S18x54.7	S20x75	S15x42.9
7	C8x18.75	C8x18.75	C8x18.75	C8x18.75	C8x18.75
8	C8x18.75	C8x18.75	C8x18.75	C8x18.75	C8x18.75
9	C6x8.2	C9x13.4	C7x9.8	C9x13.4	C6x13
10	C15x33.9	C15x33.9	C15x33.9	C15x33.9	C12x25
11	C7x12.25	C6x10.5	C6x8.2	C8x18.75	C4x5.4
12	CGS-21	CGS-14	CGS-26	CGS-21	CGS-14
13	CRS-14	CRS-15	CRS-14	CRS-14	CRS-14

Table F.12 Optimal sets of sizing parameters for model B3.

Structural Component No.	Cross Section Designation				
	MESO-ABC	MESO-BA	MESO-DE	MESO-PSO	MESO-SA
1	S15x50	S18x54.7	S15x50	S15x42.9	S18x54.7
2	S18x54.7	S15x50	S15x50	S18x70	S18x54.7
3	S20x86	S18x54.7	S20x75	S20x75	S18x70
4	S20x96	S20x86	S20x96	S20x96	S20x75
5	4 x 2 1/2 x 1/4	S20x96	4 x 2 1/2 x 1/4	4 x 2 1/2 x 1/4	S20x96
6	4 x 2 1/2 x 1/4	4 x 2 1/2 x 1/4	4 x 2 1/2 x 1/4	4 x 2 1/2 x 1/4	4 x 2 1/2 x 1/4
7	5 x 3 x 1/8	4 x 2 1/2 x 1/4	6 x 2 x 3/16	5 x 3 x 1/8	4 x 2 1/2 x 1/4
8	5 x 4 x 3/16	5 x 4 x 3/16	5 x 4 x 3/16	6 x 2 x 3/16	5 x 4 x 3/16
9	6 x 3 x 1/4	6 x 2 x 3/16	7 x 3 x 1/2	7 x 4 x 1/2	6 x 2 x 3/16
10	7 x 5 x 1/2	6 x 3 x 1/4	7 x 4 x 1/2	8 x 2 x 3/8	6 x 3 x 1/4
11	9 x 3 x 5/16	7 x 5 x 1/2	9 x 3 x 5/16	9 x 3 x 5/16	7 x 4 x 1/2
12	8 x 6 x 3/8	7 x 3 x 1/2	8 x 6 x 3/8	8 x 4 x 5/16	7 x 4 x 1/2
13	C9x15	8 x 3 x 3/8	C8x13.75	C9x13.4	7 x 5 x 1/2
14	C10x15.3	9 x 3 x 5/16	C10x15.3	C9x20	9 x 3 x 5/16
15	C10x30	9 x 5 x 1/2	C10x30	C10x30	9 x 3 x 5/16
16	S18x70	C9x20	S18x70	S18x54.7	C9x13.4
17	S18x54.7	C9x13.4	S18x70	S15x50	C9x15
18	NA	C10x15.3	NA	NA	C10x15.3
19	NA	C10x30	NA	NA	C10x30
20	NA	S15x50	NA	NA	S18x70
21	NA	S15x42.9	NA	NA	S15x50

Table F.13 Optimal sets of sizing parameters for model C3.

Structural Component No.	Cross Section Designation				
	MESO-ABC	MESO-BA	MESO-DE	MESO-PSO	MESO-SA
1	12 x 10 x 5/16	16 x 8 x 3/8	16 x 12 x 5/16	10 x 3 x 3/8	14 x 10 x 5/8
2	12 x 6 x 1/4	12 x 10 x 5/16	12 x 8 x 3/8	12 x 6 x 1/4	12 x 4 x 1/4
3	12 x 6 x 1/4	14 x 6 x 1/2	12 x 10 x 5/16	10 x 4 x 5/16	12 x 8 x 3/8
4	16 x 8 x 3/8	10 x 6 x 1/2	12 x 4 x 1/4	14 x 6 x 1/2	16 x 8 x 3/8
5	18 x 12 x 3/8	16 x 8 x 3/8	14 x 10 x 5/8	18 x 6 x 5/8	18 x 12 x 3/8
6	20 x 12 x 3/8	18 x 12 x 3/8	18 x 6 x 5/8	20 x 12 x 3/8	20 x 12 x 3/8
7	20 x 12 x 3/8	20 x 12 x 3/8	20 x 12 x 3/8	20 x 12 x 3/8	20 x 12 x 3/8
8	L6 x 4 x 3/4	20 x 12 x 3/8	20 x 12 x 3/8	L5 x 5 x 5/16	L6 x 6 x 5/16
9	L6 x 6 x 9/16	L6 x 4 x 3/4	L6 x 4 x 3/4	L5 x 5 x 5/16	L6 x 6 x 5/16
10	L8 x 6 x 1/2	L6 x 4 x 3/4	L6 x 6 x 7/16	L5 x 5 x 5/16	L8 x 8 x 1/2
11	L6 x 6 x 3/4	L8 x 6 x 1/2	L8 x 6 x 5/8	L7 x 4 x 5/8	L7 x 4 x 5/8
12	L6 x 6 x 3/4	L8 x 6 x 1/2	L8 x 4 x 3/4	L8 x 8 x 7/8	L6 x 6 x 9/16
13	L8 x 8 x 7/8	L6 x 6 x 7/16	L6 x 6 x 9/16	L8 x 8 x 7/8	L8 x 8 x 5/8
14	L8 x 8 x 7/8	L7 x 4 x 7/16	L6 x 6 x 3/4	L8 x 8 x 7/8	L8 x 8 x 7/8
15	C8x18.75	L8 x 8 x 7/8	L8 x 8 x 7/8	C7x12.25	C9x13.4
16	C9x15	L8 x 8 x 7/8	L8 x 8 x 7/8	C7x12.25	C9x15
17	C12x30	C7x12.25	C8x11.5	C12x30	C12x20.7
18	C8x13.75	C9x13.4	C8x18.75	C15x33.9	C8x11.5
19	C12x30	C12x20.7	C12x25	C15x33.9	C12x25
20	C15x33.9	C8x13.75	C8x18.75	C15x33.9	C15x33.9
21	S15x42.9	C9x15	C9x13.4	S12x31.8	S15x42.9
22	S12x40.8	C15x33.9	C15x33.9	S12x31.8	S12x40.8
23	NA	C15x33.9	C15x33.9	NA	NA
24	NA	S18x54.7	S18x54.7	NA	NA
25	NA	S12x50	S12x40.8	NA	NA

Table F.14 Optimal sets of sizing parameters for model E3.

Structural Component No.	Cross Section Designation				
	MESO-ABC	MESO-BA	MESO-DE	MESO-PSO	MESO-SA
1	S20x96	S20x96	S20x86	S20x96	S20x96
2	S20x86	S20x86	S20x66	S20x96	S20x75
3	S18x54.7	S20x75	S18x54.7	S20x66	S15x42.9
4	S12x50	S12x50	S12x40.8	S12x40.8	S12x50
5	S24x90	S24x90	S24x100	S24x80	S24x100
6	S24x100	S24x100	S24x100	S24x100	S24x100
7	S24x100	S24x100	S24x100	S24x100	S24x100
8	9 x 3 x 5/16	S24x100	9 x 5 x 1/2	S24x100	8 x 4 x 5/16

9	**7 x 4 x 1/2**	**9 x 7 x 1/2**	**7 x 5 x 1/2**	**9 x 5 x 1/2**	**6 x 5 x 5/16**
10	**9 x 7 x 1/2**	**8 x 3 x 3/8**	**10 x 3 x 3/8**	**8 x 2 x 3/8**	**9 x 5 x 1/2**
11	**10 x 3 x 3/8**	**7 x 5 x 1/2**	**10 x 4 x 5/16**	**7 x 4 x 1/2**	**10 x 3 x 3/8**
12	**10 x 5 x 3/8**	**10 x 3 x 3/8**	**10 x 5 x 3/8**	**9 x 5 x 1/2**	**10 x 6 x 1/2**
13	**10 x 6 x 1/2**	**10 x 4 x 5/16**	**10 x 5 x 3/8**	**10 x 4 x 5/16**	**10 x 6 x 1/2**
14	**9 x 7 x 1/2**	**10 x 6 x 1/2**	**10 x 2 x 3/8**	**10 x 6 x 1/2**	**9 x 7 x 1/2**
15	**8 x 3 x 3/8**	**10 x 5 x 3/8**	**8 x 6 x 3/8**	**10 x 6 x 1/2**	**8 x 6 x 3/8**
16	**9 x 3 x 5/16**	**9 x 5 x 1/2**	**10 x 2 x 3/8**	**9 x 5 x 1/2**	**10 x 2 x 3/8**
17	**10 x 3 x 3/8**	**7 x 4 x 1/2**	**9 x 7 x 1/2**	**7 x 3 x 1/2**	**10 x 2 x 3/8**
18	**10 x 4 x 5/16**	**7 x 5 x 1/2**	**10 x 4 x 5/16**	**7 x 5 x 1/2**	**10 x 6 x 1/2**
19	**10 x 6 x 1/2**	**10 x 3 x 3/8**	**10 x 6 x 1/2**	**9 x 3 x 5/16**	**10 x 5 x 3/8**
20	**C7x9.8**	**10 x 3 x 3/8**	**C6x13**	**10 x 3 x 3/8**	**C6x10.5**
21	**C8x18.75**	**10 x 5 x 3/8**	**C8x13.75**	**10 x 5 x 3/8**	**C8x18.75**
22	**C9x20**	**10 x 6 x 1/2**	**C9x13.4**	**10 x 6 x 1/2**	**C10x15.3**
23	**C10x25**	**C7x9.8**	**C10x25**	**C6x10.5**	**C10x25**
24	**C10x20**	**C9x15**	**C10x20**	**C9x15**	**C10x20**
25	**C10x30**	**C8x18.75**	**C10x25**	**C10x25**	**C12x25**
26	**NA**	**C9x20**	**NA**	**C12x20.7**	**NA**
27	**NA**	**C10x25**	**NA**	**C10x30**	**NA**
28	**NA**	**C9x15**	**NA**	**C8x18.75**	**NA**
29	**NA**	**C12x25**	**NA**	**C12x20.7**	**NA**

List of References:

Abolbashari, M.H. and Keshavarzmanesh, S. (2006) 'On Various Aspects of Application of the Evolutionary Structural Optimization Method for 2D and 3D Continuum Structures', *Finite Elements in Analysis and Design*, 42(6), pp. 478-491.

Aghazadeh, F. and Meybodi, M.R. (2011) 'Learning Bees Algorithm For Optimization', *International Conference on Information and Intelligent Computing*, 18(1), pp. 115-122.

Akay, B. and Karaboga, D. (2012) 'A Modified Artificial Bee Colony Algorithm for Real-parameter Optimization', *Information Sciences*, 192, pp. 120-142.

Akpinar, Ş. and Baykasoğlu, A. (2014) 'Multiple Colony Bees Algorithm for Continuous Spaces', *Applied Soft Computing*, 24, pp. 829-841.

Al-Taee, H.H., Al-Moosawy, A.A. and Al-Shojary, M.A. (2008) 'Optimum Design of Stiffened Plate-Structure Subjected to Static Loading', *Al-Khwarizmi Engineering Journal*, 4(2), pp. 46-58.

Alatas, B. (2010) 'Chaotic Bee Colony Algorithms for Global Numerical Optimization', *Expert Systems with Applications*, 37(8), pp. 5682-5687.

Ansola, R., Canales, J. and Tárrago, J.A. (2006) 'An Efficient Sensitivity Computation Strategy for the Evolutionary Structural Optimization (ESO) of Continuum Structures Subjected to Self-Weight Loads', *Finite Elements in Analysis and Design*, 42(14–15), pp. 1220-1230.

Ansola, R., Veguería, E., Canales, J. and Tárrago, J.A. (2007) 'A Simple Evolutionary Topology Optimization Procedure for Compliant Mechanism Design', *Finite Elements in Analysis and Design*, 44(1–2), pp. 53-62.

API 620 (2002) *Design and Construction of Large, Welded, Low-Pressure Storage Tanks*. 1220 L Street, NW, Washington, DC 20005-4070, USA: API Publishing Services.

API Standard 650 (2013) *Welded Tanks for Oil Storage*. 1220 L Street, NW, Washington, DC 20005-4070, USA: API Publishing Servicesstandards@api.org.

ASCE7-10 (2010) *ASCE 7-10: Minimum Design Loads for Buildings and Other Structures*. 1801 Alexander Bell Drive, Reston, Virginia 20191: American Society of Civil Engineerswww.pubs.asce.org.

Asl, R.N., Aslani, M. and Panahi, M.S. (2016) 'Sizing Optimization of Truss Structures Using a Hybridized Genetic Algorithm', *Mathematical Optimization Criteria*, 1, pp. 1-19.

ASTM-A283/A283M − 13 (2013) *Standard Specification for Low and Intermediate Tensile Strength Carbon Steel Plates A283/A283M − 13*. 100 Barr Harbor Drive, PO Box C700, West Conshohocken, PA 19428-2959. United States: ASTM Int'lwww.astm.org.

ASTM-A 36/A 36M − 01 (2001) *Standard Specification for Carbon Structural Steel A 36/A 36M - 01*. 100 Ban Harbor Drive, West Conshohocken, PA 19428-2959, United States.: ASTM Int'lwww.astm.org.

Auld, F.A. (1970) *The Stress Distribution in, and Stability of Space Frames with Particular Reference to Radial Ribbed Domes*. Newcastle upon Tyne University.

Awad, N.H., Ali, M.Z., Suganthan, P.N. and Jaser, E. (2016) 'A Decremental Stochastic Fractal Differential Evolution for Global Numerical Optimization', *Information Sciences*, 372, pp. 470-491.

Aydoğdu, İ., Akın, A. and Saka, M.P. (2016) 'Design optimization of real world steel space frames using artificial bee colony algorithm with Levy flight distribution', *Advances in Engineering Software*, 92, pp. 1-14.

Babaei, M. and Sheidaii, M. (2013) 'Optimal Design of Double Layer Scallop Domes Using Genetic Algorithm', *Applied Mathematical Modelling*, 37(4), pp. 2127-2138.

Babaei, M. and Sheidaii, M.R. (2014) 'Automated Optimal Design of Double-layer Latticed Domes Using Particle Swarm Optimization', *Structural and Multidisciplinary Optimization*, 50(2), pp. 221-235.

Babazadeh, A., Poorzahedy, H. and Nikoosokhan, S. (2011) 'Application of Particle Swarm Optimization to Transportation Network Design Problem', *Journal of King Saud University - Science*, 23(3), pp. 293-300.

Bai, L. (2014) *Interactive Buckling in Thin-Walled I-Section Struts*. Imperial College of Science, Technology and Medicine.

Baykasolu, A., Özbakır, L. and Tapkan, P. (eds.) (2007) *Artificial Bee Colony Algorithm and Its Application to Generalized Assignment Problem*. Vienna, Austria: Itech Education and Publishing.

Bendsoe, M.P. (1989) 'Optimal Shape Design as A Material Distribution Problem', *Structural Optimization*, 1, pp. 193-202.

Bendsøe, M.P. and Kikuchi, N. (1988) 'Generating Optimal Topologies in Structural Design Using a Homogenization Method', *Computer Methods in Applied Mechanics and Engineering*, 71(2), pp. 197-224.

Blessmann, J. (1996) 'Researches on Wind Effects on Domes in Brazil', *Journal of Wind Engineering and Industrial Aerodynamics*, 65(1), pp. 167-177.

Borenstein, Y. and Moraglio, A. (eds.) (2014) *Theory and Principled Methods for the Design of Metaheuristics*. Verlag Berlin Heidelberg: Springer.

Brown, D.E. and Huntley, C.L. (1992) 'A Practical Application of Simulated Annealing to Clustering', *Pattern Recognition*, 25(4), pp. 401-412.

Bu, F. and Qian, C. (2015) 'A Rational Design Approach of Intermediate Wind Girders on Large Storage Tanks', *Thin-Walled Structures*, 92, pp. 76-81.

Burgos, C.A., Batista-Abreu, J.C., Calabró, H.D., Jaca, R.C. and Godoy, L.A. (2015) 'Buckling Estimates for Oil Storage Tanks: Effect of Simplified Modeling of the Roof and Wind Girder', *Thin-Walled Structures*, 91, pp. 29-37.

Cai, Y. and Wang, J. (2015) 'Differential Evolution with Hybrid Linkage Crossover', *Information Sciences*, 320, pp. 244-287.

Camp, C.V. and Farshchin, M. (2014) 'Design of space trusses using modified teaching–learning based optimization', *Engineering Structures*, 62-63, pp. 87-97.

Cao, H., Qian, X. and Zhou, Y. (2017) 'Large-scale structural optimization using metaheuristic algorithms with elitism and a filter strategy', *Structural and Multidisciplinary Optimization*, 57(2), pp. 799-814.

Cao, S., Tamura, Y., Kikuchi, N., Saito, M., Nakayama, I. and Matsuzaki, Y. (2015) 'A Case Study of Gust Factor of a Strong Typhoon', *Journal of Wind Engineering and Industrial Aerodynamics*, 138(1), pp. 52-60.

Carbas, S. (2008) *Optimum Topological Design of Geometrically Nonlinear Single Layer Lamella Domes Using Harmony Search Method*. Middle East Technical University.

Çarbaş, S. and Saka, M.P. (2009) 'Optimum Design of Single Layer Network Domes Using Harmony Search Method', *ASIAN JOURNAL OF CIVIL ENGINEERING (BUILDING AND HOUSING)*, 10(1), pp. 97-112.

Chacko, P., V S, D. and P.M, M. (2014) 'Finite Element Analysis of Ribbed Dome', *International Journal of Engineering Research and Applications (IJERA)*, 1(1), pp. 25-32.

Chai-ead, N., Aungkulanon, P. and Luangpaiboon, P. (2011) *Proceedings of the International MultiConference of Engineers and Computer Scientists (IMECS)*. Hong Kong, March, 16-18, 2011.

Chang, P.-C. and Yeh, W.-C. (2013) *ICUIMC(IMCOM)'13*. Kota Kinabalu, Malaysia, January, 17–19, 2013. Association for Computing Machinery (ACM).

Cheng, J., Yen, G.G. and Zhang, G. (2016) 'A Grid-based Adaptive Multi-objective Differential Evolution Algorithm', *Information Sciences*, 367-368, pp. 890-908.

Cheng, W., Liu, F. and Li, L.J. (2013) 'Size and Geometry Optimization of Trusses Using Teaching-Learning-Based Optimization', *INTERNATIONAL JOURNAL OF OPTIMIZATION IN CIVIL ENGINEERING*, 3(3), pp. 431-444.

Chu, D.N. (1997) *Evolutionary Structural Optimization Method for Systems with Stiffness and Displacement Constraints*. Victoria University of Technology [Online]. Available at: http://vuir.vu.edu.au/15282/1/Chu_1997_compressed.pdf.

Chu, D.N., Xie, Y.M., Hira, A. and Steven, G.P. (1996) 'Evolutionary Structural Optimization for Problems with Stiffness Constraints', *Finite Elements in Analysis and Design*, 21(4), pp. 239-251.

Corana, A., Marchesi, M., Martini, C. and Ridella, S. (1987) 'Minimizing Multimodal Functions of Continuous Variables with the 'Simulated Annealing" Algorithm', *ACM Transactions on Mathematical Software*, 13(3), pp. 262-280.

Das, S., Mullick, S.S. and Suganthan, P.N. (2016) 'Recent Advances in Differential Evolution – An Updated Survey', *Swarm and Evolutionary Computation*, 27, pp. 1-30.

Degertekin, S.O. and Hayalioglu, M.S. (2013) 'Sizing truss structures using teaching-learning-based optimization', *Computers & Structures*, 119, pp. 177-188.

Degertekin, S.O. and Lamberti, L. (2013) *The Fourteenth International Conference on Civil, Structural and Environmental Engineering*. Stirlingshire, UK. Civil-Comp Press.

Degertekin, S.O., Lamberti, L. and Ugur, I.B. (2018) 'Sizing, layout and topology design optimization of truss structures using the Jaya algorithm', *Applied Soft Computing*, 70, pp. 903-928.

Du, K.-L. and Swamy, M.N.S. (2016) 'Simulated Annealing', in *Search and Optimization by Metaheuristics*. Switzerland: Springer International Publishing Switzerland 2016, pp. 29-36.

Duysinx, P. and Bendsøe, M.P. (1998) 'Topology Optimization of Continuum Structures with Local Stress Constraints', *International journal for numerical methods in engineering*, 43(8), pp. 1453-1478.

El-Abd, M. (2011) 'Opposition-Based Artificial Bee Colony Algorithm', *GECCO*. Dublin, Ireland. ACM, pp. 109-115.

El-Abd, M. (2012) 'Performance Assessment of Foraging Algorithms vs. Evolutionary Algorithms', *Information Sciences*, 182(1), pp. 243-263.

Elsayed, S.M., Sarker, R.A. and Essam, D.L. (2011) 'Multi-operator Based Evolutionary Algorithms for Solving Constrained Optimization Problems', *Computers & Operations Research*, 38(12), pp. 1877-1896.

Esslinger, M., Ahmed, S. and Schroeder, H. (1971) 'Stationary Wind Loads of Open-Topped and Roof-Topped Cylindrical Silos', *Journal of Wind Engineering and Industrial Aerodynamics*, 1(1), pp. 1-8.

Fahmy, A.A. (2012) 'Using the Bees Algorithm to Select the Optimal Speed Parameters for Wind Turbine Generators', *Journal of King Saud University - Computer and Information Sciences*, 24(1), pp. 17-26.

Falcinelli, O.A., Elaskar, S.A. and Godoy, L.A. (2011) 'Influence of Topography on Wind Pressures in Tanks Using CFD', *Latin American Applied Research*, 41(1), pp. 379-388.

Fleetwood, K. (2001) 'An Introduction to Differential Evolution', *Evolutionary Multiobjective Optimization*, 1, pp. 1-40.

Flores, F.G. and Godoy, L.A. (1998) 'Buckling of Short Tanks Due to Hurricanes', *Engineering Structures*, 20(8), pp. 752-760.

Gao, W.-f. and Liu, S.-y. (2012) 'A Modified Artificial Bee Colony Algorithm', *Computers & Operations Research*, 39(3), pp. 687-697.

Gao, W., Liu, S. and Huang, L. (2012) 'A Global Best Artificial Bee Colony Algorithm for Global Optimization', *Journal of Computational and Applied Mathematics*, 236(11), pp. 2741-2753.

García-Villoria, A. and Pastor, R. (2009) 'Introducing Dynamic Diversity into a Discrete Particle Swarm Optimization', *Computers & Operations Research*, 36(3), pp. 951-966.

Ghaffarianjam, H.R. and Abolbashari, M.H. (2009) 'On the Convergence of Morphing Evolutionary Structural Optimization Method to the

Global Optimum for the Beam Design', *8th World Congress on Structural and Multidisciplinary Optimization*. Lisbon, Portugal. Organization of Structural and Multidisciplinary Optimization, p. 1.

Ghaffarianjam, H.R. and Abolbashari, M.H. (2010) 'Performance of the Evolutionary Structural Optimization-based Approaches with Different Criteria in the Shape Optimization of Beams', *Finite Elements in Analysis and Design*, 46(4), pp. 348-356.

Ghaffarianjam, H.R., Abolbashari, M.H. and Farshidianfar, A. (2011) 'Quantitative Verification of the Morphing Evolutionary Structural Optimization Method for Some Benchmark Problems Using a New Performance Index', *Scientia Iranica B*, 18(3), pp. 383-392.

Ghasemishabankareh, B., Li, X. and Ozlen, M. (2016) 'Cooperative Coevolutionary Differential Evolution with Improved Augmented Lagrangian to Solve Constrained Optimisation Problems', *Information Sciences*, 369, pp. 441-456.

Gholizadeh, S., Barzegar, A. and Gheyratmand, C. (2011) 'Shape Optimization of Structures by Modified Harmony Search', *INTERNATIONAL JOURNAL OF OPTIMIZATION IN CIVIL ENGINEERING*, 3, pp. 485-494.

Ghosh, A., Das, S., Chowdhury, A. and Giri, R. (2011) 'An Improved Differential Evolution Algorithm with Fitness-Based Adaptation of the Control Parameters', *Information Sciences*, 181(18), pp. 3749-3765.

Gidófalvy, K. (2010) 'Effect of Connection Rigidity on the Behaviour of Single-Layer Steel Grid Shells', *Conference of Junior Researchers in Civil Engineering*. 2010. pp. 58-65.

Godoy–PI, L.A. and Portela–GS, G. (2005) 'A Review of Wind-Tunnel Results of Pressures on Tank Models', *Universidad nacional de cordoba official website*.

Goffe, W.L., Ferrier, G.D. and Rogers, J. (1992) 'Global Optimization of Statistical Functions with Simulated Annealing', *Journal of Econometrics*, 60, pp. 65-99.

Gomes, H.M. (2011) 'Truss optimization with dynamic constraints using a particle swarm algorithm', *Expert Systems with Applications*, 38(1), pp. 957-968.

Haftka, R.T. (2013) 'Design Procedure for Steel Frame Structures According to BS 5950', in USA: MSO, pp. 26-71.

Hasancebi, O., Erdal, F. and Saka, M.P. (2010) 'Optimum Design of Geodesic Steel Domes under Code Provision Using Meta-Heuristic Techniques', *International Journal of Engineering and Applied Sciences (IJEAS)*, 2(2), pp. 88-103.

Henderson, D., Jacobson, S.H. and Johnson, A.W. (2008) 'The Theory and practice of Simulated Annealing', in *Simulated Annealing Strategy*. USA, pp. 287-319.

Ho-Huu, V., Nguyen-Thoi, T., Le-Anh, L. and Nguyen-Trang, T. (2016a) 'An Effective Reliability-based Improved Constrained Differential Evolution for Reliability-based Design Optimization of Truss Structures', *Advances in Engineering Software*, 92, pp. 48-56.

Ho-Huu, V., Nguyen-Thoi, T., Nguyen-Thoi, M.H. and Le-Anh, L. (2015) 'An Improved Constrained Differential Evolution Using Discrete Variables (D-ICDE) for Layout Optimization of Truss Structures', *Expert Systems with Applications*, 42(20), pp. 7057-7069.

Ho-Huu, V., Nguyen-Thoi, T., Vo-Duy, T. and Nguyen-Trang, T. (2016b) 'An Adaptive Elitist Differential Evolution for Optimization of Truss Structures with Discrete Design Variables', *Computers & Structures*, 165, pp. 59-75.

Holroyd, R.J. (1983) 'On the Behavior of Open-Topped Oil Storage Tanks in High Winds. Part I', *Aerodynamic aspects. J. Wind Eng. Ind. Aerodyn.*, 12(1), pp. 329-352.

Holroyd, R.J. (1985) 'On the Behavior of Open-Topped Oil Storage Tanks in High Winds. Part II', *Structural aspects. J. Wind Eng. Ind. Aerodyn.*, 18(1), pp. 53-73.

Hsaine, N. and Franklin, F. (2016) *International Conference for Students on Applied Engineering*. Newcastle upon Tyne, UK. IEEE.

Hu, X.-g., Cheng, H.-m. and Tao, Y. (2012) 'Modified Rejection Ratio for Multiple Load Cases Evolutionary Structural Optimization', *Procedia Engineering*, 31, pp. 627-633.

Huang, X. and Xie, Y.M. (2007) 'Optimal Design of Periodic Structures Using Evolutionary Topology Optimization', *Structural and Multidisciplinary Optimization*, 36(6), pp. 597-606.

Huang, X., Zuo, Z.H. and Xie, Y.M. (2010) 'Evolutionary Topological Optimization of Vibrating Continuum Structures for Natural Frequencies', *Computers & Structures*, 88(5-6), pp. 357-364.

INGBER, L. (1993) 'Simulated Annealing: Practice versus Theory', *Mathematical Computational Modelling*, 18(11), pp. 29-57.

Jahangiri, M., Fakhrabadi, M.H. and Jahangiri, M. (2013) 'Computational Buckling Analysis of Wind Loaded Cylindrical Storage Tanks', *Majlesi Journal of Energy Management*, 1(4), pp. 23-31.

Jamshidi, M. (2012) 'Dynamic Study of Double Layer Lattice Domes', *Trends in Applied Sciences Research*, 7(3), pp. 221-230.

Jármai, K., Snyman, J.A. and Farkas, J. (2006) 'Minimum Cost Design of a Welded Orthogonally Stiffened Cylindrical Shell', *Computers & Structures*, 84(12), pp. 787-797.

Jiang, M., Luo, Y.P. and Yang, S.Y. (2007) 'Stochastic Convergence Analysis and Parameter Selection of the Standard Particle Swarm Optimization Algorithm', *Information Processing Letters*, 102(1), pp. 8-16.

Kameshki, E.S. and Saka, M.P. (2007) 'Optimum Geometry Design of Nonlinear Braced Domes Using Genetic Algorithm', *Computers & Structures*, 85(1-2), pp. 71-79.

Kang, B.S., Choi, W.S. and Park, G.J. (2001) 'Structural Optimization under Equivalent Static Loads Transferred from Dynamic Loads Based on Displacement', *Computers and Structures*, 79(1), pp. 145-154.

Karaboga, D. (2005) *An Idea Based on Honey Bee Swarm for Numerical Optimization* (TR06). Kayseri/Türkiye: Erciyes University, Engineering Faculty, Computer Engineering Department.

Karaboga, D. and Akay, B. (2009) 'A Comparative Study of Artificial Bee Colony Algorithm', *Applied Mathematics and Computation*, 214(1), pp. 108-132.

Karaboga, D. and Akay, B. (2011) 'A Modified Artificial Bee Colony (ABC) Algorithm for Constrained Optimization Problems', *Applied Soft Computing*, 11(3), pp. 3021-3031.

Karaboga, D. and Basturk, B. (2007a) 'Artificial Bee Colony (ABC) Optimization Algorithm for Solving Constrained Optimization Problems', *New Trends in Intelligent Technologies*, 1, pp. 789-798.

Karaboga, D. and Basturk, B. (2007b) 'A Powerful and Efficient Algorithm for Numerical Function Optimization: Artificial Bee Colony (ABC) Algorithm', *Journal of Global Optimization*, 39(3), pp. 459-471.

Karaboga, D. and Basturk, B. (2008) 'On the Performance of Artificial Bee Colony (ABC Algorithm', *Applied Soft Computing*, 8(1), pp. 687-697.

Karaboga, D. and Ozturk, C. (2011) 'A Novel Clustering Approach: Artificial Bee Colony (ABC) Algorithm', *Applied Soft Computing*, 11(1), pp. 652-657.

Kassim, M.A.B.A. (2015) *Finite Element Analysis of a Geodesic Dome Structure by Using Staadpro Software*. Universiti Malaysia Pahang.

Kaveh, A. and Ghazaan, M.I. (2015) 'Optimal Design of Dome Truss Structures with Dynamic Frequency Constraints', *Structural and Multidisciplinary Optimization*, 53(3), pp. 605-621.

Kaveh, A. and Javadi, S.M. (2013) 'Shape and size optimization of trusses with multiple frequency constraints using harmony search and ray optimizer for enhancing the particle swarm optimization algorithm', *Acta Mechanica*, 225(6), pp. 1595-1605.

Kaveh, A., Kalateh-Ahani, M. and Masoudi, M.S. (2011) 'The CMA Evolution Strategy Based Size Optimization of Truss Structures', *INTERNATIONAL JOURNAL OF OPTIMIZATION IN CIVIL ENGINEERING*, 2, pp. 233-256.

Kaveh, A. and Talatahari, S. (2008) 'A Hybrid Particle Swarm and Ant Colony Optimization for Design of Truss Structures', *ASIAN JOURNAL OF CIVIL ENGINEERING (BUILDING AND HOUSING)*, 9(4), pp. 329-348.

Kaveh, A. and Talatahari, S. (2009a) 'A Particle Swarm Ant Colony Optimization for Truss Structures with Discrete Variables', *Journal of Constructional Steel Research*, 65(8-9), pp. 1558-1568.

Kaveh, A. and Talatahari, S. (2009b) 'Particle swarm optimizer, ant colony strategy and harmony search scheme hybridized for optimization of truss structures', *Computers & Structures*, 87(5-6), pp. 267-283.

Kaveh, A. and Talatahari, S. (2009c) 'Size Optimization of Space Trusses Using Big Bang–Big Crunch Algorithm', *Computers & Structures*, 87(17-18), pp. 1129-1140.

Kaveh, A. and Talatahari, S. (2010a) 'Geometry and Topology Optimization of Geodesic Domes Using Charged System Search', *Structural and Multidisciplinary Optimization*, 43(2), pp. 215-229.

Kaveh, A. and Talatahari, S. (2010b) 'Optimal Design of Schwedler and Ribbed Domes via Hybrid Big Bang–Big Crunch Algorithm', *Journal of Constructional Steel Research*, 66(3), pp. 412-419.

Kaveh, A. and Zolghadr, A. (2012) 'Truss optimization with natural frequency constraints using a hybridized CSS-BBBC algorithm with trap recognition capability', *Computers & Structures*, 102-103, pp. 14-27.

Kaveh, A. and Zolghadr, A. (2014) 'Comparison of nine meta-heuristic algorithms for optimal design of truss structures with frequency constraints', *Advances in Engineering Software*, 76, pp. 9-30.

Kennedy, J. and Eberhart, R. (1995) 'Particle Swarm Optimization', *IEEE*, 1, pp. 1942-1948.

Kim, N.-I., Park, Y.-S., Fu, C.C. and Kim, M.-Y. (2008) 'Stiffness Matrix of Thin-Walled Curved Beam for Spatially Coupled Stability Analysis', *International Journal of Mechanical Sciences*, 50(4), pp. 788-803.

Kirkpatrick, S., Gelatt, C.D. and Vecchi, M.P. (1983) 'Optimization by Simulated Annealing', *American Association for the Advancement of Science.*, 220(4598), pp. 671-680.

KLEIN, R.W. and DUBES, R.C. (1989) 'Experiments in Projection and Clustering by Simulated Annealing', *Pattern Recognition*, 22(2), pp. 213-220.

Ko$, E. (2010) *The Bees Algorithm Theory, Improvements and Applications*. University of Wales, Cardiff [Online]. Available at: https://orca.cf.ac.uk/55027/1/U585416.pdf.

Koc, E. (2010) *The Bees Algorithm Theory, Improvements and Applications*. University of Wales, Cardiff.

Kong, X., Liu, S. and Wang, Z. (2013) 'An Improved Artificial Bee Colony Algorithm and Its Application', *International Journal of Signal Processing, Image Processing and Pattern Recognition*, 6(6), pp. 259-274.

Kuan, S.Y. (2009) *Design, Construction and Operation of the Floating Roof Tank*. University of Southern Queensland.

Kulkarni, M.N.K., Patekar, M.S., Bhoskar, M.T., Kulkarni, M.O., Kakandikar, G.M. and Nandedkar, V.M. (2015) 'Particle Swarm Optimization Applications to Mechanical Engineering- A Review', *Materials Today: Proceedings*, 2(4-5), pp. 2631-2639.

Kuo, R.J. and Huang, C.C. (2009) 'Application of Particle Swarm Optimization Algorithm for Solving Bi-level Linear Programming Problem', *Computers & Mathematics with Applications*, 58(4), pp. 678-685.

Lagaros, N.D., Fragiadakis, M. and Papadrakakis, M. (2004) 'Optimum Design of Shell Structures with Stiffening Beams', *AIAA Journal*, 42(1), pp. 175-184.

Lamberti, L. (2008) 'An Efficient Simulated Annealing Algorithm for Design Optimization of Truss Structures', *Computers & Structures*, 86(19-20), pp. 1936-1953.

Lamberti, L. and Pappalettere, C. (2013) 'Truss Weight Minimization Using Hybrid Harmony Search and Big Bang–Big Crunch Algorithms', *Metaheuristic Applications in Structures and Infrastructures*, 1, pp. 207-240.

Lee, H.-A. and Park, G.-J. (2013) 'Development of an Optimization Software System for Nonlinear Dynamics Using the Equivalent Static Loads Method', *10th World Congress on Structural and Multidisciplinary Optimization*. Orlando, Florida, USA, 19-24 May 2013. Orlando, Florida, USA: May 19 -24, 2013, Orlando, Florida, USA, pp. 1-10.

Lee, H.-A. and Park, G.-J. (2015) 'Nonlinear Dynamic Response Topology Optimization Using the Equivalent Static Loads Method', *Computer Methods in Applied Mechanics and Engineering*, 283, pp. 956-970.

Lee, K.S. and Geem, Z.W. (2004) 'A New Structural Optimization Method Based on the Harmony Search Algorithm', *Computers & Structures*, 82(9-10), pp. 781-798.

Li, G., Lin, Q., Cui, L., Du, Z., Liang, Z., Chen, J., Lu, N. and Ming, Z. (2016) 'A Novel Hybrid Differential Evolution Algorithm with Modified CoDE and JADE', *Applied Soft Computing*, 47, pp. 577-599.

Li, H. and Landa-Silva, D. (2011) *Evolutionary Computation*. University of Nottingham, United Kingdom. Massachusetts Institute of Technology.

Li, H., Liu, K. and Li, X. (2010) 'A Comparative Study of Artificial Bee Colony, Bees Algorithms and Differential Evolution on Numerical Benchmark Problems', *ISICA*, 1, pp. 198-207.

Li, L.J., Huang, Z.B. and Liu, F. (2009) 'A Heuristic Particle Swarm Optimization Method for Truss Structures with Discrete Variables', *Computers & Structures*, 87(7-8), pp. 435-443.

Li, Q., Steven, G.P. and Xie, Y.M. (1999) 'On Equivalence Between Stress Criterion and Stiffness Criterion in Evolutionary Structural Optimization', *Structural optimization*, 18(1), pp. 67-73.

Li, Q., Steven, G.P. and Xie, Y.M. (2000) 'Evolutionary Structural Optimization for Stress Minimization Problems by Discrete Thickness Design', *Computers and Structures*, 78(1), pp. 769-780.

Liang, J.J., Qin, A.K., Suganthan, P.N. and Baskar, S. (2006) 'Comprehensive Learning Particle Swarm Optimizer for Global Optimization of Multimodal Functions', *IEEE Transactions on Evolutionary Computation*, 10(3), pp. 281-295.

Liang, Q.Q. and Steven, G.P. (2002) 'A Performance-Based Optimization Method for Topology Design of Continuum Structures with Mean Compliance Constraints', *Computational Methods in Applied Mechanics and Engineering*, 191, pp. 1471-1489.

Liang, Q.Q., Xie, Y.M. and Steven, G.P. (2001) 'A Performance Index for Topology and Shape Optimization of Plate Bending Problems with Displacement Constraints', *Structural and Multidisciplinary Optimization*, 21(5), pp. 393-399.

Lieu, Q.X., Do, D.T.T. and Lee, J. (2018) 'An Adaptive Hybrid Evolutionary Firefly Algorithm for Shape and Size Optimization of Truss Structures with Frequency Constraints', *Computers & Structures*, 195(1), pp. 99-112.

Mahfoud, S.W. and Goldberg, D.E. (1995) 'Parallel Recombinative Simulated Annealing: A Genetic Algorithm', *Parallel Computing*, 21, pp. 1-28.

Mallipeddi, R., Suganthan, P.N., Pan, Q.K. and Tasgetiren, M.F. (2011) 'Differential Evolution Algorithm with Ensemble of Parameters and Mutation Strategies', *Applied Soft Computing*, 11(2), pp. 1679-1696.

Maraveas, C., Balokas, G.A. and Tsavdaridis, K.D. (2015) 'Numerical Evaluation on Shell Buckling of Empty Thin-Walled Steel Tanks under Wind Load According to Current American and European Design Codes', *Thin-Walled Structures*, 95, pp. 152-160.

Mezura-Montes, E., Miranda-Varela, M.E. and Gómez-Ramón, R.d.C. (2010) 'Differential Evolution in Constrained Numerical Optimization: An Empirical Study', *Information Sciences*, 180(22), pp. 4223-4262.

Miguel, L.F.F., Lopez, R.H. and Miguel, L.F.F. (2013) 'Multimodal size, shape, and topology optimisation of truss structures using the Firefly algorithm', *Advances in Engineering Software*, 56, pp. 23-37.

Mohamed, A.W. and Sabry, H.Z. (2012) 'Constrained Optimization Based on Modified Differential Evolution Algorithm', *Information Sciences*, 194, pp. 171-208.

Mortazavi, A. and Toğan, V. (2016) 'Simultaneous size, shape, and topology optimization of truss structures using integrated particle swarm optimizer', *Structural and Multidisciplinary Optimization*, 54(4), pp. 715-736.

Mortazavi, A. and Toğan, V. (2017) 'Sizing and layout design of truss structures under dynamic and static constraints with an integrated particle swarm optimization algorithm', *Applied Soft Computing*, 51, pp. 239-252.

Moslemi, M. and Kianoush, M.R. (2012) 'Parametric Study on Dynamic Behavior of Cylindrical Ground-Supported Tanks', *Engineering Structures*, 42, pp. 214-230.

Nha, C.D., Xie, Y.M. and Steven, G.P. (1998) 'An Evolutionary Structural Optimization Method for Sizing Problems with Discrete Design Variables', *Computers & Structures*, 68(4), pp. 419-431.

Nha Chu, D., Xie, Y.M., Hira, A. and Steven, G.P. (1997) 'On Various Aspects of Evolutionary Structural Optimization for Problems with Stiffness Constraints', *Finite Elements in Analysis and Design*, 24(4), pp. 197-212.

Özkal, F.M. and Uysal, H. (2009) 'General Aspects of Evolutionary Structural Optimization: A Review', *Pamukkale University Journal of Engineering Sciences*, 15(3), pp. 383-393.

Ozkis, A. and Babalik, A. (2013) 'Accelerated ABC (A-ABC) Algorithm for Continuous Optimization Problems', *Lecture Notes on Software Engineering*, 1(3), pp. 262-266.

Özkis, A. and Babalik, A. (2013) *International Conference on Systems, Control and Informatics*. Konya, Turkey. Selcuk University.

Pan, Q.-K., Suganthan, P.N., Wang, L., Gao, L. and Mallipeddi, R. (2011) 'A Differential Evolution Algorithm with Self-adapting Strategy and Control Parameters', *Computers & Operations Research*, 38(1), pp. 394-408.

PARK, G.J. and KANG, B.S. (2003) 'Validation of a Structural Optimization Algorithm Transforming Dynamic Loads into Equivalent Static Loads', *JOURNAL OF OPTIMIZATION THEORY AND APPLICATIONS*, 118(1), pp. 191-200.

Patel, V., Tiwari, A. and Patel, A. (2016) *ICIA-16*. Pondicherry, India, August, 25-26, 2016. Association for Computing Machinery (ACM).

Pedersen, N.L. (2000) 'Maximization of Eigenvalues Using Topology Optimization', *Structural and Multidisciplinary Optimization*, 20(1), pp. 2-11.

Pham, D.T., Ghanbarzadeh, A., Koc, E., Otri, S., Rahim, S. and Zaidi, M. (2005) 'Bee Algorithm A Novel Approach to Function Optimisation', *The Manufacturing Engineering Centre*, 1, pp. 1-40.

Pham, D.T., Ghanbarzadeh, A., Koç, E., Otri, S., Rahim, S. and Zaidi, M. (2007) 'The Bees Algorithm – A Novel Tool for Complex Optimisation Problems', *Manufacturing Engineering Centre*, pp. 1-6.

Pholdee, N. and Bureerat, S. (2014) 'Comparative Performance of Meta-heuristic Algorithms for Mass Minimisation of Trusses with Dynamic Constraints', *Advances in Engineering Software*, 75, pp. 1-13.

Piotrowski, A.P. (2017) 'Review of Differential Evolution Population Size', *Swarm and Evolutionary Computation*, 32, pp. 1-24.

Portela, G. and Godoy, L.A. (2005) 'Wind Pressures and Buckling of Cylindrical Steel Tanks with a Dome Roof', *Journal of Constructional Steel Research*, 61(6), pp. 808-824.

Price, K.V. (1996) 'Differential Evolution: A Fast and Simple Numerical Optimizer', *IEEE*, 1, pp. 524-527.

Purdy, D., Maher, P. and Frederick, D. (1967) 'Model Studies of Wind Loads on Flat-Top Cylinders', *Journal of the Structural Division, ASCE*, 93(1), pp. 379-395.

Querin, O.M., Young, V., Steven, G.P. and Xie, Y.M. (2000) 'Computational Efficiency and Validation of Bi-directional Evolutionary Structural Optimization', *Computational Methods in Applied Mechanics and Engineering*, 189(1), pp. 559-573.

Rajasekhar, A., Lynn, N., Das, S. and Suganthan, P.N. (2017) 'Computing with the Collective Intelligence of Honey Bees – A Survey', *Swarm and Evolutionary Computation*, 32, pp. 25-48.

Rini, D.P., Shamsuddin, S.M. and Yuhaniz, S.S. (2011) 'Particle Swarm Optimization: Technique, System and Challenges', *International Journal of Computer Applications*, 14(1), pp. 19-27.

Ronkkonen, J. and Lampinen, J. (2007) *Genetic and Evolutionary Computation Conference Companion-07*. London, England, United Kingdom, July, 7-11, 2007. Association for Computing Machinery (ACM).

Rutenbar, R.A. (1989) 'Simulated Annealing Algorithms: An Overview', *IEEE*, 1, pp. 19-26.

Saka, M.P. (2007a) 'Optimum Geometry Design of Geodesic Domes Using harmony Search Algorithm', *Advances in Structural Engineering*, 10(6), pp. 595-606.

Saka, M.P. (2007b) 'Optimum Topological Design of Geometrically Nonlinear Single Layer Latticed Domes Using Coupled Genetic Algorithm', *Computers & Structures*, 85(21-22), pp. 1635-1646.

Saka, M.P. and Geem, Z.W. (2013) 'Mathematical and Metaheuristic Applications in Design Optimization of Steel Frame Structures: An Extensive Review', *Mathematical Problems in Engineering*, 2013, pp. 1-33.

Saka, M.P., Hasançebi, O. and Geem, Z.W. (2016) 'Metaheuristics in structural optimization and discussions on harmony search algorithm', *Swarm and Evolutionary Computation*, 28, pp. 88-97.

Salam, S.A., EL-shihy, A., Eraky, A. and Salah, M. (2015) 'Optimum Design of Trussed Dome Structures', *International Journal of Engineering and Innovative Technology (IJEIT)*, 4(8), pp. 124-130.

Sarac, Y. (2005) *Optimum Design of Pin-Jointed 3-D Dome Structures Using Global Optimization Techniques*. Middle East Technical University.

Savsani, V.J., Tejani, G.G., Patel, V.K. and Savsani, P. (2017) 'Modified Meta-heuristics Using Random Mutation for Truss Topology Optimization with Static and Dynamic Constraints', *Journal of Computational Design and Engineering*, 4(2), pp. 106-130.

Seifi, H., Xie, Y.M., O'Donnell, J. and Williams, N. (2016) 'Design and Fabrication of Structural Connections Using Bi-Directional Evolutionary Structural Optimization and Additive Manufacturing', *Applied Mechanics and Materials*, 846(1), pp. 571-576.

Sevim, O., Sonmez, M. and Toprak, B. (2016) 'Optimum Design of Truss Structure Using Artificial Bee Colony Algorithm', *International Journal of Soft Computing and Artificial Intelligence*, 4(1).

Shirkhanghah, B., Darabadi-Zare, A., Eimani-Kalesar, H. and Pahlevan, B. (2012) 'Investigation into behavior of Suspen-Domes in Comparison with Single-Layer Domes', *International Journal of Civil, Environmental, Structural, Construction and Architectural Engineering*, 6(9), pp. 745-752.

Silva, R.C.P., Lopes, R.A. and Guimarães, F.G. (2011) *Genetic and Evolutionary Computation Conference Companion-11*. Dublin, Ireland, July, 12–16, 2011. Association for Computing Machinery (ACM).

Sonmez, M. (2010) 'Discrete optimum design of truss structures using artificial bee colony algorithm', *Structural and Multidisciplinary Optimization*, 43(1), pp. 85-97.

Sonmez, M. (2011) 'Artificial Bee Colony algorithm for optimization of truss structures', *Applied Soft Computing*, 11(2), pp. 2406-2418.

Sosa, E.M. and Godoy, L.A. (2010) 'Challenges in the Computation of Lower-Bound Buckling Loads for Tanks under Wind Pressures', *Thin-Walled Structures*, 48(12), pp. 935-945.

Steven, G.P., Li, Q. and Xie, Y.M. (2002) 'Multicriteria Optimization that Minimizes Maximum Stress and Maximizes Stiffness', *Computers & Structures*, 80(27-30), pp. 2433-2448.

Storn, R. and Price, K. (1995) *Differential Evolution: A Simple and Efficient Adaptive Scheme for Global Optimization Over Continuous Spaces*.

Storn, R. and Price, K. (1997) 'Differential Evolution – A Simple and Efficient Heuristic for Global Optimization over Continuous Spaces', *Journal of Global Optimization*, 11, pp. 341–359.

Suganthan, P.N., Hansen, N., Liang, J.J., Deb, K., Chen, Y.-P., Auger, A. and Tiwari, S. (2005) *Problem Definitions and Evaluation Criteria for the CEC 2005 Special Session on Real-Parameter Optimization*. Nanyang Technological University, Singapore: IIT Kanpur Computing, N.

Sui, Y. and Yi, G. (2013) *10th World Congress on Structural and Multidisciplinary Optimization*. Orlando, Florida, USA, May 19-24, 2013. Orlando, Florida, USA: National Natural Science Foundation of China.

Talatahari, S., Gandomi, A.H. and Yun, G.J. (2014) 'Optimum design of tower structures using Firefly Algorithm', *The Structural Design of Tall and Special Buildings*, 23(5), pp. 350-361.

Talbi, E.-G. (2009) *Metaheuristics: From Design to Implementation*. Hoboken, New Jersey: JohnWiley & Sons, Inc.

Talukder, S. (2010) *Mathematical Modelling and Applications of Particle Swarm Optimization*. Blekinge Institute of Technology.

Tanskanen, P. (2002) 'The Evolutionary Structural Optimization Method: Theoretical Aspects', *Computer Methods in Applied Mechanics and Engineering*, 191(47–48), pp. 5485-5498.

Tejani, G.G., Savsani, V.J., Patel, V.K. and Savsani, P.V. (2018) 'Size, shape, and topology optimization of planar and space trusses using mutation-based improved metaheuristics', *Journal of Computational Design and Engineering*, 5(2), pp. 198-214.

Trivedi, A., Srinivasan, D., Biswas, S. and Reindl, T. (2016) 'A Genetic Algorithm – Differential Evolution Based Hybrid Framework: Case Study on Unit Commitment Scheduling Problem', *Information Sciences*, 354, pp. 275-300.

Tsai, H.-C. (2014) 'Novel Bees Algorithm: Stochastic Self-adaptive Neighborhood', *Applied Mathematics and Computation*, 247, pp. 1161-1172.

Uematsu, Y., Yasunaga, J. and Koo, C. (2015) 'Design Wind Loads for Open-Topped Storage Tanks in Various Arrangements', *Journal of Wind Engineering and Industrial Aerodynamics*, 138, pp. 77-86.

Vanneschi, L., Codecasa, D. and Mauri, G. (2010) *Genetic and Evolutionary Computation Conference Companion-10*. Portland, Oregon, USA, July, 7–11, 2010. Association for Computing Machinery (ACM).

Varma, A. (2015) 'Compression Member Design', in *Design of Steel Structures*. Michigan: Michigan State University.

Wetter, M. and Wright, J. (2004) 'A Comparison of Deterministic and Probabilistic Optimization Algorithms for Nonsmooth Simulation-based Optimization', *Building and Environment*, 39(8), pp. 989-999.

Wu, Y., Li, Q., Hu, Q. and Borgart, A. (2017) 'Size and Topology Optimization for Trusses with Discrete Design Variables by Improved Firefly Algorithm', *Mathematical Problems in Engineering*, 2017, pp. 1-12.

Xiang, W.-l. and An, M.-q. (2013) 'An Efficient and Robust Artificial Bee Colony Algorithm for Numerical Optimization', *Computers & Operations Research*, 40(5), pp. 1256-1265.

Xie, Y.M. and Steven, G.P. (1993) 'A Simple Evolutionary Procedure for Structural Optimization', *Computers & Structures*, 49(5), pp. 885-896.

Xie, Y.M. and Steven, G.P. (1994) 'Optimal Design of Multiple Load Case Structures Using an Evolutionary Procedure', *Engineering Computations*, 11(1), pp. 295-302.

Xie, Y.M. and Steven, G.P. (1996) 'Evolutionary Structural Optimization for Dynamic Problems', *Computers & Strucutures*, 58(6), pp. 1067-1073.

Xu, Y., Fan, P. and Yuan, L. (2013) 'A Simple and Efficient Artificial Bee Colony Algorithm', *Mathematical Problems in Engineering*, 2013, pp. 1-9.

Yang, M., Cai, Z. and Li, C. (2013) *Genetic and Evolutionary Computation Conference Companion-13*. Amsterdam, The Netherlands, July, 6–10, 2013. Association for Computing Machinery (ACM).

Yang, M.X. (1999) *Bi-directional Evolutionary Method for Stiffness and Displacement Optimization*. Victoria University of Technology.

Yang, S., Jiang, S. and Jiang, Y. (2016) 'Improving the Multiobjective Evolutionary Algorithm Based on Decomposition with New Penalty Schemes', *Soft Computing*, pp. 1-15.

Yi, W., Zhou, Y., Gao, L., Li, X. and Mou, J. (2016) 'An Improved Adaptive Differential Evolution Algorithm for Continuous Optimization', *Expert Systems with Applications*, 44, pp. 1-12.

Yu, W.-j. and Zhang, J. (2012) *Genetic and Evolutionary Computation Conference Companion-12*. Philadelphia, Pennsylvania, USA, July, 7–11, 2012. Association for Computing Machinery (ACM).

Yu, W.-j., Zhang, J. and Chen, W.-n. (2013) *Genetic and Evolutionary Computation Conference Companion*. Amsterdam, The Netherlands, July, 6–10, 2013. Association for Computing Machinery (ACM).

Zaharie, D. (2005) 'Extensions of Differential Evolution Algorithms for Multimodal Optimization', *West University of Timisoara*, pp. 1-12.

Zamanzadeh, Z., Abdolpour, H. and Behravesh, A. (2010) 'Investigating the Buckling Behaviour of Single Layer Dome Form of Space Structures', *Challenges, Opportunities and Solutions in Structural Engineering and Construction*, 1(1), pp. 399-403.

Zavala, A.E.M.n., Aguirre, A.H.a. and Diharce, E.R.V. (2005) *Genetic and Evolutionary Computation Conference Companion-05*. Washington, DC, USA, June, 25–29, 2005. Association for Computing Machinery (ACM).

Zhao, C., Steven, G.P. and Xie, Y.M. (1996) 'Evolutionary Natural Frequency Optimization of Thin Plate Bending Vibration Problems', *Structural Optimization*, 11(3-4), pp. 244-251.

Zhao, Y. and Lin, Y. (2014) 'Buckling of Cylindrical Open-Topped Steel Tanks under Wind Load', *Thin-Walled Structures*, 79, pp. 83-94.

Zhou, M. and Haftka, R.T. (1995) 'A Comparison of Optimality Criteria Methods for Stress and Displacement Constraints', *Computational Methods in Applied Mechanics and Engineering*, 124(1), pp. 253-271.

Zou, D., Liu, H., Gao, L. and Li, S. (2011a) 'A Novel Modified Differential Evolution Algorithm for Constrained Optimization Problems', *Computers & Mathematics with Applications*, 61(6), pp. 1608-1623.

Zou, W., Zhu, Y., Chen, H. and Shen, H. (2011b) *Genetic and Evolutionary Computation Conference Companion-11*. Dublin, Ireland, July, 12–16, 2011. Association for Computing Machinery (ACM).